Volume 67 • Number 3 • June 2019

Acta Geophysica

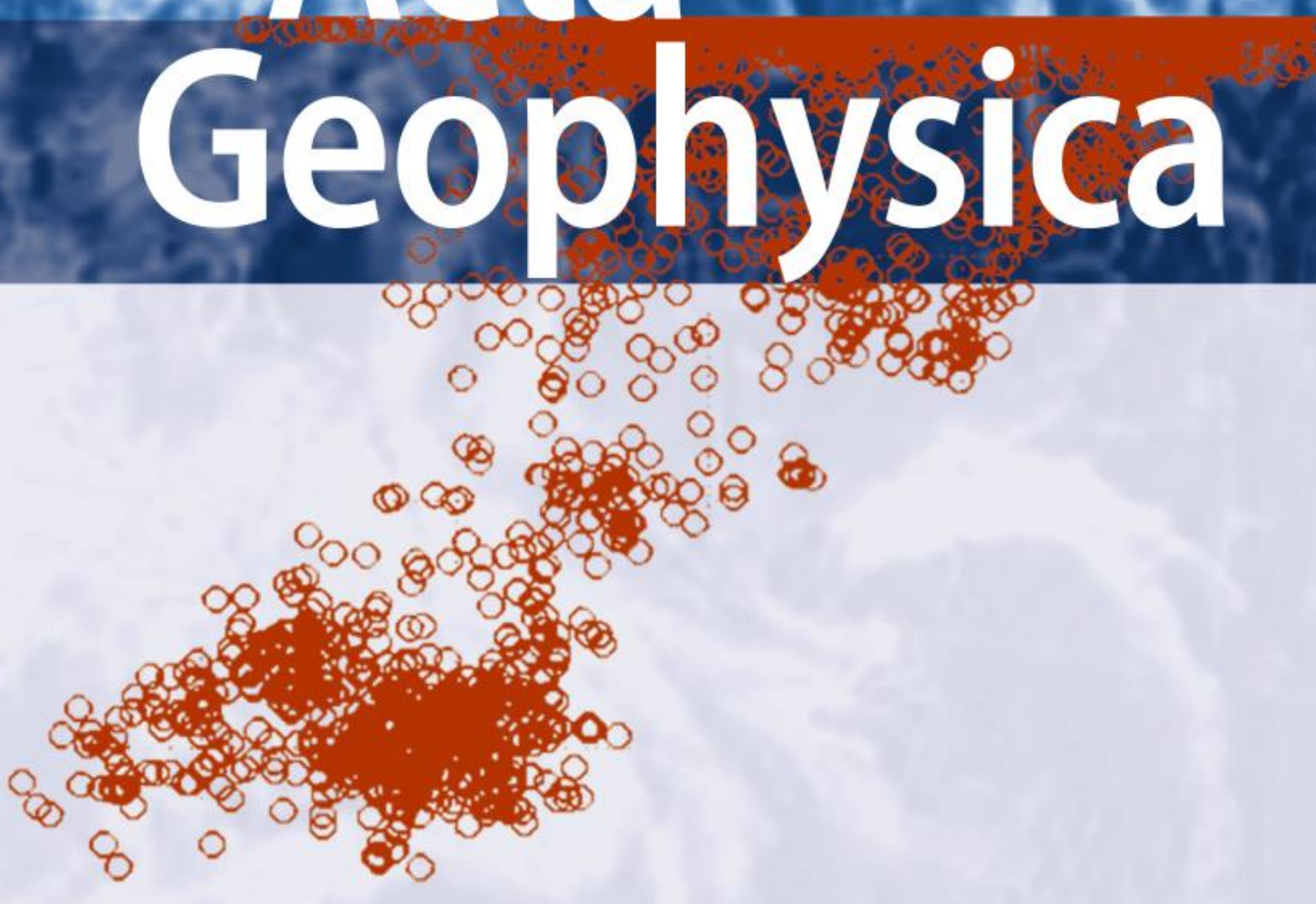

PAN
POLISH ACADEMY OF SCIENCES

Institute of Geophysics
Polish Academy of Sciences

Springer

Acta Geophysica (2019) 67:739–752
https://doi.org/10.1007/s11600-019-00284-4

REVIEW ARTICLE - SOLID EARTH SCIENCES

Modeling the earthquake occurrence with time-dependent processes: a brief review

Ourania Mangira[1] · **Christos Kourouklas**[1] · **Dimitris Chorozoglou**[1] · **Aggelos Iliopoulos**[1] · **Eleftheria Papadimitriou**[1]

Received: 5 January 2019 / Accepted: 30 March 2019 / Published online: 10 April 2019

Abstract

The complexity of seismogenesis tantalizes the scientific community for understanding the earthquake process and its underlying mechanisms and consequently, precise earthquake forecasting, although a realistic target, is yet far from being a practice. Therefore, seismic hazard assessment studies are focused on estimating the probabilities of earthquake occurrence. For a more precise representation of seismicity-regarding time, space and magnitude stochastic modeling is engaged. The candidate models deal with either a single fault or fault segment, or a broader area, leading to fault-based or seismicity-based models, respectively. One important factor in stochastic model development is the time scale, depending upon the target earthquakes. In the case of strong earthquakes, the interevent times between successive events are relatively large, whereas, if we are interested in triggering and the probability of an event to occur in a small time increment then a family of short-term models is available. The basic time-dependent models that can be applied toward earthquake forecasting are briefly described in this review paper.

Keywords Time-dependent seismicity models · Stochastic · Long- and short-term · Earthquakes forecasting

Introduction

Estimating the occurrence time of future earthquakes, in a given area, is an indispensable component in seismic hazard assessment studies. It can be made possible through the analysis of the temporal seismicity properties, and consequently the development of models that can imitate the earthquakes temporal behavior. The application of stochastic rather than deterministic models is affected by the limited number of the available data (instrumental records and historical seismic catalogs) as well as the fact that seismogenesis is a self-organized system, related with many complex phenomena (e.g., fault heterogeneity). While a deterministic model aims at fully describing the phenomenon and making exact predictions, a stochastic model introduces a certain level of randomness into the physical process under study, resulting in a forecast of future events. Regarding this distinction, earthquake forecasts based on stochastic models are given in terms of occurrence probabilities. Stochastic models may be based on the memoryless Poisson process or on other processes containing memory, such as short- and long-term cluster behavior (Kagan and Jackson 1991) or quasi-periodic occurrence (Papazachos et al. 1997a). Given that earthquakes are clustered in time, some kind of memory is implied and thus, the most appropriate models are the time-dependent ones.

Two different main approaches prevail when developing and applying time-dependent stochastic models. In the "fault based" approximation the studies deal with the interevent times between successive strong earthquakes occurring on an individual fault or fault segment above a certain magnitude threshold. The target of these models is the estimation of the long-term recurrence of strong events in a given area where faults are well known. As already mentioned, earthquake occurrence is a complex physical process including

✉ Ourania Mangira
omangira@geo.auth.gr

Christos Kourouklas
ckouroukl@geo.auth.gr

Dimitris Chorozoglou
chorozod@geo.auth.gr

Aggelos Iliopoulos
ailiopou@gmail.com

Eleftheria Papadimitriou
ritsa@geo.auth.gr

[1] Geophysics Department, Aristotle University of Thessaloniki, GR54124 Thessaloniki, Greece

fault heterogeneity and interaction between nearby faults leading to a collective behavior, which can potentially cause triggering of adjacent fault segments in short-term time scales. These physical processes can be modeled through the second family of stochastic approaches, the so-called seismicity based ones, which assume that the future earthquakes are characterized by the temporal properties of the past events within a specific region due to all possible seismic sources, not only the large and well known but also the smaller ones (Frankel 1995).

Fault-based models

The construction of a fault-based model

The available data (geological and geodetic) along with the longest possible record of past ruptures (historical and instrumental) of the fault segments under study are required for the development of a fault-based model. Using this information, the model can then be built with the combination of the assumptions of the time-predictable model (Shimazaki and Nakata 1980) and the characteristic earthquake hypothesis (Schwartz and Coppersmith 1984). The time-predictable model assumes that the occurrence of an earthquake is observed when stress surpasses a given constant threshold. Thus, the estimation of the next event is achieved considering the coseismic slip of the previous earthquake (Fig. 1). According to the characteristic earthquake hypothesis, strong earthquakes on a fault occur regularly and they are characterized by similar physical mechanisms. Thus, a future strong earthquake occurs as the result of the long-term tectonic loading on a given segment.

Consequently, the final output of such a model will be single or multi-segment long-term Earthquake Rupture Forecasts (ERF) in a specific time window. The distribution of the recurrence time of strong earthquakes constrained with the occurrence time of the last strong earthquake on a certain fault segment is given by the formula:

$$P(T \leq t \leq T + \Delta T | t > T) = \frac{\int_{T}^{T+\Delta T} f(t)\mathrm{d}t}{\int_{T}^{\infty} f(t)\mathrm{d}t}$$

where t stands for the time relative to the previous earthquake under the condition that T years passed since the last event, ΔT stands for the duration of the forecast and $f(t)$ stands for the probability density function of the recurrence time (Field 2015).

The problem of the distribution fitting

The major task for these renewal models is the selection of the appropriate distribution that the recurrence time follows. Among the most common distributions used for this purpose, the Weibull, the Lognormal and the Brownian passage time (BPT) distributions dominate (Convertito and Faenza 2014). The Weibull distribution probability density function (pdf) is given by

$$f(t|a,b) = \frac{b}{a}\left(\frac{t}{a}\right)^{(b-1)} \exp\left\{-\left(\frac{t}{a}\right)^{b}\right\}$$

where α and b stand for the scale and the shape parameter, respectively. An interesting feature of this distribution, which is connected with the seismicity, is the value of the shape parameter, b. If the parameter b is equal to 1 ($b = 1$) then the distribution is reduced into the exponential one. If b is less than 1 ($b < 1$), then the model can be considered as a short-term clustering one, while if b is greater than 1 ($b > 1$), then the model can be characterized as quasi-periodic, which is the case in the fault-based models.

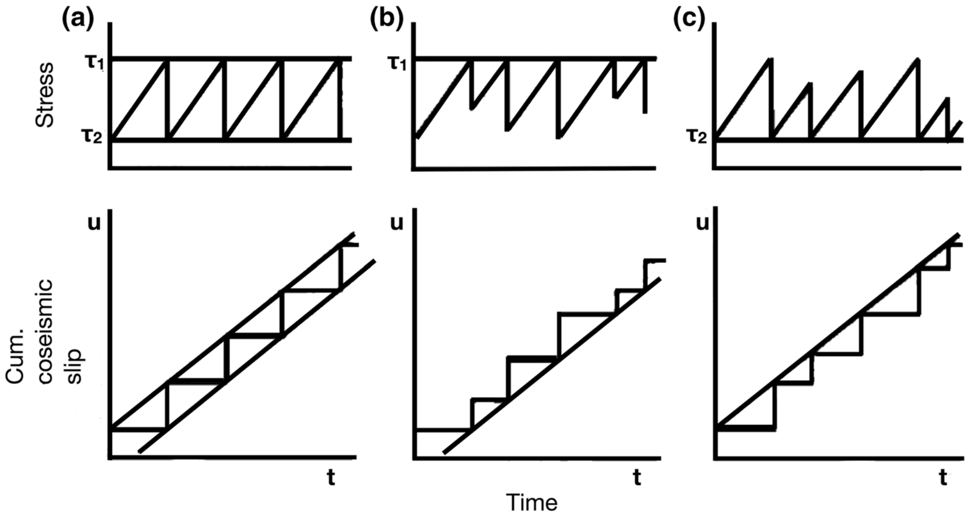

Fig. 1 Representation of the evolution of stress (upper panel) and corresponding slip (lower panel) with time on a certain fault, considering characteristic (**a**), time-predictable (**b**) and slip-predictable (**c**) earthquake occurrence models. (modified from Shimazaki and Nakata 1980)

The lognormal distribution pdf is formulated by the equation

$$f(t|\mu,\sigma)=\frac{1}{\sqrt{2\pi}\sigma t}\exp\left\{-\frac{(lnt-\mu)^2}{2\sigma^2}\right\}$$

where μ is the mean and σ is the standard deviation of the natural logarithm of the data sample, such as the recurrence intervals between strong earthquakes. Lognormal distribution is one of the so-called heavy tail distributions, which return high values of probability for variables that have larger return periods than the average one.

Kagan and Knopoff (1987) tried to describe the earthquake occurrence by modeling the evolution of stress as a random walk, or in other words as a Brownian motion, incorporating the inverse Gaussian distribution. The pdf of the inverse Gaussian distribution is given by

$$f(t|\mu,\lambda)=\sqrt{\frac{\mu}{2\pi t^3}}\exp\left\{\frac{-\lambda(t-\mu)^2}{2\mu^2 t}\right\}$$

where μ and λ are the mean value of the data sample and the shape parameter. Ellsworth et al. (1999) and later Matthews et al. (2002) extended the aforementioned idea and proposed a renewal model based on an experimental one introducing the Brownian Relaxation Oscillator (BRO). This model assumes that the earthquake occurrence is driven by the equation

$$X(t)=\lambda t+\sigma W(t)$$

where $X(t)$ is the stress level, λ is the constant loading rate and $\sigma W(t)$ is a random factor following the properties of the Brownian motion in which σ is a nonnegative scale parameter and *W(t)* is the standard Brownian motion. The resulting recurrence properties of the model (the recurrences of strong earthquakes) are described by the Brownian passage time (BPT) distribution, which is an alternative form of the inverse Gaussian one given from the relation

$$f(t|\mu,\alpha)=\sqrt{\frac{\mu}{2\pi\alpha^2 t^3}}\exp\left\{\frac{-(t-\mu)^2}{2\mu\alpha^2 t}\right\}$$

where μ is the mean value of the data sample and α is the model's aperiodicity, which must take values greater than 0 ($0<\alpha<\infty$). Aperiodicity can be considered as the analogous of the coefficient of variation of the Gaussian distribution, and it represents the model level of randomness. As α tends to 0, the model becomes increasingly periodic. As α tends to ∞ the model becomes increasingly aperiodic. All the intermediate cases represent quasi-periodic models with a certain level of randomness. In most strong earthquakes recurrence studies, the value of a ranges between 0.3 and 0.7 ($0.3\le a\le 0.7$) (e.g., Field et al. 2015).

Zoller et al. (2008) introduced an alternative expression of the BPT distribution, where the contribution of small and intermediate earthquakes on the state changes before strong earthquake occurrence is taken into account. Following this approach, we assume that the on-fault seismicity provokes delay of the next large events by unloading the fault, while the off-fault seismicity loads the fault. If these effects are considered approximately equivalent, then the aperiodicity is related to the b-value of the instrumental catalog of the corresponding fault according to the following relation

$$\alpha=\sqrt{\frac{b}{3-b}}$$

where b must be ranging between $0<b<3$. Then, the BPT pdf can be written as

$$f(t|\mu,b)=\sqrt{\frac{\mu(3-b)}{2\pi t^3 b}}\exp\left\{\frac{-(t-\mu)^2(3-b)}{2tb\mu}\right\}$$

BPT model has become the most popular one over the years in studies dealing with the recurrence times of strong earthquakes. This is due to the fact that the temporal behavior of strong earthquakes is fairly explained through its hazard function (Fig. 2). The values of the hazard function, i.e., the hazard rate, which is equivalent to the conditional probability, are very low immediately after the occurrence of an event and then they exhibit an increasing trend with time. The maximum value is obtained at some finite time near the mean recurrence time. Then, the hazard rate decreases asymptotically to $1/\left(2\mu\alpha^2\right)$. In contrast, the Weibull hazard function increases monotonically with time after a strong event (e.g., the blue line of Fig. 2 right panel) and the lognormal hazard function increases to a maximum and then decreases asymptotically to zero.

An alternative distribution has been proposed by Polidoro et al. (2013), the Erlang distribution, which is a Gamma distribution with pdf

$$f(t|k,\lambda)=\frac{\lambda(\lambda t)^{k-1}}{\Gamma(k)}\exp\{-\lambda t\},$$

where k is the shape parameter, λ is the scale parameter and Γ is the gamma function. Regarding the probabilistic seismic hazard analysis, the aforementioned distribution suggests that in a small time interval the occurrence of more than one earthquake is unlikely. The inverse Gamma distribution is also proposed by Polidoro et al. (2013), assuming that the load on the fault increases linearly over time, with a rate that varies randomly from event to event. The pdf is given by the following relation

$$f(t|\gamma,\beta)=\frac{\beta^\gamma}{\Gamma(\gamma)}\left(\frac{1}{t}\right)^{\gamma+1}\exp\left\{-\frac{\beta}{t}\right\},$$

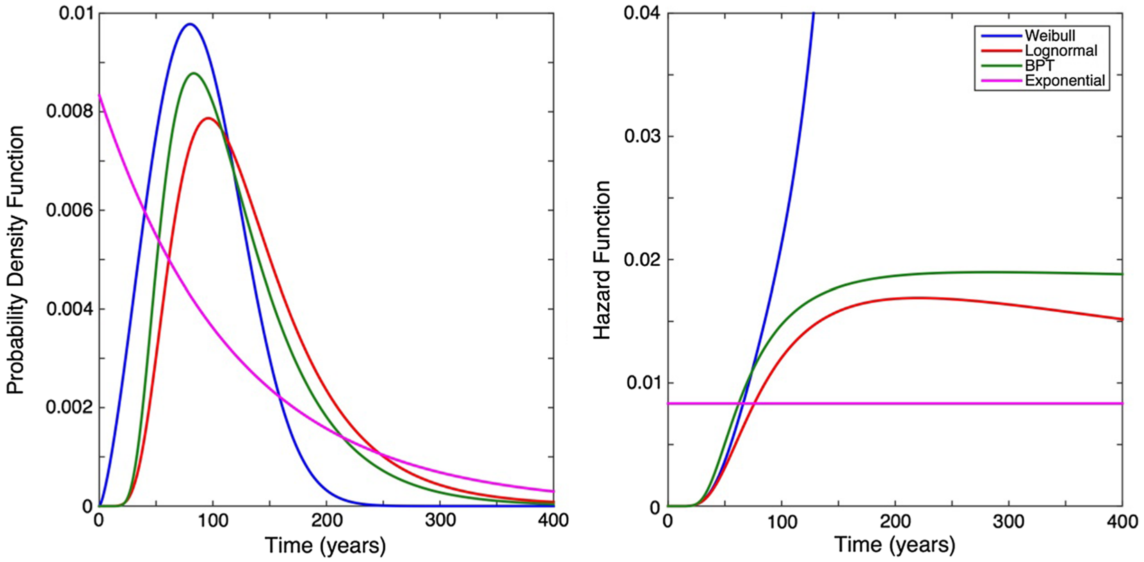

Fig. 2 Example of probability density functions (left) and their corresponding hazard functions (right) of the main renewal models (Weibull, Lognormal and BPT) against the memoryless one

where γ and β the shape and scale parameters, respectively. Over the years, recurrence models were refined more and more, aiming at improving their predictive power and increasing the accuracy of their estimations for seismic hazard, incorporating processes like the permanent and temporal stress perturbations in combination with a particular pdf of recurrence time (Stein et al. 1997; Hardebeck 2004; Gomberg et al. 2005).

Applications

One of the first relevant applications was performed by Hagiwara (1974), who used the Weibull distribution assuming that the crust is strained under a constant speed. Earthquakes with $M \geq 6.0$ along South Kanto District in Japan were considered and it was found that the maximum value of the conditional probability of a future event is expected in 84 years after the last earthquake. Rikitake (1974, 1976) used the same distribution to estimate the probabilities of strong future events ($M \geq 8.0$) along the subduction zones of Japan, Kurile, Aleutian Islands, Kamchatka, and Americas (North, Central and South) considering that the ultimate crustal stain increases linearly with time and that immediately after a strong event is nearly zero. He evidenced the long-term time dependence (e.g., for the Kanto area in Japan, where the last strong event occurred in 1925 with $M = 7.9$ the probability values were found equal to 0.2, 0.5 and 0.8 for the next 55, 105 and 155 years, respectively). More recently, Abaimov et al. (2008) also applied the Weibull distribution on characteristic events of Parkfield and Wrightwood fault segments of San Andreas fault zone. Their best fitting models resulted in quite similar mean and standard deviation values to the observed ones, suggesting Weibull as the most suitable distribution for such studies.

Nishenko and Bulland (1987), attempting a time-dependent probabilistic approach to describe earthquake occurrence and its corresponding seismic hazard, proposed a generic recurrence time model adopting the Lognormal distribution. They concluded that the Lognormal distribution exhibits a significant better fit than the Weibull using recurrence times of earthquakes with *Mo* between 10^{17} and 10^{23} Nm, occurred in the major fault segments of Mexico, Chile, California, Japan and Alaska through a normalized function. Following their suggestion, Jackson et al. (1995) summarized the results of the Working Group on California Earthquake Probabilities (WGCEP), adopting the Lognormal as the optimal statistical model. Their model estimates a probability equal to 80%–90% for an $M \geq 7.0$ expected earthquake in California before 2024. The Lognormal distribution was also used by Paradisopoulou et al. (2010) in fault segments across Western Turkey, incorporating the static stress changes into the probability estimates.

Ogata (2002) used the BPT distribution constructing a slip-size dependent renewal model, incorporating the knowledge of the slip associated with strong earthquake ruptures. The application of the model was performed on the large historical earthquakes along Nankai Trough ($M \approx 8.0$) and Off Toyooka fault ($6.0 \leq M \leq 7.0$) in Japan. He found that the single BPT model for the Nankai Trough returned a likely occurrence time around 2070, but with large uncertainty (> 100 years). When the slip-size dependent model was used considering the last three events of this catalog, then the estimated hazard function assumes that the next earthquake's occurrence is expected around 2040. The model was also used for the second data set exhibiting that the next occurrence time in this case is decreasing. Parsons (2004) applied the BPT model for the estimation of $M \geq 7.0$ earthquakes occurrence probabilities on single fault segments beneath the Sea of Marmara, after taking into account the coseismic and postseismic stress transfer in the calculations. The same author (Parsons 2008) modeled the recurrence times of characteristic earthquakes on Hayward fault segment in California with the use of the BPT model and concluded in the superiority of this renewal model in respect to the memoryless one. Console et al. (2008) studied the effect of such stress interactions between nearby faults of Central and South Apennines region in Italy also using the BPT model, concluding that this effect was relatively small. Parsons et al. (2012) and Murru et al. (2016) took into account the effect of static stress transfer from previous earthquakes to the next ones in Nankai Trough in Japan and Sea of Marmara in Turkey fault systems, respectively, using the BPT distribution on their recurrence modeling.

Focusing on similar applications in Greece, Console et al. (2013) applied two renewal models, the BPT and the Weibull, against the memoryless Poisson one, in each one of the eight fault segments consisting the Corinth Gulf fault system, after taking into account the effect of stress transfer in their calculations of conditional occurrence probability values (Fig. 3). The North Aegean Trough (NAT) fault system was also studied under the BPT renewal model, considering a new segmentation model and two different assumptions of strong earthquakes magnitude completeness (Kourouklas et al. 2018).

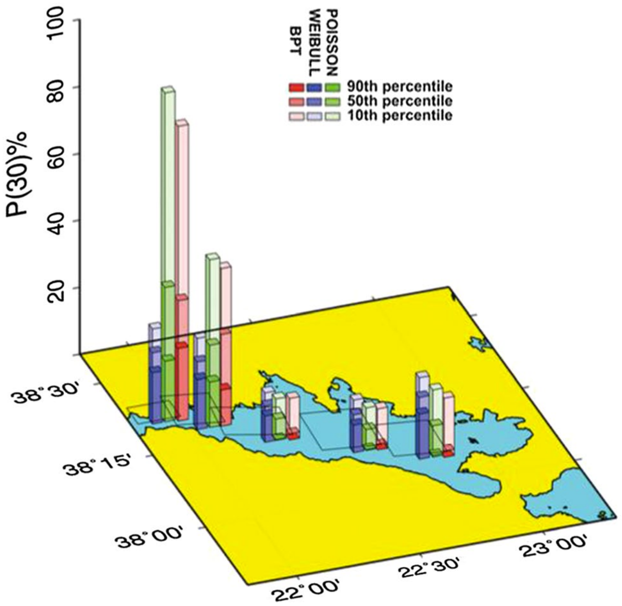

Fig. 3 Thirty years conditional occurrence probabilities along Corinth Gulf fault system according to Poisson, BPT and Weibull models. (From Console et al. 2013)

Polidoro et al. (2013) applied many different distributions, among them the BPT, the inverse Gaussian and the Erlang distribution, in the Paganica fault (Central Italy). They found that when the time elapsed since the last earthquake is about half of the return period of the event, then all models exhibit similar results. This means that the longer is the time since the last event, the more critical is selecting the appropriate model. For example, a decreasing occurrence probability implied by some distributions is not representative of seismogenesis.

Special mention must be paid to the Uniform California Earthquake Rupture Forecast (UCERF) versions 2 (Field et al. 2009) and 3 (Field et al. 2015), which are the best developed models for long-term time-dependent probability estimations. These approaches combine a large variety of seismological, geological and geodetic information constructing different fault, deformation and earthquake rate models for each fault segment of California, which form a logic tree with a large number of branches (e.g., version 3 has a total number of 5760) with their corresponding weights. Then the probability calculations were based on the aforementioned assumptions having as final product different estimations of the next earthquakes in California, with their corresponding weights and uncertainties. The renewal model used in these estimations is the BPT once again.

Seismicity-based models

Assumptions and forecast windows

"Seismicity based" models belong to the second category of stochastic models assuming that the future earthquakes follow the temporal properties of the past seismicity within a given region due to all possible seismic sources. These models combine both physical processes related to strong earthquakes occurrence, such as the accumulation, release and transfer of stress, and the well-known empirical laws of Seismology, namely the Gutenberg–Richter (GR) (Gutenberg and Richter 1949) and the Omori's (Omori 1894). Model applications can provide either long-term or short-term estimations of next earthquakes in a given region.

Long-term regional models

Starting with the long-term ones, Papazachos (1989) suggested a time-predictable model for earthquake occurrence in seven distinctive regions of Greece, using all available

$M \geq 5.5$ earthquakes located in the area. He claimed that the magnitude of the preceding shock, Mp, influences the repeat time, T, of the next mainshocks. The model he developed is based on the linear fit between the logarithm of T and Mp:

$$logT = cMp + a.$$

Papadimitriou (1993) applied the aforementioned model in 8 zones of the western coast of South and Central America. Papazachos (1992) and Papazachos and Papaioannou (1993) extended the time-predictable model to the time and magnitude one. They are given by two relations: one between the logarithm of T and the minimum magnitude considered in the dataset, $Mmin$, the magnitude of the previous shock, M_p, and the logarithm of the annual moment rate, m_o, and a second relation linking the magnitude of the following mainshock, M_f, and the above mentioned parameters as,

$$logT = bMmin + cMp + dlogm0 + q$$

and

$$Mf = BMmin + CMp + Dlogm0 + m.$$

This extended model was used in several studies all over the world. For example, Karakaisis (1993, 1994a, b) applied the models in New Guinea–Bismarck Sea, North and East Anatolian Fault Zones and Iran regions. Panagiotopoulos (Panagiotopoulos 1994, 1995) applied the time- and magnitude-predictable models in Solomon Islands, Central America and Caribbean Sea, Papadimitriou (Papadimitriou 1994a, 1994b) in North Pacific and Tonga–New Zealand seismic zones, Papazachos et al. (1994, 1997a, b) in Japan, circum–Pacific and Alpine–Himalayan belts and a few years later Shanker and Papadimitriou (2004) in the Hindu Kush–Pamir–Himalayan region. Similar to these studies Musson et al. (2002) proposed a similar time-dependent model connecting the natural logarithm of interarrival times, $lnIAT$, with their magnitudes, M, above a given threshold:

$$lnIAT = a + bM$$

and applied it in Japan and Greece. Later, Chingtham et al. (2015) applied this model in Northwest Himalaya and its adjoining regions.

A connection between seismicity and physics is accomplished through the Stress Release Model (Vere-Jones 1978; Vere-Jones and Deng 1988) which is built under the assumptions of stress loading due to elastic rebound and energy released when an event occurs (Fig. 4). The main variable is the stress level which can be written as

$$X(t) = X(0) + \rho t - S(t),$$

where $X(0)$ is the initial stress level, ρ is the loading rate (which is considered constant) and $S(t)$ is the accumulated stress release during $(0, t)$. The conditional intensity function

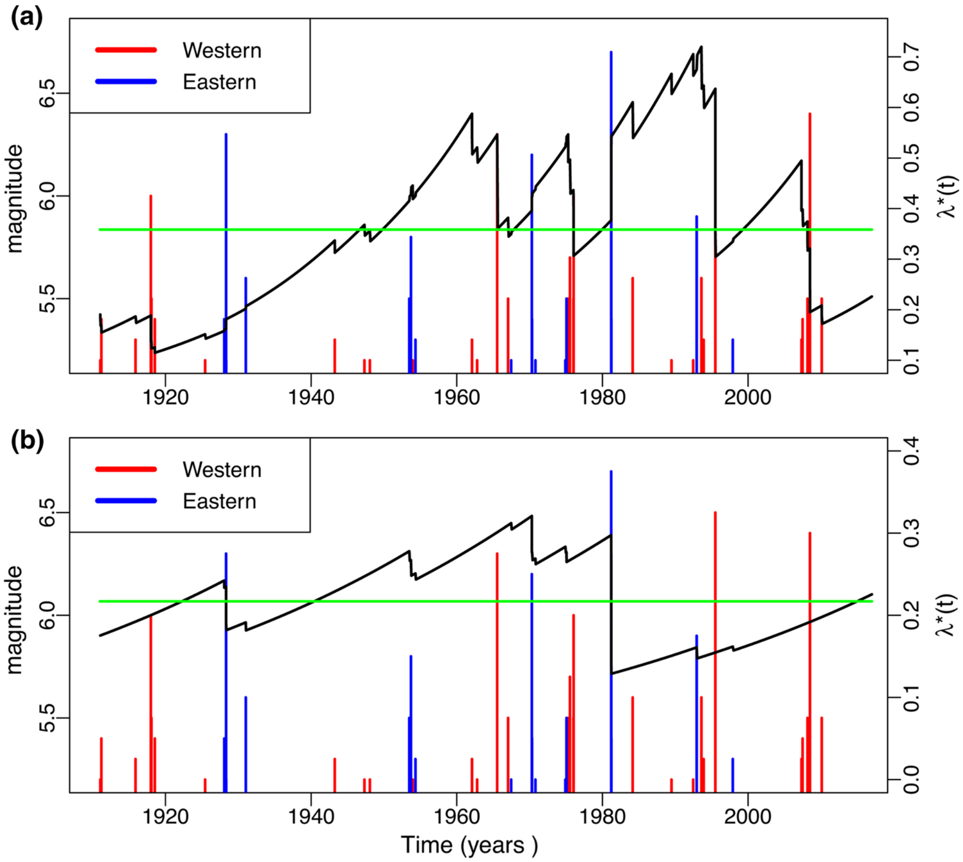

Fig. 4 Plots of the conditional intensity functions when the LSRM is applied in the Corinth Gulf (Greece) **a** Western part, **b** Eastern part. The mean occurrence level of the Poisson model is represented by a green line (From Mangira et al. 2018)

$\lambda * (t)$, (Daley and Vere-Jones 2003) determines the stochastic behavior of the point process. The most common form adopted is the exponential

$$\lambda * (t) = \Psi(X(t)) = \exp\{a + b[t - cS(t)]\}$$

where a, b and c are parameters to be estimated.

In the case of the Linked Stress Release Model (Liu et al. 1998), the conditional intensity function becomes

$$\lambda_i^*(t) = \exp\left\{ a_i + b_i \left[t - \sum_j c_{ij} S(t,j) \right] \right\}.$$

In this model, stress transfer and interactions between subareas are introduced. Many applications of the model have been performed worldwide. The first applications include Chinese (Liu et al. 1999), and Japanese data (Lu et al. 1999). Lu and Vere-Jones (2000) compared the results applying the model in two different tectonic regimes (North China and New Zealand), whereas Bebbington and Harte (2001) examined the model from a statistical point of view. SRM was also applied in Italy, where Varini and Rotondi (2015) and Varini et al. (2016) used a Bayesian approach. Romania (Imoto and Hurukawa 2006) and Greece (Rotondi and Varini 2006; Votsi et al. 2011; Mangira et al. 2017, 2018) have also been study areas for the SRM. Bebbington and Harte (2003) conducted an extensive study regarding the determination of the regions, the sensitivity to catalog errors optimization techniques, and the selection of the most appropriate model. Numerical simulations by Kuehn et al. (2008) aimed at investigating how the occurrence probability distributions are affected by the coupling between different areas.

The observed foreshock activity before strong earthquakes in many regions around the world (Jones and Molnar 1979; Sykes and Jaume 1990; Bakun et al. 2005) was also used as a tool aiming at the development of physics-based models for forecasting. A relevant approach, so-called Accelerating Moment Release (AMR) model or critical earthquake concept, was developed under the assumption that before a large earthquake, and the rate of seismic moment released from precursory intermediate magnitude (e.g., $M \geq 5.0$) seismic activity is increased with an accelerating component (Bufe and Varnes 1993; Bowman et al. 1998; Jaume and Sykes 1999; Mignan 2008).

Bufe and Varnes (1993) proposed that the cumulative Benioff strain,$\varepsilon(t)$, over time, which is equal to the summation of the square of the seismic moment of the ith foreshock, Ei, defined as

$$\varepsilon(t) = \sum_{i=1}^{N(t)} \sqrt{E_i}$$

can be expressed by the equation

$$\varepsilon(t) = A - B\left(t_f - t\right)^m$$

where t_f is the time of a mainshock or in other words the critical occurrence time of the upcoming strong earthquake, A and B are constants and m is a positive exponent ranging from 0.1 to 0.5 ($0.1 \leq m \leq 0.5$) with mean value equal to 0.3. The AMR model has been applied in many studies and in various regions worldwide such as California (Bowman et al. 1998), Italy (Di Giovambattista and Tyupkin 2000), China (Jiang and Wu 2006), Western, South and Central America (Papazachos et al. 2008) and Greece (Papazachos et al. 2006, 2007).

Another class of stochastic models includes the hidden Markov (HMMs) and semi-Markov (HSMM) models. The main concept of the HMMs applied in seismology is to reveal features of the earthquake generation process which cannot be directly observed. Toward that direction, Votsi et al. (2013) applied a HMM, where the states of the model correspond to levels of the stress field. Their application is performed in a set of strong ($M \geq 6.5$) earthquakes that occurred in Greece and its surrounding areas, since 1845. In order to overcome the drawback that derives from the geometrically distributed sojourn times of the HMM states and allow arbitrary distributions, the same authors (Votsi et al. 2014) suggested a discrete-time semi-Markov model. Pertsinidou et al. (2016) extended their work proposing Poisson, Logarithmic and Negative Binomial distributions for the sojourn times. Their application is performed in moderate ($M \geq 5.5$) earthquakes in the areas of North and South Aegean Sea (Greece) where the hidden states represent different stress levels classified into five types according to the earthquake magnitude and location.

Different occurrence rates are also considered as hidden states in the case of Markovian Arrival Processes suggested by Bountzis et al. (2018). MAP consists a generalization of the Poisson process and renewal models preserving the Markovian structure. The model captures temporal fluctuations that characterize Corinth Gulf seismicity for earthquakes with $M \geq 4.5$ since 1964.

Short-term modeling of regional earthquake activity

In addition to the long-term earthquake forecasting, extensive research was performed on short time scales. One of the most crucial elements regarding an earthquake time series is their tendency to clustering. It is generally accepted that seismic activity is increased after the occurrence of a strong event for several years (Utsu et al. 1995) and for long distances (Kagan and Jackson 1998; Dreger and Savage 1999). When the magnitude of an event is smaller than that of the previous one, the triggered event is called an aftershock. Defining an aftershock is quite arbitrary though and separating triggering earthquakes from the others is not a trivial task. Since the classification of an earthquake foreshock, mainshock, or aftershock—is often hard, it is useful to investigate models that do not presuppose such distinction. In addition, aftershocks constitute the greatest proportion in a catalog and thus, a thorough analysis of their occurrence can give an insight for understanding the whole seismic cycle. Ogata (1988) introduced a model where there is no need to distinguish between mainshocks and aftershocks, between independent and triggering events, since each one, irrespective of whether it is small or large, can trigger its own offspring. The ETAS (Epidemic-Type Aftershock Sequence) model, named after the analogy with the spread of epidemics, belongs to the family of self-exciting Hawkes processes (Hawkes and Oakes 1974). It is assumed that each event is followed by its own aftershock activity; this assumption stands even for the aftershocks of the previous events. The modified Omori formula (Utsu 1961) is employed for the representation of the aftershock activity. The appropriate form of the response function for the causal relation with subsequent events is the key for the application of the model. The conditional intensity is given by

$$\lambda(t,m) = \beta e^{\beta(m-m_0)}\{\mu + A\sum_{i:t_i<t} e^{a(m-m_0)} f(t-t_i)\},$$

where μ represents the background seismicity,A is related to the criticality of the process, a is related to the productivity, i.e., the influence of magnitude in the production of the offspring and $\beta = b\ln 10$ is linked to the G–R law. $f(t) = (p-1)\left(1+\frac{t}{c}\right)^{-p}/c$ refers to the Omori–Utsu formula and it is the pdf of the time difference between the parent event and its offspring. Based on the temporal model of Ogata (1988) many applications have been performed. For example, Ogata (2005) tried to detect anomalous seismicity patterns using it as a stress change sensor. Hainzl and Ogata (2005) and Lombardi et al. (2010) used the ETAS model for detecting fluid signals. They interpreted the increase in the background seismicity as fluid-driven earthquake triggering.

In a similar manner with the temporal ETAS model, Ogata (1998) deals with the response function for time and space causal relationship introducing the spatiotemporal ETAS model. The concept of this model is to investigate the magnitude scale of the clusters and also to understand whether the clusters are constrained to well-defined areas or if seismic activity is extended in areas beyond the aftershock regions. When space is involved the conditional intensity takes the form

$$\lambda(t,x,m) = \beta e^{\beta(m-m_0)}\{\mu h(x) + A\sum_{i:t_i<t} e^{a(m-m_0)} f(t-t_i) g(x-x_i)\}.$$

The new terms added in the model are the spatial density, h, of the background events and the density, g, of the location of a triggered event. The model proposed by Ogata (1998) underwent several modifications, particularly concerning the spatial component (Zhuang et al. 2002, 2004, 2005; Ogata and Zhuang 2006), and it is broadly accepted and applied.

Based on the assumption that every event is potentially triggered by all the previous ones and every event can trigger subsequent ones according to their relative time–space distance, Console and Murru (2001) proposed a spatiotemporal model for short-term clustering that returns the occurrence rate of events expected at each point of the location–time–magnitude space. They concluded that instead of using as a null hypothesis the Poisson model against other more sophisticated earthquake hypotheses, the clustering hypothesis (the space–time ETAS model) should be adopted since it exhibits a much higher likelihood. Console et al. (2003) refined the formulation of the clustering model. The expected earthquake rate density takes then the form

$$\lambda(x,y,t,m) = f_r\lambda_0(x,y,m) + \sum_{i=1}^{N} H(t-t_i)\lambda_i(x,y,t,m),$$

where the f_r, called failure rate, expresses the proportion of events that are considered independent, a factor revealing the so-called spontaneous background seismicity. The $\lambda_0(x,y,m)$ is the spatial magnitude distribution, $H(t)$ the step function, i.e., $H(t) = \begin{cases} 0, & \mathit{if}\ t \le 0 \\ 1, & \mathit{if}\ t > 0 \end{cases}$ and $\lambda(x,y,t,m)$ is the kernel of the previous events. In this equation, the two terms of the right-hand side show that seismicity is a mixture of the background, the independent events, and the induced ones. The model could provide daily expected seismicity rates, information extremely critical during a seismic excitation. Examples of expected daily seismicity rate forecast provided by the ETAS modelare shown in Fig. 5 (From Murru et al. 2014).

The ETAS model examines earthquake clustering from a purely statistical point of view. Fault interaction consists of a way to connect seismicity and physics. Since it is broadly recognized that sudden Coulomb stress changes due to the coseismic slip of preceding earthquakes can modify the proximity to failure of subsequent events, Console et al. (2006a, b) proposed a modification of the clustering model by including the rate-and-state theory developed by Dieterich (1994) in the concept of the ETAS model. According to this theory, the seismicity rate $R(t)$ of earthquakes when a stress change is observed at time $t = 0$ is written:

$$R(t) = \frac{R_o}{1 - \left[1 - \exp\left(-\frac{\Delta\tau}{A\sigma}\right)\right]\exp\left(\frac{-t}{t_a}\right)}$$

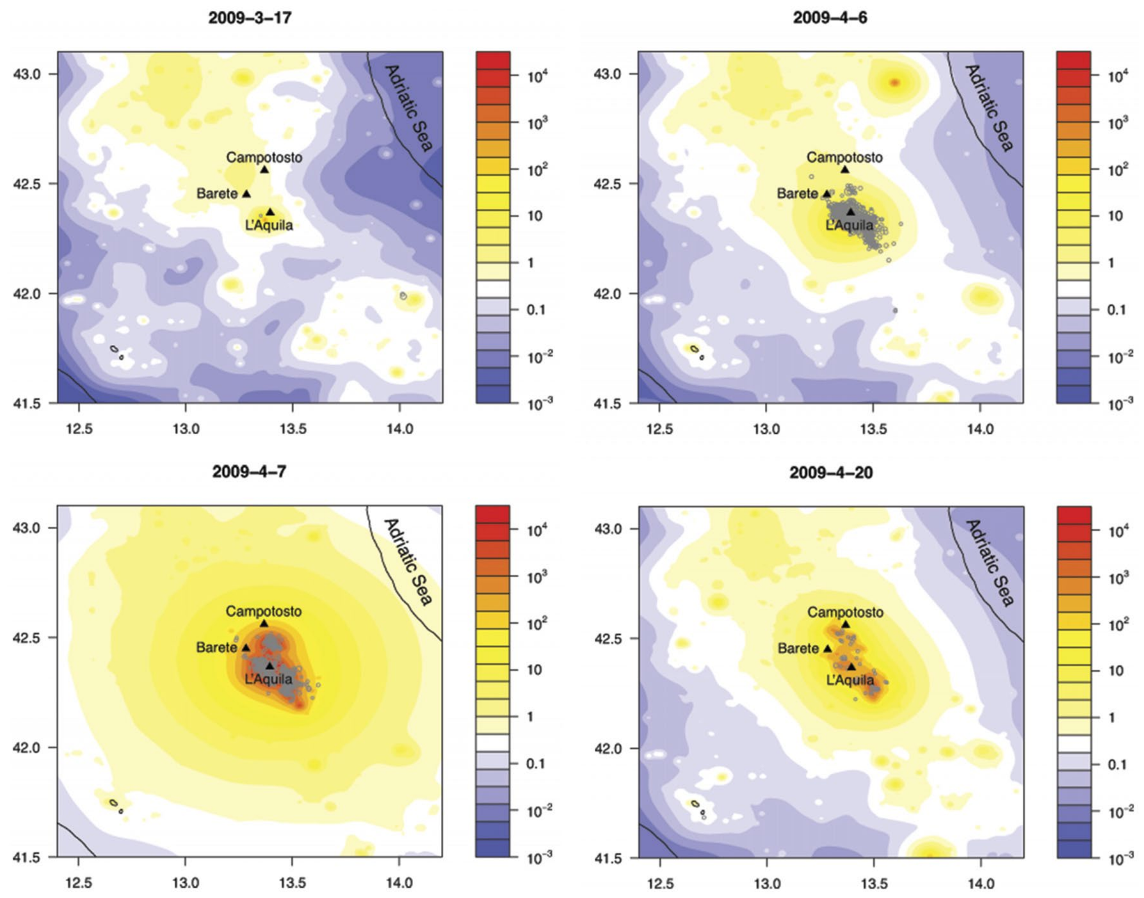

Fig. 5 Examples of expected daily seismicity rate forecast by ETAS at 00:00 UTC on the days: **a** March 17, 2009, **b** April 6, 2009 (1 h and 32 min before the L'Aquila mainshock M_w6.3), **c** April 7, 2009 (the second-largest shock in the Abruzzi region occurred on April 7, 2009, at 17:47 UTC, with M_w5.6) and **d** April 20, 2009. The color scale represents the number of events in units of magnitude larger than 2.0 in cells of 1° .1°per day (From Murru et al. 2014)

where R_o is the background rate density, $\Delta\tau$ is the shear stress change, and A, σ and t_a are parameters of the constitutive law. By fixing some of the parameters based on published results, the authors reduced the number of the model-free parameters, explaining in parallel more thoroughly their physical meaning. The new stochastic model applied to the Japanese seismicity performs as well as the purely stochastic ETAS model. The two models were also tested in Console et al. (2007) with data from California. Despite the poor performance of the model under the constraint of the rate-and-state constitutive law, it is considered that its physical meaning may provide insights into seismogenic processes and should not be rejected.

Another approach focusing on probabilistic aspects is conducted by Iervolino et al. (2014). They analytically combined results of probabilistic seismic hazard analysis (PSHA) and aftershock probabilistic seismic hazard analysis (APSHA) in order to get a seismic hazard integral accounting for mainshock–aftershocks seismic sequences. Their results are particularly interesting from an earthquake engineering perspective since seismic hazard is expressed in terms of occurrence rate causing the exceedance of an acceleration threshold.

Despite the wide variety of purely temporal models and time-independent spatial models, in practice the spatiotemporal models have not been fully exploited, mainly due to the fact that the implementation of such models demands heavy and complicated numerical computations. The concept of epidemic models though has been particularly popular, like the spatiotemporal ETAS model (Ogata 1998) that has been extensively applied in the context of earthquake short-term clustering (Helmstetter and Sornette 2002; Marzocchi et al. 2012; Murru et al. 2014). Another model that has common elements with the ETAS model is the EEPAS-Every Earthquake is a Precursor According to Scale-model. The EEPAS model by Evison and Rhoades (2004) and Rhoades and Evison (2004) is based on predictive scaling relations derived from many examples of the precursory scale increase phenomenon —an increase in the magnitude and occurrence rate of minor earthquakes that precede most major earthquakes on a time scale ranging from months to decades, depending on magnitude. Even though extensive studies were conducted and many relationships between precursory earthquakes and subsequent strong mainshocks have been suggested, regarding the magnitude, time, and location, in practice there are no tools for recognizing precursory earthquakes in advance. In this stochastic forecasting model, the identification of precursory earthquakes is set aside and every event is considered a long-range precursor period taking into account a scale based on its magnitude. The conditional intensity of the EEPAS process has a similar form with the ETAS, as

$$\lambda^*(t,m,x) = \mu\lambda_0(t,m,x) + \sum_{t_i<t} w_i\eta\left(m_i\right)r(M|M_i)f(t-t_i|M_i)g(x-x_i|M_i),$$

where λ_o is a reference rate density, which can be considered as the null hypothesis, e.g., the Poisson model, μ is a parameter that can be considered as the rate of events that are observed without a sequence of precursory earthquakes that can be predicted and η is a function of magnitude. Although the ETAS and the EEPAS models have similar forms of the conditional intensity, they differ in their details. For example, the functions f and g are not based in the Omori formula, which is an indispensable element of the ETAS model. Nevertheless, the weights w_i that are usually set to 1 could be obtained from an initial stochastic declustering that depends on the ETAS model. The EEPAS model has been used in several earthquake catalogs worldwide, e.g., New Zealand and California (Rhoades and Evison 2004; Rhoades 2007), Japan (Rhoades and Evison 2005, 2006) and Greece (Console et al. 2006a, b), and in synthetic catalogs as well (Rhoades et al. 2011).

The aforementioned rate density λ_o is related to the Proximity to Past Earthquakes (PPE). The PPE model, as its name reveals, relies on the proximity to previous shocks, taking into consideration their magnitudes. Most of its characteristics are associated with the forecasting model of Jackson and Kagan (1999). The PPE model gets the form

$$\lambda_{PPE}(t,m,x,y) = g_o(m)h(t,x,y),$$

where

$$g_o(m) = \beta exp\left[-\beta\left(m-m_c\right)\right]\left(m > m_c\right)$$

and

$$h(t,x,y) = \frac{1}{t-t_o}\sum_{t_i<t} h_{eq}(i)$$

where

$$h_{eq}(i) = \frac{a\left(m_i-m_c\right)}{\pi\left(d^2+\Delta_i^2\right)} + s$$

and Δi is the distance from (x, y) to (xi, yi). The parameters β, α, d, and s are to be fitted from data. Here $\beta = bln(10)$, where b is the G–R b–value, α is a normalization parameter, d is a smoothing distance in kilometers, and s is a spatially uniform background rate (occurrence per day per kilometer squared) that accounts events occurring far from the previous ones. As a result, the earthquake occurrence–rate density is high near the locations of past earthquakes and low far away from all past earthquakes. Regarding the magnitude, the larger the nearby past earthquakes are, the greater is the rate density. The PPE and EEPAS model have been candidate models in the CSEP Earthquake Forecast Testing Centers in New Zealand and California (Gerstenberger and Rhoades 2010; Rhoades and Stirling 2012; Schneider et al. 2014; Rhoades et al. 2018). An example of the rate of earthquake occurrence given by the EEPAS model is shown in Fig. 6 (From Console et al. 2006b).

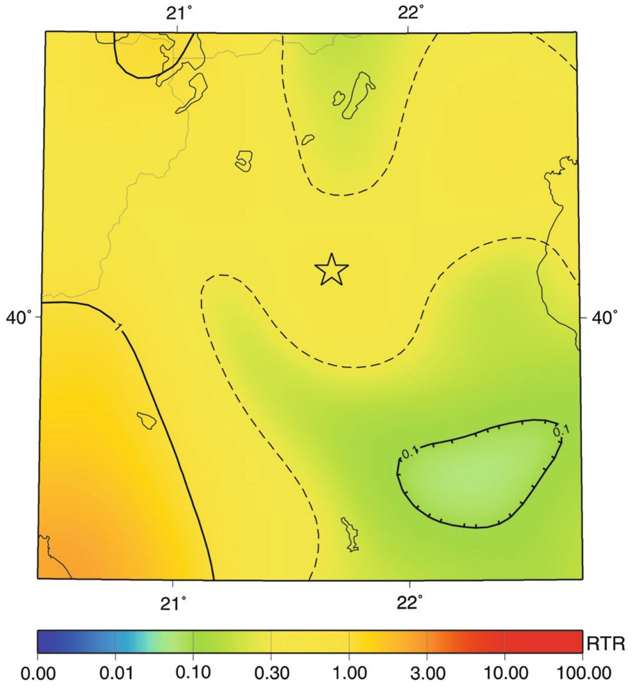

Fig. 6 Average rate of earthquake occurrence for $M > 6.35$ over the year 1995 under the EEPAS model, using data up to the end of 1994 in the area of Kozani (Greece). The rate is expressed relative to a reference scale (RTR) in which there is an expectation of 1 earthquake per year exceeding any magnitude m in an area of 1 $10^m km^2$. The epicenter of the M6.6 earthquake of 13 May 1995, 0847:17.0 UT is depicted by a star (From Console et al. 2006a, b)

Another candidate spatiotemporal model of earthquake occurrence is the double branching model by Marzocchi and Lombardi (2008), which is applied in two steps. The first step includes the application of the ETAS model so that triggered events are removed from the catalog. The next step consists of the reapplication of the model—the same or one with high resemblance—to the rest of the seismicity so that the long-term clustering is described.

Summary

The approaches for modeling and forecasting seismogenesis revealed that understanding earthquake phenomena which are complex and trying to predict them could be achieved by developing and applying progressively sophisticated and refined stochastic models. Their development and application could bridge the gap between the underlying physics and the small amount of the available data.

Selecting the most suitable model among all the competing ones is not a trivial issue. For that reason, rigorous tests and experiments should be implemented. In that direction, a collective international attempt has been made feasible in the Collaboratory for the Study of Earthquake Predictability (CSEP) experiment, for several regions all over the world. Their goal, since its inception in California in 2007, is to test alternative scientific hypotheses, their predictive abilities and consequently improve seismic hazard assessment.

The innovative concept of CSEP is that scientists are requested to submit their models for testing in pre-agreed datasets and standardized statistical tests. In that way, full independence is guaranteed and the comparisons between the models are objective (Schorlemmer et al. 2018). The next steps of CSEP include tests of fault-based forecasts where finite-fault information is provided instead of just testing the locations of hypocenters, forecasts based in simulations, tests where earthquake clustering is better approximated, and tests of ground-motion measures that achieve direct probabilistic seismic hazards assessments (Michael and Werner 2018).

Acknowledgments The constructive comments of two reviewers are acknowledged for their contribution to the improvement of the paper. Gratitude is also extended to Prof. Zuniga for his editorial assistance and constructive suggestions. The financial support by the European Union and Greece (Partnership Agreement for the Development Framework 2014–2020) for the Project "Development and application of time-dependent stochastic models in selected regions of Greece for assessing the seismic hazard" is gratefully acknowledged, MIS5004504. Geophysics Department Contribution 922.

References

Abaimov SG, Turcotte DL, Shcherbakov R, Runlde JB, Yakovlev G, Goltz C, Newman WI (2008) Earthquakes: recurrence and interoccurrence times. Pure appl Geophys 165:777–795. https://doi.org/10.1007/s00024-008-0331-y

Bakun WH, Aagaard B, Dost B, Ellsworth WL, Hardebeck JL, Harris RA, Ji C, Johnston MJS, Langbein J, Lienkaemper JJ, Michael AJ, Murray JR, Nadeau RM, Reasenberg PA, Reichle MS, Roeloffs EA, Shakal A, Simpson RW, Waldhausen F (2005) Implications for prediction and hazard assessment from the 2004 Parkfield earthquake. Nature 437:969–974

Bebbington M, Harte D (2001) On the statistics of the linked stress release process. J Appl Probab 38:176–187

Bebbington M, Harte D (2003) The linked stress release model for spatio-temporal seismicity: formulations, procedures and applications. Geophys J Int 154:925–946

Bountzis P, Papadimitriou E, Tsaklidis G (2018) Estimating the earthquake occurrence rates in Corinth Gulf (Greece) through Markovian arrival process modeling. J Appl Stat. https://doi.org/10.1080/02664763.2018.1531977

Bowman DD, Ouillon G, Sammis CG, Sornette A, Sornette D (1998) An observational test of the critical earthquake concept. J Geophys Res 103:24359–24372

Bufe CG, Varnes DJ (1993) Predictive modeling of the seismic cycle of the greater San Francisco Bay region. J Geophys Res 98:9871–9883

Chingtham P, Yavad RBS, Chopra S, Yavad AK, Gupta AK, Roy PNS (2015) Time-dependent seisimicity analysis in the Northwest Himalaya and its adjoining regions. Nat Hazards 80:1783–1800. https://doi.org/10.1007/s11069-015-2031-0

Console R, Murru M (2001) A simple and testable model for earthquake clustering. J Geophys Res 106:8699–8711

Console R, Murru M, Lombardi AM (2003) Refining earthquake clustering models. J Geophys Res 108:2468

Console R, Murru M, Catalli F (2006a) Physical and stochastic models of earthquake clustering. Tectonophysics 417:141–153

Console R, Rhoades DA, Murru M, Evison FF, Papadimitriou EE, Karakostas VG (2006b) Comparative performance of time-invariant, long range and short-range forecasting models on the earthquake catalogue of Greece. J Geophys Res 111:B09304. https://doi.org/10.1029/2005JB004113

Console R, Murru M, Catalli F, Falcone G (2007) Real time forecasts through an earthquake clustering model constrained by the rate-and-state constitutive law: comparison with a purely stochastic ETAS model. Seismol Res Let 78:49–56

Console R, Murru M, Falcone G, Catalli F (2008) Stress interaction effect on the occurrence probabilities of characteristic earthquakes in Central Apennines. J Geophys Res 113:B08313. https://doi.org/10.1029/2007JB0005418

Console R, Falcone G, Karakostas V, Murru M, Papadimitriou E, Rhoades D (2013) Renewal models and coseismic stress transfer in the Corinth Gulf, Greece, fault system. J Geophys Res Solid Earth 118:3655–3673. https://doi.org/10.1002/jgrb.50277

Convertito V, Faenza L (2014) Earthquake Recurrence. In: Beer M, Kougioumtzoglou IA, Patelli E, Siu-Kui Au I (eds) Encyclopedia of earthquake engineering. Springer, Berlin, pp 1–22. https://doi.org/10.1007/978-3-642-36197-5-236-1

Daley D, Vere-Jones D (2003) An introduction to the theory of point processes, 2nd edn. Springer, New York, pp 211–287

Di Giovambattista R, Tyupkin YS (2000) Spatial and temporal distribution of the seismicity before the Umbria-Marche September 26, 1997 earthquakes. J Seismol 4:589–598

Dieterich J (1994) A constitutive law for rate of earthquake production and its application to earthquake clustering. J Geophys Res 99:2601–2618

Dreger D, Savage B (1999) Aftershocks of the 1952 Kern County, California, earthquake sequence. Bull Seismol Soc Am 89:1094–1108

Ellsworth WL, Matthews MV, Nadeau RM, Nishenko SP, Reasenberg PA (1999) A physically based recurrence model for estimation of long-term earthquake probabilities. US Geol Surv Rept 99:522

Evison FF, Rhoades DA (2004) Demarcation and scaling of long-term seismogenesis. Pure appl Geophys 161:21–45

Field EH (2015) Computing elastic—rebound—motivated earthquake probabilities in unsegment fault models: a new methodology supported by physics—based simulators. Bull Seismol Soc Am 105:544–559. https://doi.org/10.1785/0120140094

Field EH, Dawson TE, Felzer KR, Frankel AD, Gupta V, Jordan TH, Parsons T, Petersen MD, Stein RS, Weldon RJ II, Wills CJ (2009) Uniform California rupture forecast, version 2 (UCERF 2). Bull Seismol Soc Am 99:2053–2107. https://doi.org/10.1785/0120080049

Field EH, Biasi GP, Bird P, Dawson TE, Felzer KR, Jackson DD, Johnson KM, Jordan TH, Madden C, Michael AJ, Milner KR, Page MT, Parsons T, Powers PM, Shaw BE, Thatcher WR, Weldon RJ II, Zeng Y (2015) Long-term time-dependent probabilities for the third uniform California earthquake rupture forecast (UCERF3). Bull Seismol Soc Am 105:511–543. https://doi.org/10.1785/0120140093

Frankel AM (1995) Mapping seismic hazard in the central and eastern United States. Seismol Res Let 60:8–21

Gerstenberger MC, Rhoades DA (2010) New Zealand earthquake forecast testing centre. Pure appl Geophys 167:877–892. https://doi.org/10.1007/s00024-010-0082-4

Gomberg M, Belardinelli ME, Cocco M, Reasenberg P (2005) Time-dependent earthquake probabilitied. J Geophys Res 110:B05S04. https://doi.org/10.1019/2004jb003405

Gutenberg B, Richter C (1949) Seismicity of the earth and associated phenomena, 2nd edn. University Press, Princeton

Hagiwara Y (1974) Probability of earthquake occurrence as obtained from a Weibull distribution analysis of crustal strain. Tectonophysics 23:313–318

Hainzl S, Ogata Y (2005) Detecting fluid signals in seismicity data through statistical earthquake modeling. J Geophys Res 110:B05S07

Hardebeck JL (2004) Stress triggering and earthquake probability estimated. J Geophys Res 109:B04310. https://doi.org/10.1029/2003JB002437

Hawkes AG, Oakes D (1974) A cluster process representation of a self-exciting process. J Appl Prob 11:493–503

Helmstetter A, Sornette D (2002) Sub-critical and supercritical regimes in epidemic models of earthquake aftershocks. J Geophys Res 107:2237

Iervolino I, Giorgio M, Polidoro B (2014) Sequence-based probabilistic seismic hazard analysis. Bull Seismol Soc Am 104(2):1006–1012. https://doi.org/10.1785/0120130207

Imoto M, Hurukawa N (2006) Assessing potential seismic activity in Vrancea, Romania, using a stress-release model. Earth Planets Space 58:1511–1514

Jackson DD, Kagan YY (1999) Testable earthquake forecasts for 1999. Seismol Res Lett 70:393–403

Jackson DD, Aki K, Cornell CA, Dieterich JH, Henyey TL, Mahdyiar M, Schwartz D, Ward SN (1995) Seismic hazard in Southern California: Probable earthquakes, 1994 to 2024. Bull Seism Soc Am 85:379–439

Jaume SC, Sykes LR (1999) Evolving towards a critical point: a review of accelerating seismic moment/energy release prior to large and great earthquakes. Pure appl Geophys 155:279–306

Jiang C, Wu Z (2006) Benioff strain release before earthquakes in China: accelerating or not? Pure appl Geophys 163:965–976

Jones LM, Molnar P (1979) Some characteristics of foreshocks and their possible relationship to earthquake prediction and premonitory slip on faults. J Geophys Res 84(B7):3596–3608

Kagan YY, Jackson DD (1991) Long-term earthquake clustering. Geophys J Int 104:117–133

Kagan YY, Jackson DD (1998) Spatial aftershock distribution: effect of normal stress. J Geophys Res 103:24453–24467

Kagan YY, Knopoff L (1987) Random stress and earthquake statistics: time dependence. Geoplys JR Astron Soc 88:723–731

Karakaisis GF (1993) Long term earthquake prediction in the New Guinea-Bismarck Sea region based on the time and magnitude predictable model. J Phys Earth 41:365–389

Karakaisis GF (1994a) Long-term earthquake prediction along the North and East Anatolian Fault Zones based on the time and magnitude predictable model. Geophys J Int 116:198–204

Karakaisis GF (1994b) Long term earthquake prediction in Iran based on the time and magnitude predictable model. Phys Earth Planet Inter 83:129–145

Kourouklas C, Papadimitriou E, Tsaklidis G, Karakostas V (2018) Earthquake recurrence models and occurrence probabilities of strong earthquakes in North Aegean Trough (Greece). J Seismol 22:1225–1246. https://doi.org/10.1007/s10950-018-9763-8

Kuehn NM, Hainzl S, Scherbaum F (2008) Non-Poissonian earthquake occurrence in coupled stress release models and its effect on seismic hazard. Geophys J Int 174:649–658

Liu J, Vere-Jones D, Ma L, Shi Y, Zhuang JC (1998) The principal of coupled stress release model and its application. Acta Seismol Sin 11:273–281

Liu C, Chen Y, Shi Y, Vere-Jones D (1999) Coupled stress release model for timedependent seismicity. Pure appl Geophys 155:649–667

Lombardi AM, Cocco M, Marzocchi W (2010) On the increase of background seismicity rate during the 1997–1998 Umbria-Marche, central Italy, sequence: apparent variation or fluid-driven triggering? Bull Seismol Soc Am 100:1138–1152

Lu C, Vere-Jones D (2000) Application of linked stress release model to historical earthquake data: comparison between two kinds of tectonic seismicity. Pure appl Geophys 157:2351–2364

Lu C, Harte D, Bebbington M (1999) A linked stress release model for historical Japanese earthquakes: coupling among major seismic regions. Earth Planets Space 51:907–916

Mangira O, Vasiliadis G, Papadimitriou E (2017) Application of a linked stress release model in Corinth gulf and Central Ionian Islands (Greece). Acta Geophys. https://doi.org/10.1007/s11600-017-0031-z

Mangira O, Console R, Papadimitriou E, Vasiliadis G (2018) A restricted linked stress release model (LSRM) for the Corinth gulf (Greece). Tectonophysics 723:162–171

Marzocchi W, Lombardi AM (2008) A double branching model for earthquake occurrence. J Geophys Res 113:317

Marzocchi W, Murru M, Lombardi AM, Falcone G, Console R (2012) Daily earthquake forecasts during the May-June 2012 Emilia earthquake sequence (northern Italy). Ann Geophys 55(4):561–567

Matthews VM, Ellsworth WL, Reasenberg PA (2002) A Brownian model for recurrent earthquakes. Bull Seism Soc Am 92:2233–2250

Michael AJ, Werner MJ (2018) Preface to the focus section on the collaboratory for the study of earthquake predictability (CSEP): new results and future directions. Seismol Res Lett 89(4):1226–1228. https://doi.org/10.1785/0220180161

Mignan A (2008) The non-critical precursory accelerating sesmicity theory (NC PAST) and limits of the power-law fit methodology. Tectonophysics. https://doi.org/10.1016/j.tecto.2008.02.010

Murru M, Zhuang Z, Console R, Falcone G (2014) Short-term earthquake forecasting experiment before and during the L'Aquila (central Italy) seismic sequence of April 2009. Ann Geophys 57(6):S0649. https://doi.org/10.4401/ag-6583

Murru M, Akinci A, Falcone G, Pucci S, Console R, Parsons T (2016) $M \geq 7.0$ earthquake rupture forecast and time-dependent probability for the Sea of Marmara region, Turkey. J Geophys Res Solid Earth 1:121. https://doi.org/10.1002/2015jb012595

Musson RMW, Tsapanos T, Nakas CT (2002) A power-law function for earthquake interarrival time and magnitude. Bull Seismol Soc Am 92:1783–1794

Nishenko SP, Bulland R (1987) A generic recurrence interval distribution for earthquake forecasting. Bull Seism Soc Am 77:1382–1399

Ogata Y (1988) Statistical models for earthquake occurrences and residual analysis for point processes. J Am Stat Assoc 83:9–27

Ogata Y (1998) Space-time point-process models for earthquake occurrences. Ann Inst Stat Math 50:379–402

Ogata Y (2002) Slip-size-dependent renewal processes and Bayesian inferences for uncertainties. J Geophys Res 107:2268. https://doi.org/10.1029/2001JB000668

Ogata Y (2005) Detection of anomalous seismicity as a stress change sensor. J Geophys Res 110:B05S06

Ogata Y, Zhuang J (2006) Space–time ETAS models and an improved extension. Tectonophysics 413:13–23

Omori F (1894) On the aftershocks of earthquakes. J Coll Sci Imp Univ Tokyo 7:111–200

Panagiotopoulos DG (1994) Long term earthquake prediction along the seismic zone of Solomon Islands and New Hebrides based on the time and magnitude predictable model. Nat Hazards 11:17–43

Panagiotopoulos DG (1995) Long term earthquake prediction in central America and Caribbean Sea based on the time and magnitude predictable model. Bull Seismol Soc Am 85:1190–1201

Papadimitriou EE (1993) Long-term earthquake prediction along the Western Coast of South and Central America based on a Time Predictable Model. Pure appl Geophys 140:301–316

Papadimitriou EE (1994a) Long term prediction in North Pacific seismic zone based on the time and magnitude predictable model. Nat Hazards 9:303–321

Papadimitriou EE (1994b) Long term prediction of large shallow mainshocks along the Tonga-Kermadec-New Zealand seismic zone based on a time and magnitude predictable model. Tectonophysics 235:347–360

Papazachos BC (1989) A time-predictable model for earthquake generation in Greece. Bull Seismol Soc Am 79:77–84

Papazachos BC (1992) A time and magnitude predictable model for generation of shallow earthquakes in the Aegean area. Pure appl Geophys 138:287–308

Papazachos BC, Papaioannou CA (1993) Long-term earthquake prediction in the Aegean area based on a time and magnitude predictable model. Pure appl Geophys 140:593–612

Papazachos BC, Papadimitriou EE, Karakaisis GF, Tsapanos TM (1994) An application of the time and magnitude predictable model for the long term prediction of strong shallow earthquakes in Japan area. Bull Seismol Soc Am 84:426–437

Papazachos BC, Papadimitriou EE, Karakaisis GF, Panagiotopoulos DG (1997a) Long-term Earthquake Prediction in the Circum-Pacific Convergent Belt. Pure appl Geophys 149:173–217

Papazachos BC, Karakaisis GF, Papadimitriou EE, Papaioannou CA (1997b) The regional time and magnitude predictable model and its application to the Alpine-Himalayan belt. Tectonophysics 271:295–323

Papazachos BC, Karakaisis GF, Scordilis EM, Papazachos CB (2006) New observational information on the precursory accelerating and decelerating strain energy release. Tectonophysics 423:83–96. https://doi.org/10.1016/j.tecto.2006.03.004

Papazachos BC, Karakaisis GF, Papazachos CB, Scordilis EM (2007) Evaluation of the results for an intermediate-term prediction of the 8 January 2006 M_w 6.9 Cythera Earthquake in Southwestern Aegean. Bull Seismol Soc Am 97:347–352. https://doi.org/10.1785/0120060075

Papazachos BC, Papaioannou CA, Scordilis EM, Papazachos CB, Karakaisis GF (2008) A forward test of the Decelerating–Accelerating Seismic Strain model to western, south and central America. Tectonophysics 454:36–43. https://doi.org/10.1016/j.tecto.2008.03.012

Paradisopoulou PM, Papadimitriou EE, Karakostas VG, Taymaz T, Kilias A, Yolsal S (2010) Seismic hazard evaluation in Western Turkey as revealed by stress transfer and time-dependent probability calculations. Pure appl Geophys 167:1013–1048. https://doi.org/10.1007/s00024-010-0085-1

Parsons T (2004) Recalculated probability of $M \geq 7.0$ earthquakes beneath the Sea of Marmara, Turkey. J Geophys Res 109:B05304. https://doi.org/10.1029/2003jb002667

Parsons T (2008) Earthquake recurrence on the south Hayward fault is more consistent with a time dependent, renewal process. Geophys Res Lett 35:L21301. https://doi.org/10.1029/2008GL035887

Parsons T, Console R, Falcone G, Murru M, Yamashina K (2012) Comparison of characteristic and Guterberg–Richter models for time-dependent $M \geq 7.9$ earthquake probability in the Nankai-Tokai subduction zone, Japan. Geophys J Int 190:1673–1688. https://doi.org/10.1111/j.1365-246X.2012.05595.x

Pertsinidou C, Tsaklidis G, Papadimitriou E, Limnios N (2016) Application of hidden semi-Markov models for the seismic hazard assessment of the North and South Aegean Sea, Greece. J Appl Stat 44:1064–1085

Polidoro B, Iervolino I, Chioccarelli E, Giorgio M (2013) In: Proceedings of 11th conference on structural safety and reliability ICOSSAR 13, New York, June 16–20

Rhoades DA (2007) Application of the EEPAS model to forecasting earthquakes of moderate magnitude in southern California. Seismol Res Lett 78(1):110–115

Rhoades DA, Evison FF (2004) Long-range earthquake forecasting with every earthquake a precursor according to scale. Pure appl Geophys 161:47–72

Rhoades DA, Evison FF (2005) Test of the EEPAS forecasting model on the Japan earthquake catalogue. Pure appl Geophys 162(6/7):1271–1290

Rhoades DA, Evison FF (2006) The EEPAS forecasting model and the probability of moderate-to-large earthquakes in central Japan. Tectonophysics 417(1/2):119–130

Rhoades DA, Stirling MW (2012) An earthquake likelihood model based on proximity to mapped faults and cataloged earthquakes. Bull Seismol Soc Am 102(4):1593–1599

Rhoades DA, Robinson R, Gerstenberger MC (2011) Long-range predictability in physics-based synthetic earthquake catalogues. Geophys J Int 185:1037–1048

Rhoades DA, Christophersen A, Gerstenberger MC, Liukis M, Silva F, Marzocchi W, Werner MJ, Jordan TH (2018) Highlights from the first ten years of the New Zealand earthquake forecast testing center. Seismol Res Lett 89(4):1229–1237. https://doi.org/10.1785/02201800322

Rikitake T (1974) Probability of earthquake occurrence as estimated from crustal strain. Tectonophysics 23:299–312

Rikitake T (1976) Recurrence of great earthquakes at subduction zones. Tectonophysics 35:335–362

Rotondi R, Varini E (2006) Bayesian analysis of marked stress release models for timedependent hazard assessment in the western Gulf of Corinth. Tectonophysics 423:107–113

Schneider M, Clements R, Rhoades DA, Schorlemmer D (2014) Likelihood- and residual-based evaluation of medium-term earthquake forecast models for California. Geophys J Int 198(3):1307–1318. https://doi.org/10.1093/gji/ggu178

Schorlemmer D, Werner MJ, Marzocchi W, Jordan TH, Ogata Y, Jackson DD, Mak S, Rhoades DA, Gerstenberger MC, Hirata N, Liukis M, Maechling PJ, Strader A, Taroni M, Wiemer S, Zechar JD, Zhuang J (2018) The collaboratory for the study of earthquake predictability: achievements and priorities. Seismol Res Lett 89(4):1305–1313. https://doi.org/10.1785/0220180053

Schwartz DP, Coppersmith KJ (1984) Fault behavior and characteristic earthquakes: examples from Wasatch and San Andreas fault zones. J Geophys Res 89:5681–5698

Shanker D, Papadimitriou EE (2004) Regional time-predictable modeling in the Hindukush-Pamir-Himalayas region. Tectonophysics 390:129–140

Shimazaki K, Nakata T (1980) Time-predictable recurrence model for large earthquakes. Geophys Res Lett 7:279–282

Stein RS, Barka AA, Dieterich JH (1997) Progressive failure on the North Anatolian fault since 1939 by earthquake stress triggering. Geophys J Int 128:594–604

Sykes LR, Jaume SC (1990) Seismic activity on neighbouring faults as a long-term precursor to large earthquakes in San Francisco Bay area. Nature 348:595–599

Utsu T (1961) A statistical study on the occurrence of aftershocks. Geophysics 30:521–605

Utsu T, Ogata Y, Matsu'ura S (1995) The centenary of the Omori Formula for a decay law of aftershock activity. J Phys Earth 43:1–33

Varini E, Rotondi R (2015) Probability distribution of the waiting time in the stress release model: the Gompertz distribution. Environ Ecol Stat 22:493–511

Varini E, Rotondi R, Basili R, Barba S (2016) Stress release models and proxy measures of earthquake size. Application to Italian seismogenic sources. Tectonophysics 682:147–168

Vere-Jones D (1978) Earthquake prediction—a statistician's view. J Phys Earth 26:129–146

Vere-Jones D, Deng YL (1988) A point process analysis of historical earthquakes from North China. Earthq Res China 2:165–181

Votsi I, Tsaklidis G, Papadimitriou E (2011) Seismic hazard assessment in Central Ionian Islands area based on stress release models. Acta Geophys 59:701–727

Votsi I, Limnios N, Tsaklidis G, Papadimitriou E (2013) Hidden markov models revealing the stress field underlying the earthquake generation. Phys A 392:2868–2885

Votsi I, Limnios N, Tsaklidis G, Papadimitriou E (2014) Hidden semi-Markov modeling for the estimation of earthquake occurrence rates. Commun Stat Theory Methods 43:1484–1502

Zhuang J, Ogata Y, Vere-Jones D (2002) Stochastic declustering of space-time earthquake occurrences. J Am Stat Assoc 97:369–380

Zhuang J, Ogata Y, Vere-Jones D (2004) Analyzing earthquake clustering features by using stochastic reconstruction. J Geophys Res B5:301

Zhuang J, Chang CP, Ogata Y, Chen YI (2005) A study on the background and clustering seismicity in the Taiwan region by using a point process model. J Geophys Res 110:B05S13

Zoller G, Hainzl S, Holschneider M (2008) Recurrent large earthquakes in a fault region: what can be inferred from small and intermediate events? Bull Seismol Soc Am 98:2641–2651. https://doi.org/10.1785/0120080146

Acta Geophysica (2019) 67:753–763
https://doi.org/10.1007/s11600-019-00281-7

RESEARCH ARTICLE - SOLID EARTH SCIENCES

Time-dependent shake map for Uttarakhand Himalayas, India, using recorded earthquakes

Himanshu Mittal[1] · **Yih-Min Wu**[2,3,4] · **Ting-Li Lin**[1] · **Cédric P. Legendre**[4] · **Sushil Gupta**[5] · **Benjamin M. Yang**[2]

Received: 21 September 2018 / Accepted: 22 March 2019 / Published online: 27 March 2019

Abstract

Uttarakhand Himalayas are highly sensitive to seismic hazard with possible occurrence of high-magnitude earthquakes. Fewer waveforms are available from previously recorded earthquakes, which are insufficient for carrying out seismic hazard studies. The recently installed strong motion instrumentation network (SMIN) in India, particularly, in Indian Himalayas is providing useful data. Using recorded data from SMIN, time-dependent peak ground acceleration and observed peak ground velocity shake maps are drawn for two earthquakes widely recorded by SMIN in Uttarakhand region of Indian Himalayan belt. Open-source Earthworm software with new algorithms is used for drawing these shake maps. The source mechanism is computed for April 4, 2011 earthquake using waveform inversion technique to relate it to the trend of shake maps. The computed focal mechanism shows one of the nodal planes in NW–SE, which are consistent with shake maps for the same earthquake. These time-dependent plotted shake maps provide useful information on the initial rupture, as well as the potential directivity of the rupture.

Keywords Shake map · PGA · PGV · Uttarakhand Himalaya · Earthworm

Introduction

The formation of Tibetan Plateau is result of the convergence of the Indian and Eurasian plates that started 50 Myr ago (Gansser 1964; Legendre et al. 2015a). Indian subcontinent is prone to earthquakes in both the inter-plate and intra-plate regions. Collision of Eurasian and Indian plates resulted in the formation of Lesser Himalaya, Main Central Thrust and Great Himalayas (Valdiya 1980; Legendre et al. 2015b). The great Himalayas are an active tectonic region where larger-magnitude earthquakes can occur occasionally (Fig. 1). Some belts which did not generate any bigger earthquakes ($M \geq 8$) in the last century but can generate larger earthquakes are regarded as seismic gaps. Several seismic gaps exist in Indian Himalayan belt, one of which is the central seismic gap (CSG) having a length of 600 km that extends from the eastern edge of rupture zone of 1905 Kangra earthquake to western edge of 1934 Bihar–Nepal earthquake rupture zone (Seeber and Armbruster 1981; Khattri 1999). Kangra earthquake (M 7.8) of 1905 occurred on the west of CSG, and Bihar earthquake (M 8.3) of 1934 occurred to the eastern side. Higher-magnitude earthquakes can occur within the CSG. The possibility of occurrence of high magnitude ($M \geq 8$) in CSG is estimated to be 59% in coming 80 years (Khattri 1999). Some higher-magnitude earthquakes happened in CSG in last 100 years; examples include: 1803 and 1833 earthquakes having magnitude < 8, but those cannot be attributed to being gap filling (Khattri 1999; Bilham 1995). The recent devastating Gorkha earthquake in 2015 (Mw 7.8) caused a lot of destructions in Nepal and the eastern side of India, but it also occurred toward the eastern side of CSG (Yagi and Okuwaki 2015). Though this Gorkha earthquake reduced the aerial distribution of CSG toward the eastern side, but the possibility of happening of a bigger seismic event cannot be denied in future. The

---

✉ Himanshu Mittal
himanshumitt10@gmail.com

[1] Department of Earth Sciences, National Cheng Kung University, Tainan 701, Taiwan

[2] Department of Geosciences, National Taiwan University, Taipei 10617, Taiwan

[3] NTU Research Center for Future Earth, National Taiwan University, Taipei 10617, Taiwan

[4] Institute of Earth Sciences, Academia Sinica, Taipei 11529, Taiwan

[5] Risk Modeling and Insurance, RMSI, Noida, India

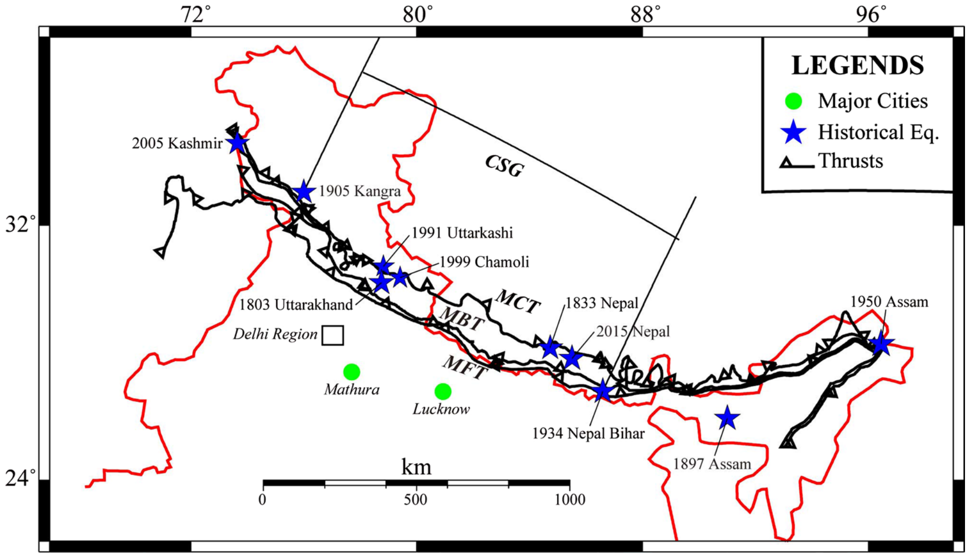

Fig. 1 A map showing the tectonic environment of Himalayan belt. Various seismic gaps along Himalayan region are shown. The Uttarakhand Himalayas, the focus of the present study lies in between central seismic gap (CSG) that extends from eastern edge of 1905 Kangra earthquake to western edge of 1934 Nepal–Bihar earthquake. The various earthquakes located in CSG like Uttarkashi earthquake of 1991, Chamoli earthquake of 1999 and recent Gorkha earthquake of 2015 are also shown

expected magnitude ≥ 8 earthquake in CSG would have a destructive impact on human society as well as casualties. In recent times, remarkable developments in population growth and industrial activity are continuing to grow in the Uttarakhand Himalayas classified in seismic zone IV and V of seismic hazard maps according to seismic hazard zonation map of India (BIS 2002). Most of the houses in Uttarakhand are constructed using brunt brick and stones, without following earthquake-resistant design guidelines. The population of the Uttarakhand is approximately 10 million people, who are under threat from natural disasters including earthquakes. Therefore, delineating the possible regions with potentially high seismic risk or shaking is of high importance.

Strong motion seismographs are used to record ground motions when routinely short-period seismographs go off the scale. The most critical role of strong motion networks is to provide on-scale recordings of potentially damaging earthquakes over a broad frequency band (50 Hz or higher). The strong motion data are fundamental for earthquake engineering studies such as site effects, advanced structural analyses and seismic hazard evaluation. Shaking and damage patterns in a seismically active region are generally characterized using peak ground acceleration (PGA) and peak ground velocity (PGV) (Wald et al. 1999; Wu et al. 2016, 2018; Legendre et al. 2017). These patterns are important information for mitigating seismic risk. The obtained data from strong motion network in Uttarakhand provide an opportunity to unravel the seismotectonics of the region, as well as improved knowledge on the potential damage regions. Ground shaking distribution caused by earthquakes can be represented using shake maps. The real-time or near-real-time shake maps are useful to assess the shaking induced by an earthquake in a specific region. Shake maps display the shaking at different sites based on source to site distance and site condition (soil or rock). PGV is supposed to be a better indicator of damage in comparison with PGA (Wu et al. 2004) because it provides relatively more stable information in damage assessment and in intensity estimation. A region where the seismic instrumentation is dense (having instruments at a regular interval of 10–15 km) will portray an accurate picture of shaking and damage scenario. In the present study, shake maps are plotted for two earthquakes recorded in Uttarakhand Himalayas using Earthworm software. Earthworm is an open-source, robust and well-functioning software that is widely distributed in different parts of the world (Olivieri and Clinton 2012; Chen et al. 2015). Earthworm is the outcome of the project that started in the early 1990s at the US Geological Survey (Johnson et al. 1995). This software is commonly used for data acquisition and processing in addition to interpretation. The user can select usage of this software in accordance with his requirements. Open-source Earthworm software with new algorithms is used to estimate PGA and PGV for each station. This further allows us to plot contours for PGA and PGV and evaluate the potential region with risk of damage for buildings and population.

Seismotectonics

Uttarakhand Himalayas are seismically active and have experienced earthquakes since ancient times (Gupta et al. 2012). Several tectonic faults exist in the region, which are capable of generating large-magnitude earthquakes (Srivastava and Mitra 1994). The most prominent of these are Main Boundary Thrust (MBT), Main Central Thrust (MCT) and Main Frontal Thrust (MFT), displayed in Fig. 1. Along with these Himalayan thrusts, several other faults also exist in region under consideration. Most important features that run transverse to Himalayan faults are Mahendragarh–Dehradun Fault (MDF), Great Boundary Fault (GBF) and Moradabad Fault (MF), which exists in the Delhi–Moradabad region (Fig. 2).

The seismicity in Uttarakhand Himalayas is particularly of inter-plate type. Most of the earthquakes lie around MCT, the central part of east–west extended Himalayan mountain zone (Seeber and Armbruster 1981; Kumar et al. 2009). This portion is denoted as Himalayan seismic belt focused around MCT with a southern boundary extending toward MBT, and the seismicity between MBT and MCT is linked to reactivation of the parallel low-angle detachment thrust faults (Khattri et al. 1989).

Based on available fault plane solutions in Uttarakhand Himalayas, and in general in the entire Himalayas, the tectonic features are marked as thrust dipping toward the northeast (Gahalaut and Rao 2009). Uttarakhand Himalaya unveils moderate to high instrumental and historic seismicity which is demonstrated on the basis that many moderate- to large-size earthquakes occurred in Uttarakhand. The available fault plane solutions from USGS for prominent instrumental recorded earthquakes like Uttarkashi earthquake of 1991 (Mw 6.8), Chamoli earthquake of 1999 (Mw 6.5), Nepal–Uttarakhand earthquake of 2011 (Mw 5.4) and recent Gorkha earthquake of April 2015 (Mw 7.8) are found to support the theory of thrust dominance in the region. Generally earthquakes occurring in this region are located in upper crust (Gaur et al. 1985; Liang et al. 2008). Substantial destruction was caused in Uttarakhand by Uttarkashi and Chamoli earthquakes, because of occurrence at shallow depths (10–15 km).

Strong motion instrumentation network

The strong motion instrumentation network (SMIN) of India consists of 300 stations (Mittal et al. 2006; Kumar et al. 2012). The instruments installed in states like Himachal Pradesh and Uttarakhand are cataloged as zone IV and V according to seismic zonation map of India (BIS 2002). In peninsular India, strong motion records of engineering importance are available from Koyna region (Gupta and Gupta 2004). The instruments are located mainly in three geological conditions, i.e., rock sites, medium soil site and soft soil sites. The site classification beneath the instruments is based on surface geology, as reported by Mittal et al. (2012). Out of these 300 stations, 35 instruments are installed in different parts of Uttarakhand, which is the target region of this study. The inter-station spacing between instruments is 25–30 km. Most of the stations in Uttarakhand have recorded tens of small to moderate earthquakes

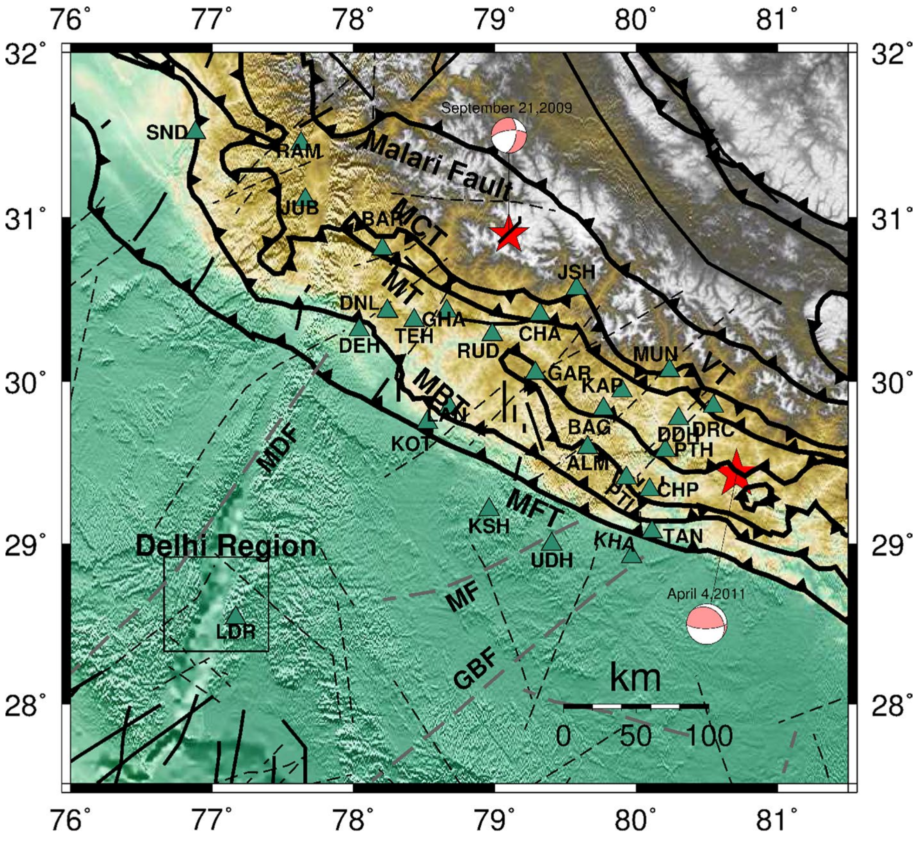

Fig. 2 Seismotectonic setup of Uttarakhand Himalayas. The prominent fault responsible for major seismicity in the region, namely Main Boundary Thrust (MBT), Main Central Thrust (MCT), Main Frontal Thrust (MFT), Vartica Thrust (VT), Munsiari Thrust (MT), are shown. Some other faults, namely Malari Fault, Mahendragarh–Dehradun Fault (MDF), Great Boundary Fault (GBF) and Moradabad fault (MF), are also shown. The epicenters of April 4, 2011 earthquake and September 21, 2009 earthquake are shown as red stars. All the strong motion recording these earthquakes is shown as triangles

since their operation. Earlier analog strong motion accelerographs (SMA) installed in Uttarakhand became obsolete and were replaced by digital strong motion instruments in one of the projects sponsored by Ministry of Earth Sciences (MoES), Government of India. This network of digital SMA has recorded more than 50 earthquakes in Uttarakhand since its installation in 2005. Some small- to moderate-size earthquakes, for example, the most prominent being the December 14, 2005 (M 5.2); July 22, 2007 (M 5.0); September 4, 2008 (M 5.1); September 21, 2009 (M 4.7); February 22, 2010 (M 4.7); May 1, 2010 (M 4.6); July 6, 2010 (M 5.1); April 4, 2011 (M 5.4); April 5 2011(M 5.0), are recorded by this network. M is the magnitude reported for these events by Indian Meteorological Department (IMD, nodal agency in India for reporting earthquakes). Since this network is set in triggering mode and the triggering threshold is somewhat high, most of the earthquakes are recorded at few sites only. However, by the time April 4, 2011 earthquake occurred, the threshold was lowered to 2 gals (1 gal = 1 cm/s^2) and allowed this event to be recorded at many stations. Here April 4, 2011 earthquake is used for plotting PGA and PGV shake maps, as this is the widespread recorded earthquake by SMIN in Uttarakhand Himalayas. In the past also, some studies made use of April 4, 2011 earthquake (Mittal and Kumar 2015; Kumar and Khandelwal 2015; Mittal et al. 2016b). In addition, another earthquake which occurred on September 21, 2009, is also used for plotting shake maps.

Source mechanism

The seismotectonic environment of any region can be studied using the data from small- to moderate-magnitude earthquakes in that region. P-wave polarity method is the most common and widely used approach for determining the focal mechanism and other source parameters of earthquakes. The main disadvantage of this approach is that it requires a large number of stations having good station coverage as well as signal-to-noise ratio. In the absence of sufficient station coverage, the solution obtained from this conventional approach is prone to errors. To keep the solution error-free, the waveform fitting approach is used as an alternate for calculating routine inversions of source parameters. Nowadays, the moment tensor waveform inversion is a well-established technique to determine the fault mechanism (e.g., Frohlich and Apperson 1992; Mozziconacci et al. 2009; Chao et al. 2011; Ekström et al. 2012).

We use strong motion data of April 4, 2011 earthquake in the region to determine the focal mechanisms by combining P-wave polarity method with cross-correlations between recorded and synthetic waveforms (Chao et al. 2011). The vertical component of accelerograms is used. The accelerograms are processed to remove mean and linear trend before the P-wave arrivals and then integrated to obtain velocity waveforms. Green's function database is obtained by the finite-difference method. We opt the strain Green's tensor (SGT) approach (Zhao et al. 2006), where 3D SGTs are calculated by a fourth-order staggered-grid finite-difference method (Olsen 1994; Graves 1996). In addition, we used a realistic 3D velocity model for the study region (Kanaujia et al. 2016). In order to improve the results, the grid search method based on genetic algorithm is used for computing exact depth and fault plane solution. A simple inversion is performed to minimize the overall difference between synthetic and observed seismograms (Fig. 3). As obtained data are recorded by strong motion instruments, the less fitting is found between observed and synthetic seismograms. However, the computed focal mechanism is in close agreement with other reporting agencies. Though source mechanism has nothing to do with time-dependent shake map mechanism, we simply compute it to compare our source mechanism with source mechanism reported by other organizations like USGS and relate shake map trend to source mechanism.

Near-real-time shake maps

Shake maps can be drawn in a better way where data are received continuously from all stations in real time, i.e., at least 5- to 10-min data can be used to compute shake maps. However, in our case data are recorded by SMIN in triggered mode, i.e., when triggering threshold exceeds 2 gals, instruments starts recording. So in that case, we have mostly 60- to 120-s record for each station. For a country like Taiwan, shake maps are plotted when 10 or 12 instruments confirm PGA to be larger than 1.2 gals (Wu et al. 2013, 2016; Wu 2015; Legendre et al. 2017). As we do not have so many instruments installed in the region, we have reduced threshold number of recording station to 3. So when 3–5 instruments confirm PGA to be more than 2 gals, the shake maps are automatically generated. The recorded data of various channels from both earthquakes are combined together into two different files, called Tank files. These files can be played in Earthworm software in order of the timestamp of each record line. By this method, we could pass the recorded data to our algorithm in a similar manner, as it would have streamed during the real-time event. The algorithm is then tested, and the parameter values can be optimized. Earthworm module Pick_EEW automatically detects the P-wave arrival using Allen et al. (2009) algorithm, and the peak values of velocity (P_v), and acceleration (P_a) are estimated once predefined conditions are met after the P-wave arrival. When ground motion data flow into Earthworm software, our module computes the PGA for every second and then passes the results to the shake map module for evaluation. The shake map module tests the trigger criteria to tell whether it is an

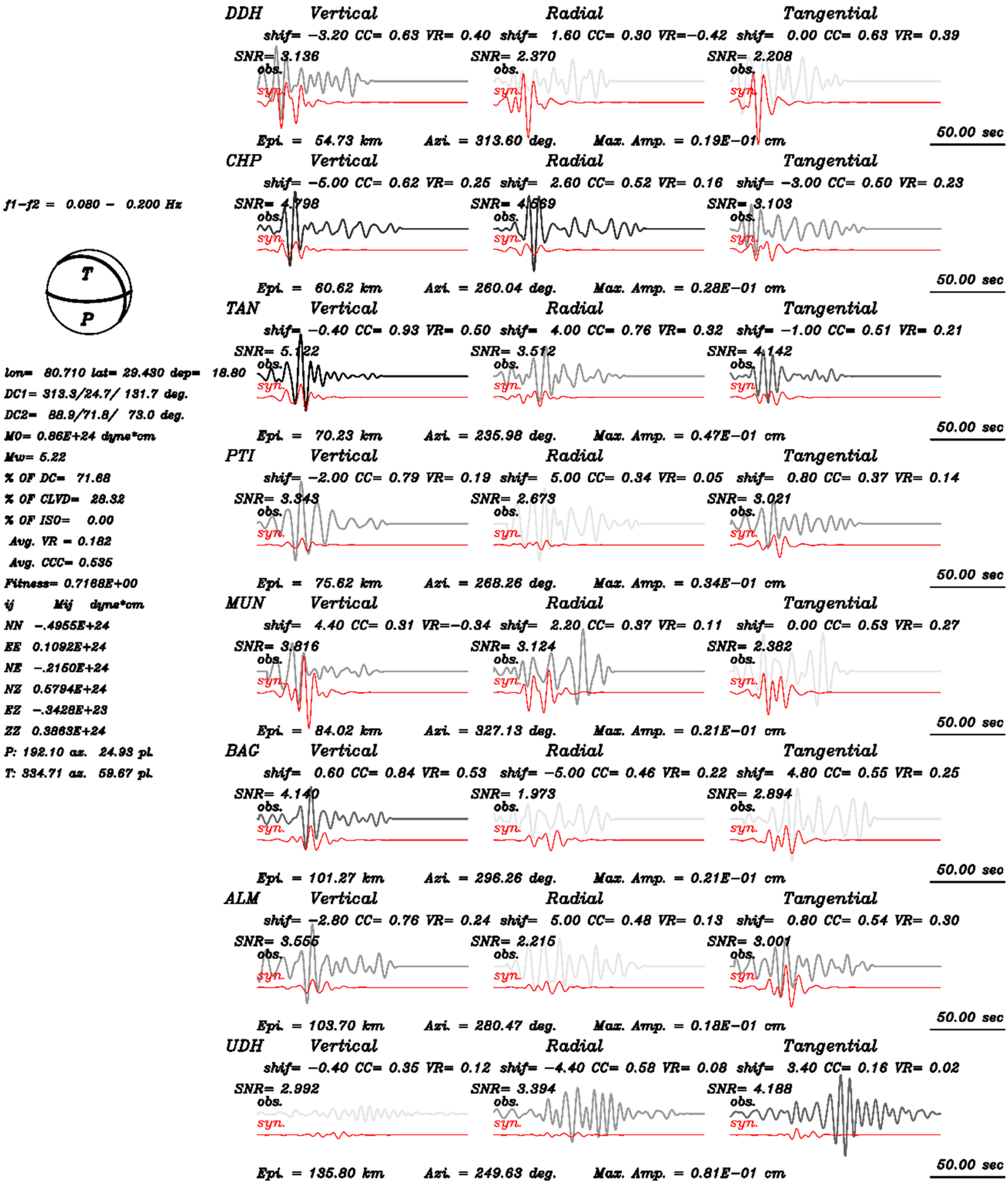

Fig. 3 Estimated focal mechanism for April 4, 2011 earthquake following Chao et al. (2011). This algorithm is based on minimizing the error between observed and synthetic seismogram

event. The trigger criteria (Mittal et al. 2018a) are empirical and are derived previously. The peak value of P_a is picked directly from seismograms, while these seismograms are integrated to get the values of P_v. A high-pass 0.075-Hz recursive Butterworth filter is applied to remove low-frequency drift during the integration process. The information from Pick_EEW is transferred to another shared memory Pick_Ring, which in turn provides information to TCPD module for calculation of earthquake source parameters.

Since SMIN is in triggered mode, less data length is available for drawing shake maps. Along with data length, some other problems also exist in the dataset which we used. For having an automated algorithm to plot shake maps, all the instruments should have the same component name and network name. Right now, in the Indian network, all the stations have different component and network names. All the data were corrected for having uniform information about component and network names. Above all, the most critical thing for plotting shake map is GPS timings, which is not correct in some of the instrumental records. For April 4, 2011 earthquake, 4 instruments out of 24 were not having correct GPS timings. These records were corrected for timing. Table 1 lists all the instruments recording April 4, 2011 earthquake along with observed PGA and computed PGV using shake map approach. In a network, where instruments operate in triggered mode instead of continuous recording, an alternate approach can be used for producing shake maps. This approach is based on using real-time data (continuous recording) from one hard rock site station (instead of all stations) and the transfer functions (amplification) of other sites w.r.t. hard rock site (Mittal et al. 2013c, 2015, 2018b). Transfer functions can be estimated using different approaches (Borcherdt 1970; Mittal et al. 2013a, b, 2016a).

Table 1 Detail of all the instruments recording April 4, 2011 (M 5.4) earthquake along with observed PGA and computed PGV using shake map approach

Station	Station code	PGA (cm/s^2) Observed	PGV (cm/s) Observed
Almora	ALM	11.56	1.09
Bageshwar	BAG	12.08	1.08
Barkot	BAR	6.77	0.95
Chamoli	CHA	17.57	3.71
Champawat	CHP	30.88	1.59
Didihat	DDH	17.58	2.38
Delhi	LDR	1.77	0.43
Dehradun	DEH	3.33	0.67
Dhanaulti	DNL	8.47	1.81
Dharchula	DRC	150.07	7.62
Fix	FIX	11.73	1.68
Garsain	GAR	21.68	2.01
Joshimath	JSH	10.71	1.86
Khatima	KHA	26.45	1.87
Kashipur	KSH	9.64	0.90
Kotdwar	KOT	6.43	0.61
Munsiari	MUN	23.03	2.16
Pithoragarh	PTH	63.19	5.29
Patti	PTI	9.37	3.90
Roorkee	ROO	4.70	0.92
Rudraprayag	RUD	8.14	0.78
Tanakpur	TAN	13.15	1.21
Tehri	TEH	6.78	0.88
U. S. Nagar	UDH	11.73	2.19

Results and discussion

For April 4, 2011 earthquake, the determination of the focal solutions was performed. The earthquake is located to the western edge of Nepal and eastern edge of India. According to earthquake report published by US Geological Survey (USGS), the hypocenter of the earthquake is reported at 29.698°N and 80.754°E having a focal depth of 26.1 km. USGS has also proposed fault plane solution of this earthquake, which suggests thrust mechanism (http://earthquake.usgs.gov/earthquakes/eventpage/usp000hz8k#moment-tensor). The moment tensor solution provided by Global Centroid Moment Tensor (GMCT) also suggests thrust mechanism as that of USGS but having a shallower depth of 18.8 km only. This earthquake was also reported by IMD. According to IMD, the earthquake is located at 29.67°N and 80.84°E with a focal depth of 10 km. Figure 3 shows the fault plane solution obtained for April 4, 2011 earthquake using the methodology of Chao et al. (2011), which is consistent with focal solution published by USGS as well as GMCT. According to the focal mechanism solution, one fault plane is found to dip toward NNE having strike direction parallel to the MCT. The matching is not so good between observed and synthetic records owing to the improper orientation of strong motion records. But, still, a good focal mechanism in agreement with other agencies is found; justifying our results. The focal solution was also performed for the September 21, 2009 earthquake, which also suggests thrust mechanism. We were not able to compare its focal mechanism with other agencies, as this is a smaller earthquake (Mw 4.5) and is prevented from being reported by the other international agencies. The focal mechanism of Uttarkashi and Chamoli earthquake also suggest the thrust mechanism, which is the general trend in this part of Himalayas (Ekström et al. 2012).

The recorded PGA and estimated PGV contours are plotted for two earthquakes. As the earthquake occurred on the eastern edge of the SMIN for April 4, 2011, there are fewer constraints on recorded PGA values toward the eastern side. Most of the instruments are located on the west, south and north sides of epicenter; which provides a good picture of PGA map in all three directions. We have tried to follow the PGA or PGV contour interval scheme from Wald et al. (1999), but keeping maximum values in mind, the contour values have been lowered. The SMIN generates very sparse shake map with a limited number of stations. In a country like Taiwan, with a dense array in operation, the shake map from the P-alert system provides much detailed shaking conditions (Wu et al. 2016).

PGA map (Fig. 4) for April 4, 2011 earthquake is consistent with the focal mechanism of the earthquake. The first PGA map is plotted as soon as five instruments experience PGA to be 2 gals. Being very near to epicenter, DRC station conceives maximum acceleration value during the first map only. As DRC station falls toward the eastern side of India very close to Nepal border, maximum PGA contours are formed initially toward the eastern side only. The PGA values decay rapidly toward SW, as other stations have not received maximum PGA, though they have triggered because of the threshold of 2 gals. The recording stations are the best indicator of recorded values; however, for all other places having no recording instrument, the shaking contours are drawn using interpolation involving distance inverse method. In terms of our interpolation method, the distance inverse method is quite commonly used and is quite a robust method. The most recent use of this method is discussed in ShakingAlarm (Yang et al. 2018). The second map is plotted after triggering of 11 instruments. By this time, around 7 instruments have received maximum PGA. This PGA is stored in memory for plotting final map. By the time, the third PGA map gets plotted, around 22 instruments have triggered. At this moment, the maximum PGA contour is confined toward the eastern side. Only one or two stations have recorded PGA to be over 100 gal, where site effect also plays an important role. The fourth map is the final PGA

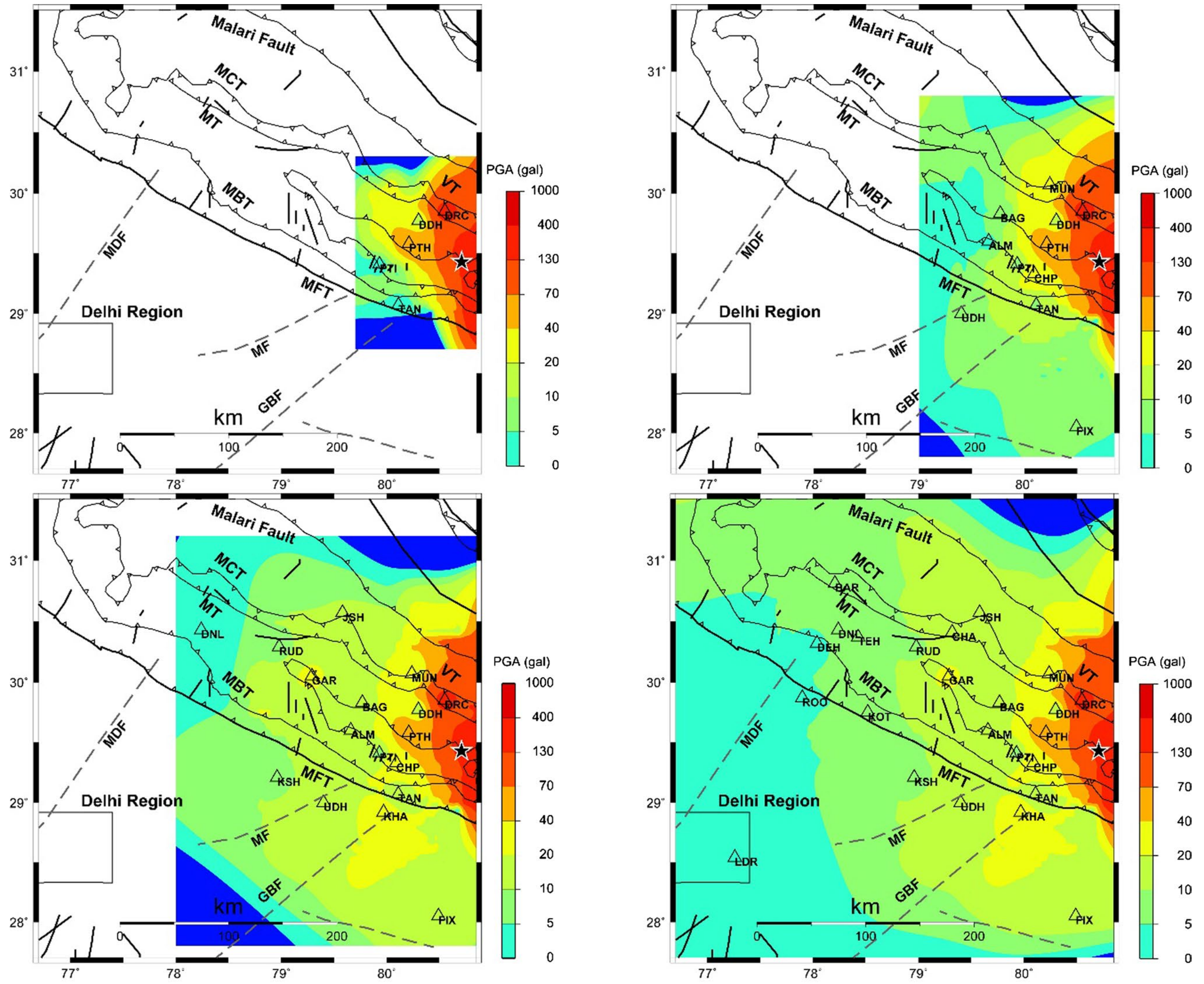

Fig. 4 PGA maps for April 4, 2011 earthquake. The first map is plotted after triggering of 5 instruments, second after 11 instruments, third after 22 instruments and fourth when all the instruments have conceived their maximum PGA. The PGA maps are consistent with focal mechanism of earthquake

map, where all 24 instruments have triggered with maximum PGA value. Almost the same kind of observation is made for PGV contours as shown in Fig. 5a–d. In a conventional real-time shake map methodology, the shake maps are plotted after every 1 min, once 10–12 instruments confirm PGA to be higher than 1.2 gals (Wu et al. 2013, 2016). This type of methodology is helpful in a country/region, where a dense array of recording instruments is in operation. PGV is supposed to be a better indicator of damage pattern than PGA (Boatwright et al. 2001; Wu 2015). During this earthquake, low computed PGV values are obtained. This may be the reason that much destruction was not reported during this earthquake, and even higher PGA values were reported in Dharchula area. We do not have any control on PGA and PGV values on the east side of the epicenter, as no recording instrument is there. All the instruments that are less than 15 km from the earthquake epicenter (EE) are considered to have PGA equal to EE.

Figure 6 gives the PGA shake maps for September 21, 2009 earthquake, which was recorded by 11 instruments. For this earthquake also, all the recording instruments lie toward the south of the epicenter. As no instrument is found toward the north of the epicenter, less constraint is there on PGA values toward the north.

Besides being helpful in damage assessment, shake maps provide useful information about source rupture direction (e.g., Wu et al. 2016, 2018). The source parameters of April 4, 2011 earthquake have been estimated in addition to confirming from USGS and GMCT. Based on the common focal mechanism solutions from all agencies, two nodal fault

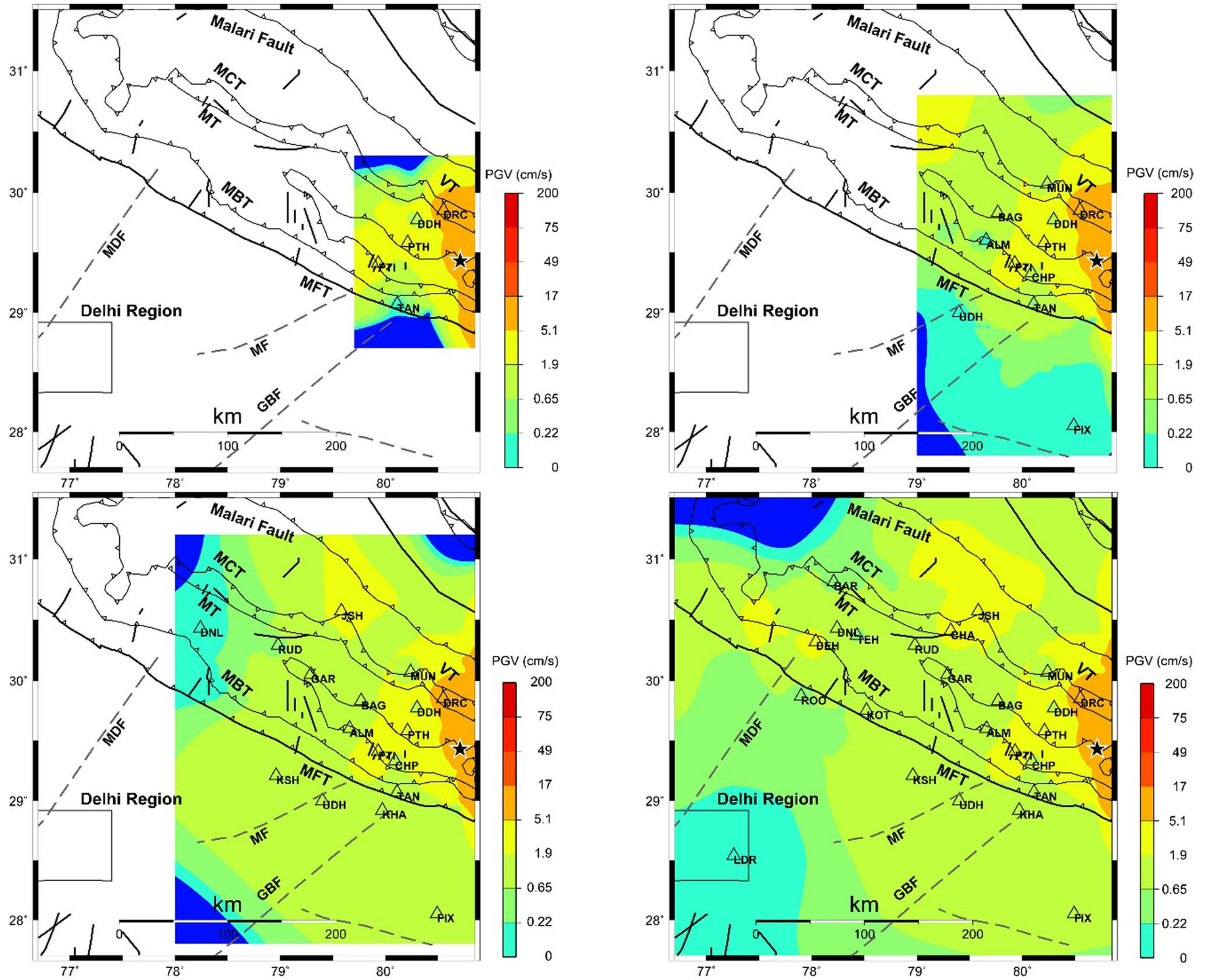

Fig. 5 PGV maps for April 4, 2011 earthquake (M 5.4). The general trend of PGV map is same as that of PGA maps. In general, PGV is better indicator of damage than PGA. During this earthquake, maximum PGV values are found to be less than 10 cm/s, which can be related to less/no damage during this earthquake

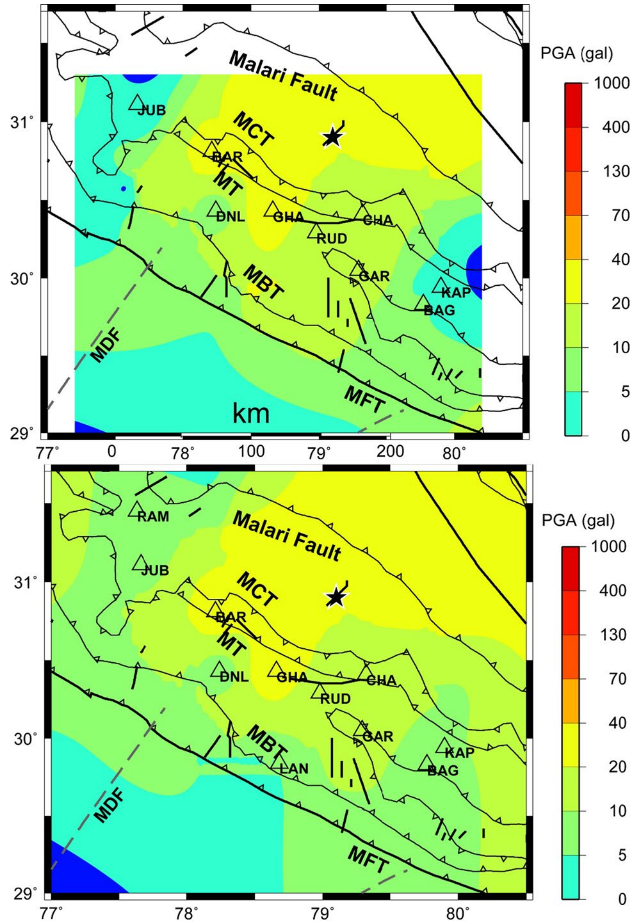

Fig. 6 PGA maps for September 21, 2009 earthquake (M 4.7). The first map is plotted after triggering of 9 instruments, while second is plotted when all the instruments have conceived their maximum PGA. No constraint is found on PGA values in northern side in the absence of recording instruments

planes have strikes about NW–SE. According to fault plane solution and PGA and PGV shake map results, the higher values are found to occur on the northwestern and southeastern side of the epicenter. Obviously, the fault plane may be the NW–SE one and the source may rupture northwestward. However, our interpretation regarding rupture direction is based on the available instrumental records. As no instrument was found on the eastern side of the epicenter, it is very difficult to comment about the rupture in the eastern side. From here, it can be inferred that source effect plays an important role.

Conclusions

Strong ground motion records provide an excellent opportunity to access damage pattern and risk mitigation in a particular region. The strong ground motion network (SMIN) in Uttarakhand, India, has provided useful data. Taking advantage of recorded data, an endeavor has been made to generate PGA and PGV shake maps for two earthquakes. The April 4, 2011 earthquake is well documented by different agencies including USGS and GMCT, which provides an opportunity to compare our estimated fault plane solution with the solution provided by others. The solution for this earthquake suggests thrust mechanism, which is in a good agreement with others and well as the general trend in Uttarakhand Himalayas. Although the fault mechanism has nothing to do in real-time shake map methodology, it is computed to compare with shake map pattern. The PGA and PGV contour maps for this earthquake are consistent with rupture process. The contours are also plotted for September 21, 2009 earthquake. Since this was recorded at 11 instruments only and we do not have any recording instrument toward the north side of the epicenter, less constraint is there on plotted shake maps. This kind of study for plotting shake maps using recorded data is first of its kind. For a country like Taiwan, plotting shake maps is a routine activity after the occurrence of any moderate earthquake. The densely installed instruments across the whole country assure the shake maps to be precise. Presently SMIN operates in threshold mode. Once it is changed to operate in real time, it will be very helpful for accessing the damage pattern. Simultaneously, an earthquake early warning (EEW) system is being installed in Uttarakhand Himalayas, a region where these two earthquakes were recorded. Earthworm software is used in EEW for receiving real-time data and computing various parameters. If these shake map algorithms can be implemented along with EEW algorithms that would be very helpful in identifying strong shaking areas, while an earthquake is happening. The shake maps in the present work are plotted using data from instruments where inter-station spacing is about 25 km. In the EEW system, the inter-station spacing is 10–15 km like Taiwan, so plotting shake map using combined data from these EEW and SMIN will be very helpful in generating accurate shake maps.

Data and resources

The strong motion waveform records used in this study are obtained from the Department of Earthquake Engineering, Indian Institute of Technology, Roorkee. The authors thankfully acknowledge www.pesmos.in (last accessed January 7, 2018) for providing waveforms to be used in this study.

Acknowledgements The authors are profusely thankful to the Ministry of Science and Technology of the Republic of China for funding the project, under which this study was carried out. The author (HM) is really thankful to Dr. Wei-An Chao for providing his code to estimate focal mechanism. GMT software from Wessel and Smith (1998) is used in the plotting part of the figures and is gratefully acknowledged.

References

Allen RM, Brown H, Hellweg M, Khainovski O, Lombard P, Neuhauser D (2009) Real-time earthquake detection and hazard assessment by ElarmS across California. Geophys Res Lett 36:L00B08. https://doi.org/10.1029/2008gl036766

Bilham R (1995) Location and magnitude of the Nepal earthquake and its relation to the rupture zones of the contiguous great Himalayan earthquakes. Curr Sci 69:101–128

BIS, IS, 1893–2002 (Part 1) Indian standard criteria for earthquake resistant design of structures, part 1—general provisions and buildings. Bureau of Indian Standards, New Delhi

Boatwright J, Thywissen K, Seekins L (2001) Correlation of ground motion and intensity for the 17 January 1994 Northridge California Earthquake. Bull Seismol Soc Am 91:739–752

Borcherdt RD (1970) Effects of local geology on ground motion near San Francisco Bay. Bull Seismol Soc Am 60:29–61

Chao WA, Zhao L, Wu YM (2011) Centroid fault-plane inversion in three-dimensional velocity structure using strong-motion records. Bull Seismol Soc Am 101(3):1330–1340

Chen DY, Hsiao NC, Wu YM (2015) The Earthworm based earthquake alarm reporting system in Taiwan. Bull Seismol Soc Am 105:568–579. https://doi.org/10.1785/0120140147

Ekström G, Nettles M, Dziewoński AM (2012) The global CMT project 2004–2010: centroid-moment tensors for 13,017 earthquakes. Phys Earth Planet Inter 200:1–9

Frohlich C, Apperson KD (1992) Earthquake focal mechanisms, moment tensors, and the consistency of seismic activity near plate boundaries. Tectonics 11(2):279–296

Gahalaut K, Rao NP (2009) Stress field in the western Himalaya with special reference to the 8 October 2005 Muzaffarabad earthquake. J Seismol 13:371–378

Gansser A (1964) Geology of the Himalayas. Interscience, New York, p 289

Gaur VK, Chander R, Sarkar I, Khattri KN, Sinvhal H (1985) Seismicity and state of stress from investigations of local earthquakes in the Kumaun Himalaya. Tectonophysics 118:243–251

Graves RW (1996) Simulating seismic wave propagation in 3D elastic media using staggered-grid finite differences. Bull Seismol Soc Am 86:1091–1106

Gupta S, Gupta ID (2004) Prediction of earthquake peak ground acceleration in Koyna region, India. 13 WCEE, Vancouver, Canada, Aug 1–6, 2004, paper no. 1437

Gupta S, Kumar S, Wason HR, Das R (2012) A statistical analysis of completeness of earthquake data around Dehradun city and its implications for seismicity evaluation. 15WCEE, Lisbon, Portugal, Sept 24–28, 2012, paper no. 3539

Johnson CE, Bittenbinder A, Bogaert B, Dietz L, Kohler W (1995) Earthworm: a flexible approach to seismic network processing. Inc Res Inst Seismol Newsl 14(4):1–4

Kanaujia J, Kumar A, Gupta SC (2016) Three-dimensional velocity structure around Tehri region of the Garhwal Lesser Himalaya: constraints on geometry of the underthrusting Indian plate. Geophys J Int 205(2):900–914

Khattri KN (1999) An evaluation of earthquakes hazard and risk in northern India. Himalayan Geol 20:1–46

Khattri KN, Chander R, Gaur VK, Sarkar I, Kumar S (1989) New seismological results on the tectonics of the Garhwal Himalaya. Proc Indian Acad Sci (Earth Planet Sci) 98:91–109

Kumar N, Khandelwal DD (2015) Strong motion data analysis of the 4 April 2011 Western Nepal earthquake (M 5.7) and its implications to the seismic hazard in the Central Himalaya. Curr Sci 109(10):1822–1830

Kumar N, Sharma J, Arora BR, Mukopadhyay S (2009) Seismotectonic model of the Kangra-Chamba sector of Northwest Himalaya: constraints from joint hypocenter determination and focal mechanism. Bull Seismol Soc Am 99:95–109

Kumar A, Mittal H, Sachdeva R, Kumar A (2012) Indian Strong Motion Instrumentation Network. Seismol Res Lett 83(1):59–66

Legendre CP, Deschamps F, Zhao L, Chen QF (2015a) Rayleigh-wave dispersion reveals crust-mantle decoupling beneath eastern Tibet. Sci Rep 5:16644. https://doi.org/10.1038/srep16644

Legendre CP, Zhao L, Chen QF (2015b) Upper-mantle shear-wave structure under East and Southeast Asia from Automated Multimode Inversion of waveforms. Geophys J Int 203(1):707–719. https://doi.org/10.1093/gji/ggv322

Legendre CP, Tseng TL, Mittal H, Hsu CH, Karakhanyan A, Huang BS (2017) Complex wave propagation revealed by peak ground velocity maps in the Caucasus Area. Seismol Res Lett 88(3):812–821

Liang X, Zhou S, Chen YJ, Jin G, Xiao L, Liu P, Fu Y, Tang Y, Lou X, Ning J (2008) Earthquake distribution in Southern Tibet and its tectonic implications. J Geophys Res 113:B12409. https://doi.org/10.1029/2007JB005101

Mittal H, Kumar A (2015) Stochastic finite-fault modeling of M w 5.4 earthquake along Uttarakhand-Nepal border. Nat Hazards 75(2):1145–1166

Mittal H, Gupta S, Srivastava A, Dubey RN, Kumar A (2006) National strong motion instrumentation project: an overview. In: 13th Symposium on earthquake engineering, Indian Institute of Technology, Roorkee, Dec 18–20, 2006, 107–115, New Delhi: Elite Publishing

Mittal H, Kumar A, Ramhmachhuani R (2012) Indian national strong motion instrumentation network and site characterization of its stations. Int J Geosci 3(6):1151–1167

Mittal H, Kumar A, Kumar A (2013a) Site effects estimation in Delhi from the Indian strong motion instrumentation network. Seismol Res Lett 84(1):33–41

Mittal H, Kamal, Kumar A, Singh SK (2013b) Estimation of site effects in Delhi using standard spectral ratio. Soil Dyn Earthq Eng 50:53–61

Mittal H, Kumar A, Kamal (2013c) Ground motion estimation in Delhi from postulated regional and local earthquakes. J Seismol 17(2):593–605

Mittal H, Kumar A, Kumar A, Kumar R (2015) Analysis of ground motion in Delhi from earthquakes recorded by strong motion network. Arab J Geosci 8(4):2005–2017

Mittal H, Wu YM, Chen DY, Chao WA (2016a) Stochastic finite modeling of ground motion for March 5, 2012, Mw 4.6 earthquake and scenario greater magnitude earthquake in the proximity of Delhi. Nat Hazards 82(2):1123–1146

Mittal H, Kumar A, Wu YM, Kumar A (2016b) Source study of M w 5.4 April 4, 2011 India-Nepal border earthquake and scenario events in the Kumaon-Garhwal Region. Arab J Geosci 9(5):348

Mittal H, Wu YM, Sharma ML, Yang BM, Gupta S (2018a) Testing the performance of earthquake early warning system in northern India. Acta Geophys 67:59–75. https://doi.org/10.1007/s11600-018-0210-6

Mittal H, Wu YM, Sharma ML, Lin TL, Yang BM (2018b) Shake maps generation for Delhi region using two different algorithms. In: 16th symposium on earthquake engineering, Indian Instiute of Technology, Roorkee, Dec 20–22

Mozziconacci L, Delouis B, Angelier J, Hu JC, Huang BS (2009) Slip distribution on a thrust fault at a plate boundary: the 2003 Chengkung earthquake, Taiwan. Geophys J Int 177(2):609–623

Olivieri M, Clinton J (2012) An almost fair comparison between Earthworm and Seiscomp3. Seismol Res Lett 83:720–727

Olsen KB (1994) Simulation of three-dimensional wave propagation in the Salt Lake Basin. Ph.D. Thesis, University of Utah, Salt Lake City, Utah

Seeber L, Armbruster JG (1981) Great detachment earthquakes along the Himalayan arc and long-term forecasting. In: Earthquake prediction: an international review. Maurice Ewing Series 4, American Geophysical Union, Washington, DC, pp 259–277

Srivastava P, Mitra G (1994) Thrust geometries and deep structure of the outer and lesser Himalaya, Kumaon and Garhwal (India): implications for evolution of the Himalayan fold-and-thrust belt. Tectonics 13(1):89–109

Valdiya KS (1980) Geology of Kumaun Lesser Himalaya, interim record: Dehradun. Dehradun, Wadia Institute of Himalayan Geology, p 289

Wald DJ, Quitoriano V, Heaton TH, Kanamori H, Scrivner CW, Worden CB (1999) TriNet "ShakeMaps": rapid generation of peak ground motion and intensity maps for earthquakes in southern California. Earthq Spectra 15(3):537–555

Wessel P, Smith WHF (1998) New, improved version of generic mapping tools released. Eos, Trans Am Geophys Union. https://doi.org/10.1029/98EO00426

Wu YM (2015) Progress on development of an earthquake early warning system using low cost sensors. Pure appl Geophys 172:2343–2351. https://doi.org/10.1007/s00024-014-0933-5

Wu YM, Hsiao NC, Teng TL (2004) Relationships between strong ground motion peak values and seismic loss during the 1999 Chi-Chi, Taiwan earthquake. Nat Hazards 32:357–373

Wu YM, Chen DY, Lin TL, Hsieh CY, Chin TL, Chang WY, Li WS, Ker SH (2013) A high density seismic network for earthquake early warning in Taiwan based on low cost sensors. Seismol Res Lett 84:1048–1054. https://doi.org/10.1785/0220130085

Wu YM, Liang WT, Mittal H, Chao WA, Lin CH, Huang BS, Lin CM (2016) Performance of a low-cost earthquake early warning system (P-alert) during the 2016 ML 6.4 Meinong (Taiwan) Earthquake. Seismo Res Lett 87(5):1050–1059. https://doi.org/10.1785/0220160058

Wu YM, Mittal H, Huang TC, Yang BM, Jan JC, Chen SK (2018) Performance of a low-cost earthquake early warning system (P-alert) and shake map production during the 2018 Mw 6.4 Hualien (Taiwan) Earthquake. Seismol Res Lett (accepted)

Yagi Y, Okuwaki R (2015) Integrated seismic source model of the 2015 Gorkha, Nepal, earthquake. Geophys Res Lett 42(15):6229–6235

Yang BM, Huang TC, Wu YM (2018) ShakingAlarm: a nontraditional regional earthquake early warning system based on time-dependent anisotropic peak ground-motion attenuation relationships. Bull Seismol Soc Am 108(3A):1219–1230. https://doi.org/10.1785/0120170105

Zhao L, Chen P, Jordan TH (2006) Strain Green's tensors, reciprocity and their applications to seismic source and structure studies. Bull Seismol Soc Am 96:1753–1763

Acta Geophysica (2019) 67:765–773
https://doi.org/10.1007/s11600-019-00282-6

RESEARCH ARTICLE - SOLID EARTH SCIENCES

Seismicity evaluation of Mongton area of Salween in Myanmar

Chao Lian[1,2] · **Yuyang Kong**[1,2] · **Xinqiang Chen**[1,2] · **Yueqiang Qiao**[1,2]

Received: 21 November 2018 / Accepted: 25 March 2019 / Published online: 28 March 2019

Abstract

The area of Mongton is located in the central part of main stream of Salween. There has a straight-line distance of 200 km to the border of China's Yunnan Province and 90 km to the border of Chiang Mai Province of Thailand. There are two earthquake concentrating regions of destructive earthquakes within this area. It reflects the collision between the Indian plate and the Eurasian plate. The main regional seismic activity characteristics are summarized as follows in accordance with the spatial-temporal distribution characteristics of the seismic activity and the estimated future seismic trend of the area under analysis: (1) There are 132 times of destructive earthquake occurrences of $M \geq 4.7$ that occurred ever since the record within this area. There are 2915 modern small earthquakes of $4.6 \geq M \geq 2.0$ being recorded within this area totally since 1966. (2) Orientation of axis P of the maximum principal compressive stress of the regional focal mechanism solutions is mainly distributed in the angular domain in the direction of NNE–NE–NEE and under the horizontal action, which indicates that the distribution of the tectonic stress fields within the area is very complicated with the spreading of the earthquake fracture planes displaying a characteristic multi-directionality. (3) This area is located at the intersection of the Himalayan Seismic Belt and the Southwestern Yunnan Seismic Belt; the seismic activities involved display an obvious alternate quiescence and active phenomenon. It will experience a strong seismic activity level similar to that of the previous 100 years in the future 100 years. Large earthquakes are likely to occur within this area.

Keywords Seismic activity characteristics · Salween in Myanmar · Earthquake engineering

Introduction

Mongton hydropower station is located at around 20 km upstream of Wan Hsa-la Village between Mongton and Mong Pan at the middle reach of the trunk stream of Salween River within the territory of Myanmar. The site has a straight-line distance of 200 km to the border of China's Yunnan Province and 90 km to the border of Chiang Mai Province of Thailand. Currently, there is an upper and a lower optional dam site apart from each other at a distance no more than 10 km at the most. And their geographic coordinates are E98.588°, N20.608° and E98.604°, N20.548°, respectively. According to the project design, the normal storage water level is 395 m, the installed capacity is 7100 MW and the average annual energy generation is 35.823 billion kw h. The dam is preliminarily designed to have a dam height of 230 m or so and the elevation of the available rock foundation face of the deepest foundation of the riverbed around 170 m with the dam type to be decided. The seismicity of the research area is quite active. In the area, the small earthquakes are concentrated and large earthquakes are seriously absent. The lack of seismic research makes more difficult to construct the major local projects and to do geology, geophysics and earthquake engineering studies. Because of the economic and political reasons in this area, no relevant research has been done before. Soe and Aye (2002) do the study about the seismicity and seismological work of Myanmar. But the work is overall study

✉ Chao Lian
lianchao9612@163.com

Yuyang Kong
46277899@qq.com

Xinqiang Chen
81604268@qq.com

Yueqiang Qiao
yjsfeng@163.com

[1] Hubei Key Laboratory of Earthquake Early Warning, Institute of Seismology, China Earthquake Administration, Hongshan Sideway #40, Wuhan 430071, China

[2] Wuhan Institute of Earthquake Engineering Co., Ltd, Hongshan Sideway #40, Wuhan 430071, China

with strong earthquakes and do not include specific research. In our study, the catalogues of earthquakes are collected from many research institutes and organizations. Many of earthquakes have not been systematically collated and published. Based on a large number of seismic data, the temporal and spatial distribution characteristics of earthquake are evaluated. The focal mechanism on the area indicates that the distribution of tectonic stress field within the region is relatively complicated and the earthquake fracture plane is multi-directional. The seismicity study in Mongton area will bring convenience to other disciplines and engineering constructions.

Data range

Given that the structures within the region are very complicated and earthquakes are active at Ruili and Canglan to the north and Central Myanmar Basin to the west with extremely developed seismic structures, it is determined upon comprehensive consideration that the area shall be moderately expanded to Ruili Basin to the north and to Sagaing and Boba to the west, including partial Central Myanmar Basin with the research range to be 18.5°N–24.0°N; 95.73°E–110.13°E.

Study area range

According to the seismic belt delineation plan in the 2001 version Seismic Ground Motion Parameter Zonation Map of China, in addition to the seismic geological factor, seismic activity, and other consistent factors in multiple aspects under consideration, it also emphasizes the characteristics of them as the statistical units in determining the seismic activity parameters in the delineation of the seismic zones and seismic belts. Further modification and improvements have been made through applications and practices in the parameter determination and trend analysis as well as consultation with related experts for comments.

Seismic data

The seismic data are the basic data for the study of the seismic activity. In this report, a catalogue of destructive earthquakes within the range of this area has been compiled and discussions on the basis and integrity of the seismic data selection are provided as well.

Basis of seismic data

The research area included two part areas. Most of the area is located inside Myanmar and its eastern and northern parts are located in China's Yunnan Province and Thailand. The seismic data are mainly acquired through citing and checking the Catalogue of World Earthquakes (1900 AD—1980) (Shi et al. 1986), Catalogue of Chinese Historical Strong Earthquakes (23rd century BC—1911) (Earthquake Disaster Prevention Center of China Earthquake Administration 1995), Catalogue of Chinese Modern Earthquakes (1912 AD—1990) (Earthquake Disaster Prevention Center of China Earthquake Administration 1999) and Catalogue of Chinese Earthquakes (1831 BC–1969 AD) (Gongxu 1983). The observation data from the regional earthquake networks in Yunnan, the catalogue of earthquakes of China Earthquake Network Center (CENC) (http://www.csndmc.ac.cn/newweb/, in Chinese) and simple catalogue of world earthquakes (1975–2010) provided by USGS of the USA (https://earthquake.usgs.gov/earthquakes/). The origin time of earthquake is uniformly calibrated to the Greenwich Mean Time (GMT). The catalogue of China Earthquake Network Center is located by using the absolute earthquake location method Hypo2000. The expression forms of earthquake magnitudes adopted in each catalogue are different, and it is generally converted into M. In order to compile the magnitudes of instrumental recorded earthquake and historical earthquakes together, we rescaled the M_L, M_b and M_s into M. The magnitude M_s is approximate as M. The conversion between M_b and M_L with the magnitude (M) is obtained by the formulas of $M = 1.13\ M_L - 1.08$ and $M = 1.17\ M_b - 0.41$ (The Earthquake Disaster Defense Department of the State Seismological Bureau 1990). The expression forms for relatively uncertain earthquakes are selectively adopted sometimes due to their different representations in various cited references. Taking the $M8$ earthquake in Taunggyi of Myanmar in 1912 for example, it has been represented in some cited references (Li and Zhu 1995; Fu and Wang 1992) but has not been mentioned in most of the data. It has been taken into consideration in the delineation of the potential seismic source zones, but this seismic factor has not been taken as a key consideration in terms of the influences on the site for its calculated result is smaller than the biggest influence result due to the limitation of the data available.

Analysis of the integrity of regional seismic data

This area has a relatively large range, and very few historical records of earthquakes, among which the early seismic data are missing, that of the earthquakes lower than $M5$ is seriously missing and the record of the destructive earthquakes originated from 1128 AD. Along with the gradual establishment of the earthquake networks around the world since 1900, the seismic records observed by instruments started from 1906 in this area and 98% of the strong earthquakes from then on have instrument-observed data, from which it is estimated that the possibility of omitted records of earthquakes over $M6$ is very low. This area is involved with the

Himalayan Seismic Belt and Southwestern Yunnan Seismic Belt. Judging from the seismic records and activity study of these two seismic belts, the earthquakes of $M \geq 5$ of the Himalayan Seismic Belt and Southwestern Yunnan Seismic Belt are basically complete since 1900.

The regional seismic networks in Yunnan Province of our country can basically cover the overall province since 1970 and the earthquake-monitoring capability therefore has been increased to some extent, which can basically control the earthquakes over $M3.0$ within Yunnan Province and a surrounding area of about 100–150 km to the perimeter of Yunnan Province. Moreover, the earthquakes of this area after 1970 could be retrieved in the catalogue of earthquakes of China Seismograph Network (CSN). It is concluded through analysis that the earthquakes over $M3.0$ within Yunnan Province and its surrounding areas are basically complete since 1970 and the possibility of omitted records of earthquakes over $M4.0$ within the area is very low (Fig. 1).

In order to analyze the integrity of earthquakes which have been collected, the Gutenberg–Richter curve is shown in Fig. 2. In Fig. 2, x-axis shows the number of earthquakes with different magnitude. Y-axis is the frequent of these earthquakes. The b which is the slope on the line is 0.6362. The integrity of the regional destructive earthquakes is satisfied to meet with the requirement of seismicity study of Mongton area of Salween in Myanmar. Compared with adjacent area, the integrity of regional destructive earthquakes in Mongton area of Salween in Myanmar is relatively complete (Chen and Fu 2007). The result could be used as the reference basis for the study of the regional seismic activity and the estimation of their parameters in this project.

Regional seismic activity

Temporal characteristics of the seismic activity

The seismic activity patterns and trends could be understood through the studies on the spatial-temporal distribution characteristics of the regional seismic activities. The analysis of the historical seismic influence tells us that seismic damage suffered by this area any destruction in the recorded history. Scientific and reasonable seismic environment assessment within the region is the basis of the seismic safety evaluation which is helpful for reasonably dividing the potential seismic source zones and determining the seismic activity parameters.

A catalogue of regional destructive earthquakes ($M \geq 4.7$) has been compiled based on the aforementioned seismic data. Table 1 is a statistic table of the magnitudes and frequencies of the regional destructive earthquakes.

As is shown in Table 1, there are 132 times of destructive earthquakes ($M \geq 4.7$) recorded within this area totally from the year of 1611 AD to the year of 2011 including 93 times

Fig. 1 Map of the site (Site: black triangle)

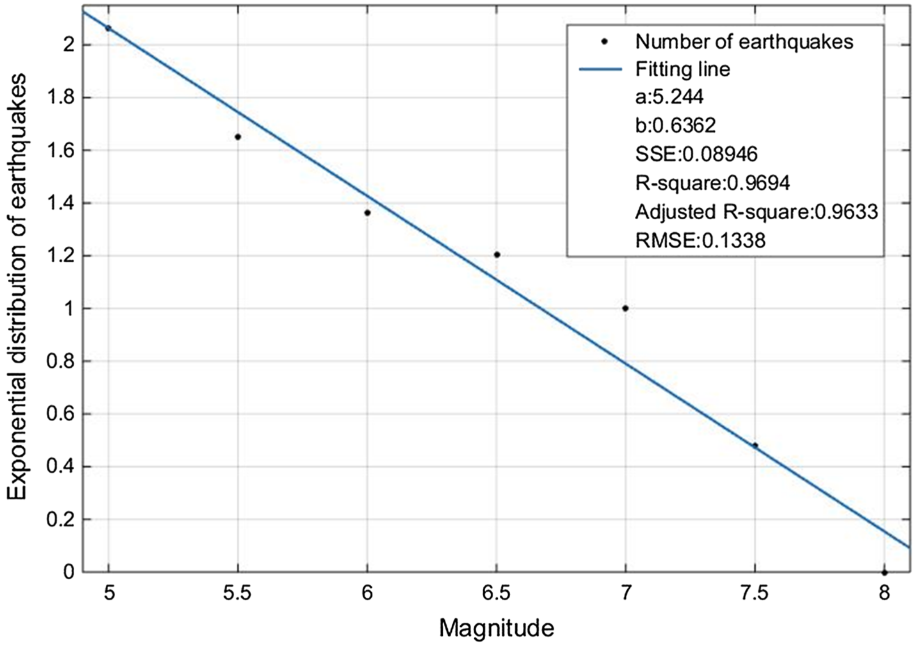

Fig. 2 The Gutenberg–Richter curve for the earthquake catalogue. **a** The intercept of fitting line; **b** the slope of fitting line; SSE: the sum of squares due to error; R-square: coefficient of determination; adjusted R-square: degree-of-freedom adjusted coefficient of determination; RMSE: root mean squared error

Table 1 Summary of magnitudes and frequencies of regional destructive earthquakes (1611–December 2011, $M \geq 4.7$)

Magnitude grade	4.7–4.9	5.0–5.9	6.0–6.9	7.0 and above
Earthquake number	16	93	13	10

Table 2 Summary of magnitude grades and earthquake number of regional modern small earthquakes (1966–December 2011, $3.0 \leq M \leq 4.6$)

Magnitude grade	2.0–2.9	3.0–3.9	4.0–4.6
Earthquake number	2359	502	54

at *M*5.0–5.9, 13 times at *M*6.0–6.9 and 10 times at *M*7.0–7.9. Among which, the earliest earthquake in history was the $M4\frac{3}{4}$ earthquake that occurred in Ruili of Yunnan in April, 1611; the biggest earthquake was the *M*8 earthquake that occurred in Taunggyi of Myanmar in May 23, 1912.

It is known from Table 1 that this area has a relatively higher level both in the seismic activity frequency and strength.

The catalogue of the regional modern small earthquakes (1966–2011, $4.0 \leq M \leq 4.6$) had been compiled. Then, the statistics is making. Table 2 is the summary of the magnitude grades and numbers of the regional modern small earthquakes.

As is shown in Tables 3 and 4, the modern small earthquakes within the area since 1970 are mainly small earthquakes and micro-earthquakes with 2915 earthquakes of $2.0 \leq M \leq 4.6$ being recorded including 2359 earthquakes of *M*2–2.9, 502 earthquakes of *M*3–3.9 and 54 earthquakes of *M*4–4.6. Since the western area is located within Myanmar, most of the records of the modern instruments are records provided by earthquake networks in China's Yunnan Province with the records of the small earthquakes being seriously missing.

It could be seen from Table 3 that the earliest recorded earthquake among the regional modern small earthquakes of $M4.0 \leq M \leq 4.6$ was the *M*4.0 earthquake that occurred in Myanmar on June 14, 1966; the latest earthquake was the *M*4.2e earthquake that occurred in Myanmar in June 23, 2007.

It is known from Tables 3 and 4 that the activity frequency of the regional modern small earthquakes is intermediate (Li and Zhu 1995).

Distribution characteristics of the seismic source

The distribution map of epicenters of regional destructive earthquakes (Fig. 3) and the distribution map of epicenters of regional modern small earthquakes (Fig. 4) are compiled on the basis of the catalogue of regional destructive earthquakes ($M \geq 4.7$) and the catalogue of regional modern small earthquakes ($2.0 \leq M \leq 4.6$) to display the spatial distribution characteristics of the regional seismic activities. There are two earthquake concentrating regions of destructive earthquakes within this area: the northern mountain area in middle Myanmar where the northeast striking seismic stripes and belts gradually change its orientation into near north–south from the south to the north and the earthquake concentrating region near Naypyidaw both reflecting the collision of Indian Plate and Eurasian Plate; and the Cangyuan–Lancang region in the northeastern part of the

Table 3 Regional focal mechanism solutions of earthquakes

No.	Earthquake occurrence time	Location of epicenter			Magnitude	Nodal surface *A*		Nodal surface *B*		Axis *P*		Axis *T*	
	Y-M-D	Latitude/°	Longitude/°	Reference place name		Strike	Dip angle	Strike	Dip angle	Orientation	Dip angle	Orientation	Dip angle
1	19411226	22.7	99.9	Lancang of Yunnan	7	232	85	141	89	96	3	186	4
2	19500203	21.7	100.1	Southwestern Menghai of Yunnan	7			77	80	347	55		
3	19500203	22.1	99.9	Southeastern Menglian of Yunnan	$6\frac{3}{4}$	149	85	59	90	194	4	284	4
4	19520619	22.7	99.8	Near Lancang of Yunnan	6.5	153	90	63	77	19	9	287	9
5	19521218	22.9	99.7	Northwestern Lancang of Yunnan	$5\frac{3}{4}$	341	90	251	77	26	9	295	10
6	19810912	21.06	99.35	Common border of Myanmar and China	5.4	77	60	341	79	32	12	295	29
7	19840423	22.04	99.14	Common border of Myanmar and China	6.5	84	69	349	78	37	6	305	24
8	19881106	22.92	99.79	Northern Lancang of Yunnan	7.4	333	78	64	84	198	4	289	13
9	19881107	23.37	99.52	Southern Gengma of Yunnan	5.4	122	55	6	58	65	2	333	51
10	19881115	23.18	99.71	Southeastern Gengma of Yunnan	5.6	333	70	63	90	196	14	290	14
11	19881127	22.74	99.94	Common border of Myanmar and China	5.8	71	61	334	78	25	11	289	29
12	19881130	22.76	99.95	Common border of Myanmar and China	6.5	167	75	76	87	31	12	122	9
13	19890301	21.75	97.94	Myanmar	5.4	73	79	341	82	27	2	297	14
14	19890507	23.52	99.62	Common border of Myanmar and China	6.2	335	76	68	79	201	3	292	18
15	19890928	20.33	98.82	Myanmar	5.7	76	72	167	89	33	14	300	12
16	19890930	20.24	98.85	Myanmar	5.6	85	78	352	78	308	17	38	0
17	19910105	23.50	96.00	Myanmar	7.6	2	68	97	77	228	6	321	25
18	19920423	22.30	99.10	Common border of Myanmar and China	6.7	354	77	262	79	218	17	308	1
19	19920423	22.60	99.00	Common border of Myanmar and China	6.9	345	68	252	84	207	20	301	11
20	19920615	23.99	95.89	Myanmar	6.3	8	69	275	83	229	20	323	10
21	19921028	19.00	96.28	Myanmar	5.6	68	65	335	84	24	13	289	22
22	19940911	19.59	99.52	Southwestern Asia	5.2	64	27	206	68	89	63	309	21
23	19950710	22.00	99.20	Common border of Myanmar and China	6.2	64	66	333	88	21	15	286	19
24	19950711	22.00	99.30	Common border of Myanmar and China	7.3	60	85	330	89	15	3	285	4
25	20030921	19.83	95.76	Myanmar	5.3	8	71	100	83	233	8	326	19
26	20031030	19.81	95.74	Myanmar	5.9	121	42	336	54	50	6	301	71
27	20031219	19.85	95.70	Myanmar	6.1	136	39	346	55	63	8	304	73
28	20050208	19.82	95.80	Myanmar	5.7	129	46	356	55	64	5	323	64
29	20060802	19.08	95.74	Myanmar	4.7	4	87	274	88	229	4	319	1
30	20070107	22.02	98.20	Common border of Myanmar and China	4.8	92	71	182	89	49	15	316	13
31	20070623	21.47	99.78	Common border of Myanmar and China	5.6	61	81	330	82	15	1	285	12
32	20070623	21.55	99.91	Common border of Myanmar and China	5.4	334	60	237	79	192	30	289	12
33	20070730	19.31	95.61	Myanmar	5.6	322	44	127	47	225	1	325	82

Table 3 (continued)

No.	Earthquake occurrence time	Location of epicenter		Reference place name	Magnitude	Nodal surface A		Nodal surface B		Axis P		Axis T	
	Y-M-D	Latitude/°	Longitude/°			Strike	Dip angle	Strike	Dip angle	Orientation	Dip angle	Orientation	Dip angle
34	20070731	19.24	95.61	Myanmar	5.0	313	43	138	47	226	2	95	86
35	20081220	22.75	95.90	Myanmar	5.2	359	79	90	82	224	2	315	13
36	20081225	23.97	97.57	Common border of Myanmar and China	5.1	353	76	84	84	218	6	309	14
37	20100319	21.36	100.11	Common border of Myanmar and China	5.1	234	63	332	74	195	31	101	7
38	20110324	20.72	99.82	Myanmar	7.2	339	79	70	85	204	4	295	11
39	20110324	20.59	99.86	Myanmar	5.2	347	72	80	79	213	4	304	21
40	20110325	20.68	99.74	Myanmar	5.9	8	63	104	78	233	10	329	28

No. 1, 3–5, 36 from Yunnan Earthquake Administration, CEA; No. 2, 6–35, 37–40 from HR

area within the territory of China where the earthquakes are concentrated in groups and distributed in a rough north-northwest direction and a belt shape. Chen (2007) believes that the fault generated by the Longling $M7.3$ and $M7.4$ earthquakes in 1976. The $M7.3$ earthquake is the developed northeast fault zone (called as Zhaoyang fault zone) and that by the $M7.4$ earthquake the northeast—east fault zone (called as Jinzhuping fault zone) in the granite body through comprehensive analysis based on the aftershocks spatial distribution maps and distribution of surface seismic crack belts.

Within this area, the record of earthquakes by the modern instrument is relatively complete in China's Yunnan Province while the record of small earthquakes by the modern instrument is seriously missing in the western area for it is within the territory of Myanmar.

Cummins (2007) developed that there is a potential tsunami threat in this area.

Generally speaking, the seismic activity within the area is at a relatively high level.

There are 121 historical earthquakes been recorded within this area. In this report, these earthquakes have been utilized to analyze the regional seismic source depth characteristics. Figure 5 is the profile of the regional seismic source depth. According to the statistics, the average seismic source depth is 35 km, which indicates that the earthquakes are mainly concentrated in the earth crust and belonging to the shallow focus earthquakes.

Regional focal mechanism solution and modern tectonic stress field

Focal mechanism solution

The eastern area covers the western area of Yunnan Province and the middle and western area includes the northern areas of Myanmar and Thailand. The program Seiscap was used for the focal mechanisms of $M \geq 4.6$, and earthquakes during 1981–2011 are obtained totally in the study area (Table 3). The collected data of the areas within China's territory are mainly obtained from the Seismological Bureau of Yunnan Province; the data of the overseas areas are obtained from Harvard University (HRV) in the USA (https://www.globalcmt.org/). Figure 6 is the diagram of regional focal mechanism solutions.

The focal mechanism solutions of earthquake and stress fields of the seismic source within the area display a good consistency. The orientation of Axis P of the maximum principal compressive stress is mainly distributed in the angular domain in the direction of NNE–NE–NEE with the minority in the angular domain in the direction of SSE–SE and the dip angles mostly smaller than 30°. In the Nodal Surface I, mainly characteristic of right-lateral strike-slip dislocation,

Table 4 Summary of nodal surface dip angles and principal compressive stress axis angles of altitude of focal mechanism solutions in local and neighboring areas

Parameter	Dip angle or angle of altitude %						
	> 60	45–60	≥ 45	30–44	15–29	< 15	< 30
Nodal surface I	56	29	85	13	2	0	2
Nodal surface II	75	25	100	0	0	0	0
Axis *P*	6	0	6	8	17	69	86
Axis *T*	15	4	19	21	27	33	60
Axis *N*	46	27	73	4	10	13	23

The result is obtained by statistics of collected focal mechanism solutions. One part of the focal mechanism solutions are from the Seismological Bureau of Yunnan Province. Another part of the focal mechanism solutions are from Harvard University (HRV) in the USA

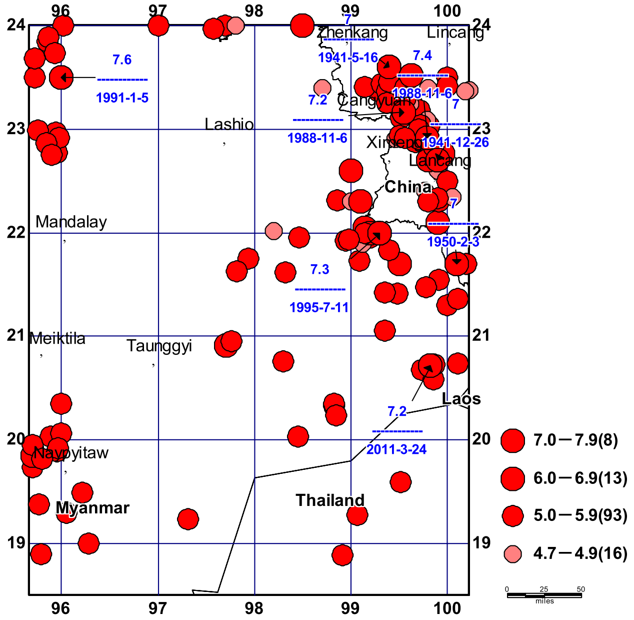

Fig. 3 Distribution map of epicenters of regional destructive earthquakes (1611–December 2011, $M \geq 4.7$; the earthquakes which's magnitude are bigger than *M*7.0 had been marked)

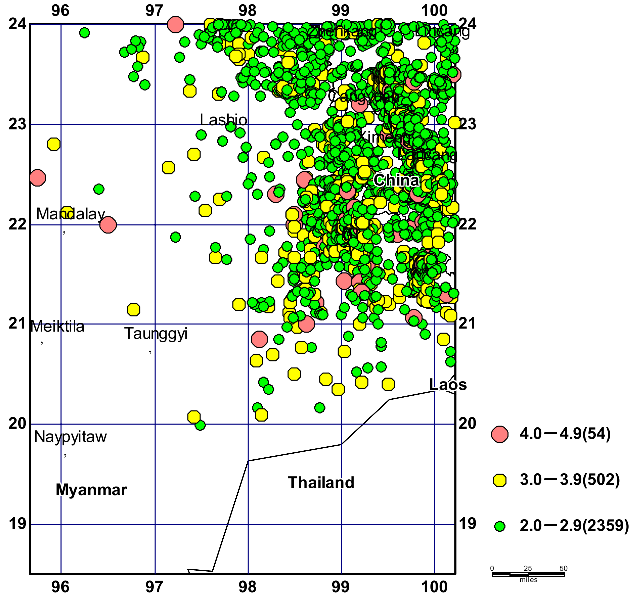

Fig. 4 Distribution map of epicenters of regional modern small earthquakes (1970–December 2010, $2.0 \leq M \leq 4.6$)

the strikes and orientations are mainly distributed in the angular domain in the direction of NNW–NW–NWW; in the Nodal Surface II mainly characteristic of left-lateral strike-slip dislocation, the strikes and orientations are mainly distributed in the angular domain in the direction of NNE–NE–NEE, which indicate that the distribution of the tectonic stress fields within the area is very complicated with the spreading of the earthquake fracture planes displaying a characteristic multi-directionality.

Average stress field

Analysis and studies (Li and Qin 1994) are carried out on the spatial distribution characteristics of the tectonic stress fields of earthquakes in the local and neighboring areas through the comprehensive analysis of the acquired data and in accordance with the findings of the multi-phase researches on the regional modern tectonic stress fields in the southwestern area of China, Myanmar and other neighboring countries over years. This area belongs to the stress fields of the subregion of Sichuan–Yunnan Block of Qinghai–Tibet Plateau Tectonic Region in the southwestern area of China (including Myanmar) and the subregion of Western Yunnan–Myitkyina Block of Southwestern Yunnan–Indo-China Tectonic Region, respectively. In the Southwestern Yunnan Block fault belts (The study area occupies only a small part.) at the southwest of Jinsha River–Red River Fault Zone to the east of Tengchong–Longling–Gengma–Lancang belt, the preferred orientation of principal compressive stress of the regional modern tectonic stress field is in the direction of SSE–SE mainly under the horizontal action, which reflects the extrusion of the earth crust materials from Qinghai–Tibet Plateau. Tengchong–Longling–Gengma–Lancang Seismic Belt and its western area including the middle and

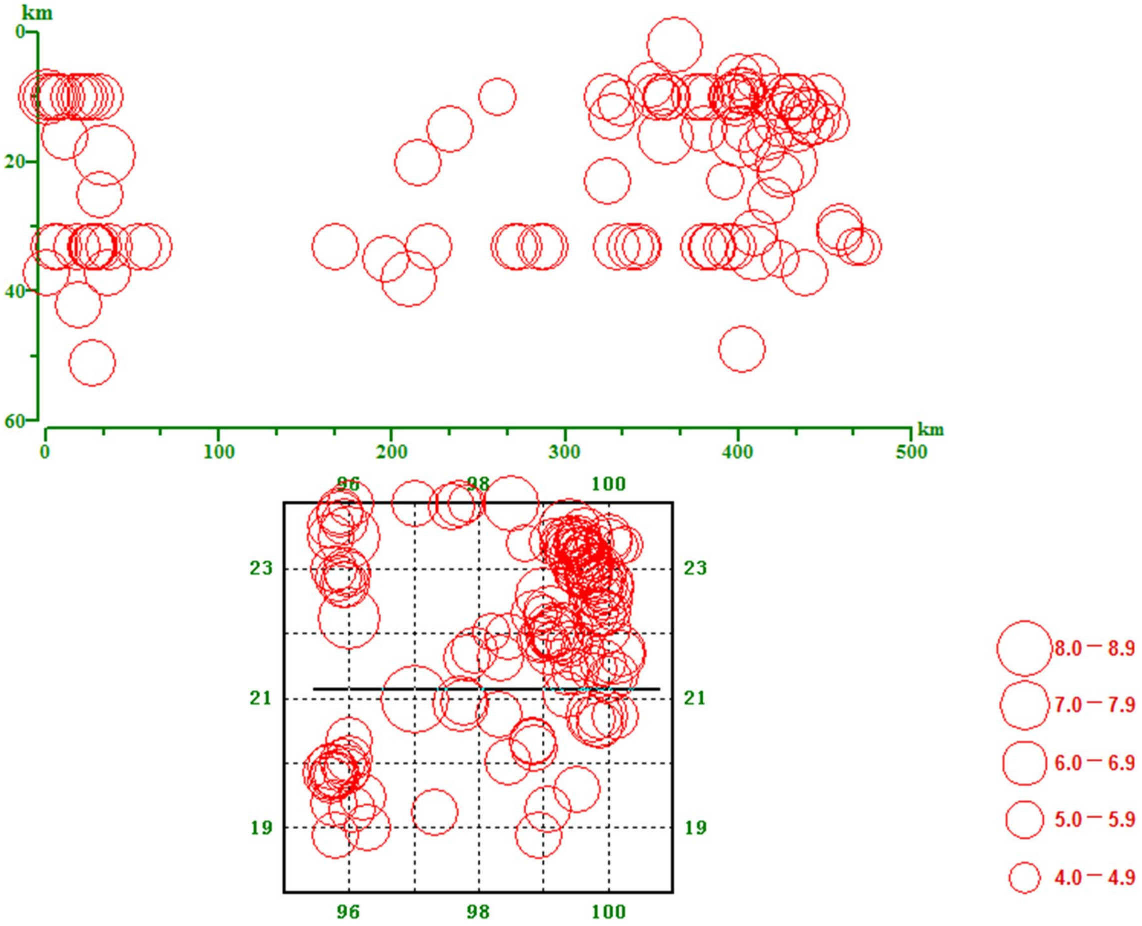

Fig. 5 Profile of regional destructive earthquakes' depth (upper figure) and figure of profile trend on the map (lower figure) (The black line in the lower figure shows profile trend direction)

northern parts of Myanmar to the western boundary of Myanmar Plate belong to the tectonic stress fields (Most of the study area falls within this subregion.) of Southwestern Yunnan–Indo-China Region, in which the preferred orientation of principal compressive stress of the regional modern tectonic stress field is in the direction of NNE–NE also mainly under the horizontal action (Table 4), which reflects the wide right-lateral shear tectonic deformation zone with extrusion components at western Yunnan, middle and northern parts of Myanmar and the areas to the west of them.

Conclusions

1. Under most circumstances, the record of regional historical earthquakes is not complete and so far, total 132 destructive earthquakes ($M \geq 4.7$) are recorded in historical documentations (Before 1970) and seismographs (After 1970), among which the earliest recorded earthquake was $M4\frac{3}{4}$ Ruili earthquake of Yunnan Province in April 1611 AD and the strongest earthquake was $M9$ Dongzhi earthquake of Burma on May 23, 1912.
2. The regional destructive earthquakes often occur in two earthquake prone regions: The first is the middle part of the region—northern mountain area of Burma, seismic belt changes from northeast direction to trending near south–north direction from south to north, together with the earthquake concentrating region near Naypyitaw and the two regions jointly reflect the plate collision effect of Indian plate and Eurasian plate; the second is the northeast part—earthquake concentrating region in Cangyuan–Lancang in China, which roughly presents zonal distribution in north-northwestern direction. Since the record for historical earthquakes is not complete, most of the records for destructive earthquakes are those after 1900. Since the most parts of the region located in the border of Burma, the records for small earthquakes by modern instruments are seriously missing. In general, the regional seismic activities level is relatively high.
3. The orientation of the maximum principal stress axis P of the focal mechanism solution is mainly distributed in

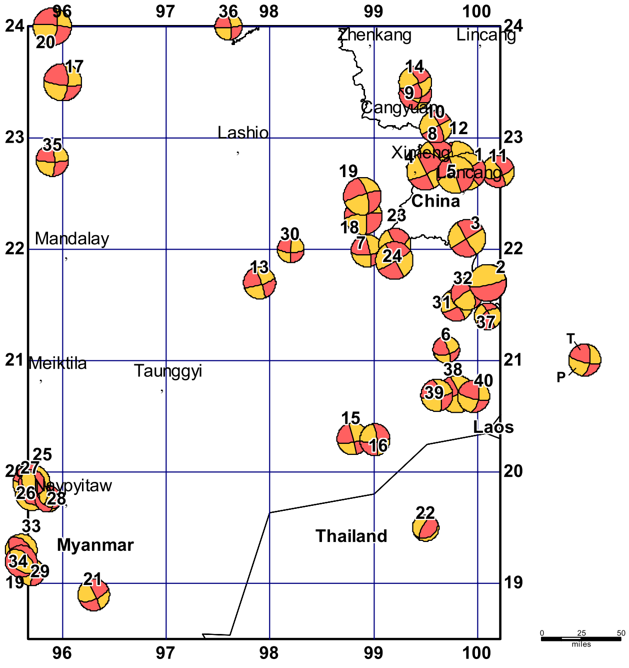

Fig. 6 Diagram of regional focal mechanism solutions

NNE–NE–NEE direction angular domain and is dominated by horizontal action, which indicates that the distribution of tectonic stress field within the region is relatively complicated and the earthquake fracture plane is multi-directional.

Compliance with ethical standards

Conflict of interest We declare that we have no financial and personal relationships with other people or organizations that can inappropriately influence our work; there is no professional or other personal interest of any nature or kind in any product, service and/or company that could be construed as influencing the position presented in, or the review of, the manuscript entitled.

References

Chen L, Fu H (2007) Relativity study between Andaman arc and strong earthquakes in Burma and Yunnan, China. Earthq Study 30(1):14–17 **(in Chinese)**

Cummins PR (2007) The potential for giant tsunami genic earthquakes in the northern Bay of Bengal. Nat Lett 449:75

Earthquake Disaster Prevention Center of China Earthquake Administration (1995) Catalogue of historical earthquakes in China (23rd century BC–1911 AD). Seismological Press, Beijing **(in Chinese)**

Earthquake Disaster Prevention Center of China Earthquake Administration (1999) Catalogue of Chinese earthquakes in modern times (1912 AD–1990 AD, $Ms \geq 4.7$). General Science Press of China, Beijing **(in Chinese)**

Fu X, Wang S (1992) Abnormal varation characteristics in near-fault of *M*67 and 69 earthquakes of Burma on April 23. Earthq Study 17(4):350–354 **(in Chinese)**

Gu G (1983) Catalogue of Chinese earthquakes (1831 BC–1969 AD). Science Press, Beijing **(in Chinese)**

Li H, Qin J (1994) Focal mechanism and present stress field of burma arc and its surrounding areas. Acta Seismol Sin 16(4):463–471 **(in Chinese)**

Li H, Zhu C (1995) Seismic activities and earthquake disaster alleviation of Burma. Recent Dev World Seismol 1:36–38 **(in Chinese)**

Shi Z, Zhao R, Shuzhen W, Jingxian W et al (1986) Catalogue of global earthquakes (1900–1980, $M \geq 6$). SinoMaps Press, Beijing **(in Chinese)**

Soe W, Aye K (2002) The seismicity and seismological work of Myanmar. Earthq Res China 16(3):225–235

The Earthquake Disaster Defense Department of the State Seismological Bureau (1990) The seismic work manual. Seismological Press, Beijing **(in Chinese)**

Acta Geophysica (2019) 67:775–787
https://doi.org/10.1007/s11600-019-00287-1

RESEARCH ARTICLE - SOLID EARTH SCIENCES

Theoretical and experimental investigation of sliding instability in blocky rock system triggered by external disturbance

Hai-ming Jiang[1] · Jie Li[1] · Shu-xin Deng[2]

Received: 19 December 2017 / Accepted: 9 April 2019 / Published online: 3 May 2019

Abstract

Based on the structural hierarchy theory, rock masses can be considered as a blocky rock system capable of storing various kinds of a large amount of energy. As the development and utilization of underground space has extended to thousands of meters, the increasingly frequent rockbursts pose a great danger to the constructors and equipment at the construction field. According to its mechanism, rockburst can be broadly divided into strain failure type caused by rock volume damage and sliding failure type caused by fault-slip event. This paper focused on investigating the triggering mechanism of sliding type rockbursts induced by external disturbance. With the simplified theoretical model of contact slipping between rock masses under the condition of initial stress, a non-dimensional impact energy parameter I was derived to quantify the critical conditions of different types of sliding failure events along structural plane. Then the necessary conditions for the occurrence of fault-slip rock burst were derived: Firstly, the contact surfaces of the rock block are in the quasi-stable state with the high initial stress in the tangential direction; secondly, the impact energy factor which characterizes the movement of the rock mass reaches a critical value under the dynamic disturbance. To verify the theoretical result, a series of sliding tests were carried out for purple sandstone blocky system under various horizontal pulls and vertical impact loadings. Both the irreversible displacement and sustained sliding instability are observed, and the critical energy conditions of above-mentioned phenomenon are obtained, which are consistent with the theoretical model. Furthermore, numerical modeling calculations considering rock mass vibration and the slip rate weakening mode of rock friction were performed to better understand the mechanism of sliding instability caused by external disturbances. These results provide a theoretical reference on the safety of underground tunnel construction.

Keywords Fault-slip burst · External disturbance · Sliding instability · Triggering mechanism

List of symbols

c	Damping coefficient
C_R	Cohesive strength between block's surfaces
f	Dynamic disturbing force
f_h	Pull force
F_0	Initial active force
F_d	Residual force
F_τ	Shear force
F_δ	Active force provided by surrounding rocks
F_p	Peak static friction force
H	Height of rock block
I	Non-dimensional impact energy factor
k_1	Elastic modulus of pre-peak phase
k_2	Elastic modulus of post-peak phase
k_δ	Stiffness modulus of surrounding rock
L	Length of rock block
m	Mass of rock block
N	Normal force
p	Vertical impact loading
S	Area of the rock block
U_{eff}	Total energy acting on rock block
V	Rock block's volume
W_d	Work done by $p(t)$
W_τ	Work done by the shear force
W_δ	Work done by the surrounding rock
x	Horizontal displacement of rock block
x_0	Initial horizontal displacement
x_c	Critical horizontal displacement
x_p	Yield horizontal displacement

✉ Jie Li
lijierf@163.com

[1] State Key Laboratory for Disaster Prevention and Mitigation of Explosion and Impact, Army Engineering University of PLA, Nanjing, China

[2] School of Mechanical Engineering, Nanjing University of Science and Technology, Nanjing, Jiangsu, China

γ_p	Yield strain
μ	Frictional coefficient
μ_d	Dynamic frictional coefficient
μ_s	Static frictional coefficient
τ_p	Peak shear stress between block's surfaces
δ	Displacement of the surrounding rock

Introduction

The increasing world's population, energy shortages and many other problems require the development of underground spaces to gradually reach into deeper areas, including mines, hydraulic and hydroelectric engineering projects, deep borehole disposal, etc. With the increase in the buried depth, rock bursts occur frequently in mineral exploitation and other construction of underground projects, which has sparked widespread concerns in the international rock mechanics engineering community (Zhang et al. 2012; Blake and Hedley 2003; Cook et al. 1966). Rockburst is a phenomenon of a sudden and violent failure of rock mass in deep mining or excavation (Kaiser et al. 1996). Rockbursts in tunnels pose a tremendous danger to the constructors and construction equipment, as well as a detrimental factor with respect to performance on tunneling contracts. For instance, a serious destructive rockburst occurred in the parallel tunnels of the Jinping II Hydropower Station Project on November 28, 2009, unfortunately causing the death of seven workers and damaging a tunnel boring machine (Zhang et al. 2012).

Several researchers suggested two basic mechanisms in the rockbursts literatures: (1) strain burst caused by the brittle volume failure in high geo-stress region and (2) fault-slip burst due to the shear failure along the preexisting or newly generated discontinuities of different scales (Ryder 1988; Ortlepp and Stacey 1994; Linkov 1996; Qian 2014). The accumulated evidences convey the conclusion that among South African mine tremendous failures, the bursts resulting from the shear failure along the preexisting planes of weakness, play a dominant role (Ryder 1988). The damage caused by fault-slip burst is typically far more extensive than strain bursts, confirmed by the fact that several tens even hundreds of meters of roadways would be destroyed in a single excavation-induced seismicity (Stacey 2011). However, the effective researches of revealing the mechanism of fault-slip burst are rather scarce, comparing with the extensive studies of strain bursts.

The physical nature of the sliding type rockburst is considered to be deformation instability of the contact surface (Salamon 1970). Summarizing the geological features of the rockburst sites in Jinping II Hydropower Station in China, the structural plane in the vicinity of the tunnels was closely related to the occurrence of rockburst (Zhou et al. 2015; Meng et al. 2016). Excess shear stress (ESS) was first used to numerically evaluate the probability and intensity of the general shear-type seismic hazards in African mining excavations (Napier 1987; Ryder 1988; Spottiswoode 1988). Barton's shear strength criterion was introduced to explain the influence of the asperity of the structural surfaces on fault-slip, and a case of numerical analysis indicated that the rough faults would be intended to cause much more serious geo-hazards than the smooth faults (Sainoki and Mitri 2014). Otherwise, some researchers (Liu et al. 2017; Meng et al. 2019) conducted shear tests on filled and non-filled rock joints to reveal the mechanical response of rock jointing under dynamic loads. Direct shear tests at a variety of shear velocities under different normal stresses were performed with splitting granite jointing, the results of which suggested that the peak shear strength decreased to some extent as the shear rate increased, as well as the residual strength (Meng et al. 2019).

A common premise triggering dynamic geological hazards is that historical quasi-static loading results in the storage of large amounts of energy in the rock mass, including excavation-induced seismicity and rockburst. These fault-slip events always take place after external disturbances, such as natural distant seismic waves, nearby drilling and blasting vibration during excavation, stress waves generated by rock bursts in adjacent caverns (Mazaira and Konicek 2015; Yan et al. 2015; Castro et al. 2009; Huang and Wang 1999). Huang and Wang (1999) pointed out that when the dynamic compression wave arrives at the tunnel wall, it reflects into tension wave and produces tension stress in the tunnel surrounding rock. Once the tensile stress exceeds rock mass strength, the rockburst will probably occur. Xu et al. (2010) performed a spectrum analysis on the seismic wave signal of seismicity events, which confirmed that the dynamic disturbance is a necessary condition for the occurrence of rockburst. Therefore, the occurrence of rockburst depends not only on the accumulated energy stored in the rock mass, but also on the triggering effect of external disturbances. Nonetheless, the energy contained in the external disturbance is small and negligible compared to the energy released by a case of rockburst (Xia et al. 2004; Johnson and Jia 2005). However, the triggering mechanism and main influencing factors of these shear-slip events have not been systematically studied.

In view of the above discussion, this study attempted to investigate the mechanism of shear-slip type disasters in underground openings. Firstly, this paper studied the key block sliding instability of surrounding rock from the theoretical point of view, and the main influencing factors and critical conditions for fault-slip bursts are analyzed. A non-dimensional impact energy parameter was derived to quantify the critical conditions of different types of sliding failure events along structural plane. To verify the theoretical results, a series of sliding tests were carried out for purple sandstone blocky system under various horizontal pulls and vertical impact loadings. Furthermore, numerical modeling calculations considering rock mass vibration and the slip rate weakening mode of rock friction were performed to develop a better understanding of the mechanism of sliding instability caused by external disturbances. These results provide a theoretical reference on the safety of underground tunnel construction.

Triggering instability of rock mass under external disturbance

Based on the structural hierarchy theory, rock mass can be described as a blocky rock system, involving various grades of sizes from microscopic to macroscopic scale (Kurlenya et al. 1993; Qi et al. 2008). It is accepted that the joints between these blocks tend to have much lower effective strength and poorer deformation characteristic (Shilko et al. 2010; Grigoriev et al. 2016). Numerous practical in situ observations show that the physical and mechanical properties of structural planes and their partitioned blocky rock seriously affect the stability of underground engineering structures. According to the reference (Goodman and Shi 1985), there are three situations for finite-size rock blocks segmented by the discontinuities in the tunnel surrounding shown in Fig. 1.

Block 1 is the key block, which is the most unstable block and likely to move under the action of excess shear force and external disturbance. It can cause the domino effect of the movement of other adjacent blocks, which leads to instability of the cavity. Block 2 is the potentially key block, which tends to move toward the tunnel free face after the falling of the key block, if the frictional resistance on the potentially sliding face is extremely small, or there are additional loads driving the displacement. Block 3 belongs to the stable block, which has a favorable orientation with respect to the resultant force and would be unlikely to lift from its home since its virtual movement is away from the excavated space.

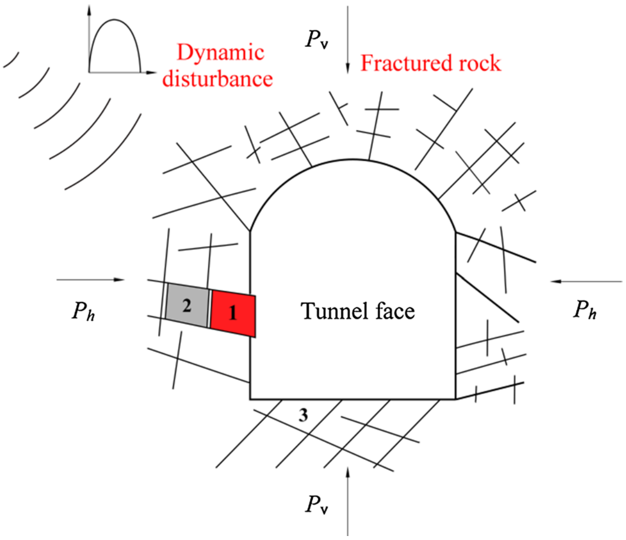

Fig. 1 Blocky system of the tunnel surrounding rock mass (P_v and P_h denote the geo-stress)

In this paper, the mechanism of fault-slip of key block under dynamic disturbance is discussed. From the perspective of force analysis, the existing key block in tunneling surrounding rock is simplified as the one-dimensional mechanical analytic model seen in Fig. 2. The shear resistance of the block sliding along fracture surface F_τ is determined by the friction and the cohesive strength on the surface, and the active force F_δ that causes the rock mass to generate slip deformation is provided by the spring element with stiffness k_δ, which indicates the stiffness of the surrounding rock. At the tunnel boundary, the key block is limited to move freely owing to the shear strength so that the blocky rock system can be stabilized.

Dynamic disturbances, such as blasting and TBM vibration, play a crucial role in the transition of rock mass from stable state to instability. According to the previous research (Wang et al. 2016), the external disturbance makes the tectonic block to vibrate, which is equivalent to superimposing an effective potential energy on the original steady-state energy field. With the action of dynamic disturbances, the key rock block will become movable and the initial equilibrium state of surrounding rock will be further damaged. Under this circumstance, the work of all forces on the blocky rock can be written as the following equation:

$$U_{\mathrm{eff}} = -W_\delta + W_\tau - W_{\mathrm{d}} \tag{1}$$

where U_{eff} is the total potential, W_δ is the work done by the surrounding rock, W_τ is the work done by the frictional resistance, W_{d} is the vibrational kinetic energy from external disturbance and can be presented as:

$$W_{\mathrm{d}} = \frac{1}{2} m\bar{v}^2 = \frac{\bar{f}^2}{2m\omega^2} \tag{2}$$

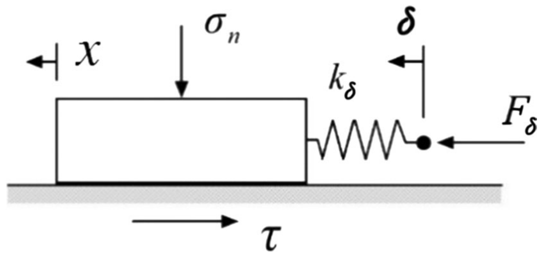

Fig. 2 The simplified force analysis of the key rock block

where m is the mass of the rock block, and f denotes the dynamic disturbance with the form of $f = f_1\cos(\omega t) + f_2\sin(\omega t), \bar{f}^2 = \left(f_1^2 + f_2^2\right)/2$.

For the assumed displacement of surrounding rock δ and the rock block x, the active force acting on the rock block can be expressed as:

$$F_\delta = k_\delta(\delta - x) \tag{3}$$

Thus, the work applied by the surrounding rock can be written as:

$$W_\delta = \int_0^x F_\delta \mathrm{d}x = \int_0^x k_\delta(\delta - x)\mathrm{d}x = k_\delta \delta x - \frac{1}{2}k_\delta x^2 \tag{4}$$

Similarly, the work applied by the frictional resistance can be written as:

$$W_\tau = \int_0^x F_\tau(x)\mathrm{d}x \tag{5}$$

Assume the relation between the shear force and the displacement of the rock sliding is shown in Fig. 3. Under the static condition, the initial stress F_0 is confined at the boundary of the rock mass. Then when the slip displacement reaches a critical value x_p, the shear force F_τ increases to the maximum F_p, which can be expressed as:

$$F_\mathrm{p} = \tau_\mathrm{p} \cdot S = \left(\mu_\mathrm{s}\sigma_\mathrm{n} + C_\mathrm{R}\right) \cdot S \tag{6}$$

where τ_p denotes the peak shear stress between the rock block slipping surface, S denotes the area of the slip surface, σ_n is the normal stress, μ_s denotes static frictional coefficient, C_R denotes the cohesive strength.

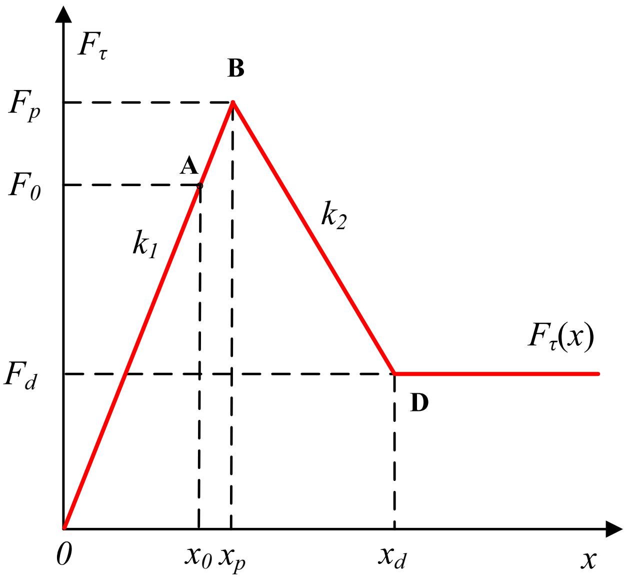

Fig. 3 Relation curve between the displacement and shear force for the rock interface

As the sliding displacement reaches a limited value x_d, the cohesive strength is essentially lost, and the shear force reduces to the residual dynamic friction F_d:

$$F_\mathrm{d} = \left(\mu_\mathrm{d}\sigma_\mathrm{n}\right) \cdot S \tag{7}$$

where μ_d denotes dynamic frictional coefficient. The remarkable drop in friction is considered to be a significant reason accountable for accelerating the slippage process of the fault-slip.

According to the variation principle, when the formulation of first-order variation satisfies $\delta U_\mathrm{eff} \le 0$, the system will transition to unstable state. The first-order variation for Eq. (1) on x is conducted, considering:

$$\frac{\partial}{\partial x}\left[v^2\right] = \frac{\partial}{\partial x}\left[\left(\frac{\partial x}{\partial t}\right)^2\right] = 2\frac{\partial}{\partial t}\left(\frac{\partial x}{\partial t}\right) = 2\frac{\partial^2 x}{\partial t^2} \tag{8}$$

The following expression was obtained:

$$\frac{\mathrm{d}U_\mathrm{eff}}{vx} = -k_\delta(\delta - x) + F_\tau(x) - m\frac{\partial^2 x}{\partial t^2} \tag{9}$$

Substituting the condition $\delta U_\mathrm{eff} \le 0$ into Eq. (9), the listed below condition should be met for the instability:

$$m\frac{\partial^2 x}{\partial t^2} \ge F_\tau(x) - F_\delta(x) \tag{10}$$

Conducting the integration on x for Eq. (10), we obtain:

$$\frac{1}{2}m\bar{v}^2 \ge \int_{x_0}^x \left[F_\tau(x) - F_\delta\right]\mathrm{d}x \tag{11}$$

Equation (11) can be expressed intuitively by the relation curves shown in Fig. 4. In Fig. 4, F_τ curve represents the change in the frictional resistance on the fracture surface, F_δ curve shows the pressure change of surrounding rock during the rebound process, which can be expressed as:

$$F_\tau(x) = \tau \cdot A = \begin{cases} k_1 x & 0 \le x < x_\mathrm{p} \\ -k_2\left(x - x_\mathrm{p}\right) + F_\mathrm{p} & x_\mathrm{p} \le x < x_\mathrm{d} \\ F_\mathrm{d} & x \ge x_\mathrm{d} \end{cases} \tag{12}$$

$$F_\delta(x) = -k_\delta\left(x - x_0\right) + F_0 \quad x \ge x_0 \tag{13}$$

In the initial state (see point A), the system is in the pre-peak stable equilibrium state, the cumulative displacement x_0 is generated by the initial active force F_0. The integration $\int_{x_0}^x \left[F_\tau(x) - F_\delta\right]\mathrm{d}x$ denotes the area enclosed by F_δ curve and F_τ curve. The physical meaning of Eq. (11) is that when the disturbance can assists the surrounding rock mass to overcome the friction resistance F_τ, the system deformation changes from the pre-peak stage to the post-peak state (see point C). Since then $F_\delta - F_\tau > 0$, the rock mass will slip

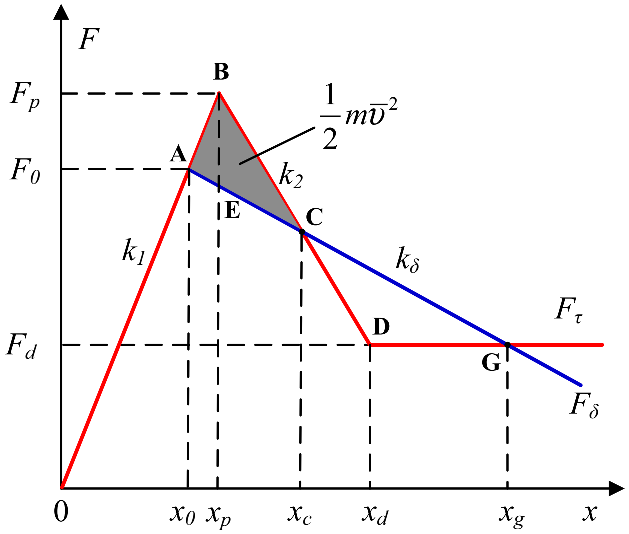

Fig. 4 Relationship between the surrounding rock pressure and shear resistance in the process of sliding

along its fault surface under the effect of stress difference. In general, as the slip increases, the friction force rapidly decreases to the dynamic friction force F_d, while the surrounding rock pressure F_δ gradually decreases with the increase of slip. Until $F_\delta - F_\tau < 0$ (see point G), the slippage motion of rock mass will decelerate. When the rock mass is separated from the surrounding rock, the fault-slip rockburst occurs if the remaining kinetic energy exists.

Consequently, the critical point of sliding instability can be symbolized by the state of point *C*, which is the second intersection of F_δ curve and F_τ curve shown in Fig. 5. Based on Eq. (11), the critical conditions for sustained slip failure is obtained:

$$W_d \geq \int_{x_0}^{x_c} \left[F_\tau(x) - F_\delta\right] dx = \frac{\frac{1}{2}\left(1 + \frac{k_2}{k_1}\right)\left(1 + \frac{k_\delta}{k_1}\right)\left(F_p - F_0\right)^2}{\left(k_2 - k_\delta\right)} \tag{14}$$

In Ref (Wang et al. 2016), a dimensionless impact energy factor *I* is introduced to reflect the energy density of disturbance energy in the process of deformation and failure, which can be expressed as:

$$I = \frac{W_d}{\tau_p V} = \frac{W_d}{F_p H} \tag{15}$$

where τ_p is the peak shear strength, *H* and *V* represent the length and volume of rock block, respectively. When the impact energy factor reaches a certain critical threshold, it can induce the release of the stored energy, thus promoting the deformation of the rock mass. Thus, the dimensionless impact energy factor *I* for sustained slipping instability can be represented as:

$$\begin{aligned} I &= \frac{W_d}{\tau_p V} \geq \frac{1}{\tau_p V} \int_{x_0}^{x_c} \left[F_\tau(x) - F_\delta\right] dx \\ &= \frac{\gamma_p}{2} \frac{L}{H} \left(1 + \frac{k_2}{k_1}\right) \frac{k_1 + k_\delta}{k_2 - k_\delta} \left(1 - \frac{F_0}{F_p}\right)^2 \end{aligned} \tag{16}$$

where $\gamma_p = \frac{x_p}{L}$ denotes the yield strain regarding to its peak shear strength.

Further, the critical condition for the key rock to begin to slip can be symbolized by the state of point *B*, and the corresponding non-dimensional impact energy factor *I* can be represented as:

$$I = \frac{W_d}{\tau_p V} \geq \frac{1}{\tau_p V} \int_{x_0}^{x_p} \left[F_\tau(x) - F_\delta\right] dx = \frac{\gamma_p}{2} \frac{L}{H} \left(1 + \frac{k_\delta}{k_1}\right) \left(1 - \frac{F_0}{F_p}\right)^2 \tag{17}$$

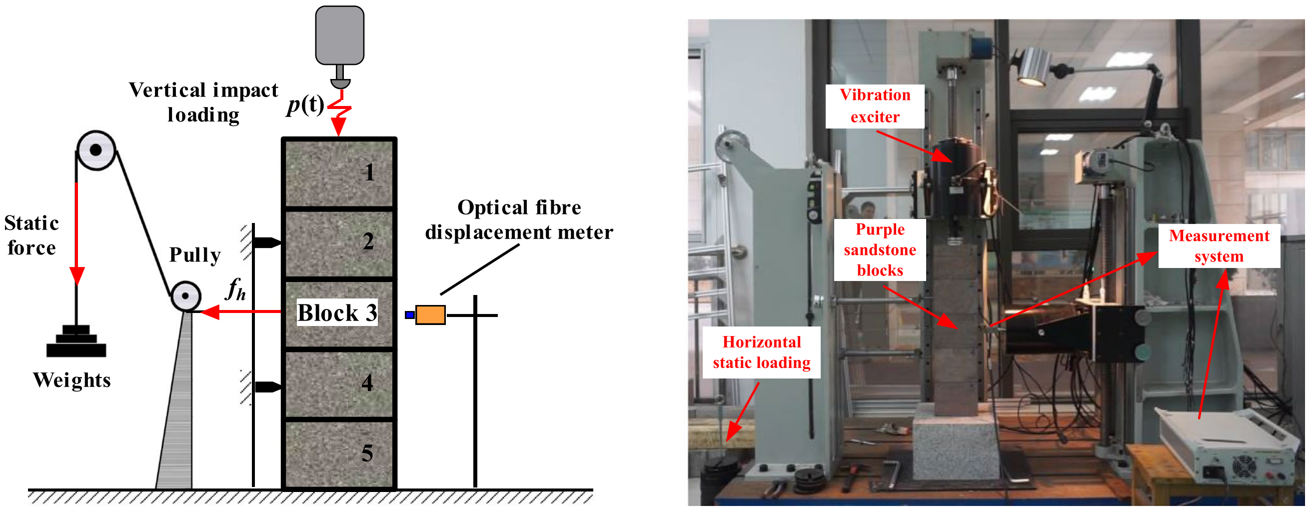

Fig. 5 Triggering sliding instability caused by external disturbance in a blocky rock system

For further simplification, it is supposed that the surrounding rock mass pressure remains constant during deformation ($F_\delta(x) = F_0, k_\delta = 0$). The corresponding dimensionless impact energy factor I can be simplified as:

$$I = \frac{W_\mathrm{d}}{\tau_\mathrm{p} V} = \begin{cases} \frac{\gamma_\mathrm{p}}{2}\frac{L}{H}\left(1 - \frac{F_0}{F_\mathrm{p}}\right)^2 & \text{(irreversible displacement)} \\ \frac{\gamma_\mathrm{p}}{2}\frac{L}{H}\left(1 + \frac{k_1}{k_2}\right)\left(1 - \frac{F_0}{F_\mathrm{p}}\right)^2 & \text{(sustained slip instability)} \end{cases} \tag{18}$$

It can be deduced from Eq. (18) that the critical threshold of impact energy factor depends on the physical and mechanical properties of rock mass and the initial stress state, which is a function of the yield strain (γ_p), the length–height ratio (L/H), the ratio of stiffness coefficients (k_1/k_2), the shear–strength ratio (F_0/F_p). Specifically, the non-dimensional energy factor I is a significant characteristic parameter, which can characterize the influence of external disturbances on the stability of blocky rock system.

The calculation result in Eq. (18) is derived from the idealized linear model. For the actual displacement–force curve of the rock mass, the shear force and the displacement show a linear elastic character in the stage of small deformation. When the shear force along the slip surface is close to the peak value, the shear force and displacement show a strong nonlinear character. From the perspective of dimensional analysis, the impact energy factor of block rock mass slipping caused by the external disturbance can be expressed as a general form:

$$I = A \cdot \left(1 - \frac{F_0}{F_\mathrm{p}}\right)^B \tag{19}$$

Experimental verification of proposed model

Experimental system

To testify the theoretical model in Sect. 2, a series of experiments were performed as illustrated in Fig. 5. The phenomenon of sliding instability induced by external disturbance was investigated in blocky rock system, which consists of five purple sandstone blocks stacked from top to bottom, with dimensions of 160 × 125 × 125 mm and each block weighing 6.2 kg. The third block is taken as the working block, with the application of horizontal static force provided by the gravitational force of weights. In the vertical direction, the block model system is subjected to an impact loading by the way of an electrodynamic exciter, which can be considered as a symbol of external disturbance. Horizontal absolute displacement of block 3 is measured by a fiber-optic displacement sensor under different horizontal forces and vertical loadings. In order to measure the absolute displacement of the block 3, the left horizontal movements of block 2 and block 4 are limited.

Experimental procedures

Step 1: The maximum static friction force of block 3 in blocky rock system shown in Fig. 5 was measured to provide parameter basis for determining initial horizontal pulls and modeling calculation. Without the vertical impact loads, the horizontal pull was steadily increased through adding weight until the obvious movement of block 3 was observed. This measurement step was repeated three times to minimize operational accidental errors. The maximum static friction force was averaged as F_p = 200 N, and the static frictional coefficient μ_s can be calculated as follows:

$$\mu_\mathrm{s} = \frac{F_\mathrm{p}}{N} = \frac{F_\mathrm{p}}{5\ mg} = 0.65 \tag{20}$$

where N denotes the total normal force, m denotes the weight of sandstone block, and g denotes the gravitational acceleration.

Step 2: A series of sliding tests were conducted for purple sandstone blocky system under various horizontal pulls and vertical impact loadings to reappear the sliding events of the working block. After the blocky system applying a certain static force $f_\mathrm{h}(f_\mathrm{h} < F_\mathrm{p})$ is stabilized, the gradually increasing impact loading is implemented until the occurrence of slip instability. At the same time, the horizontal dynamic displacement of the working block is measured and recorded. And a positive stop device is employed to prevent the collapse of the system, i.e., when the working block attains a limited displacement, the motion of the rock mass is stopped.

The force–time curve shown in Fig. 6 caused by the electrodynamic exciter was measured by the force transducer. Considering the fact that impact loading force acts only during a short time, the total disturbance energy W_d receiving from the external field source is determined:

$$W_\mathrm{d} = \frac{1}{2m}\left|\int_0^\infty p(t)\mathrm{d}t\right|^2 = \frac{I_\mathrm{m}^2}{2m} \tag{21}$$

where $p(t)$ represents force–time curve, I_m denotes the momentum.

Experimental results

Figure 7 shows the displacements–time curves of the working block under a combined effect of different vertical impact loads and horizontal static forces.

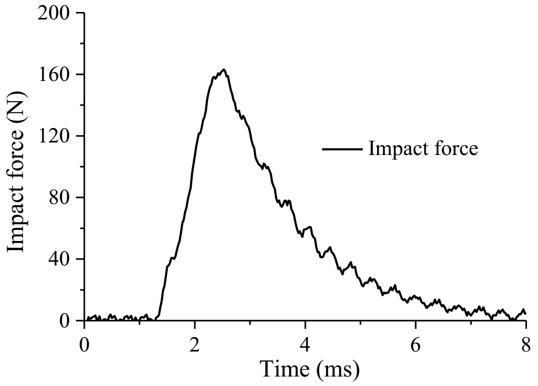

Fig. 6 Curve of the impact force

The experimental results shown in Fig. 7 can be described as follows:

Firstly, for a given horizontal static force, the horizontal displacement of block 3 increases with increasing vertical impact energy. Taking Fig. 7b as an example, where the horizontal pull force is 180 N, the residual displacements of block 3 are 94, 374, 700 μm, corresponding to the impact energies of 2, 4, 10 mJ, respectively. According to the experimental data, Fig. 8 shows the influence of the vertical impact energy on the displacement of block 3 with the horizontal static force ranging from 50 to 190 N. Figure 8 indicates that with the increase in horizontal force, the slippage of rock block is extremely sensitive to the impact loading. When the horizontal pull approaches the peak static friction force, even a relatively weak disturbance can cause a great irreversible displacement.

Secondly, for a certain shear force, there is an energy threshold for the irreversible displacement induced by the impact loading. When the horizontal force is 50 N (Fig. 7g), the impact loading below 80 mJ does not cause the irreversible displacement phenomenon. As the shear force increases, the energy threshold of the irreversible displacement decreases rapidly. When the horizontal force increases to 90 N, the energy threshold becomes 40 mJ.

Thirdly, in the case of an impact energy of 4 mJ and horizontal pull force of 190 N (Fig. 7a), the working block slides freely, implying that the sliding instability phenomenon occurs. The same phenomena are similarly observed in Fig. 7b–d, and the vertical impact energies of impact load triggering sliding instability are 20, 80, 300 mJ, corresponding to the horizontal static force of 180 (Fig. 7b), 170 (Fig. 7c), 160 N (Fig. 7d), respectively.

Finally, when the horizontal shear force decreases to a certain threshold, regardless of how the impact energy increases, there is only an irreversible displacement between the rock blocks, and the slip instability does not occur. For example, when the working rock mass is reduced horizontally to $F = 150$ N (Fig. 7e), even if we increase the impact energy to 300 mJ, the working block does not slip out, and only an irreversible displacement of 2640 μm occurs.

According to Eq. (18), the experimental results are nondimensionalized, and the energy threshold conditions for irreversible displacement and sliding instability under different shear forces are obtained, as shown in Fig. 9. The round and square symbols denote the test results, while the solid lines denote the fitting results, which are presented as:

$$\begin{aligned} I_1 &= 0.012 \cdot \left(1 - F_0/F_\mathrm{p}\right)^{2.27} \quad \text{(Irreversible displacement)} \\ I_2 &= 52.4 \cdot \left(1 - F_0/F_\mathrm{p}\right)^{5.21} \quad \text{(Sustained slip instability)} \end{aligned} \tag{22}$$

In Fig. 9, there exist three zones indicating different responses of the working block with the action of external disturbances. In zone I, the horizontal pulls F_0 should be less than the peak static friction force F_p and there will be no obvious horizontal displacement. In zone II, the impact energy is great enough to give rise to irreversible displacement, but no sustained slip instability can be observed. In zone III, the horizontal pulling force F_h exceeds the dynamic friction force and the impact energy is large enough, so the working block cannot stop to slide, which may cause sliding failure type geo-hazards. Thus, the theoretical results are consistent with the experimental results, validating the feasibility of this theoretical model.

Numerical modeling of induced slip instability

Establishment of the motion equations

The current geomechanical science describes rock mass as a complex hierarchy structure of diverse scale blocks embedded in each another. Rock mass at different scale levels consists of separate rock blocks, which are fairly homogenous in physical properties bound with relatively weak joints. A model of one-dimensional chain of masses with elastic and damping elements connected in parallel is proposed, as shown in Fig. 10a (Aleksandrova et al. 2006; Ma et al. 2009). The one-dimensional mass-chain model is subjected to the external dynamic force $p(t)$, which can be represented as a half-sine load:

$$p(t) = \begin{cases} p_\mathrm{m} \sin \omega t & 0 \le t \le T \\ 0 & t \ge T \end{cases} \tag{23}$$

where T denotes the duration of impact load, ω is the angular velocity ($\omega = \pi/T$), p_m denotes the peak force. And f_h is a

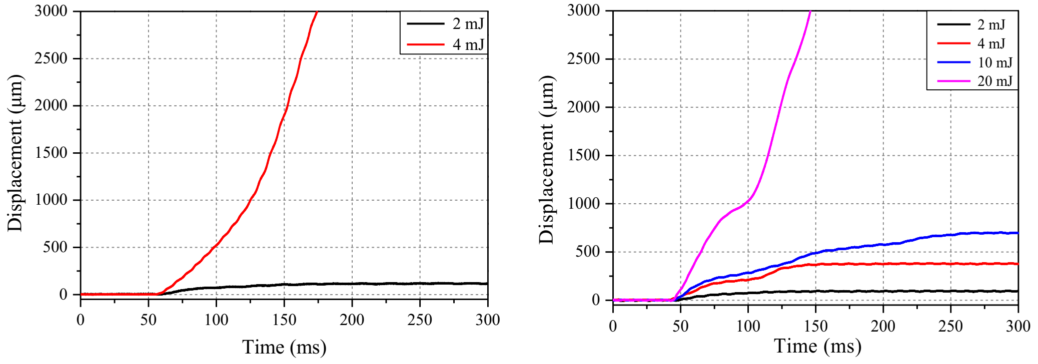

(a) Curves of displacements ($f_h = 190$ N) **(b)** Curves of displacements ($f_h = 180$ N)

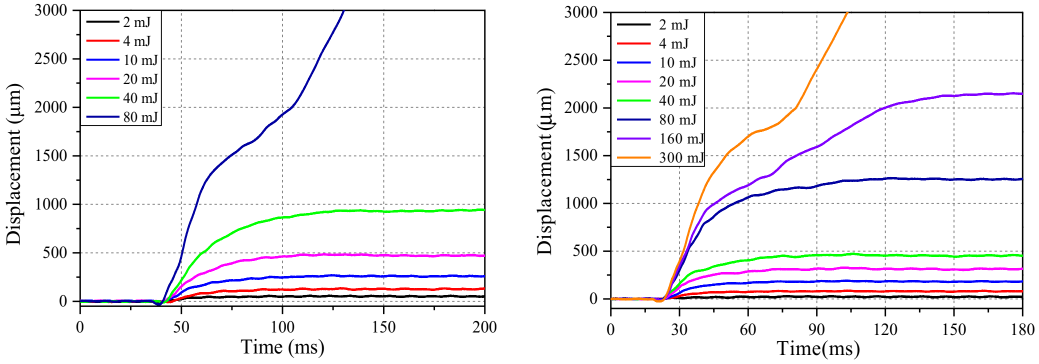

(c) Curves of displacements ($f_h = 170$ N) **(d)** Curves of displacements ($f_h = 160$ N)

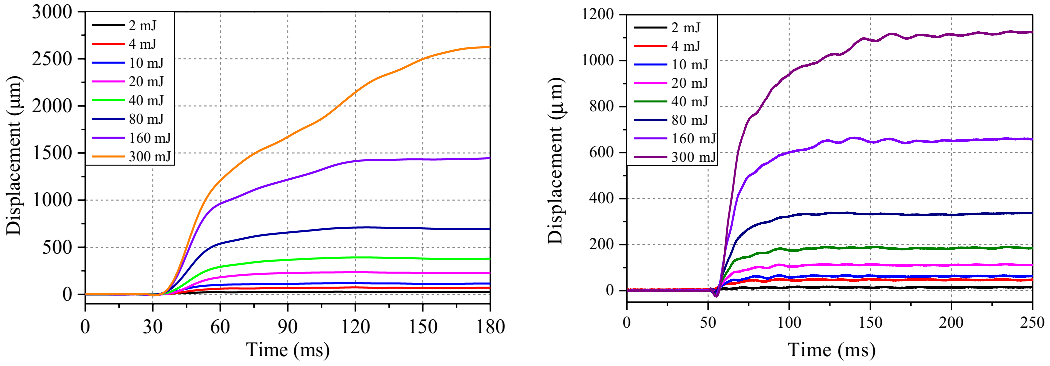

(e) Curves of displacements ($f_h = 150$ N) **(f)** Curves of displacements ($f_h = 130$ N)

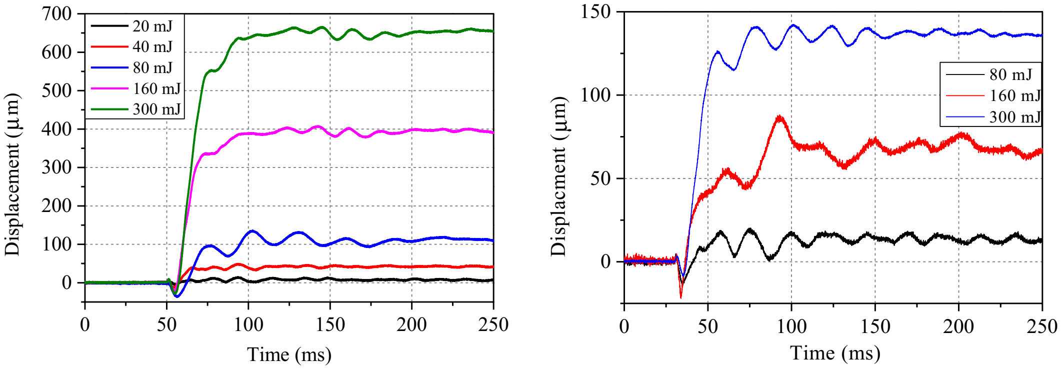

(g) Curves of displacements ($f_h = 90$ N) **(h)** Curves of displacements ($f_h = 50$ N)

Fig. 7 Displacements of the working block under vertical impact loading

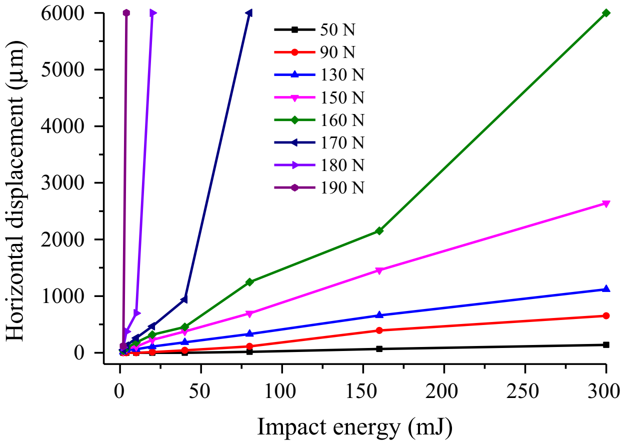

Fig. 8 Horizontal displacement vs. impact energy for block 3

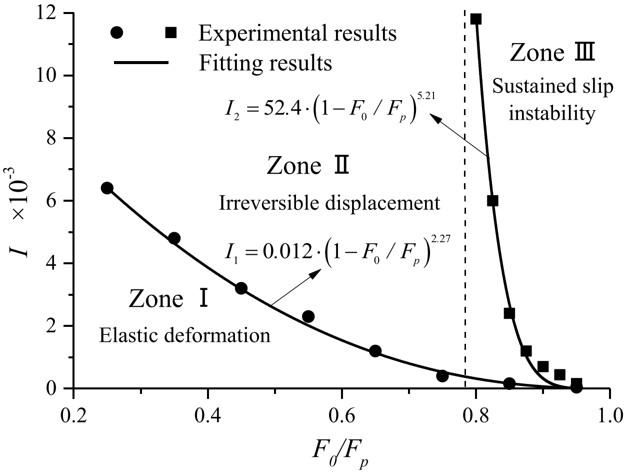

Fig. 9 Critical energy conditions of fault-slip events

static force representing the horizontal load acted on the working block.

The dynamic equations of the blocky rock structure can be expressed in a matrix form as

$$\mathbf{M}\ddot{\mathbf{y}}(t) + \mathbf{C}\dot{\mathbf{y}}(t) + \mathbf{K}\mathbf{y}(t) = \mathbf{p}(t) \tag{24}$$

where $\mathbf{M}$ denotes the mass matrix, $\mathbf{M} = \begin{bmatrix} m_1 & & & \\ & m_2 & & \\ & & \ddots & \\ & & & m_5 \end{bmatrix}$, $\mathbf{y}(t)$ denotes the displacement vector, $\mathbf{y}(t) = \begin{Bmatrix} y_1 \\ y_2 \\ \vdots \\ y_5 \end{Bmatrix}$, $\mathbf{C}$ denotes the damping matrix, $\mathbf{C} = \begin{bmatrix} c_1 & -c_1 & & & \\ -c_1 & c_1+c_2 & -c_2 & & \\ & -c_2 & c_2+c_3 & -c_3 & \\ & & -c_3 & c_3+c_4 & -c_4 \\ & & & -c_4 & c_4+c_5 \end{bmatrix}$, $\mathbf{K}$ denotes the stiffness matrix, $\mathbf{K} = \begin{bmatrix} k_1 & -k_1 & & & \\ -k_1 & k_1+k_2 & -k_2 & & \\ & -k_2 & k_2+k_3 & -k_3 & \\ & & -k_3 & k_3+k_4 & -k_4 \\ & & & -k_4 & k_4+k_5 \end{bmatrix}$, and $\mathbf{p}(t)$ is the vertical loading vector, $\mathbf{p}(t) = \begin{Bmatrix} p(t) \\ 0 \\ \vdots \\ 0 \end{Bmatrix}$.

For the working block subjected to a horizontal static force f_h (Fig. 10b), the equation of motion is

$$m\ddot{x} = f_\mathrm{h} - \mu N(t) \tag{25}$$

where x and $\ddot{x}$ are the horizontal displacement and acceleration of the working block, respectively, $N(t)$ denotes the changing normal force, and μ denotes the frictional coefficient of contact surface.

It is accepted that sliding of the blocky rock mass initiates when the ratio of the shear to normal force on the slip plane attains a value μ_s, referred as the static frictional coefficient. In case the slippage is activated, the frictional resistance reduces due to a lower dynamic frictional coefficient μ_d. The weakening effect of the slippage resistance is closely related to the microstructure, normal stress, temperature and shear rate, and may result in a dynamic instability (Blanpied et al. 1998; Shilko et al. 2010). It is to be noted that the focus of this study is not on determining the mechanism of this problem. Here, only the velocity weakening behavior of the frictional coefficient is considered, expressed as (Beeler and Tullis 1997):

$$\mu = \begin{cases} \mu_\mathrm{s} & v \le v_\mathrm{m} \\ \mu_\mathrm{d} + (\mu_\mathrm{s} - \mu_\mathrm{d}) * v_\mathrm{m}/v & v \ge v_\mathrm{m} \end{cases} \tag{26}$$

where v is the sliding velocity, v_m is the critical velocity, and here $v_\mathrm{m} = 1 \times 10^{-2}$ m/s is adopted.

Calculation results

Considering the purple sandstone block in the above experiment as the object of calculation, the mass $m = 6.2$ kg, the static frictional coefficient $\mu_\mathrm{s} = 0.65$, the dynamic frictional coefficient $\mu_\mathrm{d} = 0.5$, spring stiffness $k = 3 \times 10^6$ N/m and damping $c = 2.5 \times 10^3$ N·s/m were adopted. The theoretical result of the sliding displacement of the working block thereby obtained is shown in Fig. 11, where a horizontal constant pull force of $f_\mathrm{h} = 160$ N, series of a

Fig. 10 Modeling and analysis of the blocky rock system

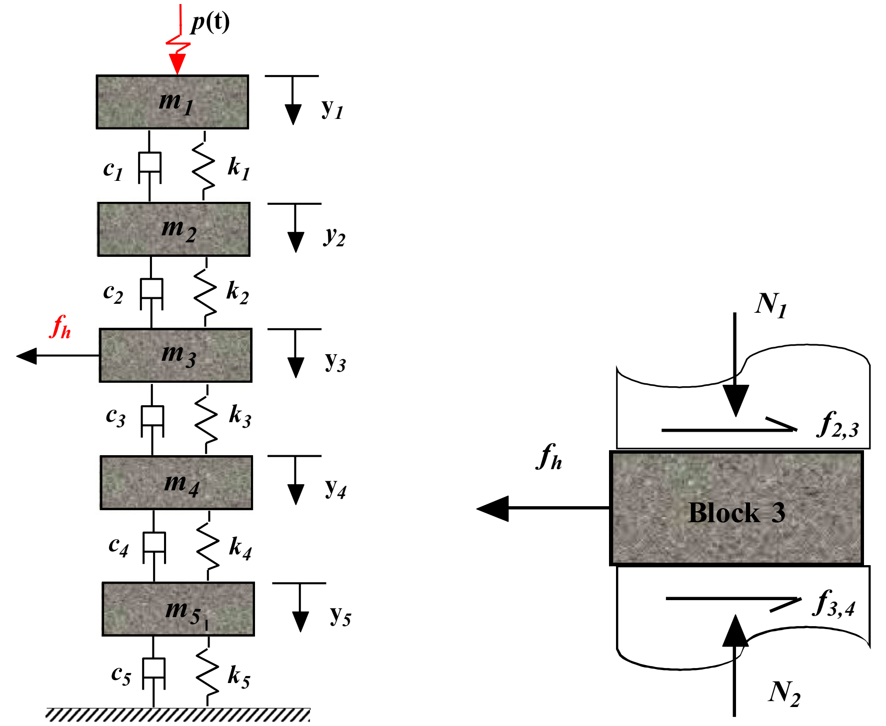

(a) Analytical model in vertical direction **(b)** Mechanical analysis of block 3

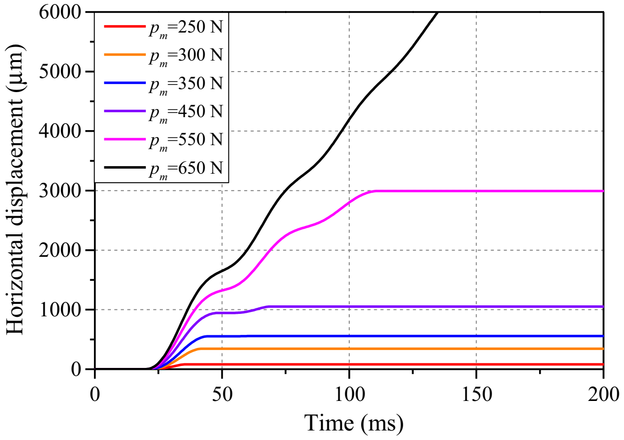

Fig. 11 Theoretical results of the sliding displacement of the working block (f_h = 160 N)

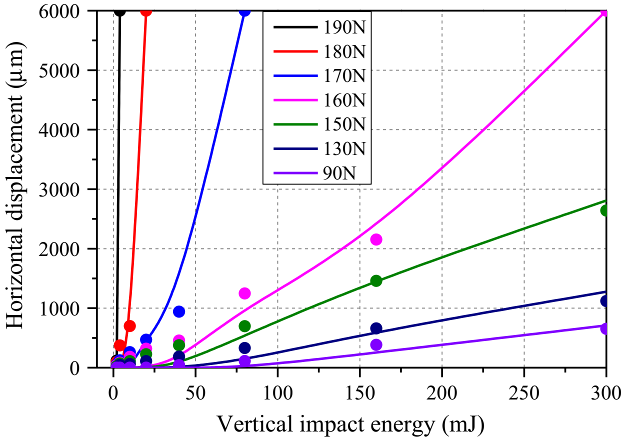

Fig. 12 Theoretical results of the slip trend and critical combination condition

half-sine load with different magnitudes of the peak force p_{m} and duration of vertical action $T = 4\ ms$ and $\omega = 250\pi$ were used.

It can be found that the irreversible displacement of the working rock block increases with the vertical impact disturbance, for a given constant force in Fig. 11. When the impact disturbance exceeds a critical value ($p_{\mathrm{m}} = 650\,N$), the working block slips freely, indicative of the sliding instability of the blocky structure. This result shows good agreement with the above-mentioned experiment.

Furthermore, the theoretical result of the effect of the impact loading energy on the sliding events is presented with the solid lines in Fig. 12, where the scatter symbols represent the experimental results shown in Fig. 8. It can be found that when the disturbance energy is small, the numerical modeling results have a slight deviation from the experimental results. However, as the disturbance energy increases, these two results show good agreement. Although there are some limitations, the sliding instability of the blocky structure was observed obviously. The numerical modeling can be improved to further study the fault-slip events occurred along non-filled or filled joint with different asperities induced by external disturbance.

Discussion

During the long-term tectonic movement in geological history, a large amount of deformation energy was stored in quasi-stable equilibrium state, due to the cohesive force, internal friction and dilatancy of rock mass. When the low-amplitude shock wave passes, the energy-stored rock mass is loaded and unloaded in cycle. Because of the significant asymmetrical deformation of the discontinuity under cyclic loading, residual deformation can be produced by the weak disturbance compared with the rock strength. Major external disturbance energies are locked in the rock masses, reflecting by the displacement accumulation. When the displacement accumulates to a critical threshold, the original equilibrium state of the rock mass is broken, which causes the release of the long-term storage of tectonic deformation energy. Thus, the slippage of the block rock mass is caused.

In nature, rock masses deform slowly before dynamic geological disasters occur, such as excavation-induced seismicity and fault-slip rockburst, while the slippage events can be appreciably accelerated under various kinds of external disturbances. Dynamic shear failure occurs instantaneously once the shear strength of the joints is overcome by the shear stress. External disturbances mainly help to diminish the restriction of the frictional force, playing a "trigger" role. Take the constant confining pressure ($F_\delta(x) = F_0$) as an example, as shown in Fig. 13. If the confining pressure is less than its residual shear resistance, i.e., $F_0 < F_\mathrm{d}$, disturbances will only increase the deformation but not induce sudden instability events. It is noted that the large cumulative deformation probably causes the collapsing of surrounding rock. For the case $F_0 > F_\mathrm{d}$, once the rock mass slips, it will continue to develop. When the rock blocks are separated from the system, there will be residual kinetic energy, which will cause dynamic disaster. As referred in Sect. 1, the total released energy from the sliding type bursts may be much greater than the external disturbance energy acted on the system, which can be explained with the theoretical model in Sect. 2. It can be found that the working block will keep slipping with a sustained sliding instability in Fig. 13. Therefore, the released energy increases continuously so that it could be much greater than the impact loading energy.

All the above-mentioned results in this paper facilitate further understanding of the mechanism of fault-slip events induced by external disturbances. The first is satisfied requirement for the occurrence of fault-slip rockbursts is high crustal stress, which is a prerequisite for adequate energy accumulation. Particularly, the considerable residual regional tectonic stress near the discontinuity will increase the probability and intensity of rockburst (Zhou et al. 2015). Secondly, the sliding instability events should occur along a specific fault easily under external disturbances, although structural planes are widely distributed in the tunneling surrounding rock. To identify the potentially risky faults, the geometric characteristic and mechanical property of the structural plane should be still involved: The structural plane (1) should be relatively close to the tunnel free face, (2) have relatively short slip length, (3) should be filled with soft soil, sand and rock fragments which possess the lower shear strength. Thirdly, dynamic disturbances are significant external cause, always triggering the geological hazards. This paper indicated that the occurrence of sliding instability is the result of the redistribution of the normal force of the rock block and the constant change in the frictional coefficient, which confirmed that the remarkable reduction in the clamping force acting on the fault may cause the occurrence of a fault-slip burst (Blake and Hedley 2003; Sainoki and Mitri 2014). From the perspective of wave propagation, the reflected tensile wave appears due to the different properties on both sides of the fault, which will adversely affect the stability of the rock mass engineering (Huang and Wang 1999; Zhou et al. 2015).

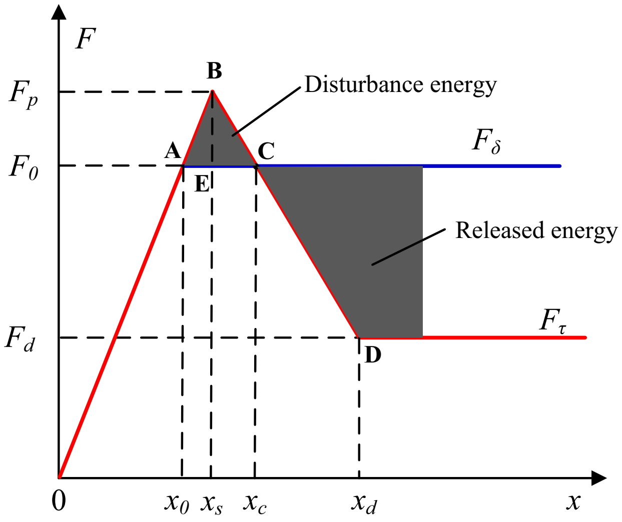

Fig. 13 Critical energy conditions of fault-slip events

Conclusion

The fault-slip rockburst has been a frequent occurrence of geological hazard during the tunnel construction, which is tightly associated with the slip of structural planes and always takes place after external disturbances. Although there are extensive researches to reveal the mechanism of fault-slip burst, the triggering mechanism for fault-slip bursts is still unclear. This paper focused on revealing the triggering mechanism of sliding type events induced by external disturbance and the critical conditions of fault-slip bursts. With variation method adopted in the simplified theoretical model for rock block sliding, the basic conditions required for sliding type rockbursts were obtained as: (1) The preexisting or the new fractural surfaces are in the quasi-steady state with the high initial tangential stress; (2) the dimensionless impact energy factor I which characterizes the movement of the rock mass should exceed the critical value presented as Eq. (18).

A series of sliding tests were carried out for purple sandstone blocky system under various horizontal pulls and vertical impact loadings. The slip displacement of the rock blocks is measured by a fiber-optic displacement sensor. Both the irreversible displacement and sustained slip instability are observed, and the critical energy conditions of above-mentioned phenomenon are obtained, which are consistent with the theoretical model. A dynamic calculation model considering rock mass vibration and the slip rate weakening mode of rock friction was established to better understand the mechanism of sliding instability caused by external disturbances. Numerical modeling calculations were presented, and the results agreed with the experimental observations.

The physical nature of the sliding type rockburst is considered to be deformation instability of the contact surface. In the long-term geotectonic movement, a large amount of deformation energy was stored in unstable equilibrium state. When external disturbances break the original equilibrium state of rock mass, the consequent deformation may be a slow process (creeping) and may also be an instantaneous dynamic process (sliding). The energy released by the rock mass deformation the greatly exceeds the external disturbance energy, so the external disturbance acts as a trigger. In practical underground engineering, the key point in preventing the fault-slip event effectively is to identify the potentially dangerous oriented fault and monitor its cumulative deformation.

Acknowledgements This study was supported by the Major Research Plan of Scientific Instruments of National Natural Science Foundation of China (Grant No. 51527810) and National Natural Science Foundation of China (Grant No. 51679249). The authors would like to thank the editors and peer reviewers for their valuable comments on this paper.

Compliance with ethical standards

Conflict of interest On behalf of all authors, the corresponding author states that there is no conflict of interest.

References

Aleksandrova NI, Chernikov AG, Sher EN (2006) On attenuation of pendulum-type waves in a block rock mass. J Min Sci 42:468–475

Beeler NM, Tullis TE (1997) The roles of time and displacement in velocity-dependent volumetric strain of faults. J Geophys Res 102:22595–22609

Blake W, Hedley DGF (2003) Rockbursts: case studies from North American hard-rock mines, society for mining, metallurgy, and exploration, New York

Blanpied ML, Tullis TE, Weeks JD (1998) Effects of slip, slip rate, and shear heating on the friction of granite. J Geophys Res 103:489–511

Castro LAM, Carter TG, Lightfoot N (2009) Investigating factors influencing fault-slip in seismically active structures. In 3rd CANUS rock mechanics symposium, Toronto

Cook NGW, Hoek E, Pretorius JPG et al (1966) Rock mechanics applied to the study of rockbursts. J S Afr I Min Metallj 66:435–528

Goodman RE, Shi GH (1985) Block theory and its application to rock mechanics. Prentice-Hall, New Jersey, pp 98–103

Grigoriev AS, Shilko EV, Astafurov SV et al (2016) Effect of dynamic stress state perturbation on irreversible strain accumulation at interfaces in block-structured media. Phys Mesomech 19:136–148

Huang RQ, Wang XN (1999) Analysis of dynamic disturbance on rock burst. Bull Eng Geol Environ 57(3):281–284

Johnson PA, Jia XP (2005) Nonlinear dynamics, granular media and dynamic earthquake triggering. Nature 437:871–874

Kaiser PK, Tannant DD, McCreath D R (1996) Canadian rockburst support handbook. Geomechanics Research Centre, Laurentian University, Sudbury, Ontario

Kurlenya MV, Oparin VN, Eremenko AA (1993) Relation of linear block dimensions of rock to crack opening in the structural hierarchy of masses. J Min Sci 29:197–203

Linkov AM (1996) Rockburst and the instability of rock masses. Int J Rock Mech Min Sci Geomech Abstr 33:727–732

Liu TT, Li JC, Li HB et al (2017) Experimental study of s-wave propagation through a filled rock joint. Rock Mech Rock Eng 50(10):2645–2657

Ma GW, An XM, Wang MY (2009) Analytical study of dynamic friction mechanism in blocky rock systems. Int J Rock Mech Min Sci 46:946–951

Mazaira A, Konicek P (2015) Intense rockburst impacts in deep underground construction and their prevention. Can Geotech J 52:150421143936002

Meng FZ, Zhou H, Wang ZQ et al (2016) Experimental study of factors affecting fault slip rockbursts in deeply buried hard rock tunnels. Bull Eng Geol Environ 76(3):1167–1182

Meng FZ, Wong LNY, Zhou H et al (2019) Shear rate effects on the post-peak shear behaviour and acoustic emission characteristics of artificially split granite joints. Rock Mech Rock Eng 52:1–20

Napier JAL (1987) The application of excess shear stress to the design of mine layouts. J S Afr Inst Min Metall 87(12):397–405

Ortlepp WD, Stacey TR (1994) Rockburst mechanisms in tunnels and shafts. Tunn Undergr Sp Tech 9:59–65

Qi CZ, Chen CS, Qian QH et al (2008) Dynamic instability of tunnel in blocky rock mass. Trans Tianjin Univ 14(6):457–463

Qian QH (2014) Definition, mechanism, classification and quantitative forecast model for rockburst and pressure bump. Rock Soil Mech 35:1–6

Ryder JA (1988) Excess shear stress in the assessment of geologically hazardous situations. J S Afr I Min Metallj 88:27–39

Sainoki A, Mitri HS (2014) Dynamic modelling of fault slip with Barton's shear strength model. Int J Rock Mech Min Sci 67:155–163

Salamon MDG (1970) Stability, instability and design of pillar workings. Int J Rock Mech Min Scie Geomech Abstr 7(6):613–631

Shilko EV, Astafurov SV, Ruzhich VV et al (2010) On the feasibility of shear stress estimation at interfaces of block-structured medium. Phys Mesomech 13:21–27

Spottiswoode SM (1988) Total seismicity, and the application of ESS analysis to mine layouts. J S Afr Inst Min Metall 88(4):109–116

Stacey TR (2011) Support of excavations subjected to dynamic (rockburst) loading. In: Proceedings of the 12th international congress of the international society of rock mechanics, pp 137–145

Wang MY, Li J, Ma LJ et al (2016) Study on the characteristic energy factor of the deep rock mass under weak disturbance. Rock Mech Rock Eng 49:3165–3173

Xia KW, Rosakis AJ, Kanamori H (2004) Laboratory earthquake: the sub-Rayleigh-to-supershear rupture transition. Science 303:1859–1861

Xu XF, Dou LM, Lu CP et al (2010) Frequency spectrum analysis on micro-seismic signal of rock bursts induced by dynamic disturbance. Min Sci Tech 20:682–685

Yan P, Zhao ZG, Lu WB et al (2015) Mitigation of rock burst events by blasting techniques during deep-tunnel excavation. Eng Geol 188:126–136

Zhang CQ, Feng XT, Zhou H et al (2012) Case histories of four extremely intense rockbursts in deep tunnels. Rock Mech Rock Eng 45:275–288

Zhou H, Meng FZ, Zhang CQ et al (2015) Analysis of rockburst mechanisms induced by structural planes in deep tunnels. Bull Eng Geol Environ 74:1435–1451

Acta Geophysica (2019) 67:789–797
https://doi.org/10.1007/s11600-019-00291-5

RESEARCH ARTICLE - APPLIED GEOPHYSICS

Brittleness index analysis of coal samples

Haibo Wu[1] · **Pingsong Zhang**[1] · **Shouhua Dong**[2] · **Yaping Huang**[2] · **Min Zhang**[3]

Received: 9 January 2019 / Accepted: 15 April 2019 / Published online: 27 April 2019

Abstract

The brittleness index (BI), which serves as a key reference for reservoir fracturing, is also an important quantitative index for the evaluation of coal-bed methane (CBM) reservoirs. To address the lack of research regarding this application of the BI, we measured the ultrasonic wave velocity of 10 coal samples collected from the Qinshui Basin, China. We then calculated the BI in three test directions, i.e., BI(90°), BI(45°), and BI(0°), as well as the BI anisotropy value (A_{BI}) using the dynamic elastic method. Analysis of the calculated results showed that BI(90°) generally had the highest values and that BI(45°) was close to BI(0°). The A_{BI} showed a positive correlation with the dynamic Young's modulus anisotropy value, dynamic Poisson's ratio anisotropy value, S-wave velocity anisotropy value, and the ratio of P-wave and S-wave velocity anisotropy values. However, the A_{BI} had an unclear correlation with the P-wave velocity anisotropy value. Further analysis of the correlation between the BI and two other reservoir parameters (coal structure type and fracture development) revealed that samples with high BI values generally corresponded to primary or fragmented types of coal and also had low Poisson's ratios, which indicates undeveloped fractures, while samples with low BI values corresponded to granulated types of coal and had high Poisson's ratios, which indicates developed fractures. We investigated these correlations in order to understand the multiparameter constraints and their combined application in brittleness evaluations, which could reduce risk and improve the precision of ideal brittleness identification in CBM reservoirs.

Keywords Ultrasonic wave · Dynamic elastic parameters · Anisotropy value · Coal structure type · Fracture development

Introduction

When compared with testing of sandstone, shale, and carbonate rocks, ultrasonic testing of coal samples has developed at a slower rate. These tests are also poorly constrained in relation to low strength, developed fractures, and significant anisotropy (Dong et al. 2016). Furthermore, the preparation of coal samples for ultrasonic tests is difficult. The parameters analyzed in the ultrasonic testing of coal samples are generally the P-wave and S-wave velocities and the anisotropic coefficients (Zhou 2012). Despite the challenges in sample preparation, previous studies have used ultrasonic testing to constrain the P- and S-wave velocities in coal, along with their respective anisotropic coefficients. Yu et al. (1991, 1993) tested the ultrasonic velocities and amplitude variations of coal samples, while also considering the influences of confining pressure and water saturation. Dong and Tao (2008) tested the ultrasonic velocities in coal samples under normal temperature and pressure (NPT) conditions and then analyzed the samples' anisotropic characteristics based on a transverse isotropic medium model. Morcote et al. (2010) and Wang and Xu (2012) tested the ultrasonic velocities of coal samples and then fitted the velocities in accordance with the density of different types of coal under various pressures and NPT conditions.

Based on the velocity and density parameters acquired from the previous studies mentioned above, reservoir prediction and evaluation can be enhanced by calculating many more elastic parameters, such as the dynamic Young's moduli, dynamic Poisson's ratios, and Lamé

✉ Haibo Wu
2016017@aust.edu.cn

[1] School of Earth and Environment, Anhui University of Science and Technology, Huainan 232001, People's Republic of China

[2] School of Resources and Geosciences, China University of Mining and Technology, Xuzhou 221116, People's Republic of China

[3] Key Laboratory of Geotechnical Mechanics and Engineering of the Ministry of Water Resources, Changjiang River Scientific Research Institute, Wuhan 430010, People's Republic of China

constants. A representative study by Wu et al. (2015) involved ultrasonic testing of coal samples, followed by the calculation and analysis of the dynamic Young's modulus and the dynamic Poisson's ratio. However, elastic parameters have limitations in relation to reservoir evaluation, such that they act as indirect parameters that describe pore structure and fluid characteristics. Therefore, another group of parameters has been developed, named reservoir parameters, which can be applied directly to the description and evaluation of reservoirs (e.g., the brittleness index (BI), coal structure type, fracture density, and fluid factor).

The BI is a recently developed reservoir parameter that can be used as an analog for fracturing and has become widely adopted in the field of non-conventional gas exploration and exploitation. Many methods exist for BI calculation in the study of shale gas reservoirs. For example, an early study had proposed that the BI should be expressed based on the results of hardness tests (Honda and Sanada 1956). However, other subsequent studies have concentrated on its expression based on stress–strain and penetration tests (Hucka and Das 1974; Quinn and Quinn 1997; Altindag 2003; Copur et al. 2003). To better constrain the BI, many different types of rock tests have been conducted that involved complex experimental operations, redundant technical processes, and high costs. Therefore, to reduce the degree of difficulty associated with testing and to provide a clear evaluation of the results, Rickman et al. (2008) proposed both a dynamic elastic method, based on dynamic elastic test results, and a static method based on the brittle mineral composition. Many subsequent studies have been conducted using both these methods (Diao 2013; Yuan et al. 2013; Chen and Xiao 2013). Additionally, many methods based on various other dynamic elastic parameters have also been studied and analyzed (Guo et al. 2013; Qian et al. 2017; Huang et al. 2015).

Most coal-bed methane (CBM) reservoirs in China rely on fracturing because of low permeability (Fu et al. 2007). Therefore, it is necessary to test and analyze the BI for CBM reservoirs. However, the BI calculated using rock mechanics data and brittle mineral content may not suitable for CBM reservoirs, due to their structure and the low brittle mineral content of coal. One of the few alternative methods is based on dynamic elastic parameters directly calculated from velocity and density data. Therefore, this study attempts to calculate and analyze the BI for CBM reservoirs by testing coal samples and serves as a reference for an in-depth study based on well-logging and seismic data. In this study, we first performed ultrasonic testing under NPT conditions on coal samples collected from the southern margin of the Qinshui Basin (China). Then, the BI and the BI anisotropy value (A_{BI}) were calculated and systematically analyzed. Finally, we analyzed the correlations between the BI and two other reservoir parameters, which we believe could improve the accuracy of BI evaluation for CBM reservoirs.

Coal sample testing method

Collection and preparation of coal samples

Anthracite coal samples were collected from multiple underground working faces in the southern margin of the Qinshui Basin (China). We cut 300-mm cube-shaped coal blocks along the direction parallel to the bedding planes using a portable CNC cutting machine (Exib). The samples were sealed in a sample box and transported immediately to the laboratory for processing. The entire processing and testing procedure was executed strictly in accordance with the standards recommended by the ISRM (Ulusay 2015). A representative coal sample after processing is shown in Fig. 1. The side length of the sample is 100 mm, with the top and bottom faces, side faces, and the diagonal faces parallel, perpendicular, and at 45° to the bedding planes, respectively. Machining error was less than 1°. Ultimately, we obtained 10 samples with smooth surfaces.

Coal sample porosity and fracture descriptions

Porosity tests were conducted using a type 9310 mercury porosimeter with a normal working pressure of 0.0028–103.08 MPa. The resolution for pore diameter recognition was 0.01 μm. The degree of fracture development on the

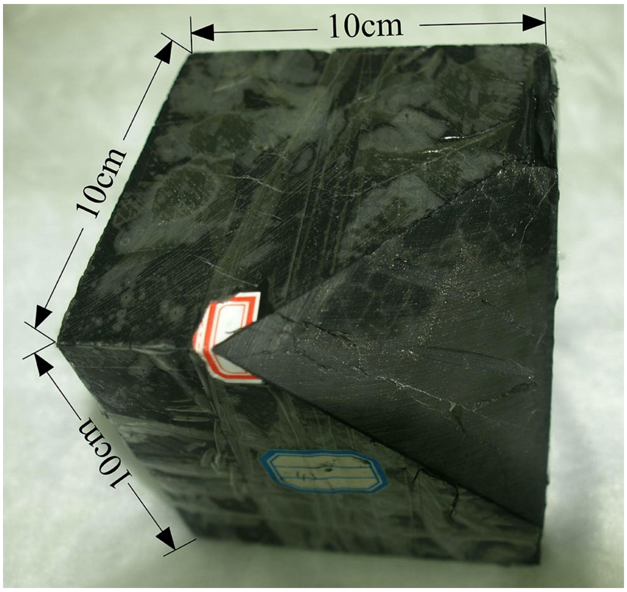

Fig. 1 A representative coal sample after processing

Table 1 Porosity and fracture descriptions of coal samples

Coal sample	Porosity (%)	Fracture description	Lithotype
A	4.67	Moderate	Bright Coal
B	4.50	Moderate	Bright Coal
C	4.31	Developed	Bright Coal
D	5.16	Developed	Bright Coal
E	4.80	Undeveloped	Bright Coal
F	5.26	Developed	Bright Coal
G	5.01	Undeveloped	Semibright Coal
H	4.30	Developed	Bright Coal
I	5.10	Developed	Bright Coal
J	5.44	Moderate	Bright Coal

surfaces of the coal samples was observed, and these details are shown in Table 1.

Ultrasonic wave test method

Ultrasonic wave tests were conducted under NPT conditions (about 25 °C, one bar pressure, and ~50% relative humidity) using a PCI-2 ultrasonic wave testing system with a working frequency range of 1 kHz to 3 MHz and sampling at 10 M/S. This system can perform several functions, including pulse signal emission, signal transformation, signal amplification with high fidelity, and automatic signal reception and transmission. The piezoelectric transducers (PZT) for the P-waves and S-waves have a main frequency of 600 kHz and a diameter of 50 mm.

Before testing, an aluminum cylinder was used to calibrate the system with the docking time being calculated. During testing, the surfaces of the test samples were smeared with honey before placement on the test bed. Each sample was tested by a single P-wave and two mutually perpendicular single S-waves on the three pairs of parallel subsurfaces (Fig. 2). We tested all 10 samples, and an example of the P-waveform is shown in Fig. 3.

Test parameter calculation method

Calculation method for coal sample velocities and densities

The velocity and density of the coal samples were calculated as follows:

$$\begin{cases} V = \frac{l}{t_{\mathrm{M}} - t_{\mathrm{T}}} \\ \rho = \frac{m}{v} \end{cases}, \quad (1)$$

where V is the ultrasonic wave velocity, l is the propagation distance, t_{M} is the travel time of the first arrival, t_{T} is the docking time of the transducer, v is the volume of the coal sample, and m is the quality of the coal sample.

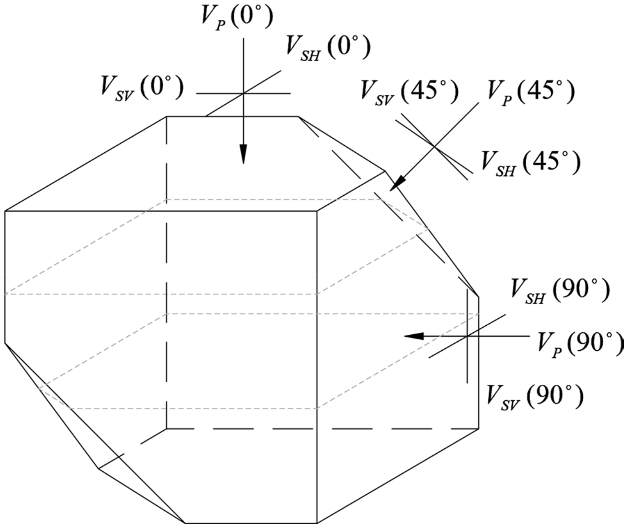

Fig. 2 Ultrasonic wave measurement of coal samples. Each sample was tested using P-waves, SH waves, and SV waves in three directions (parallel (90°), perpendicular (0°), and at 45° to the bedding planes)

Calculation method for coal sample BI and anisotropy values

The BI calculated using the dynamic elastic method based on the dynamic Young's modulus and the dynamic Poisson's ratio is shown in the following equation (Rickman et al. 2008):

$$\mathrm{BI} = \frac{\left[\frac{100(E_{\mathrm{d}} - E_{\mathrm{d\,min}})}{(E_{d\mathrm{max}} - E_{\mathrm{d\,min}})} + \frac{100(\upsilon_{\mathrm{d}} - \upsilon_{\mathrm{d\,max}})}{(\upsilon_{\mathrm{d\,min}} - \upsilon_{\mathrm{d\,max}})}\right]}{2}, \quad (2)$$

where E_{d} and υ_{d} are the dynamic Young's modulus and the dynamic Poisson's ratio, respectively, $E_{\mathrm{d\,max}}$ and $E_{\mathrm{d\,min}}$ are the maximum and minimum dynamic Young's moduli, respectively, and $\upsilon_{\max}$ and $\upsilon_{\min}$ are the maximum and minimum dynamic Poisson's ratios, respectively. In Eq. (2), the extreme values of the dynamic elastic parameters should be provided to unify the calculation standard. Generally, the dynamic Young's modulus of coal is 0.5–9.0 GPa and the dynamic Poisson's ratio is 0.22–0.46. Therefore, here we set $E_{\mathrm{d\,max}}$ and $E_{\mathrm{d\,min}}$ as 9.0 and 0.5 GPa, respectively, and we set $\upsilon_{\max}$ and $\upsilon_{\min}$ as 0.46 and 0.22, respectively.

The values of E_{d} and υ_{d} in Eq. (2) can be calculated based on the ultrasonic wave velocities as follows:

$$\begin{cases} E_{\mathrm{d}} = \rho V_S^2 \frac{(3V_P^2 - 4V_S^2)}{(V_P^2 - V_S^2)} \\ \upsilon_{\mathrm{d}} = \frac{(V_P^2 - 2V_S^2)}{2(V_P^2 - V_S^2)} \end{cases}, \quad (3)$$

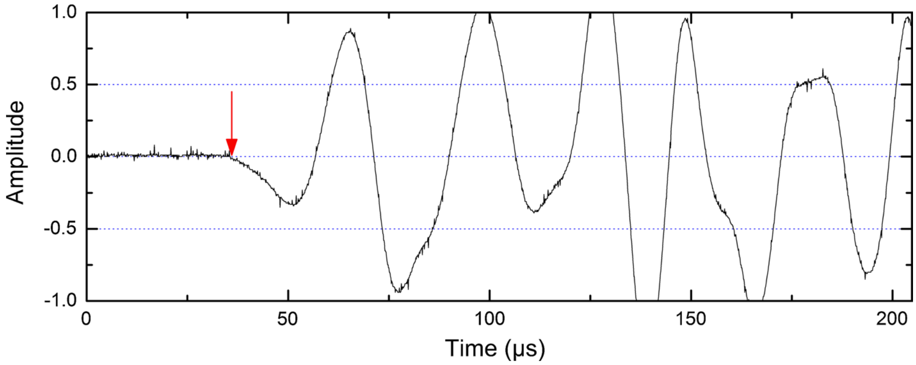

Fig. 3 Example of a P-waveform. Red arrow indicates the first break time point

where V_S is the mean value of V_{SV} and V_{SH}.

Generally, coal has obvious anisotropic characteristics that can be deduced from the differences between ultrasonic velocities in the three directions, which is also true of the BI. Therefore, we calculated the BI anisotropy value as follows (Liu et al. 2002):

$$A_{\mathrm{BI}} = \left| \frac{2(\mathrm{BI}(90°) - \mathrm{BI}(0°))}{\mathrm{BI}(90°) + \mathrm{BI}(0°)} \right| \times 100\%. \tag{4}$$

Test error calculation method

During our testing procedure, we can express any error using an error transfer formula:

$$\Delta N = \left| \frac{\partial f}{\partial x_1} \right| \Delta x_1 + \left| \frac{\partial f}{\partial x_2} \right| \Delta x_2 + \cdots + \left| \frac{\partial f}{\partial x_n} \right| \Delta x_n, \tag{5}$$

where $N = f(x_1, x_2, \ldots, x_n)$, x_n is the test parameter, and Δx_n is the test error. During calculation, the velocity error ΔV and density error $\Delta \rho$ should be calculated first:

$$\begin{cases} \Delta V = \left| \frac{1}{t_m - t_T} \right| \Delta l + \left| \frac{l}{(t_m - t_T)^2} \right| (\Delta t_m + \Delta t_T) \\ \Delta \rho = \left| \frac{1}{v} \right| \Delta m + \left| \frac{m}{v^2} \right| \Delta v \end{cases}. \tag{6}$$

Then, the errors of the dynamic elastic parameters (ΔE_{d} and $\Delta \upsilon_{\mathrm{d}}$) can be calculated using Eq. (7):

$$\begin{cases} \Delta E_{\mathrm{d}} = \left| V_S^2 \frac{(3V_P^2 - 4V_S^2)}{(V_P^2 - V_S^2)} \right| \Delta \rho + \left| \frac{2\rho V_P V_S^4}{(V_P^2 - V_S^2)^2} \right| \Delta V_P + \left| 6\rho V_S + \rho \frac{2V_S^5 - 4V_P^2 V_S^3}{(V_P^2 - V_S^2)^2} \right| \Delta V_S \\ \Delta \upsilon_{\mathrm{d}} = \left| \frac{V_P V_S^2}{(V_P^2 - V_S^2)^2} \right| \Delta V_P + \left| \frac{V_P^2 V_S}{(V_P^2 - V_S^2)^2} \right| \Delta V_S \end{cases}. \tag{7}$$

Finally, the error of the brittleness index (ΔBI) can be calculated:

$$\begin{cases} \Delta \mathrm{BI} = \left| \frac{50}{E_{\mathrm{d\,max}} - E_{\mathrm{d\,min}}} \right| \Delta E_{\mathrm{d}} + \left| \frac{50}{\upsilon_{\mathrm{d\,min}} - \upsilon_{\mathrm{d\,max}}} \right| \Delta \upsilon_{\mathrm{d}} \\ \varepsilon_{\mathrm{BI}} = \frac{\Delta \mathrm{BI}}{\mathrm{BI}} \times 100\% \end{cases}. \tag{8}$$

Results

Results of test parameters and test errors

The ultrasonic wave velocity, density, dynamic elastic parameters, BI, BI anisotropy value, and test errors for each of the coal samples are shown in Table 2. The average test error of the BI in different test directions is less than 5.0%, with 2.99% at 90°, 3.74% at 45°, and 4.34% at 0°, indicating satisfactory analytical precision. Particularly, sample I had the most significant test error of all the samples.

Analysis of BI and BI anisotropy values

The BI for each of the three directions in the test coal samples is shown in Fig. 4. The BI(90°) has the largest value of the three directions, ranging from 30.792 to 77.421, while the BI(45°) is close to BI(0°) for each sample such that the range of BI(45°) is 6.116–69.080 and the range of BI(0°) is 3.096–75.51. Sample D is unusual because its BI is high in all three directions.

The BI values of some samples are similar in all three directions, and these samples have correspondingly low BI anisotropy values (e.g., samples D and G) (Fig. 4). Conversely, many samples show obvious differences in BI in the three directions and have high BI anisotropy values, (e.g., samples A, F, and I). Sample I has the highest BI anisotropy value (1.832) with a BI(90°) value greater than 60 and BI(45°) and BI(0°) values less than 10.

No clear correlation was observed between the BI anisotropy value and P-wave velocity anisotropy value of the test coal samples, as shown in Fig. 5.

Table 2 Test and calculation results for the coal samples

Coal sample	Density (g/cm^3)	Velocity (km/s)						Dynamic Young's modulus (GPa)			Dynamic Poisson's ratio			Brittleness index (BI)			Error of brittleness index			Brittleness index anisotropy value
		V_P(90°)	V_S(90°)	V_P(45°)	V_S(45°)	V_P(0°)	V_S(0°)	90°	45°	0°	90°	45°	0°	90°	45°	0°	90° (%)	45° (%)	0° (%)	
A	1.378	2.248	1.275	1.711	0.747	1.580	0.662	5.655	2.123	1.683	0.263	0.382	0.394	71.331	25.705	20.806	3.010	3.405	3.645	1.097
B	1.454	1.961	1.135	1.670	0.837	1.581	0.778	4.673	2.711	2.359	0.248	0.333	0.340	68.617	39.564	35.887	3.182	3.262	3.338	0.626
C	1.467	2.602	1.290	2.032	1.009	1.844	0.922	6.528	3.992	3.326	0.337	0.336	0.333	61.073	46.296	43.010	2.670	2.996	3.126	0.347
D	1.485	2.516	1.388	2.428	1.301	2.078	1.219	7.331	6.528	5.462	0.281	0.299	0.238	77.421	69.080	75.510	2.781	2.795	3.124	0.025
E	1.443	2.120	1.147	1.728	0.832	1.590	0.746	4.910	2.695	2.180	0.293	0.349	0.359	60.717	36.016	30.901	2.996	3.235	3.373	0.651
F	1.432	1.955	0.935	1.519	0.525	1.360	0.462	3.381	1.129	0.875	0.352	0.432	0.435	39.465	9.464	7.430	3.072	4.906	5.707	1.366
G	1.382	1.666	0.775	1.307	0.608	1.230	0.566	2.261	1.392	1.207	0.362	0.362	0.366	30.792	25.678	23.748	3.346	3.679	3.781	0.258
H	1.440	2.313	1.097	1.714	0.769	1.550	0.643	4.692	2.337	1.662	0.355	0.374	0.396	46.522	28.685	20.156	2.834	3.320	3.671	0.791
I	1.427	2.212	1.223	1.616	0.504	1.570	0.452	5.463	1.048	0.846	0.280	0.446	0.455	66.726	6.116	3.096	2.973	6.178	9.998	1.823
J	1.472	1.986	0.942	1.514	0.636	1.200	0.580	3.536	1.659	1.335	0.355	0.393	0.348	39.724	20.803	28.328	3.033	3.655	3.681	0.335

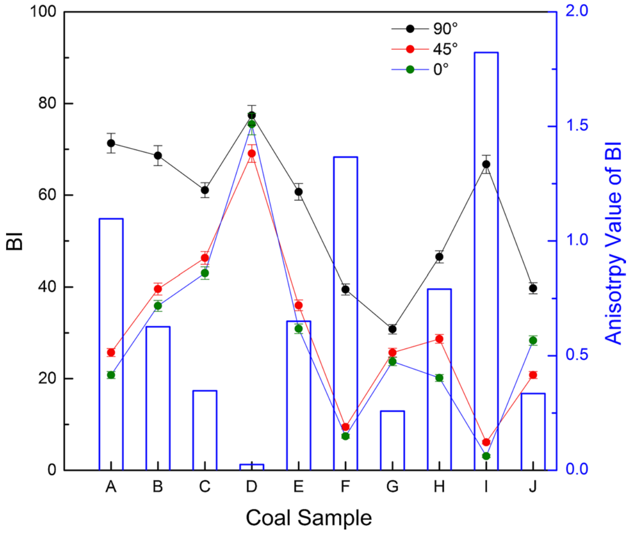

Fig. 4 BI and BI anisotropy values of test coal samples. The colored dots with error bars denote the BI of the test coal samples in three directions. Columns represent the brittleness index anisotropy value for each test sample

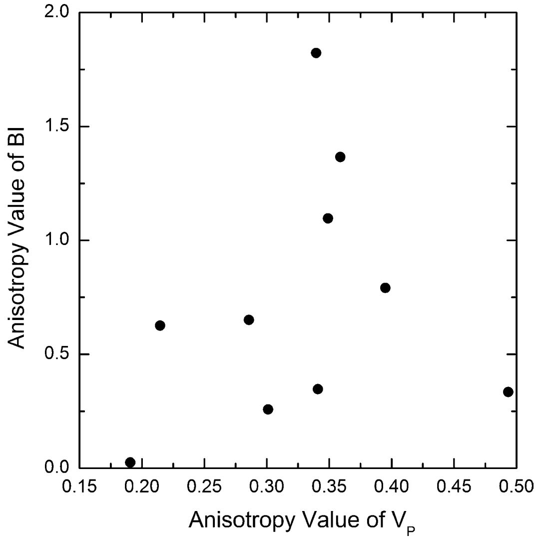

Fig. 5 Relationship between BI anisotropy value and P-wave velocity anisotropy value

A positive correlation was observed between the BI anisotropy value and dynamic elastic parameter anisotropy value, which is shown in Fig. 6, for which the fitting formulas are as follows:

$$\begin{cases} A_{\mathrm{BI}} = 1.55282 A_{E_{\mathrm{d}}} - 0.59723 \quad R = 0.93399 \\ A_{\mathrm{BI}} = 2.57656 A_{\upsilon_{\mathrm{d}}} + 0.23745 \quad R = 0.7591 \end{cases} . \tag{9}$$

Positive correlations also exist between the BI anisotropy value and the ratio of the P-wave and S-wave velocity

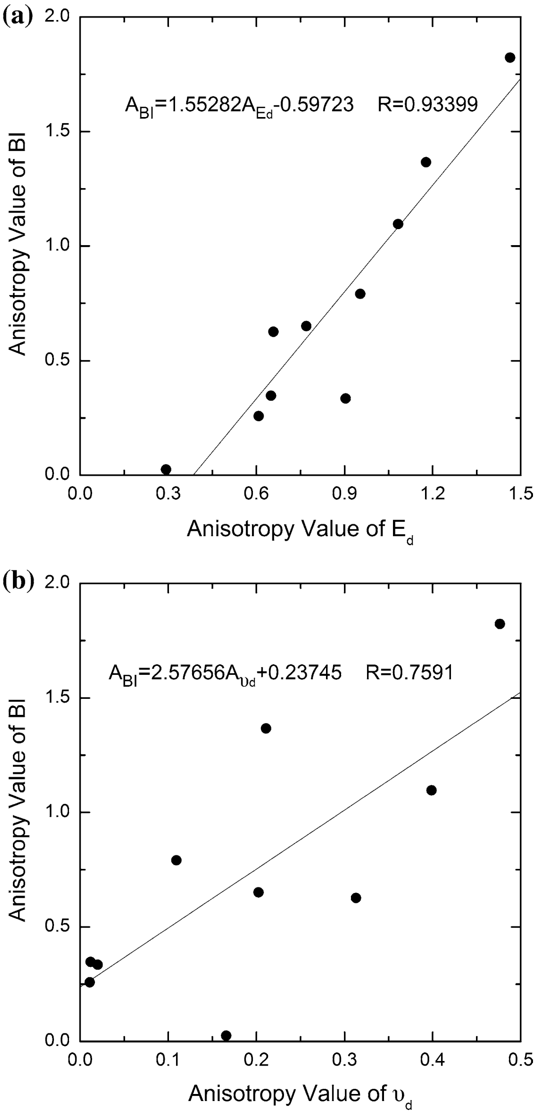

Fig. 6 Relationship between BI anisotropy value and dynamic elastic parameter anisotropy values: **a** dynamic Young's modulus and **b** dynamic Poisson's ratio

anisotropy values (Fig. 7), as well as the S-wave velocity anisotropy value (Fig. 8), for which the fitting formulas are as follows:

$$\begin{cases} A_{BI} = 2.39172A_{V_S} - 0.41594 & R = 0.95811 \\ A_{BI} = 2.70406A_r - 0.2427 & R = 0.95315 \end{cases}. \qquad (10)$$

Relationship between BI and coal type

The relationship between the BI and coal type, which acts as an important parameter for reservoir evaluation, is shown in Fig. 9. In Fig. 9, the BI values for the three directions in the test samples are marked by colored circles, and the BI values of the three coal types are indicated by colored squares (BI values for the three coal types were calculated from data provided in Peng et al. 2005).

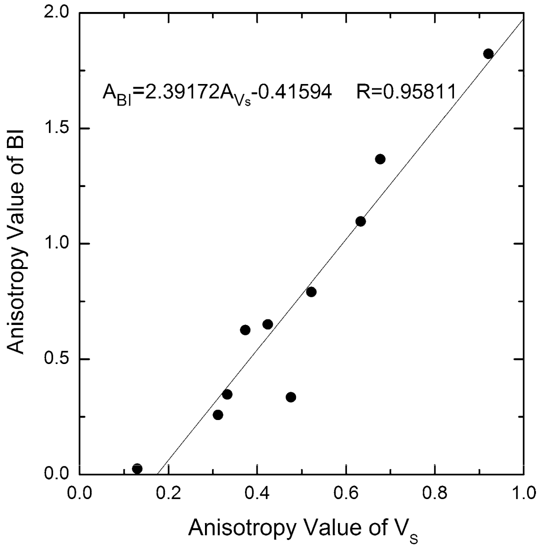

Fig. 7 Relationship between BI anisotropy values and S-wave velocity anisotropy values

The BI values for both primary and fragmented types of coal are similar: 65.056 and 60.160, respectively. A high dynamic Young's modulus for the primary coal and a low dynamic Poisson's ratio for the fragmented coal might account for this. However, granulated coal has the lowest BI value, which can be attributed to the minimum dynamic Young's modulus and the maximum dynamic Poisson's ratio, with BI generally less than 30, dynamic Young's

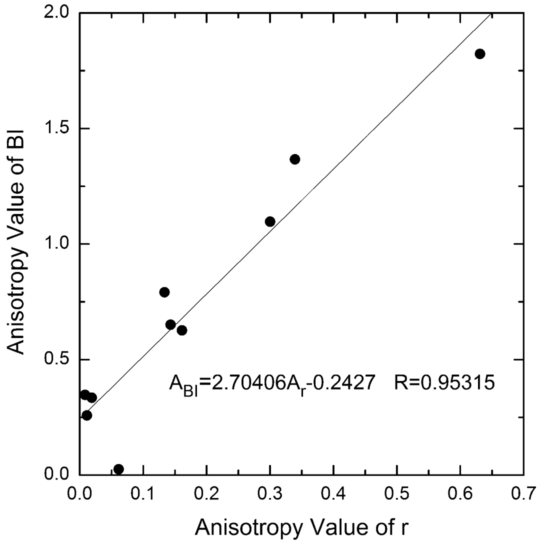

Fig. 8 Relationship between BI anisotropy values and ratio of P-wave and S-wave velocity anisotropy values

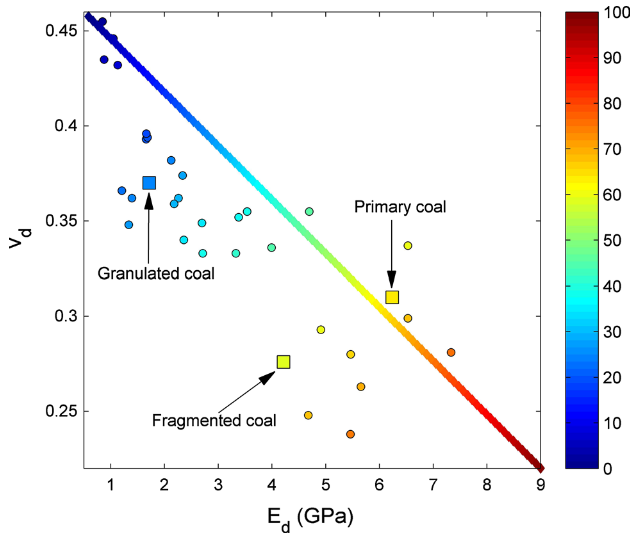

Fig. 9 Relationship between BI and coal type. Colored circles denote the BI of the test samples; colored squares represent the BI of the three coal types

modulus less than 2 GPa, and dynamic Poisson's ratio greater than 0.37.

Relationship between BI and fracture development

The degree of fracturing development in coal is a key factor for CBM permeability and exploitation and has a significant influence on BI. However, comparing Table 1 and Fig. 4 reveals a complex correlation between BI and coal fracture development. For example, coal sample D, described as having developed fractures, has high BI values in all three directions, while coal sample G, described as having undeveloped fractures, has low BI values in all three directions. Two factors could explain this situation. One is the low accuracy of the description of the surface fractures observed on the coal samples and our inability to observe any internal fractures, which might influence the fracture evaluation data. The other is the characteristics of the observed fractures (e.g., aspect ratio, connectivity, and arrangement), which might influence the variation of BI in the three directions.

Using a qualitative statistical method and according to the relationship between the dynamic Poisson's ratio and the fracture development revealed by both Ramos (1997) and Peng et al. (2006), we divided the BI values of the coal samples into three classes based on their corresponding dynamic Poisson's ratio (i.e., <0.31, 0.31–0.41, and >0.41), as shown in Fig. 10. The samples whose dynamic Poisson's ratio is <0.31 have BI values greater than 60, indicating undeveloped fractures. The samples whose dynamic Poisson's ratio is >0.41 have BI values less than 40, indicating developed fractures.

Discussion

The relationship between BI anisotropy value and the anisotropy values of the other parameters (P-wave and S-wave velocity, dynamic Young's modulus, and dynamic Poisson's ratio) can be illustrated by Eqs. (2) and (3). In Eqs. (2) and (3), BI is expressed by dynamic elastic parameters, which correlate directly with the ratio of P-wave and S-wave velocities ($r = V_P/V_S$), as well as S-wave velocity, but not P-wave velocity. Therefore, only the unclear relationship observed is that of the BI anisotropy value and P-wave anisotropy value.

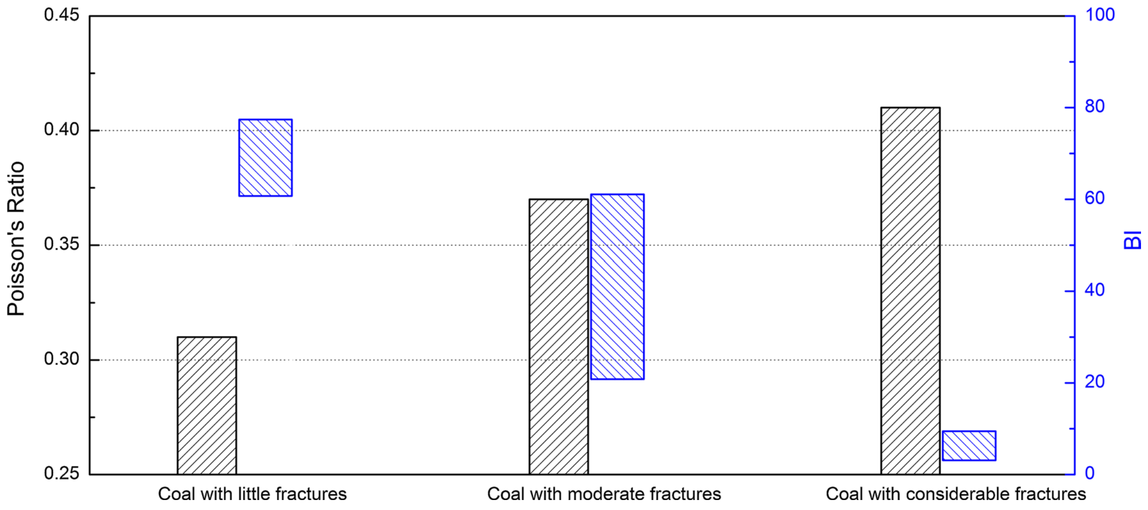

Fig. 10 Statistical analysis of BI versus fracture development in the coal samples [dynamic Poisson's ratio and fracture development data from Ramos (1997)]. Black columns represent the dynamic Poisson's ratio divided into three classes according to fracture development; blue columns denote the BI ranges for the test sample statistics according to the dynamic Poisson's ratio classes

Although the BI of a CBM reservoir has the same variation range as that of a shale gas reservoir, the meanings of the BI for both reservoirs differ. For a CBM reservoir, the BI is mostly influenced by structure (closely connected with coal type, fractures, and bedding), while for a shale gas reservoir, three or more factors may impact the BI, (structure, content, and types of brittle mineral) (Diao, 2013). The relationship between the coal type, fracture development, and BI is clear, due to coal type being divided according to its degree of fragmentation (Fu et al. 2007). Granulated coal has a soft structure and poor integrity, yet shows lower BI values. Fractures must have developed, but with poor connectivity. When fracturing in these CBM reservoirs does not effectively improve permeability, but the fracturing process may instead lead to the deterioration of reservoir permeability due to an increased amount of coal particles or pulverized coal. However, primary coal and fragmented coal are consolidated and hard with no or undeveloped fractures but have good connectivity that corresponds to a higher BI. Fracturing in these types of reservoirs is more conducive to forming a fracture system with good network connectivity. Therefore, based on the relationship mentioned above, we have reason to believe that the combined multiparameter application in brittleness evaluations may be acceptable. This has the potential to simultaneously reduce risk and improve the precision of BI evaluation.

Conclusions

To investigate the BI and A_{BI} characteristics of CBM reservoirs, we conducted the ultrasonic wave tests of 10 coal samples in three directions (parallel, perpendicular, and 45° to the bedding plane). The major conclusions are listed below.

The error of the BI calculated by the chosen method has average values lower than 5% in three test directions.

The BI(90°) generally had the highest values, while the BI(45°) values were close to the BI(0°) values. The BI anisotropy value showed a positive correlation with the dynamic Young's modulus anisotropy value, dynamic Poisson's ratio anisotropy value, S-wave velocity anisotropy value, and the ratio of P-wave and S-wave velocity anisotropy values, but its correlation with the P-wave velocity anisotropy value was unclear.

A unified relationship exists between BI and two other reservoir parameters (coal type and fracture development), which indicates that granulated coal has a soft structure with developed but poor connectivity fractures, showing high BI values. Meanwhile, primary coal and fragmented coal are consolidated and hard with no or undeveloped fractures, but whey have good connectivity that corresponds to a higher BI.

Acknowledgements We would like to thank the Anhui Key Research and Development Program (Grant No. 1804a0802203), the Natural Science Foundation of the Anhui Higher Education Institutions (Grant Nos. KJ2018A0071, KJ2016A192), and the Natural Science Foundation for Young Teachers in AUST (Grant No. QN2017202) for supporting this study. We also thank Li Donghui and Xue Haifei for their help with the coal sample testing. Finally, many thanks are due to the anonymous reviewers and the editor for their valuable suggestions.

Compliance with ethical standards

Conflict of interest On behalf of all authors, the corresponding author states that there is no conflict of interest to declare.

References

Altindag R (2003) Correlation of specific energy with rock brittleness concepts on rock cutting. J S Afr Inst Min Metall 103(3):163–171

Chen J, Xiao X (2013) Mineral composition and brittleness of three sets of Paleozoic organic-rich shales in China South area. J China Coal Soc 38(5):822–826

Copur H, Bilgin N, Tuncdemir H, Balci C (2003) A set of indices based on indentation tests for assessment of rock cutting performance and rock properties. J S Afr Inst Min Metall 103(9):589–599

Diao H (2013) Rock mechanical properties and brittleness evaluation of shale reservoir. Acta Petrol Sin 29(9):3300–3306

Dong S, Tao W (2008) Test on elastic anisotropic coefficients of gas coal. Chin J Geophys 51(3):671–677

Dong S, Wu H, Li D, Huang Y (2016) Experimental study of ultrasonic velocity and anisotropy in coal samples. J Seism Explor 25(2):131–146

Fu X, Qin Y, Wei Z (2007) Coal-bed methane geology. China University of Mining and Technology Press, Beijing

Guo Z, Li X, Liu C, Feng X, Ye S (2013) A shale rock physics model for analysis of brittleness index, mineralogy and porosity in the Barnett Shale. J Geophys Eng 10(2):1–10

Honda H, Sanada Y (1956) Hardness of coal. Fuel 35:451

Huang X, Huang J, Li Z, Yang Q, Sun Q, Cui W (2015) Brittleness index and seismic rock physics model for anisotropic tight-oil sandstone reservoirs. Appl Geophys 12(1):11–22

Hucka V, Das B (1974) Brittleness determination of rocks by different methods. Int J Rock Mech Min Sci Geomech Abstr 11(10):389–392

Liu B, Xi D, Ge N, Wang B, Kern H, Popp T (2002) Anisotropy of Poisson's ratio in Rock Samples at Different Confining Pressures. Chin J Geophys 45(6):880–890

Morcote A, Mavko G, Prasad M (2010) Dynamic elastic properties of coal. Geophysics 75(6):E227–E234

Peng S, Gao Y, Yang R, Chen H, Chen X (2005) Theory of application of AVO for detection of coalbed methane - A case from the Huainan coalfield. Chin J Geophys 48(6):1475–1486

Peng S, Chen H, Yang R, Gao Y, Chen X (2006) Factors facilitating or limiting the use of AVO for coal-bed methane. Geophysics 71(4):C49–C56

Qian K, He Z, Chen Y, Liu X, Li X (2017) Prediction of brittleness based on anisotropic rock physics model for kerogen-rich shale. Appl Geophys 14(4):463–480

Quinn J, Quinn G (1997) Indentation brittleness of ceramics: a fresh approach. J Mater Sci 32(16):4331–4346

Ramos A (1997) 3-D AVO analysis and modeling applied to fracture detection in coalbed methane reservoirs. Geophysics 62(6):1683–1695

Rickman R, Mullen M, Petre J, Grieser B, Kundert D (2008) A practical use of shale petrophysics for stimulation design optimization: all shale plays are not clones of the barnett shale. SPE Technical Conference and Exhibition. Society of Petroleum Engineers: 115258

Ulusay R (2015) The ISRM suggested methods for rock characterization, testing and monitoring: 2007–2014. Springer, Berlin

Wang Y, Xu X (2012) Characteristics of P-wave and S-wave velocities and their relationships with density of six metamorphic kinds of coals. Chin J Geophys 55(11):3754–3761

Wu H, Dong S, Li D, Huang P, Qi X (2015) Experimental study on dynamic elastic parameters of coal samples. Int J Min Sci Technol 25(3):447–452

Yu G, Vozoff K, Durney D (1991) Effects of confining pressure and water saturation on ultrasonic compressional wave velocities in coals. Int J Rock Mech Min Sci Geomech Abstr 28(6):515–522

Yu G, Vozoff K, Durney D (1993) The influence of confining pressure and water saturation on dynamic elastic properties of some Permian coals. Geophysics 58(1):30–38

Yuan J, Deng J, Zhang D, Li D, Yan W, Chen C, Cheng L, Chen Z (2013) Fracability evaluation of shale-gas reservoirs. Acta Petrol Sin 34(3):523–527

Zhou F (2012) Experiment of influence of fractures on coal/rock acoustic velocities: with carboniferous seams of Qinshui basin as example. Coal Geol Explor 40(2):71–74

Acta Geophysica (2019) 67:799–811
https://doi.org/10.1007/s11600-019-00294-2

RESEARCH ARTICLE - APPLIED GEOPHYSICS

Frequency-dependent energy attenuation and velocity dispersion in periodic layered media

Heng Zhang[1] · **Fanchang Zhang**[1] · **Yawei Lu**[1]

Received: 15 November 2018 / Accepted: 22 April 2019 / Published online: 2 May 2019

Abstract

According to Brajanovski periodic layered model, a fractural medium can be equivalent to layered media with periodic distribution of fractural layers and background layers, but the analytical solution given by Brajanovski can only interpret the dispersion and attenuation effects of single characteristic unit model. In order to study the dispersion and attenuation features of multiple characteristic units, forward modeling methods are needed. Based on the theory of two-phase medium, Biot deduced the propagation equation of longitudinal waves in fluid-saturated porous media. However, there are two problems in the forward modeling using time-domain equation. One is the influences of boundary reflection, and the other is the introduction of cumulative error. For convenience, time-domain equation is rewritten in the frequency domain, thus constructing a one-dimensional rock physics model. Then, forward method is used to study the dispersion and attenuation features of fluid-saturated medium. Numerical simulation results are found to be in good agreement with the analytical solution. Furthermore, the frequency-domain forward method can analyze the velocity dispersion and energy attenuation of longitudinal waves in any multilayered fracture medium. By analyzing those numerical simulation results, it can be obtained that, as the length of characteristic unit increases or the number of characteristic unit decreases, both the starting frequency of dispersion and the peak frequency of attenuation shift to low, whatever the attenuation peaks are equal. In addition, the effects of porosity, permeability and fluid saturation on energy attenuation and velocity dispersion are also studied. Finally, the stress field and displacement field distributions of fluid-saturated fractural medium are given by the frequency-domain forward modeling method.

Keywords Attenuation · Dispersion · Fractural medium · Frequency-domain forward modeling

Introduction

In recent years, natural fractured reservoirs have attracted the interest of geophysicists in the fields of petroleum exploration and development. In many cases, natural fractures control the permeability of the reservoir, so the ability to find and characterize natural fracture areas of the reservoir is a major challenge for seismic exploration.

When discussing the seismic response of fluid-saturated porous media, the most commonly used theory is Biot's (1939, 1941, 1956a, b, 1962) two-phase medium theory, which divides fluid-saturated porous media into solid frame and porous fluids, respectively. Biot two-phase medium theory is the beginning of research on fluid-saturated porous media. The theory predicts the longitudinal wave velocity in fluid-saturated medium under the condition that the dry rock skeleton and fluid properties are known. The energy loss between the crest and trough of a longitudinal wave is called "Biot loss." However, the loss of fluid in the macroscopic background is much less than the loss in the seismic band (Pride et al. 2004). Mavko and Nur (1979) proposed a microscopic mechanism to explain the seismic wave attenuation of porous media. When seismic wave causes particle-scale background rupture, microcrack will generate larger fluid pressure than the pore space and then cause fluid to flow from microcrack into pore, called the "squirt flow." Dvorkin

✉ Fanchang Zhang
zhangfch@upc.edu.cn

Heng Zhang
s17010186@s.upc.edu.cn

Yawei Lu
luyawei123456@gmail.com

[1] China University of Petroleum (East China), Qingdao, People's Republic of China

et al. (1994) proposed a squirt flow model for fluid-saturated rocks and combined it with Biot theory to obtain Biot/squirt (BISQ) theory. Ba and Zhao (2016) developed a new dual-porosity medium based on squirt flow theory and proposed a new boundary to predict the longitudinal wave velocity of saturated dense rock. Although the squirt flow theory can fully explain and calculate the attenuation at ultrasonic frequencies, it fails to explain the attenuation produced in the seismic band. In recent years, Rubino et al. (2009) and Ba et al. (2012) have strongly proved that the most important reason for the dispersion and attenuation of longitudinal waves in the seismic frequency band is that the waves induced fluid flow (WIFF) in the mesoscopic scale. Dvorkin (2014) and Shen et al. (2018) study the mechanism for attenuation in the seismic frequency band and establish the relationship between velocity and formation absorption parameters.

The mechanism of attenuation and dispersion due to the presence of fluid in rock pore space is broadly called WIFF. Elastic wave creates pressure gradient in the fluid phase that causes the fluid to flow until fluid pressure reaches equilibrium under the action of internal friction. Because of the effect of WIFF, elastic parameters of the medium exhibit frequency-dependent features and then cause velocity dispersion and energy attenuation when elastic waves propagate in the subsurface medium, especially in oil and gas reservoirs. Gassmann–Biot theory (Gassmann 1951; Biot 1956a) gives the expression of the bulk modulus of fluid-saturated rock in an isotropic medium at low frequencies, and the theory becomes a very classic model for fluid replacement, but it only applied to isotropic media. For anisotropic background media with cracks, fractures, etc., Brown and Korringa (1975) derived an effective elastic modulus formula for anisotropic rock skeletons and fluid-saturated rocks. This model is equally applicable to low-frequency conditions and does not work well under laboratory ultrasonic conditions. White et al. (1975) first proposed a periodic layered patchy saturated model with the interlaced superposition of water and gas layers on the premise that the mesoscopic scale was attenuated by WIFF, and described the longitudinal wave dispersion and attenuation. Hudson et al. (1996) and Chapman (2003) developed a theoretical model of attenuation and dispersion due to wave-induced flow between cracks and pores; this model is developed for sparse penny-shaped cracks in porous matrices. Chapman (2002, 2003) proposed a medium model with aligned fractures under isotropic media conditions. Galvin and Gurevich (2003) and Brajanovski et al. (2005) calculated the stiffness matrix of porous media with aligned planar fractures and then calculated the attenuation and dispersion of fast longitudinal waves. Galvin and Gurevich (2009) proposed a complex pore space model composed of penny-shaped cracks and rigid pores and gave an expression for calculating the modulus of the model. A more general approach to modeling fractural porous media is based on Biot's theory of porous elasticity. In the context of Biot's theory, fractures can be thought of as heterogeneous formations with high compliance. Based on this assumption, a model of fractural medium can be constructed and then applied to study the wave propagation in non-uniform porous media.

In this paper, we only study the elastic wave response of a one-dimensional model. The characteristic units are stacked vertically with no horizontal heterogeneity. According to the Brajanovski periodic layered model, the fractural porous medium is equivalent to a layered medium in which the fracture layer and the background layer are periodically distributed. Combined with Gurevich et al. the periodically distributed fracture layer is regarded as a layer with high compliance and high porosity embedded in background porous medium, and an equivalent model of fractural porous medium is obtained. Then based on the Biot pore elasticity equation, we use the finite difference algorithm to carry out the forward modeling, to study the elastic characteristics of the porous media with plane fractures and to analyze the energy attenuation and velocity dispersion characteristics of the fast longitudinal waves. In addition, we examine the effects of three important parameters of porosity, permeability and fluid saturation on energy attenuation and velocity dispersion.

Elastic wave response with planar fracture medium

The main reason for the attenuation of elastic waves in fluid-saturated rocks is the WIFF. When elastic waves propagate in a fluid-saturated porous medium, a local pressure gradient is formed in the fluid phase, causing liquid flow and corresponding viscous friction until the pore pressure reaches equilibrium (Müller et al. 2010). When a simple harmonic wave propagates in a fluid-saturated porous medium, a part of the rock is compressed and the other part is expanded. High pore pressure is generated in the compression zone, and the pore fluid will flow from high pore pressure to low pressure, so that the relative flow of the fluid will cause energy loss. In other words, during the propagation of the wave, dispersion and attenuation occur due to the influence of WIFF.

According to the Brajanovski periodic layered model, the fractured porous medium can be equivalent to a layered medium with periodic distribution of the fracture layer and the background layer. Gurevich et al. assume that the fracture in the periodic layered medium is a thin layer with high compliance and high porosity. Thus, the fractural porous medium is equivalent to the model shown in Fig. 1 (White et al. 1975; Galvin and Gurevich 2003), where h represents the thickness of one characteristic unit, h_1 represents the thickness of the background porous medium, and h_2 represents the thickness

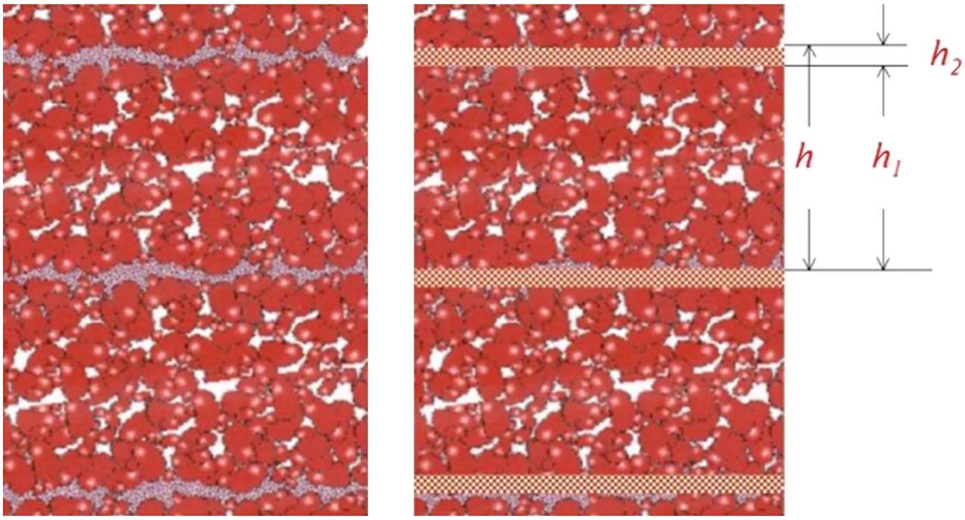

Fig. 1 Equivalent model of fractured porous media (Galvin and Gurevich 2003)

of the equivalent fracture layer; they are stacked together to form a single characteristic unit. The compressive forces cause fluid flow from the softer layer into the stiffer layer during wave propagation on the rock, which creates a pressure gradient between the layers and causes attenuation and dispersion. We will use this model to study the elastic wave response of fractural porous media at mesoscopic scale.

Assume that the symmetry axis of the medium is parallel to the *z*-axis; the layer is infinitely extended in the *xoy* plane. When the porous rock is dry or gas saturation, the stiffness matrix is as follows:

$$\mathbf{c}^{\mathrm{dry}}=\begin{bmatrix} \frac{(1-2\langle\gamma\rangle)^2}{\langle 1/L\rangle}+4\langle\mu\rangle-4\langle\gamma\mu\rangle & \frac{(1-2\langle\gamma\rangle)^2}{\langle 1/L\rangle}+2\langle\mu\rangle-4\langle\gamma\mu\rangle & \frac{1-2\langle\gamma\rangle}{\langle 1/L\rangle} & 0 & 0 & 0 \\ \frac{(1-2\langle\gamma\rangle)^2}{\langle 1/L\rangle}+2\langle\mu\rangle-4\langle\gamma\mu\rangle & \frac{(1-2\langle\gamma\rangle)^2}{\langle 1/L\rangle}+4\langle\mu\rangle-4\langle\gamma\mu\rangle & \frac{1-2\langle\gamma\rangle}{\langle 1/L\rangle} & 0 & 0 & 0 \\ \frac{1-2\langle\gamma\rangle}{\langle 1/L\rangle} & \frac{1-2\langle\gamma\rangle}{\langle 1/L\rangle} & \frac{1}{\langle 1/L\rangle} & 0 & 0 & 0 \\ 0 & 0 & 0 & \frac{1}{\langle 1/\mu\rangle} & 0 & 0 \\ 0 & 0 & 0 & 0 & \frac{1}{\langle 1/\mu\rangle} & 0 \\ 0 & 0 & 0 & 0 & 0 & \langle\mu\rangle \end{bmatrix} \tag{1}$$

In Eq. (1), the brackets $\langle\cdot\rangle$ mean the thickness weighted average of the property, that is, $\langle q\rangle = q_c h_c + q_b h_b = (1-h_b)q_c + q_b h_b$, where h_b and h_c denote the thickness fraction of background layer and fracture layer, respectively. γ are the square of the shear wave velocity to the longitudinal wave velocity ration, $L=\lambda+2\mu=K+4\mu/3$ is the equivalent P-wave modulus, λ and μ are the Lame parameters, and K is bulk modulus.

Inversion of stiffness matrix $\mathbf{c}^{\mathrm{dry}}$ yields the compliance matrix $\mathbf{s}^{\mathrm{dry}}=(\mathbf{c}^{\mathrm{dry}})^{-1}$:

$$\mathbf{s}^{\mathrm{dry}}=\begin{bmatrix} \frac{1-\langle\gamma\mu\rangle/\langle\mu\rangle}{3\langle\mu\rangle-4\langle\gamma\mu\rangle} & -\frac{1-2\langle\gamma\mu\rangle/\langle\mu\rangle}{2(3\langle\mu\rangle-4\langle\gamma\mu\rangle)} & -\frac{1-2\langle\gamma\rangle}{2(3\langle\mu\rangle-4\langle\gamma\mu\rangle)} & 0 & 0 & 0 \\ -\frac{1-2\langle\gamma\mu\rangle/\langle\mu\rangle}{2(3\langle\mu\rangle-4\langle\gamma\mu\rangle)} & \frac{1-\langle\gamma\mu\rangle/\langle\mu\rangle}{3\langle\mu\rangle-4\langle\gamma\mu\rangle} & -\frac{1-2\langle\gamma\rangle}{2(3\langle\mu\rangle-4\langle\gamma\mu\rangle)} & 0 & 0 & 0 \\ -\frac{1-2\langle\gamma\rangle}{2(3\langle\mu\rangle-4\langle\gamma\mu\rangle)} & -\frac{1-2\langle\gamma\rangle}{2(3\langle\mu\rangle-4\langle\gamma\mu\rangle)} & \left\langle\frac{1}{L}\right\rangle+\frac{(1-2\langle\gamma\rangle)^2}{3\langle\mu\rangle-4\langle\gamma\mu\rangle} & 0 & 0 & 0 \\ 0 & 0 & 0 & \left\langle\frac{1}{\mu}\right\rangle & 0 & 0 \\ 0 & 0 & 0 & 0 & \left\langle\frac{1}{\mu}\right\rangle & 0 \\ 0 & 0 & 0 & 0 & 0 & \frac{1}{\langle\mu\rangle} \end{bmatrix} \tag{2}$$

When the thickness of the fracture layer is infinite, that is, $h_\mathrm{c} \to 0$, there is $\mu_\mathrm{c}, L_\mathrm{c} \to 0$, and $\langle \mu \rangle \to \mu_\mathrm{b}$, $\langle \gamma \rangle \to \gamma_\mathrm{b}$, $\left\langle \frac{1}{\mu} \right\rangle \to \frac{1}{\mu_\mathrm{b}} + \lim\limits_{h_\mathrm{c}\to 0} \frac{h_\mathrm{c}}{\mu_\mathrm{c}}$, $\left\langle \frac{1}{L} \right\rangle \to \frac{1}{L_\mathrm{b}} + \lim\limits_{h_\mathrm{c}\to 0} \frac{h_\mathrm{c}}{L_\mathrm{c}}$, $\langle \gamma \mu \rangle \to \gamma_\mathrm{b}\mu_\mathrm{b}$. μ_b and μ_c are the shear modulus of background and fracture layers, respectively. L_b and L_c are the P-wave modulus of background and fracture layers, respectively. Substitution of these results into Eq. (2) yields the compliance matrix of the dry fractured porous medium:

$$\begin{aligned}\mathbf{s}^{\mathrm{dry}} &= \mathbf{s}_\mathrm{b}^{\mathrm{dry}} + \mathbf{s}_\mathrm{c}^{\mathrm{dry}} \\ &= \begin{bmatrix} \frac{1}{E_\mathrm{b}} & -\frac{\nu_\mathrm{b}}{E_\mathrm{b}} & -\frac{\nu_\mathrm{b}}{E_\mathrm{b}} & 0 & 0 & 0 \\ -\frac{\nu_\mathrm{b}}{E_\mathrm{b}} & \frac{1}{E_\mathrm{b}} & -\frac{\nu_\mathrm{b}}{E_\mathrm{b}} & 0 & 0 & 0 \\ -\frac{\nu_\mathrm{b}}{E_\mathrm{b}} & -\frac{\nu_\mathrm{b}}{E_\mathrm{b}} & \frac{1}{E_\mathrm{b}} & 0 & 0 & 0 \\ 0 & 0 & 0 & \frac{1}{\mu_\mathrm{b}} & 0 & 0 \\ 0 & 0 & 0 & 0 & \frac{1}{\mu_\mathrm{b}} & 0 \\ 0 & 0 & 0 & 0 & 0 & \frac{1}{\mu_\mathrm{b}} \end{bmatrix} + \lim_{h_\mathrm{c}\to 0} \begin{bmatrix} 0 & 0 & 0 & 0 & 0 & 0 \\ 0 & 0 & 0 & 0 & 0 & 0 \\ 0 & 0 & \frac{h_\mathrm{c}}{L_\mathrm{c}} & 0 & 0 & 0 \\ 0 & 0 & 0 & \frac{h_\mathrm{c}}{\mu_\mathrm{c}} & 0 & 0 \\ 0 & 0 & 0 & 0 & \frac{h_\mathrm{c}}{\mu_\mathrm{c}} & 0 \\ 0 & 0 & 0 & 0 & 0 & 0 \end{bmatrix}\end{aligned} \tag{3}$$

In Eq. (3) $E_\mathrm{b} = \mu_\mathrm{b}(3 - 4\gamma_\mathrm{b})/(1 - \gamma_\mathrm{b})$ denotes the dynamic Young's modulus of background porous layer and $\gamma_\mathrm{b} = 1 - 2\gamma_\mathrm{b}/[2(1 - \gamma_\mathrm{b})]$ denotes the dynamic Poisson's ratio of background porous layer. Matrices $\mathbf{s}_\mathrm{b}^{\mathrm{dry}}$ and $\mathbf{s}_\mathrm{c}^{\mathrm{dry}}$ are the compliance matrices caused by the dry background and dry fracture layers, respectively. Equation (3) is consistent with the equation for the compliance matrix of a fractural medium as given by linear slip deformation theory (Schoenberg and Douma 1988; Schoenberg and Sayers 2012).

Assuming the shear modulus μ_c and longitudinal modulus $K_\mathrm{c} + 4\mu_\mathrm{c}/3$ are

$\mathcal{O}(h_\mathrm{c})$ as $h_\mathrm{c} \to 0$, and defining

$$\lim_{h_\mathrm{c}\to 0} \frac{h_\mathrm{c}}{L_\mathrm{c}} = Z_\mathrm{N},\ \lim_{h_\mathrm{c}\to 0} \frac{h_\mathrm{c}}{\mu_\mathrm{c}} = Z_\mathrm{T}, \tag{4}$$

where Z_N and Z_T are called excess normal and tangential compliances, respectively, Fang et al. (2013) demonstrate the relations between Z_N, Z_T and fractures infill material properties. These results also verify the correct rationality of the assumption that the fracture layer is a thin layer with high compliance and high porosity.

However, when the pore space is saturated with fluid, the rock exhibits frequency-dependent velocity dispersion and attenuation due to the effect of WIFF between pores and fractures. Elastic waves in such a periodically layered and porous medium with periodic and segmental constant coefficients can be described by the Biot's equation of poroelasticity (Biot 1962).

The fluid-saturated P-wave modulus of layer is given by Gassmann's equation

$$C = L + \alpha^2 M \tag{5}$$

In Eq. (5), $\alpha = 1 - K_{\mathrm{dry}}/K_\mathrm{g}$ denotes Biot–Wills parameter and $1/M = (\alpha - \phi)/K_\mathrm{g} + \phi/K_\mathrm{f}$ denotes the bulk modulus of pore space.

White et al. (1975) and Norris (1993) showed that for frequencies much smaller than the Biot's characteristic frequency $\omega_\mathrm{B} = \eta\phi/\kappa\rho_\mathrm{f}$ and also much smaller than the resonant frequency of the layering $\omega_\mathrm{R} = V_\mathrm{p}/H$, the P-wave modulus c_{33}^{sat} of a periodic lamellar porous medium composed of alternating fracture layers and background layers in fluid saturation can be expressed as:

$$\frac{1}{c_{33}^{\mathrm{sat}}} = \left\langle \frac{1}{C} \right\rangle + \frac{2}{\sqrt{i\omega\eta H}} \frac{\left(\frac{\alpha_\mathrm{b} M_\mathrm{b}}{C_\mathrm{b}} - \frac{\alpha_\mathrm{c} M_\mathrm{c}}{C_\mathrm{c}} \right)^2}{\sqrt{\frac{M_\mathrm{b} L_\mathrm{b}}{C_\mathrm{b} \kappa_\mathrm{b}}} \cot\left(\sqrt{\frac{i\omega\eta C_\mathrm{b}}{\kappa_\mathrm{b} M_\mathrm{b} L_\mathrm{b}}} \frac{h_\mathrm{b} H}{2} \right) + \sqrt{\frac{M_\mathrm{c} L_\mathrm{c}}{C_\mathrm{c} \kappa_\mathrm{c}}} \cot\left(\sqrt{\frac{i\omega\eta C_\mathrm{c}}{\kappa_\mathrm{c} M_\mathrm{c} L_\mathrm{c}}} \frac{h_\mathrm{c} H}{2} \right)} \tag{6}$$

In Eq. (6) ω is circular frequency, η is the viscosity of the pore fluid.

H denotes the thickness of a characteristic unit, and h_b and h_c are the thickness fraction of background layer and fracture layer, respectively. κ_b and κ_c are the permeability of the background layer and fracture layer, respectively. Subscript b indicates the elastic parameters of the background layer, and subscript c indicates the elastic parameters of fracture layer.

After obtaining the equivalent longitudinal wave modulus of the fluid-saturated medium in the vertical direction, the velocity dispersion and energy attenuation perpendicular to the layered medium can be obtained by the following Eq. (7).

$$\begin{aligned} V_\mathrm{p} &= \sqrt{c_{33}^{\mathrm{sat}}/\rho} \\ 1/Q &= \mathrm{Im}(c_{33}^{\mathrm{sat}})/\mathrm{Re}(c_{33}^{\mathrm{sat}}) \end{aligned} \tag{7}$$

In Eq. (7) $\rho = h_\mathrm{b}[\phi_\mathrm{b}\rho_\mathrm{f} + (1 - \phi_\mathrm{b})\rho_\mathrm{g}] + h_\mathrm{c}[\phi_\mathrm{c}\rho_\mathrm{f} + (1 - \phi_\mathrm{c})\rho_\mathrm{g}]$ denotes the density of the rock. ρ_b and ρ_c are the density of the background and fracture layers, respectively. ϕ_b and ϕ_c are the porosity of the background and fracture layers, respectively.

One-dimensional frequency-domain forward method

The analytical solution given in the previous section can only describe the attenuation and dispersion features of a single characteristic unit. In order to study the seismic response of multiple characteristic units, we will use the numerical simulation method of finite difference forward modeling based on Biot theory. Under the assumption of linear elasticity and isotropic medium, Biot gives the equation that P-waves satisfy in fluid-saturated porous media:

$$\begin{aligned}&-\nabla\cdot\sigma+\alpha\nabla p=f\\&\frac{\partial}{\partial t}\left(\frac{p}{M}+\alpha\nabla\cdot\mathbf{u}\right)-\nabla\cdot\frac{\kappa}{\eta}\nabla p=g\end{aligned}\tag{8}$$

where f and g are the body forces and fluid forces acting on the porous medium, respectively. σ is stress, p is fluid pressure, $\mathbf{u}$ are solid displacement matrix; α is Biot–Wills coefficient, M is the bulk modulus of pore space, κ is permeability, and η is fluid viscosity.

To simplify the research, we just consider a P-wave propagating in the z-direction, assuming that the body forces and fluid forces are vanishing, Eq. (8) can be simplified as:

$$\begin{aligned}&-(\lambda+2\mu)\frac{\partial^2u}{\partial z^2}+\alpha\frac{\partial p}{\partial z}=0\\&\frac{\partial}{\partial t}\left(\frac{p}{M}+\alpha\frac{\partial u}{\partial z}\right)-\frac{\kappa}{\eta}\frac{\partial^2p}{\partial z^2}=0\end{aligned}\tag{9}$$

where λ and μ are the Lame parameters. In order to perform the forward modeling, the differential processing of the above formula is as follows:

$$\begin{aligned}&-\frac{U_{i-1}^{t+1}-2U_i^{t+1}+U_{i+1}^{t+1}}{\Delta z^2}+\frac{P_i^{t+1}-P_{i-1}^{t+1}}{\Delta z}=0\\&\frac{1}{\Delta t}\left(\frac{P_{i+1}^{t+1}}{M}-\frac{P_i^t}{M}+\frac{U_{i+1}^{t+1}-U_i^{t+1}}{\Delta z}-\frac{U_{i+1}^{t+1}-U_i^{t+1}}{\Delta z}\right)\\&=\frac{1}{2}\frac{\kappa}{\eta}\left(\frac{P_{i-1}^{t+1}-2P_i^{t+1}+P_{i+1}^{t+1}}{\Delta z^2}+\frac{P_{i-1}^t-2P_i^t+P_{i+1}^t}{\Delta z^2}\right)\end{aligned}\tag{10}$$

where U is the solid-phase displacement, P is the fluid pressure, superscript indicates different nodes, and subscripts indicate different moments. Δt is time step, and Δz is space grid step size. In order to ensure the stability of the differential forward, it is required that within a time step Δt, the wavelength does not pass more than one grid step Δz (Yang et al. 2003).

Equation (10) can be used to calculate the fluid pressure and solid displacement field distribution at any time when the wave propagates in a two-phase medium. If we want to obtain the velocity dispersion and attenuation of the medium, the absorbing boundary condition needs to be added. However, the forward modeling in the time domain needs to consider whether the boundary reflection is completely absorbed, and it is also possible that the iterative operation produces a large cumulative error, which has a great influence on the result. So we consider using the frequency-domain forward modeling method to study the elastic wave response in two-phase media.

Under the assumption that the stress divergence of the porous medium is zero, the one-dimensional form of the quasi-static Biot equation of linear consolidation coupling in the frequency-space domain is:

$$\begin{aligned}&\frac{\partial\tau_{zz}}{\partial z}=0\\&\tau_{zz}=\left(K_{\mathrm{dry}}+\frac{4}{3}\mu_{\mathrm{dry}}\right)\frac{\partial U_{\mathrm{s}}}{\partial z}-\alpha P\\&\frac{\partial U_{\mathrm{f}}}{\partial z}+\alpha\frac{\partial U_{\mathrm{s}}}{\partial z}+\frac{P}{M}=0\\&j\omega U_{\mathrm{f}}+\frac{\kappa}{\eta}\frac{\partial P}{\partial z}=0\end{aligned}\tag{11}$$

where τ_{zz} is the strain of the solid frame, P is the fluid pressure, U_{s} is the displacement of the solid, U_{f} is the displacement of fluid relative to solid, and K_{dry} and μ_{dry} are the bulk modulus and shear modulus of the solid frame, respectively. α is Biot–Wills parameter, M is the bulk modulus of pore space, ω is circular frequency, κ is permeability, and η is the viscosity of pore fluid.

Using the Taylor series expansion to expand Eq. (11) into the frequency-domain difference format, we obtain the following:

$$\begin{aligned}&\frac{\tau_{zz}(i+1)-\tau_{zz}(i-1)}{2\mathrm{d}z}=0\\&\tau_{zz}(i)=\left(K_{\mathrm{dry}}+\frac{4}{3}\mu_{\mathrm{dry}}\right)\frac{U_{\mathrm{s}}(i+1)-U_{\mathrm{s}}(i-1)}{2\mathrm{d}z}-\alpha P(i)\\&\frac{U_{\mathrm{f}}(i+1)-U_{\mathrm{f}}(i-1)}{2\mathrm{d}z}+\alpha\frac{U_{\mathrm{s}}(i+1)-U_{\mathrm{s}}(i-1)}{2\mathrm{d}z}+\frac{P(i)}{M}=0\\&j\omega U_{\mathrm{f}}(i)+\frac{\kappa}{\eta}\frac{P(i+1)-P(i-1)}{2\mathrm{d}z}=0\end{aligned}\tag{12}$$

where i is the ith grid point.

When numerical simulation is performed using Eq. (12), it is necessary to apply an external force at the upper and lower interfaces to simulate the role of simple harmonics wave. In addition, in order to ensure the closed condition of the petrophysical model, the fluid displacement of the upper and lower boundaries is zero. So the boundary conditions are:

$$\begin{aligned}&\tau_{zz}^{\mathrm{upper}}=\tau_{zz}^{\mathrm{lower}}=p_0\\&U_{\mathrm{f}}^{\mathrm{upper}}=U_{\mathrm{f}}^{\mathrm{lower}}=0\end{aligned}\tag{13}$$

where $\tau_{zz}^{\mathrm{upper}}$ and $\tau_{zz}^{\mathrm{lower}}$ are the stress of the upper interface and lower interface, respectively. $U_{\mathrm{f}}^{\mathrm{upper}}$ and $U_{\mathrm{f}}^{\mathrm{lower}}$ are the relative displacement of fluid at the upper and lower interfaces (Wu and Wu 2018), respectively.

Using the frequency-domain difference format Eq. (12), combined with the boundary condition Eq. (13), the finite

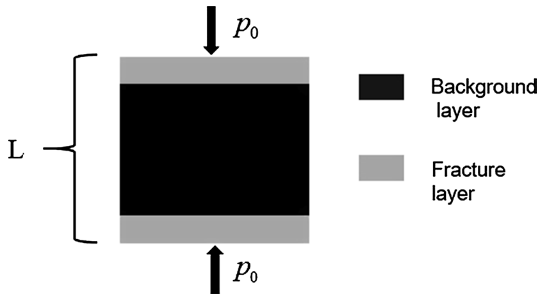

Fig. 2 Sketch of the model

difference numerical simulation method can be used to obtain the solid displacement value U_s at any point in the model medium. In the case of a known solid displacement field distribution, the overall strain of the model medium can be determined to satisfy:

$$e = \frac{U_s^{\text{lower}} - U_s^{\text{upper}}}{L} \tag{14}$$

where U_s^{upper} and U_s^{lower} are the solid displacement of the upper interface and lower interface, respectively.

When the medium is subjected to an external force p_0, the medium generates a bulk strain e, their ratio is the equivalent plane wave modulus E of the medium.

$$E = \frac{p_0}{e} \tag{15}$$

Because of the effect of WIFF, the modulus is frequency dependent, $E(\omega)$, and then velocity dispersion and energy attenuation satisfy:

$$\begin{aligned} V_P(\omega) &= \sqrt{\mathrm{Re}[E(\omega)]/\rho} \\ Q^{-1}(\omega) &= \mathrm{Im}[E(\omega)]/\mathrm{Re}[E(\omega)] \end{aligned} \tag{16}$$

where Re( ) and Im( ) are the real and imaginary parts of the plural, respectively.

ρ is the density satisfying:

$$\rho = h_b[\rho_g \cdot (1 - \phi_b) + \rho_f \cdot \phi_b] + h_c[\rho_g \cdot (1 - \phi_c) + \rho_f \cdot \phi_c] \tag{17}$$

where h_b, ρ_b and ϕ_b are the thickness fraction, density and porosity of the background layer, respectively. h_c, ρ_c and ϕ_c are the thickness fraction, density and porosity of the fracture layer, respectively.

Numerical simulation

It is assumed that the fluid-saturated horizontal layered is periodically arranged alternately, and the lateral is infinitely extended. In order to study the elastic wave response of layered porous media with planar fractures, firstly, we compare the agreement between the white analytical solution and the frequency-domain forward modeling to verify the correctness and rationality of frequency-domain forward modeling, and then we change the parameters such as the number of

Table 1 Porous media parameter

Skeleton parameter	Fluid parameter	Fracture layer parameter	Background layer parameter
$K_g = 33.4$ Gpa	$K_f = 2.2$ Gpa	$K_{dry} = 0.6$ Gpa	$K_{dry} = 6$ Gpa
$\mu_g = 22$ Gpa	$\rho_f = 1000\ \mathrm{kg/m^3}$	$\mu_{dry} = 0.3$ Gpa	$\mu_{dry} = 5$ Gpa
$\rho_g = 2650\ \mathrm{kg/m^3}$	$\eta = 1 \times 10^{-3}$ pa s	$\phi_c = 0.8$	$\phi_b = 0.2$
		$k_c = 5 \times 10^{-10}\ \mathrm{m^2}$	$k_b = 3 \times 10^{-13}\ \mathrm{m^2}$

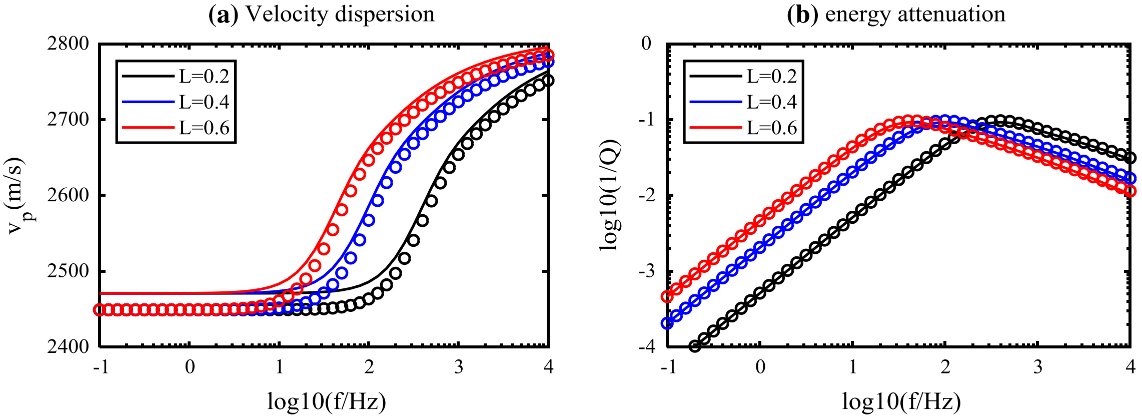
(a) Velocity dispersion **(b)** energy attenuation

Fig. 3 P-wave velocity dispersion (**a**) and energy attenuation (**b**)

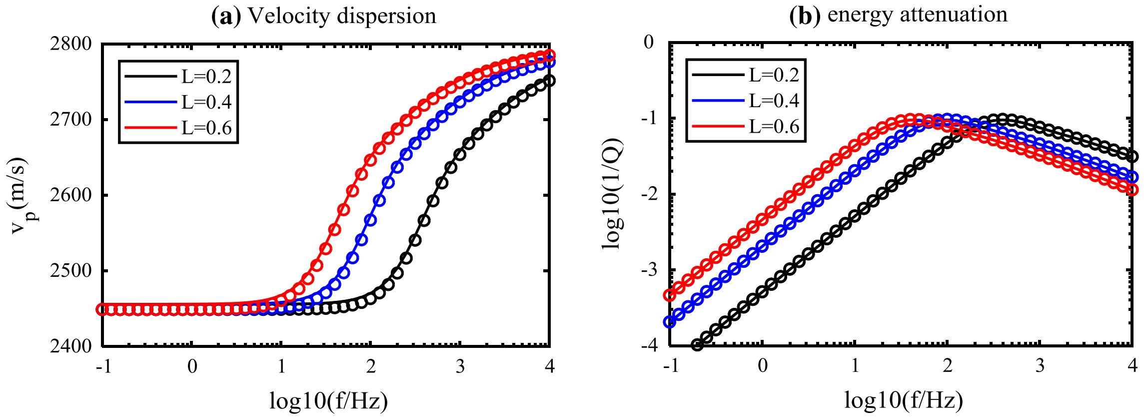

Fig. 4 P-wave velocity dispersion (**a**) and energy attenuation (**b**)

characteristic units, fracture thickness, fluid saturation, background porosity and permeability, to analyze the variation of the elastic wave response and compare with the previous research results to confirm the correctness of the research results (Galvin and Gurevich 2003; Brajanovski et al. 2005; Galvin and Gurevich 2009; Wu and Wu 2018).

Suppose the model contains only one characteristic unit and the thickness of the fracture layer is 0.1L; the sketch of the model is shown in Fig. 2. In Fig. 2, p_0 is an external force applied to the upper and lower interfaces. From top to bottom, there are fracture layer with thickness of 0.05L, background layer with thickness of 0.9L, and fracture layer with thickness of 0.05L; these three parts form a single characteristic unit.

Correctness, accuracy and computational efficiency of frequency-domain forward modeling

Firstly, we will verify the correctness of the frequency-domain forward method. Depending on the model in Fig. 2 and pore medium parameters in Table 1, the velocity dispersion and energy attenuation of Brajanovski layered medium with planar fractures are studied by analytical solution expression and frequency-domain numerical simulation. Their results are shown in Figs. 3 and 4.

Figure 3 and 4 shows the P-wave velocity dispersion and energy attenuation, the solid line represents the Brajanovski analytical solution, and the dotted line denotes the result of numerical simulation. The black curve, the blue curve and the red curve correspond to the characteristic unit thicknesses of 0.2 m, 0.4 m and 0.6 m, respectively. In Fig. 3, the model is divided into 400 grid points in the vertical direction for numerical simulation, and we can see the results of numerical simulation are in poor agreement with the analytical solution, especially in the low-frequency region. We deduce the reason for this error may be because the grid step size is too large. So we split the model into 900 grid points and the obtained results are shown in Fig. 4; the numerical simulation results are consistent with the analytical solution results. By comparing Fig. 3 with Fig. 4, we can conclude that when the grid points are small, it may cause the forward to produce dispersion phenomenon. Appropriately

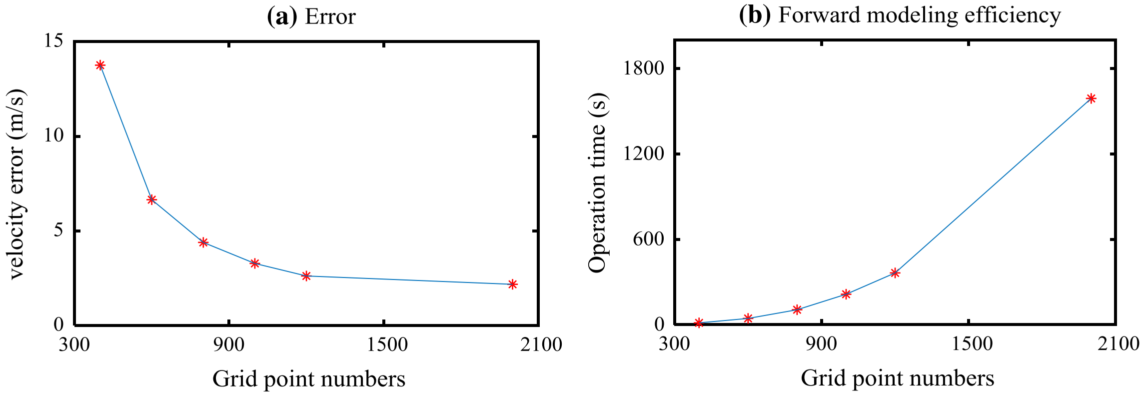

Fig. 5 Calculation accuracy (**a**) and efficiency (**b**) of finite difference forward modeling

increasing the number of gridding points can effectively weaken the dispersion phenomenon and reduce the error between the numerical simulation results and the analytical solution.

The relationship between accuracy and efficiency of differential forward modeling and the number of grid points is analyzed. Assuming that the model length is 0.2 m and contains only one characteristic unit, the model parameters used in the numerical simulation are shown in Table 1. The result is presented in Fig. 5.

It can be observed in Fig. 5 that, as the number of grid points increases, the error between numerical simulation and analytical solution decreases rapidly. When the number of grid points is greater than 800, the longitudinal wave velocity error is not more than 5 m/s. When the number of grid points is further increased, the velocity error does not decrease significantly, and the time spent on numerical simulation increases rapidly. In summary, we believe that when the number of grid points is between 800 and 1000, the calculation accuracy and efficiency can be satisfied. So in later studies, the model was divided into 800 grid points in the vertical direction.

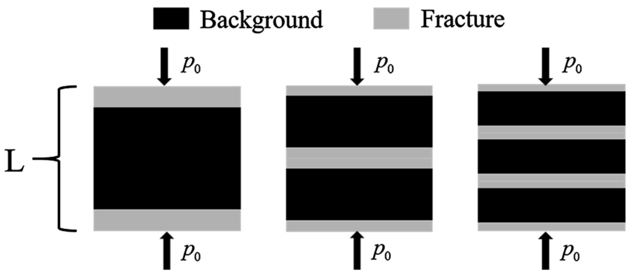

Fig. 6 Media model with different characteristic units

Influence of the length and number of characteristic units and thickness of fracture layer on elastic wave response

Firstly, we analyze the velocity dispersion and energy attenuation corresponding to different lengths of the characteristic unit. From the left of Fig. 4, we can see that as the length of the characteristic unit increases, the starting frequency of the velocity dispersion decreases, but the velocity corresponding to the low-frequency limit and the high-frequency limit does not vary. As can be seen on the right of Fig. 4, the attenuation peak remains unchanged, but the peak frequency shifts toward low frequency as the length of the characteristic unit increases.

Then, we analyze velocity dispersion and energy attenuation corresponding to multiple characteristic units. Assume that the total thickness of the medium is constant, divided it into different numbers of characteristic units, and the fracture thickness fraction in each characteristic unit is 10%. The model media with different numbers of characteristic units are forwarded separately to study the attenuation and dispersion features of the porous media with planar fractures.

As shown in Fig. 6, the model is divided into one, two and three characteristic units for forward modeling, and the corresponding elastic wave response is shown in Fig. 7. It can be seen from Fig. 7a that as the number of characteristic unit increases, the low-frequency limit velocity does not change, but the high-frequency limit velocity decreases, and the dispersion start frequency shifts to high-frequency direction. In Fig. 7b, the energy attenuation peaks have the same magnitude, but the frequency corresponding to the attenuation peak shifts toward high-frequency direction as the number of characteristic unit increases. This is because as the number of characteristic unit increases, the thickness of the single characteristic unit and the thickness of the fracture

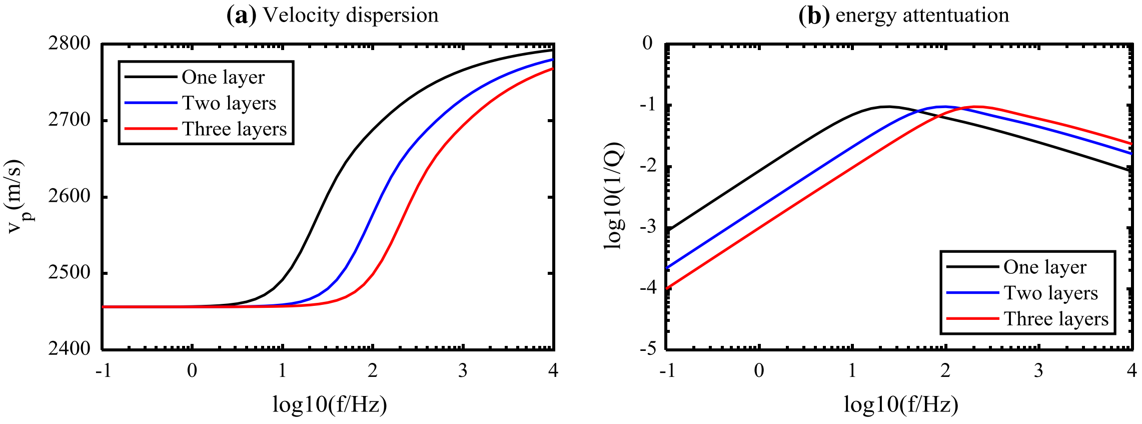

Fig. 7 Velocity dispersion (**a**) and attenuation (**b**) corresponding to the number of different feature units

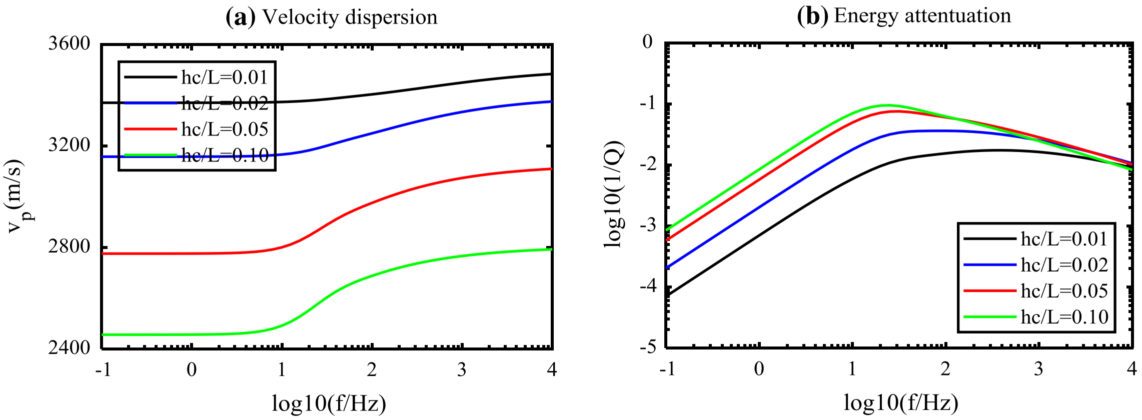

Fig. 8 Velocity dispersion (**a**) and attenuation (**b**) for different crack thicknesses

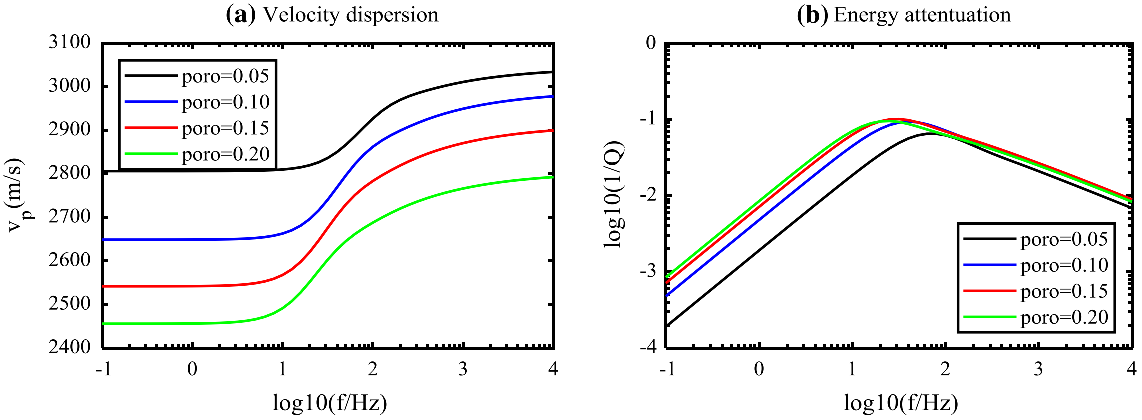

Fig. 9 Velocity dispersion (**a**) and attenuation (**b**) of porosity in different background layers

layer decrease, causing the initial frequency of the velocity dispersion and energy attenuation to move to high frequency.

Further study is carried out when the thickness of the medium $L = 0.4$ m remains unchanged, the variation features of velocity dispersion and energy attenuation when the thickness of fracture layer is changed. Assuming that the media contains only one characteristic unit, the thickness of fracture layer accounts for 0.01, 0.02, 0.05 and 0.1 of the total thickness of the medium, respectively. The forward result is shown in Fig. 8. It can be seen from the curve shown in Fig. 8a that as the thickness of fracture layer increases, the medium velocity decreases overall and the velocity dispersion is more severe in the seismic band. In Fig. 8b, the attenuation peak becomes larger and the peak frequency shifts toward low frequency. The reason for the velocity decrease is that the compliance of the medium increases due to the increase in the soft layer volume fraction, and the equivalent plane wave modulus of the medium decreases. At the same time, the increase in the fracture layer thickness leads to an increase in the overall porosity of the medium, so that the relative flow of the fluid is more likely to occur, thereby generating a stronger energy attenuation.

Influence of porosity, permeability and gas saturation on elastic wave response

Keep the porosity of fracture layer unchanged, and study the attenuation and dispersion features of porous medium when the porosity of the background layer changes. Assuming that the medium is a single feature unit, background layer porosity is 0.05, 0.10, 0.15 and 0.20, respectively. It can be observed in Fig. 9 that as the porosity of background layer increases, the wave velocity decreases as a whole, and the dispersion degree first increases and then slowly decreases. Attenuation peak increases first and then decreases, and the peak frequency gradually shifts to low frequency. At low frequencies, the fluid pressure of the medium can reach equilibrium in half a wave period, but it cannot reach equilibrium at high frequencies. However, as the porosity of background layer increases, the difficulty of the internal pressure of the

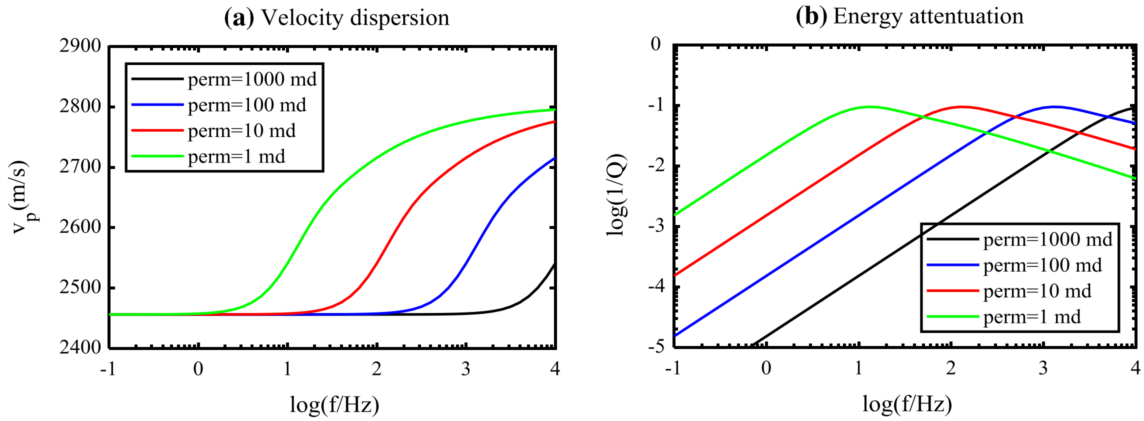

Fig. 10 Velocity dispersion (**a**) and attenuation (**b**) at different background layer permeabilities

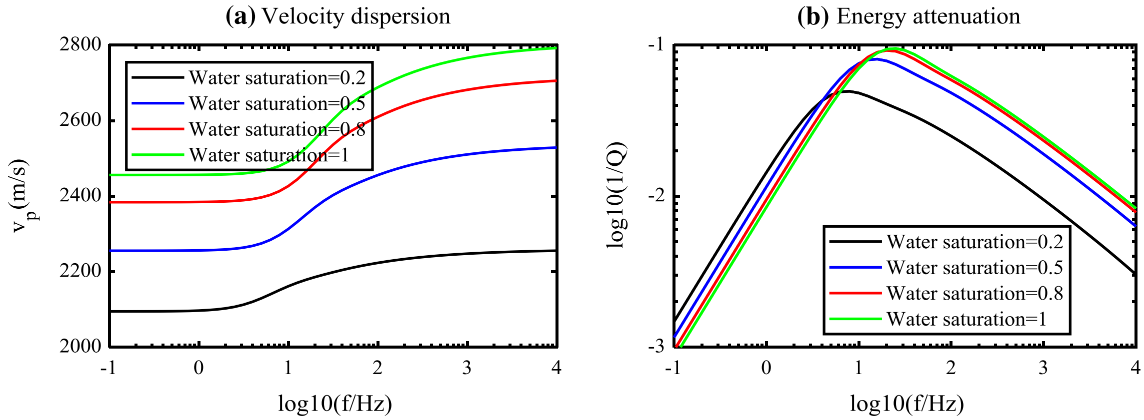

Fig. 11 Velocity dispersion (**a**) and attenuation (**b**) for different fluid saturations

medium reaching equilibrium is gradually reduced. Especially at high frequencies, due to the increase in porosity, the fluid still has a certain flow capacity at high frequencies, which reduces the high-frequency limit of bulk modulus, resulting in a decrease in the high-frequency velocity, causing the energy attenuation to increase first and then slowly decrease.

The effect of changing background layer permeability on the velocity dispersion and energy attenuation is studied when the fracture layer permeability remains ($k_c = 5 \times 10^{-10}\ \mathrm{m}^2$) unchanged. Assuming that the medium contains one characteristic unit, the permeability of background layer is $1 \times 10^{-12}\ \mathrm{m}^2$, $1 \times 10^{-13}\ \mathrm{m}^2$, $1 \times 10^{-14}\ \mathrm{m}^2$ and $1 \times 10^{-15}\ \mathrm{m}^2$, respectively. It can be seen from the curve shown in Fig. 10 that as the permeability of the background layer increases, the low-frequency velocity of the medium remains substantially unchanged, the high-frequency velocity decreases, and the initial frequency of the velocity dispersion shifts toward high-frequency direction. Energy attenuation peak remains substantially unchanged, and the peak frequency shifts to high frequency. We can deduce that the greater the difference in permeability between the background layer and the fracture layer, the lower the starting frequency of velocity dispersion and the peak frequency of energy attenuation.

We also study the elastic wave response when the fluid saturation in porous medium is different, assuming that the pores are filled with two fluids, gas and water. The saturation of water is s_a, the saturation of the gas is s_b, and $s_a + s_b = 1$ is established. The water saturation used for the forward performance is 0.2, 0.5, 0.8 and 1.0, respectively. It can be seen from Fig. 11 that as the water saturation increases, the velocity of the low-frequency limit and high-frequency limit increases, but the shape of the velocity dispersion curve is basically maintained constant. The energy attenuation peak is slightly increased, and the corresponding peak frequency shifts slightly to high-frequency direction, which is consistent with the conclusions obtained by the predecessors (Masson and Pride 2010; Zhang and He 2015). We believe that this phenomenon is caused by an increase in water saturation, which increases the equivalent P-wave modulus, resulting in an increase in velocity. And the increase in water saturation

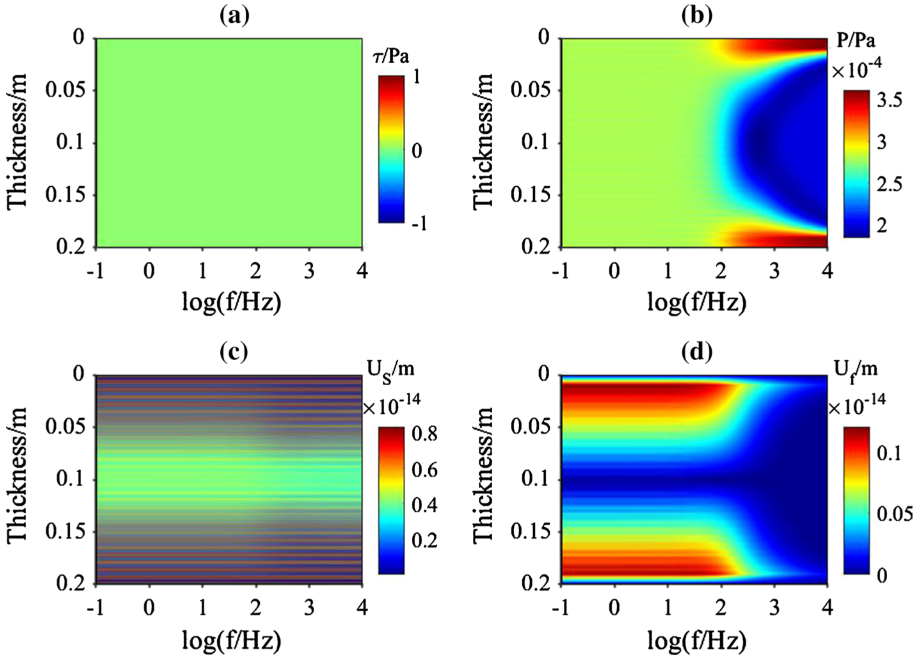

Fig. 12 Force field and displacement field distribution in a model under constant pressure: (**a**) the stress on the solid skeleton, (**b**) the force of the pore fluid, (**c**) the displacement of the solid skeleton under the external force and (**d**) the fluid displacement under pressure

means a decrease in gas saturation. Since water is more difficult to compress than gas, when the water saturation increases, the resistance of the elastic wave propagating in the medium also increases, resulting in an increase in the attenuation peak.

In addition, we can use forward modeling to simulate the force field and displacement field distribution in layered media. Assume that the model length is 0.2 m, the model extends wirelessly in the horizontal direction, which contains only one characteristic unit, the proportion of fracture layer is 10% of the total thickness, and elastic parameters of the medium are shown in Table 1. The model is divided into 800 grid points in the vertical direction for numerical simulation, and a constant force is applied to the upper and lower interfaces of the model. The distribution of the force field and the displacement field inside the model can be obtained as shown in Fig. 12.

It can be seen from Fig. 12a that the solid stress is uniform and independent of frequency, satisfying the assumption that the stress divergence of the porous medium is zero as previously mentioned. And in Fig. 12b the fluid pressure in the fracture layer and background layer is about 2.7×10^{-4} pa at low frequencies, but the fluid pressure in the fracture layer increases at high frequencies, while the fluid pressure in the background pores is reduced. In Fig. 12c, the solid displacement is sensitive to the combination of characteristic unit, because the fracture has high compliance and is easy to be compressed, so the solid-phase displacement of the fracture layer is large, while the displacement of the background porous medium is small. In Fig. 12d, the fluid displacements at the upper and lower boundaries of the model are zero, and near the fracture layer are obviously larger than the background layer at low frequencies, but at high frequencies the fluid displacement is zero. The reason for fluid pressure and fluid displacement is frequency dependent is that fluid movement is hindered at high frequencies, resulting in fracture layer is subjected to more external forces as a highly compliant layer.

It is worth mentioning that the model used in all numerical simulations is that the fracture layer is distributed at the top and bottom, and the external force acts directly on it. When we change the combination of the characteristic units, the fracture layer is embedded in the background porous medium. At this time, the top and bottom of the model is the background porous medium, and then loading stresses at the boundaries of the model to study the elastic wave response. From the results of velocity dispersion and energy attenuation of different characteristic units, under the same fracture volume fraction, the elastic wave energy attenuation and velocity dispersion curves of the characteristic unit models with different combinations are also different. However, it is worth noting that the high- and low-frequency limits of different feature unit velocities are consistent and that the energy attenuation is on the order of magnitude. At the same time, the curve change features caused by the change of elastic parameters are consistent. The corresponding figure is not included for brevity.

Discussion

The numerical simulation method in this paper can obtain high-precision results for the frequency-domain seismic wave attenuation and dispersion of the one-dimensional model, but the theory is not applicable when the model is transverse anisotropy or even more complex. From the results of numerical simulation, we can infer that when the fluid-saturated reservoir contains a certain amount of gas, the seismic wave attenuation is relatively large, indicating the potential value of using the seismic wave attenuation for oil and gas prediction. In addition, the attenuation coefficient of the low-frequency band is linear with the frequency in the logarithmic coordinate system and thus can be used as a constraint condition for the inversion coefficient parameter Q. And it can qualitatively explain the high-frequency dispersion and high attenuation in the actual rock of the seismic frequency band.

Conclusion

The dispersion property of periodically layered medium with planar fracture is characterized by the finite difference forward method in frequency domain. By increasing the number of differential meshes, the natural dispersion of differential algorithm can be effectively weakened, and the frequency-domain forward results agreed with the Brajanovski analytical solution, which verified the correctness of frequency-domain differential forward method. It provides an accurate and reasonable method for studying the elastic wave response of Brajanovski layered media with planar fractures.

The dispersion and attenuation of fluid-saturated medium with different porosities, permeabilities and fluid saturations are analyzed. The results show that the thicker the fractural layer, the more easily the velocity dispersion occurs, and the larger the attenuation peak, the lower the peak frequency. As the porosity increases, the frequency of dispersion shifts to low frequency, the attenuation peak increases first and then decreases, and the peak frequency gradually moves to the low-frequency direction. As the permeability increases, the high-frequency velocity decreases slightly, the starting frequency of dispersion moves toward high-frequency direction, and the peak of attenuation is nearly the same, while the peak frequency moves to the high-frequency direction. As the water saturation increases, the velocity increases as a whole, the degree of dispersion increases, the peak of energy attenuation increases, and the peak frequency increases slightly.

For the horizontally layered medium with high-angle fracture, the corresponding dispersion and attenuation properties such as HTI media need to be further studied.

Acknowledgements We are grateful to the reviewers for their constructive comments on this paper. This research is supported by the following funds: the National Natural Science Foundation of China (Nos. 41874146 and 41874149).

Compliance with ethical standards

Conflict of interest On behalf of all authors, the corresponding author states that there is no conflict of interest.

References

Ba J, Carcione JM, Cao H et al (2012) Velocity dispersion and attenuation of P waves in partially-saturated rocks: wave propagation equations in double-porosity medium. Chin J Geophys 55(1):219–231. https://doi.org/10.6038/j.issn.0001-5733.2012.01.021

Ba J, Zhao J, Carcione JM et al (2016) Compressional wave dispersion due to rock matrix stiffening by clay squirt flow. Geophys Res Lett 43(12):6186–6195. https://doi.org/10.1002/2016GL069312

Biot MA (1939) Non-linear theory of elasticity and the linearized case for a body under initial stress. Philos Mag 27(183):468–489. https://doi.org/10.1080/14786443908562246

Biot MA (1941) General theory of three-dimensional consolidation. J Appl Phys 12(2):155–164. https://doi.org/10.1063/1.1712886

Biot MA (1956a) Theory of propagation of elastic waves in a fluid-saturated porous solid. I. Low-frequency range. J Acoust Soc Ame 28(2):168–178. https://doi.org/10.1121/1.1908239

Biot MA (1956b) Theory of propagation of elastic waves in a fluid-saturated porous solid. II. Higher frequency range. J Acoust Soc Am 28(2):179–191. https://doi.org/10.1121/1.1908241

Biot MA (1962) Mechanics of deformation and acoustic propagation in porous media. J Appl Phys 33(4):1482–1498. https://doi.org/10.1063/1.1728759

Brajanovski M, Gurevich B, Schoenberg M (2005) A model for P-wave attenuation and dispersion in a porous medium permeated by aligned fractures. Geophys J R Astron Soc 163(1):372–384. https://doi.org/10.1111/j.1365-246X.2005.02722.x

Brown RJS, Korringa J (1975) On the dependence of the elastic properties of a porous rock on the compressibility of the pore fluid. Geophysics 40(4):608–616. https://doi.org/10.1190/1.1440551

Chapman M (2003) Frequency dependent anisotropy due to meso-scale fractures in the presence of equant porosity. Geophys Prospect 51(5):369–379. https://doi.org/10.1046/j.1365-2478.2003.00384.x

Chapman M, Zatsepin SV, Crampin S (2002) Derivation of a micro-structural poroelastic model. Geophys J R Astron Soc 151(2):427–451. https://doi.org/10.1046/j.1365-246X.2002.01769.x

Dvorkin J, Nolenhoeksema RC, Nur A (1994) The squirt-flow mechanism: macro-scopic description. Geophysics 59(3):428–438. https://doi.org/10.1190/1.1443605

Dvorkin J, Gutierrez MA, Grana D (2014) Seismic reflections of rock properties. Cambridge University Press, Cambridge. https://doi.org/10.1017/cbo9780511843655

Fang X, Shang X, Fehler M (2013) Sensitivity of time-lapse seismic data to fracture compliance in hydraulic fracturing. Geophys J Int 195(3):1843–1861. https://doi.org/10.1190/segam2013-0732.1

Galvin RJ, Gurevich B (2003) Frequency-dependent anisotropy of porous rocks with aligned fractures. In: ASEG 16th geophysical conference and exhibition, Adelaide. https://doi.org/10.1111/1365-2478.12177

Galvin RJ, Gurevich B (2009) Effective properties of a poroelastic medium containing a distribution of aligned cracks. J Geophys Res Solid Earth 114(1):1–11. https://doi.org/10.1029/2008JB006032

Gassmann F (1951) Über die Elastizität Poröser Medien: Vierteljschrift.der naturforschenden. Gesellschaft in zürich 96:1–23

Hudson JA, Liu E, Crampin S (1996) The mechanical properties of materials with interconnected cracks and pores. Geophys J R

Astron Soc 124(1):105–112. https://doi.org/10.1111/j.1365-246X.1996.tb06355.x

Masson YJ, Pride SR (2010) Finite-difference modeling of Biot's poroelastic equations across all frequencies. Geophysics 75(2):33–41. https://doi.org/10.1190/1.3332589

Mavko GM, Nur A (1979) Wave attenuation in partially saturated rocks. Geophysics 44(2):161–178. https://doi.org/10.1190/1.440958

Müller TM, Gurevich B, Lebedev M (2010) Seismic wave attenuation and dispersion resulting from wave-induced flow in porous rocks—a review. Geophysics 75(5):147–164. https://doi.org/10.1190/1.3463417

Norris AN (1993) Low-frequency dispersion and attenuation in partially saturated rocks. J Acoust Soc Am 94(1):359–370. https://doi.org/10.1121/1.407101

Pride SR, Berryman JG, Harris JM (2004) Seismic attenuation due to wave-induced flow. J Geophys Res 109(1):1–19. https://doi.org/10.1029/2003JB002639

Rubino JG, Ravazzoli CL, Santos JE (2009) Equivalent viscoelastic solids for heterogeneous fluid-saturated porous rocks. Geophysics 74(1):1–13. https://doi.org/10.1190/1.3008544

Schoenberg M, Douma J (1988) Elastic-wave propagation in media with parallel fractures and aligned cracks. Geophys Prospect 36(6):571–590. https://doi.org/10.1111/j.1365-2478.1988.tb.2181.x

Schoenberg M, Sayers CM (2012) Seismic anisotropy of fractured rock. Geophysics 60(1):204–211. https://doi.org/10.1190/1.1443748

Shen Y, Dvorkin J, Li Y (2018) Improving seismic Qp estimation using rock physics constraints. Geophysics 83(3):1–56. https://doi.org/10.1190/geo2016-0655.1

White JE, Mihailova N, Lyakhovitsky F (1975) Low-frequency seismic waves in fluid-saturated layered rocks. J Acoust Soc Am J 11(10):654–659. https://doi.org/10.1121/1.1995164

Wu J, Wu G (2018) Quantitative virtual rock physics method in one-dimensional frequency domain. Pet Geophys Prospect 53(1):105–112. https://doi.org/10.13810/j.cnki.issn.1000-7210.2018.01.013

Yang J, Song E, Chen Z (2003) Analysis of two compression waves of saturated soil by finite difference method of u-w equation. Chin J Appl Mech 20(4):89–92. https://doi.org/10.3969/j.issn.1000-4939.2003.04.020

Zhang H, He B (2015) Propagation and attenuation of P-waves in patchy saturated porous media. Appl Geophys 12(3):401–408. https://doi.org/10.1007/s11770-015-0497-x

Acta Geophysica (2019) 67:813–824
https://doi.org/10.1007/s11600-019-00296-0

RESEARCH ARTICLE - APPLIED GEOPHYSICS

Effective denoising of magnetotelluric (MT) data using a combined wavelet method

Zhenbao Ling[1] · **Peiyuan Wang**[2] · **Yunxia Wan**[1] · **Tonglin Li**[3]

Received: 28 December 2016 / Accepted: 26 April 2019 / Published online: 2 May 2019

Abstract

Noise interference, especially from human noise, seriously affects the quality of magnetotelluric (MT) data. Strong human noise distorts the apparent resistivity curve, known as the near-source effect, causing poor reliability of MT data inversion. Based on analyzing the frequency characteristics of human noise resulting from the surrounding environment, a new wavelet-based denoising method is proposed for both synthetic and real MT data in this paper. The new technique combines multi-resolution analysis with a wavelet threshold algorithm based on Bayes estimation and has a remarkable effect on denoising at all band frequencies. The multi-resolution analysis method was employed to reduce long-period noise, and a wavelet threshold algorithm was used to eliminate strong high-frequency noise. In this research, the improved algorithm was assessed via simulated experiments and field measurements with regard to the reduction in human noises. This study demonstrates that the new denoising technique can increase the signal-to-noise ratio by at least 112% and provides an extensive analysis method for mineral resource exploration.

Keywords Combined Denoising Method · Wavelet Transforms · Magnetotellurics · Apparent Resistivity

Introduction

The main research focus of the magnetotelluric (MT) sounding method is natural electromagnetic fields. However, MT data are rarely clean, and the signals are characterized by wide and weak bands that are often heavily contaminated by human noise from different sources (e.g., moving vehicles, power grids, and electrical equipment) (Goubau et al. 1978; Cooper 2014). However, noise makes it difficult to accurately measure MT signals in the field and may even affect exploration results. Therefore, to extract useful information from raw data, an efficient sound denoising method is often required.

Many noise-processing and denoising algorithms have been developed. For instance, to minimize bias caused by correlated noise and to obtain impedance tensor estimates that are unbiased by noise in the self-power, Goubau et al. (1978) discussed cross-power spectrum phase methods that are applicable to four-channel MT data. Gamble et al. (1979a, b) subsequently developed an analysis method that is applicable to most remote reference MT data. Egbert and Booker (1986) proposed an automatic robust analysis scheme that accounts for the systematic increase in errors that occurs with increasing power and that automatically reduces the noise contamination from the source. However, source-related noises cannot be completely removed when the denoising effect is no longer apparent. In addition to these two milestone studies, a new method of analyzing nonlinear and nonstationary data that eliminates the need for false harmonics in signal representation was developed by Huang et al. (1998). Nonstationarity in electromagnetic data affects the computation of Fourier spectra and therefore affects the traditional estimation of MT transfer functions

---

✉ Yunxia Wan
wanyx@jlu.edu.cn

Zhenbao Ling
lingzhenbao@jlu.edu.cn

Peiyuan Wang
499162677@qq.com

Tonglin Li
litl@jlu.edu.cn

[1] College of Instrumentation & Electrical Engineering, Jilin University, Changchun, China

[2] Shanxi Engineering Vocational College, Taiyuan, China

[3] College of Geoexploration Science & Technology, Jilin University, Changchun, China

(TFs). A TF estimation scheme based on emerging nonlinear and nonstationary time series was established to address the nonstationary effects that challenged traditional methods (Neukirch and Garcia 2014). A concise review of sophisticated MT signal processing based on the Fourier transform was given by Garcia et al. (1997), who noted that nonstationarity is a problem that affects TF estimation.

Another approach is the use of wavelet techniques to search for MT sources or to remove noise in a time series. As an improvement to Fourier transform analysis, wavelet analysis is a popular topic in many research fields (Myint et al. 2015). Wavelet transform has been investigated and applied in MT data processing due to its innovative mathematical framework for multi-scale time–frequency signal analysis. Cunha et al. (2015) provided a new method of selecting the wavelet basis to determine the number of wavelet decomposition levels based on the energy spectral density of the signals and a scale-dependent algorithm; this method can be used to select the wavelet functions based on the signal-to-noise ratio (SNR) computed from the wavelet coefficients. Escalas et al. (2013) used wavelet analysis to study the polarization properties of cultural noise sources in MT time series and proposed a new method of detecting cultural noise sources in MT data. This method involved a polarization analysis of MT time series in the time–frequency domain using a wavelet scheme.

Among several noise reduction algorithms that have been proposed, a denoising algorithm based on the wavelet technique is the most commonly used approach to reduce wide-band noise. A new combined denoising method is proposed in this study to improve the effectiveness of MT data strongly affected by human noise.

The rest of this paper is organized as follows: Section "Proposed technique" discusses the proposed combined denoising method. In section "Experimental procedure," synthetic and experimental MT data are denoised to verify the algorithm. Section "Conclusions" presents a detailed discussion and the conclusions.

Proposed technique

Basic wavelet transform

The continuous wavelet transform (CWT) of an arbitrary signal $f(t) \in L^2(R)$ is defined in Eq. (1):

$$W_f(a,b) = |a|^{-\frac{1}{2}} \int_R f(t)\overline{\psi\left(\frac{t-b}{a}\right)}\mathrm{d}t, \tag{1}$$

where $\psi(t)$ is the "mother wavelet," a and b are the wavelet scale parameter and wavelet translation, respectively, and R represents a set of real numbers. By choosing a wavelet basis $\psi(t)$, the denoising signal $f(t)$ is obtained through the inverse wavelet transform, which is given by Eq. (2):

$$f(t) = \frac{1}{c_\psi}\int_{-\infty}^{+\infty}\int_{-\infty}^{+\infty}\frac{1}{a^2}W_f(a,b)\psi\left(\frac{t-b}{a}\right)\mathrm{d}a\mathrm{d}b. \tag{2}$$

However, in practical applications, the discrete wavelet transform (DWT) is the most frequently used wavelet transform. The mathematical expression of the DWT is presented in Eq. (3):

$$W_f(j,k) = \int_R f(t)\frac{1}{\sqrt{2^j}}\psi\left(\frac{t}{2^j} - k\right)\mathrm{d}t, \tag{3}$$

where j and k are linked to the scaling parameters of $\psi(t)$, k is time localization, and j is frequency localization. Similarly, once an orthonormal wavelet basis is chosen, the signal can be reconstructed by using the wavelet coefficient $W_f(j,k)$, which represents the wavelet coefficient at scale j; k is a variable that ranges from 1 to n (number of wavelet coefficients). In addition, inverse discrete wavelet transform (IDWT) can be expressed as shown in Eq. (4):

$$f(t) = \sum\nolimits_{j \in Z} \int W_f(j,k)\frac{1}{\sqrt{2^j}}\psi\left(\frac{t}{2^j} - k\right)\mathrm{d}k. \tag{4}$$

The multi-resolution analysis algorithm

The multi-resolution analysis (MRA) theory, which is based on the orthonormal wavelet, was proposed by Mallat (1996). This theory can be used to further decompose low-frequency signals without considering high-frequency signals. Thus, the algorithm is optimal for extracting the useful signal and suppressing low-frequency noise (such as baseline drifting and low-frequency square-wave noise). Additionally, this method is characterized by high accuracy and high disturbance resistibility. As shown in Fig. 1, the process of wavelet decomposition can be represented as a multi-level decomposition tree, where S is the processed signal at a sampling rate of 24 Hz, cA is a series of approximation coefficients, and cD is a series of detailed coefficients. Moreover, $W_f(j,k)$ is composed of cA and cD in each level. The original signal, $f(t)$, passes through two complementary filters (high and low passes) and is decomposed into two down-sampled signals, cA_1 and cD_1. The decomposition process can be iterated with successive approximations and decomposed in turn; thus, the original signal can be decomposed into many low-resolution components (Mallat 1996). The desired level of decomposition depends on the required frequency components available in the wavelet coefficient at that level and on the dominant frequency components of the signal (Kim 2011).

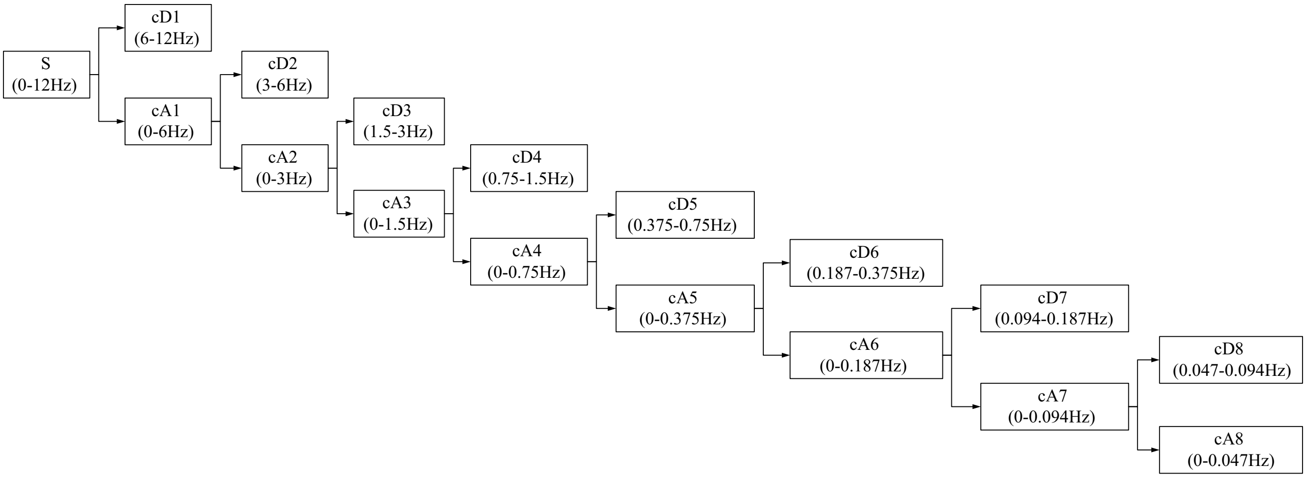

Fig. 1 Eight-level decomposition tree

In the paper, the MT data signal is from the Jiujiang-Ruichang ore concentration area, and the experimental field data are sampled at 24 Hz. According to Nyquist's theory, if the original signal has a maximum frequency of $f_{\max}$, then the required sampling frequency is $f_s = 2f_{\max}$. Thus, the frequency band of the valid MT data spectrum is in the range of 0–12 Hz. In this study, we observed low-frequency interruptive signals (quadrate wave interference, step noises, etc.) in both the time domain and frequency domain and found that the disturbance frequency is mainly concentrated in the 0.01–0.05 Hz range. According to the relationship between the effective frequency band and the sampling rate, the decomposition level was set to 8, and the Haar wavelet was chosen as the mother wavelet. Therefore, decomposing the MT signals by MRA gives signal $S = cA_8 + cD_8 + cD_7 + cD_6 + cD_5 + cD_4 + cD_3 + cD_2 + cD_1$. In this case, the approximation coefficient of level 8 (cA8) is used to estimate the low-frequency (0–0.047 Hz) signal which is low-frequency noise because of its low SNR (signal-to-noise ratio). For this reason, when reconstructed the MT useful signals, cA8 is set to zero and not involved in the reconstruction. The signal can be reconstructed without low-frequency noise using the detailed coefficients from level 1 to level 8. Then, S = cD8 + cD7 + cD6 + cD5 + cD4 + cD3 + cD2 + cD1. If possible, the wavelet base should be consistent with the characteristics of the MT signal to insure that the most of useful information remains in the reconstructed signal, and a better mother wavelet was chosen through a large number of experiments using different wavelet bases.

The wavelet threshold denoising method

In section "The multi-resolution analysis algorithm," we discussed the removal of low-frequency noise. However, there is also high-frequency interference such as impulsive noise in the MT data from the Jiujiang-Ruichang ore concentration area. Wavelet transform is also effective for processing impulsive noise in MT data (Trad and Travassos 2000). In this section, the threshold denoising method is used to reduce high-frequency noise. Compared with using the MRA wavelet algorithm, it is often less effective using more decomposition levels in the wavelet threshold method. If the decomposition level is too high, the reconstructed signal can be distorted. Therefore, noise can be efficiently canceled by choosing a suitable wavelet threshold and decomposition level. Typically, the MRA level is chosen according to the low-frequency noise range, and the level of the wavelet threshold method is determined based on experience and tests. A thresholding method adapts wavelet coefficients to obtain a smoother version of the signal (Downie and Silverman 1998). This method is effective when the number of decomposition levels ranges from 5 to 7, depending on the sampling rate and noise frequency. In this study, low-frequency interference (below 0.05 Hz) was removed using the MRA algorithm described above. Therefore, the decomposition level was chosen as 7 to compute the wavelet coefficient of each level, and the sym3 wavelet was chosen as the mother wavelet. Then, the high-frequency section (above 0.1 Hz) was processed based on an appropriate threshold. Finally, the signal was reconstructed using inverse wavelet transform.

The wavelet threshold rule

The distortion of a denoised signal is closely related to both base wavelet selection and threshold estimation. The selection of the threshold parameters determines the wavelet coefficients that are associated with noise and hence eliminated. The key factor is to determine the threshold of each level. If the threshold value is too large, signal information and noise are both filtered out, and the weak edge is substantially reduced. If the threshold value is too small, the denoising effect becomes unremarkable. There are four types of common threshold rules used in all applications (Kim 2011). In this paper, we chose the EBayes threshold rule (Spichak 2012), which is based on the empirical Bayes principle. This rule is convenient for average square error (ASE) calculations, which can ensure that the threshold is the asymptotic optimum threshold. At the different level j, the threshold $T(j)$, which is based on the empirical Bayes estimator (Johnstone and Silverman 2005) and is calculated in each level, can be obtained through the following four steps:

(i) After a decomposition level is determined, the wavelet decomposition coefficients ($\omega(k)$) at level j can be calculated via the DWT. Furthermore, k is a variable that ranges from 1 to n (number of wavelet coefficients) at level j.

(ii) The accurate estimation of high-frequency noise variance $\sigma_{W_n}(k)$ at level j can be calculated by the following function (Liu et al. 2012):

$$\sigma_{W_n}(k) = \frac{\text{median}(|\omega(k)|)}{0.6745}, \tag{9}$$

where the subscript W_n refers to noise and median($|\omega(k)|$) is the median of $\omega(k)$. The adjustment coefficient of the standard deviation of white Gaussian noise is 0.6745.

(iii) The signal variance $\sigma_{W_s}(k)$ can be more accurately determined at this stage. At the level j, according to the equation $\sigma^2_W(k) = \sigma^2_{W_s}(k) + \sigma^2_{W_n}(k)$, we obtain Eq. (10):

$$\sigma_{W_s}(k) = \sqrt{\max\left[\sigma^2_W(k) - \sigma^2_{W_n}(k), 0\right]} \tag{10}$$

where $\sigma^2_W(k) = \frac{1}{n^2}\sum_{k=1}^{n} \omega^2(k)$, the subscript W refers to the raw signal, and the subscript W_s refers to the useful signal, and n is the number of wavelet coefficients at level j.

(iv) The optimal threshold $T(j)$ can be calculated by the following function:

$$T(j) = \frac{\sigma^2_{W_n}(k)}{\sigma_{W_s}(k)}. \tag{11}$$

Selection of the threshold function

After selecting a threshold value, the thresholding is performed by selecting an appropriate algorithm. Hard and soft thresholding methods are very popular (Donoho 1995; Donoho and Johnstone 1995). A threshold is applied to the wavelet coefficients to determine how such coefficients will be attenuated or singled out to eliminate or reduce the noise distributed among the raw MT data. The hard threshold function is given by Eq. (12):

$$\hat{\omega}(j,k) = \begin{cases} \omega(j,k), & |\omega(j,k)| \geq T(j) \\ 0, & |\omega(j,k)| < T(j) \end{cases}. \tag{12}$$

The soft threshold function is given by Eq. (13):

$$\hat{\omega}(j,k) = \begin{cases} \text{sgn}(\omega(j,k))(|\omega(j,k)| - T(j)), & |\omega(j,k)| \geq T(j) \\ 0, & |\omega(j,k)| < T(j) \end{cases}. \tag{13}$$

The hard threshold function can preserve the signal magnitude characteristics, providing a better denoised result than that of the soft function; however, this can also cause instability during signal processing. When the wavelet coefficients exceed the threshold for the soft threshold function, some errors exist between $\hat{\omega}(j,k)$ and $\omega(j,k)$, which can influence the accuracy of the reconstructed signal (Mamgain and Chaudhary 2015). Therefore, an improved thresholding method is proposed based on soft thresholding. The improved threshold function is given as follows:

$$\hat{\omega}(j,k) = \begin{cases} \text{sgn}(\omega(j,k))\left[|\omega(j,k)| - \frac{1}{\exp\left(\frac{|\omega(j,k)|}{T(j)}\right)}\right], & |\omega(j,k)| \geq T(j) \\ 0, & |\omega(j,k)| < T(j) \end{cases}. \tag{14}$$

This function overcomes the shortcomings of the hard threshold function by using a discontinuous function. Additionally, it solves the problem of permanent bias in the soft threshold function.

The noise reduction results for evaluation criteria

In the field of signal analysis, two standards are commonly used to evaluate the noise reduction effect: the SNR and the root mean square error (mean squared error; MSE). The SNR is used to calculate the ratio of signal to noise (Zhang et al. 2016), and the MSE can be used to measure the perceived similarity between the original and processed signals by comparing computed MSE values with similarity assessments (Marmolin 1986). Generally, the effect of noise reduction can be either good or bad, which can be determined by analyzing these two values.

$s(t)$ represents a useful signal, and $\hat{s}(t)$ represents the signal, which may be a noisy signal or a signal after noise reduction.

SNR can be defined as follows:

$$\text{SNR} = 10\log\left(\frac{\sum_{n=1}^{N} s^2(t)}{\sum_{n=1}^{N} s^2(t) - \sum_{n=1}^{N} \hat{s}^2(t)}\right). \tag{15}$$

Additionally, MSE can be defined as follows:

$$\mathrm{MSE} = \sqrt{\frac{1}{N}\sum_{n=1}^{N}[s(t) - \hat{s}(t)]^2}. \quad (16)$$

In general, the higher the SNR is, the better the noise reduction result, and the smaller the MSE is, the higher the similarity between the signal and the useful signal after wavelet reconstruction.

Steps in the combined wavelet denoising method

In this paper, the denoising of MT data using the proposed combined wavelet transform algorithm can be summarized in the following steps, and the flowchart is shown in Fig. 2.

(i) Load a signal, and perform DWT using the signal and the MRA algorithm to obtain the approximation coefficients and detail coefficients after defining the necessary level of decomposition.
(ii) Remove the approximation coefficients of level n (the level of decomposition) to remove the low-frequency noise. Then, reconstruct the wavelet coefficients to obtain a new signal.
(iii) Use DWT with different mother wavelets of the new signal to obtain a series of new approximation coefficients and detail coefficients. Then, define the level-dependent threshold values for the thresholding rule and apply the threshold to the detail coefficients.
(iv) Perform IDWT using the modified wavelet coefficients to obtain a denoised signal.

Experimental procedure

Processing results of the simulated data

To verify the effectiveness of the combined denoising method for MT data in a human interference environment, synthetic signals were processed and analyzed. To test the denoising effect of the algorithm proposed in this paper on strong square wave and pulse interference in the data and to better reduce noise in the measured signal, the simulation data must be consistent with the measured data. After analyzing the measured data, we found that the main types of noise were square waves (0.01–0.05 Hz) and pulse noise (0.1–1 Hz). Thus, according to the characteristics of the time series of the measured signals, the synthetic signals were composed of a multi-sine wave, and square waves (0.02 Hz) and pulse noise (0.5 Hz, 0.9 Hz) were added as human interference.

The simulation experiment involved two cases. In the first case, a signal was denoised using the basic threshold rule and the hard threshold function. In the second case, as proposed in this paper, the EBayes threshold rule with the improved threshold function was used to denoise the signal (Fig. 3).

Figure 3a shows the simulated data with no interference, and Fig. 3b shows the simulated data containing square and pulse interference. The signal processed using the combined denoising method and the generalized threshold rule with the hard threshold function is shown in Fig. 3c. Finally, Fig. 3d shows signal denoising based on the EBayes threshold rule with the improved threshold function.

Comparing Fig. 3c and d with Fig. 3b suggests that the square and pulse interference were markedly suppressed, and the denoised time series are similar to the original signal shown in Fig. 3a. Moreover, no phase deviation occurred during the denoising process. Thus, noise reduction methods can eliminate interference, as useful signals are not lost. However, the obtained results prove that the denoising method based on the Bayesian threshold rule with the improved threshold generates a better denoising result than that based on generalized hard thresholding. In addition, we can evaluate the effects of signal processing by comparing the SNR and MSE values, as shown in Table 1. This table shows the SNR values and MSE values of the simulation data before and after denoising using different methods. The SNR of the signal is improved by using the combined denoising method. Additionally, with the traditional parameters, the MSE of the signal is reduced from 84.39 to 0.65, and the SNR is reduced from – 16.25 to 1.82. Alternatively, with the proposed parameters, the MSE of the signal is reduced from 84.39 to 0.33, and the SNR is reduced from – 16.25 to 2.62. All of these results suggest that the method proposed in this paper, which combines MRA and a wavelet threshold algorithm based on Bayes estimation and improved thresholding, provides a better noise reduction effect.

Processing result of MT data

MT data from a site in the Jiujiang-Ruichang ore concentration area, which is located within the Yangtze Cu-Au mineralizing belt in China, are used as an example. The data acquisition system used was the V5-2000 MT sounding system. During the experiment, the acquisition of MT signals lasted for 10 h. The

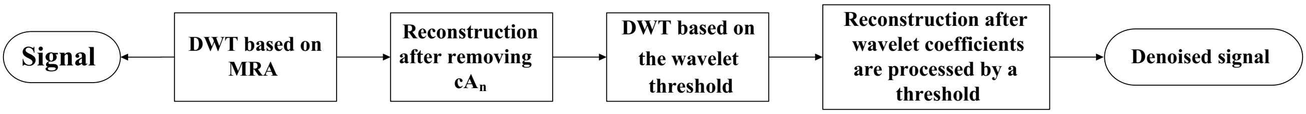

Fig. 2 Flowchart of the combined wavelet transform algorithm

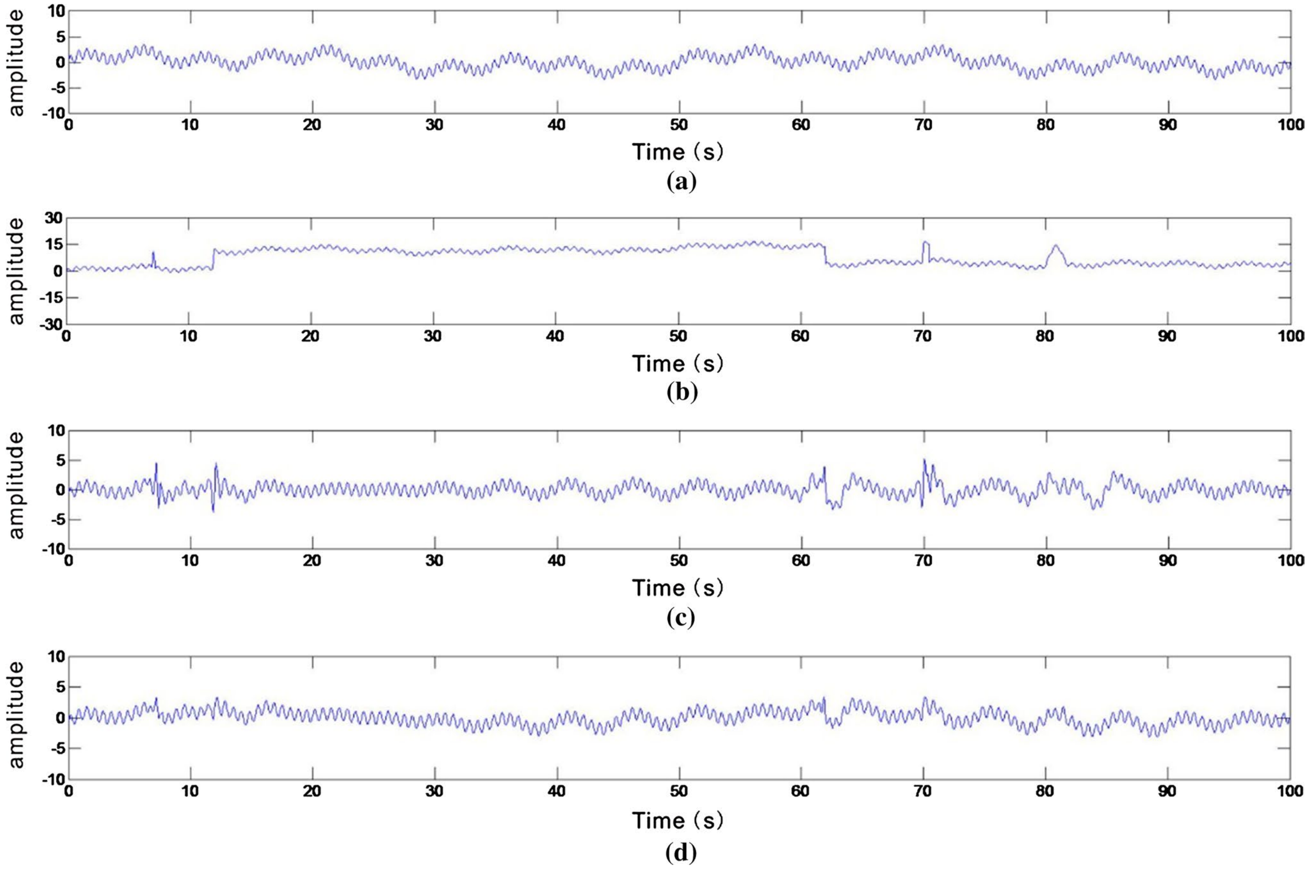

Fig. 3 Comparison of simulated data time series before and after denoising: **a** original simulated data; **b** noisy simulated data; **c** denoised simulated data based on traditional parameters; and **d** denoised simulated data based on proposed parameters

Table 1 SNR and MSE of the simulated data

Evaluation criterion	Before denoising	Denoising based on traditional parameters	Denoising based on proposed parameters
MSE	84.39	0.65	0.33
SNR	– 16.25	1.82	2.62

MT data collected near the mining area are selected to verify the rationality and validity of the novel combined denoising method. Under such circumstances, the noise mainly comes from the mining equipment, transportation, and the electric power network around the measuring point. The noise characteristics are generally associated with large-energy and wide-frequency bands, and the noises are correlated in each channel. Due to limited display space, only a short time series of the all collecting data were given in the article. The four-channel (Ex, Ey, Hx, and Hy) measured data (only a short section) before processing are illustrated in Fig. 4a. The sampling rate is 24 Hz, and the data length is 700 s. The denoising data are shown in Fig. 4b. Compared with the initial data, the denoised data show that the square and pulse noise are obviously removed at many frequencies.

To better understand the effect of interference removal, MT time series illustrations before and after denoising were enlarged to show the details of each. Figure 5 shows the partial details (Ey channel) produced from 500 to 600 s. During this period, the data are affected by violent pulse noises (Fig. 5a). In addition, the data are disturbed by high-energy square signals in the intervals from 525 s to 550 s and 562 s to 580 s. This kind of noise has not a fixed frequency. The pulse width and amplitude are varying with time, so that standard filtering techniques cannot be applied successfully. However, the wavelet has the characteristics of multi-resolution analysis, so it can be applied to the square wave signal processing of the uncertain noise frequency. Moreover, the noise frequencies are mainly concentrated at certain frequencies: 0.04 Hz, 0.25 Hz, 0.7 Hz, 0.95 Hz, and 2.3 Hz. These frequencies are highly dispersed, with values ranging from 0.01 to 1 Hz. Under the above-mentioned conditions, some of the useful signal is flooded by noise. In Fig. 5b, the large-amplitude square signal and irregular pulse signal were removed during denoising. The result indicates

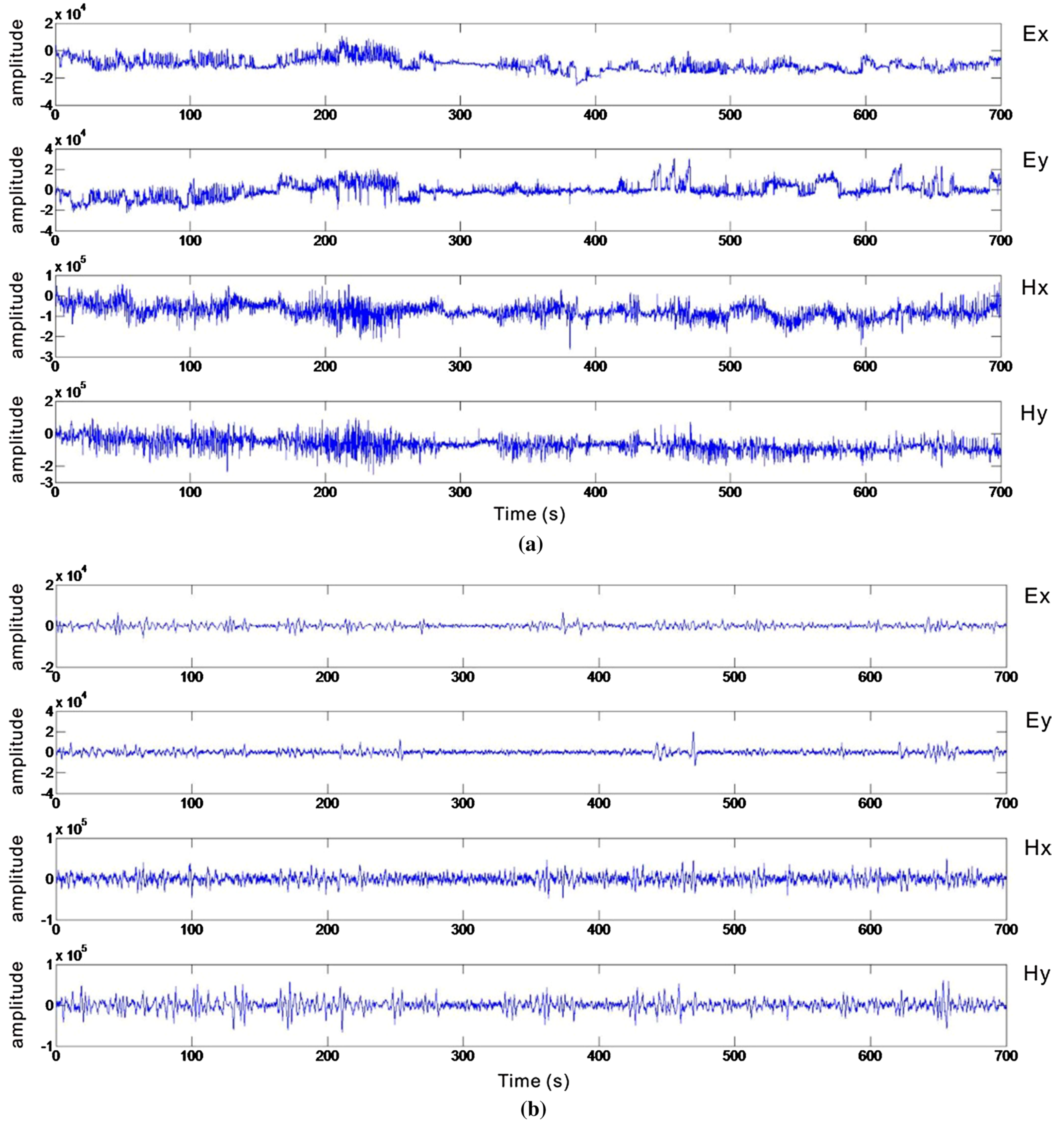

Fig. 4 Comparison of time series of measured data before and after denoising: **a** time series of the data before denoising and **b** time series of the data after denoising

that the combined denoising method is an appropriate tool for noise suppression.

In addition, the minimum (min), maximum (max), and variance (var) values of the MT data in Fig. 4 can be used to evaluate the effectiveness of the combined algorithm (Deng et al. 2015). The maximum and minimum values are based on the mathematical solution of the amplitude of the signal in the time domain. The amplitude of square waves is much larger than that of the useful signal; therefore, the effect of noise removal can be judged from an energy standpoint using the minimum, maximum, and variance values. By comparing the minimum and maximum values of the MT

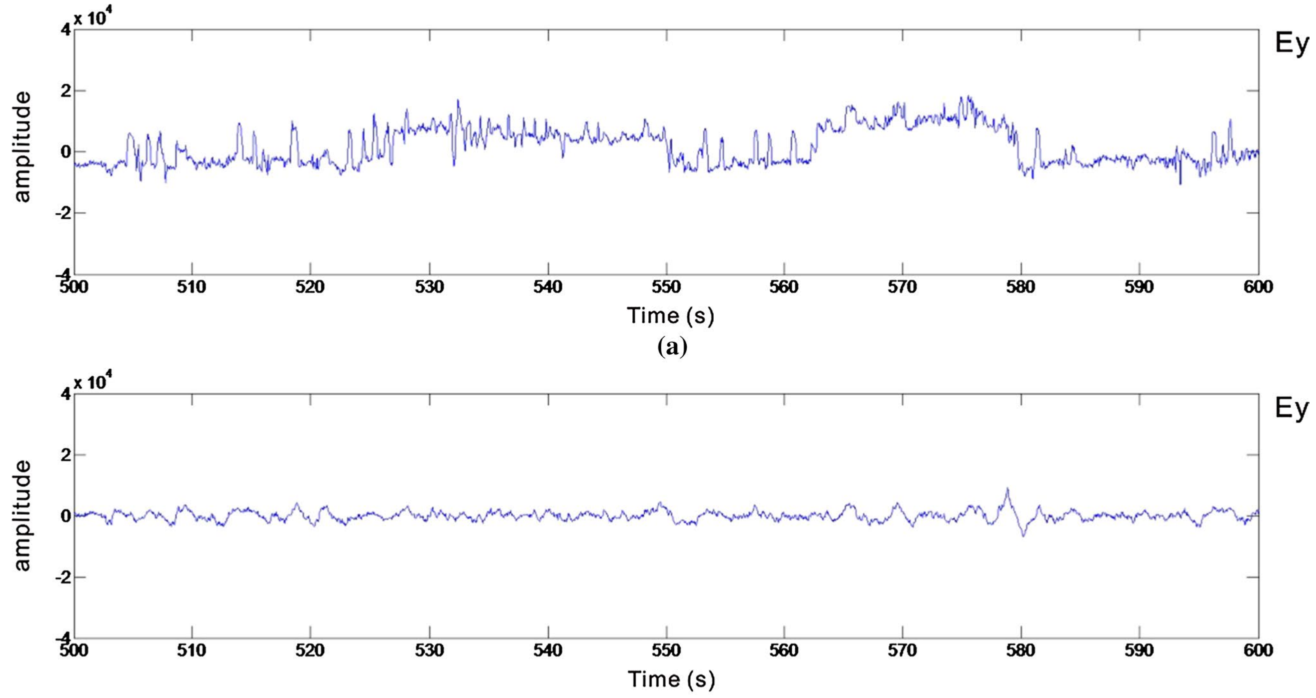

(a)

(b)

Fig. 5 Details of the MT data (Ey channel) before and after denoising: **a** time series of the data before denoising and **b** time series of the data after denoising

data before and after denoising, we can determine whether interference should be removed. The variance value indicates whether to keep the detailed features of the original signal. In Table 2, "before" and "after" refer to "before denoising" and "after denoising," respectively.

The MT data exhibit disturbed apparent resistivity and phase curves between 0.001 and 1 Hz for both components. The source of MT data is a natural earth electromagnetic field from high altitude. Therefore, the MT signal can be treated as plane wave, and the apparent resistivity of underground medium can be calculated using the Cagniard resistivity formula. If the collected electromagnetic data contain near-field interference (the human electromagnetic interference near the receiving point), the apparent resistivity curve calculated by Cagniard resistivity formula will produce distortion. The high-frequency part of the electromagnetic field affected by the near-field noise goes into the far field earlier than the low-frequency part. Generally, the near-source effect is more serious at middle and low frequency of the MT data, and the apparent resistivity curve tends to rise in the low-frequency direction (Zhu et al. 2011). "Near-source effect" specifically appeared as follows: The apparent resistivity curve has a rising trend of about 45 degrees in the low-frequency section, and the value of the apparent resistivity increases by several orders of magnitude in a narrow frequency range. Moreover, the apparent resistivity curves of two modes of XY and YX are separated, and the phase value is 0° or − 180° (Xu 2012). Combined with the time series of electromagnetic signals and apparent resistivity curves, it is determined that the MT data are seriously disturbed by near source. And with processing, the characteristics of near-source interference of apparent resistivity curve are obviously reduced. The details of the apparent resistivity are shown in Fig. 6.

In Fig. 6, the circular points represent the apparent resistivity of Ex-Hy before denoising; the square points represent the apparent resistivity of Ex-Hy after denoising; the rhomboid points represent the apparent resistivity of Ey-Hx

Table 2 Minimum, maximum, and variance of the MT data

	Ex		Ey		Hx		Hy	
	Before	After	Before	After	Before	After	Before	After
Max	10,441	6542	30,665	18,090	72,089	49,300	95,677	60,694
Min	− 25,654	− 5766	− 22,207	− 11,319	− 264,492	− 47,200	− 250,734	− 65,714
Var	2.3e + 7	1.6e + 5	4.9e + 7	3.5e + 6	1.2e + 9	2.3e + 7	1.6e + 9	3.4e + 7

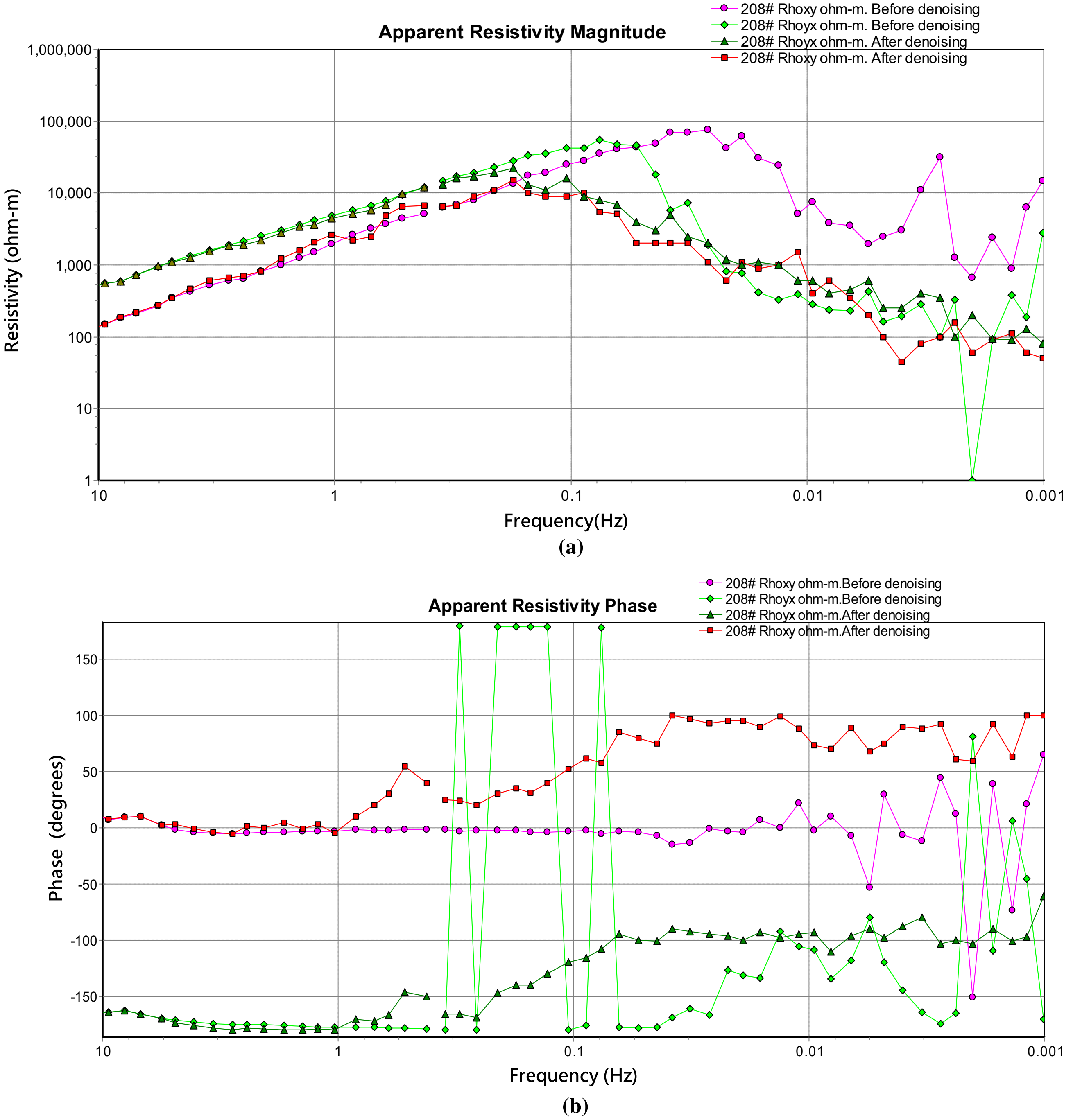

Fig. 6 Comparison of the apparent resistivity at point 208 (#208): **a** comparison of the magnitude before and after denoising and **b** comparison of the phase before and after denoising

before denoising; and the triangular points represent the apparent resistivity of Ey-Hx after denoising. Between 1 and 0.03 Hz on the line with circular points, the apparent resistivity exhibits a trend of approximately 45°, and the corresponding phase values are approximately 0. These observations indicate that the MT data are affected by typical near-source interference. However, after using the method proposed in this paper, these phenomena were moderated. For the line with square points, the 45° trend disappears, and the phase values are better than those of the line with circular points. Additionally, the apparent resistivity curve is smoother than the previous curve.

Polarization orientation was proposed by Weckmann et al. (2005) to reflect the human disturbance of MT data. Generally,

Fig. 7 Comparison of the polarization direction before and after denoising: **a** polarization direction at 0.04 Hz before denoising; **b** polarization direction at 0.04 Hz after denoising; **c** polarization direction at 0.7 Hz before denoising; and **d** polarization direction at 0.7 Hz after denoising

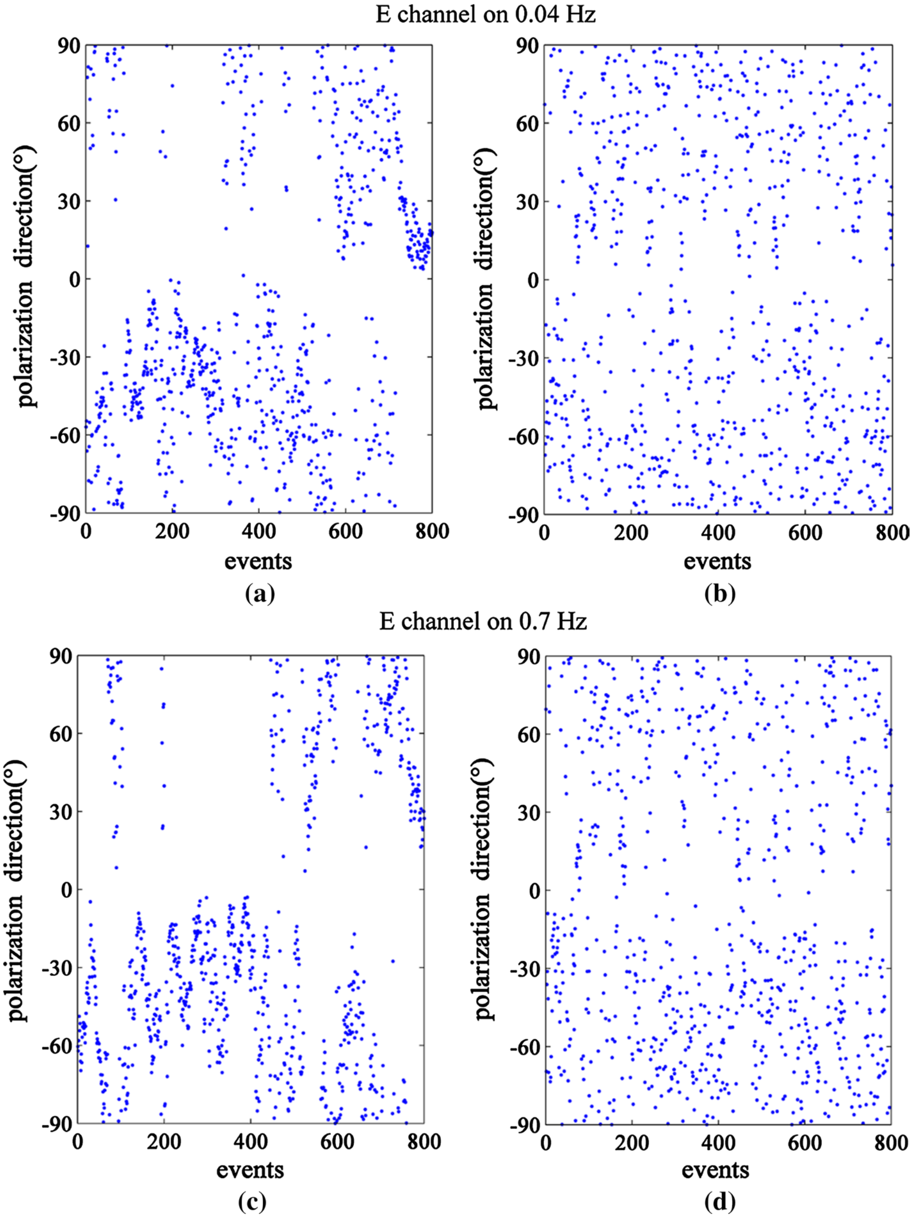

natural MT signals come from all directions, and the polarization direction is random; however, for near-source interference, the randomness of the signal will be destroyed, and polarization will accumulate in a particular direction. This phenomenon is illustrated by the polarization direction of the signals. The polarization directions α_E and α_H of the electric and magnetic wave fields are given in Eqs. (17) and (18), respectively:

$$\alpha_E = \arctan \frac{2 \cdot \mathrm{Re}([E_x E_y^*])}{[E_x E_x^*] - [E_y E_y^*]}, \tag{17}$$

and

$$\alpha_H = \arctan \frac{2 \cdot \mathrm{Re}([H_x H_y^*])}{[H_x H_x^*] - [H_y H_y^*]}, \tag{18}$$

where $[E_x E_y^*]$ and $[H_x H_y^*]$ are the cross-power spectra; $[E_x E_x^*]$, $[E_y E_y^*]$, $[H_x H_x^*]$, and $[H_y H_y^*]$ are the self-power spectra; and Re(*) refers to the extracted real part of the data.

We calculated the polarization angles of the MT data at 0.04 Hz and 0.7 Hz before and after processing, and those of the Ey channel are shown in Fig. 7. In this case, most of the unprocessed data exhibit a strongly polarized electric field direction (see Fig. 7a, c), which indicates the presence of strong near-source interference in the MT data. After denoising, the distribution of the polarization direction approximately obeys a comparatively decentralized distribution (see Fig. 7b, d).

Conclusions

In this paper, we demonstrate that a joint algorithm based on MRA and the wavelet threshold algorithm is an effective tool for signal denoising. In general, all observed electromagnetic field components are contaminated with noise to some extent. MRA is used to remove long-period noise, and the wavelet threshold algorithm combined with Bayesian estimation removes short-period interference. Selecting the appropriate wavelet function, decomposition layer, and threshold is critical for achieving an optimal denoising effect. Therefore, the results are improved only if appropriate parameters are selected.

The example data clearly show that both the electrical and magnetic channels are influenced by noise between 0.001 and 1 Hz. After analyzing the observed data in the frequency domain, the Haar wavelet is selected as the base wavelet to address the long-period noise at eight decomposition levels. In addition, the sym3 wavelet is considered a suitable base wavelet for processing short-period interference with Bayesian estimation, and the MT data are decomposed into seven layers using the wavelet threshold algorithm.

The time series of MT data are affected by human disturbance, and the apparent resistivity and phase curves exhibit distortion. After processing, the MT signals are recovered from the contaminated data. In addition, the apparent resistivity and phase approach reasonable values. As an evaluation criterion, the calculated polarization angle of the processed data indicates that the electromagnetic influence from a certain direction is reduced. However, the results for frequencies between 0.7 and 1 Hz do not suggest successful application because the software provided by the manufacturer considers data with a high sampling rate (320 Hz and 1560 Hz); however, the data at a sampling rate of 24 Hz were denoised. Therefore, the results may be affected by high sampling rates, which will be a topic of future research. Overall, the combined method proposed in this paper solves most of the problems caused by human electromagnetic noise.

Acknowledgements This paper was funded by a grant from the National Natural Science Foundation of China (No. 41404094).

References

Cooper GRJ (2014) The automatic determination of the location and depth of contacts and dykes from aeromagnetic data. Pure Appl Geophys 171:2417–2423. https://doi.org/10.1007/s00024-014-0789-8

Cunha CFFC, Carvalho AT, Petraglia MR, Lima ACS (2015) A new wavelet selection method for partial discharge denoising. Electr Power Syst Res 125:184–195. https://doi.org/10.1016/j.epsr.2015.04.005

Deng JZ, Chen H, Yin CC, Zhou BH (2015) Three-dimensional electrical structures and significance for mineral exploration in the Jiujiang-Ruichang District. J Geophys 58(12):4465–4477. https://doi.org/10.6038/cjg20151211 **(in Chinese)**

Donoho DL (1995) De-noising by soft-thresholding. IEEE Trans Inform Theory 41:613–627. https://doi.org/10.1109/18.382009

Donoho DL, Johnstone IM (1995) Adapting to unknown smoothness via wavelet shrinkage. J Am Stat Assoc 90:1200–1224. https://doi.org/10.1080/01621459.1995.10476626

Downie TR, Silverman BW (1998) The discrete multiple wavelet transform and thresholding methods. IEEE Trans Signal Process 46:2558–2561. https://doi.org/10.1109/78.709546

Egbert GD, Booker JR (1986) Robust estimation of geomagnetic transfer functions. Geophys J Int 87:173–194. https://doi.org/10.1111/j.1365-246X.1986.tb04552.x

Escalas M, Queralt P, Ledo J, Marcuello A (2013) Polarisation analysis of magnetotelluric time series using a wavelet-based scheme: a method for detection and characterisation of cultural noise sources. Phys Earth Planet Inter 218:31–50. https://doi.org/10.1016/j.pepi.2013.02.006

Gamble TD, Goubau WM, Clarke J (1979a) Magnetotellurics with a remote magnetic reference. Geophysics 44:53–68

Gamble TD, Goubau WM, Clarke J (1979b) Error analysis for remote magnetotellurics. Geophysics 44:959–968. https://doi.org/10.1190/1.1440988

Garcia X, Chave AD, Jones AG (1997) Robust processing of magnetotelluric data from the all auroral zone. J Geomagn Geoelectr 49:1451–1468. https://doi.org/10.5636/jgg.49.1451

Goubau WM, Gamble TD, Clarke J (1978) Magnetotelluric data analysis: removal of bias. Geophysics 43:1157–1166. https://doi.org/10.1190/1.1440885

Huang NE, Shen Z, Long SR, Wu MC, Shih HH, Zheng Q, Yen NC, Tung CC, Liu HH (1998) The empirical mode decomposition and the Hilbert spectrum for nonlinear and non-stationary time series analysis. Proc R Soc A Math Phys Eng Sci 454:903–995. https://doi.org/10.1098/rspa.1998.0193

Johnstone IM, Silverman BW (2005) Ebayesthresh: R programs for empirical Bayes thresholding. J Stat Softw 12:1–38. https://doi.org/10.18637/jss.v012.i08

Kim IS (2011) Fault detection algorithm of the photovoltaic system using wavelet transform. In: 2010 India international conference on power electronics (IICPE). IEEE, pp 1–6. https://doi.org/10.1109/iicpe.2011.5728156

Liu B, Rong MT, Liu WJ, Wang RL (2012) A fast and accurate algorithm of noise variance estimation. Inf Technol 1:8–11. https://doi.org/10.13274/j.cnki.hdzj.2012.01.034

Mallat S (1996) Wavelets for a vision. Proc IEEE 84:604–614. https://doi.org/10.1109/5.488702

Mamgain P, Chaudhary S (2015) Implementation of adaptive wavelet thresholding and nonlocal means for medical image enhancement for noise reduction. IJCTT 24:23–28. https://doi.org/10.14445/22312803/IJCTT-V24P105

Marmolin H (1986) Subjective mse measures. IEEE Trans Syst, Man, Cybern 16:486–489. https://doi.org/10.1109/TSMC.1986.4308985

Myint SW, Zhu T, Zheng B (2015) A novel image classification algorithm using overcomplete wavelet transforms. IEEE Geosci Remote Sens Lett 12:1232–1236. https://doi.org/10.1109/LGRS.2015.2390133

Neukirch M, Garcia X (2014) Nonstationary magnetotelluric data processing with instantaneous parameter. J Geophys Res Solid Earth 119:1634–1654. https://doi.org/10.1002/2013JB010494

Spichak VV (2012) Evaluation of the feasibility of recovering the magma chamber's parameters by 3D Bayesian statistical inversion of synthetic MT data. Acta Geophys 60:942–958. https://doi.org/10.2478/s11600-012-0008-x

Trad DO, Travassos JM (2000) Wavelet filtering of magnetotelluric data. Geophysics 65:482–491. https://doi.org/10.1190/1.1444742

Weckmann U, Magunia A, Ritter O (2005) Effective noise separation for magnetotelluric single site data processing using a frequency domain selection scheme. Geophys J Int 161:635–652. https://doi.org/10.1111/j.1365-246X.2005.02621.x

Xu ZM (2012) Study of magnetotelluric interference noise of Luzong. Central South University

Zhang G, Tuo XG, Wang XB, Zhang W, Luo W (2016) Analysis on remote reference magnetotelluric effect under different parameters. Prog Geoghys 31(6):2458–2466. https://doi.org/10.6038/pg20160614 **(in Chinese)**

Zhu W, Fan CS, Yao DW, Wang G (2011) Noise source analysis and noise characteristics study of MT in an ore concentration area. Geophys Geochem Explor 35(5):658–662 **(in Chinese)**

Acta Geophysica (2019) 67:825–836
https://doi.org/10.1007/s11600-019-00298-y

RESEARCH ARTICLE - APPLIED GEOPHYSICS

Comprehensive prediction of coal seam thickness by using in-seam seismic surveys and Bayesian kriging

Mengbo Zhu[1,2] · **Jianyuan Cheng**[1,2] · **Weixiong Cui**[2] · **Hui Yue**[2]

Received: 25 December 2018 / Accepted: 27 April 2019 / Published online: 6 May 2019

Abstract

Quantitative determination of the coal seam thickness distribution within the longwall panel is one of the primary works before integrated mining. In-seam seismic (ISS) surveys and interpolations are essential methods for predicting thickness. In this study, a new quantitative method that combines ISS and Bayesian kriging (BK), called ISS–BK, is proposed to determine the thickness distribution. ISS–BK consists of the following six steps. (1) The group velocity of Love waves is plotted by using the simultaneous iterative reconstruction technique under a constant frequency value. (2) An approximate quantitative relationship between the thickness and the group velocity is fitted based on sampling points of the coal seam thickness, which are measured during the process of entry development. (3) The group velocity map is translated into a primary thickness map according to the above-mentioned fitted equation. (4) By subtracting the ISS prediction result from the actual thickness at a sampling point, the residual variable is created. (5) The residual distribution is interpolated within the whole longwall panel by applying BK. The residual map establishes the interconnection between the ISS survey and BK. (6) A refined thickness distribution map can be obtained by overlapping the primary thickness map and the residual map. The application of this method to the No. 2408 longwall panel of Yuhua Coal Mine using ISS–BK showed a considerable improvement in thickness prediction accuracy over ISS. The residuals of ISS and ISS–BK mainly lie in the intervals (− 3.0, 3.0 m) and (− 1.0, 3.0 m), respectively. The accurate prediction rates [where the residual lies in the interval (0, 0.1 m)] of ISS and ISS–BK are 9.39% and 50.28%, respectively, and the effective prediction rates (where the residual is less than 1.0 m) of ISS and ISS–BK are 61.88% and 77.90%, respectively. All the above statistics reflect a considerable improvement in the ISS–BK method over the ISS method.

Keywords In-seam seismic · Love wave · Dispersion · Bayesian kriging · Coal seam thickness · Longwall panel

Introduction

Quantitative determination of the coal seam thickness distribution within the longwall panel is essential in coal mining. The importance can be summarized into three aspects. First, both the entry development and mining plan can be optimized with an accurate coal seam thickness distribution (Dresen and Bochum 1995). Therefore, production cost is reduced, and recovery is increased. Second, gas and geo-stress concentration tend to be associated with the area where the coal seam thickness changes dramatically. Geological hazards are likely to be induced during mining without predetermined coal seam thickness distributions, such as coal–gas outbursts and rock bursts (Dresen and Bochum 1995; álvarez-Fernández et al. 2009). Third, unmanned intelligent mining could be achieved by the automatic control of the shearer rocker arm when the coal seam thickness in front of the working face is ascertained (Yuan 2017). Quantitative determination of the coal seam thickness distribution not only has the benefit of shearer protection but also improves mining efficiency and reduces the gangue rate.

To address the problem of coal seam thickness determination, many studies have been conducted, and various methods have been proposed. These methods can be grouped into four types according to methodology and data type: geo-statistical methods (Du and Peng 2010), seismic attributes analysis methods (Wang et al. 2017; Zou et al. 2018),

✉ Jianyuan Cheng
cjy6608@163.com

[1] China Coal Research Institute, Beijing, China

[2] Xi'an Research Institute, China Coal Technology & Engineering Group Corp, Xi'an, China

coal-rock recognition methods (Slavinskii et al. 1985; Sun and Chen 2017) and integrated mining geophysical methods (Wang et al. 2011). Integrated mining geophysical methods mainly include mine transient electromagnetic (TEM) surveys (Sahalos and Kyriacou 1985), ISS (Dresen and Bochum 1995; Cheng et al. 2012; Schott and Waclawik 2015; Hu et al. 2018), geological radar (also called ground penetrating radar, GPR) and others. A review of coal seam thickness prediction can be found in Wang et al. (2011). However, both theories and applications show that each method has applicable conditions, and it is hard for a single method to ascertain coal seam thickness and geological anomalies effectively, especially for the lengthening and widening longwall panels.

In this paper, an integrated, quantitative method is proposed to determinate coal seam thickness within a longwall panel based on an in-seam seismic survey and Bayesian kriging. We call this method ISS–BK in the following sections. This new method combines the merits of ISS and BK. In the areas with dense sampling points of coal seam thickness, the thicknesses mainly depend on the hard data. In areas lacking sampling points, the thicknesses mainly depend on the ISS survey results (soft data). The application shows that ISS–BK achieved a better performance compared with the ISS survey.

In-seam seismic surveys

In-seam seismic surveys are widely applied to detect various geological anomalies, such as minor faults, collapse columns, coal seam variation zones, goaves and abandoned laneways. Moreover, they are characterized by large detection ranges, high precision, strong anti-interference and obvious waveform features. ISS includes transmission and reflection surveys (Dresen and Bochum 1995), and their schematics are shown in Fig. 1a, b, respectively. By applying transmission surveys, the geological structures can be judged according to the energy variation in ISS waves. Then, the coal seam structure and thickness distribution can be investigated by applying ISS tomography (Dresen and Bochum 1995).

The ISS waves recorded by seismography consist of Rayleigh waves and Love waves. The former is formed by the interference of P-waves and SV-waves, and the latter is formed by the interference of SH-waves. In practice, in-seam seismic surveys are simpler to perform on the basis of Love seam waves than on the basis of Rayleigh seam waves. On the other hand, the Rayleigh wave within the seam is more complex due to its complicated interpretation (Dresen and Bochum 1995). In addition, Love waves are more sensitive to coal seam thickness. Therefore, Love waves are generally used in ISS (Dresen and Bochum 1995; Schott and Waclawik 2015; Hu et al. 2018). When the ISS wave is used in the following section, it refers to the Love wave.

Dispersion of Love waves

For forward modelling of the dispersion of the Love wave, a model consisting of three horizontal layers is considered, as shown in Fig. 2. The upper, middle and lower layers represent the roof stratum (index 1), the coal seam (index 2) and the floor stratum (index 3), respectively. All three layers are assumed to be elastic, homogeneous and isotropic. Their shear wave velocities and densities are expressed using β_i and ρ_i ($i=1, 2, 3$), respectively, and the thickness of the coal seam is expressed by d.

With the above information, the dispersion equation of a Love wave under the three-layer model is derived based on the phase recursion algorithm (Räder et al. 1985), as shown in Eq. (1).

$$\begin{cases} \tan(\xi_2+\omega\gamma_2 d) = i\frac{\mu_3\gamma_3}{\mu_2\gamma_2} \\ \tan(\xi_2) = -i\frac{\mu_1\gamma_1}{\mu_2\gamma_2} \end{cases} \tag{1}$$

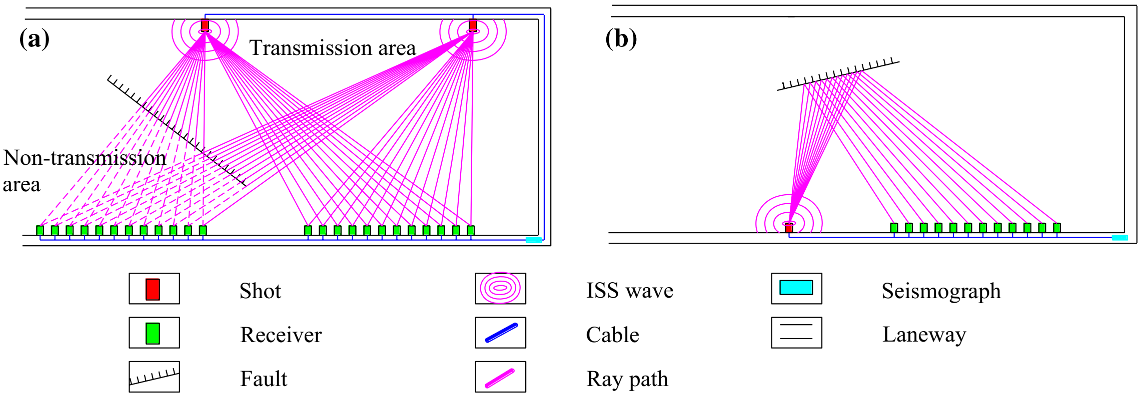

Fig. 1 Schematics of transmission (**a**) and reflection (**b**) ISS surveys

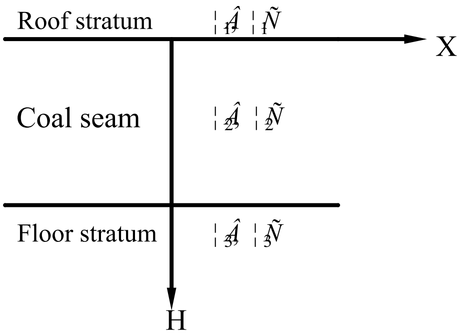

Fig. 2 Three-layer model used to derive the dispersion equation of the Love wave

where ξ_2 is the phase shift in the coal seam; $\omega = 2\pi f$ is the angular frequency; f is the frequency; $\gamma_i = \sqrt{\frac{1}{\beta_i^2} - \frac{1}{c^2}}$ is the propagation factor; c is the phase velocity; i is the imaginary unit; and $\mu_i = \rho_i \beta_i^2$ is the rigidity.

Equation (1) can be transformed into a single formula based on the arc tangent transformation, as shown in Eq. (2).

$$\omega\gamma_2 d = \arctan\left(i\frac{\mu_3\gamma_3}{\mu_2\gamma_2}\right) + \arctan\left(i\frac{\mu_1\gamma_1}{\mu_2\gamma_2}\right) + n\pi \tag{2}$$

where n is the modal order.

Traditionally, it is assumed that the roof and floor strata consist of identical rocks; i.e. μ_1 equals μ_3 and γ_1 equals γ_3. Only the fundamental mode is considered, i.e. n equals 0. Then, Eq. (2) is further simplified as Eq. (3).

$$\omega\gamma_2 d = 2\arctan\left(i\frac{\mu_1\gamma_1}{\mu_2\gamma_2}\right) \tag{3}$$

Equation (3) can be solved to find the explicit solution for the coal seam thickness d.

$$d = \frac{2}{\omega\gamma_2}\arctan\left(i\frac{\mu_1\gamma_1}{\mu_2\gamma_2}\right) \tag{4}$$

Equation (4) shows the relationship between the phase velocity c and the coal seam thickness d. However, the mathematical relationship between the group velocity u and the coal seam thickness d must be established to determine the thickness distribution of the longwall panel. The group velocity u is defined as follows:

$$u = \frac{d\omega}{dk} \tag{5}$$

where $k = \frac{2\pi f}{c}$ is the wavenumber.

The differential of k is found as shown in Eq. (6).

$$dk = \frac{-2\pi f}{c^2}dc + \frac{2\pi}{c}df \tag{6}$$

Equation (6) applied to Eq. (5) derives the following equation between the group velocity u and phase velocity c.

$$\begin{aligned} u &= \frac{d\omega}{\frac{-2\pi f}{c^2}dc + \frac{2\pi}{c}df} = \frac{c}{\frac{-2\pi f}{c}\frac{dc}{d\omega} + 2\pi\frac{df}{d\omega}} \\ &= \frac{c}{-\frac{\omega}{c}\Big/\frac{d\omega}{dc} + 1} \end{aligned} \tag{7}$$

Equation (3) applied to Eq. (7) derives the following dispersion equation of the group velocity:

$$u = c\frac{g(c) - (2\pi f)d}{g(c) - (2\pi f)d\left(1 + \gamma_2^2 c^2\right)} \tag{8}$$

where $g(c) = \frac{2i\mu_1\mu_2\left(\gamma_2^2 - \gamma_1^2\right)}{\gamma_1\left(\mu_2^2\gamma_2^2 - \mu_1^2\gamma_1^2\right)}$.

Equations (4) and (8) define the mathematical relation of velocity-frequency-thickness. When the frequency f and the thickness d are given, the phase velocity c is solved based on Eq. (4). Then, the corresponding group velocity u is calculated based on Eq. (8). Therefore, the curve $u = F(d)$ can be calculated when the frequency f is kept constant. Similarly, the curve $u = F(f)$ can also be calculated.

Inversion of coal seam thickness

From the analysis in "Dispersion of Love waves" section, the variation in coal seam thickness has an obvious influence on the dispersion of Love waves. As the coal seam thickness increases, the dominant frequency band moves towards the lower frequency. Therefore, there is a negative correlation between coal seam thickness and group wave velocity (group velocity) under a certain frequency, i.e. the group velocity is higher in the region with a small thickness and lower in the region with a large thickness. The travel time of each ray can be calculated by subtracting the phase arrival time and the shot time. Then, the velocity tomography can be plotted by utilizing the SIRT algorithm (Gersztenkorn and Scales 1988). During the preparation stage of the coal mining face, many sampling points of coal seam thickness were recorded through drilling and entry development. These known points are used to establish a mathematical model between the group velocity and thickness, and the coal seam thickness distribution within the longwall panel is predicted based on the above model and velocity tomography.

The modification of the thickness map with Bayesian kriging

Theoretical derivation

Many sampling points of coal seam thickness (hard data) are measured during entry development. These data are distributed along the two sides of the longwall panel and are characterized by high precision. The thickness map surveyed by ISS (soft data) reflects the distribution of coal thickness within the longwall panel. However, its accuracy is relatively low compared with the hard data. In areas close to the hard data, such as roadways, kriging interpolation is closer to the actual coal thickness than the ISS results. However, in areas that are far from the hard data, such as in the middle of the longwall panel, the ISS results are closer to the actual thickness. Therefore, the question of how to combine the advantages of ISS and kriging is worth studying.

Let the regionalized variables $\{Z(x);x \in A\}$ and $\{M(x);x \in A\}$ denote the hard and soft data, respectively, where A is the whole longwall panel. Assume the second-order moments of $M(x)$ are known a priori, i.e. the expectation and covariance of $M(x)$ are defined as

$$\begin{array}{ll} E[M(x')] = \mu_M(x') & x' \in A \\ \mathrm{Cov}[M(x'), M(x'')] = C_M(x', x'') & x', x'' \in A \end{array} \tag{9}$$

The variogram of $M(x)$ is defined as

$$\begin{aligned} \gamma_M(x', x'') &= \tfrac{1}{2}\mathrm{Var}[M(x') - M(x'')] \\ &= [C_M(x', x'') + C_M(x', x'')]/2 - C_M(x', x'') \quad x', x'' \in A \end{aligned} \tag{10}$$

The covariance and variogram are dependent on both x' and x'' , not only on their relative locations. Let the conditional expectation and the conditional covariance of $Z(x)$ be defined as in Eq. (11).

$$\begin{array}{ll} E[Z(x')|M(x);x \in A] = a_0 + M(x') & x' \in A \\ \mathrm{Cov}[Z(x'), Z(x'')|M(x);x \in A] = C_{Z|M}(x' - x'') & x', x'' \in A \end{array} \tag{11}$$

where a_0 is a constant.

The relationship between $Z(x)$ and $M(x)$ is defined by Eq. (11), and $M(x)$ can be interpreted as a reasonable guess of $Z(x)$ with uncertainty. The introduction of a_0 is to reduce the influence of $M(x)$.

The conditional expectation and the conditional covariance of $Z(x)$ are deduced based on a linear Bayesian formula.

$$\begin{aligned} &\mu_Z(x') = E[Z(x')] = E[E[Z(x')|M(x);x \in A] = a_0 + \mu_M(x');x' \in A \\ &\gamma_z(x', x'') = \tfrac{1}{2}\mathrm{Var}[Z(x') - Z(x'')] = \gamma_{z|M}(x' - x'') + \gamma_M(x', x'') \end{aligned} \tag{12}$$

Assume an observation set of $Z(x)$ is available

$$\{Z(x_i); i = 1, \dots, N\} \tag{13}$$

The expected function of $Z(x)$ is a constant because the expected function of $M(x)$ is $\mu_M(x')$, and a_0 is a constant, as shown in Eqs. (9) and (11). A new random variable $Z^{\mathrm{T}}(x)$ can be introduced.

$$\{Z^{\mathrm{T}}(x) = Z(x) - \mu_M(x); x \in A\} \tag{14}$$

The observation set of $Z^{\mathrm{T}}(x)$ is

$$\{Z^{\mathrm{T}}(x_i) = Z(x_i) - \mu_M(x_i); i = 1, \dots, N\} \tag{15}$$

Therefore, the linear estimator for $Z^*\left(x_0\right)$ with an arbitrary location x_0 within A is calculated as follows:

$$Z^*(x_0) = \sum_{i=1}^{N} \alpha_i Z^{\mathrm{T}}(x_i) + \mu_M(x_0) \tag{16}$$

where α_i is the ith weight.

Based on the un-biasedness and minimizing variance requirements of the estimator, the Bayesian kriging equations are established:

$$\begin{cases} \sum\limits_{i=1}^{N} \alpha_i[\gamma_{Z|M}(x_i - x_j) + \gamma_M(x_i, x_j)] + \beta_1 = \gamma_{Z|M}(x_0 - x_j) + \gamma_M(x_0, x_j) \\ \quad j = 1, \dots, N \\ \sum\limits_{i=1}^{N} \alpha_i = 1 \end{cases} \tag{17}$$

where β_1 is a Lagrange multiplier.

The coal seam thickness estimator $Z(x_0)$ at x_0 can be calculated based on the solution to the above Bayesian kriging equations (Eqs. 16, 17).

Based on "Inversion of coal seam thickness" section and the present section, the steps of the ISS–BK method are summarized as follows:

Step 1 Applying group velocity tomography to the transmission data.

Step 2 Fitting an approximate quantitative relationship between the thickness d and the group velocity u according to the sampling points, i.e. $d = f(u)$.

Step 3 Converting the group velocity map into a primary thickness map based on the above function, $d = f(u)$.

Step 4 Creating the residual variable $Z^{\mathrm{T}}(x)$ according to Eq. (14).

Step 5 Interpolating the residual variable $Z^{\mathrm{T}}(x)$ within the longwall panel by using Bayesian kriging.

Step 6 Calculating the final prediction of the coal seam thickness, $Z^*\left(x_0\right)$, according to Eq. (17).

Characteristics of the ISS–BK method

The characteristics of ISS–BK can be summarized based on the special cases discussed in (Omre 1987).

(1) When the location x_0 matches the location of one of the thickness sampling points, the corresponding weight equals 1, and the weights of the other sampling points equal 0. Then, the final prediction of ISS–BK, $Z^*(x_0)$, equals the actual thickness, $Z(x_0)$. That is, ISS–BK is equipped with exact interpolation properties.

(2) When the location x_0 is farther from any sampling point than the ranges of both $\gamma_{ZIM}(\cdot)$ and $\gamma_M(\cdot)$, the weights are independent of x_0. Then, the final prediction of ISS–BK, $Z^*(x_0)$, mainly depends on the ISS results, $M(x_0)$.

A case study for ISS–BK

To evaluate the prediction accuracy for the coal seam thickness, the ISS–BK method was applied to determine the thickness distribution of the No. 2408 longwall panel of Yuhua Coal Mine.

Overview of the longwall panel

The No. 2408 longwall panel is in the No. 2 panel of Yuhua Coal Mine, Tongchuan City, Shaanxi Province, China, with a strike length of 1775 m and a face width of 240 m. The coal seam thickness varies from 4.5 to 11.7 m with an average of 7.5 m.

In total, 181 sampling points of coal seam thickness were collected across the life cycle of the No. 2408 longwall panel. Forty-two, thirty-eight and five of those sampling points lie in intake airways, return airways and the start-up room, respectively (Fig. 3, symbol "o"). Two surface exploratory drilling boreholes that penetrate coal seams are also within the longwall panel (Fig. 3, red dots). In addition, ninety-four sampling points were measured during the mining process (Fig. 3, symbol "×"). The coal seam thins between the stations located 1000 and 1200 m, and the thickness is between 4.5 and 6.5 m. In this area, the full-face coal seam was mined integrally; that is, there was no top coal caving. Therefore, none of the sampling points were measured in this area. The sampling points from the intake and return airways, the start-up room and the drilling boreholes can be used both in prediction and validation. However, the sampling points collected during mining are only used to validate.

ISS survey and the primary thickness distribution

Design of the observation system layout

The observation system layout was designed based on the forward modelling results produced by GeoCoal, an ISS data processing system developed by the Xi'an branch of the China Coal Technology and Engineering Group Corp. A total of 354 receiver stations were set up every 10 m along the return and intake airways (Fig. 4, green dots). Similarly, a total of 118 source stations were set every 30 m along

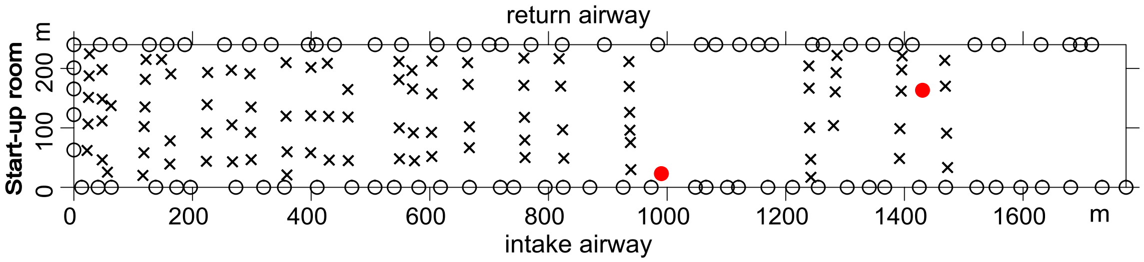

Fig. 3 Distribution of thickness sampling points in the No. 2408 longwall panel

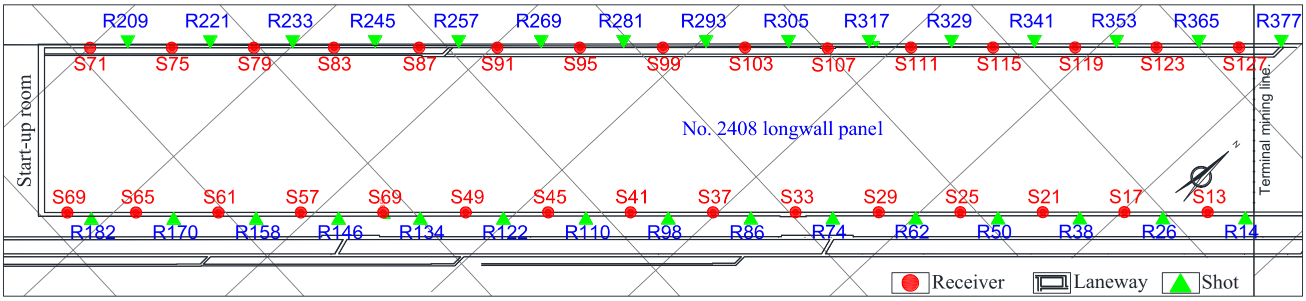

Fig. 4 Observing system layout of the ISS survey (locations of all the source and receiver stations)

the return and intake airways, shown as red dots in Fig. 4. Detailed information of the observation system is shown in Table 1 and Fig. 4.

The geophone probes were mounted on the outcrops of rock bolts located in the approximate centre of the coal wall. Every probe contained a geophone that was oriented perpendicular to the direction of the longwall panel length. Therefore, the Y-component of the transmitted Love wave was recorded. At every source station, a blast hole that was oriented perpendicular to the coal wall was drilled. The depth of the blast holes was approximately 2.40 m. Explosives weighing approximately 0.25 kg were ignited to generate seismic waves. The YTZ-3 nodal seismographs were applied to record the ISS waves. The sampling interval and recording times were 0.25 ms and 2.00 s, respectively.

Data acquisition and ISS wave identification

The rays cover the whole longwall panel. In total, 115 valid shot gathers were recorded during the ISS survey. The recorded seismic traces have a high signal-to-noise ratio (SNR). An example of the ISS waves recorded in this survey is shown in Fig. 5. The data from source station S106 recorded at receiver stations S11–S187 are displayed. To improve the SNR, a band-pass filter with a wide band was used to suppress noise, such as in the P- and S-waves and in the surface waves and sound waves. Figure 6 shows the denoised seismic record from common-shot gather S106.

ISS tomography

The physical parameters of the layers were measured by a qualified rock mechanics laboratory before the ISS survey. The results are shown in Table 2. Then, the dispersion curves of group velocity for different coal seam thicknesses and the dependency between group velocity and coal seam thickness for different constant frequency values were calculated based on Eqs. (4) and (8), as shown in Figs. 7 and 8. Figure 7 shows that the group velocity increases significantly as the thickness decreases. Similarly, Fig. 8 indicates that a pre-defined frequency only reacts on a certain thickness range. When the group velocity is greater than the minimum, there is a negative correlation between the thickness and the velocity at a given frequency. In addition, a lower frequency tends to plot a thicker coal seam. However, a lower frequency may result in noise interference because the frequency of noise mainly goes up to 50 Hz. Therefore, an appropriate frequency should be selected to determine the group travel time of every ray trace by using the multiple filter technique (MFT) (Dziewonski et al. 1969). Then, by means of ISS tomography, the group velocity within the survey area can be plotted.

In this ISS survey, an investigation of the coal seam thickness distribution of the whole longwall panel, including the extension of coal seam thinning and its boundary, was needed. Considering Fig. 7, the dispersion curve of the group velocity for an average thickness of 7.5 m should

Table 1 Detailed information of the observation system

Tunnels	Serial number of the source	Source span (m)	No. of Sources	Serial number of the receiver	Receiver span (m)	No. of receivers
Intake airway	S11–S69	30	59	R11–R187	10	177
Return airway	S70–S128	30	59	R201–R377	10	177
Total			118			354

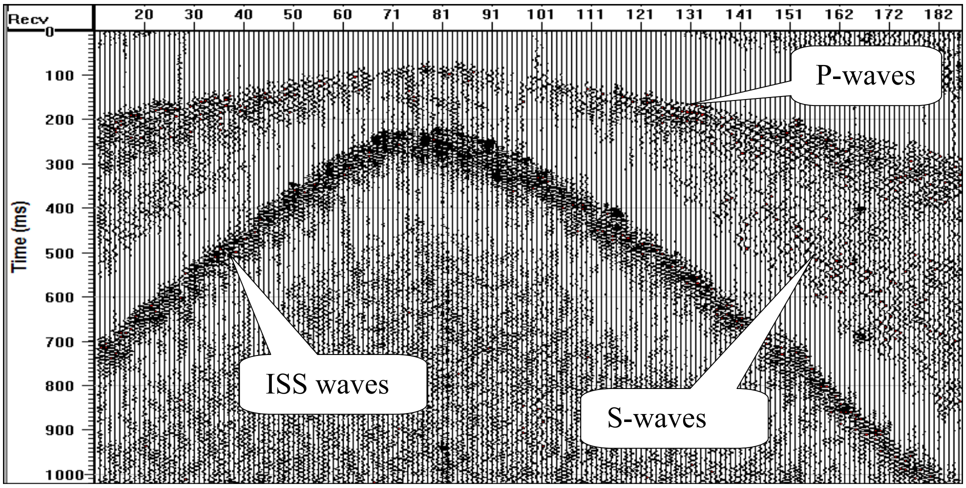

Fig. 5 Seismic record from common-shot gather S106

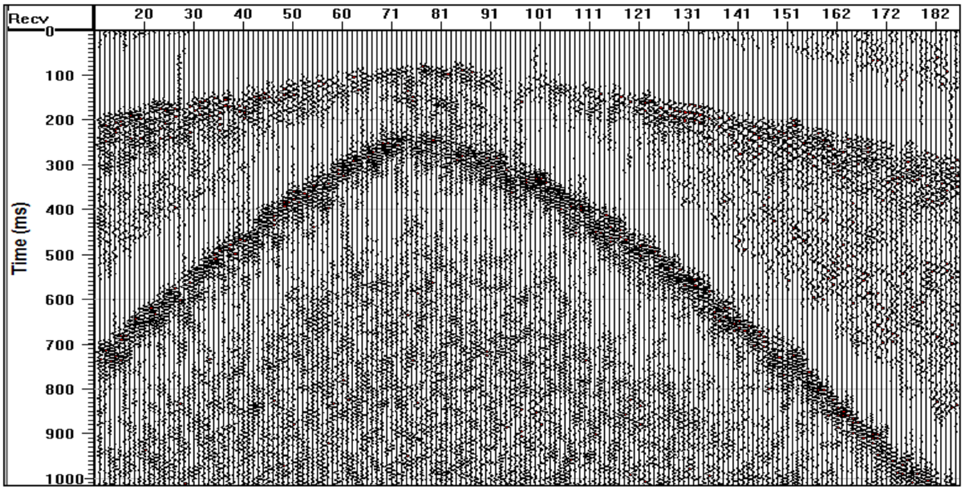

Fig. 6 Band-pass filtering seismic record from common-shot gather S106

Table 2 Physical parameters of the surrounding rock and coal seam

Layer	Physical parameters		
	P-wave velocity (m/s)	S-wave velocity (m/s)	Density (kg/m^3)
Roof and floor strata	4300	2280	4100
Coal seam	1755	1025	1400

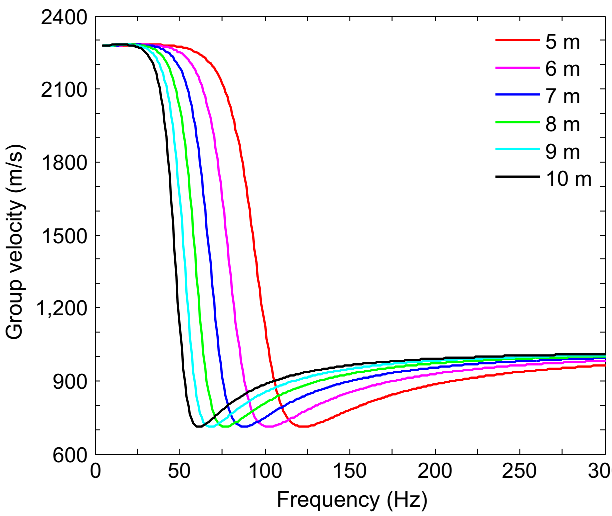

Fig. 7 Love wave dispersion curves for different coal seam thicknesses and parameters gathered in the laboratory

lie between the minimums of the blue and green curves. Therefore, in this application, a narrow frequency band of 75 Hz was selected to determine the travel time of every ray trace, considering the noise frequency distribution and the thickness distribution together. A high SNR seismic record numbered S63-R281 was selected to validate the above analysis by applying the MFT. Figure 9 shows the result of the dispersion extraction, and the warm colours indicate a high-energy concentration. There was good consistency between the theoretical dispersion curve and the dispersion spectra. Finally, the group velocity tomography was plotted by utilizing the SIRT algorithm, as shown in Fig. 10.

Inversion of the thickness distribution

As shown in Eqs. (4) and (8), many parameters affect the group velocity of the Love waves, such as the S-wave velocities, the densities of the three layers, the coal seam thickness and the frequency. In addition, there is no explicit solution for the thickness, *d*, in terms of the group velocity, *u*. However, an approximate quantitative relationship between the thickness and the group velocity can be fitted based on the sampling points that were collected during entry development, as shown in Fig. 11. Then, the group velocity map (Fig. 10) can be translated into a thickness map (Fig. 12) based on the above equation.

Figure 12 shows that the coal seam thickness is mainly distributed within the range of 7–8 m for the whole longwall panel. The two thin-coal areas where the thickness is less than 7 m are located in the middle and in the start-up room of the longwall panel, as shown in the blue areas in Fig. 12. The thinnest coal seam in the middle of the longwall panel is approximately 5 m. The coal seam thickness revealed by the laneway is approximately 4 m at its thinnest, and it is located near the start-up room.

Refining the primary thickness distribution with BK

Bayesian kriging has three steps for refining the primary thickness distribution, i.e. steps 4 to 6 in "Theoretical derivation" section. The sampling points located in laneways

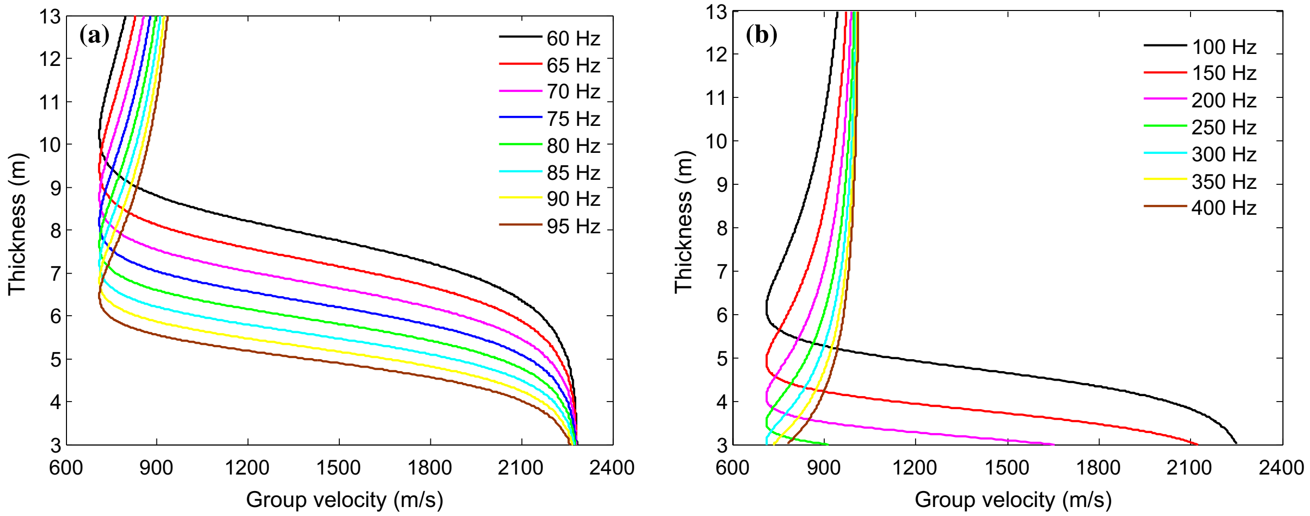

Fig. 8 Theoretical dependencies between the group velocity and the coal seam thickness for different constant frequency values

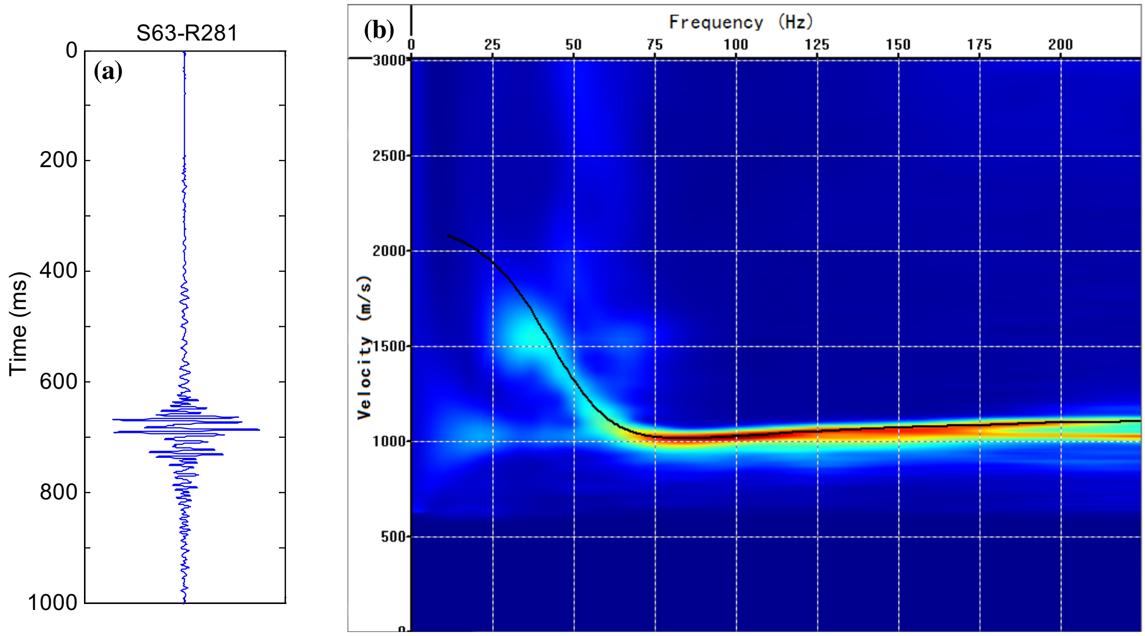

Fig. 9 No. S63-R281 seismic trace (**a**) and the corresponding dispersion spectra (**b**). In the serial number of the seismic trace, “S63” and “R281” denote the shot and receiver stations, respectively. The black line in the dispersion spectra (**b**) is the theoretical group velocity dispersion curve of the average coal thickness (7.5 m)

and the two surface exploratory drilling boreholes are used to create the residual variable, $Z^{\mathrm{T}}(x)$, $x = 1, 2, \ldots, 87$. The distribution of the residual variable, $Z^{\mathrm{T}}(x)$, can be estimated by kriging. The interpolation result of the residual variable is shown in Fig. 13. According to Eq. (16), the refined thickness map can be obtained by adding the primary thickness distribution to the kriging interpolation of $Z^{\mathrm{T}}(x)$, as shown in Fig. 14.

Validation

The No. 2408 longwall panel was completely mined out based on the result of ISS–BK. Ninety-four sampling points were measured during the process of mining, shown by “×” in Fig. 3. Thus, there are a total of 181 sampling points that can be used to validate the coal seam thickness distribution produced by ISS–BK.

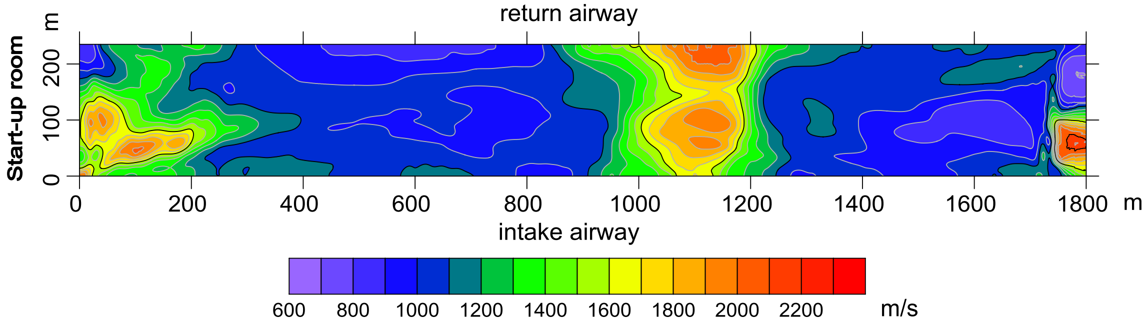

Fig. 10 Group velocity distribution of the Love wave for a constant frequency value of 75 Hz

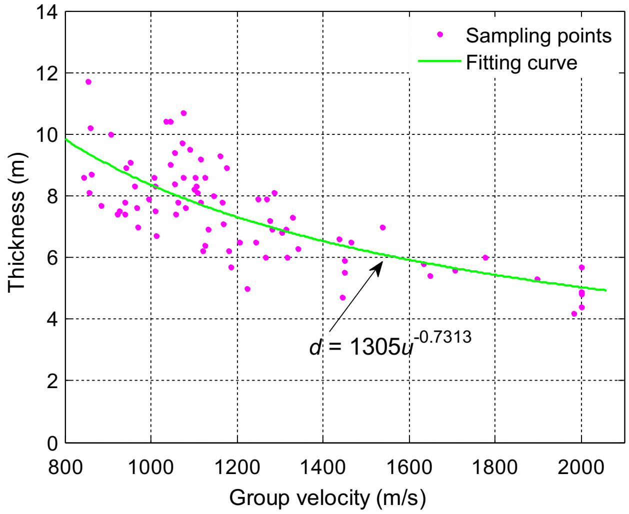

Fig. 11 Fitting curve between the coal seam thickness and the group velocity for a constant frequency value of 75 Hz

If we regard all the sampling points as exploratory drilling boreholes, then the exploratory grid of the longwall panel is approximately 45 m × 45 m. Compared with the surface exploratory grid, the grid of the longwall panel is much smaller. Therefore, the thickness map interpolated by all the sampling points (both from the roadways and the longwall face) is the closest to the actual thickness distribution. The thickness map is shown in Fig. 15. If we regard this thickness map as the actual thickness distribution, then the residual maps of ISS and ISS–BK can be calculated by subtracting the primary and final thickness maps from the actual thickness map, respectively. The residual maps of ISS and ISS–BK are shown in Fig. 16a, b, respectively. Both maps share the same colour scale. The violet and red areas indicate large residuals. Compared with the residual map of ISS, the violet and red areas in the residual map of ISS–BK are much smaller, especially along the return and intake

Fig. 12 Primary coal seam thickness distribution from the ISS survey

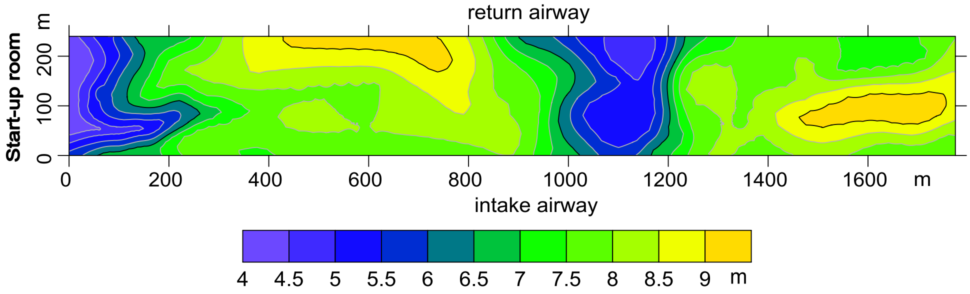

Fig. 13 Kriging interpolation of the residual variable, $Z^{\mathrm{T}}(x)$

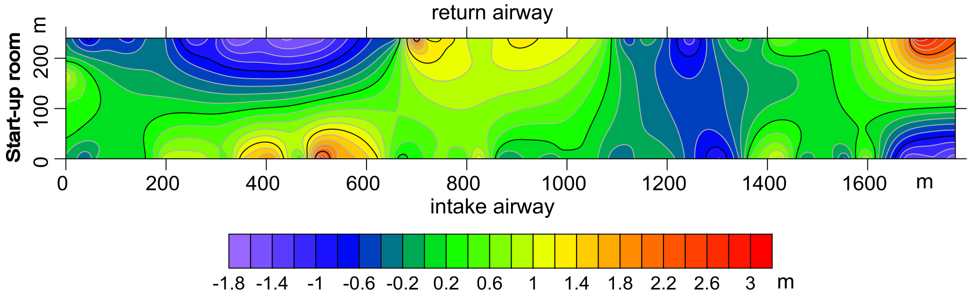

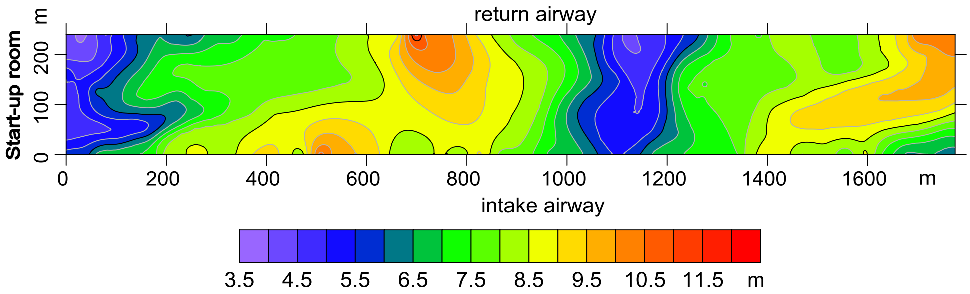

Fig. 14 Final thickness distribution by using ISS–BK

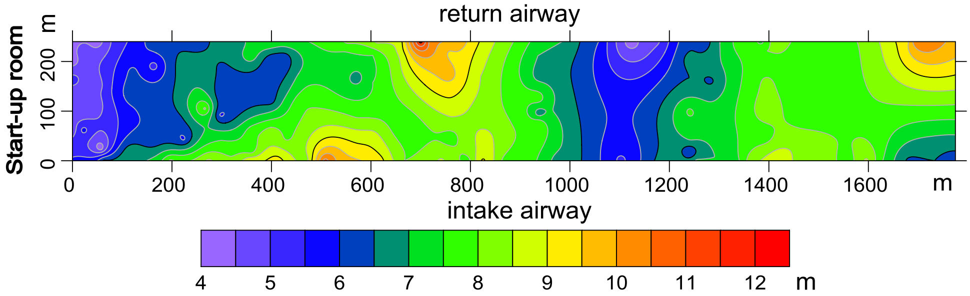

Fig. 15 Thickness map interpolated by all the hard data

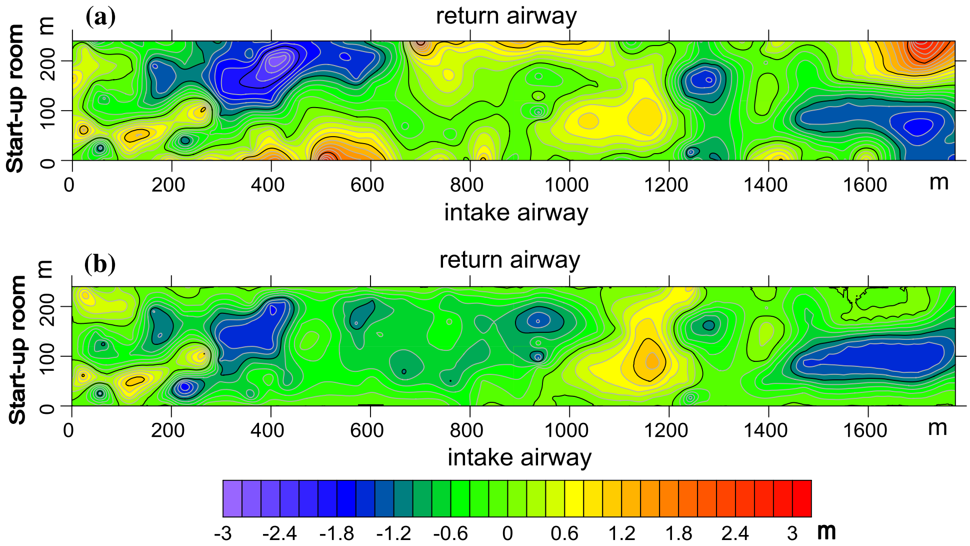

Fig. 16 Residual maps of ISS (**a**) and ISS–BK (**b**)

airways. That is, it is a considerable advantage to apply the ISS–BK method to coal seam thickness prediction.

The prediction residual histograms of ISS and ISS–BK are shown in Fig. 17a, b, respectively. Figure 17 shows that the residuals of ISS and ISS–BK mainly lie in the intervals (− 3, 3) and (− 1, 3), respectively. The residuals of ISS are approximately normally distributed, but the residuals of ISS–BK are not. Intuitively, the accuracy of coal seam thickness prediction was greatly improved after the Bayesian kriging.

All the residuals were classified into four intervals, (0, 0.1], (0.1, 0.5], (0.5, 1.0] and (1.0, +∞), and the results are shown in Table 3. As Table 3 shows, the prediction accuracy of ISS–BK is higher than that of ISS. If we regard the results whose residuals lie in the interval (0, 0.1] as the accurate predictions, then the accurate prediction rates of ISS and ISS–BK are 9.39% and 50.28%, respectively. If we regard the results whose residuals are less than 1.0 m as the effective predictions, then the effective prediction rates of ISS and ISS–BK are 61.88% and 77.90%, respectively. All the above statistics reflect a considerable improvement in ISS–BK compared to ISS.

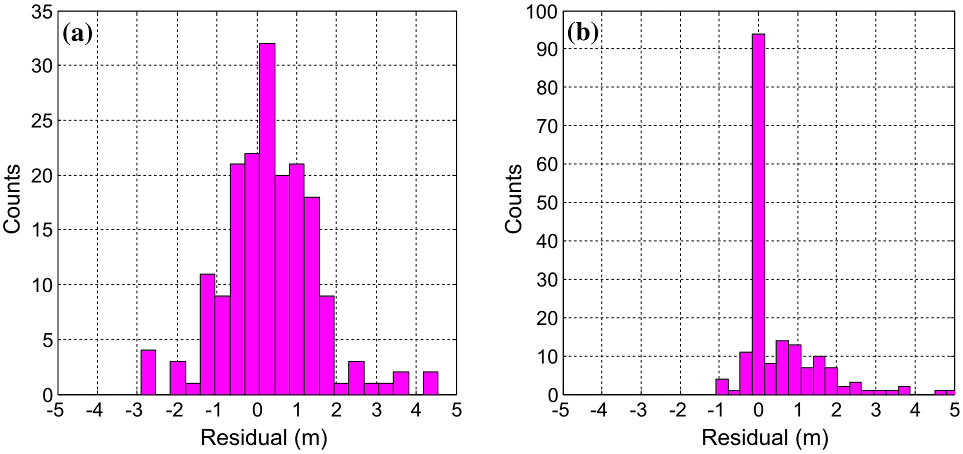

Fig. 17 Histograms of the coal seam thickness prediction residuals for ISS (**a**) and ISS–BK (**b**)

Table 3 Absolute residual distribution intervals for ISS and ISS–BK

Method	Error intervals (m)				Total
	(0, 0.1]	(0.1, 0.5]	(0.5, 1.0]	(1.0, +∞)	
ISS	17	57	38	69	181
ISS–BK	91	28	22	40	181

Conclusions

ISS surveys are widely used to investigate geological disturbances and thickness distributions within coal seams. An ISS transmission survey can give a primary thickness distribution for the whole longwall panel. The primary thickness map can be refined by utilizing Bayesian kriging. The resulting thickness distribution map gives guidance for the selection of mining methods, mining plans and safety management.

(1) The dominant frequency of Love waves stretches towards the lower frequency with the increase in coal seam thickness. There exists a negative correlation between group velocity and coal thickness for a predetermined constant frequency. Each frequency value can only invert a specific range of thicknesses. A higher frequency is appropriate for thinner coal seams; a lower frequency is appropriate for thicker coal seams. In this paper, a narrow frequency band of 75 Hz was selected to determine the travel times of every ray trace, considering the noise frequency distribution and the thickness distribution together. Then, the group velocity was plotted by using the SIRT algorithm.

(2) An approximate quantitative relationship between the thickness and the group velocity was fitted based on the sampling points of the coal seam thickness, which were collected during entry development. In this paper, a power function was used. Then, a primary thickness map was plotted by applying the above function to the group velocity map.

(3) By applying the BK to interpolate the residual distribution in the whole longwall panel, a residual map was produced. Thus, the residual map establishes the relationship between ISS and BK. The thickness values predicted by ISS–BK from the sampling points are equal to the actual values, because ISS–BK has inherited the exact interpolation property of BK. The final prediction of ISS–BK mainly depends on the ISS results when the location is farther away than the ranges of both $\gamma_{Z|M}(\cdot)$ and $\gamma_M(\cdot)$ from any sampling points.

(4) The application in the No. 2408 longwall panel of Yuhua Coal Mine by using the ISS–BK method showed a considerable improvement in thickness prediction accuracy compared with the ISS method. The statistics show that the accurate prediction rates of ISS and ISS–BK are 9.39% and 50.28%, respectively, and the effective prediction rates of ISS and ISS–BK are 61.88% and 77.90%, respectively. In conclusion, by applying Bayesian kriging to refine the thickness map of ISS, the prediction accuracy of the thickness is greatly improved.

Acknowledgements The authors gratefully acknowledge the financial support from the National Key Research and Development Plan (No. 2018YFC0807804) and the Guizhou Science and Technology Major Project (No. [2018]3003-1). Special thanks are given to the anonymous reviewers for their assistance, comments and suggestions.

References

álvarez-Fernández MI, González-Nicieza C, álvarez-Vigil AE, Herrera García G, Torno S (2009) Numerical modelling and analysis of the influence of local variation in the thickness of a coal seam on surrounding stresses: application to a practical case. Int J Coal Geol 79(4):157–166

Cheng J, Ji G, Zhu P (2012) Resolution analysis of in-seam seismic tomographic inversion for coal thickness. J China Coal Soc 37(01):67–72

Dresen L, Bochum R (1995) Seismic coal exploration, Part B. In-seam seismics. RuhrUniversität Bochum, Institut für Geophysik, Bochum

Du W, Peng S (2010) Coal seam thickness prediction with geostatistics. Chin J Rock Mech Eng 29(s1):2762–2767

Dziewonski AM, Bloch S, Landisman M (1969) A technique for the analysis of transient seismic signals. Bull Seismol Soc Am 59:427–444

Gersztenkorn A, Scales JA (1988) Smoothing seismic tomograms with alpha-trimmed means. Geophys J 92(1):67–72

Hu Z, Zhang P, Xu G (2018) Dispersion features of transmitted channel waves and inversion of coal seam thickness. Acta Geophys 66(5):1001–1009

Omre H (1987) Bayesian kriging: merging observations and qualified guesses in kriging. Math Geol 19(1):25–39

RäDer D, Schott W, Dresen L, RüTER H (1985) Calculation of dispersion curves and amplitude-depth distributions of love channel waves in horizontally-layered media. Geophys Prospect 33(6):800–816

Sahalos JN, Kyriacou G (1985) On the electromagnetic detection of the thickness of a coal or lignite seam with slate backing. J Franklin Inst 320(2):83–101

Schott W, Waclawik P (2015) On the quantitative determination of coal seam thickness by means of in-seam seismic surveys. Can Geotech J 52:1496–1504

Slavinskii VM, Shilov VI, Chernyak ZA (1985) The output function and calibration curve for a natural-radioactivity coal-seam thickness gauge. Meas Tech 28(8):704–706

Sun J, Chen B (2017) Coal-rock recognition approach based on CLBP and support vector guided dictionary learning. J China Coal Soc 42(12):3338–3348

Wang B, Liu S, Jiang Z, Huang L (2011) Advanced forecast of coal seam thickness variation by integrated geophysical method in the laneway. In: First international symposium on mine safety science and engineering

Wang X, Li Y, Chen T et al (2017) Quantitative thickness prediction of tectonically deformed coal using extreme learning machine and principal component analysis: a case study. Comput Geosci 101(C):38–47

Yuan L (2017) Scientific conception of precision coal mining. J China Coal Soc 42(1):1–7

Zou G, Xu Z, Peng S, Fan F (2018) Analysis of coal seam thickness and seismic wave amplitude: a wedge model. J Appl Geophys 148:245–255

Acta Geophysica (2019) 67:837–847
https://doi.org/10.1007/s11600-019-00289-z

RESEARCH ARTICLE - ANTHROPOGENIC HAZARD

Simple GMPE for underground mines

Aleksander J. Mendecki[1]

Received: 5 November 2018 / Accepted: 11 April 2019 / Published online: 6 May 2019

Abstract

A simple ground motion prediction equation (GMPE) is developed for peak ground velocity, PGV, and for cumulative absolute displacement, CAD, for underground mines. Assuming the ground velocity at source, $\mathrm{PGV}_0 = 0.63 v_S \Delta\epsilon$ where v_S is S-wave velocity and $\Delta\epsilon$ is the average strain change at seismic sources (Brune in J Geophys Res 75(26):4997–5009, 1970; Kanamori in Phys Earth Planet Inter 5:426–434, 1972), is independent of seismic potency, P, then $\overline{\mathrm{PGV}}(P,R) = \mathrm{PGV}_0 \cdot B$, where $B = \left[c_L P^{1/3} / \left(R + c_L P^{1/3}\right)\right]^{c_R}$ and R is distance. Assuming after Eshelby that at source $\mathrm{CAD}_0 = q_0\, \Delta\epsilon^{2/3} P^{1/3}$, then $\overline{\mathrm{CAD}}(P,R) = \mathrm{CAD}_0 \cdot B$, where $q_0 = 0.828494$. The S-wave velocity and the strain drop are strongly constrained by the type of rock and can be assumed, therefore both GMPE have only two parameters to be inverted from ground motion data: c_L and c_R. There is no provision made for site effect since in mines almost all sensors are placed in boreholes away from excavations. The basic outcome of ground motion hazard analysis for a given site is a seismic hazard curve that shows the annual rate, or probability, at which a specific ground motion level will be exceeded. It is expected that CAD that includes both the peak and the duration of ground motion may be a better indicator of damage potential than PGV alone, being a single measurement over the whole waveform. Two simple applications are presented. (1) A graphical trigger for damage inspection when the PGV predicted for an event at selected sites exceeds a predetermined level. (2) The cumulative CAD plot that may be a useful tool to monitor the consumption of the deformation capacity of the support due to seismicity.

Keywords Ground motion prediction · Near-source ground motion · Cumulative absolute displacement

Motivation

Underground structures, specifically those embedded in hard rock, are far more resilient to shaking than surface ones. Therefore, with the exception of large events, most damage caused by seismic events in underground mines is observed in excavations relatively close to their sources. Since the maximum ground velocity at source is controlled by the strength of the rock mass, small and large events produce similar ground motion at source, but large events affect a substantial volume of rock, hence, the probability of hitting a vulnerable structure is considerably higher. In smaller mines, the strong ground velocities associated with larger events may affect the entire infrastructure.

There is not much literature on GMPE for mining-induced seismicity. McGarr et al. (1981) used ground motion data recorded 3 km underground in a South African gold mine to develop the relationship $\log(R \cdot \mathrm{PGV}) = 3.95 + 0.57 m_\mathrm{L}$, where both R and the peak ground velocity, PGV, are in cm/s and m_L is local magnitude. Kaiser and Maloney (1997) proposed a similar equation but with the exponent $a^* = 0.5$ as a scaling law for support design in rockburst conditions. It is written in the form, $\mathrm{PGV} = C^* \cdot M^{a^*}/R$, where M is seismic moment expressed in GNm. The parameter C^* depends on the stress drop environment and, based on data form the Creighton Mine, $C^* = 0.1$ to 0.3 for events with stress drops less than 2.5 MPa and with $C^* = 0.5$ to 1.0 for higher stress drop events. However, it is recommended to adjust C^* to a specific data set at hand. Translating to the seismic potency domain gives $\mathrm{PGV} = C^* P^{1/2}/R$, where PGV is in m/s, P in m^3 and R in metres. Taking into account that $M = \mu P$ and $\mu = 30$ GPa, the parameter $C^* = (1.1$ to $1.64)$ for events with stress drop less than 2.5 MPa and $C^* = (2.74$ to $5.48)$ for higher stress drop events. The relation by McGarr et al. (1981) and by Kaiser and Maloney (1997) do not cater for attenuation and the near-source saturation.

✉ Aleksander J. Mendecki
Aleksander.Mendecki@IMSeismology.org

[1] Institute of Mine Seismology, 50 Huntingfield Avenue, Huntingfield, TAS 7055, Australia

McGarr and Fletcher (2005) developed GMPE for PGV and PGA based on the ground motion recorded on surface due to coal mining that generated events with $m \leq 2.2$, recorded at distances of 500 m to 10 km. Mendecki (2008) developed and compared the GMPE-PGV for four underground mines: two gold mines in South Africa, one in Australia and an iron ore mine in Sweden, all based on data recorded by three-component geophones installed in boreholes drilled from underground excavations. Atkinson (2015) used the NGA-West 2 database, containing horizontal component response spectra and PGV for events $3.0 \leq m \leq 6.0$ recorded on surface at distances up to 40 km to develop a GMPE that could be applied to induced seismicity. She concluded that ground motion from small-to-moderate induced events may be significantly larger than that predicted by most currently used GMPE.

The development of a GMPE for underground mines is in some respects different to that in earthquake seismology. There are very few accelerometers installed in mines, and in most cases, these are piezoelectric which are not strong ground motion instruments. They deliver high accelerations at high frequencies which are of little interest since at those frequencies there is not much ground velocity and even less ground deformation. Double integration of frequently noisy acceleration waveforms to displacement may also prove difficult. It is only recently that the semiconductor micro-electromechanical systems accelerometers, MEMS, are being used in mines.

Most mines install a mixture of 4.5 and 14 Hz geophones, and only recently have lower frequency sensors been deployed. For larger events, the higher frequency sensors filter lower frequencies and underestimate the ground motion parameters, and to some degree seismic potency and energy. Figure 1 shows the three-component velocity and integrated displacement waveforms of a $\log P = 2.86$ event recorded at a distance 2252 m from the source by a 1 Hz sensor and a 4.5 Hz sensor located next to each other in the same borehole. While the shape of the waveforms is similar, the 4.5 Hz sensor recorded significantly lower ground motions. PGV recorded by the 4.5 Hz sensors is 1.8 times lower, PGD is 3.5 times lower and the cumulative absolute displacement, CAD, is 2.3 times lower. The 14-Hz geophone would record even lower ground motion. For smaller events, the differences are less significant. It is therefore advisable to select

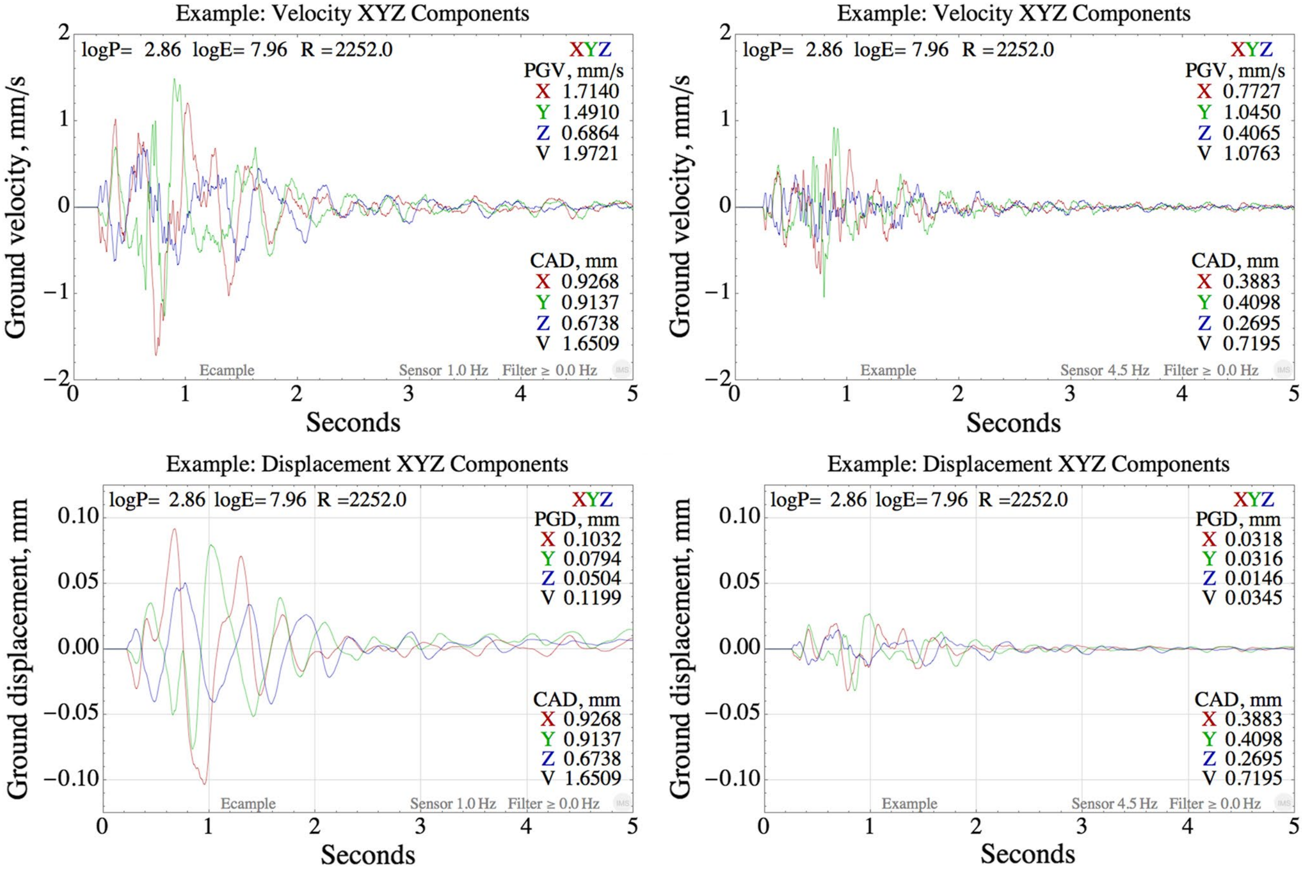
Example: Velocity XYZ Components

Example: Velocity XYZ Components

Example: Displacement XYZ Components

Example: Displacement XYZ Components

Fig. 1 Velocity and displacement waveforms of a $\log P = 2.86$ event recorded by 1 Hz (left column) and 4.5 Hz sensors (right column), located at the same site

PGV and CAD recorded by the same type of sensors while developing GMPE.

One can increase the signal range and the travel limits of geophones by overdamping. With normal damping of 0.7, the frequency response is flat to ground velocity above the natural frequency, f_n, and is proportional to f_n^2 below, which is caused by a double pole at that frequency, see Fig. 2. As the damping increases beyond 1, the poles separate, in such a way that the product of the pole frequencies remains constant. Between these poles, the velocity response is proportional to frequency, effectively making it flat to acceleration over this frequency range. For 4.5 Hz geophones, the maximum damping which can reasonably be achieved is 3.4 which means the acceleration response covers the frequency band from 0.7 to 30 Hz. In this configuration, the ADC voltage clip limit is raised by a factor of 5 to 0.5 m/s which is then slightly greater than the minimum internal displacement clip limit. The spectra need to be corrected for this response when calculating source parameters.

Traditionally, the most important ground motion parameter in underground mines was the instrumental PGV which is used for support design. Recently, Mendecki (2018) developed a GMPE for the cumulative absolute displacement, CAD, to be applied to monitor the consumption of the deformation capacity of support due to seismicity. The main interest for mines is the ground motion parameters at distances between 50 and 1000 m. Larger distances are of interest for surface structures, e.g. tailings dams or processing plants. For the sizes of events in mines, the PGV may drop by two orders of magnitude between 100 and 1000 m from the source. CAD decays more slowly with distance than PGV, mainly because of the increased duration of waveforms with distance due to scattering. Although we caution that the GMPE is not the best tool to estimate the near-source ground motion (Mendecki 2016), the geotechnical engineers, lacking other credible data, resort to such extrapolation when considering support specifications. Therefore, there is a need to constrain PGV at source to a physically acceptable level.

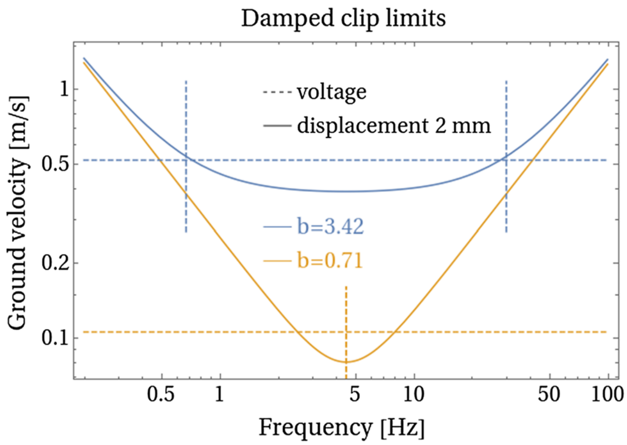

Fig. 2 The solid lines show the ground velocity required to produce 2-mm peak internal displacement in a 4.5 Hz geophone, for over-damped and maximally flat responses. The voltage limits for a typical audio ADC are marked by dashed horizontal lines, and pole frequencies by dashed vertical lines, after Mountfort and Mendecki (2019, in preparation)

Seismic systems in mines are designed to locate events and to estimate their source parameters. For this reason sensors are installed at least 6–10 m into boreholes to avoid the very site effects that amplify ground motion at the skin of excavations. Since the GMPE derived from such measurements certainly underestimate seismic load, mines conduct separate site amplification measurements at selected locations (Milev and Spottiswood 2005; Cichowicz 2008; Mendecki 2013, 2016, 2017; Dineva et al. 2016; Cuello and Mendecki 2017).

Unlike crustal seismology, in mines the bulk rock mass properties are changing due to rock extraction, specifically in caving and open stoping mines, and because new strong ground motion data are coming fast, the GMPE needs to be updated at least once a year. For the same reason, the GMPE developed for mines are characterised by large scatter. Moreover, many waveforms of larger events recorded at closer distances are displacement clipped or voltage saturated, which limits the number of observations in the near field. The distances to larger and intermediate size events are also uncertain because of the unknown orientation of sources and the complex nature of larger events.

Potency, magnitude and ground motion characteristics

Potency. Seismic potency of a single dislocation source is the product of an average slip and source area, $P = \bar{u}A$ (Ben-Menahem and Singh 1981). For a complex source, potency is the product of the source strain and the source volume, $P = \Delta\epsilon V$ (Madariaga 1979), where $\Delta\epsilon = \Delta\sigma/\mu$, $\Delta\sigma$ is an averaged stress drop and μ is the rigidity of the rock mass surrounding the source. Seismic moment $M = \mu P = \mu\Delta\epsilon V = \Delta\sigma V$.

Magnitude. Different mines use different magnitude scales that in many cases differ significantly and, in some cases, are not consistent over time. Therefore, here the common logarithm of seismic potency, $\log P$, is used as a measure of magnitude. $\log P$ is simple, appropriate for the range of sizes of seismic events recorded in mines and independent of rigidity, thus seismic hazard may be objectively compared between different mines and between different periods of time for the same mine. Table 1 translates selected $\log P$ to Hanks–Kanamori potency magnitude, $m_{\mathrm{HK}} = 2/3 \log P + 5.92$ (Hanks and Kanamori 1979), to the average source size $L = \sqrt[3]{3.5P/\Delta\epsilon}$ and the maximum source slip, $u_{\max} = 0.04865\sqrt[3]{P}$ (Eshelby 1957) assuming $\Delta\epsilon = 5 \times 10^{-4}$. The conversion from Hanks–Kanamori magnitude to $\log P$ is $\log P = 1.5m_{\mathrm{HK}} - 1.425$.

There are a number of parameters that measure the intensity of ground motion and its potential for damage. They are mainly based on measured maximum amplitude, energy and duration.

Peak ground characteristics. Ground motion characteristics include peak ground acceleration, PGA, velocity, PGV and displacement, PGD. The PGA is the most convenient for structural engineers, since the maximum force experienced by a rigid structure of mass m is $F_{\max} = m \cdot \mathrm{PGA}$. However, the PGA is a poor parameter for evaluating potential for damage. For example, a large PGA associated with a high frequency pulse may be absorbed by the inertia of the structure with little deformation, since $\mathrm{PGD} \propto \mathrm{PGA}/f^2$, where f is frequency. On the other hand, a more moderate acceleration associated with a long duration pulse of low frequency may result in significant deformation of structures. The PGV is less sensitive to the higher frequencies than PGA, can be measured directly and reliably and provides a better indication of damage potential.

Duration. Degradation of the stiffness and strength of rock is sensitive not only to the amplitude of ground motion but also to its duration and the associated number of load or stress reversals above the elastic regime. The *bracketed duration* measures the duration of the ground motion from the first to the last occurrence of amplitude exceeding a specified threshold. The *uniform duration* is defined as the sum of the time intervals during which the ground motion is greater than the threshold see Bommer et al. (2009) for more details. The *significant duration* defines ground motion duration as the length of the time interval between the accumulations of two specified levels of ground motion energy at the site. Trifunac and Brady (1975) defined duration as the length of the time interval between the accumulations of two specified levels of ground motion energy at the site, e.g. the amount of time in which the central 90% of the integral of the squared velocity or acceleration takes place, t_{90}.

Cumulative absolute velocity. $\mathrm{CAV} = \int_0^{t_d} |a(t)|\mathrm{d}t$, where $a(t)$ is the acceleration time history, has units of velocity, m/s (EPRI 1988). However, in mines, the utility of *CAV* is limited for two reasons. Mines mostly employ velocity transducers and the highest accelerations recorded by piezoelectric accelerometers are associated with very high frequencies, where there is little displacement and little or no damage potential.

Cumulative absolute displacement. CAD is defined as the integral of the absolute value of a velocity time series, $\mathrm{CAD} = \int_0^{t_d} |v(t)|\mathrm{d}t$, where $v(t)$ is the velocity time history, has units of displacement. CAD is the area under the absolute velocity time history and is more sensitive to lower frequency ground motion, i.e. to larger displacements. CAD is a better indicator of damage potential than a single point measurement PGV, and can be used to monitor the consumption of the deformation capacity of rock support due to seismicity. Figure 3 shows the three-component velocity and displacement waveforms of a $\log P = 2.12$ event at the Beaconsfield mine, BCF, recorded by 14 Hz sensors and X, Y and Z components of the absolute velocity that after integration deliver CAD. The PGV and CAD values are shown in the right margin of each graph.

Simple GMPE for PGV and CAD

Ground motion prediction equation. The ground motion prediction equation (GMPE) gives the expected value of a given ground motion parameter, GMP, e.g. peak ground velocity PGV or the cumulative absolute displacement CAD, as a function of seismic potency or energy or magnitude and distance. Its main utility in mines is to predict ground motion in the near and intermediate fields of larger events that may occur in the future, on the basis of observations of ground motion caused by smaller events.

We start with the following prediction equation for a ground motion parameter, GMP, caused by an event of potency P at distance R,

$$\overline{\mathrm{GMP}}\,(P,R) = c \cdot P^{c_P}\left(R + c_L \cdot P^{1/3}\right)^{-c_R}, \qquad (1)$$

where R should be measured orthogonal to the characteristic rupture plane, unless source sizes are small compared with the distances involved, c_P is the potency dependence parameter, c_R controls the geometrical attenuation rate and c is a free parameter (Esteva 1970; Campbell 1981). The term $c_L P^{1/3}$ is introduced to modulate ground motion at small

Table 1 Hanks–Kanamori m_{HK} for selected $\log P$, source displacement $u_{\max}$, and average source sizes, L

$\log P$	− 4.0	− 3.0	− 2.0	− 1.0	0.0	1.0	2.0	3.0	4.0
Hanks–Kanamori m_{HK}	− 1.72	− 1.05	− 0.38	0.28	0.95	1.62	2.28	2.95	3.62
Source size, L (m)	0.9	1.9	4.1	8.9	19.1	41.2	89	191	412
$u_{\max}$ (cm)	0.023	0.049	0.01	0.002	0.0487	1.05	2.26	4.86	10.48

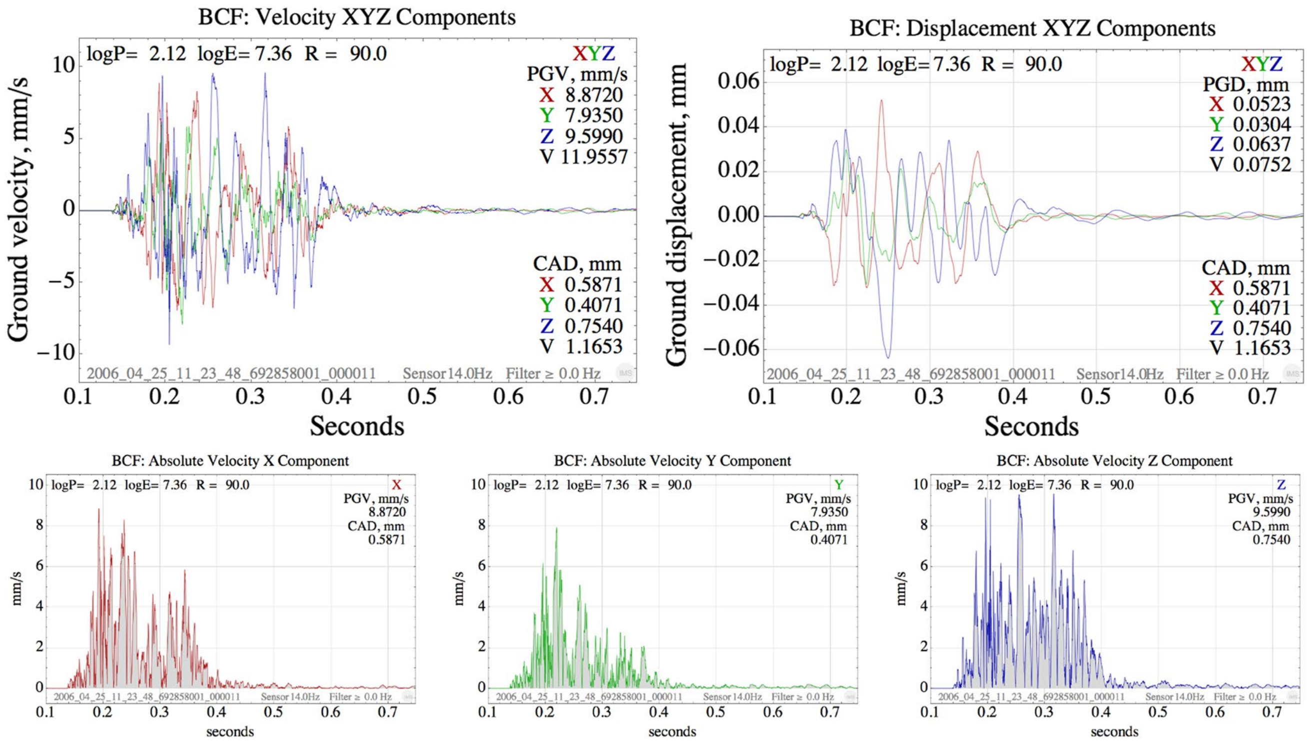

Fig. 3 Velocity waveforms and integrated displacements (top) of a $\log P = 2.12$ ($m2.36$) and energy $\log E = 7.36$ event recorded 90 m from source. X, Y and Z components of the absolute velocity that after integration delivers CAD (bottom). At the bottom of each graph there is the date and time of the event and information on sensor and filter applied to processing

distances, where geometric attenuation is small, and to saturate them at source.

The amplitudes of GMP predicted by the GMPE above are positively correlated with c_P and c and negatively with c_R and c_L. The term $c_P \log P$ is consistent with the definition of earthquake magnitude as a logarithmic measure of the amplitude of ground motion. The term $-c_R \log R$ is consistent with the geometric spreading of the seismic wave front as it propagates away from the source, and it also caters in part for the attenuation due to an elasticity and scattering. The term $c_L P^{1/3}$ is introduced to modulate ground motion at small distances, where geometric attenuation is small, and to saturate them at source.

The GMPE at source gives $\mathrm{GMP}(R=0) = c c_L^{-c_R} P^{c_P - c_R/3}$, i.e. at source $\log \mathrm{GMP}$ is a linear function of $\log P$. For $c_P = c_R/3$, the GMP at source is independent of event size, $\mathrm{GMP}(R=0) = c/c_L^{c_R}$. For $c_P > c_R/3$, it delivers larger GMP's at source for events with larger potencies. The case $c_P < c_R/3$ predicts that lower potencies generate higher GMP's at source than larger potencies which is rather unlikely. The case $c_R = 1.0$ with no attenuation and for $c_L = 0$, gives the familiar $\mathrm{GMP} = cP^{c_P}/R$ (McGarr et al. 1981; Kaiser and Maloney 1997).

From the GMPE given by Eq. (1), we can calculate $R = (cP^{c_P}/\mathrm{GMP})^{1/c_R} - c_L P^{1/3}$, i.e. the distance over which seismic source with potency P generates the ground motion parameter $\geq \mathrm{GMP}$. We can also calculate the minimum potency, or $\log P$ that delivers a given level of GMP at a distance R. The case $c_P = c_R/3$ gives $P(R) = R^3/\left[(c/\mathrm{GMP})^{1/c_R} - c_L\right]^3$, but in the general case the solution must be obtained numerically.

There are many forms of GMPE, most of them developed for predicting surface ground motion resulting from earthquakes, see Douglas (2018) for a review. Some of them are complex and have more than 5 or even 10 coefficients to cater for magnitude, distance, site effects, source mechanisms (normal, strike slip or reverse faulting) and, in some cases even directivity. However, more complex models are more susceptible to the danger of overfitting, i.e. modelling spurious details of the data rather than the data generating process. The inversion procedure for parameters in the GMPE equation should therefore be carried out in two stages to decouple potentially correlated variables, in this case c_P and c_R (Joyner and Boore 1993, 1994) or Abrahamson and Youngs (1992). However, such a process can only alleviate the problem and the real physical meaning of these parameters may be lost, a point well made by McGarr and Fletcher (2005).

Simple GMPE-PGV. Equation (1) for PGV is $\overline{\mathrm{PGV}}(P,R)=cP^{c_P}\left(R+c_L\cdot P^{1/3}\right)^{-c_R}$, which at source, for $R=0$, gives $\overline{\mathrm{PGV}}(P,R=0)=cc_L^{-c_R}P^{c_P-c_R/3}$.

Ambraseys (1969) postulated that the near-source PGV of earthquakes should be limited by the strength or maximum stresses of the rocks. Brune (1970) showed that if a stress pulse is applied instantaneously over the whole source, the initial ground velocity is $\mathrm{PGV}_0=\sigma_{\mathrm{eff}}v_S/\mu$, where σ_{eff} is the applied effective stress available to accelerate the two sides of the source, v_S is the S-wave velocity and μ is the rigidity of the rock surrounding the source. The ratio $\epsilon_{\mathrm{eff}}=\sigma_{\mathrm{eff}}/\mu$ is the effective strain on both sides of a slip type source, so we can write $\mathrm{PGV}_0=v_S\epsilon_{\mathrm{eff}}$.

For a finite circular source of radius r with instantaneous stress release, the effects of the edges of the crack will abate the ground velocity with time. For the simple taper given by Brune (1970), integration of $v_S\epsilon_{\mathrm{eff}}\exp\left(-v_St/r\right)$ over the process time, r/v_S (Kanamori 1972; Mendecki 2016, p. 59), gives the average ground velocity at source, which is adopted in this paper,

$$\mathrm{PGV}_0=0.63v_S\epsilon_{\mathrm{eff}}. \tag{2}$$

The near-source ground velocity, for a finite source and finite rupture velocity, for different source models are quoted in Table 2.

For $\sigma_{\mathrm{eff}}=25$ MPa, $\rho=2700$ kg/m^3, $v_S=3300$ m/s, assuming the rupture velocity $v_r=0.75v_S$, the estimates of the near-source ground motion would vary between 1.0 and 2.1 m/s. In general, the faster the rupture the faster the slip and the higher the near field ground motion.

The effective stress cannot be measured directly but one can assume that it is equal to the bulk shear strength of the rock within the volume of interest, which for hard rock varies between 10 MPa, for an inhomogeneous rock to 100 MPa for an intact homogeneous hard rock. This, assuming the rigidity of the order of 10 GPa, translates to $10^{-4}\le\epsilon_{\mathrm{eff}}\le10^{-3}$. A more practical proxy for σ_{eff} or ϵ_{eff} is the upper limit of the static stress drop, $\Delta\sigma$, or strain change, $\Delta\epsilon$, derived from waveforms recorded in the area of interest.

Now, from $\overline{\mathrm{PGV}}(P,R=0)=0.63v_S\Delta\epsilon=cc_L^{-c_R}P^{c_P-c_R/3}$, we can derive $c=0.63v_S\Delta\epsilon c_L^{c_R}P^{-c_P+c_R/3}$. For $c_P=c_R/3$, parameter $c=0.63v_S\Delta\epsilon c_L^{c_R}$ is independent of potency P and the GMPE for $\overline{\mathrm{PGV}}$ can be written as,

$$\overline{\mathrm{PGV}}(P,R)=0.63v_S\Delta\epsilon\left(\frac{c_LP^{1/3}}{R+c_LP^{1/3}}\right)^{c_R}. \tag{3}$$

While this expression has 4 parameters: v_S, $\Delta\epsilon$, c_L and c_R, two of them, v_S, $\Delta\epsilon$, are constrained by the type of rock and can be assumed and the other two, c_L and c_R need to be inverted from data.

Simple GMPE-CAD. Equation (1) for CAD is $\overline{CAD}(P,R)=c\cdot P^{c_P}\left(R+c_L\cdot P^{1/3}\right)^{-c_R}$. For a circular crack with a uniform strain change $\Delta\epsilon$ over the source surface, the displacement profile is given by $u(x)=24\Delta\epsilon\sqrt{r^2-x^2}/(7\pi)$, where x is the radial distance from the centre of the crack and r is the radius of the crack (Eshelby 1957). The maximum displacement is in the middle of the crack, i.e. at $x=0$, therefore $u_{\max}=24r\Delta\epsilon/(7\pi)$. Integration over the crack length in polar coordinates, (x,φ), gives the mean displacement at source $\bar{u}=24\Delta\epsilon/\left(7\pi^2r^2\right)\cdot\int_0^r x\mathrm{d}x\int_0^{2\pi}\mathrm{d}\varphi\sqrt{r^2-x^2}$, which translates to $\bar{u}=48\Delta\epsilon/\left(7\pi r^2\right)\cdot\int_0^r\sqrt{r^2-x^2}x\mathrm{d}x$, and finally $\bar{u}=16r\Delta\epsilon/(7\pi)$. This gives seismic potency, $P=\bar{u}\pi r^2=(16/7)r^3\Delta\epsilon$, the source radius $r=(7/16)^{1/3}(P/\Delta\epsilon)^{1/3}$ and,

$$u_{\max}=1.5\bar{u}=q_0\Delta\epsilon^{2/3}P^{1/3}, \tag{4}$$

where the constant $q_0=(24/7\pi)(7/16)^{1/3}=0.828494$. For the average strain change at source $\Delta\epsilon=5\times10^{-4}$, the maximum displacement $u_{\max}=0.004865\sqrt[3]{P}$, which is not far from $u_{\max}=0.0046\sqrt[3]{P}$ given by McGarr and Fletcher (2003).

If we assume that the cumulative absolute displacement at the source is equal to the maximum source displacement, i.e. $\mathrm{CAD}_0=u_{\max}=q_0\Delta^{2/3}P^{1/3}$, then at source, $\overline{\mathrm{CAD}}(P,R=0)=cc_L^{-c_R}P^{c_P-c_R/3}=\mathrm{CAD}_0=q_0\Delta\epsilon^{2/3}P^{1/3}$.For $c_P=\left(1+c_R\right)/3$, parameter $c=q_0\Delta\epsilon^{2/3}c_L^{c_R}$ is independent of potency P and, after simple algebra the GMPE for $\overline{\mathrm{CAD}}$ can be written as

$$\overline{\mathrm{CAD}}(P,R)=q_0\Delta\epsilon^{2/3}P^{1/3}\left(\frac{c_LP^{1/3}}{R+c_LP^{1/3}}\right)^{c_R}. \tag{5}$$

Table 2 Models of near-source ground velocity, v, as a function of rupture velocity according to Burridge (1969)$^{(1)}$, Ida (1973)$^{(2)}$ and McGarr and Fletcher (2001)$^{(3)}$, where $f\left(v_r\right)$ is a monotonic function that ranges from 0.11 to 0.4 as rupture velocity increases from $0.6v_S$ to $0.9v_S$

Model	$\langle v\rangle$	for $v_r=0.75v_S$
Bilateral rupture$^{(1)}$	$\langle v\rangle=\sigma_{\mathrm{eff}}/\left[\rho v_S\left(1+v_S/v_r\right)\right]$	$\langle v\rangle=0.43\sigma_{\mathrm{eff}}/\left(\rho v_S\right)$
Dynamic cohesive rupture$^{(2)}$	$\langle v\rangle=\sigma_{\mathrm{eff}}v_r/\left(\rho v_S^2\right)$	$\langle v\rangle=0.75\sigma_{\mathrm{eff}}/\left(\rho v_S\right)$
Dynamic rupture scaling$^{(3)}$	$\langle v\rangle=0.8\sigma_{\mathrm{eff}}/\left[\rho v_Sf\left(v_r\right)\right]$	$\langle v\rangle=0.36\sigma_{\mathrm{eff}}/\left(\rho v_S\right)$

Equation (5) has three parameters, $\Delta\epsilon$, c_L and c_R and since $\Delta\epsilon$ is constrained by the type of rock and can be assumed, the other two, c_L and c_R need to be inverted from data.

Example

We analysed the ground motion data of selected seismic events recorded at BCF mine from 03 August 2005 to 25 April 2006, i.e. 265 days. Figure 4 shows in plan (left) and in section (right) seismic sensor sites and all seismic events with $\log P \geq -1.0 (m \geq 0.28)$ selected for analysis.

There are 448 observations of PGV and 429 of CAD derived from 51 events of the potency range $-1.0 \leq \log P \leq 2.12$, recorded at distances between 35 and 591 m from source. The minimum PGV is 0.002 cm/s and the maximum 3.2 cm/s. The minimum CAD is 0.0015 cm and the maximum 0.1656 cm.

Figure 5 shows $\log P$ versus PGV and $\log P$ versus CAD of the final data set accepted for fitting.

Figure 6 shows $\log \Delta\epsilon$ versus $\log P$ (left) and $\log f_0$ versus $\log P$, where f_0 is an average P- and S-wave corner frequency, for a constant strain change at source (right) of events at BCF accepted for fitting. The upper limit of strain change at source is of the order of 5×10^{-4}.

GMPE-PGV. Assuming $v_S = 3250$ m/s and $\Delta\epsilon = 5 \times 10^{-4}$, the GMPE for PGV is obtained as,

$$\overline{\mathrm{PGV}}(P,R) = 102.375\left(\frac{2.8027P^{1/3}}{R+2.8027P^{1/3}}\right)^{1.6381}, \qquad (6)$$

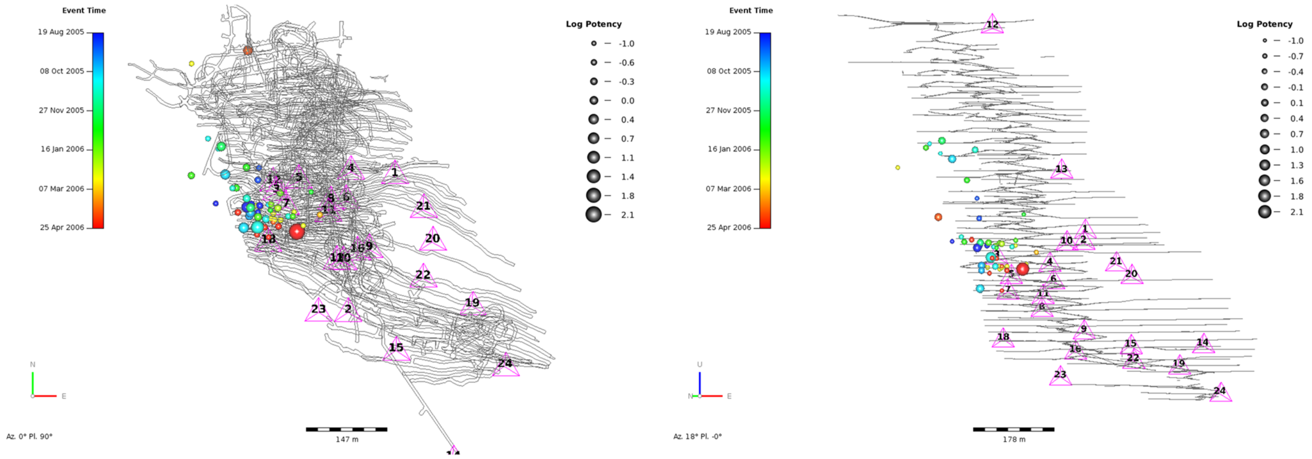

Fig. 4 Seismic events, sites and characteristics of the final data sets for fitting at BCF mine

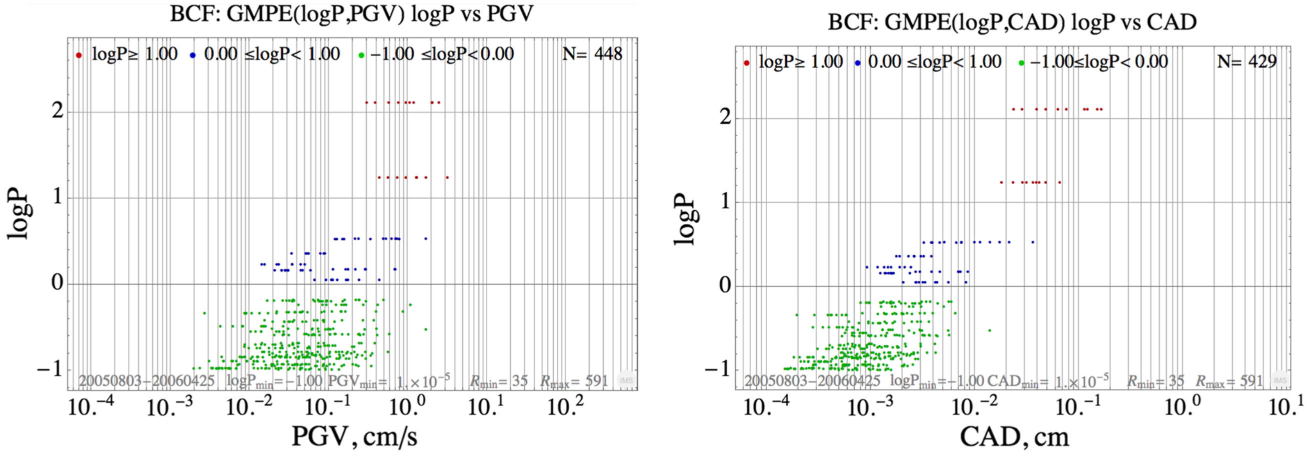

Fig. 5 $\log P$ versus PGV (left) and $\log P$ versus CAD (right) of the final data sets accepted for fitting the simple GMPE

where PGV is in cm/s, P in m^3 and R in metres. Inversion was done in the $\log \mathrm{PGV}$ domain with weighting $w_j = \left(\log \mathrm{PGV}_j - \log \mathrm{PGV}_{\mathrm{min}}\right) / \left(\log \mathrm{PGV}_{\mathrm{max}} - \log \mathrm{PGV}_{\mathrm{min}}\right)$ The standard errors of $c_R = \pm 0.0443$ and $c_L = \pm 0.3343$ and the standard deviation $\sigma_{\log \mathrm{PGV}} = 0.1753$. If we assume 5% uncertainty in v_S and 25% uncertainty in $\Delta\epsilon$, then the expected peak ground velocity at source is $\mathrm{PGV}_0 = 102.375$ cm/s ± 30%, i.e. it would vary between $72.94 \leq \mathrm{PGV}_0 \leq 134.37$ cm/s, irrespective of magnitude. Figure 7 left shows the data selected for fitting with dots coloured by size range and the GMPE fit plotted in the middle of each potency range with grey bands indicating 95% confidence limits. The predicted PGV's for larger potency events are shown in Fig. 7 right.

Figure 8 shows the results of residual analysis: on the left log (Obs/Pred) as a function of distance and, right, log (Pred) versus log (Obs).

GMPE-CAD. Assuming $\Delta\epsilon = 5 \times 10^{-4}$, the GMPE for CAD is obtained as,

$$\overline{\mathrm{CAD}}(P, R) = 0.63 \cdot P^{1/3} \left(\frac{1.3805 P^{1/3}}{R + 1.3805 P^{1/3}} \right)^{1.068}, \qquad (7)$$

where CAD is in cm, P in m^3 and R in metres. The standard errors of $c_R = \pm 0.0294$ and $c_L = \pm 0.1969$ and the standard deviation $\sigma_{\log \mathrm{CAD}} = 0.167$. If, in addition, we assume 25% uncertainty in $\Delta\epsilon$, the expected maximum seismic deformation at source for $\log P = 3.0$ would vary between 4.31 and 6.06 cm. Figure 9 left shows data selected for fitting with dots coloured by $\log P$ range and the GMPE fit plotted in the middle of each potency range with grey bands indicating 95% confidence limits. The predicted CAD's for larger potency events are shown in Fig. 9 right.

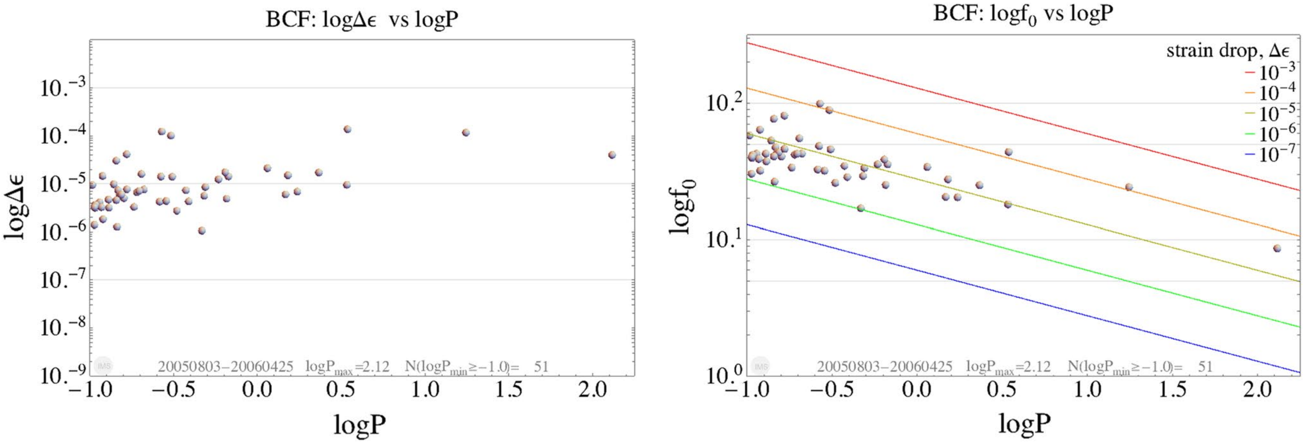

Fig. 6 $\log \Delta\epsilon$ versus $\log P$ (left) and $\log f_0$ versus $\log P$ (right) of events accepted for fitting

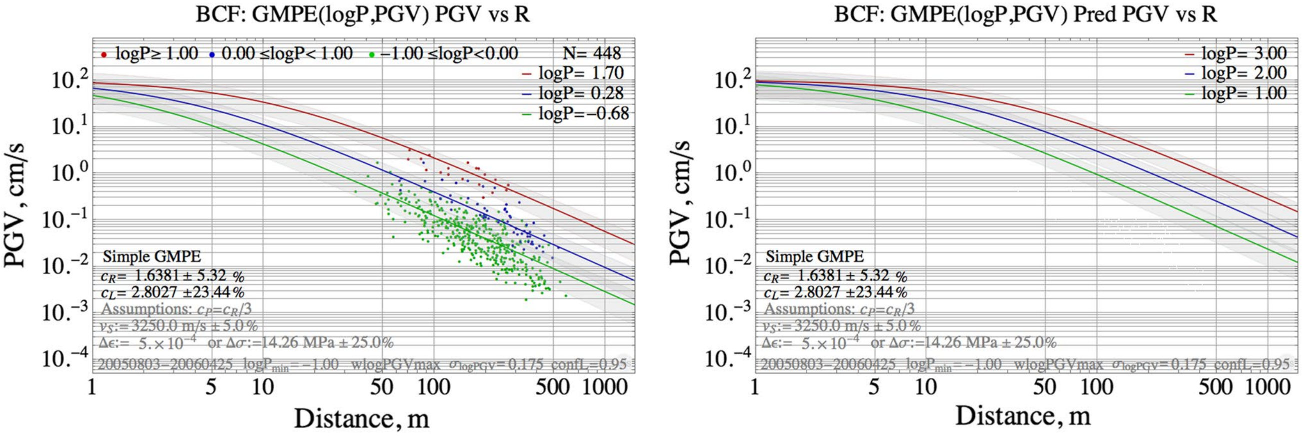

Fig. 7 The GMPE-PGV fit and data (left) and predictions for larger potencies (right)

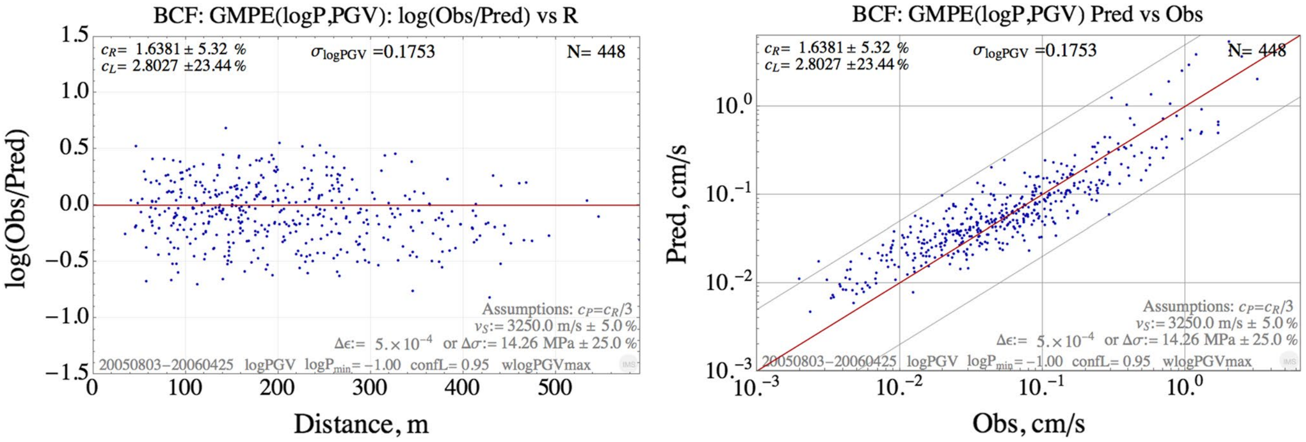

Fig. 8 $\log\left(\mathrm{PGV}_{\text{obs}}/\mathrm{PGV}_{\text{pred}}\right)$ versus distance (left) and $\log \mathrm{PGV}_{\text{pred}}$ versus $\log \mathrm{PGV}_{\text{obs}}$ (right)

Figure 10 shows the results of residual analysis: on the left log (Obs/Pred) as a function of distance and, on the right, log (Pred) versus log (Obs).

Applications of GMPE for underground mines

The basic outcome of ground motion hazard analysis for a given site is a seismic hazard curve that shows the annual rate, or probability, at which a specific ground motion level will be exceeded. This is outside the scope of this paper. It is expected that CAD that includes the peak and the duration of ground motion may be a better indicator of damage potential than the PGV alone, being a single measurement over the whole waveform. Below, we present two simple applications: the potential damage inspection plot and the cumulative CAD plot.

From the simple GMPE-PGV given by Eq. (3), we can calculate the distance, R, over which a seismic source with potency P generates the velocity of ground motion ≥ PGV,

$$R = c_L P^{1/3}\left[\left(\mathrm{PGV}_0/\mathrm{PGV}\right)^{1/c_R} - 1\right]. \tag{8}$$

We can also calculate the minimum potency, or $\log P$ that delivers a given level of PGV as a function of distance,

$$P(R) = \left(R/c_L\right)^3\left[\left(\mathrm{PGV}_0/\mathrm{PGV}\right)^{1/c_R} - 1\right]^{-3}. \tag{9}$$

Now, we can plot $\log P$ versus distance R of seismic events, on the background of envelopes of a minimum $\log P$ that delivers a given level of PGV as a function of distance, for a number of strategic sites. Figure 11 left shows the $\log P \geq -2.0$ versus distance of 277 events at the BCF mine that occurred between 02 August 2005 and 25 April 2006 and the thresholds of ground motion, PGV_x, set as 1, 2.5, 5 and 10 cm/s. The envelopes of a minimum $\log P$ stop where,

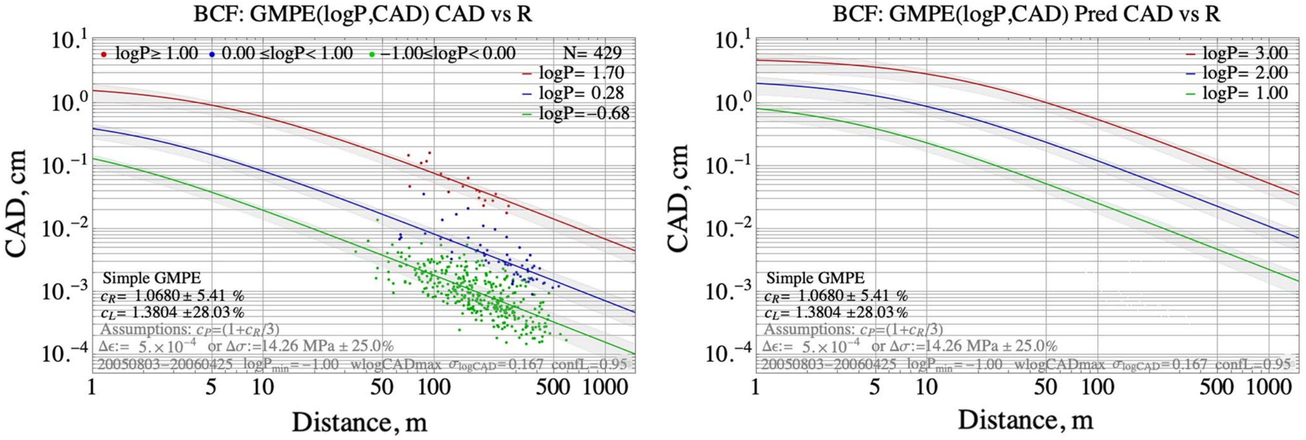

Fig. 9 The GMPE-CAD fit and data (left) and predictions for larger potencies (right)

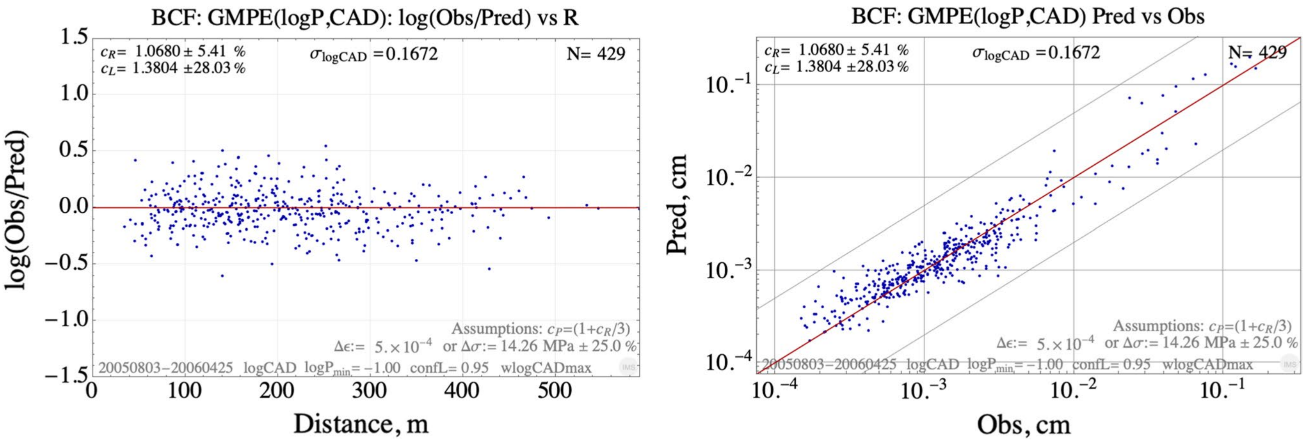

Fig. 10 $\log\left(\text{CAD}_{\text{obs}}/\text{CAD}_{\text{pred}}\right)$ versus distance (left) and $\log \text{CAD}_{\text{pred}}$ versus $\log \text{CAD}_{\text{obs}}$ (right)

according to the GMPE, a $\log P_{\max}$ event cannot deliver a given PGV beyond that distance. We assumed that for BCF mine $\log P_{\max} = 3.06(m_{\text{HK}} = 2.99)$. A seismic event that crosses the calibrated envelope for a given site should trigger damage inspection. If the threshold for the three test sites is set at 1 cm/s in solid rock then over the 265 days period, there would be 6 damage inspections: four to Site3, one to Site4 and one to Site11. Note that the developed GMPE does not take into account site effects, i.e. the amplification of ground motion at the skin of excavations, therefore all these estimates are in solid rock.

Another useful application is monitoring the consumption of the deformation capacity of the support due to seismicity.

Figure 11 right shows the cumulative seismic deformation, CAD, due to 277 seismic events with $\log P \geq -2.0$ at the same 3 sites over the same period as before. The red dots indicate events with seismic strain, $\text{PGV}/v_S \geq 10^{-6}$, which is considered inelastic for hard rock. It shows that all three sites were subjected to a relatively low level of seismic deformation. The highest level of seismic deformation in the intact rock over that time was recorded at Site3. Note that all the observed CAD were recorded by sensors in boreholes, therefore, they do not take into account the amplifying effect of the fracture zone close to excavations and the reaction of the support.

Acknowledgements I thank Peter Mountfort for discussion on seismic sensor characteristics and for assistance with testing the quality of data. Peter Hills assisted in data collection from the BCF mine. I would like to thank Peter Kaiser for motivating me to develop GMPE for CAD. I would also like to thank the anonymous reviewer whose comments and recommendations improved the text.

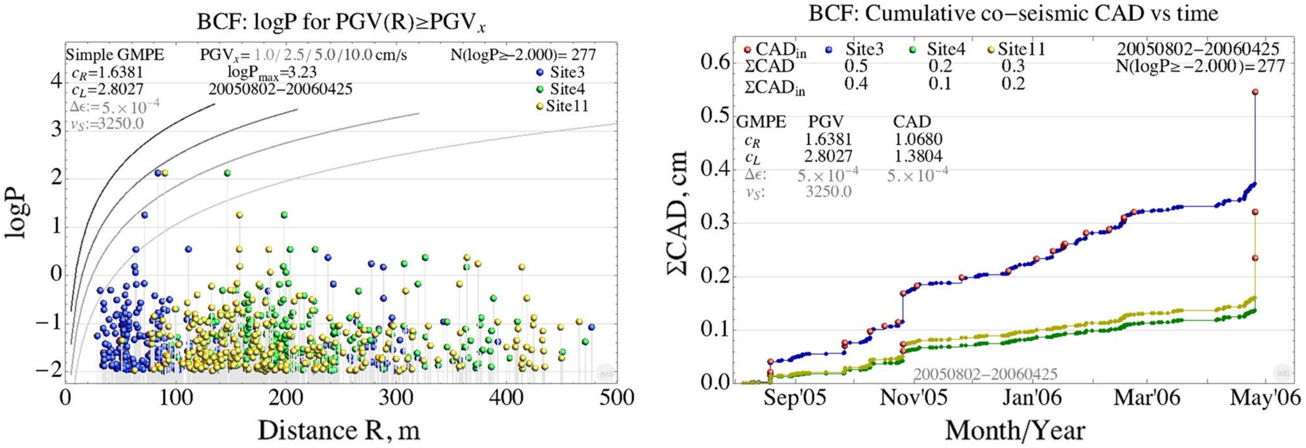

Fig. 11 Left. $\log P$ of 277 seismic events that occurred between 02 August 2005 and 25 April 2006 versus distances to three sites at the BCF mine. The grey envelopes indicate a minimum $\log P$, that delivers $1.0 \leq \text{PGV}_x \leq 10.0$ cm/s as a function of distance. Right. Estimates of cumulative co-seismic displacement at the same sites over the same period of time

References

Abrahamson NA, Youngs RR (1992) A stable algorithm for regression analyses using the random effects model. Bull Seismol Soc Am 82(1):505–510

Ambraseys NN (1969) Maximum intensity of ground movements caused by faulting. In: Proceedings of the 4th world conference on earthquake engineering, Santiago, A2, pp 154–171

Atkinson GM (2015) Ground motion prediction equation for small to moderate events at short hypocentral distances, with application to induced seismicity hazards. Bull Seismol Soc Am 105(2A):981–992. https://doi.org/10.1785/0120140142

Ben-Menahem A, Singh SJ (1981) Seismic waves and sources. Springer, New York

Bommer JJ, Stafford PJ, Alarcon JE (2009) Empirical equations for the prediction of the significant, bracketed, and uniform duration of earthquake ground motion. Bull Seismol Soc Am 99(6):3217–3233. https://doi.org/10.1785/0120080298

Brune JN (1970) Tectonic stress and the spectra of seismic shear waves from earthquakes. J Geophys Res 75(26):4997–5009

Burridge R (1969) The numerical solution of certain integral equations with non-integrable kernels arising in the theory of crack propagation and elastic wave diffraction. Philos Trans R Soc Lond A 265:353–381

Campbell KW (1981) Near-source attenuation of peak horizontal acceleration. Bull Seismol Soc Am 71(6):2039–2070

Cichowicz A (2008) Near-field pulse-type motion of small events in deep gold mines: observations, response spectra and drift spectra. In: 14th World conference on earthquake engineering, Beijing, China

Cuello D, Mendecki AJ (2017) Ground motion amplification at the skin of excavations. In: Vallejos J (ed) Proceedings 9th international symposium on rockbursts and seismicity in mines, Santiago, Chile

Dineva S, Mihaylov D, Hansen-Haug J, Nystrom A, Woldemedhin B (2016) Local seismic systems for study of the effect of seismic waveson rock mass and ground support in Swedish underground mines Zinkgruvan, Garpenberg, Kiruna. Ground Support 2016. Lulea, Sweden, pp 1–11

Douglas J (2018) Ground motion prediction equations 1964–2018. Review, University of Strathclyde, Glasgow

EPRI (1988) A criterion for determining exceedance of the operating basis earthquake. Technical report EPRI NP-5930, Electrical Power Research Institute, Palo Alto, California

Eshelby JD (1957) The determination of the elastic field of an ellipsoidal inclusion and related problems. Proc R Soc Lond Ser A Math Phys Sci 241(1226):376–396

Esteva L (1970) Seismic risk and seismic design decisions. In: Hansen RJ (ed) Seismic risk and seismic design criteria for nuclear power plants. MIT Press, Cambridge, pp 142–182

Hanks TC, Kanamori H (1979) A moment magnitude scale. J Geophys Res 84:2348–2350

Ida Y (1973) The maximum acceleration of seismic ground motion. Bull Seismol Soc Am 63(3):959–968

Joyner WB, Boore DM (1993) Methods for regression analysis of strong motion data. Bull Seismol Soc Am 83(2):469–487

Joyner WB, Boore DM (1994) Methods for regression analysis of strong motion data: errata. Bull Seismol Soc America 84(3):955–956

Kaiser PK, Maloney SM (1997) Scaling laws for the design of rock support. Pure Appl Geophys 150(3–4):415–434

Kanamori H (1972) Determination of effective tectonic stress associated with earthquake faulting. The Tottori earthquake of 1943. Phys Earth Planet Inter 5:426–434

Madariaga R (1979) On the relation between seismic moment and stress drop in the presence of stress and strength heterogeneity. J Geophys Res 84(B5):2243–2250

McGarr A, Fletcher JB (2001) A method for mapping apparent stress and energy radiation applied to the 1994 Northridge earthquake fault zone: revisited. Geophys Res Lett 28(18):3529–3532. https://doi.org/10.1029/2001GL013094

McGarr A, Fletcher JB (2003) Maximum slip in earthquake fault zones, apparent stress, and stick-slip friction. Bull Seismol Soc Am 93(6):2355–2362

McGarr A, Fletcher JB (2005) Development of ground-motion prediction equations relevant to shallow mining induced seismicity in the Trail Mountain area. Bull Seismol Soc Am 95(1):31–47. https://doi.org/10.1785/0120040046

McGarr A, Green RWE, Spottiswoode SM (1981) Strong ground motion of mine tremors: some implications for near-source ground motion parameters. Bull Seismol Soc Am 71(1):295–319

Mendecki AJ (2008) Forecasting seismic hazard in mines. In: Potvin Y, Carter J, Diskin A, Jeffrey R (eds) Proceedings 1st Southern Hemisphere international rock mechanics symposium. Australian Centre for Geomechanics, Perth, pp 55–69

Mendecki AJ (2013) Characteristics of seismic hazard in mines: keynote lecture. In: Malovichko A, Malovichko DA (eds) Proceedings 8th international symposium on rockbursts and seismicity in mines. St Petersburg, Moscow, pp 275–292. ISBN 978-5-903258-28-4

Mendecki AJ (2016) Mine seismology reference book: seismic hazard, 1st edn. Institute of Mine Seismology, St. Petersburg. ISBN 978-0-9942943-0-2

Mendecki AJ (2017) Mapping seismic ground motion hazard: keynote lecture. In: Vallejos J (ed) Proceedings 9th international symposium on rockbursts and seismicity in mines, Santiago, Chile

Mendecki AJ (2018) Ground motion prediction equations for DMLZ. Technical PTFI-REP-GMPE-201801-AJMv1, Institute of Mine Seismology

Milev AM, Spottiswood SM (2005) Strong ground motion and site response in deep South African mines. J S Afr Inst Min Metall 105:1–10

Trifunac MD, Brady AG (1975) A study on the duration of strong earthquake ground motion. Bull Seismol Soc Am 65(3):581–626

Acta Geophysica (2019) 67:849–861
https://doi.org/10.1007/s11600-019-00295-1

ORIGINAL PAPER - HYDROLOGY

Modelling spatial variation of extreme precipitation over Ho Chi Minh City under nonstationary condition

Le Thi Hoa Binh[1,2] · **V. Agilan**[3] · **N. V. Umamahesh**[1] · **E. V. Rathnam**[1]

Received: 24 August 2018 / Accepted: 25 April 2019 / Published online: 2 May 2019

Abstract

Understanding the magnitude and spatial variation of extreme rainfall events are required for decision making and adaptation strategies for flood risk. In Ho Chi Minh City (HCMC), heavy rainfall, which is considered as a main cause of floods, witnessed an increase in frequency and magnitude in last few decades. Although nonstationarity in extreme rainfall has been proved in many places of the world, research into nonstationarity feature in extreme rainfall in HCMC has not been paid attention thoroughly. In this study, the spatial variation of extreme precipitation over Ho Chi Minh City is modelled under nonstationary condition. The generalized extreme value (GEV) distribution with location made a nonlinear function of time is applied to annual maximum daily rainfall. The study results show that the nonstationary GEV model is found to be superior in capturing extreme precipitation events when compared to the stationary GEV model. The extreme rainfall estimates under the stationary condition are lower than those under the nonstationary condition in most stations. Besides, the spatial variation of extreme rainfall under nonstationary condition shows a significant difference in extreme estimates between the periods of 1980–1984 and 2010–2014 in study area.

Keywords Ho Chi Minh City · Extreme rainfall · Nonlinear · Nonstationary · Spatial variation · GEV

Introduction

In recent years, changes in rainfall characteristics and hydrological cycle have been reported for many places of the world, especially increasing in rainfall extremes, due to the change in global climate related to human activities (Berg et al. 2013; Groisman et al. 2005; Milly et al. 2008; Trenberth 2011). These changes propose that the assumption of stationarity in hydro-meteorological time series may no longer suitable (Khaliq et al. 2006; Sugahara et al. 2009). As such, the concept of nonstationary extreme value analysis has been well developed and used in modelling the behavior of rainfall extremes in many regions as Taiwan, China, West Central Florida, South Korea and Greece and so on (Chu et al. 2013; Feng et al. 2007; Kioutsioukis et al. 2010; Nadarajah 2005; Park et al. 2011; Westra et al. 2013).

In other hand, the previous studies have reported that extreme rainfall is influenced by the physical processes such as the El Nino-Southern Oscillation (ENSO), the North Atlantic Oscillation (NAO), the Indian Ocean Dipole (IOD) or the Pacific Decadal Oscillation (PDO) (Agilan and Umamahesh 2015; Cai and Rensch 2012; Kenyon and Hegerl 2010; Mondal and Mujumdar 2015;

Electronic supplementary material The online version of this article (https://doi.org/10.1007/s11600-019-00295-1) contains supplementary material, which is available to authorized users.

✉ N. V. Umamahesh
mahesh@nitw.ac.in

Le Thi Hoa Binh
binhlth@tlu.edu.vn

V. Agilan
agilan@nitc.ac.in

E. V. Rathnam
evr@nitw.ac.in

[1] Department of Civil Engineering, National Institute of Technology, Warangal 506004, India

[2] Division of Water Resources and Environment, Thuyloi University, Ho Chi Minh 700000, Vietnam

[3] Department of Civil Engineering, National Institute of Technology, Calicut 673601, India

Villafuerte et al. 2015). That is a reason why the large-scale climate variables have been commonly used in frequency analysis as the factors causing nonstationarity in extreme rainfall. For example, Villafuerte et al. (2015) found that ENSO has significant impact on the changes in extreme rainfall in the Philippines. Mondal and Mujumdar (2015) reported that the global warming, local temperature changes and ENSO play a significant role in causing nonstationarity in rainfall extremes over India. Hence, the physical processes associated with extreme rainfall have a periodicity component in it (Agilan and Umamahesh 2016a). Introducing periodicity feature in extreme rainfall frequency analysis is therefore needed, which could significantly impact on the chosen design values.

Most of the studies in modelling extreme rainfall under nonstationary condition, the linear trend was commonly adopted to express the function of parameters of chosen distribution. In particular, Wi et al. (2016) constructed nonstationary generalized extreme value (GEV) distribution and generalized Pareto distribution (GPD) models by introducing linear trend in location and scale parameters. Villafuerte et al. (2015) investigated the changes in extreme rainfall in the Philippines using GEV distribution with linear form of location parameter. Cheng and AghaKouchak (2014) used a nonstationary GEV distribution with linear trend in location parameter to develop the rainfall intensity–duration–frequency curves. However, Agilan and Umamahesh (2016a) recommended that using time covariate based linear form could lead to increase the bias of nonstationary model. Um et al. (2017) suggested that nonlinear function could be a useful option when applied to the nonstationary frequency analysis of extreme rainfall. And the use of flexible nonlinear forms to model nonstationarity in extreme rainfall could be found in many researches (Agilan and Umamahesh 2016b; Panagoulia et al. 2014; Sugahara et al. 2009; Yilmaz et al. 2016). Thus, among many nonlinear forms that were established and used in the past, choosing an appropriate form for modelling nonstationary extreme rainfall mimicking all involved physical processes is essential.

The main objective of this study is to model the spatial variation of extreme rainfall over Ho Chi Minh City, a flood-prone city in the South of Vietnam, using appropriate nonstationary GEV model. In order to address this objective, the observed data is firstly checked for the possible trend by using the Mann–Kendall test. The nonlinear trend in the extreme rainfall time series is developed by the use of multi-objective generic algorithm. The best model is chosen by the Akaike Information Criterion and the likelihood ratio test. Finally, the best nonstationary model is used to investigate the spatial variation of extreme rainfall corresponding to different return periods.

Study area and data

Background of Ho Chi Minh City (HCMC)

HCMC is located in the South of Vietnam and belongs to a transitional region between the southeastern and Mekong River delta regions. This city is considered as a typical example of a vulnerable coastal city. Much of HCMC is located in low-lying lands of the Saigon-Dongnai River basin that are prone to frequent flooding (Lasage et al. 2014; World Bank 2010). Total 154 of the city's 322 communes and wards have a history of regular flooding, affecting 12 percent of the HCMC population (around 971,000 people) (ADB 2010). HCMC's climate is governed by monsoon regime and divided into rainy and dry season. Ninety percent of annual rainfall occurs in rainy season from May to October (ADB 2010). The heavy rainfall in a short period of time is considered as a main cause of floods in rainy season (ADB 2010; Le Vo 2007).

In last few decades, beside huge challenges related to fast-growing population, urbanization and industrialization (Le Vo 2007; World Bank 2010), HCMC also has to cope with climate problems such as increases in frequency and magnitude of extreme rainfall events (ADB 2010). In addition, the impacts of ENSO and PDO on rainfall regimes in Vietnam has been investigated by recent studies (Chan and Zhou 2005; Chen et al. 2013; Gobin et al. 2015; Nguyen et al. 2014; Yen et al. 2011), which partly influence the extreme rainfall in HCMC. Since extreme rainfall continuously result in severe floods and inundations, it is necessary to detect the trends and develop the spatial variation of extreme rainfall over the entire HCMC, which can be used for the city government in urban planning or infrastructure design purpose.

Data

In this study, the daily rainfall data are carefully selected from the National Hydro–Meteorological Service (NHMS) of Vietnam. The stations which had numerous days of missing data in a year are excluded from this study. Only rain gauges with longer rainfall records are selected for this study because the length of data records has a significant influence on the accuracy of parameter estimation of the extreme value distribution (Yilmaz et al. 2016). In particular, the dataset contains 8 stations within HCMC and10 stations outside HCMC (i.e. Binh Duong, Dong Nai, Ba Ria Vung Tau, Long An and Tay Ninh provinces) that have long-term precipitation observations and spread over the entire study area (Fig. 1) is used. The average record length is 40 years. The details of selected stations, including name, location and the length of data, are shown in Table 1.

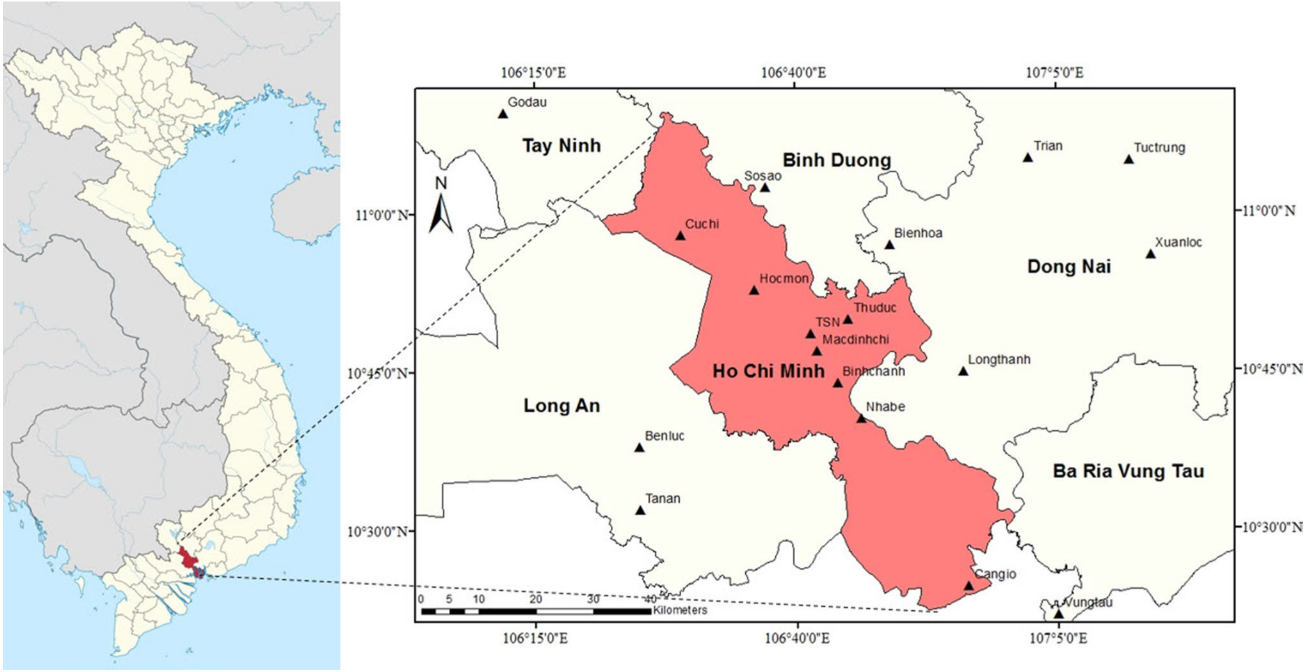

Fig. 1 Study area and locations of selected rainfall stations

Table 1 Details of selected rain gauges for the study

Region	Station name	Longtitude	Latitude	Data period
HCMC	Cuchi	106°29′00″	10°58′00″	1980–2014
	Hocmon	106°36′00″	10°53′00″	1980–2014
	Thuduc	106°45′00″	10°50′00″	1980–2014
	Macdinhchi (MDC)	106°42′01″	10°47′02″	1980–2014
	Tansonnhat (TSN)	106°40′00″	10°49′00″	1956–2014
	Binhchanh	106°44′00″	10°44′00″	1980–2014
	Nhabe	106°47′00″	10°41′00″	1980–2014
	Cangio	106°59′00″	10°24′00″	1980–2014
Binh Duong	Sosao	106°37′07″	11°02′33″	1958–2013
Tay Ninh	Godau	106°12′00″	11°09′36″	1980–2014
Dong Nai	Bienhoa	106°49′30″	10°57′25″	1958–2015
	Longthanh	106°35′00″	11°49′00″	1980–2014
	Tuctrung	107°12′00″	11°05′00″	1978–2015
	Xuanloc	107°14′00″	10°56′00″	1949–2015
	Trian	107°02′22″	11°05′15″	1980–2014
Long An	Benluc	106°25′00″	10°38′00″	1980–2014
	Tanan	106°25′00″	10°32′00″	1980–2014
Ba Ria Vung Tau	Vungtau	107°05′00″	10°22′00″	1949–2015

Figure 2a provides the average annual rainfall of all selected stations. It can be seen that there is a wide variation in the average annual rainfall amount between rain gauges. The stations located in Dong Nai province have the high values of annual rainfall, around 2000 mm (e.g. Longthanh, Trian, Tuctrung, Xuanloc). Whilst the stations located within HCMC have the lower values of annual rainfall, especially in Cangio station. Figure 2b shows the maximum daily rainfall over surveyed period of all stations. It is observed that the highest daily rainfall above 300 mm occurred in Xuanloc station, whereas the lowest value of 140 mm occurred in Hocmon station. Figure 3 shows the maximum annual daily rainfall time series with the linear trends of Tansonnhat (TSN) and Hocmon

Fig. 2 Diagram of **a** average annual rainfall and **b** maximum daily rainfall of all surveyed stations

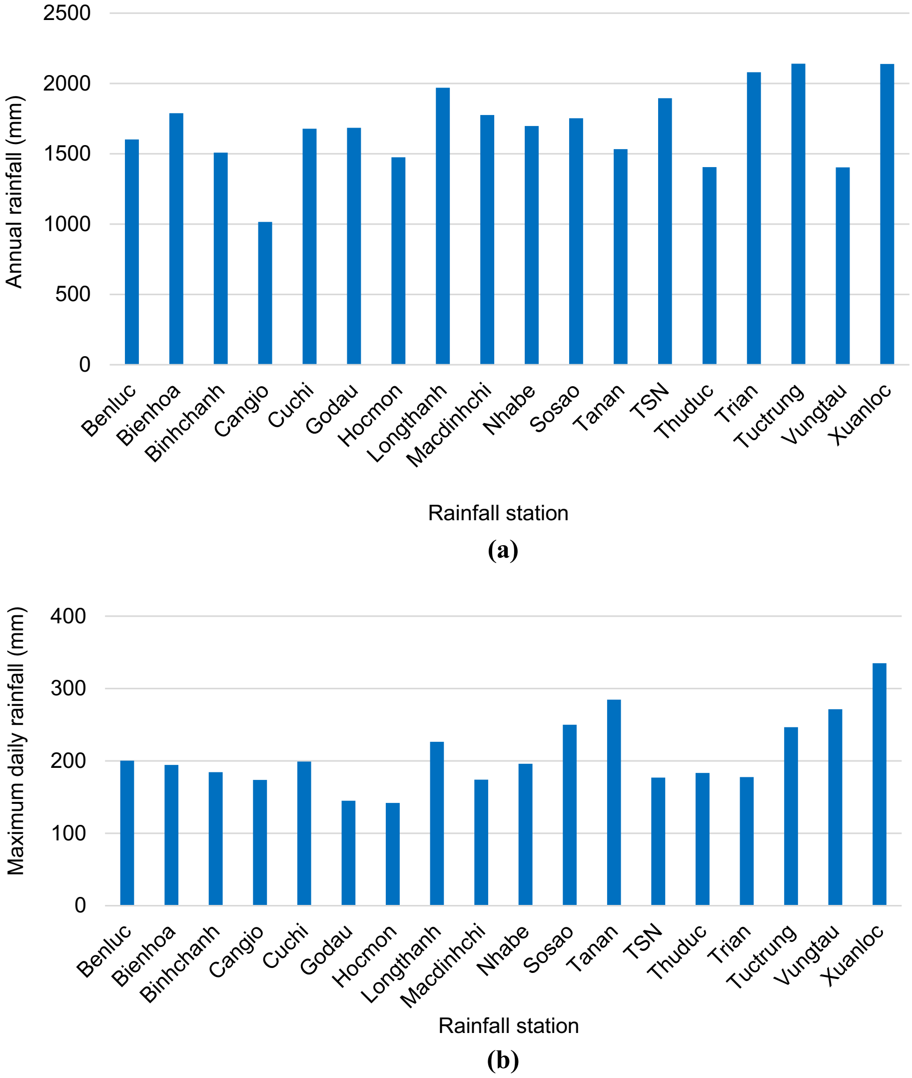

Fig. 3 The maximum annual daily rainfall time series with the linear trends (dotted lines) of Tansonnhat (TSN) and Hocmon stations during the observed period

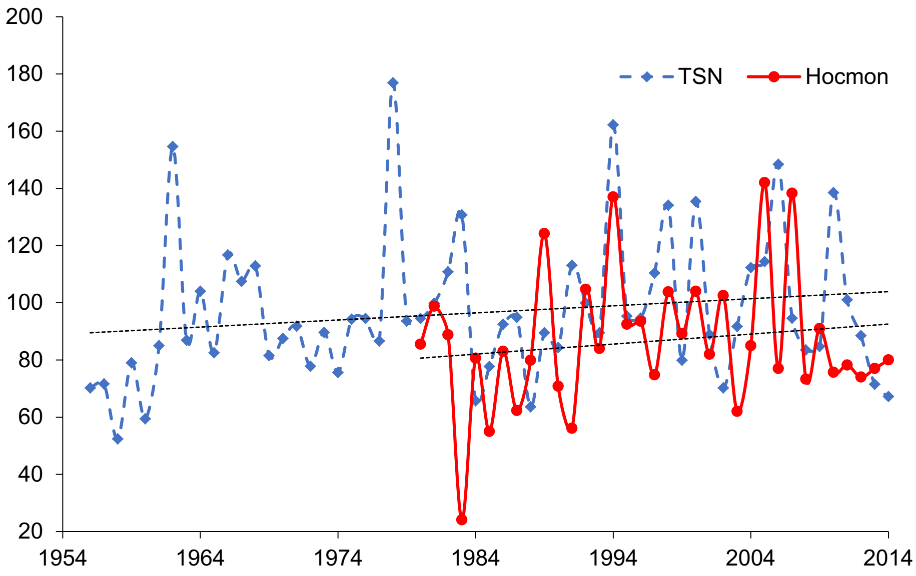

stations during the observed period. Through this figure, time variability of mean and standard deviation of the two series from neighboring stations can be seen. The dates of maximum daily rainfall of both these stations for a period of 1980–2014 are also provided in Fig. S1 in the supplementary material.

Methodology

The methodology of this study is organized as follows. The nonstationarity in rainfall time series is firstly detected using statistical test. Then the nonstationary GEV models are developed in which location parameter is expressed as a function of non-linear trend. The best model for each station could be found by Akaike Information Criterion and the likelihood ratio test. Based on the best models, the spatial variation of extreme rainfall over in HCMC and adjacent areas are mapped corresponding to the return periods of 5, 25 and 50 years. The methodology flowchart is shown in Fig. 4.

Mann–Kendall (M–K) test

Climatic extremes, particularly heavy rainfall events, have significantly increased in the past few decades due to human activities, urbanization and global climate change (Berg et al. 2013; Cheng and AghaKouchak 2014; Min et al. 2011; Trenberth 2011). Hence, the rainfall time series may have a nonstationary component. Normally, trend analysis is used to detect the nonstationarity signal in the rainfall time series. The M–K test (Kendall 1962; Mann 1945), a non-parametric statistical test, is widely used to analyze the monotonic trends in series of environmental data, climate data or hydrological data (Douglas and Fairbank 2010; Guhathakurta et al. 2011; Katz 2013; Pingale et al. 2014; Pohlert 2016; Rakhecha and Soman 1994; Westra et al. 2013; Zhang et al. 2008).

GEV model development

The asymptotic distribution of extreme rainfall series extracted using the annual maximum method is the GEV distribution and it has been previously used to model the extreme rainfall series under nonstationary condition (Agilan and Umamahesh 2016a; Cheng et al. 2014; Villafuerte

Fig. 4 Flowchart to determine the return levels

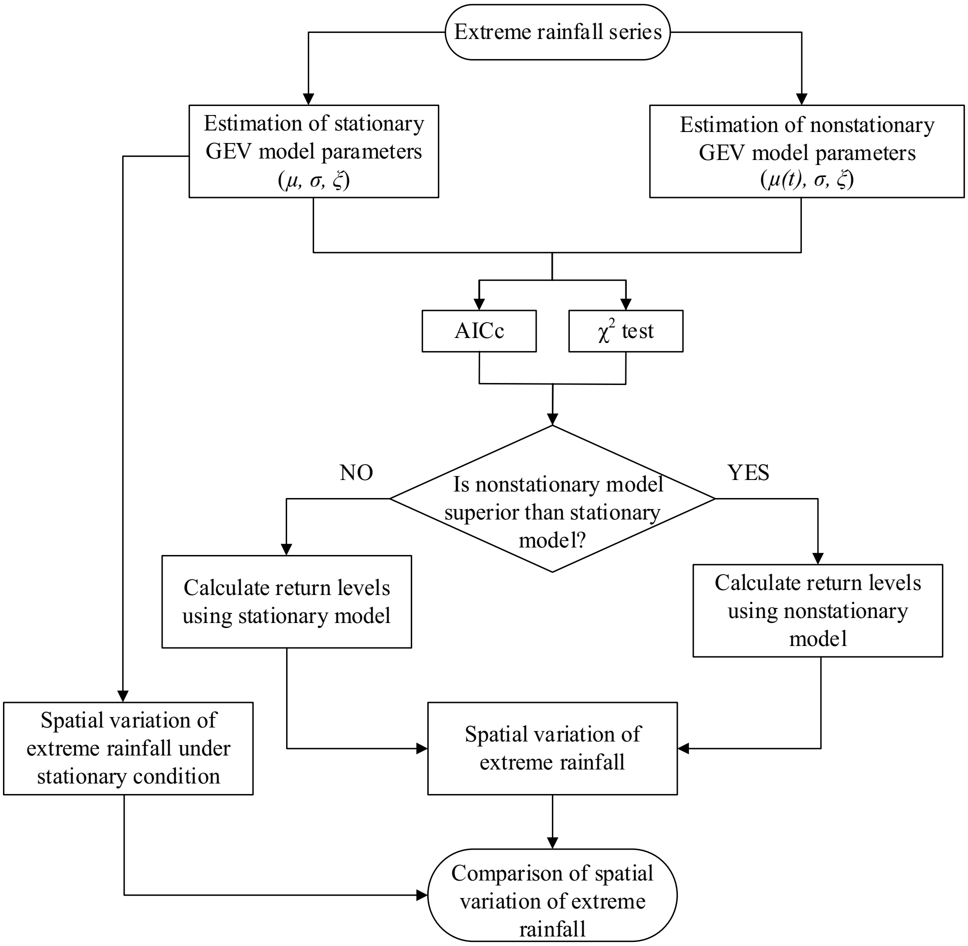

et al. 2015; Yilmaz et al. 2016). Therefore, in this study, the GEV distribution is used to model extreme rainfall series. Suppose $x = x_1, x_2, x_3, \ldots, x_n$ denote the annual maximum rainfall of n independent and identically distributed random variables. The cumulative distribution function of the GEV is given by Eq. (1) (Coles 2001; Katz et al. 2002):

$$G(x;\mu,\sigma,\xi) = \exp\left\{-\left[1+\xi\left(\frac{x-\mu}{\sigma}\right)\right]^{-1/\xi}\right\}, \quad 1+\xi\left(\frac{x-\mu}{\sigma}\right) > 0,\ \sigma > 0 \tag{1}$$

where μ, σ and ξ denote the location, scale and shape parameters. The location parameter (μ) specifies the center of the distribution, the scale parameter (σ) represents the size of deviations around the location parameter, and the shape parameter (ξ) governs the tail behavior of the GEV distribution. The GEV has three types of distribution determined by the sign of the shape parameter, i.e. Fréchet-type ($\xi > 0$), Weibull type ($\xi < 0$), and Gumbel type ($\xi = 0$).

Nonstationary GEV model

In the nonstationary case, the parameters of the models are allowed to vary with covariates (e.g. time or climatological covariates) (Coles 2001). In this study, we developed nonstationary models considering time as covariate. In particular, the parameters of the GEV distribution are expressed as a function of time, known as $\mu(t)$, $\sigma(t)$, $\xi(t)$, and $t = 1, 2, \ldots n$. For this study, we did not consider nonstationarity in scale (σ) and shape parameter (ξ). Because precise estimation of ξ is difficult, and it is unrealistic to assume it as a smooth function of time (Coles 2001). Besides, modelling temporal changes in σ and ξ reliably requires long-term observations which are usually unavailable for practical applications (Cheng et al. 2014). Hence, under nonstationary condition, the parameters of GEV model are expressed as a function of the covariate [$f(t)$] (Eq. 2):

$$\mu(t) = \mu_0 + \mu_1 \times f(t); \quad \sigma(t) = \sigma; \quad \xi(t) = \xi \tag{2}$$

where μ_1 denotes as the slope parameter and it represents the trend in the location parameter due to covariate $f(t)$.

As mentioned earlier, extreme rainfall events are affected by global climate change and many physical processes which have a different periodicity. Besides, directly using time covariate based linear form in nonstationary modelling may create more bias. Agilan and Umamahesh (2016a) suggested a non-linear form which is based on time and concern the incorporation of both long-term trend and periodicity concurrently. The covariate equation is given as follows (Agilan and Umamahesh 2016a):

$$f(t) = t^{a_1} + \sin\left(a_2 \times t\right) + \cos\left(a_3 \times t\right) \tag{3}$$

where a_1 is the variable that controls the magnitude of the long-term trend, and variables a_2 and a_3 control the periodicity. The estimation of a_1, a_2 and a_3 values is implemented by the multi-objective genetic algorithm (MOGA). The generic algorithm (GA), one of the efficient global search methods, is a computerized search and optimization algorithm based on the mechanics of natural genetics and natural selection. Unlike single objective problem, multi-objective problem based on multiple objectives functions is usually considered for estimating robust solution. In this study, we have used MOGA to estimate the value of a_1, a_2 and a_3. As such, the corrected version of Akaike Information Criterion (AICc), a distance function based on correlation coefficient (r) and root mean square error (RMSE) are considered as three objective functions of the GA is used to identify the best solution. The package nsga2R in R programming language is used to perform MOGA in this study. For more details about MOGA, the reader is referred to Agilan and Umamahesh (2016a).

Parameters estimation

The method of maximum-likelihood has been widely used for estimating the parameters of (non)stationary GEV model. The maximum-likelihood estimates of μ, σ and ξ are taken to be those values which maximize the likelihood function (Katz 2013). For the nonstationary model, the likelihood function can be represented as a function of parameters (i.e. μ_0, μ_1, σ, ξ). Let x_1, x_2, …, x_n be annual maximum precipitation series of n years. The log-likelihood function can be written as follows:

For $\xi \neq 0$,

$$\begin{aligned} L(\mu,\sigma,\xi|X) = {} & -n\log\sigma - \left(1+\frac{1}{\xi}\right) \\ & \times \sum_{i=1}^{n} \log\left[1+\xi\left(\frac{x_i-(\mu_0+\mu_1\times f(T))}{\sigma}\right)\right] \\ & - \sum_{i=1}^{n}\left[1+\xi\left(\frac{x_i-(\mu_0+\mu_1\times f(T))}{\sigma}\right)\right]^{-\frac{1}{\xi}}, \\ & 1+\xi\left(\frac{x_i-(\mu_0+\mu_1\times f(T))}{\sigma}\right) > 0 \end{aligned} \tag{4}$$

For $\xi = 0$,

$$\begin{aligned} L(\mu,\sigma|X) = {} & -n\log\sigma - \sum_{i=1}^{n}\left(\frac{x_i-(\mu_0+\mu_1\times f(T))}{\sigma}\right) \\ & - \sum_{i=1}^{n}\exp\left[-\left(\frac{x_i-(\mu_0+\mu_1\times f(T))}{\sigma}\right)\right] \end{aligned} \tag{5}$$

For the purpose of optimization, minimization of negative log-likelihood (Katz 2013) can be adopted to arrive at the estimates of parameters instead of maximizing log-likelihood. Therefore, minimization the negative log-likelihood function is used for parameters estimation in this study.

Model selection

Selection of the best model is a complex process and need to consider several different measures. A single measure may fail to determine an appropriate model, which lead to underestimate or overestimate the probability of extreme rainfall. In this paper, we use two measures to identify the best model for annual maximum extreme rainfall. Besides, the graphical approach (The probability–probability plot and quantile–quantile plots) is also used to check the quality of fitted model.

The Akaike information criterion

The AIC has been used commonly to select the best model among candidate models. In the comparison of AIC values between various models, the model with the lowest AIC value is considered to be the most efficient, and hence should be selected. However, Hurvich and Tsai (1995) showed that the AIC may have serious deficiencies, and they recommend a corrected version, namely AICc, which was developed for small samples to mitigate the bias and avoid overfitting the data. Thus, we use AICc for selecting the appropriate model in this study. The AICc is given by Eq. 6:

$$\mathrm{AICc} = -2\log L(\theta|X) + 2k + \frac{2k(k+1)}{n-k-1} \tag{6}$$

where n is the sample size, k is the number of parameters in a given model, $-\log\ L(\theta|X)$ is the minimized negative log-likelihood function. In addition, Burnham and Anderson (2004) suggested a rescaled form of AICc (denoted Δ_i) which is used in this work for ranking and comparison among the GEV models.

$$\Delta_i = \mathrm{AICc} - \min(\mathrm{AICc}) \tag{7}$$

where min(AICc) is the smallest value of AICc among candidate models. The model having $\Delta_i = 0$ is considered as the best model, whereas the model with larger Δ_i is less plausible. The model which has $\Delta_i \leq 2$ is considered reasonable selection for the given time series (Agilan and Umamahesh 2016a; Burnham and Anderson 2004).

The likelihood ratio test

The likelihood ratio test allows to determine the significance of the trend parameter in the nonstationary model by comparing negative log-likelihood of stationary and nonstationary models (Katz 2013). For example, if the stationary model and nonstationary model are denoted by (M_0) and (M_1) respectively, the negative log-likelihood of model (M_0) and (M_1) can be written:

$$l_0\left(M_0\right) = -\log L(x_1, x_2, \ldots, x_n; \mu, \sigma, \xi) \tag{8}$$

$$l_1\left(M_1\right) = -\log L(x_1, x_2, \ldots, x_n; a_1, a_2, a_3, \mu_0, \mu_1, \sigma, \xi) \tag{9}$$

Under null hypothesis of no trend ($\mu_1 = 0$), the likelihood ratio test statistic, based on twice the difference between $l_0(M_0)$ and $l_1(M_1)$ [Eqs. (8) and (9)], approximately follows Chi square distribution with four degree of freedom [denoted by χ^2 (4)] as the different between number of parameters in model (M_0) and (M_1) (Katz 2013). The test is given by:

$$2\left\{l_0\left(M_0\right) - l_1\left(M_1\right)\right\} \sim \chi^2(4) \tag{10}$$

The graphical diagnostics

In order to check the quality of fitting for a chosen model, the graphical approach of the probability–probability plot (P–P) and quantile–quantile plot (Q–Q) can be used. To develop the P–P and Q–Q plots, it is necessary to transform the data into a standardized form (Coles 2001). Here we use standard Gumbel distribution, and the transformed variable is defined by (Coles 2001; Katz 2013):

$$\varepsilon_i = \frac{1}{\hat{\xi}} \log\left(1 + \hat{\xi}\left(\frac{x_i - \hat{\mu}}{\hat{\sigma}}\right)\right) \tag{11}$$

where $\hat{\mu}, \hat{\sigma}, \hat{\xi}$ are estimated location, scale and shape parameter. Let $\hat{\varepsilon}$ is order value of ε, the P–P plot points and the Q–Q plot points are given by Eqs. (12) and (13) respectively (Coles 2001)

$$\left(\frac{i}{n+1}, \exp\left(-\exp\left(-\hat{\varepsilon}\right)\right)\right) \tag{12}$$

$$\left(-\log\left(1 - \frac{i}{(n+1)}\right), \hat{\varepsilon}\right) \tag{13}$$

Return level estimation

Once the best model for the given extreme rainfall series is determined, the T-year return level z_p corresponding to the T-year return period can be obtained. Here, the location parameter value in the nonstationary model varies over the time. Some authors suggested the low-risk approach for calculating location parameter by taking the 95 percentiles of the location parameter values in historical observation (Agilan and Umamahesh 2016a; Cheng and AghaKouchak 2014). However, in this study, we have used two ways to compute return levels by using mean value of location parameter for the years 1980–1984, say first 5 years, and the period of 2010–2014, say last 5 years. It is the fact that the rainfall process has periodicity as it is controlled by many physical processes (such as the ENSO cycle). As mentioned earlier, the rainfall of the study area is controlled by one of the dominant teleconnections, i.e. ENSO cycle. The El Nino and La Nina events (positive and negative phases of the ENSO cycle) will occur once in 2–5 years. In other words, the periodicity of the ENSO cycle is less than 5 years. Besides, a study related to nonstationarity analysis of Chawla and Mujumdar (2018) suggested that the hydrologic cycle in a river catchment can change every 5-year period. Consequently, we have calculated the average of 5 years thereby the interannual variations in the rainfall can be eliminated. This concept allows compare the difference between the first and the last periods of rainfall values at a certain station. Estimation of the T-year return level for the first(last) 5-year period can be given by Eq. (14):

$$z_{pF} = \begin{cases} \hat{\mu}_{5F(5L)} - \frac{\hat{\sigma}}{\hat{\xi}}\left[1 - \left\{-\log\left(1-\frac{1}{T}\right)\right\}^{-\hat{\xi}}\right], & \text{for } \hat{\xi} \neq 0 \\ \hat{\mu}_{5F(5L)} - \hat{\sigma}\log\left\{-\log\left(1-\frac{1}{T}\right)\right\}, & \text{for } \hat{\xi} = 0 \end{cases} \tag{14}$$

where $\hat{\mu}_{5F}$ and $\hat{\mu}_{5L}$ are the mean value of the location parameter of first 5 years and last 5 years respectively. By substituting the values of estimated parameters into Eq. (14), we can obtain the estimates of the return levels.

Result and discussion

Trends in extreme rainfall

As mentioned earlier, the M–K test is applied to indicate the increasing or decreasing trend in the rainfall data. In Table 2, the results of the Mann–Kendall test with all rain gauges are shown. The negative value of *Tau* indicates decreasing trend, in contrast, the positive value of *Tau* indicates increasing trend. Decreasing trend has been found in 8 stations, of which 2 stations are inside HCMC (i.e. Thuduc and MDC) and 6 stations outside HCMC (i.e. Sosao, Godau, Tuctrung, Benluc, Tanan, Vungtau). Increasing trend is observed in the annual maximum precipitation series of remaining stations.

Table 2 Results of M–K test for trend for all gauging stations

Stations	*Tau* value	*p* value	Stations	*Tau* value	*p* value
Cuchi	0.08	0.504	Godau	− 0.15	0.227
Hocmon	0.02	0.898	Bienhoa	0.07	0.497
Thuduc	− 0.15	0.218	Longthanh	0.17	0.156
MDC	− 0.22	0.080	Tuctrung	− 0.06	0.597
TSN	0.15	0.110	Xuanloc	0.16	0.071
Binhchanh	0.08	0.514	Trian	0.07	0.580
Nhabe	0.24	0.057	Benluc	− 0.02	0.865
Cangio	0.38	0.001	Tanan	− 0.05	0.660
Sosao	− 0.12	0.221	Vungtau	− 0.03	0.727

In addition, the p value shown in Table 2 points out that only 1 station in the Southeast side (i.e. Cangio) has a significant trend at 5% significant level. The trends in annual maximum series of Macdinhchi, Nhabe, Xuanloc stations are significant at 10% significance level. None of the test statistics of remaining stations is significant at 10% significant level.

Some researchers found that the characteristic of rainfall is changing (Min et al. 2011; Westra et al. 2013). It includes the increases in extreme rainfall in most places of the world, although only limited rain gauges indicate a statistically significant nonstationary behavior. Cheng and AghaKouchak (2014) also mentioned that ignoring the nonstationarity may lead to remarkable underestimation of extreme events, which may result in the increase in risk of infrastructure design and construction. Besides, these authors also suggested that the nonstationary condition can be applied to all datasets regardless of their trend, avoiding a subjective significance measure. Hence, the nonstationary GEV model is constructed for all 18 stations in this study.

Nonstationary GEV model

Before developing the stationary and nonstationary GEV models for extreme rainfall analysis, it is required to determine the value of variables a_1, a_2 and a_3 in Eq. (3). Upon estimating the value of variables a_1, a_2 and a_3 by multi-objective genetic algorithm, the stationary and nonstationary GEV models are constructed for each station. The values of a_1, a_2 and a_3 are shown in Table 3 for all stations.

Table 4 shows estimated parameter values of two models along with Δ_i values and likelihood ratio test results. The results show that the nonstationary GEV model is the best model for all stations. Further, as mentioned in the methodology section, the P–P and Q–Q plots are used to check the quality of a fitted model. The diagnostic plots of Tansonnhat station are shown in Fig. 5. It is observed that the nonstationary model shows a better match (Fig. 5b) than the stationary model (Fig. 5a). The P–P and Q–Q plots for remaining stations also indicate a good fit of extreme rainfall data by nonstationary GEV models. For brevity, P–P and Q–Q plots of remaining stations are not shown in this paper.

Spatial variation of rainfall extremes

Figure 6 shows the annual maximum daily rainfall return levels corresponding to 5, 25 and 50 years return period over HCMC. In the nonstationary case, extreme rainfall values of

Table 3 Estimated values of a_1, a_2 and a_3

Stations	Variables			Stations	Variables		
	a_1	a_2	a_3		a_1	a_2	a_3
Cuchi	−1.87	5.13	8.31	Godau	−0.92	−5.94	6.04
Hocmon	−4.01	2.99	2.45	Bienhoa	−0.75	7.24	9.83
Thuduc	−0.67	−5.24	6.44	Longthanh	−1.87	6.76	1.40
MDC	−2.35	9.31	2.51	Tuctrung	−10.00	7.61	0.43
TSN	0.15	−0.48	9.18	Xuanloc	−3.77	−4.92	8.30
Binhchanh	−8.32	−8.86	1.85	Trian	−0.87	−9.13	8.00
Nhabe	−0.88	4.76	4.10	Benluc	−10.00	−5.11	1.44
Cangio	−0.29	−6.14	6.16	Tanan	−1.84	1.34	6.02
Sosao	−9.28	7.03	7.83	Vungtau	−1.56	6.50	3.49

Table 4 Parameter estimates, likelihood ratio test results and Δ_i values

Stations	Parameters value of stationary model				Parameters value of nonstationary model					Likelihood ratio test
	μ	σ	ξ	Δ_i	μ_0	μ_1	σ	ξ	Δ_i	p value
Cuchi	84.32	24.80	0.09	3.08	83.66	19.01	17.53	0.35	0.00	5.97E−03
Hocmon	77.74	22.93	−0.22	3.09	79.55	13.93	18.78	−0.26	0.00	5.95E−03
Thuduc	79.28	29.18	−0.07	4.62	79.92	20.23	20.75	0.11	0.00	2.85E−03
MDC	92.32	23.15	−0.04	5.65	94.06	14.56	16.48	0.08	0.00	1.58E−03
TSN	85.27	19.42	0.01	15.84	84.51	10.23	13.12	0.31	0.00	3.68E−05
Binhchanh	71.07	21.97	0.07	5.07	70.20	14.06	14.36	0.39	0.00	2.33E−03
Nhabe	77.27	23.80	0.06	0.32	74.72	−10.06	15.87	0.44	0.00	1.52E−02
Cangio	41.67	30.25	0.17	11.29	45.14	−22.58	20.17	0.32	0.00	1.48E−04
Sosao	87.66	25.67	0.01	9.47	87.45	−13.70	19.32	0.18	0.00	6.48E−04
Godau	75.03	20.78	−0.13	18.72	73.47	−16.71	10.03	0.39	0.00	4.68E−06
Bienhoa	86.02	20.34	0.10	10.76	86.66	−10.82	15.26	0.25	0.00	3.45E−04
Longthanh	90.00	29.56	0.03	1.79	91.66	−16.51	23.20	0.11	0.00	1.05E−02
Tuctrung	98.63	22.83	0.10	7.92	97.46	−12.01	14.99	0.40	0.00	8.04E−04
Xuanloc	88.79	24.23	0.15	10.54	87.21	11.02	18.01	0.39	0.00	4.62E−04
Trian	91.65	17.45	−0.02	1.82	91.98	−11.24	13.27	0.12	0.00	1.04E−02
Benluc	88.88	24.63	0.12	5.65	87.55	−10.63	17.47	0.39	0.00	1.91E−03
Tanan	78.28	24.12	0.08	4.52	76.30	−17.06	15.79	0.40	0.00	3.12E−03
Vungtau	80.66	24.10	0.16	12.56	81.21	11.23	18.76	0.30	0.00	1.91E−04

each station are estimated for the periods of first 5 years and last 5 years by using mean value of location parameter for the years of 1980–1984 and 2010–2014 respectively.

Under the nonstationary condition, there is a large variation among rain gauges for the first 5 years' period compared to current years (the last 5 years' period). For instance, the estimated return levels corresponding to the 5-year return period vary between 55 and 210 mm per day for the first 5 years' period, whereas those values for the last 5 years' period are within range of 100–144 mm per day.

Figure 6 also shows that the differences in estimate rainfall values derived from nonstationary models are more significant in Tanan, Cangio, Thuduc, Godau when comparing first 5 years and last 5 years periods. In more detail, the difference in extreme rainfall estimates between these periods reaches 66.5 mm for Tanan station corresponding to 50-year return period, while those values for Cangio, Godau and Thuduc are approximately 53 mm, 37 mm and 20 mm respectively. Remaining stations do not show significant differences in estimated extreme rainfall between concerned periods.

Besides, it can be seen that the values of the return levels based on the best nonstationary models have significant difference compared with stationary models, especially in the South and Northeast of study area. Considering Tanan station as an example, the 50-year annual maximum rainfall values are 189 and 260 mm per day under stationary and nonstationary (for last 5 years' period) conditions respectively. Table 5 shows the percentage when nonstationary return levels are greater than stationary return levels for

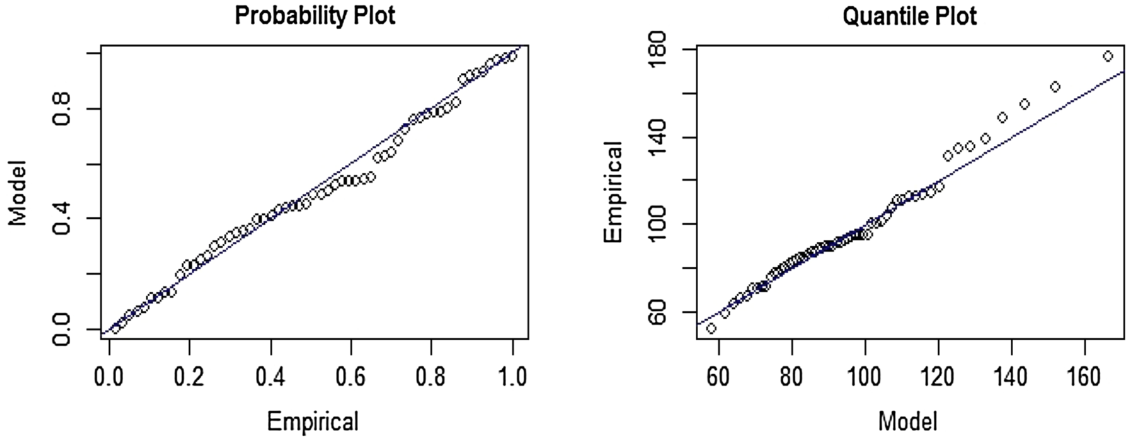

(a) Stationary model

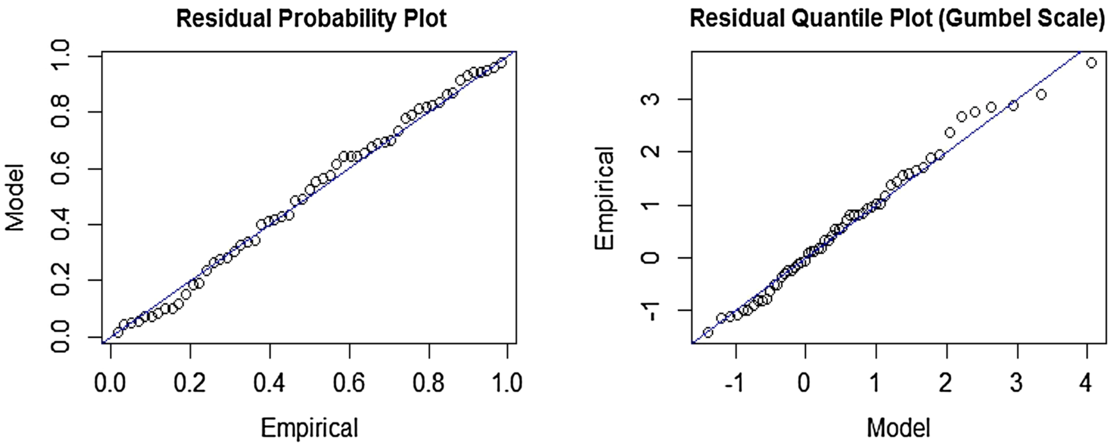

(b) Nonstationary model

Fig. 5 P–P and Q–Q plots of Tansonnhat (TSN) station

50-year return period for all stations. It can be seen that the magnitudes of extreme rainfall under the stationary condition are much lower than those under the nonstationary condition for most of the stations. These results point out that the assumption of stationarity could lead to underestimation of extreme rainfall events, hence choosing the design value for hydraulic structures under stationary or nonstationary condition should be considered thoroughly.

Summary and conclusion

Under the influence of global climate change and physical processes as ENSO and PDO, extreme rainfall in HCMC has been proven to increase in frequency and magnitude in last few decades. Therefore, the reality of nonstationary extreme rainfall should be paid more attention in the design of water infrastructure and flood mitigation projects since the extreme value distribution models with constant parameters may no longer be suitable. This present paper is aimed to model the spatial variation of extreme precipitation at HCMC and adjacent areas under nonstationary condition. In particular, the trend in time series is firstly determined by the nonparametric method, known as M–K test, before constructing nonstationary GEV model. In order to introduce nonstationarity into extreme rainfall frequency analysis, a nonlinear trend representing the long-term trend and periodicity of physical processes is suggested for the location parameter, whereas the scale and shape parameters (σ and ξ) are kept constant. The best nonstationary model for each station is found based on AICc value and likelihood ratio test. Based on the results of M–K test, only one station has a significant trend at the 5% significant level, and three stations have significant trend at 10% significant level. The remaining stations do not show a significant trend in the annual maximum precipitation data.

The findings indicate that the nonstationary model can be considered as the best model for modelling extreme rainfall when comparing to stationary model. The chosen

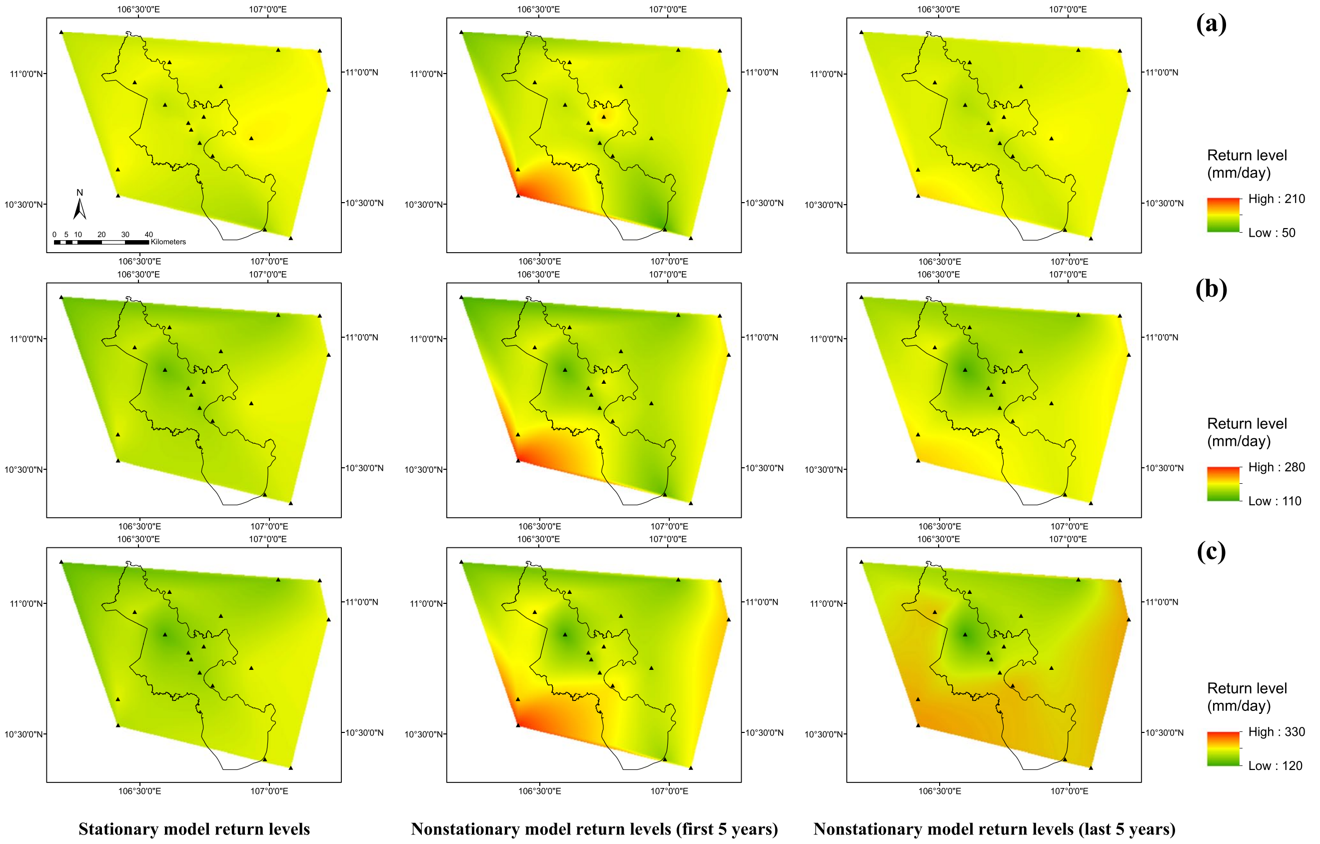

Stationary model return levels **Nonstationary model return levels (first 5 years)** **Nonstationary model return levels (last 5 years)**

Fig. 6 The variation of return levels for the return period of **a** 2-year; **b** 5-year; **c** 10-year; **d** 25-year; **e** 50-year

nonstationary GEV model also has better goodness of fit performance. Moreover, the extreme rainfall estimates under the stationary condition are much lower than those under the nonstationary condition in a major part of study area.

Regarding two concerned periods, first 5 years and last 5 years, it can be seen that the differences in estimate rainfall values derived from nonstationary models are significant, especially in Tanan, Cangio, Thuduc, Godau stations.

Table 5 The percentage when nonstationary return levels are greater than stationary return levels for 50-year return period for all stations

Station	Percentage (%)	Station	Percentage (%)
Cuchi	91.2	Godau	100
Hocmon	17.1	Bienhoa	69.2
Thuduc	58.8	Longthanh	37.1
MDC	31.3	Tuctrung	97.4
TSN	100	Xuanloc	100
Binhchanh	100	Trian	62.9
Nhabe	100	Benluc	100
Cangio	42.9	Tanan	97.1
Sosao	68.5	Vungtau	81.8

In a nut shell, we regard the present study as an important step towards flood mitigation projects and flood risk management in HCMC. Not only because it is the first of its kind, as authors' knowledge, but also because of proposed method, which considers the impact of global climate change and physical processes on extreme rainfall of study areas. In other word, it is suggested that extreme rainfall should be analysed under both stationary and nonstationary condition before using as initial inputs of hydrological and hydrodynamic models since the global climate is continuously changing and unpredictable. The findings are also able to provide useful information on nonstationary extreme rainfall of HCMC for decision makers in choosing appropriate design values. The future work may be continued by considering local factors and assessing the uncertainties in modelling extreme precipitation.

Acknowledgements The authors are grateful to the National Hydro-Meteorological Service (NHMS) of Vietnam for providing long-term rainfall data for this study. The R programming language and R packages "nsga2R", "ismev", "Kendall" are used in this study.

Compliance with ethical standards

Conflict of interest On behalf of all authors, the corresponding author states that there is no conflict of interest.

References

ADB (2010) Ho Chi Minh City adaptation to climate change: summary report. Asian Development Bank. https://www.adb.org/publications/ho-chi-minh-city-adaptation-climate-change-summary-report. Accessed 19 Dec 2016

Agilan V, Umamahesh N (2015) Detection and attribution of non-stationarity in intensity and frequency of daily and 4-h extreme rainfall of Hyderabad, India. J Hydrol 530:677–697. https://doi.org/10.1016/j.jhydrol.2015.10.028

Agilan V, Umamahesh N (2016a) Modelling nonlinear trend for developing non-stationary rainfall intensity–duration–frequency curve. Int J Climatol. https://doi.org/10.1002/joc.4774

Agilan V, Umamahesh N (2016b) What are the best covariates for developing non-stationary rainfall intensity–duration–frequency relationship? Adv Water Resour. https://doi.org/10.1016/j.advwatres.2016.12.016

Berg P, Moseley C, Haerter JO (2013) Strong increase in convective precipitation in response to higher temperatures. Nat Geosci 6:181–185. https://doi.org/10.1038/ngeo1731

Burnham KP, Anderson DR (2004) Multimodel inference understanding AIC and BIC in model selection. Sociol Methods Res 33:261–304. https://doi.org/10.1177/0049124104268644

Cai W, Rensch P (2012) The 2011 southeast Queensland extreme summer rainfall: a confirmation of a negative Pacific Decadal Oscillation phase? Geophys Res Lett. https://doi.org/10.1029/2011GL050820

Chan JC, Zhou W (2005) PDO, ENSO and the early summer monsoon rainfall over south China. Geophys Res Lett. https://doi.org/10.1029/2004GL022015

Chawla I, Mujumdar P (2018) Partitioning uncertainty in streamflow projections under nonstationary model conditions. Adv Water Resour 112:266–282

Chen W, Feng J, Wu R (2013) Roles of ENSO and PDO in the link of the East Asian winter monsoon to the following summer monsoon. J Clim 26:622–635. https://doi.org/10.1175/JCLI-D-12-00021.1

Cheng L, AghaKouchak A (2014) Nonstationary precipitation intensity–duration–frequency curves for infrastructure design in a changing climate. Sci Rep. https://doi.org/10.1038/srep07093

Cheng L, AghaKouchak A, Gilleland E, Katz RW (2014) Non-stationary extreme value analysis in a changing climate. Clim Change 127:353–369. https://doi.org/10.1007/s10584-014-1254-5

Chu L, McAleer M, Chang C-H (2013) Statistical modelling of extreme rainfall in Taiwan. http://hdl.handle.net/1765/38227. Accessed 19 Dec 2016

Coles S (2001) An introduction to statistical modeling of extreme values, vol 208. Springer, London. https://doi.org/10.1007/978-1-4471-3675-0

Douglas EM, Fairbank CA (2010) Is precipitation in northern New England becoming more extreme? Statistical analysis of extreme rainfall in Massachusetts, New Hampshire, and Maine and updated estimates of the 100-year storm. J Hydrol Eng 16:203–217. https://doi.org/10.1061/(ASCE)HE.1943-5584.0000303

Feng S, Nadarajah S, Hu Q (2007) Modeling annual extreme precipitation in China using the generalized extreme value distribution. J Meteorol Soc Jpn 85:599–613. https://doi.org/10.2151/jmsj.85.599

Gobin A, Nguyen H, Pham V, Pham H (2015) Heavy rainfall patterns in Vietnam and their relation with ENSO cycles. Int J Climatol. https://doi.org/10.1002/joc.4451

Groisman PY, Knight RW, Easterling DR, Karl TR, Hegerl GC, Razuvaev VN (2005) Trends in intense precipitation in the climate record. J Clim 18:1326–1350. https://doi.org/10.1175/JCLI3339.1

Guhathakurta P, Sreejith O, Menon P (2011) Impact of climate change on extreme rainfall events and flood risk in India. J Earth Syst Sci 120:359. https://doi.org/10.1007/s12040-011-0082-5

Hurvich CM, Tsai C-L (1995) Model selection for extended quasi-likelihood models in small samples. Biometrics. https://doi.org/10.2307/2533006

Katz RW (2013) Statistical methods for nonstationary extremes. In: Extremes in a changing climate. Springer, Dordrecht, pp 15–37. https://doi.org/10.1007/978-94-007-4479-0_2

Katz RW, Parlange MB, Naveau P (2002) Statistics of extremes in hydrology. Adv Water Resour 25:1287–1304. https://doi.org/10.1016/S0309-1708(02)00056-8

Kendall MG (1962) Rank correlation methods. Hafner Publishing Company, New York

Kenyon J, Hegerl GC (2010) Influence of modes of climate variability on global precipitation extremes. J Clim 23:6248–6262. https://doi.org/10.1175/2010JCLI3617.1

Khaliq M, Ouarda T, Ondo J-C, Gachon P, Bobée B (2006) Frequency analysis of a sequence of dependent and/or non-stationary hydro-meteorological observations: a review. J Hydrol 329:534–552. https://doi.org/10.1016/j.jhydrol.2006.03.004

Kioutsioukis I, Melas D, Zerefos C (2010) Statistical assessment of changes in climate extremes over Greece (1955–2002). Int J Climatol 30:1723–1737. https://doi.org/10.1002/joc.2030

Lasage R, Veldkamp T, De Moel H, Van T, Phi H, Vellinga P, Aerts J (2014) Assessment of the effectiveness of flood adaptation strategies for HCMC. Nat Hazards Earth Syst Sci 14:1441–1457. https://doi.org/10.5194/nhess-14-1441-2014

Le Vo P (2007) Urbanization and water management in Ho Chi Minh City, Vietnam-issues, challenges and perspectives. GeoJournal 70:75–89. https://doi.org/10.1007/s10708-008-9115-2

Mann HB (1945) Nonparametric tests against trend. Econometrica 13:245–259. https://doi.org/10.2307/1907187

Milly PC, Betancourt J, Falkenmark M, Hirsch RM, Kundzewicz ZW, Lettenmaier DP, Stouffer RJ (2008) Stationarity is dead: whither water management? Science 319:573–574. https://doi.org/10.1126/science.1151915

Min S-K, Zhang X, Zwiers FW, Hegerl GC (2011) Human contribution to more-intense precipitation extremes. Nature 470:378–381. https://doi.org/10.1038/nature09763

Mondal A, Mujumdar PP (2015) Modeling non-stationarity in intensity, duration and frequency of extreme rainfall over India. J Hydrol 521:217–231. https://doi.org/10.1016/j.jhydrol.2014.11.071

Nadarajah S (2005) Extremes of daily rainfall in West Central Florida. Clim Change 69:325–342. https://doi.org/10.1007/s10584-005-1812-y

Nguyen KC, Katzfey JJ, McGregor JL (2014) Downscaling over Vietnam using the stretched-grid CCAM: verification of the mean and interannual variability of rainfall. Clim Dyn 43:861–879. https://doi.org/10.1007/s00382-013-1976-5

Panagoulia D, Economou P, Caroni C (2014) Stationary and nonstationary generalized extreme value modelling of extreme precipitation over a mountainous area under climate change. Environmetrics 25:29–43. https://doi.org/10.1002/env.2252

Park JS, Kang HS, Lee YS, Kim MK (2011) Changes in the extreme daily rainfall in South Korea. Int J Climatol 31:2290–2299. https://doi.org/10.1002/joc.2236

Pingale SM, Khare D, Jat MK, Adamowski J (2014) Spatial and temporal trends of mean and extreme rainfall and temperature for the 33 urban centers of the arid and semi-arid state of Rajasthan, India. Atmos Res 138:73–90. https://doi.org/10.1016/j.atmosres.2013.10.024

Pohlert T (2016) Non-parametric trend tests and change-point detection. The R Foundation. https://cran.mtu.edu/web/packages/trend/vignettes/trend.pdf. Accessed 19 Dec 2016

Rakhecha P, Soman M (1994) Trends in the annual extreme rainfall events of 1 to 3 days duration over India. Theor Appl Climatol 48:227–237. https://doi.org/10.1007/BF00867053

Sugahara S, Da Rocha RP, Silveira R (2009) Non-stationary frequency analysis of extreme daily rainfall in Sao Paulo, Brazil. Int J Climatol 29:1339–1349. https://doi.org/10.1002/joc.1760

Trenberth KE (2011) Changes in precipitation with climate change. Clim Res 47:123–138. https://doi.org/10.3354/cr00953

Um M-J, Kim Y, Markus M, Wuebbles DJ (2017) Modeling nonstationary extreme value distributions with nonlinear functions: an application using multiple precipitation projections for US cities. J Hydrol 552:396–406. https://doi.org/10.1016/j.jhydrol.2017.07.007

Villafuerte MQ, Matsumoto J, Kubota H (2015) Changes in extreme rainfall in the Philippines (1911–2010) linked to global mean temperature and ENSO. Int J Climatol 35:2033–2044. https://doi.org/10.1002/joc.4105

Westra S, Alexander LV, Zwiers FW (2013) Global increasing trends in annual maximum daily precipitation. J Clim 26:3904–3918. https://doi.org/10.1175/JCLI-D-12-00502.1

Wi S, Valdés JB, Steinschneider S, Kim T-W (2016) Non-stationary frequency analysis of extreme precipitation in South Korea using peaks-over-threshold and annual maxima. Stochastic Environ Res Risk Assess 30:583–606

World Bank (2010) Climate risks and adaptation in Asian coastal megacities: a synthesis report. http://documents.worldbank.org/curated/en/866821468339644916/Climate-risks-and-adaptation-in-Asian-coastal-megacities-a-synthesis-report. Accessed 20 Dec 2016

Yen M-C, Chen T-C, Hu H-L, Tzeng R-Y, Dinh DT, Nguyen TTT, Wong CJ (2011) Interannual variation of the fall rainfall in Central Vietnam. J Meteorol Soc Jpn 89:259–270. https://doi.org/10.2151/jmsj.2011-A16

Yilmaz AG, Imteaz MA, Perera BJC (2016) Investigation of non-stationarity of extreme rainfalls and spatial variability of rainfall intensity–frequency–duration relationships: a case study of Victoria, Australia. Int J Climatol 37:430–442. https://doi.org/10.1002/joc.4716

Zhang Q, Xu C-Y, Zhang Z, Chen YD, C-l Liu, Lin H (2008) Spatial and temporal variability of precipitation maxima during 1960–2005 in the Yangtze River basin and possible association with large-scale circulation. J Hydrol 353:215–227. https://doi.org/10.1016/j.jhydrol.2007.11.023

Acta Geophysica (2019) 67:863–877
https://doi.org/10.1007/s11600-019-00266-6

RESEARCH ARTICLE - HYDROLOGY

A critical evaluation of the variability induced by different mathematical equations on hydraulic conductivity determination using disc infiltrometer

Biplab Ghosh[1] · Sreeja Pekkat[1]

Received: 2 July 2018 / Accepted: 12 February 2019 / Published online: 18 March 2019

Abstract

Infiltration measurements are mandatory input for hydrological modelling. Disc infiltrometer is used for determining infiltration in the field by allowing three-dimensional flow of water under the negative head at the surface. There are steady-state and transient mathematical equations for obtaining hydraulic characteristics based on disc infiltrometer measurements. Different assumptions and formulations adopted by these equations may induce analysis-dependent variability in hydraulic parameter determination from the disc infiltrometer measurements. In this study, a critical evaluation of nine mathematical equations used for determining near-surface saturated hydraulic conductivity based on mini-disc infiltrometer (MDI) measurements in the field for two different seasons is carried out. The saturated hydraulic conductivity determined by Guelph permeameter was used as the reference for evaluating the appropriateness of equations considered in this study. Considering different statistical procedures, Wooding–Gardner, Weir's Refinement, van Genuchten Zhang, Ankeny, and Haverkamp equations identified by Bland–Altman plot are recommended as the most reliable mathematical equations that can be used for analysing MDI measurements. The appropriateness of the mathematical equation for MDI analysis with respect to soil type needs to be investigated further.

Keywords Infiltration · Disc infiltrometer · Guelph permeameter · Hydraulic conductivity · Critical evaluation

Introduction

Infiltration is the measure of water entry into the soil at the ground surface. Infiltration capacity is a mandatory input for various hydrological projects such as groundwater recharge, water and solute transport through soils, irrigation, drainage, and flood modelling (Hillel 1998; Mishra et al. 2003; Revol et al. 1997). Hence, quantification of near-surface hydraulic conductivity based on infiltration measurements is of utmost importance in watershed management (Chahinian et al. 2006; Zhou et al. 2015; Pitt et al. 2008; Bean et al. 2007; Lee et al. 2016). There are several well-established infiltrometers for determining near-surface hydraulic conductivity in the field (Angulo-Jaramillo et al. 2000). The conventional ring infiltrometers are heavy with less portability, cumbersome procedure, time-consuming, and requirement of more water, thereby limiting its extensive measurements with adequate repetitions on catchment scale and on difficult grounds (McKenzie et al. 2002). In this context, a miniature version of disc infiltrometer, mini-disc infiltrometer (MDI), as shown in Fig. 1, has gained popularity due to its relative ease, high portability, a noninvasive and non-intrusive procedure for measuring the near-surface and near-saturated hydraulic conductivity (Dohnal et al. 2010). It allows extensive spatio-temporal measurements using MDI in the field with adequate repetitions (David and César 2009; Latorre et al. 2015). Past studies have determined the hydraulic conductivity of vegetated soils and different plant covers using MDI (Homolák et al. 2009; Gadi et al. 2017).

Researchers have proposed short-term transient methods and long-term steady-state methods for analysing disc infiltrometer data (Ankeny et al. 1991; Logsdon and Jaynes 1993; Jacques et al. 2002; Angulo-Jaramillo et al. 2000, 2016). These methods adopt different assumptions,

---

✉ Sreeja Pekkat
sreeja@iitg.ac.in

Biplab Ghosh
g.biplab@iitg.ac.in

[1] Department of Civil Engineering, Indian Institute of Technology Guwahati, Guwahati, Assam 781039, India

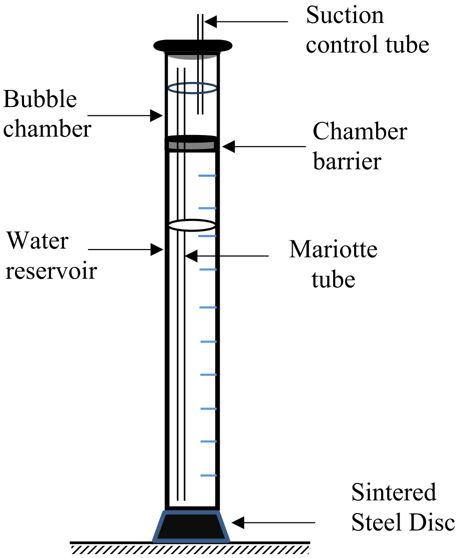

Fig. 1 Schematic diagram of mini-disc infiltrometer (MDI)

mathematical formulations, and boundary conditions for estimating hydraulic characteristics (David and César 2009; Haverkamp et al. 1994; Reynolds et al. 2002). This may lead to the variability in the determination of surface hydraulic conductivity using MDI (Verbist et al. 2013). MDI measures near-saturated hydraulic conductivity $\left(K_{h_0}\right)$ corresponding to a negative pressure head $\left(h_0\right)$ applied at the ground surface. There are comparisons of different infiltrometer results (Ghosh and Sreeja 2019) and insightful discussions on the theoretical formulations used for MDI (Angulo-Jaramillo et al. 2016). Ronayne et al. (2012) have compared Guelph permeameters with disc infiltrometers and ring infiltrometers. The variabilities in the hydraulic conductivity depending on the measurement techniques are appraised in the literature (Verbist et al. 2013). However, there is no conclusive recommendation on the appropriateness of any particular measurement methodology. It is mainly due to the lack of reference true value for hydraulic conductivity in the field (Morbidelli et al. 2017). Researchers have carried out studies to evaluate different physically based, semi-empirical, and empirical infiltration equations in different types of soil (Hsu et al. 2002; Mishra et al. 2003; Chahinian et al. 2005; Sihag et al. 2017). However, there are not many studies that critically evaluate the appropriateness of different mathematical equations for determining hydraulic conductivity based on MDI measurements under identical field conditions and different seasons.

The primary objective of this study is to evaluate nine popular mathematical equations that can be used to determine hydraulic conductivity based on MDI measurements taken at 14 sites within a sub-catchment of north-east India for two different seasons. A well-established Guelph permeameter (GP) was used as the reference for saturated hydraulic conductivity (K_s) measurement in the field (Salverda and Dane 1993; Reynolds and Elrick 1985; Bagarello and Giordano 1999; Morbidelli et al. 2017). Some of the mathematical equations considered in this study determine K_{h_0} instead of K_s. For such cases, K_{h_0} measured at a water head h_0 lower than zero was extrapolated to h_0 equal to zero for determining K_s. The research indicates that Wooding–Gardner, Weir's Refinement, van Genuchten–Zhang (vG–Z), Ankeny, and Haverkamp equations are appropriate mathematical equations that can be used for analysing MDI results for the field conditions identical to this study. To explore the role of soil type on the appropriateness of the mathematical equation for MDI analysis needs further studies.

Mathematical equations for MDI analysis

Infiltration beneath the MDI is governed by axisymmetric three-dimensional water flow into an initially unsaturated porous medium. For a given field condition, MDI measures cumulative infiltration with time for a specific time interval. These raw data are analysed using different steady-state and transient mathematical equations for determining K_{h_0}. The details of mathematical equations considered in this study are briefly discussed as follows.

Wooding–Gardner equation

According to Wooding (1968), the steady-state flux, q_{h_0} entering into the soil at a tension head h_0, from a shallow circular pond of radius r, can be approximated by a three-dimensional axisymmetric infiltration equation (Eq. 1):

$$q_{h_0} = K_{h_0}\left[1 + 4\lambda_c/(\pi r)\right] \tag{1}$$

where $\lambda_c = 1/\alpha_c$ is the macroscopic capillary length and K_{h_0} is the near-saturated hydraulic conductivity which is a function of h_0. The first term of Eq. 1 represents the one-dimensional vertical infiltration below the disc under gravity. The second term designates the lateral spread under the capillary metric force. The Gardner (1958) exponential function for the estimation of hydraulic conductivity (K_{h_0}) can be expressed as:

$$K_{h_0} = K_s \exp\left(\alpha_c h_0\right), \text{ when } h_0 \le 0 \tag{2}$$

where K_s is the saturated hydraulic conductivity. Combining both Wooding and Gardner equations, K_s can be determined by Eq. 3.

$$Q_{h_0} = \pi r^2 K_s \exp(\alpha_c h_0)\left(1 + \frac{4}{\pi r \alpha_c}\right) \tag{3}$$

where Q_{h_0} is the steady-state flow rate under a given tension h_0. The unknowns in this equation are K_s and α_c, which can be estimated by conducting infiltration measurements with a fixed disc radius and multiple negative pressure heads (Wang et al. 1998).

Weir's Refinement method

For water flow from a small surface source such as MDI disc, Weir (1987) observed that Wooding's approximate solution might not be representative. The flow rate and the infiltrometer disc radius, r_0, were normalized into the following dimensionless form:

$$Q^* = \frac{\alpha_c}{r_0 K_s \exp\left(\alpha_c h_0\right)} Q_{h_0} \tag{4}$$

$$r^* = \frac{1}{2}\alpha_c r_0 \tag{5}$$

Wooding's relationship was modified as:

$$Q^* = 4 + 2\pi r^* \tag{6}$$

For $r^* < 0.4$, Weir (1987) found that Eq. 6 may not be precise and thereby proposed an alternative estimate for Q^* given by Eq. 7.

$$Q^* = \frac{4\pi \sin^2\left(r^*\right)}{r^*\pi \sin\left(r^*\right)\cos\left(r^*\right) + 2r^* \sin^2\left(r^*\right)\ln\left(r^*\right) - 1.073\left(r^*\right)^3} \tag{7}$$

The experimental fitting parameter α_c is determined from the known steady-state flow rates at two tensions h_1 and h_2 using Eq. 8.

$$\alpha_c = \frac{\ln\left[Q\left(h_2\right)/Q\left(h_1\right)\right]}{h_2 - h_1} \tag{8}$$

The saturated hydraulic conductivity can be estimated by Weir's equation as:

$$K_s = \frac{\alpha_c}{r_0}\exp\left(-\alpha_c h_1\right)\frac{Q\left(h_1\right)}{Q^*} \tag{9}$$

van Genuchten–Zhang method

Zhang (1997a) proposed a method for determining near-saturated hydraulic conductivity, K_{h_0} from the measured cumulative infiltration versus the square root of the time response of relatively dry soil. The measured result was fitted with a second-order polynomial equation for determining the hydraulic conductivity and sorptivity of the soil. Zhang (1997a) used simulated data of cumulative infiltration under the disc infiltrometer for the determination of constants C_1 and C_2. The near-saturated hydraulic conductivity K_{h_0} and sorptivity S_{h_0} was estimated by

$$K_{h_0} = \frac{C_2}{A_2} \tag{10}$$

$$S_{h_0} = \frac{C_1}{A_1} \tag{11}$$

where A_1 and A_2 are the dimensionless coefficients. Using numerous numerical experiments, the empirical relationships were established for A_1 and A_2 as functions of soil retention parameters, infiltrometer parameters, and initial water content (Zhang and van Genuchten 1994; Zhang 1997a). The dimensionless coefficients alter with the total infiltration time, although the variation becomes insignificant as infiltration time increases and the coefficients can be treated as constants. By considering van Genuchten (1980) soil water retention function, the coefficients are given by the following equations:

$$A_1 = \frac{1.4b^{0.5}\left(\theta_0 - \theta_i\right)^{0.25}\exp\left[3(n - 1.9)\alpha_c h_0\right]}{\left(\alpha_c r_0\right)^{0.15}} \tag{12}$$

$$A_2 = \frac{11.65\left(n^{0.1} - 1\right)\exp\left[2.92(n - 0.19)\alpha_c h_0\right]}{\left(\alpha_c r_0\right)^{0.91}} \quad n \geq 1.9 \tag{13}$$

$$A_2 = \frac{11.65\left(n^{0.1} - 1\right)\exp\left[7.5(n - 0.19)\alpha_c h_0\right]}{\left(\alpha_c r_0\right)^{0.91}} \quad n < 1.9 \tag{14}$$

n and α_c represents the van Genuchten soil parameters, $h_0(< 0)$ is the pressure head of the infiltrometer, r_0 is the radius of the infiltrometer, θ_0 is the water content at h_0, θ_i is the initial water content, and b is the parameter equal to 0.55. The van Genuchten parameters for different soil texture can be obtained from Carsel and Parrish (1988).

White and Sully method

White and Sully (1987) proposed a method to determine the value of α_c in Gardner (1958) exponential hydraulic conductivity function (Eq. 2) as follows:

$$\alpha_c = \frac{\left(\theta_{h_0} - \theta_n\right)\left(K_{h_0} - K_n\right)}{bS_{h_0}^2} \tag{15}$$

where S_{h_0}, θ_{h_0}, and K_{h_0} are the sorptivity, moisture content, and hydraulic conductivity at pressure head h_0, respectively, θ_n and K_n are the initial moisture content and the corresponding hydraulic conductivity, respectively, and b is a shape factor. Linking Eqs. 15 and 1 with an assumption that K_n is insignificant, White et al. (1992) proposed the equation:

$$K_{h_0} = q_{h_0} - \frac{4bS_{h_0}^2}{(\theta_{h_0} - \theta_n)\pi r_0} \tag{16}$$

where q_{h_0} is the flow rate at steady state for pressure head h_0, S_{h_0} was determined from early-time cumulative infiltration versus square root of the time response of MDI by following vG–Z method (Eq. 11), θ_{h_0} is obtained from the soil surface instantly after the measurement, θ_n is determined before the measurement, and b is taken as 0.55.

Simunek–Wooding

(Šimunek et al. 1998) presumed that in the interval between two adjacent heads, the parameter α_c in Gardner (1958) exponential hydraulic conductivity function was constant. This assumption was used to find out the hydraulic conductivity in the middle of the interval between two successive heads, h_i and h_{i+1}. The parameter α_c was given as:

$$\alpha_c = \frac{\ln \frac{q_{i+1}}{q_i}}{h_{i+1} - h_i} \quad i = 1, \dots, n-1 \tag{17}$$

The average steady-state infiltration rate can be described as:

$$q_{h_0} = \sqrt{q_{i+1} \times q_i + 1} \quad i = 1, \dots, n-1 \tag{18}$$

Then, the near-saturated hydraulic conductivity, K_{h_0}, was estimated as:

$$K_{h_0} = \frac{q_{h_0}}{1 + \frac{4}{r_0\alpha_c}} \tag{19}$$

Ankeny method

Ankeny et al. (1991) proposed a multiple head method for the determination of near-saturated hydraulic conductivity using two consecutive tension heads. The parameter α_c in Gardner (1958) exponential hydraulic conductivity function was estimated by

$$\alpha_c = \frac{\ln \frac{Q_{h_1}}{Q_{h_2}}}{h_1 - h_2} \tag{20}$$

where Q_{h_1} and Q_{h_2} are the steady-state fluxes at h_1 and h_2, respectively.

Corresponding to two tension heads, $h_0 = h_1$ and h_2, two values of K_{h_0} can be obtained as:

$$K_{h_1} = \frac{Q_{h_1}}{\pi r_0^2 + \frac{4r_0}{\alpha_c}} \tag{21}$$

$$K_{h_2} = \frac{Q_{h_2}}{\pi r_0^2 + \frac{4r_0}{\alpha_c}} \tag{22}$$

Zhang method-I

Zhang (1998) suggested a procedure to reduce the time for field infiltrometer experiments drastically which do not require steady-state infiltration rates but infiltration data at any time by modifying Ankeny et al. (1991) procedure. In this method, the correction factors were proposed as follows:

$$f_1 = 1 + \frac{0.4431 r_0 \left(\theta_1 - \theta_i\right)^{0.5}}{\left(K_{h_1}\lambda t_1\right)^{0.5}} - 0.216 \exp\left[-\frac{4.01K_{h_1}\lambda t_1}{\left(\theta_1 - \theta_i\right) r_0^2}\right] \tag{23}$$

$$f_2 = 1 + \frac{0.4431 r_0 \left(\theta_2 - \theta_i\right)^{0.5}}{\left(K_{h_2}\lambda t_2\right)^{0.5}} - 0.216 \exp\left[-\frac{4.01K_{h_2}\lambda t_2}{\left(\theta_2 - \theta_i\right) r_0^2}\right] \tag{24}$$

where K_{h_1} and K_{h_2} are the hydraulic conductivity values and θ_1 and θ_2 are the final water contents at tensions $h_0 = h_1$ and h_2, respectively, θ_i is the initial water content, Q_1 and Q_2 are the measured flux at infiltration time t_1 and t_2, and λ is the macroscopic capillary length, which are unknowns. The modified method in the matrix form can be expressed as:

$$\begin{bmatrix} f_1\pi r_0^2 & 0 & 4f_1 r_0 K_{h_1} \\ 0 & f_2\pi r_0^2 & 4f_2 r_0 K_{h_2} \\ 0.5\Delta h & 0.5\Delta h & K_{h_2} - K_{h_1} \end{bmatrix} \begin{bmatrix} K_{h_1} \\ K_{h_2} \\ \lambda \end{bmatrix} = \begin{bmatrix} Q_{h_1} \\ Q_{h_2} \\ 0 \end{bmatrix} \tag{25}$$

where Q_{h_1} and Q_{h_2} are the measured flux at infiltration time t_1 and t_2 for the tension h_1 and h_2. Matrices are nonlinear because the coefficients are functions of the unknowns K_{h_1}, K_{h_2}, and λ. A Picard iteration with an incremental solution technique was used to solve the nonlinear equations assuming the initial approximate solution (Zhang 1998).

Zhang method-II

Zhang (1997b) proposed the infiltration model of the disc infiltrometers which is known as the second method of Zhang as:

$$I = C_1\sqrt{t} + C_2 t \tag{26}$$

where I is the cumulative infiltration, C_1 and C_2 are parameters, and t is the time.

The relationship for infiltration rate i is derived as:

$$i = 0.5C_1 t^{-0.5} + C_2 \tag{27}$$

If the steady-state infiltration rate $i_s = C_2$, then

$$f = \frac{Q}{Q_s} = \frac{i}{i_s} = 1 + 0.5\frac{C_1}{C_2}t^{-\frac{1}{2}} \tag{28}$$

where Q_s is the steady-state flow rate.

For the tensions h_1 and h_2, the correction factors f_1 and f_2 can be expressed as:

$$f_1 = \frac{Q_1}{Q_{1s}} = 1 + 0.5\frac{C_{11}}{C_{12}}t_1^{-\frac{1}{2}} \tag{29}$$

$$f_2 = \frac{Q_2}{Q_{2s}} = 1 + 0.5\frac{C_{21}}{C_{22}}t_2^{-\frac{1}{2}}. \tag{30}$$

Fitting Zhang (1997b) equation to cumulative infiltration data from 0 to t_1 for tension h_1 and 0 to t_2 for tension h_2, the coefficients C_{11}, C_{12}, C_{21}, and C_{22} were determined. In accordance with the first method of Zhang, t_1 and t_2 can be any infiltration time. Using known values of f_1 and f_2 for any definite time, the hydraulic conductivity can be found out by Zhang (1998) as follows:

$$K_{h_1} = \frac{\frac{Q_1}{f_1}}{\pi r_0^2 + 4\pi r_0} \tag{31}$$

$$K_{h_2} = \frac{\frac{Q_2}{f_2}}{\pi r_0^2 + 4\pi r_0} \tag{32}$$

Haverkamp method

Haverkamp et al. (1994) developed a physically based quasi-exact equation describing the three-dimensional unsaturated cumulative infiltration (I) curve for disc infiltrometers expressed as:

$$-\frac{1}{1-\beta}\ln\left(\left\{e^{\frac{2\beta(K_{h_0}-K_n)}{S_{h_0}^2}}\left\{I - K_n t - \left[\frac{\gamma S_{h_0}^2}{r_0(\theta_{h_0}-\theta_n)}\right]t\right\} + (\beta-1)\right\}\beta^{-1}\right)$$
$$\frac{2(K_{h_0}-K_n)^2}{S_{h_0}^2}t = \frac{2}{1-\beta}\frac{(K_{h_0}-K_n)}{S_{h_0}^2}\left\{I - K_n t - \left[\frac{\gamma S_{h_0}^2}{r_0(\theta_{h_0}-\theta_n)}\right]t\right\} \tag{33}$$

where r_0 is the radius of the disc, θ_n and θ_{h_0} are the initial and final volumetric water content, respectively, S_{h_0} is the sorptivity, γ is the proportionality constant, K_{h_0} and K_n are the soil hydraulic conductivity values corresponding to θ_{h_0} and θ_n, and β is a shape constant.

Haverkamp et al. (1994) assumed K_n to be negligible and simplified the above equation for short to a medium time interval as:

$$I = C_1\sqrt{t} + C_2 t \tag{34}$$

where $C_1 = S_{h_0}$.

$$C_2 = \frac{2-\beta}{3}K_{h_0} + \frac{\gamma S_{h_0}^2}{r_0(\theta_{h_0}-\theta_n)} \tag{35}$$

Using this expression, Vandervaere et al. (2000) suggested the differentiated linearization (DL) method to infer soil hydraulic properties using linear regression. The DL method is only applicable for short to medium time and the validity of this method is questioned when the capillary forces are predominant (Angulo-Jaramillo et al. 2000). The technique consists of differentiating it with respect to the square root of time which gives

$$\frac{\mathrm{d}I}{\mathrm{d}\sqrt{t}} = C_1 + 2C_2\sqrt{t} \tag{36}$$

Plotting the $\frac{\mathrm{d}I}{\mathrm{d}\sqrt{t}}$ term as a function of $\sqrt{t}$ gives C_1 as the intercept and C_2 as the slope of the corresponding regression lines. Haverkamp et al. (1999, 2005) proposed an average value of 0.75 for γ and 0.6 for β. Knowing C_1 and C_2 from the DL method (Eq. 36) K_{h0} is obtained by using Eq. 35. The summary of all the equations, their designation, different parameters, and initial conditions required for the calculation of hydraulic conductivity are listed in Table 1.

Measurement methodology

In this study, MDI was used to measure infiltration characteristics and K_{h_0} whereas a GP was used to determine K_s.

Mini-disc infiltrometer (MDI)

The MDI (Meter Group, USA 2018) depicted in Fig. 1 is a miniature tension disc infiltrometer ideal for field measurements due to its compact size and small amount of water requirement. The total length of MDI is 32.7 cm, with an adjustable suction range of 0.5–7 cm. The diameter of the bottom sintered stainless steel disc through which water infiltrate is 4.5 cm. The top chamber is used to control the suction head by using the Marriott principle. Water is filled in both the upper and lower chambers of the MDI. The lower chamber contains the volume of water that infiltrates into the soil at a suction head delegated on the disc through the bubble chamber. In order to prevent the water leak in the open air, a porous sintered stainless steel disc is provided at the bottom of the MDI. After preparing the MDI, it was placed on the soil surface, and the volume of water infiltrating into the soil was noted as a function of

Table 1 Parameters and initial conditions for different equations

S. no.	Equation	Designation	Equation parameters			Parameters determined		References
						Near-saturated hydraulic conductivity	Saturated hydraulic conductivity	
1	Wooding–Gardner	W–G	α_c, λ_c			Wooding equation (Eq. 1)	Gardner equation (Eq. 2)	Gardner (1958) and Wooding (1968)
2	Weir's Refinement	W-R	$\alpha_c = \frac{\ln[Q(h_2)/Q(h_1)]}{h_2 - h_1}$ $\lambda_c = 1/\alpha_c$			Weir equation (Eq. 4)	Gardner equation (Eq. 2)	Weir (1987), Gardner (1958) and Wang et al. (1998)
3	van Genuchten–Zhang	vG–Z	n	Sand	2.68	vG–Z (Eq. 10)	Extrapolation method	Zhang (1997a) and van Genuchten (1980)
				Loam	1.56			
				Silt	1.37			
			α_c	Sand	0.145			
				Loam	0.036			
				Silt	0.016			
4	White and Sully	W–S	$\alpha_c = \frac{(\theta_{h_0} - \theta_n)(K_{h_0} - K_n)}{bS_{h_0}^2}$ $\lambda_c = 1/\alpha_c$			White Equation (Eq. 16)	Extrapolation method	White and Sully (1987) and White et al. (1992)
5	Simunek–Wooding	S–W	$\alpha_c = \frac{\ln \frac{q_{i+1}}{q_i}}{h_{i+1} - h_i}$			$K_{h_0} = \frac{q_{h_0}}{1 + \frac{4}{r_0 \alpha_c}}$	Extrapolation method	Šimunek et al. (1998)
6	Ankeny	A	$\alpha_c = \frac{\ln \frac{Q_{h1}}{Q_{h2}}}{h_1 - h_2}$			$K_{h_1} = \frac{Q_{h_1}}{\pi r^2 + \frac{4r}{\alpha_c}}$	Extrapolation method	Ankeny et al. (1991)
7	Zhang method-I	Z-I	$K_{h_1}, K_{h_2}, \lambda_c$			Zhang matrix form (Eq. 25)	Extrapolation method	Zhang (1998)
8	Zhang method-II	Z-II	$K_{h_1}, K_{h_2}, \lambda_c$			Zhang equation (Eqs. 31 and 32)	Extrapolation method	Zhang (1997b)
9	Haverkamp	H	γ		0.75	Differential linearization method (Eq. 36)	Extrapolation method	Haverkamp et al. (1994, 1999, 2005) and Vandervaere et al. (2000)
			K_n		0			
			β		0.6			

time. This gives the cumulative infiltration versus time response for a given field condition, which approaches a linear trend after some duration indicating quasi-steady state. The MDI measurements at every location were obtained for four different tensions in the order of 6, 4, 2, and 0.5 cm. For every tension head, the initial condition was kept identical by shifting the MDI after each measurement. Hydraulic conductivity was determined by different steady and transient mathematical equations explained above based on the MDI measurements (cumulative infiltration versus time).

Guelph permeameter (GP)

The Guelph permeameter (GP) is a borehole constant head permeameter method for measuring field-saturated hydraulic conductivity at a depth below the ground surface (15–75 cm) (Reynolds and Elrick 1985; Morbidelli et al. 2017; Salverda and Dane 1993; Hayashi and Quinton 2004). For better comparison with MDI, GP measurements were taken at a depth of approximately 15 cm. A constant ponding depth of water varying from 5 cm and 10 cm was maintained in the borehole using the Marriott principle. Under the constant head, there is a steady-state three-dimensional flow of water into the adjacent unsaturated soil. This results in the formation of saturated soil bulb around the ponding depth depending on the type of soil, the radius, and head of water in the well. Once the unique bulb is established, the outflow of water from the well reaches steady state, which can be measured. The steady-state flow rate was used for the determination of K_s as given by Eq. 37, which is based on one ponding depth. The details of working methodology and mathematical formulations for GP for the determination of K_s are well established in the literature (Morbidelli et al. 2017; Elrick and Reynolds 1992; Reynolds et al. 1985) and hence not repeated in this study.

$$K_s = \frac{C_1 Q_1}{2\pi H_1^2 + \pi a^2 C_1 + 2\pi\left(\frac{H_1}{a^*}\right)} \tag{37}$$

where H_1 is the ponding depth, Q_1 is the steady-state outflow from the GP, a is the auger hole radius equal to 3 cm, a^* is the capillary length factor and C_1 is the shape factor. The values of a^* and C_1 were estimated based on the soil type (Elrick et al. 1989).

Description of the study area

The study area is in the sub-basin of river Brahmaputra, north-east India, with the elevation of the site varying from 49 m to 97 m above mean sea level with its geographic location between 26°11′3.434″ N and 26°11′55.122″N latitude and 91°41′14.324″ E and 91°42′10.578″ E longitude. The measurements were taken at 14 locations (designated as S1 to S14 in Table 2) in the study area to take into account the spatial variability of infiltration characteristics and for December 2014 and June 2015 representing two different seasons. The surface soils were characterized for specific gravity, grain-size distribution, field density, and initial moisture content (ASTM D2487-2011; IS 2720-29 1975; ASTM D 854-2014; ASTM D 7928-2017; ASTM D 6938-2015; ASTM D 2216-2010). The grain-size distribution was used to classify the soils based on the Unified Soil Classification System (ASTM D 2487-2011) and is listed in Table 2. In the study area, it was confirmed that the depth of the topsoil layer is more than 1 m at all the sites evading the influence of soil layering (inhomogeneity) on infiltration measurements. The soil surface was bare with no influence of vegetation on MDI measurements and free from anthropogenic activities.

There are four types of soils, viz. loamy sand, loam, sand, and silt, in the study area with varying field densities which are listed in Table 2. A typical layout of the infiltration measurement scheme and repetitions performed in the site for a particular station is depicted in Fig. 2. Symbols denote the location of infiltration measurement for each instrument.

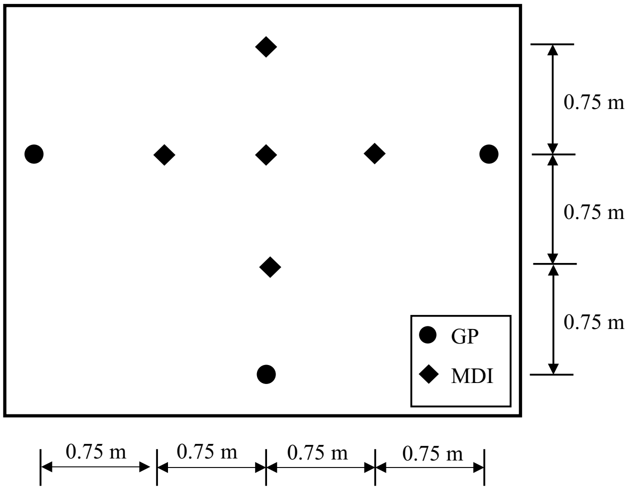

Fig. 2 Positions of the MDI and GP measurements in the study area (not to scale)

Table 2 Details of soils at different sites of the study area

Site no.	Soil description	Particle size fraction (%)				Soil type	USCS[a]	van Genuchten parameters		Field dry density (gm/cc)	Specific gravity (G_s)
		Gravel	Sand	Silt	Clay			α	n		
S1	Fill soil	23	53	17	7	Sand	SM	0.145	2.68	1.74	2.580
S2	Soil from hill cutting	4	56	34	6	Loamy sand	SM	0.124	2.28	1.40	2.525
S3	Hard compacted	2	82	16	0	Sand	SM	0.145	2.68	1.76	2.410
S4	Hard compacted	1	87	12	0	Sand	SM	0.145	2.68	2.02	2.410
S5	Hard rocky	13	64	15	8	Sand	SM	0.145	2.68	1.85	2.535
S6	Soil from hill cutting	2	45	40	13	Loam	MH	0.036	1.56	1.57	2.560
S7	Soil from hill cutting	2	40	55	3	Silt	MH	0.016	1.37	1.42	2.545
S8	Fill soil	3	42	53	2	Silt	MH	0.016	1.37	1.49	2.495
S9	Fill soil	2	52	45	1	Loam	SM	0.036	1.56	1.59	2.495
S10	Fill soil with organic	3	59	38	0	Loam	SM	0.036	1.56	1.71	2.510
S11	Fill soft soil	3	56	38	3	Loam	SM	0.036	1.56	1.58	2.470
S12	Fill soft soil	3	48	39	10	Loam	SM	0.036	1.56	1.68	2.505
S13	Fill soft soil	1	53	46	0	Loam	SM	0.036	1.56	1.67	2.580
S14	Hard compacted	1	67	25	7	Loamy sand	SM	0.124	2.28	1.88	2.560

[a] Unified soil classification system (ASTM D 2487)

Similar layout of infiltration measurements was followed for all the 14 sites. It needs to be noted that adequate space was provided to rule out the interference of adjacent measurements. To ensure this, a minimal distance of 0.75 m was maintained between each measurement as shown in Fig. 2. All MDI measurements were repeated five times for all four tensions 0.5, 2, 4, and 6 cm, and the Guelph permeameter was repeated three times under identical initial conditions. Before performing infiltration measurements, initial gravimetric water content (w) and field dry density (ρ_d) of all the locations were measured according to the procedure mentioned in ASTM D 2216-2010 and ASTM D 6938-2015, respectively.

Results and discussion

The critical evaluation of different mathematical equations used for determining hydraulic conductivity from the measured results of MDI necessitates a reliable reference value. In this study, GP was considered as the reference because it is an established method for measuring field K_s. In this study, the depth of GP measurement is near to the ground surface (15 cm). The homogeneity of soil was confirmed at all the measurement sites. Barring any unforeseen errors and assuming similar pore structure within 15 cm depth, K_s determined by MDI and GP should theoretically be the same. Therefore, the K_s estimated from MDI measurements was compared with the results of GP. Most of the mathematical equations (except Wooding–Gardner and Weir's refinement method) evaluated in this study gives near-saturated hydraulic conductivity for which there is no independent reference value. Therefore, K_{h_0} corresponding to different tension heads $\left(h_0\right)$ obtained from MDI was linearly extrapolated to estimate the field-saturated hydraulic conductivity at $h_0 = 0$ as shown in Fig. 3. It can be noted that the variation in K_{h_0} corresponding to h_0 of 0.05–0.6 kPa (or 0.5–6 cm) is linear (Zhang (1997a) and hence the linear extrapolation to $h_0 = 0$ is justified. Figure 3 shows the log-transformed values of mean hydraulic conductivity as a function of h_0 for station 1 in December 2014 using method 3 (Table 1). For statistical analysis, the hydraulic conductivity was log-transformed based on the understanding that hydraulic conductivity generally follows log-normal distribution (Bouwer 1969; Nielsen et al. 1973; Buckland 1988).

The K_s estimated from the results of MDI using different mathematical equations is compared with GP measurements for all the sites and two seasons as shown in Fig. 4. Owing to the marginal standard deviation of these measurements, the error bars are not shown in the figure. It is evident that the K_s measurements of GP for both the seasons match well indicating the invariant behaviour of K_s for a particular soil and pore structure. Unlike GP, the results from MDI are not the same for both the seasons, thereby violating the condition of invariance. The MDI measurements in December gave higher K_s as compared to June even though the difference between two seasons is well within one order of magnitude. It may be noted that the GP measurements were taken at a depth of 15 cm below the ground surface, whereas MDI measurements were taken on the ground surface. The major reason for the difference in K_s (from MDI) corresponding to different seasons can be attributed to the higher sensitivity of MDI measurements to surface pore structure changes with seasons as compared to GP.

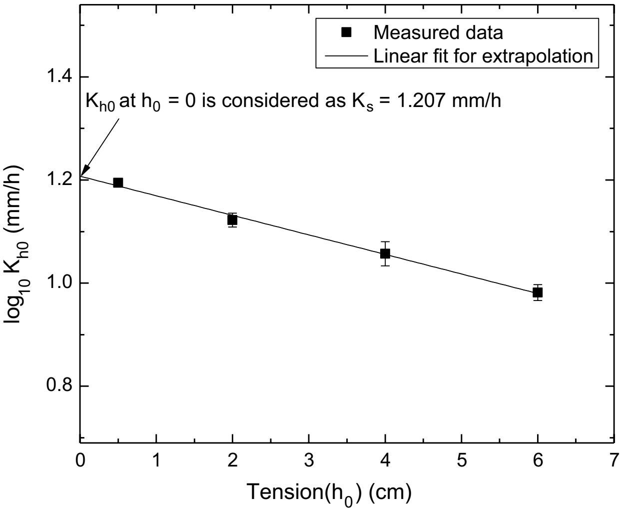

Fig. 3 Extrapolation for determining saturated hydraulic conductivity from MDI results

In general, the observations in Fig. 4 indicate that the mathematical equations can be divided into three sets. The first set of equations including W–G, W-R, vG–Z, S–W, A, and H listed in Table 1 gave comparable K_s based on the MDI measurements. The K_s from the second set of equations Z-I and Z-II is lesser and third set of equation W–S is higher as compared to first set. It is worth noting that the first set includes both steady-state and transient equations for determining K_s. From the initial observation, it is difficult to comment on the comparison of K_s determined from different equations with GP results. It can be noted that for some stations, the first set of equations performed reasonably well depending on the season. Statistical analysis was performed in the ensuing section for better understanding of the comparisons of K_s determined from mathematical equations with GP measurements.

Variability of hydraulic conductivity

The statistical difference between K_s determined from GP and different mathematical equations (using MDI results) was assessed quantitatively by using Bland–Altman plot (BAp) as shown in Fig. 5, where each panel refers to a single equation applied to all the sites and seasons. Bland–Altman

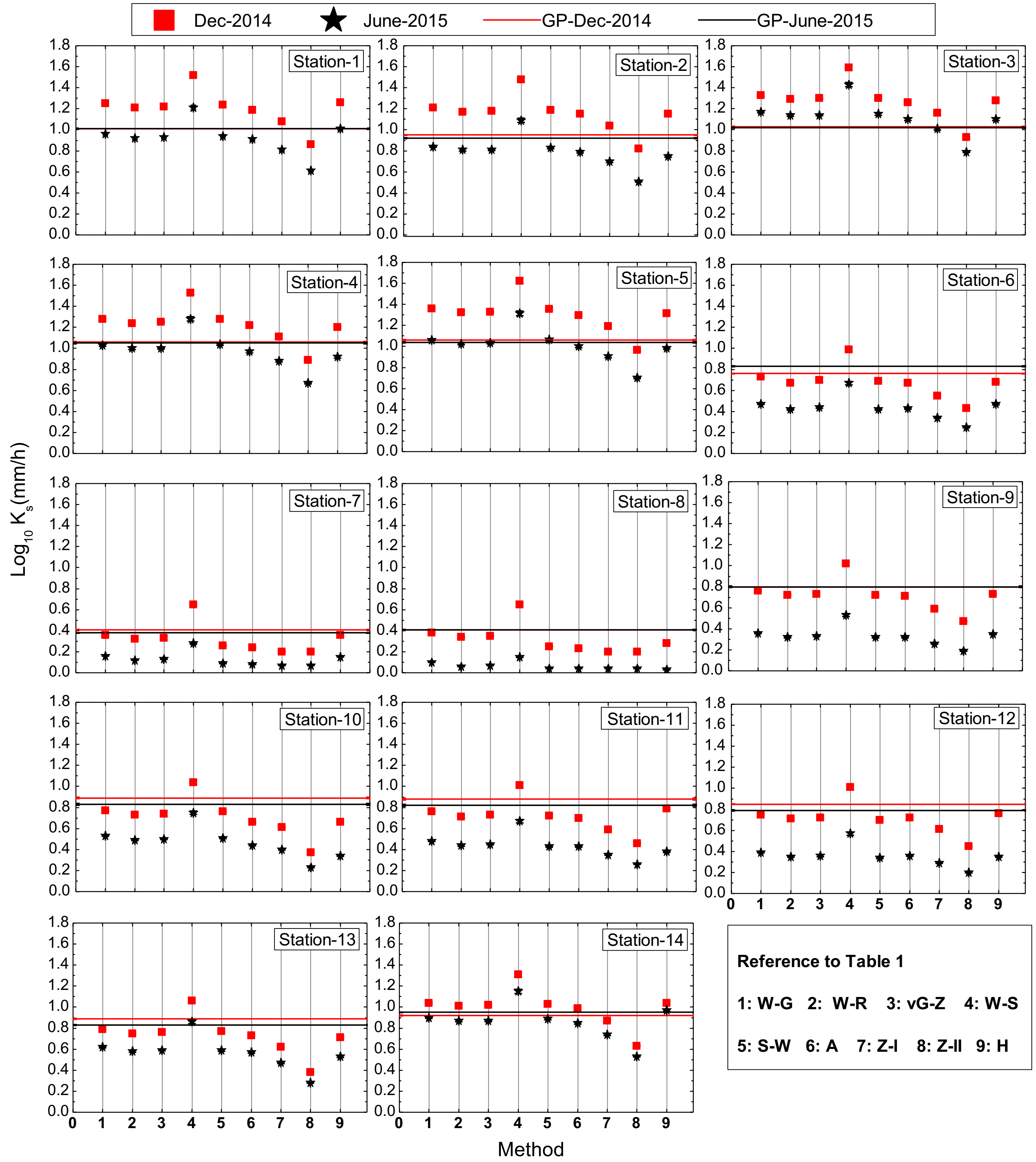

Fig. 4 Comparison of saturated hydraulic conductivity (mm/h) determined from MDI and GP

plot is an established graphical statistical method to compare the agreement between two measurement techniques (Braždžionyte and Macas 2007). In this plot, the difference between MDI and GP is plotted on the Y-axis and mean of the two methods are plotted on the X-axis. In Fig. 5, “bias” is the mean of the difference between the two methods. The 95% upper and lower limits of agreement (LoA) are equal to ± 1.96 times the standard deviation of the difference between the two methods. The BAp helps to compare two methods based on the magnitude and direction of the bias,

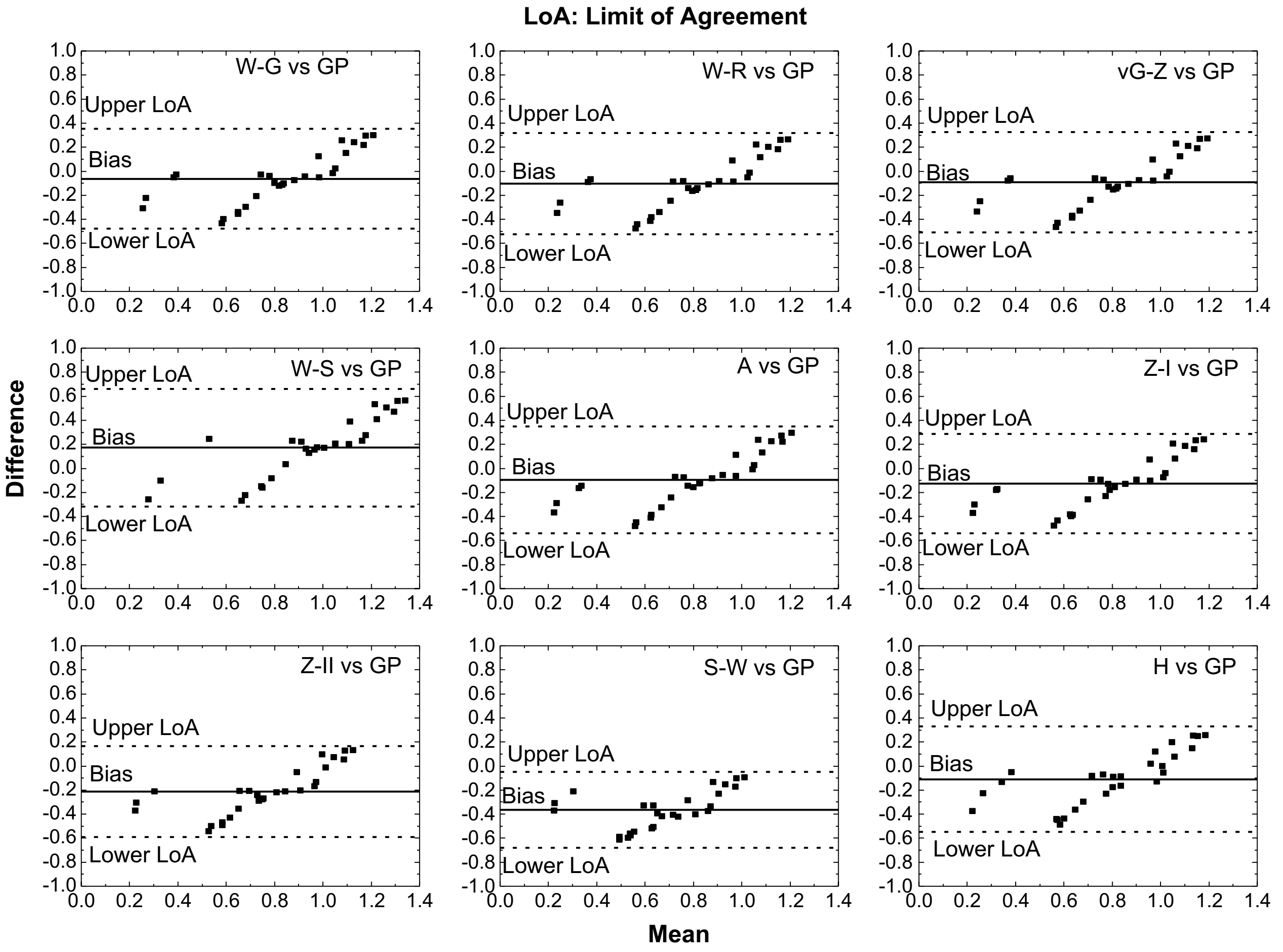

Fig. 5 Bland–Altman plot for statistical comparison between K_s determined from Guelph permeameter and different equations (based on MDI)

width of LoA, and whether there is any systematic trend between the difference and the mean. It is understood that the K_s comparisons with minimal bias and LoA can be considered to be better. The details of parameters for BAp for different equations are listed in Table 3.

Figure 5 shows that the majority of the data points falls within the LoA. With GP as the reference method, LoA indicates the total error of a given mathematical equation (Krouwer 2002) used for determining K_s. Smaller LoA means the majority of the data falls within smaller error

Table 3 Statistical analysis of hydraulic conductivity determined using different equations

S. no.	Method	Bias (mm/h)	Lower LoA	Upper LoA	Width of LoA	Pearson coefficient	p value
1	W–G	−0.063*	−0.479	0.353	0.832	0.86	0.0037
2	W-R	−0.103	−0.524	0.319	0.843	0.86	0.0020
3	vG–Z	−0.092*	−0.508	0.324	0.832	0.86	0.0023
4	W–S	***0.173***	−0.316	0.661	0.977	0.84	**0.0513**
5	S–W	−0.365	−0.680	−0.050	0.630	0.81	0.0033
6	A	−0.096*	−0.539	0.348	0.887	0.88	0.0003
7	Z-I	−0.126	−0.539	0.287	0.826	0.88	0.0003
8	Z-II	−0.211	**−0.590**	0.169	0.759	0.86	0.0004
9	H	−0.109	−0.549	0.331	0.880	0.84	0.0032

*Bias is close to zero; italics value shows the positive bias, and bold values indicate failed to reject the null hypothesis ($p > 0.05$)

limit. It is noted that LoA is comparable for the majority of the mathematical equations considered with maximum LoA for W–S and minimum for S–W. However, LoA alone may not be sufficient for deciding the appropriateness of the equations. The bias between the two data sets also needs to be considered. Among all the equations, W–S versus GP is having a positive bias, which means that W–S overestimated K_s as compared to GP. The three equations W–G, vG–Z, and A exhibited minimum bias (<0.1) with GP. For a better understanding, LoA is plotted with respect to bias as shown in Fig. 6. Based on Fig. 6, it can be noted that there is not much of difference in LoA for all the equations considered. At the same time, there is a wider range of bias exhibited by these equations. Considering both LoA and bias, K_s determined by equations W–G, W-R, vG–Z, A, and H is found to compare well with the results of GP.

It can be noted further from Fig. 5 that there is a systematic difference in K_s determined from equations and GP results. There is a visible increase in difference with the mean for all the equations and the trends are quite consistent. For mid-range of mean, the difference is centred around bias. For those methods with low bias, this means that mid-range values of K_s determined from equations exhibited a better comparison with GP results as compared to the higher and lower range of K_s. The definition of low, mid- and high range of K_s is entirely dependent on the data from this study. The impact of the systematic difference of K_s determined from different equations and GP measurements on the modelling of various hydrological processes is not clear from this study and needs to be investigated in detail.

An effort was made to explore the correlation between K_s from different equations and GP measurements. The details of the Pearson correlation coefficient (Verbist et al. 2013) and the p values are listed in Table 3. It can be noted that the Pearson correlation coefficient was found to vary between 0.81 and 0.88, indicating a fair correlation. However, it is difficult to adjudge the effectiveness of equations in determining K_s based on the Pearson correlation coefficient. In the case of White and Sully (W–S) method, even though the Pearson coefficient was 0.84, the bias and the p value (from Pearson correlation) indicated a marginal comparison of K_s with GP.

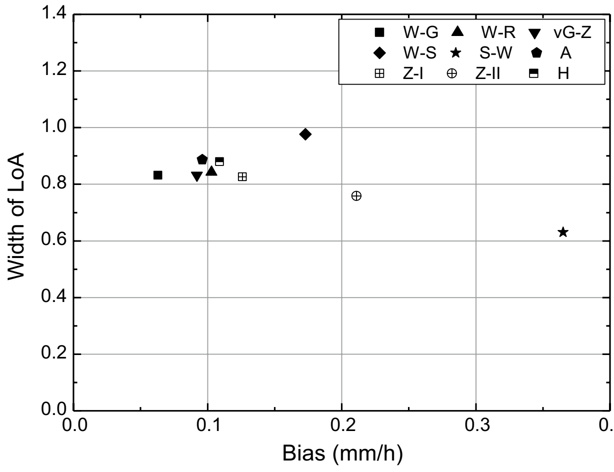

Fig. 6 Limit of agreement versus bias plot for K_s determined from different mathematical equations

For cross-verifying the observations from BAp, a comparison diagram was plotted between K_s determined by different equations and GP measurements as shown in Fig. 7. It can be observed that the equations W–G, W-R, vG–Z, S–W, A, Z-II, and H gave the majority of K_s values within 25% variation. The results from BAp indicated a subset of this group of equations, which performed better. Similar to the finding from Fig. 5, it can be noted that the mid-range of K_s exhibited a better match between equations and GP. A few of the December data exhibited overestimation and July data showed underestimation in the higher and lower range of K_s, respectively. The root mean square error (RMSE) of all the equations was estimated by considering GP as the reference value of K_s and is illustrated in Fig. 8. In general, W–S, Z-I, and Z-II equations were found to perform poorly in different locations considered in this study. For silt dominant sites S7 and S8, RMSE of all equations was found to be comparable. The above discussion reveals the fact that different mathematical equations can induce variability in K_s for the same measured data of MDI.

Based on all the statistical procedures, the smallest subset of equations identified by BAp (W–G, W-R, vG–Z, A, and H) is recommended for estimating near-surface hydraulic conductivity based on MDI results. Among the equations, W–G, W-R, and A are based on the Wooding's steady-state formulations, whereas vG–Z and H are transient methods. The steady-state equations that determined K_s directly (W–G and W-R) were found to be superior to those which relied on extrapolation (W–S, S–W, Z-I, and Z-II). The equations W–G and W-R are entirely dependent on the measured results of MDI and do not depend on any estimated soil parameters. The results from W–G and W-R were found to be similar, thereby ruling out the influence of small disc radius of MDI on hydraulic conductivity determination based on W–G (Weir 1987) for the soils considered in this study. For transient state equations (vG–Z and H), extrapolation of K to K_s was found to yield satisfactory results. The adequacy of vG–Z equation indicates that neglecting the effect of sorptivity in K determination was not erroneous for the soils in the study area. The W–S equation was found to grossly overestimate K_s as compared to GP measurements. This can be attributed to the overestimation of the sorptivity parameter used in W–S equation (Jacques et al. 2002). According to Zhang (1997a), the accuracy of sorptivity is less for smaller measurement duration. The factors f_1

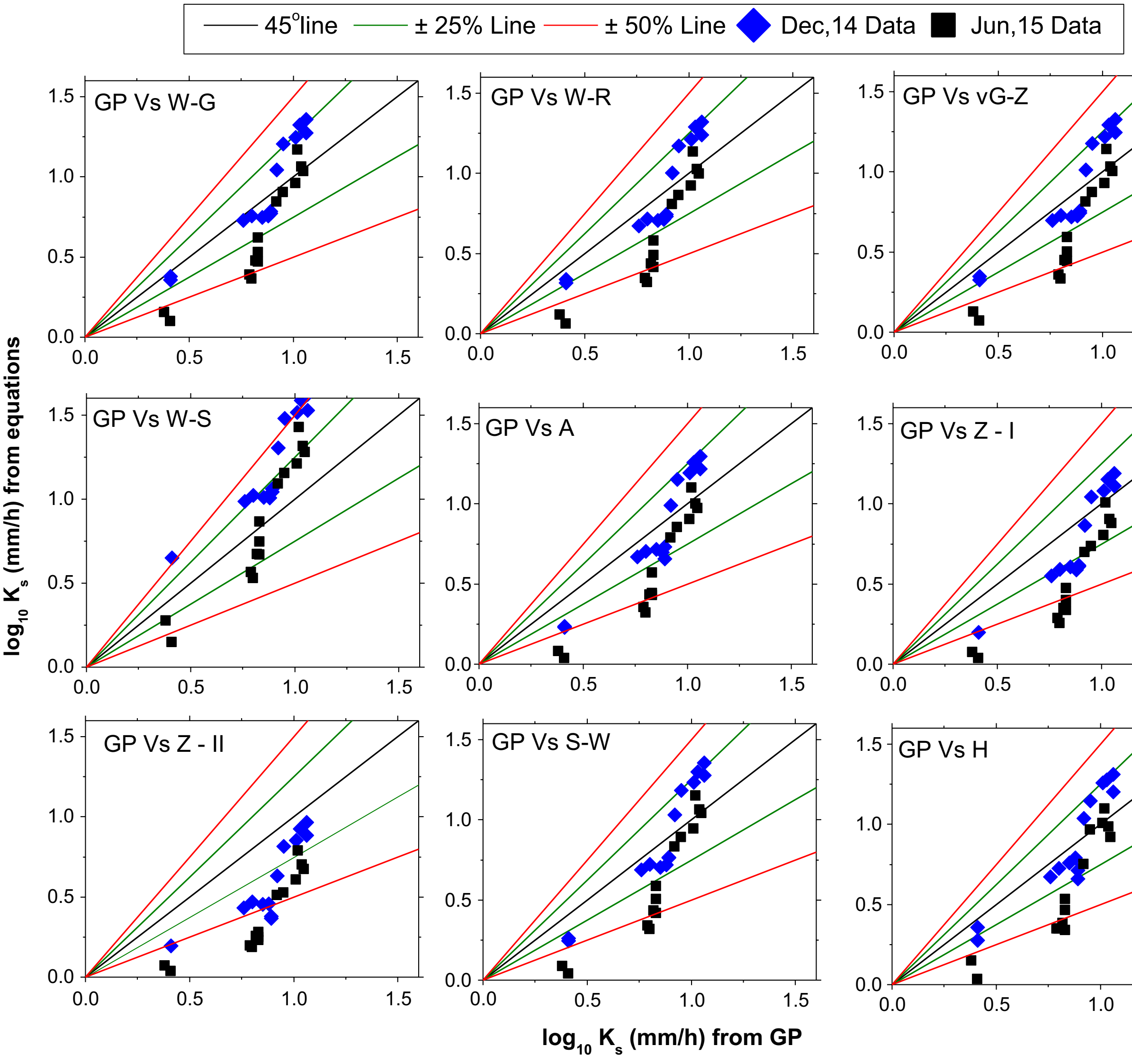

Fig. 7 Comparison of hydraulic conductivity estimated from MDI and GP measurements

and f_2 used in Z-I and Z-II equations would have resulted in the underestimation of K_s as compared to GP measurements. The role of soil type in deciding the appropriate equation for MDI analysis is not explicit from this study. This would necessitate the formulation of an extensive measured database and using data analytics tools such as artificial intelligence (Garg et al. 2017a) as well as optimization methods (Garg et al. 2017b, c).

Conclusion

The present study performed a critical evaluation of nine mathematical equations for determining near-surface saturated hydraulic conductivity (K_s) based on mini-disc infiltrometer (MDI) measurements corresponding to different field conditions. A well-established Guelph permeameter (GP) was used as a reference measurement for K_s in the field. The nine equations considered in this study include Wooding–Gardner (W–G), Weir's Refinement (W–R), van Genuchten–Zhang (vG–Z), White and Sully (W–S), Simunek–Wooding (S–W), Ankeny (A), Zhang method-I (Z-I), Zhang method-II (Z-II) and Haverkamp (H). It was noted that the measurements of GP matched well for two consecutive seasons indicating the invariant nature of K_s for a particular soil and pore structure. Unlike GP, MDI measurements in December gave higher K_s as compared to June which can be attributed to the sensitivity of MDI measurements to surface pore structural changes with seasons.

The statistical difference between K_s determined from GP and different mathematical equations (using MDI results) was assessed quantitatively by using Bland–Altman

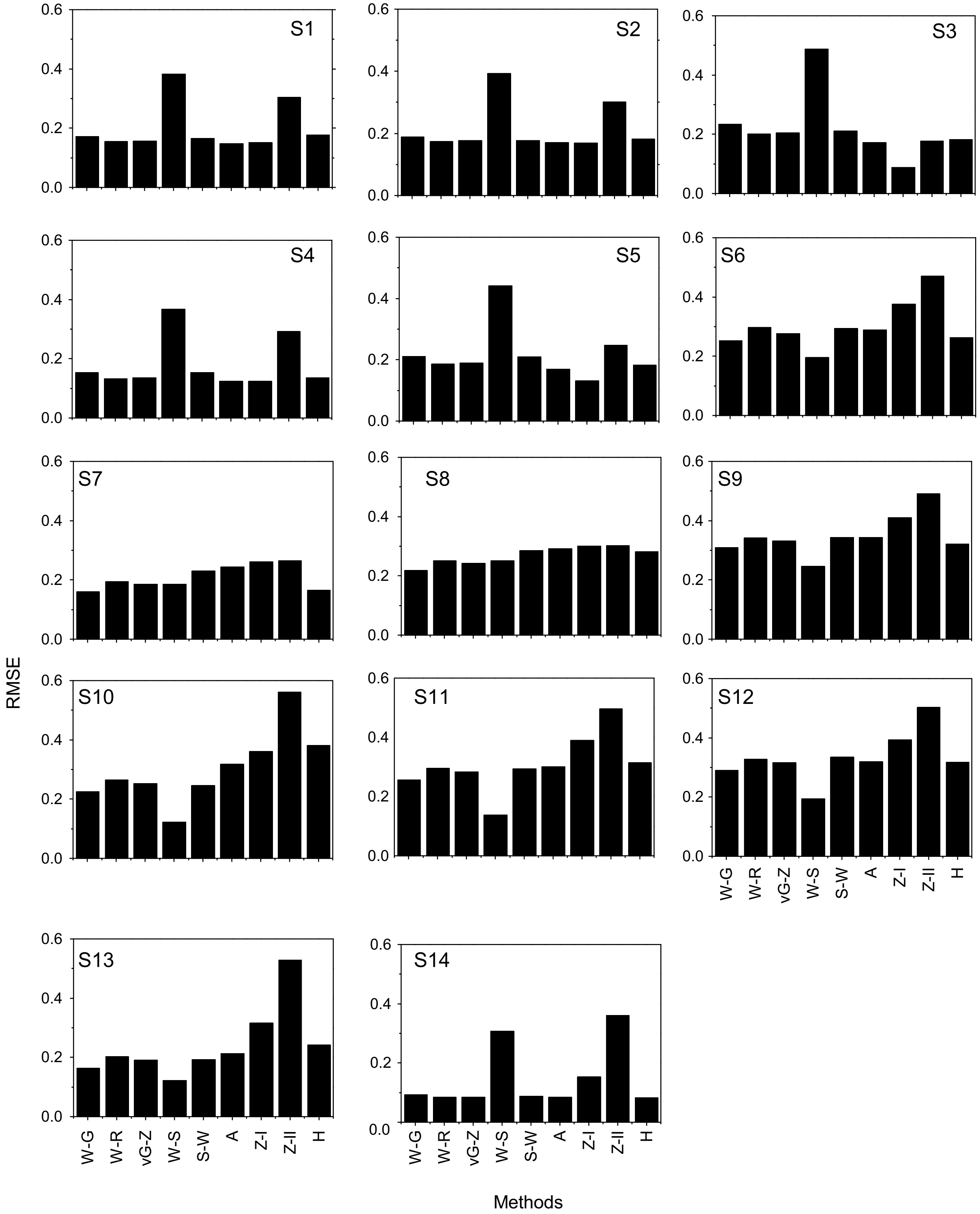

Fig. 8 RMSE of saturated hydraulic conductivity estimated from different mathematical equations based on MDI results

plot (BAp), Pearson's correlation coefficient and root mean square error (RMSE). Analysing the limits of agreement (LoA) and bias used in BAp, it was noted that K_s determined by W–G, W-R, vG–Z, A, and H equations compared well with the results of GP. The BAp also revealed a systematic difference in K_s determined from equations and GP results. For those equations with low bias, the mid-range values of K_s exhibited a better comparison with GP results as compared to higher and lower range of K_s. The impact of the systematic difference of K_s determined from different equations and GP results on the modelling of various hydrological processes needs to be investigated in detail.

The K_s determined from different equations exhibited a fair and comparable correlation with GP measurements with the Pearson correlation coefficient ranging from 0.81 to 0.88. Hence, the correlation coefficient was not an effective method for evaluating the appropriateness of the equation for determining K_s. For example, in the case of the W–S equation, even though the Pearson coefficient was 0.84, and the bias and *p* value indicated that there is a marginal comparison of K_s with GP. From the comparison plot, it was observed that W–G, W-R, vG–Z, S–W, A, Z-II, and H gave the majority of K_s values within 25% variation. W–S equation was found to grossly overestimate, and Z-I underestimates K_s as compared to GP measurements. Based on RMSE, equations W–S, Z-I, and Z-II were found to perform poorly. For those locations where the soil is predominantly silt, gave comparable RMSE for all equations. Considering all the statistical procedures, the smallest subset of equations given by BAp (W–G, W-R, vG–Z, A, and H equations) is recommended as the most reliable mathematical equations that can be used for estimating K_s based on MDI results. The reliability of MDI measurement for determining near-surface near-saturated hydraulic conductivity can be improved by choosing the correct mathematical equation for analysing the results. The role of soil type on deciding the appropriateness of the mathematical equation for MDI analysis needs to be investigated further.

Compliance with ethical standards

Conflict of interest On behalf of all authors, the corresponding author states that there is no conflict of interest.

References

Angulo-Jaramillo R, Vandervaere J, Roulier S, Thony J, Gaudet J, Vauclin M (2000) Field measurement of soil surface hydraulic properties by disc and ring infiltrometers-a review and recent developments. Soil Tillage Res 55:1–29

Angulo-Jaramillo R, Bagarello V, Iovino M, Lassabatere L (2016) Infiltration measurements for soil hydraulic characterization. Springer, Switzerland

Ankeny MD, Ahmed M, Kaspar TC, Horton R (1991) Simple field method for determining unsaturated hydraulic conductivity. Soil Sci Soc Am J 55:467–470

ASTM D 2216 (2010) Standard test methods for laboratory determination of water (moisture) content of soil and rock by mass. ASTM International, West Conshohocken

ASTM D 2487 (2011) Standard practice for classification of soils for engineering purposes (Unified Soil Classification System). ASTM International, West Conshohocken

ASTM D 6938 (2015) Standard test methods for in-place density and water content of soil and soil-aggregate by nuclear methods (Shallow Depth). ASTM International, West Conshohocken

ASTM D 7928 (2017) Standard test method for particle-size distribution (gradation) of fine-grained soils using the sedimentation (hydrometer) analysis. ASTM International, West Conshohocken

ASTM D 854 (2014) Standard test methods for specific gravity of soil solids by water pycnometer. ASTM International, West Conshohocken

Bagarello V, Giordano G (1999) Comparison of procedures to estimate steady flow rate in field measurement of saturated hydraulic conductivity by the guelph permeameter method. J Agric Eng Res 74(1):63–71

Bean EZ, Hunt WF, Bidelspach DA (2007) Field survey of permeable pavement surface infiltration rates. J Irrig Drain Eng 133(3):249–255

Bouwer H (1969) Planning and interpreting soil permeability measurements. J Irrig Drain Div Proc Am Soc Civil Eng 95(3):391–402

Braždžionytė J, Macas A (2007) Bland–Altman analysis as an alternative approach for statistical evaluation of agreement between two methods for measuring hemodynamics during acute myocardial infarction. Medicina 43:208–214

Buckland GD (1988) Graph for estimating field scale hydraulic conductivity sampling requirements. Can Agric Eng 30:323–324

Carsel RF, Parrish RS (1988) Developing joint probability distribution of soil water retention characteristics. Water Resour Res 24:755–769

Chahinian N, Moussa R, Andrieux P, Voltz M (2005) Comparison of infiltration models to simulate flood events at the field scale. J Hydrol 306(1):191–214

Chahinian N, Moussa R, Andrieux P, Voltz M (2006) Accounting for temporal variation in soil hydrological properties when simulated surface runoff on tilted plots. J Hydrol 326:135–152

David MF, César GC (2009) New method for monitoring soil water infiltration rates applied to a disc infiltrometer. J Hydrol 379:315–322

Dohnal M, Dusek J, Vogel T (2010) Improving hydraulic conductivity estimates from minidisc infiltrometer measurements for soils with wide pore-size distributions. Soil Sci Soc Am J 74(3):804–811

Elrick DE, Reynolds WD (1992) Methods of analyzing constant head well permeameter data. Soil Sci Soc Am J 56:320–323

Elrick DE, Reynolds WD, Tan KA (1989) Hydraulic conductivity measurements in the unsaturated zone using improved well analyses. Ground Water Monitor Rev 9(3):184–193

Gadi VK, Tang Y-R, Das A, Monga C, Garg A, Berretta C, Sahoo L (2017) Spatial and temporal variation of hydraulic conductivity and vegetation growth in green infrastructures using infiltrometer and visual technique. CATENA 155:20–29

Gardner W (1958) Some steady-state solutions of the unsaturated moisture flow equation with application to evaporation from a water table. Soil Sci 85:228–232

Garg A, Li J, Hou J, Berretta C, Garg A (2017a) A new computational approach for estimation of wilting point for green infrastructure. Measurement 111:351–358

Garg A, Vijayaraghavan V, Zhang J, Lam JSL (2017b) b) Robust model design for evaluation of power characteristics of the cleaner energy system. Renew Energy 112:302–313

Garg A, Vijayaraghavan V, Zhang J, Li S, Liang X (2017c) Design of robust battery capacity model for electric vehicle by incorporation of uncertainties. Int J Energy Res 41(10):1436–1451

Ghosh B, Sreeja P (2019) A critical evaluation of measurement induced variability in infiltration characteristics for a river sub-catchment. Measurement 132:47–59

Haverkamp R, Ross PJ, Smettem KRJ, Parlange JY (1994) Three–dimensional analysis of infiltration from the disc infiltrometer. Water Resour Res 30:2931–2935

Haverkamp RF, Bouraoui C, Zammit R, Angulo-Jaramillo R, Delleur JW (1999) Soil properties and moisture movement in the unsaturated zone. In: Delleur JW (ed) The handbook of groundwater engineering. CRC, Boca Raton, pp 2931–2935

Haverkamp R, Leij FJ, Fuentes C, Sciortino A, Ross PJ (2005) Soil water retention: I. Introduction of a shape index. Soil Sci Soc Am J 69:1881–1890

Hayashi M, Quinton WL (2004) A constant-head well permeameter method for measuring field-saturated hydraulic conductivity above an impermeable layer. Can J Soil Sci 84:255–264

Hillel D (1998) Environmental soil physics: fundamentals, applications, and environmental considerations. Academic Press, Waltham

Homolák M, Capuliak J, Pichler V, Lichner Ľ (2009) Estimating hydraulic conductivity of a sandy soil under different plant covers using minidisk infiltrometer and a dye tracer experiment. Biologia 64(3):600–604

Hsu SMPE, Ni C-F, Hung P-F (2002) Assessment of three infiltration formulas based on model fitting on richards equation. J Hydrol Eng 7(5):373–379

IS 2720-29 (1975) Methods of test for soils part 29: determination of dry density of soils, in-place by the core-cutter method. Bureau of Indian Standards Publications, New Delhi

Jacques D, Mohanty BP, Feyen J (2002) Comparison of alternative methods for deriving hydraulic properties and scaling factors from single-disc tension infiltrometer measurements. Water Resour Res 38(7):25-1–25-14

Krouwer JS (2002) Setting performance goals and evaluating total analytical error for diagnostic assays. Clin Chem 48(6):919–927

Latorre B, Peña C, Lassabatere L, Angulo-Jaramillo R, Moret-Fernández D (2015) Estimate of soil hydraulic properties from disc infiltrometer three-dimensional infiltration curve. Numerical analysis and field application. J Hydrol 527:1–12

Lee RS, Welker AL, Traver RG (2016) Modeling soil matrix hydraulic properties for variably-saturated hydrologic analysis. J Sustain Water Built Environ 2(2):04015011

Logsdon SD, Jaynes DB (1993) Methodology for determining hydraulic conductivity with tension infiltrometers. Soil Sci Soc Am J 57:1426–1431

METER Group Inc. USA (2018) Mini Disc Infiltrometer User's Manual. 10564-11, Meter Group, 2365 Northeast Hopkins Court, Pullman, WA 99163, USA

McKenzie N, Coughlan K, Cresswell H (2002) Soil physical measurement and interpretation for land evaluation. Australian soil and land survey handbooks series. CSIRO Publishing, Clayton

Mishra SK, Tyagi JV, Singh VP (2003) Comparison of infiltration models. Hydrol Process 17(13):2629–2652

Morbidelli R, Saltalippi C, Flammini A, Cifrodelli M, Picciafuoco T, Corradini C, Govindaraju RS (2017) In situ measurements of soil saturated hydraulic conductivity: assessment of reliability through rainfall–runoff experiments. Hydrol Process 31:3084–3094

Nielsen DR, Biggar JW, Erh KT (1973) Spatial variability of field-measured soil-water properties. Hilgardia 42(7):215–260

Pitt R, Chen SE, Clark SE, Swenson J, Ong CK (2008) Compaction's impacts on urban storm-water infiltration. J Irrig Drain Eng 134(5):652–658

Revol P, Clothier BE, Mailhol JC, Vachaud G, Vauclin M (1997) Infiltration from a surface point source and drip irrigation 2. An approximate time-dependent solution for wet-front position. Water Resour Res 33(8):1869–1874

Reynolds WD, Elrick DE (1985) In situ measurement of field-saturated hydraulic conductivity, sorptivity and α-parameter using the Guelph permeameter. Soil Sci 140:292–302

Reynolds WD, Elrick DE, Clothier BE (1985) The constant head well permeameter: effect of unsaturated flow. Soil Sci 139:172–180

Reynolds WD, Elrick DE, Youngs EG (2002) Single-ring and double-or-concentric-ring infiltrometer. In: Dane JH, Topp GC (eds) Methods of soil analysis. Soil Science Society of America, Madisson, pp 821–826

Ronayne MJ, Houghton TB, Stednick JD (2012) Field characterization of hydraulic conductivity in a heterogeneous alpine glacial till. J Hydrol 458–459:103–109

Salverda AP, Dane JH (1993) An examination of the Guelph permeameter for measuring the soil's hydraulic properties. Geoderma 57(4):405–421

Sihag P, Tiwari NK, Ranjan S (2017) Estimation and inter-comparison of infiltration models. Water Sci 31(1):34–43

Šimunek J, van Genuchten MT, Gribb MM, Hopmans JW (1998) Parameter estimation of unsaturated soil hydraulic properties from transient flow processes. Soil Tillage Res 47:27–36

van Genuchten MT (1980) A closed-form equation for predicting the hydraulic properties of unsaturated soils. Soil Sci Soc Am J 44:892–898

Vandervaere J-P, Vauclin M, Elrick DE (2000) Transient flow from tension infiltrometers-I: the two-parameter equation. Soil Sci Soc Am J 64(4):1263–1272

Verbist KMJ, Cornelis WM, Torfs S, Gabriels D (2013) Comparing methods to determine hydraulic conductivities on stony soils. Soil Sci Soc Am J 77(1):25–42

Wang D, Yates SR, Lowery B, van Genuchten MT (1998) Estimating soil hydraulic properties using tension infiltrometer with varying disc diameters. Soil Sci 163(5):356–361

Weir GJ (1987) Steady infiltration from small shallow circular ponds. Water Resour Res 23(4):733–736

White I, Sully MJ (1987) Macroscopic and microscopic capillary length and time scales from field infiltration. Water Resour Res 23:1514–1522

White I, Sully MJ, Perroux KM (1992) Measurement of surface-soil hydraulic properties: disc permeameters, tension infiltrometers and other techniques. In: Topp CG, Reynolds WD, Green RE (eds) Advances in measurement of soil physical properties: bringing theory into practice. Soil Science Society of American Journal of Special Publication 30, SSSA, Madisson, pp 69–103

Wooding RA (1968) Steady infiltration from large shallow circular pond. Water Resour Res 4:1259–1273

Zhang R (1997a) Determination of soil sorptivity and hydraulic conductivity from the disc infiltrometer. Soil Sci Soc Am J 61:1024–1030

Zhang R (1997b) Infiltration models for the disc infiltrometer. Soil Sci Soc Am J 61:1597–1603

Zhang R (1998) Estimating soil hydraulic conductivity and macroscopic capillary length from the disc infiltrometer. Soil Sci Soc Am J 62:1513–1521

Zhang R, van Genuchten MT (1994) New models for unsaturated soil hydraulic properties. Soil Sci 158:77–85

Zhou SM, Warrington DN, Lei TW, Lei Q-X, Zhang M-L (2015) Modified CN method for small watershed infiltration simulation. J Hydrol Eng 20(9):04014095

Acta Geophysica (2019) 67:879–889
https://doi.org/10.1007/s11600-019-00279-1

RESEARCH ARTICLE - HYDROLOGY

Quantification of historical drought conditions over different climatic zones of Nigeria

Samuel Ogunjo[1] · **Oluwatobi Ife-Adediran**[1] · **Eunice Owoola**[1] · **Ibiyinka Fuwape**[1,2]

Received: 23 November 2018 / Accepted: 9 March 2019 / Published online: 16 March 2019

Abstract

The impact of extreme climate such as drought and flooding on agriculture, tourism, migration and peace in Nigeria is immense. There is the need to study the trend and statistics for better planning, preparation and adaptation. In this study, the statistical and temporal variation of climatic indices Standardized Precipitation Index (SPI) and Standardized Precipitation Evapotranspiration Index (SPEI) was computed for eighteen (18) stations covering four climatic zones (Sahel, Midland, Guinea Savannah and Coastal) of tropical Nigeria. Precipitation, minimum and maximum temperature from 1980 to 2010 obtained from the archives of the Nigerian Meteorological Services were used to compute both the SPI and SPEI indices at 1-, 3- 6- and 12-month timescales. The temporal variation of drought indices showed that droughts were more prominent at 6- and 12-month timescales. SPI and SPEI were found to be better correlated at longer timescales than short timescales. Predominant small, positive and significant trend across the region suggest an increasing trend due to climate change.

Keywords Climate indices · Standardized Precipitation Index · Standardized Precipitation Evapotranspiration Index · Nigeria · Climate change

Introduction

Drought is an unusual period of dryness as a result of low precipitation or high temperature (Sordo-Ward et al. 2017). A drought event is characterized by a continuous shortage of water due to low rainfall over a period of time (Chen et al. 2009). The occurrence of drought in a location over a long period of time is referred to as severe drought (Muhammad et al. 2017). Droughts have become a consistent global climatic occurrence (Pereira et al. 2009). Intense drought conditions have been linked to the accumulation of greenhouse gases especially from decades of industrial activities (Gudmundsson and Seneviratne 2015; Stocker 2014; Field et al. 2012). Drought events in different regions of the globe vary in intensity (severity or magnitude), frequency of occurrence and duration (Wilhite 1993; Dracup et al. 1980). The effects of drought have far reaching impact on agriculture, ecology, health. Droughts that have direct effects on crop growth and yield as a result of dryness in their roots are referred to as agricultural droughts. Ahmad et al. (2004) reported that agricultural drought occurred in Pakistan during years 2000 and 2001. During the same period, there was a severe drought in North Korea that led to a significant drop in food production (Josserand et al. 2008). Other types of physical droughts are: meteorological and hydrological droughts (Khan et al. 2018). Keyantash and Dracup (2002) described a non-physical form of drought referred to as socioeconomic drought. Blain (2012) emphasized the slowly accumulating effect of drought and the need for its early detection. Notably, there is an expected increase in the severity, spread and effect of drought in some African countries by 2020 (Pachauri and Reisinger 2008) and increase in politically neglected people (Detges 2017).

Several indices have been developed to quantify the effect and impact of drought. These include the Standardized Precipitation Index (SPI), Standardized Precipitation Evapotranspiration Index (SPEI), Percent of Normal (PN), Effective Drought Index (EDI), Surface Water Supply Index (SWSI), Palmer Drought Severity Index (PSDI),

---

✉ Samuel Ogunjo
stogunjo@futa.edu.ng

Ibiyinka Fuwape
iafuwape@futa.edu.ng

[1] Department of Physics, Federal University of Technology, Akure, Ondo State, Nigeria

[2] Present Address: Michael and Cecilia Ibru University, Ughelli, Delta State, Nigeria

Reconnaissance Drought Index (RDI) and Normalized Difference Water Index (NDWI). The choice of a drought index depends on the type of drought as each index in use has its uniqueness and application; some of which were highlighted in Khan et al. (2018) and Mishra and Singh (2010). SPI has an advantage in its usefulness for impact assessment of agricultural droughts (Zargar et al. 2011). Furthermore, the SPI is also recommended for the characterization of meteorological droughts all over the world (Blain 2012). Statistical relationship has been established between some of the indices. Oloruntade et al. (2017) found high correlations values of 0.65 and 0.55 between SPI and SPEI at 3 months and 12 months in the Niger-South Basin area of Nigeria. SPI and SPEI values were found to produce similar droughts characteristics over the Volta basin with a correlation of 0.97 in observed and simulated data (Oguntunde et al. 2017).

The role of large-scale oscillations in continental drought phenomena have been investigated by several authors. Positive correlation has been reported between Atlantic Nino 1 along the coastal regions of West Africa, while a negative correlation prevails in the Sahel region (Adeniyi and Dilau 2018). Ndehedehe et al. (2016) reported that El Nino Southern Oscillation (ENSO), Atlantic Multi-decadal Oscillation and Atlantic Meridional Mode (AMM) are associated with extreme rainfall conditions with statistically significant relationship between Atlantic Multi-decadal Oscillation (AMO) and SPI at 12 months. Coupled ocean–atmosphere phenomena has been found to influence drought events within the Greater Horn of Africa region (Mpelasoka et al. 2018). The role of large-scale oscillation in drought over West Africa was investigated by Ogunjo et al. (2019). The authors reported that Southern Oscillation Index showed positive correlation with drought in the West African region, while Pacific Decadal Oscillation and North Atlantic Oscillation both showed negative correlation with drought in the region.

Estimated drought vulnerability index over Africa during the period 1960–2015 showed that northern African countries such as Egypt, Tunisia and Algeria were the least drought vulnerable countries, and the trend will continue in the future (Ahmadalipour and Moradkhani 2018). Studies on drought over Nigeria have always considered subregions. Report by Oloruntade et al. (2017) showed that the Niger-South basin is dominated by wet conditions in the period 1970–2008. The investigation by Ndehedehe et al. (2016) around the Lake Chad basin showed relatively wet conditions in the last two decades using SPI at 12 month scale. Using data from 1916 to 1987, the length and severity of drought in the northern part of the country were found to vary from sub-area to sub-area with very low interannual persistence (Oladipo 1993). High-resolution, multiproxy paleolimnological record from northeastern Nigeria suggests that abrupt cooling events and intense El Nino Oscillation might have been responsible for prolonged drought in the region (Street-Perrott et al. 2000). Statistical investigation of drought in the savanna region of Nigeria revealed a significant long-term increasing trend in the region (Oladipo 1995). Using the Bhalme and Mooley Drought Index (BMDI) approach, the intensity of drought in the Sudano-Sahelian region of Nigeria, low intensity drought was found to be prevalent in the region from 1948- 2010 (Kayode and Francis 2012)

In this study, we aim to investigate the statistics of drought across the different climatic zones of Nigeria using SPI and SPEI. The correlation between the two drought indices will be investigated, as well as, their regression analysis, trend and frequency distributions. Results from this study are expected to show the comparative drought risks across the different regions in Nigeria and provide information for strategic planning and adaptation.

Methodology

Eighteen locations across the four climatic zones of Nigeria, as described by Adeyemi and Emmanuel (2011), were considered in this study. The geographical coordinates and statistics of the location are presented in Table 1, and the temporal variation of mean regional precipitation is shown in Fig. 1. Stations were chosen based on availability of data in the study period. Monthly precipitation, minimum temperature and maximum temperature data were obtained from the archives of the Nigerian Meteorological Services from 1980 to 2010. To compute the impact of drought, the Standardized Precipitation Index (SPI) and Standardized Potential Evapotranspiration Index (SPEI) were chosen for their simplicity. They require simple and ready to use atmospheric variable, easy to compute and generally recognized as efficient in capturing drought events. To analyze the results, the linear correlation, regression and trend analyses were used. While correlation shows how one variable changes with respect to another, linear regression gives quantitative value to the dependence of a variable on another. Mann–Kendall analysis is used to detect consistently increasing or decreasing trends in a given data. As a nonparametric test, it does not make assumption about the distribution of the data.

The Standardized Precipitation Index (SPI) is based on the use of probability distribution to evaluate the departure of precipitation during a time span from the mean value (Oguntunde et al. 2017). The parameters, α and β, of a gamma distribution obtained are from maximum likelihood estimation when precipitation data are fitted to a gamma distribution given by

$$G(x) = \frac{1}{\beta^{\theta}\Gamma(\theta)} \int_0^x x^{\theta-1} e^{-x/\beta} \mathrm{d}x \tag{1}$$

where $x > 0$, Γ is the gamma function, α and β are the form and scale parameter, respectively. The Standardized Potential evapotranspiration Index is computed in the same way,

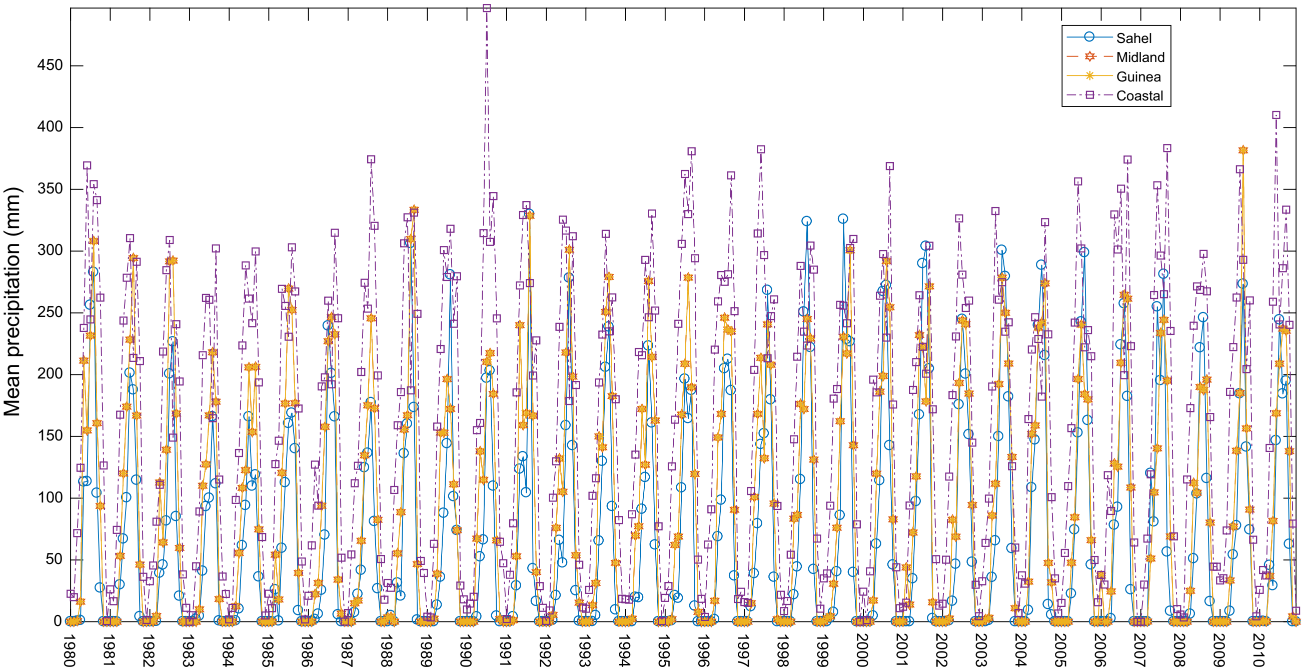

Fig. 1 Mean monthly precipitation across the regions

Table 1 Geographical coordinates and statistics of study locations in the period 1980–2010

Region	Location	Latitude	Longitude	Total (mm)	Mean (mm)	SD
Sahel	Sokoto	13.03	5.12	36,057.0	96.93	116.29
	Maiduguri	11.50	13.10	17,847.7	47.98	75.60
	Kano	12.02	8.32	31,236.3	83.97	130.51
	Katsina	12.51	7.33	15,390.3	41.37	83.50
Midland	Kaduna	10.28	7.25	32,226.0	86.63	112.66
	Minna	9.38	6.31	37,312.2	100.30	106.65
	Yola	9.15	12.30	27,500.9	73.93	84.38
Guinea Savannah	Lokoja	7.47	6.37	38,280.5	102.90	101.79
	Markudi	7.45	8.53	36,528.8	98.20	109.41
	Warri	5.52	5.75	85,674.7	230.31	189.02
Coastal	Lagos	6.61	3.62	50,944.4	136.95	146.50
	Akure	7.25	5.19	44,495.6	119.61	94.67
	Port Harcourt	4.41	6.59	71,602.6	192.48	147.79
	Owerri	5.27	6.59	73,599.8	197.85	161.34
	Enugu	6.27	7.29	53,822.4	144.68	131.01
	Calabar	4.58	8.21	90,572.6	243.47	181.65
	Ogoja	6.66	8.79	58,444.0	157.11	148.04
	Abeokuta	7.15	5.15	36,002.0	100.01	90.81

however, with the consideration of potential evapotranspiration (Oguntunde et al. 2017; Oloruntade et al. 2017). In the computation of SPEI, the difference between precipitation and potential evapotranspiration is used instead of precipitation in SPI. To compute the potential evapotranspiration, the method proposed by Thornthwaite (1948) was used because of its simplicity. The drought indices are classified as

$$\mathrm{SPI} = \begin{cases} \mathrm{SPI} \geq 2.00, & \text{Extremely wet (EW);} \\ 1.50 \leq \mathrm{SPI} < 2.00, & \text{Very wet (VW);} \\ 1.00 \leq \mathrm{SPI} < 1.50, & \text{Moderately wet (MW);} \\ -1.00 \leq \mathrm{SPI} < 1.00, & \text{Near Normal (NN);} \\ -1.50 \leq \mathrm{SPI} < -1.00, & \text{Moderately drought (MD);} \\ -2.00 \leq \mathrm{SPI} < -1.50, & \text{Severely drought (SD);} \\ \mathrm{SPI} < -2.00, & \text{Extreme drought (ED).} \end{cases} \tag{2}$$

Correlation coefficient shows the degree of association between two variables. The Pearson's correlation coefficient, ρ is defined as

$$\rho = \frac{\sum_{i=1}^{n}(x_i - \bar{x})(y_i - \bar{y})}{\sqrt{\sum_{i=1}^{n}(x_i - \bar{x})^2 \sum_{i=1}^{n}(y_i - \bar{y})^2}} \tag{3}$$

The values of ρ in the ranges $-1 \leq \rho \leq 0$ and $0 \leq \rho \leq 1$ represent positive and negative correlation, respectively. If $\rho = 0$, the two time series are said to be uncorrelated. The linear relationship between SPI and SPEI was computed using the regression analysis. Regression analysis shows the dependence of a variable on another (Fuwape and Ogunjo 2018). A simple linear regression is of the form $y = ax + b$, where x and y are the independent and dependent variable, respectively, a and b are constants to be determined by minimizing the function

$$Q = \sum_{i=1}^{n} \left(y_i - (ax_i + b)\right) = 0 \tag{4}$$

The Mann–Kendall test statistics S is based on the pairwise comparison of each data points with all preceding data points.

$$S = \sum_{k=1}^{n-1} \sum_{j=k+1}^{n} sgn(x_j - x_k) \tag{5}$$

where n is the length of the time series $x_1, \ldots, x_n$, $sgn(\cdot)$ is a sign function, while x_j and x_k are values in years. The variance of S is computed as:

$$\sigma^2(S) = \frac{1}{18}\left[n(n-1)(2n+5) - \sum_{p=1}^{q} t_p(t_p - 1)(2t_p + 5)\right] \tag{6}$$

where q is the number of tied groups and t_p is the number of data values in the pth group (Oguntunde et al. 2017; Fuwape and Ogunjo 2018). The test statistic Z obtained as:

$$Z = \begin{cases} \frac{S-1}{\sqrt{\sigma^2(S)}}, & \text{if } S > 0; \\ 0, & \text{if } S = 0; \\ \frac{S+1}{\sqrt{\sigma^2(S)}}, & \text{if } S < 0. \end{cases} \tag{7}$$

If the trend of a time series is assumed to be linear and of the form $f(t) = Qt + B$, Sen slope (Q) can be estimated from the expression

$$Q_i = \frac{x_j - x_k}{j - k} \tag{8}$$

where $j > k$. The Sen estimate of the slope is the median value of Q_i (Oguntunde et al. 2017; Fuwape and Ogunjo 2018).

Results and discussion

The temporal evolution of mean SPI and SPEI values at 1-, 3-, 6- and 12-month timescales is presented in Figs. 2, 3, 4 and 5, respectively. The SPEI values at 1-month in the Sahel and Midland region showed periodic occurrences which can be attributed to the short but intense dry seasons experienced in the regions (Fig. 2a, b). The drought intensity in these regions tends to be higher than the intensity in the Guinea Savannah and Coastal regions. At 3-month scale (Fig. 3), the seemingly periodicity in mean SPI/SPEI values persists in the Sahel but not in the Midlands. A significant drought event could be seen in 1982–1983 in the Coastal region. Considering the temporal variation of the indices at 6- and 12-month timescales, periodicity was no more obvious in the Sahel region. Prominent drought regimes and general agreement between SPI and SPEI could be observed in 1983, 1990, 1992/93 and 2004. The drought periods observed are in agreement with reported drought periods in the region (Oguntunde et al. 2017; Ndehedehe et al. 2016).

The linear correlation between SPI and SPEI at different timescales (1, 3, 6, 12) for the locations in each climatic zones is presented in Table 2. In the Sahel region, the strongest was observed at 12-month. Maiduguri has the lowest correlation values at both 3- and 6-month scales, while Sokoto and Katsina have the lowest correlation values between SPI and SPEI at 1- and 12-month scale, respectively. In the Midland area, Kaduna has the highest correlation values between SPI and SPEI, while the lowest correlation values were observed in Yola. Warri, in the Guinea savannah, was found to have the highest correlation values for the region at all scales. The lowest correlation values were obtained at the 1-month scale. An unusually low correlation value was observed at 3-month scale for Calabar in the coastal region. The correlation values were observed to increase in the progression Sahel–Midland area–Guinea Savanna–coastal area. This increasing trend could be attributed to the reducing effect of evapotranspiration as one moves from the northern region to the coastal area of the country. In a study over the Niger-South basin of Nigeria, (Oloruntade et al. 2017) obtained correlation in the range 0.56–0.66. The study by Oloruntade et al. (2017) used gridded dataset produced by the Climate Research Unit, University of East Anglia for the period 1970–2008, while our investigation considered in situ data from the Nigerian Meteorological Services for the period for the period 1980–2010. This range is lower than the values obtained in this work for the same region.

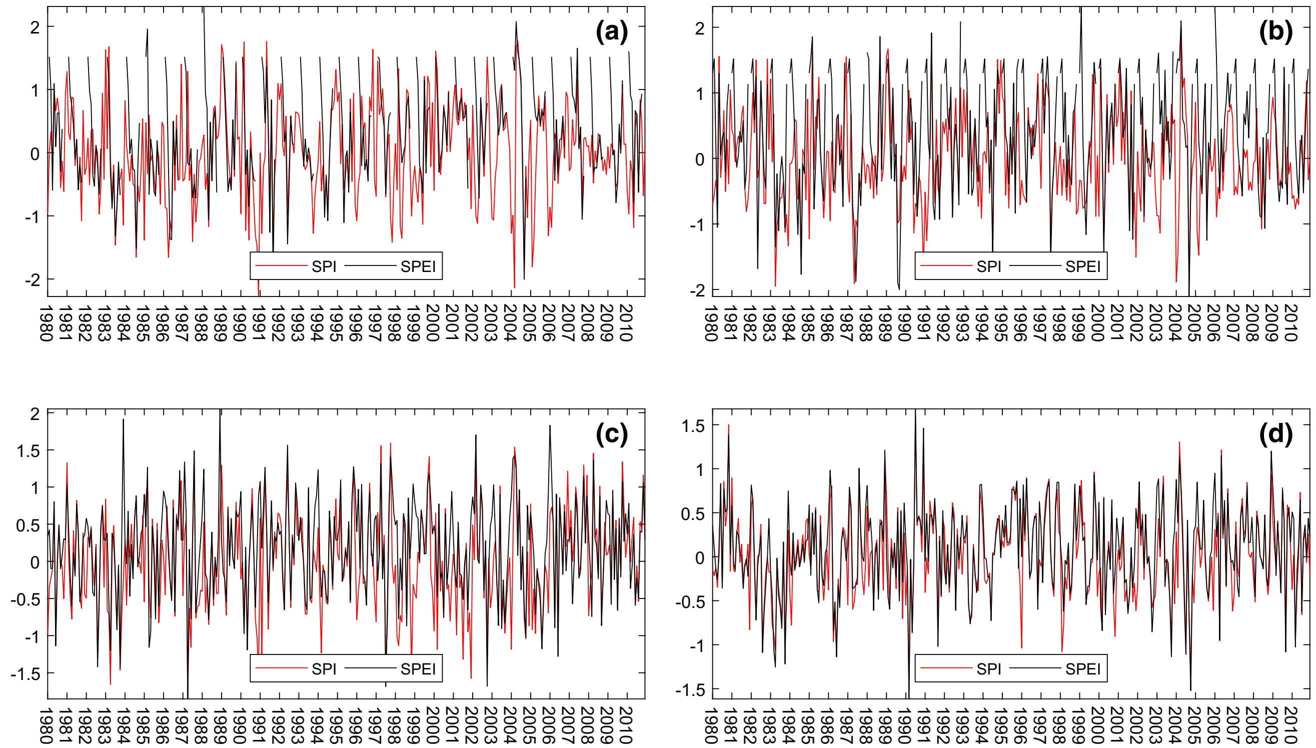

Fig. 2 Mean SPI and SPEI values for **a** Sahel, **b** Midland, **c** Guinea Savanna and **d** Coastal regions at 1-month timescale

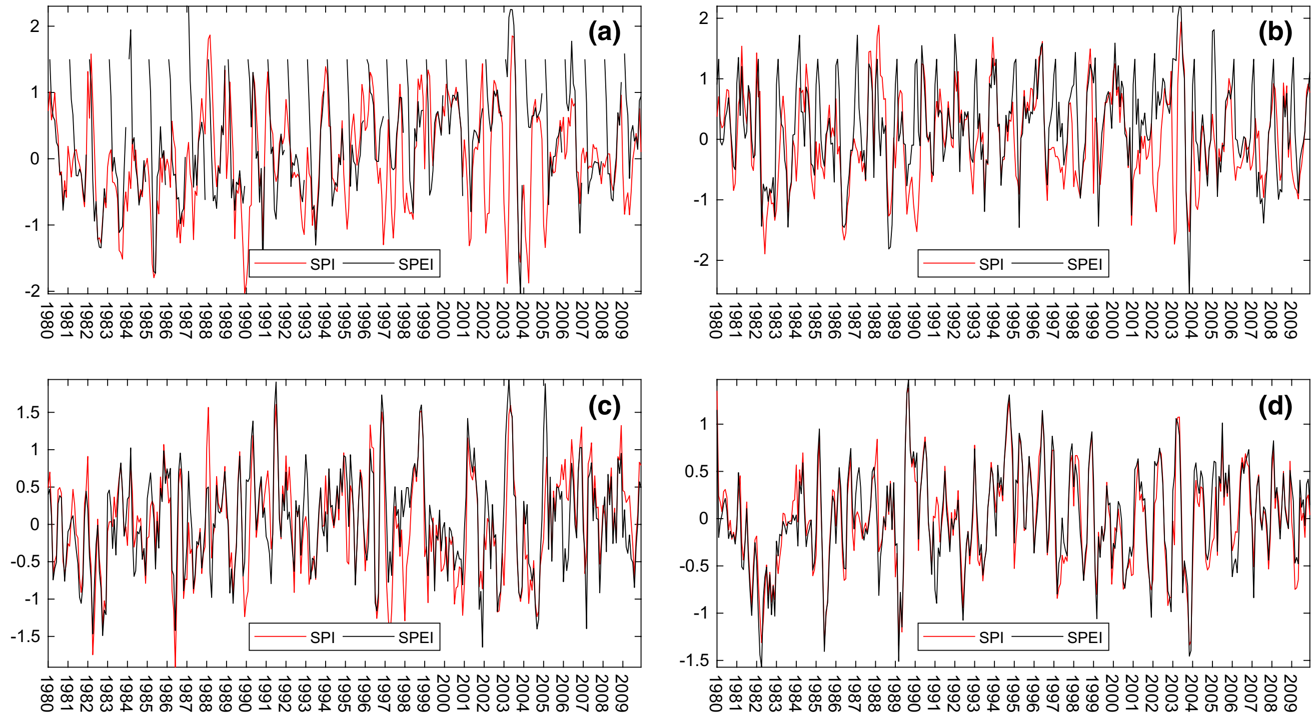

Fig. 3 Mean SPI and SPEI values for **a** Sahel, **b** Midland, **c** Guinea Savanna and **d** Coastal regions at 3-month timescale

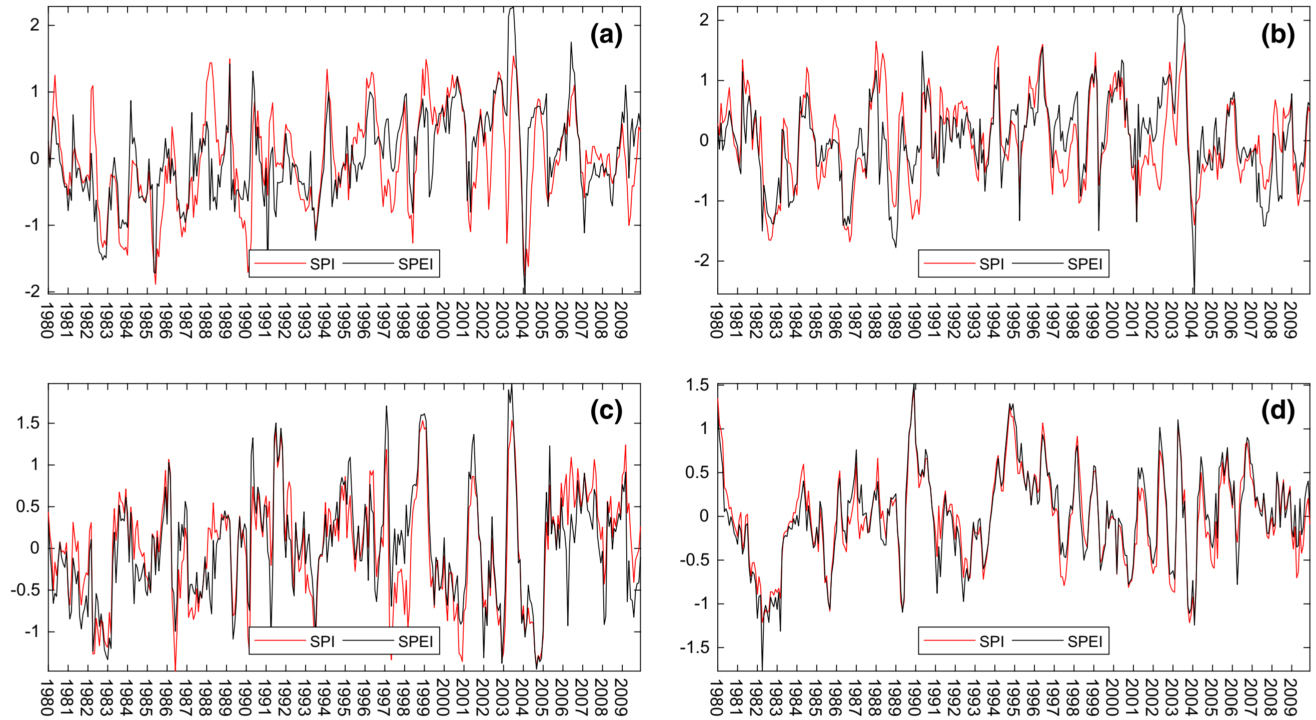

Fig. 4 Mean SPI and SPEI values for **a** Sahel, **b** Midland, **c** Guinea Savanna and **d** Coastal regions at 6-month timescale

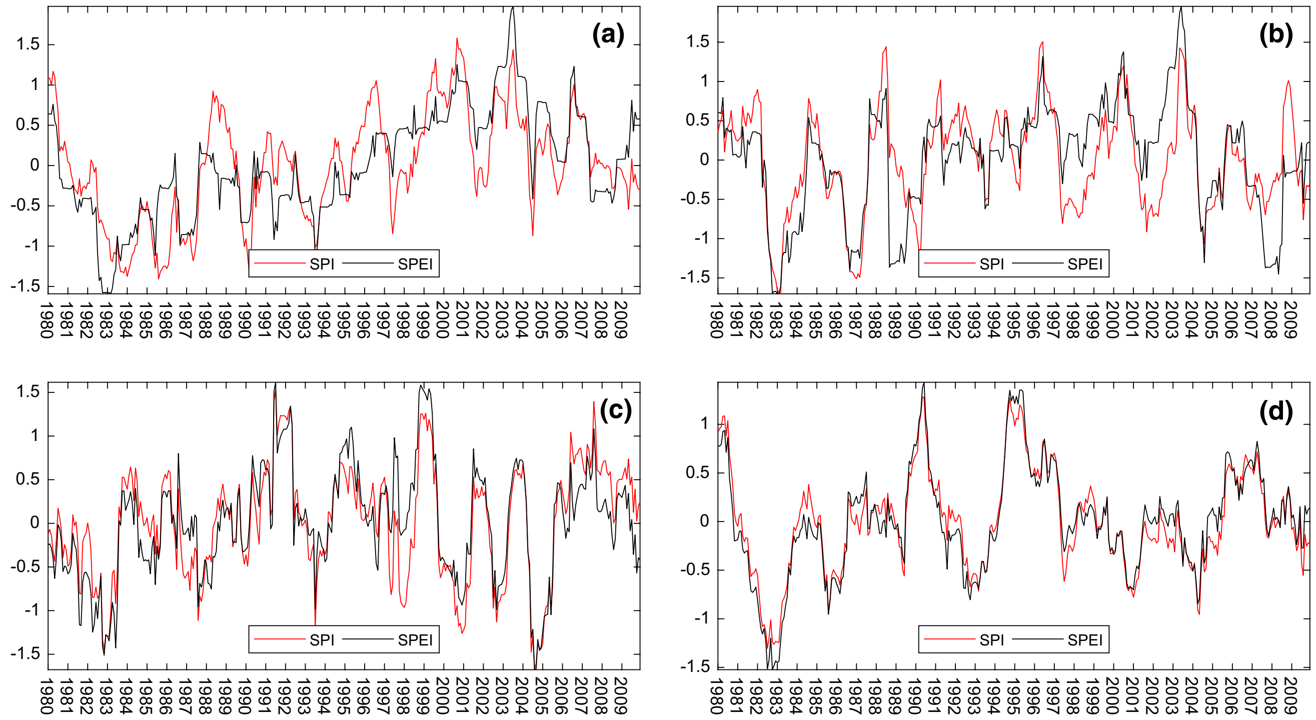

Fig. 5 Mean SPI and SPEI values for **a** Sahel, **b** Midland, **c** Guinea Savanna and **d** Coastal regions at 12-month timescale

The differences can be attributed to different data sources and time range. SPI and SPEI have better comparative performance at longer timescales than shorter durations.

A linear regression of the two indices showed the same trend as correlation analysis (Table 3). The best fit in the Sahel region was found in Kano at 12-month

Table 2 Linear correlation between SPI and SPEI for different locations at different timescales (month)

Region	Location	Scale			
		1	3	6	12
Sahel	Sokoto	0.607	0.631	0.734	0.787
	Maiduguri	0.651	0.609	0.645	0.736
	Kano	0.699	0.693	0.783	0.899
	Katsina	0.712	0.649	0.667	0.733
Midland	Kaduna	0.726	0.706	0.830	0.869
	Minna	0.650	0.718	0.792	0.781
	Yola	0.639	0.548	0.622	0.542
Guinea Savannah	Lokoja	0.765	0.793	0.855	0.877
	Markudi	0.685	0.791	0.876	0.922
	Warri	0.932	0.955	0.958	0.946
Coastal	Lagos	0.899	0.928	0.944	0.956
	Akure	0.860	0.847	0.876	0.858
	Port Harcourt	0.932	0.908	0.935	0.954
	Owerri	0.915	0.924	0.939	0.939
	Enugu	0.796	0.876	0.942	0.953
	Calabar	0.945	0.069	0.974	0.973
	Ogoja	0.822	0.870	0.936	0.949
	Abeokuta	0.827	0.849	0.861	0.859

scale with slope and r^2 values close to 1. The weakest fits were observed in Sokoto at 1- and 3-month scales. The regression fit for the Sahel region showed better fit at 12-month scale compared to other scales. In the Midland region, the worst regression fit could be found in Yola. The location has the lowest slope and r^2 values for the region. The performance of the fit was better in the Guinea Savannah and the Coastal region. Calabar showed perfect fits with good coefficient of determination for the Coastal region. The Guinea Savannah and Coastal regions of Nigeria have longer wet seasons, short dry seasons and larger amount of precipitation than the Midland and Sahel region.

Trend over the study period was computed for SPI and SPEI (Table 4) using Mann–Kendall algorithm. Trends in SPI and SPEI at all timescales were in the range −0.00349 –0.00587 and −0.00135–0.007, respectively. The trend values obtained for SPI are less than the range of −0.026–0.011 obtained in Southern Portugal at 12-month timescale (Costa 2011). In the Sahel region, all locations exhibit positive trends at all timescales except Sokoto which has negative trends. In the Midland region, Minna has positive trends at all timescales, while the other two locations in the region showed negative trends. In the Guinea Savannah, Warri is the exception with negative trend at all timescales, while in the Coastal region, Lagos, Akure and Owerri are the stations with negative trends. The varying trend signs within regions are attributed to local dynamics and topography. Locations in all the regions have the same trend sign in both SPI and SPEI except Markudi, Warri and Akure at the 1-month

Table 3 Linear regression between SPI and SPEI for different locations at different timescales (month)

Region	Location	Regression slope				r^2			
		Scale				Scale			
		1	3	6	12	1	3	6	12
Sahel	Sokoto	0.634	0.656	0.752	0.804	0.369	0.398	0.538	0.619
	Maiduguri	0.645	0.612	0.644	0.753	0.424	0.371	0.417	0.542
	Kano	0.681	0.663	0.760	0.916	0.488	0.481	0.614	0.809
	Katsina	0.667	0.624	0.661	0.748	0.507	0.421	0.445	0.537
Midland	Kaduna	0.758	0.737	0.842	0.888	0.526	0.498	0.689	0.755
	Minna	0.662	0.697	0.802	0.781	0.423	0.516	0.627	0.610
	Yola	0.655	0.567	0.636	0.556	0.408	0.300	0.387	0.294
Guinea Savannah	Lokoja	0.727	0.763	0.871	0.897	0.586	0.629	0.731	0.769
	Markudi	0.632	0.746	0.886	0.941	0.470	0.626	0.767	0.851
	Warri	0.901	0.955	0.978	0.964	0.868	0.913	0.918	0.895
Coastal	Lagos	0.850	0.930	0.960	0.980	0.808	0.861	0.892	0.913
	Akure	0.800	0.852	0.889	0.874	0.740	0.718	0.768	0.736
	Port Harcourt	0.914	0.927	0.951	0.976	0.869	0.824	0.874	0.909
	Owerri	0.883	0.937	0.952	0.960	0.837	0.855	0.882	0.883
	Enugu	0.742	0.877	0.968	0.976	0.634	0.768	0.887	0.908
	Calabar	0.921	1.000	1.000	1.000	0.893	0.939	0.949	0.948
	Ogoja	0.755	0.861	0.953	0.966	0.676	0.756	0.966	0.901
	Abeokuta	0.788	0.854	0.887	0.880	0.685	0.721	0.741	0.739

Table 4 Trend analysis for SPI and SPEI for different locations at different timescales (month)

Region	Location	SPI				SPEI			
		Scale				Scale			
		1	3	6	12	1	3	6	12
Sahel	Sokoto	– 0.00159	– 0.00214	– 0.00255[a]	– 0.00349[a]	– 0.00047	– 0.00071	– 0.00082	– 0.00135
	Maiduguri	0.0004	0.00107	0.00207	0.00354	0.00288	0.00373	0.00431	0.00645
	Kano	0.00132	0.00225	0.0037	0.00587	0.00403	0.00444	0.00474	0.007
	Katsina	0.00142	0.0024	0.00345	0.00457	0.00188	0.00273	0.00294	0.00356
Midland	Kaduna	– 0.00026	– 0.00057	– 0.00069	– 0.00095	– 0.00047	– 0.00071	– 0.00082	– 0.00135
	Minna	0.00082	0.00131	0.00222	0.00362[a]	0.00124	0.00192	0.00325	0.00517
	Yola	– 0.00094	– 0.00099	– 0.00142[a]	– 0.00201[a]	– 0.00024	– 0.00001	0.00008	– 0.00013
Guinea Sav.	Lokoja	0.00169	0.00249	0.00308	0.00369	0.00092	0.00176	0.00275	0.00377
	Markudi	– 0.00005	0.00024	0.00075	0.00082	0.00014	0.00055	0.00108	0.00095
	Warri	– 0.00002	– 0.00058	– 0.00094	– 0.00148	0.00007	– 0.00039	– 0.00075	– 0.00099
Coastal	Lagos	– 0.00008	– 0.00005	– 0.0002	– 0.00069	– 0.00001	0.00022	0.00009	– 0.00026
	Akure	– 0.00079	– 0.00131	– 0.0017	– 0.00211	0.00011	0.00004	– 0.00041	– 0.0006
	Port H.	0.00016	0.00037	0.00024	0.00043	0.00025	0.00063	0.00067	0.0009
	Owerri	– 0.00044	– 0.00062	– 0.00082	– 0.00116	– 0.00003	0.00025	0.00015	0.0001
	Enugu	0.00047	0.00112	0.00116	0.00129	0.0006	0.00133	0.0017	0.00203
	Calabar	0.00063	0.00137	0.00149	0.00172	0.00063	0.00165	0.00183	0.00214
	Ogoja	0.00097	0.00174	0.00227	0.00254	0.00079	0.00146	0.00215	0.00286
	Abeokuta	0.00021	0.00068	0.00126	0.00171	0.00089	0.0016	0.00242	0.00325

Nonsignificant values at 95% confidence interval are represented by [a]

timescale; Lagos, Owerri and Akure at 3-month timescale; Yola, Lagos and Owerri at 6-month timescale; and Owerri at 12-month timescale. All these locations have negative signs in SPI but positive signs in SPEI computation. The trends were found to be significant at 95% confidence interval except locations in Sahel and Midland regions at 1- and 3-month timescale for SPEI and Sokoto, Minna and Yola at 6- and 12-month timescales. The trend values are similar to those obtained in Cyprus by Katsanos et al. (2018) but lower than that reported by Oguntunde et al. (2017) for the same region at 12-month scale. In the report by Oguntunde et al. (2017), a longer period of time was used, different data source as well as a different method of computing the slope was used, and ecological zones were considered rather than climatic zones at only 12-month timescale.

Frequency distribution of SPI and SPEI classes is shown in Tables 5, 6, 7 and 8 at 1-, 3-, 6-, and 12-month timescales, respectively. In the Sahel and Midland regions, the occurrences of near normal events were greater in SPI than SPEI at 1- and 3-month timescales as opposed to the occurrences being greater in SPEI for both Guinea Savannah and Coastal regions. This trend was not noticeable at 6- and 12-month timescales. This implies that both SPI and SPEI have comparative performance at higher timescales than shorter timescales. It can be inferred that atmospheric–land interactions such as El Nino and Atlantic Nino 1 influence drought at short timescales. Atlantic Nino 1 has been reported to have positive correlation with SPEI in the coastal regions of West Africa but negative correlation in the Sahel regions (Adeniyi and Dilau 2018). It has also been posited that El Nino Southern Oscillation—ENSO, Atlantic Multi-decadal Oscillation—AMO, and Atlantic Meridional Mode—AMM can be responsible for the results obtained 12-month timescale (Ndehedehe et al. 2016). Near normal condition was found to be predominant in all the analyses. A noticeable trend in all climatic zones is the higher number of occurrences of MD values in SPI than the MD values obtained under SPEI.

Conclusion

In this study, the performance and statistics of two drought indices were investigated over different climatic zones of Nigeria. The study considered eighteen locations over a period of thirty-one years. At 1- and 3-month scale, both SPI and SPEI are predominantly periodic in the Sahel and Midland regions indicating a harsh and severe dry season. At longer timescales, SPI and SPEI have stronger correlation than at shorter timescales. This trend was also reflected in the regression coefficient between the two indices. The regression fits were better in the southern part of the country than the northern part of the country. Comparative trend

Table 5 Frequency distribution of SPI and SPEI drought indices at 1-month timescale

Region	Location	SPI							SPEI						
		EW	VW	MW	NN	MD	SD	ED	EW	VW	MW	NN	MD	SD	ED
Sahel	Sokoto	5	17	43	235	49	18	5	5	42	21	173	23	10	5
	Maiduguri	5	19	42	242	40	20	4	5	6	54	158	16	5	4
	Kano	4	21	40	250	35	16	6	5	8	52	159	10	11	3
	Katsina	3	20	42	252	28	21	6	5	13	21	185	14	8	2
Midland	Kaduna	9	15	38	249	35	21	5	5	42	21	173	23	10	5
	Minna	6	15	45	245	37	20	4	7	46	53	201	17	12	5
	Yola	8	15	31	255	38	20	5	3	40	24	176	19	12	5
Guinea	Lokoja	7	15	43	243	43	15	6	10	9	37	245	26	8	6
	Markudi	7	17	37	251	39	13	8	7	20	59	253	17	13	3
	Warri	7	22	33	250	34	23	3	6	16	34	269	21	20	6
Coastal	Lagos	9	16	38	247	45	13	4	8	12	37	275	21	11	8
	Akure	7	18	36	246	38	22	5	3	14	43	269	17	22	4
	PH	7	16	41	244	41	19	4	5	17	42	255	33	13	7
	Owerri	5	22	38	249	33	19	6	5	19	36	270	24	7	11
	Enugu	7	17	41	245	38	16	8	4	23	34	276	17	13	5
	Calabar	4	24	45	235	45	14	5	3	15	45	268	23	8	10
	Ogoja	10	18	28	262	31	16	7	9	18	32	273	24	9	7
	Abeokuta	5	23	35	239	37	17	4	7	16	30	275	14	10	8

EW extremely wet, *VW* very wet, *MW* moderately wet, *NN* near normal, *MD* moderately dry, *SD* severely dry, *ED* extremely dry

Table 6 Frequency distribution of SPI and SPEI drought indices at 3-month timescale

Region	Location	SPI							SPEI						
		EW	VW	MW	NN	MD	SD	ED	EW	VW	MW	NN	MD	SD	ED
Sahel	Sokoto	4	18	45	221	50	19	3	7	40	25	211	27	12	8
	Maiduguri	4	21	34	230	52	14	5	8	7	54	197	19	10	5
	Kano	12	11	30	255	28	10	14	9	8	55	197	17	11	3
	Katsina	5	19	39	233	40	14	10	5	14	30	216	21	10	4
Midland	Kaduna	5	14	37	240	37	22	5	7	40	25	211	27	12	8
	Minna	2	23	46	231	37	13	8	5	18	33	264	22	8	10
	Yola	6	13	43	233	39	21	5	7	38	61	213	23	9	9
Guinea Sav.	Lokoja	3	18	48	228	40	18	5	7	15	41	254	24	12	7
	Markudi	7	11	49	228	40	22	3	8	11	42	254	28	16	1
	Warri	7	19	31	244	36	18	5	6	18	32	244	34	19	7
Coastal	Lagos	5	19	42	230	44	16	4	3	17	37	244	33	15	11
	Akure	7	18	35	233	45	17	5	2	14	42	235	35	23	9
	PH	4	22	28	244	39	17	6	7	11	37	252	25	18	10
	Owerri	6	18	33	236	42	21	4	7	12	30	249	37	18	7
	Enugu	7	14	31	241	46	14	7	2	18	40	257	20	12	11
	Calabar	7	17	36	239	39	12	10	8	9	40	250	26	16	11
	Ogoja	5	21	31	248	30	20	5	8	19	28	260	23	12	10
	Abeokuta	6	19	33	232	38	15	5	7	9	44	232	30	18	8

EW extremely wet, *VW* very wet, *MW* moderately wet, *NN* near normal, *MD* moderately dry, *SD* severely dry, *ED* extremely dry

analysis of drought over Nigeria using SPI and SPEI were also carried out. Results obtained indicate that small but positive significant trends were predominant over the region in the period under consideration. Finally, the statistical distribution of both SPI and SPEI at different timescales reveals the prevalence of near normal conditions. It is posited that

Table 7 Frequency distribution of SPI and SPEI drought indices at 6-month timescale

Region	Location	SPI							SPEI						
		EW	VW	MW	NN	MD	SD	ED	EW	VW	MW	NN	MD	SD	ED
Sahel	Sokoto	4	15	38	238	41	22	2	7	12	26	254	33	18	10
	Maiduguri	3	20	34	228	51	22	2	9	15	27	258	29	14	8
	Kano	13	11	25	254	35	11	11	10	12	36	250	31	18	3
	Katsina	0	23	46	225	43	20	3	6	17	42	248	26	17	4
Midland	Kaduna	6	12	39	240	34	26	3	7	12	26	254	33	18	10
	Minna	1	20	51	225	40	16	7	2	15	36	258	21	11	17
	Yola	7	15	31	244	33	23	7	4	18	25	263	27	9	14
Guinea Sav.	Lokoja	3	24	39	231	40	19	4	9	17	31	246	33	18	6
	Markudi	7	17	27	249	31	24	5	9	15	28	245	34	28	1
	Warri	4	17	44	239	31	22	3	12	11	38	243	39	12	5
Coastal	Lagos	2	22	36	237	35	24	4	0	21	34	248	27	16	14
	Akure	9	15	30	242	39	20	5	5	14	31	247	31	21	11
	PH	4	21	33	239	38	21	4	5	20	36	239	35	18	7
	Owerri	8	12	37	244	27	28	4	10	12	33	244	32	19	10
	Enugu	5	12	38	233	51	14	7	4	9	41	258	26	7	15
	Calabar	7	18	29	252	30	16	8	10	16	25	261	27	10	11
	Ogoja	4	22	39	237	32	22	4	11	18	33	244	30	14	10
	Abeokuta	2	20	42	229	34	16	5	6	11	40	228	30	28	5

EW extremely wet, *VW* very wet, *MW* moderately wet, *NN* near normal, *MD* moderately dry, *SD* severely dry, *ED* extremely dry

Table 8 Frequency distribution of SPI and SPEI drought indices at 12-month timescale

Region	Location	SPI							SPEI						
		EW	VW	MW	NN	MD	SD	ED	EW	VW	MW	NN	MD	SD	ED
Sahel	Sokoto	3	15	48	215	57	22	0	7	12	15	262	24	29	11
	Maiduguri	1	20	43	228	47	20	1	0	29	22	246	29	22	12
	Kano	7	26	20	253	40	2	12	1	30	34	222	42	31	0
	Katsina	3	17	39	227	51	23	0	2	16	66	216	28	25	7
Midland	Kaduna	5	15	36	235	36	29	4	7	12	15	262	24	29	11
	Minna	7	12	36	248	27	21	9	0	14	40	263	7	11	25
	Yola	5	23	21	245	35	27	4	0	13	42	255	24	5	21
Guinea Sav.	Lokoja	2	25	38	233	33	29	0	8	14	48	223	42	17	8
	Markudi	12	5	41	242	37	17	6	15	19	13	252	35	20	6
	Warri	3	21	47	224	43	19	3	10	12	37	238	44	14	5
Coastal	Lagos	6	16	42	235	37	21	3	3	19	38	247	27	13	13
	Akure	12	12	24	247	40	21	4	17	7	24	256	23	22	11
	PH	10	10	39	241	37	18	5	3	17	51	228	33	22	6
	Owerri	1	29	28	237	39	26	0	12	13	23	262	22	13	15
	Enugu	5	15	32	239	51	12	6	0	14	49	250	31	3	13
	Calabar	3	22	37	233	45	16	4	20	14	26	242	39	17	2
	Ogoja	1	25	56	221	45	6	6	11	20	48	226	39	10	6
	Abeokuta	0	22	56	211	40	17	2	3	17	46	217	33	20	12

EW extremely wet, *VW* very wet, *MW* moderately wet, *NN* near normal, *MD* moderately dry, *SD* severely dry, *ED* extremely dry coupled ocean–atmosphere is responsible for the statistical distribution across the different climatic regions.

There is the need for spectral analysis to determine the frequency of occurrence of drought in the region. Furthermore, the role of ocean–atmosphere coupling such as ENSO in drought frequency over the region is worthy of investigation.

References

Adeniyi MO, Dilau KA (2018) Assessing the link between Atlantic Niño 1 and drought over West Africa using CORDEX regional climate models. Theor Appl Climatol 131(3–4):937–949. https://doi.org/10.1007/s00704-016-2018-0

Adeyemi B, Emmanuel I (2011) Monitoring tropospheric radio refractivity over Nigeria using CM-SAF data derived from NOAA-15, 16 and 18 satellites. Indian J Radio Space Phys 40(6):301–310

Ahmad S, Hussain Z, Qureshi AS, Majeed R, Saleem M (2004) Drought mitigation in Pakistan: current status and options for future strategies, vol 85. IWMI

Ahmadalipour A, Moradkhani H (2018) Multi-dimensional assessment of drought vulnerability in Africa: 1960–2100. Sci Total Environ 644:520–535

Blain GC (2012) Revisiting the probabilistic definition of drought: strengths, limitations and an agrometeorological adaptation. Bragantia 71(1):132–141

Chen ST, Kuo CC, Yu PS (2009) Historical trends and variability of meteorological droughts in Taiwan. Hydrol Sci J 54(3):430–441

Costa AC (2011) Local patterns and trends of the standardized precipitation index in southern Portugal (1940–1999). Adv Geosci 30:11–16. https://doi.org/10.5194/adgeo-30-11-2011

Detges A (2017) Droughts, state-citizen relations and support for political violence in Sub-Saharan Africa: a micro-level analysis. Polit Geogr 61:88–98. https://doi.org/10.1016/j.polgeo.2017.07.005

Dracup JA, Lee KS, Paulson EG (1980) On the definition of droughts. Water Resour Res 16(2):297–302. https://doi.org/10.1029/WR016i002p00297

Field CB, Barros V, Stocker TF, Dahe Q (2012) Managing the risks of extreme events and disasters to advance climate change adaptation: special report of the intergovernmental panel on climate change. Cambridge University Press, Cambridge

Fuwape I, Ogunjo S (2018) Modeling of raining season onset and cessation of tropical rainfall for climate change adaptation in agriculture. arXiv preprint arXiv:181109677

Gudmundsson L, Seneviratne SI (2015) European drought trends. Proc Int Assoc Hydrol Sci 369:75–79

Josserand H, Morrison T, O_Dea J, Dradri S, Hidalgo Sanchis P, Xie H (2008) FAO/WFP crop and food supply assessment mission to the Democratic People's Republic of Korea. Special report. Special Reports and Alerts (FAO)

Katsanos D, Retalis A, Tymvios F, Michaelides S (2018) Study of extreme wet and dry periods in Cyprus using climatic indices. Atmos Res 208(August 2017):88–93

Kayode AJ, Francis OA (2012) Drought intensities in the Sudano-Sahelian region of Nigeria. J Sustain Soc 1(4):88–95

Keyantash J, Dracup JA (2002) The quantification of drought: an evaluation of drought indices. Bull Am Meteorol Soc 83(8):1167–1180

Khan MI, Liu D, Fu Q, Faiz MA (2018) Detecting the persistence of drying trends under changing climate conditions using four meteorological drought indices. Meteorol Appl 25(2):184–194

Mishra AK, Singh VP (2010) A review of drought concepts. J Hydrol 391(1–2):202–216

Mpelasoka F, Awange JL, Zerihun A (2018) Influence of coupled ocean–atmosphere phenomena on the Greater Horn of Africa droughts and their implications. Sci Total Environ 610–611:691–702. https://doi.org/10.1016/j.scitotenv.2017.08.109

Ndehedehe CE, Agutu NO, Okwuashi O, Ferreira VG (2016) Spatiotemporal variability of droughts and terrestrial water storage over Lake Chad Basin using independent component analysis. J Hydrol 540:106–128

Ogunjo ST, Fuwape IA, Olusegun CF (2019) Impact of large scale oscillation on drought in west africa. arXiv preprint arXiv:1901.10145

Oguntunde PG, Lischeid G, Abiodun BJ, Dietrich O (2017) Analysis of long-term dry and wet conditions over Nigeria. Int J Climatol 37(9):3577–3586. https://doi.org/10.1002/joc.4938

Oladipo EO (1993) Some aspects of the spatial characteristics of drought in northern Nigeria. Nat Hazards 8(2):171–188

Oladipo E (1995) Some statistical characteristics of drought area variations in the Savanna region of Nigeria. Theor Appl Climatol 50(3–4):147–155

Oloruntade AJ, Mohammad TA, Ghazali AH, Wayayok A (2017) Analysis of meteorological and hydrological droughts in the Niger-South Basin, Nigeria. Glob Planet Change 155:225–233. https://doi.org/10.1016/j.gloplacha.2017.05.002

Pachauri R, Reisinger A (2008) Changements climatiques 2007-rapport de synthèse. Rapport GIEC, Genève, Suisse

Pereira LS, Cordery I, Iacovides I (2009) Coping with water scarcity: addressing the challenges. Springer, Berlin

Sordo-Ward A, Bejarano MD, Iglesias A, Asenjo V, Garrote L (2017) Analysis of current and future SPEI droughts in the La Plata basin based on results from the regional eta climate model. Water 9(11):857

Stocker T (2014) Climate change 2013: the physical science basis: working group I contribution to the fifth assessment report of the intergovernmental panel on climate change. Cambridge University Press, Cambridge

Street-Perrott FA, Holmes J, Waller M, Allen M, Barber N, Fothergill P, Harkness D, Ivanovich M, Kroon D, Perrott R (2000) Drought and dust deposition in the West African Sahel: a 5500-year record from Kajemarum Oasis, northeastern Nigeria. Holocene 10(3):293–302

Thornthwaite CW (1948) An approach toward a rational classification of climate. Geogr Rev 38:55–94

Wilhite DA (eds) (1993) Planning for drought: a methodology. In: Drought assessment, management, and planning: theory and case studies. Natural resource management and policy, vol 2. Springer, Boston, MA

Zargar A, Sadiq R, Naser B, Khan FI (2011) A review of drought indices. Environ Rev 19(NA):333–349

Acta Geophysica (2019) 67:891–903
https://doi.org/10.1007/s11600-019-00283-5

RESEARCH ARTICLE - HYDROLOGY

Artificial intelligence approaches for spatial modeling of streambed hydraulic conductivity

Sujay Raghavendra Naganna[1] · **Paresh Chandra Deka**[1]

Received: 13 February 2019 / Accepted: 29 March 2019 / Published online: 3 April 2019

Abstract

Saturated hydraulic conductivity (K_s) describes the water movement through saturated porous media. The hydraulic conductivity of streambed varies spatially owing to the variations in sediment distribution profiles all along the course of the stream. The artificial intelligence (AI) based spatial modeling schemes were instituted and tested to predict the spatial patterns of *streambed hydraulic conductivity*. The geographical coordinates (i.e., latitude and longitude) of the sampled locations from where the in situ hydraulic conductivity measurements were determined were used as model inputs to predict streambed K_s over spatial scale using artificial neural network (ANN), adaptive neuro-fuzzy inference system (ANFIS) and support vector machine (SVM) paradigms. The statistical measures computed by using the actual versus predicted streambed K_s values of individual models were comparatively evaluated. The AI-based spatial models provided superior spatial K_s prediction efficiencies with respect to both the strategies/schemes considered. The model efficiencies of spatial modeling scheme 1 (i.e., Strategy 1) were better compared to Strategy 2 due to the incorporation of more number of sampling points for model training. For instance, the SVM model with $\text{NSE}=0.941$ (Strategy 1) and $\text{NSE}=0.895$ (Strategy 2) were the best among all the models for 2016 data. Based on the scatter plots and Taylor diagrams plotted, the SVM model predictions were found to be much efficient even though, the ANFIS predictions were less biased. Although ANN and ANFIS models provided a satisfactory level of predictions, the SVM model provided virtuous streambed K_s patterns owing to its inherent capability to adapt to input data that are non-monotone and nonlinearly separable. The tuning of SVM parameters via 3D grid search was responsible for higher efficiencies of SVM models.

Keywords ANN · ANFIS · Spatial modeling · Streambed hydraulic conductivity · SVM · Vented dams

Introduction

Artificial intelligence (AI) based approaches are increasingly being used nowadays for the purpose of determining spatial patterns of soil processes and many ecological variables (Kirkwood et al. 2016; Leuenberger and Kanevski 2015). The AI models have shown potential applications in various fields such as geography, geosciences, and demography. They are found applicable for spatial modeling of land use dynamics, spatial (environmental) processes that are nonstationarity, soil nutrient dynamics, air pollution exposure modeling, etc. (Forkuor et al. 2017; Grekousis et al. 2013; Reid et al. 2015). The AI-based models are known to model any spatial parameter based on their inherent ability to learn from complex input–output relationships even without considering any of the influencing physical factors.

There exist several studies using artificial intelligence (AI) algorithms for predicting soil parameters such as cation exchange capacity, soil temperature, hydraulic conductivity, soil organic carbon, and microbial diversity over spatial scales (Dai et al. 2014; Ghorbani et al. 2015; Twarakavi et al. 2009; Sanikhani et al. 2018). Several researchers indeed have successfully come up with models for estimating suspended sediment concentrations in rivers using novel data mining or AI techniques (Khosravi et al. 2018; Kisi and Yaseen 2019). Recently, by coupling ANNs with GIS, Gholami et al. (2018) modeled soil erosion at different time scales to furnish soil erosion rate maps of the hillslopes in Kasilian watershed, Iran. Here are a few literature examples related to soil hydraulic conductivity prediction using AI models.

✉ Sujay Raghavendra Naganna
sujay.gopan@gmail.com

[1] Department of Applied Mechanics and Hydraulics, National Institute of Technology Karnataka, Surathkal, Mangalore 575025, India

Soil physical and hydraulic properties such as particle-size distribution, bulk density, different pore sizes, field capacity, permanent wilting point, available water capacity etc. were used to develop using artificial neural network (ANN) and multiple linear regression models by Merdun et al. (2006) to predict soil water retention properties and saturated hydraulic conductivity of soil sampled within the Erzincan plain, Turkey. Twarakavi et al. (2009) taking the advantage of soil data that are easily obtainable such as textural information, bulk density, and retention points developed support vector machine (SVM)-based pedo-transfer function to predict soil hydraulic properties. Using terrain attributes such as slope gradient, elevation, profile curvature, slope aspect, and contour curvature as input variables, Motaghian and Mohammadi (2011) developed artificial neural network models to predict the spatial variation in saturated hydraulic conductivity. Zhao et al. (2016) evaluated the performance of multiple linear regression (MLR) and artificial neural network (ANN) models in the prediction of soil hydraulic conductivity (K_s) based on samples collected from Loess Plateau of China using bulk density, clay content, saturated soil water content, silt content (Silt), and latitude as input parameters. More and Deka (2018) employed hybrid structures such as neuro-fuzzy systems to model field-scale soil hydraulic conductivity sampled from murum soils of India.

Assessment of streambed hydraulic conductivity profiles at fine spatial and temporal resolution is necessary for river corridor studies related to stream–aquifer interaction, streambed-induced infiltration, solute retention, and contaminant transport along the streambed (Wu et al. 2015). Literature that documents the importance of streambed hydraulic conductivity and its role in surface and groundwater interactions is comprehensively reviewed in Naganna et al. (2017). Successive erosion and deposition of sediments all along the stream course affect sediment distribution profiles and the streambed hydrogeological properties. In situ measurement of streambed hydraulic conductivity all along the length of the stream may not be an ideal and cost-effective way. Hence, the applicability of the AI approaches could be tested to induce a rule-based relationship for estimating the values of streambed hydraulic conductivity at unmeasured locations using representative georeferenced neighborhood data. Limited or no studies are available in the literature related to the artificial intelligence (AI)-based spatial modeling schemes to predict the spatial patterns of streambed hydraulic conductivity. Also, several studies in the literature use various soil properties and terrain attributes as inputs to simulate soil hydraulic conductivity. In reality, if the data of such predictor variables are unavailable then the application of soil hydraulic conductivity estimation may not be possible from such models. Hence, in the present study the geographical coordinates (i.e., latitude and longitude) of the sampling locations (points) from where the in situ hydraulic conductivity measurements were made were used as model inputs to predict streambed hydraulic conductivity (K_s) over spatial scale using artificial neural network (ANN), adaptive neuro-fuzzy inference system (ANFIS) and support vector machine (SVM) paradigms. Additionally, the potential of several AI approaches in predicting streambed hydraulic conductivity was evaluated comparatively.

Theoretical overview

Artificial neural network (ANN)

The multilayer perceptron (MLP) neural network is an extremely versatile technique capable of learning most complex nonlinear interrelationships between a set of dependent and independent variables (Cross et al. 1995; Kohonen 1988). A three-layered perceptron network with one hidden layer is as shown in Fig. 1. The network is trained on a set of reference data by adjusting the parameters of the MLP network with the assistance of a Levenberg–Marquardt backpropagation (BP) algorithm. The network architecture involving a set of processing units (neurons), a specific topology of weighted links connecting the neurons, and the learning paradigm that updates the connection weights determine the efficiency of MLP neural networks (Jain et al. 1996). The activation function has to be chosen based on the type of application. In the case of nonlinear mapping, the normally used activation functions are sigmoidal and hard-limiting functions. Sigmoidal functions are continuous and differentiable; however, the hard-limiting functions are non-continuous but differentiable.

Every single input (X_n), weighted by an element (w_{ij}) of the weight matrix (W), is summated and provided to the transfer function or activation function (φ) along with a bias (B) term. The activation function constructs a nonlinear decision boundary via linear combinations of the weighted inputs and then applies a threshold to transform the net inputs from all the neuronal units into an output signal. The Levenberg–Marquardt backpropagation learning rule is a variation of Newton's method which incrementally adjusts the weight and bias terms to minimize the mean square error (MSE) of the network. The quantum of progressions made in adjusting the synaptic weights and biases at every epoch is determined by the learning rate parameter. Smaller learning rates end up in longer training time, however, warrant stability that steers to minimum errors (Sivanandam and Paulraj 2009).

Adaptive neuro-fuzzy inference system (ANFIS)

Jang (1993) introduced adaptive neuro-fuzzy inference system (ANFIS), a hybrid machine learning approach

Fig. 1 Multilayer perceptron (MLP) neural network architecture

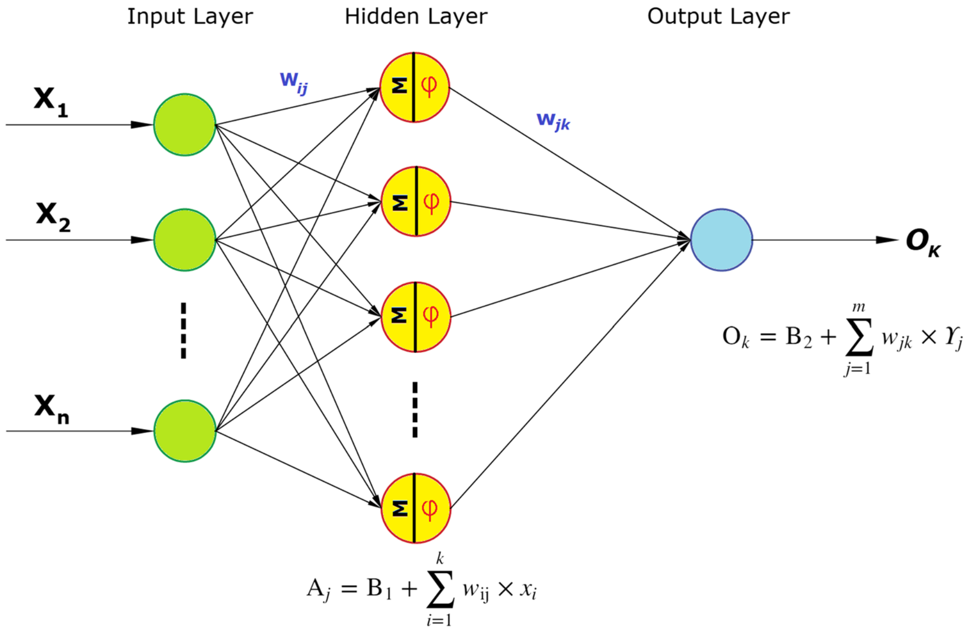

that involves a fuzzy inference system (FIS) and a backpropagation algorithm to tune the membership function parameters of FIS. Depending on the complexity of the problem addressed, sometimes the backpropagation gradient descent method in combination with the least squares method is used to adjust the parameters of FIS (Jang et al. 1997). The fuzzy inference system, based on the number of input parameters, encompasses a set of fuzzy IF–THEN rules or conditional statements to approximate nonlinear functions. ANFIS is a multilayer feedforward five-layer architecture as illustrated in Fig. 2. The fixed nodes are represented by circular outline, and the square outlines are adaptive nodes presided by parameter settings. Each node performs a particular function on incoming signals. Every node in layer 1 (adaptive node) is associated with a node function governed by premise parameters. The output of every single node of layer 2 (fixed node) represents the firing strength of a rule which is nothing but the product of all incoming signals. Similarly, the output of every single node of layer 3 (fixed node) represents the normalized firing strength. Every node in the layer 4 is an adaptive node associated with a node function governed by consequent parameters. The final fixed node in layer 5 labeled as (Σ) computes the overall output as the summation of all incoming signals (Abraham 2005). The premise and consequent parameters of ANFIS are tuned in the learning process by means of a hybrid technique which involves the gradient descent backpropagation method coupled with a least squares optimization algorithm to provide optimal outputs. Soon after the training

Fig. 2 ANFIS architecture

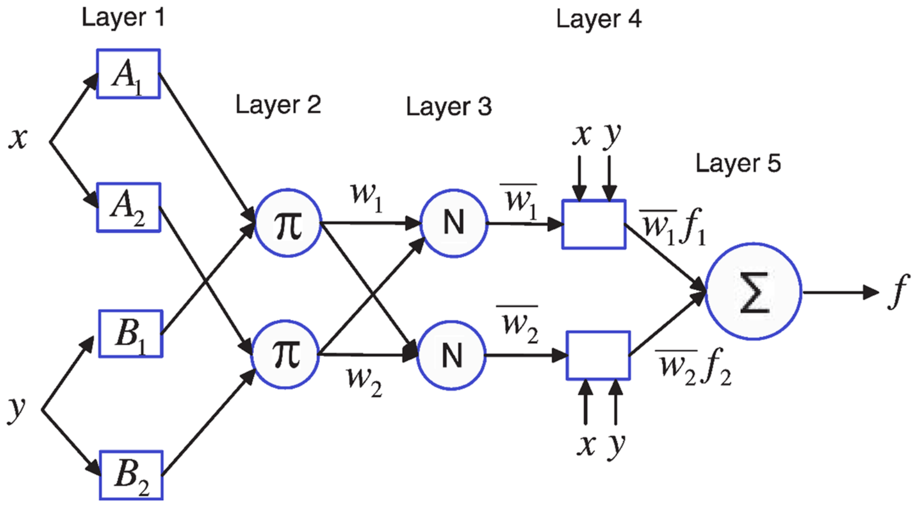

converges, the values of the premise parameters of membership function are fixed in the search space and the overall output is expressed as a linear combination of the consequent parameters (Jang 1992). Herein, grid partitioning (GP) type of the ANFIS model was employed in the streambed hydraulic conductivity modeling scheme. The performance of the ANFIS model is greatly affected by the type and number of membership functions, which are usually ascertained by trial-and-error procedure.

Support vector machine (SVM)

SVM belongs to the category of supervised learning method proposed by Vladimir Vapnik and his team (Vapnik 2000). Using suitable kernel functions, SVM maps the nonlinear datasets of the input space into a higher-dimensional feature space, to transform them into linear ones. By avoiding or else minimizing over fitting and under fitting of the data, SVM offers maximum predictive accuracy. The structural risk minimization principle of SVM takes the advantage of convex optimization algorithm to simultaneously account for both the empirical risk and the confidence interval of the learning machine by maximizing the geometric margin. SVM is known to perform efficiently in both linear and nonlinear regression tasks with the assistance from *Kernel trick*. The efficiency of SVM modeling is entirely dependent over the optimal selection of hyper-parameters (i.e., cost, kernel parameter, and loss function). Usually, a three-dimensional fine grid search will be sufficient for finding the optimal values of the SVM parameters. Figure 3 presents the general SVM architecture. For further details regarding SVM, its formulations and applications, one may refer to following literature (Cortes and Vapnik 1995; Cristianini and Shawe-Taylor 2000; Raghavendra and Deka 2014; Vapnik 1999).

Study area and data analysis

The study pertains to a part of the Pavanje River originating in the Western Ghats of India. The study is focused on the stream reach obstructed by two vented dams in sequence. The streambed hydraulic conductivity data were collected from the study reach as shown in Fig. 4 for assessing the spatial and temporal variations in streambed hydraulic conductance. The hydraulic conductivity tests using Guelph permeameter were conducted along 40 transects across the channel covering the upstream and downstream reaches of each vented dam. The spacing between each transect was 50 m and in each transect, for every 5-meter interval, streambed hydraulic conductivity (K_s) was determined (refer to Fig. 5). The details related to physiography, geological details of the basin along with streambed sampling scheme, and frequency can be referred from Naganna and Deka (2018). This study uses the data of the streambed hydraulic conductivity of two time periods (2016 and 2017) presented in Naganna and Deka (2018) for the development of AI-based spatial prediction models.

The descriptive statistics of in situ measured streambed hydraulic conductivity (K_s) along the three segments of the study reach measured at two different time periods (dry periods of 2016 and 2017) are presented in Table 1 to illustrate the overall variation in the K_s distribution. The magnitude of K_s with reference to the three segments varied by two orders of magnitude.

Methodology and performance evaluation

For spatial modeling of streambed hydraulic conductivity, two diverse schemes/strategies were adopted. In Strategy 1, the training and testing datasets were chosen in such a

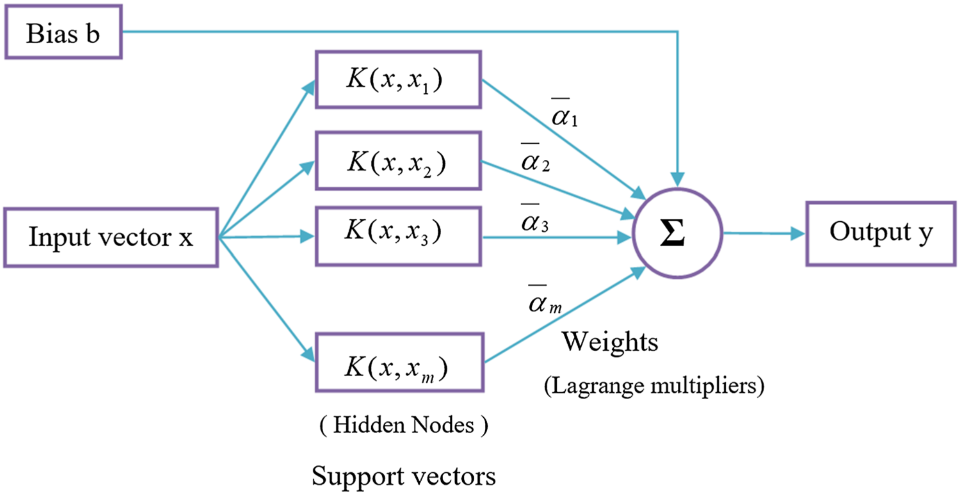

Fig. 3 General SVM architecture (adopted from Raghavendra and Deka 2014)

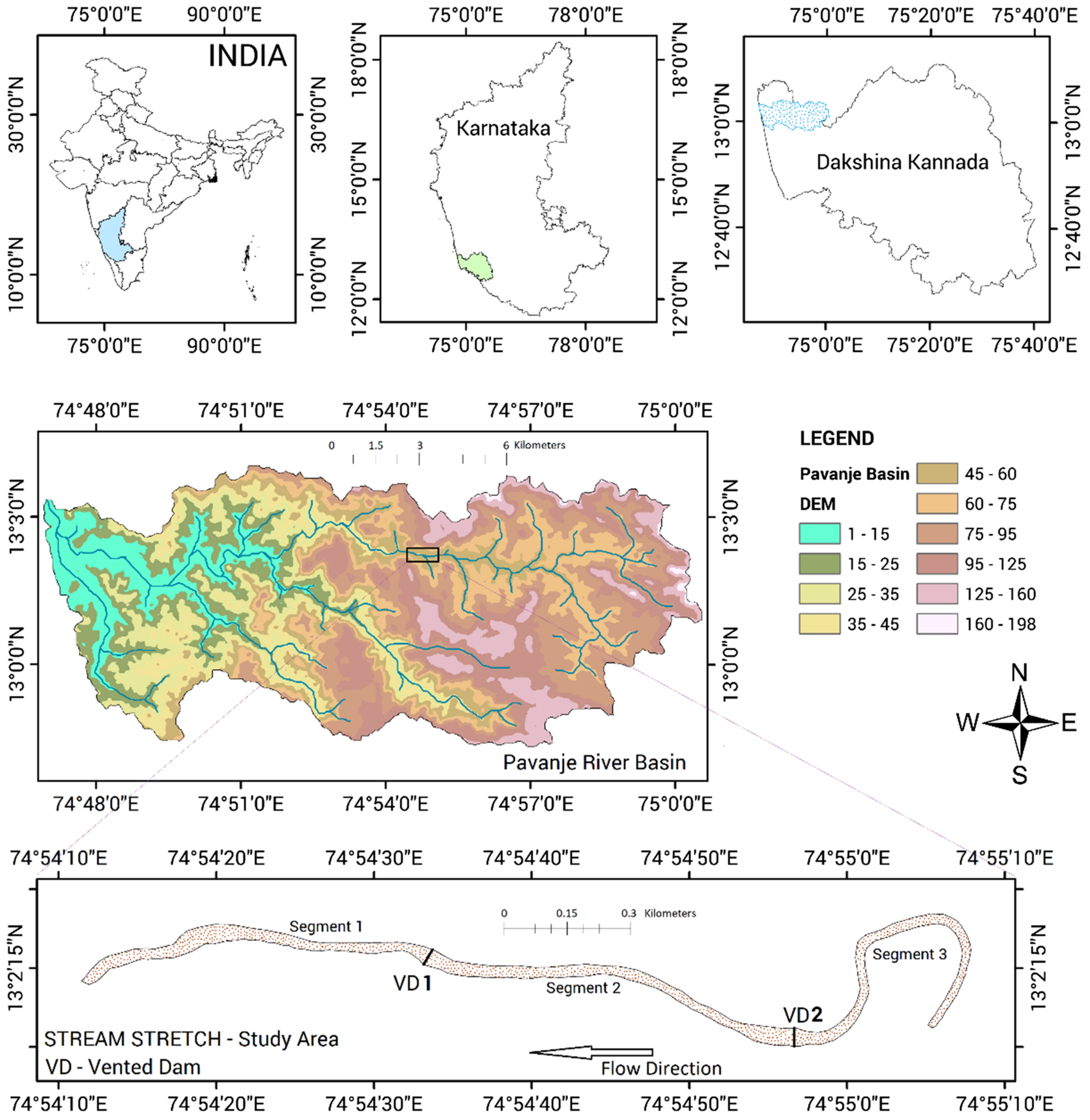

Fig. 4 Study area—stream reach obstructed by vented dams

pattern that the K_s data along a transect were estimated by considering the K_s data of two neighborhood transects both upstream and downstream. Figure 6 shows the scheme of selection of training and testing transects along the study reach. The K_s data measured at transect locations—2, 3, 5, 6, 8, 9, 11, 12, 13, 15, 16, 18, 19, 21, 22, 24, 25, 27, 28, 30, 31, 33, 34, 36, 37, 39, 40—were considered as training features, and the models were calibrated to estimate the K_s values at transects—1, 4, 7, 10, 14, 17, 20 m 23, 26, 29, 32, 35, 38. The predicted K_s values were evaluated against the observed K_s values at those transects. The sample size considered for training and testing of AI models was, respectively, 134 and 53 K_s point samples in the case of Strategy 1. During model development, the point location details (i.e., the geographical information—latitude and longitude) from where the K_s values were sampled along each transect were considered as model inputs by targeting measured K_s. Specifically, the geographical coordinates were the predictors

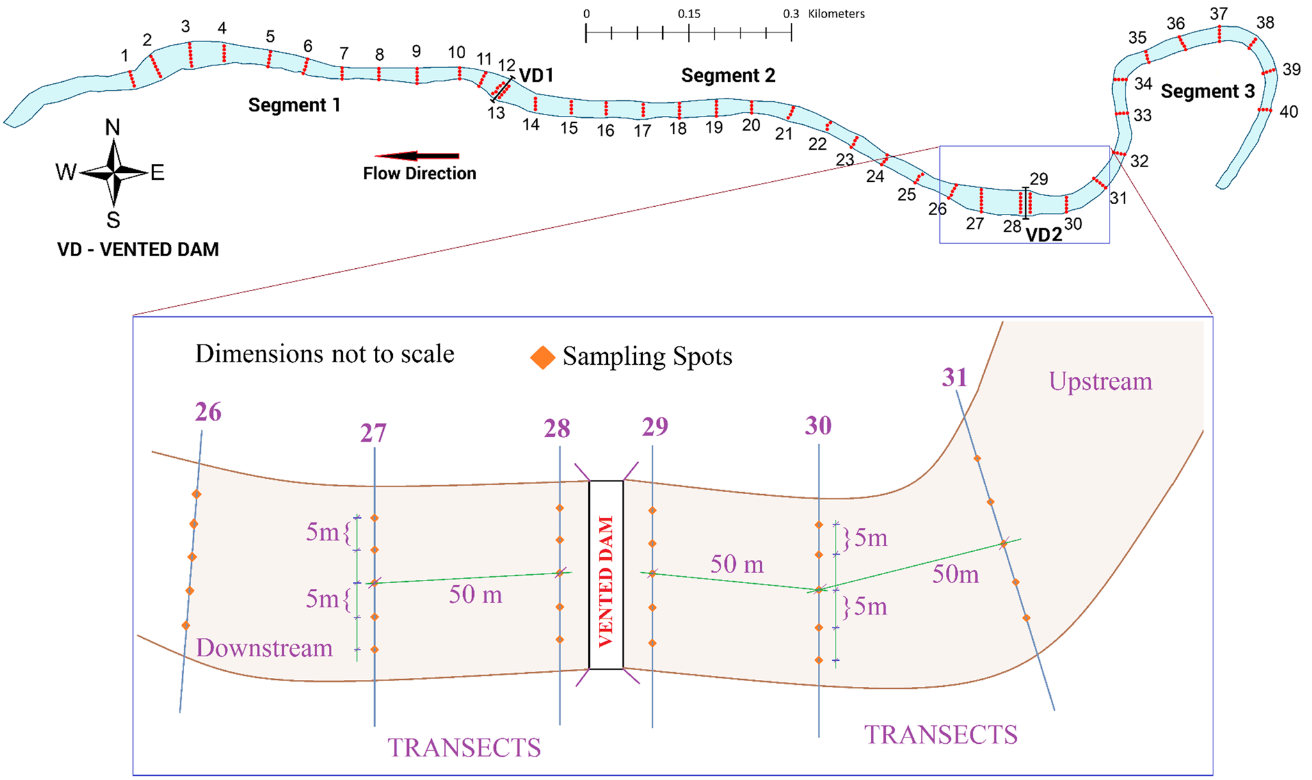

Fig. 5 Streambed hydraulic conductivity sampling scheme

Table 1 Statistical analysis of streambed hydraulic conductivity (K_s) (cm/day)

2016 Data	Min	Max	Mean	S_d	Var	Kurtosis	Skewness
Segment 1	11.634	205.2	87.015	59.339	3521.092	− 0.992	0.638
Segment 2	76.871	558.481	328.703	142.222	20,227.01	−1.125	− 0.444
Segment 3	376.678	793.886	674.809	101.678	10,338.47	1.295	−1.358
Full stretch	11.634	793.886	349.809	255.518	65,289.44	−1.337	0.283
2017 Data							
Segment 1	16.932	231.967	93.676	62.386	3892.03	− 0.646	0.775
Segment 2	65.86	547.88	332.857	141.238	19,948.25	−1.113	− 0.426
Segment 3	280.273	777.989	657.485	121.177	14,683.98	1.583	−1.503
Full stretch	16.932	777.989	348.578	249.325	62,162.71	−1.301	0.298

S_d standard deviation; *Var* variance

and the K_s values serve as predictand. The testing transects were considered to be the unknown locations where there is a necessity for prediction. While model testing, the K_s values were estimated at those testing transect locations by entering only geographical coordinates as inputs so that it becomes easier to validate the model predictions based on the observed K_s values.

Similarly, in Strategy 2, the alternate transects—one after the other—were considered as training and testing transects. The scheme of Strategy 2 is as shown in Fig. 6. In this case, the samples of upstream transects are considered for training the models. The sample size considered for training and testing of AI models was, respectively, 96 and 91 K_s point samples in the case of Strategy 2. The proposed AI models have been developed using Matlab software.

The spatial prediction performance of all the models was evaluated by computing error and efficiency statistics as given below.

Statistical criteria	Value	Inference
Root-mean-square error, $\mathrm{RMSE}=\sqrt{\frac{\left(O_i-P_i\right)^2}{N}}$	A value below half of the standard deviation	Satisfactory

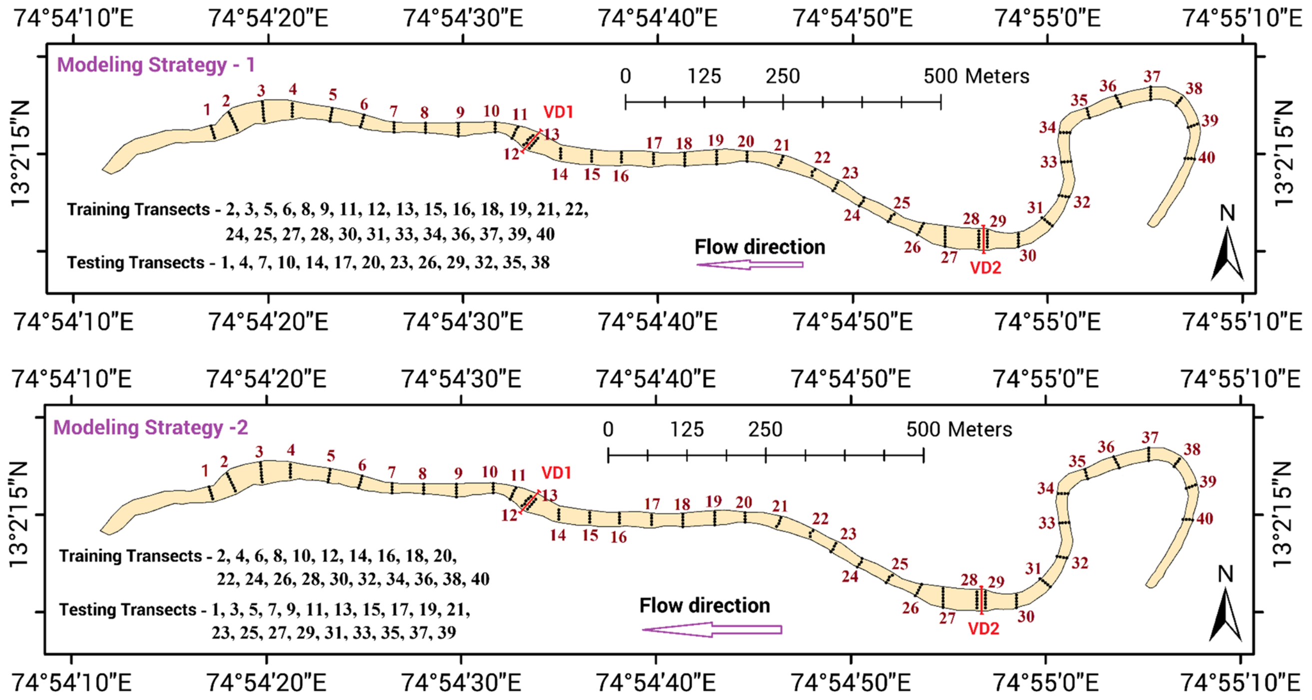

Fig. 6 Spatial modeling schemes

Statistical criteria	Value	Inference
Relative RMSE, $\mathrm{RRMSE} = \frac{RMSE}{\sigma_{obs}}$	$0.00 \le \mathrm{RRMSE} \le 0.10$	Very good
	$0.10 \le \mathrm{RRMSE} \le 0.30$	Good
	$0.30 \le \mathrm{RRMSE} \le 0.50$	Satisfactory
	$\mathrm{RRMSE} > 0.70$	Poor
Mean absolute error, $\mathrm{MAE} = \frac{\sum_{i=1}^{N} \lvert P_i - O_i \rvert}{N}$	A value below half of the standard deviation	Satisfactory
Nash–Sutcliffe efficiency, $\mathrm{NSE} = 1 - \frac{\sum_{i=1}^{N} (P_i - O_i)^2}{\sum_{i=1}^{N} (O_i - \overline{O})^2}$	$0.75 < \mathrm{NSE} < 1.00$	Very good
	$0.65 < \mathrm{NSE} \le 0.75$	Good
	$0.50 < \mathrm{NSE} \le 0.65$	Satisfactory
	$0.4 < \mathrm{NSE} \le 0.50$	Acceptable
	$\mathrm{NSE} \le 0.4$	Unsatisfactory

where O and P signpost the observed and predicted K_s values, respectively. $\overline{O}$ and $\overline{P}$ are the mean of observed and forecasted values, σ_o and σ_p are the standard deviation of observed and forecasted values, respectively. N represents the total number of data samples.

Results and discussion

Performance of ANN prediction models

Based on trial-and-error scheme, the number of hidden neurons of the multilayer perceptron neural network (ANN) was determined. The *tansig* and *purelin* were employed as input and output transfer functions along with Levenberg–Marquardt backpropagation learning rule. The model structure and performance statistics of the ANN model for each strategy are presented in Table 2 along with the performance statistics of the ANN model for each strategy. From the statistical indices, it is evident that the performance of ANN models during the testing phase was satisfactory but not up to the mark. For instance, the MAE of all the models was sufficiently high and the RRMSE values above 0.4 signpost that the spatial K_s predictions were not so accurate but fall under the satisfactory category. With reference to

Table 2 Performance indices of ANN modeling

ANN Model	Model structure	Train			Test		
		RRMSE	MAE (cm/day)	NSE	RRMSE	MAE (cm/day)	NSE
Strategy 1—2016	2-3-1	0.445	84.67	0.796	0.462	100.63	0.782
Strategy 1—2017	2-3-1	0.411	81.22	0.835	0.491	108.72	0.75
Strategy 2—2016	2-5-1	0.265	36.41	0.917	0.482	92.36	0.765
Strategy 2—2017	2-5-1	0.395	68.26	0.821	**0.458**	**85.82**	**0.788**

Strategy 1 model of 2017, even though the training results were good with an NSE = 0.835, the test performance was merely acceptable with an NSE = 0.75.

Performance of ANFIS prediction models

The adaptive neuro-fuzzy inference system (ANFIS) with grid partitioning method was calibrated by selecting the shape and optimal number of membership functions. The optimal ANFIS architectures calibrated based on trial-and-error approach for spatial modeling of streambed K_s are presented in Table 3. The 'hybrid' training algorithm which includes the backpropagation gradient descent method in combination with a least squares method was used for fitting the training data set. The performance statistics of ANFIS model for each strategy are presented in Table 4.

From the statistical indices, it is evident that the performance of all the ANFIS models during the testing phase has acceptable accuracy measures. For instance, the MAE of all the models was sufficiently less and the RRMSE values less than 0.4 and 0.3 signpost that the spatial K_s predictions were decently and highly accurate, respectively. Strategy 1 model of 2017 had a higher prediction accuracy compared to other ANFIS models with a test NSE = 0.949. The Gaussian and Gbell membership functions were found to provide better prediction accuracy for the spatial modeling strategies 1 and 2, respectively.

Performance of SVM prediction models

The support vector machine (SVM) with radial basis kernel function was employed in this study to predict the spatial streambed hydraulic conductivity. The optimal parameters of SVM (i.e., the cost, kernel, and the ε-insensitive loss function) were identified via 3D Grid Search. Table 5 presents the optimal values of SVM parameters. Hypothetically, a logarithmic grid ranging between 2^{-12} and 2^{12} is usually sufficient for arriving at the best parameter combination. In the event that the best parameters lie on the limits of the grid, the further search could be extended in that direction in a subsequent search. The performance statistics of the SVM model for each strategy are presented in Table 6.

From the statistical indices, it is evident that the performance of all the SVM models during the testing phase was of relatively higher accuracy. The MAE of all the model predictions was sufficiently less, and the RRMSE values less than 0.3 signpost superior spatial K_s predictions. Strategy 1 model of 2016 had a higher prediction accuracy compared to other SVM models with a test NSE = 0.941.

Comparative evaluation of AI models

The three AI models, namely the ANN, ANFIS, and SVM, provided more or less satisfactory spatial predictions with respect to both the strategies considered. Both SVM and ANFIS prediction models performed much better than the ANN models, and based on the error indices the SVM models performed relatively better than the ANFIS prediction models. For a comparative evaluation of all the models, Table 7 presents the evaluated statistical indices of the test phase. Figure 7 illustrates the scatter plots based on the observed vs predicted streambed K_s values of Strategy 1—ANN, ANFIS, and SVM models during the test phase. Similarly, Fig. 8 illustrates the scatter plots of Strategy 2—ANN,

Table 3 The optimal ANFIS architectures

ANFIS models	ANFIS parameters		
	Membership function		
	Number	Input	Output
Strategy 1—2016	3	Gaussmf	Constant
Strategy 1—2017	3	Gaussmf	Constant
Strategy 2—2016	3	Gbellmf	Constant
Strategy 2—2017	3	Gbellmf	Constant

Table 5 The optimal SVM architectures

SVM models	SVM parameters		
	Radial basis kernel function		
	Cost 'C'	Gamma 'γ'	Epsilon 'ε'
Strategy 1—2016	1024	38	0.0707
Strategy 1—2017	1156	44	0.1080
Strategy 2—2016	980	52	0.1785
Strategy 2—2017	1120	40	0.0967

Table 4 Performance indices of ANFIS modeling

ANFIS Model	Train			Test		
	RRMSE	MAE (cm/day)	NSE	RRMSE	MAE (cm/day)	NSE
Strategy 1—2016	0.206	40.78	0.957	0.247	56.14	0.937
Strategy 1—2017	0.216	41.78	0.955	**0.222**	**51.5**	**0.949**
Strategy 2—2016	0.279	45.278	0.931	0.372	67.386	0.86
Strategy 2—2017	0.294	47.98	0.913	0.335	64.6	0.887

Bold values represent superior performance during test phase

Table 6 Performance indices of SVM modeling

SVM model	Train			Test		
	RRMSE	MAE (cm/day)	NSE	RRMSE	MAE (cm/day)	NSE
Strategy 1—2016	0.155	50.45	0.965	**0.241**	**52.56**	**0.941**
Strategy 1—2017	0.204	51.67	0.933	0.265	56.41	0.928
Strategy 2—2016	0.264	52.567	0.927	0.322	57.66	0.895
Strategy 2—2017	0.196	50.96	0.942	0.295	55.3	0.911

Bold values represent superior performance during test phase

Table 7 Comparative evaluation of AI models with respect to test phase results

Statistic	RRMSE	MAE (cm/day)	NSE
Strategy 1—2016			
ANN	0.462	100.63	0.782
ANFIS	0.247	56.14	0.937
SVM	**0.241**	**52.56**	**0.941**
Strategy 1—2017			
ANN	0.491	108.72	0.75
ANFIS	**0.222**	**51.5**	**0.949**
SVM	0.265	56.41	0.928
Strategy 2—2016			
ANN	0.482	92.36	0.765
ANFIS	0.372	67.386	0.86
SVM	**0.322**	**57.66**	**0.895**
Strategy 2—2017			
ANN	0.458	85.82	0.788
ANFIS	0.335	64.6	0.887
SVM	**0.295**	**55.3**	**0.911**

Bold values represent superior performance during test phase

ANFIS, and SVM models during the test phase. The scatter plot displays the strength, direction, and form of the relationship between the observed and predicted streambed K_s values. The prediction performance or the relative skill of different AI models is graphically summarized via Taylor diagrams as presented in Figs. 9 and 10.

With reference to Strategy 1 model for 2016 K_s data, the SVM model provides relatively better predictions than other two based on the NSE statistic. The RRMSE = 0.24 indicates relatively good spatial K_s predictions. The instances of underestimation and overestimation of observed K_s values were better captured in scatter plots presented in Fig. 7 wherein the K_s predictions by SVM model were quite closer to the observed values. In Taylor diagram as presented in Fig. 9, three statistical indices, namely the correlation coefficient (R), the standard deviation (σ) and the root-mean-square difference (RMSD), are used to characterize the statistical relationship between the modeled and reference fields. In this case, both ANFIS and SVM predictions were analogous to each other. For a comparative evaluation of RRMSE and NSE statistic, Fig. 11 presents the pictographic representation via bar chart. The model efficiencies of spatial modeling scheme 1 (i.e., Strategy 1) were better compared to Strategy 2 due to the incorporation of more number of sampling points for model training.

Pertaining to *Strategy 1 model for 2017* K_s *data*, the performance of ANFIS prediction model was found to be relatively superior to the SVM model. The ANN model underperformed as compared to ANFIS and SVM predictions. From the scatter plots presented in Fig. 7, it can be observed that both ANFIS and SVM models were analogous in capturing the spatial variations of streambed K_s. From the Taylor diagram as presented in Fig. 9, it can be observed that the standard deviation of ANN predictions significantly differs from that of the observed K_s data. Here, the RMSD, standard deviation, and correlation coefficient of ANFIS predictions were superior to SVM predictions.

Comparing the statistical indices with regard to *Strategy 2 models* for 2016 and 2017 K_s data, it was evident that the SVM predictions outperform the other two models in terms of all the indices considered. The scatter plots presented in Fig. 8 portray the ability of individual AI models to fit the observed K_s data. From the Taylor diagrams as presented in Fig. 10, it could be seen that the standard deviation of ANFIS predictions was closer to the standard deviation curve of observed K_s data. However, the SVM predictions had better RMSD and R statistics, reaffirming the better accuracy over its comparison counterparts. Henceforth, based on NSE, RMSD and R values, the SVM model predictions were considered to be efficient even though the ANFIS predictions were less biased compared to SVM predictions.

It is always not possible to collect dense data of any variable of interest by sampling through experiments from the area of interest. In such cases, with limited data obtained through coarse sampling could be employed to predict data samples to enhance the database. For instance, in the present study, with the help of neighborhood streambed K_s data samples, the AI models provided reliable predictions of streambed K_s at two different spatial scales. The streambed K_s being an important parameter for assessing the

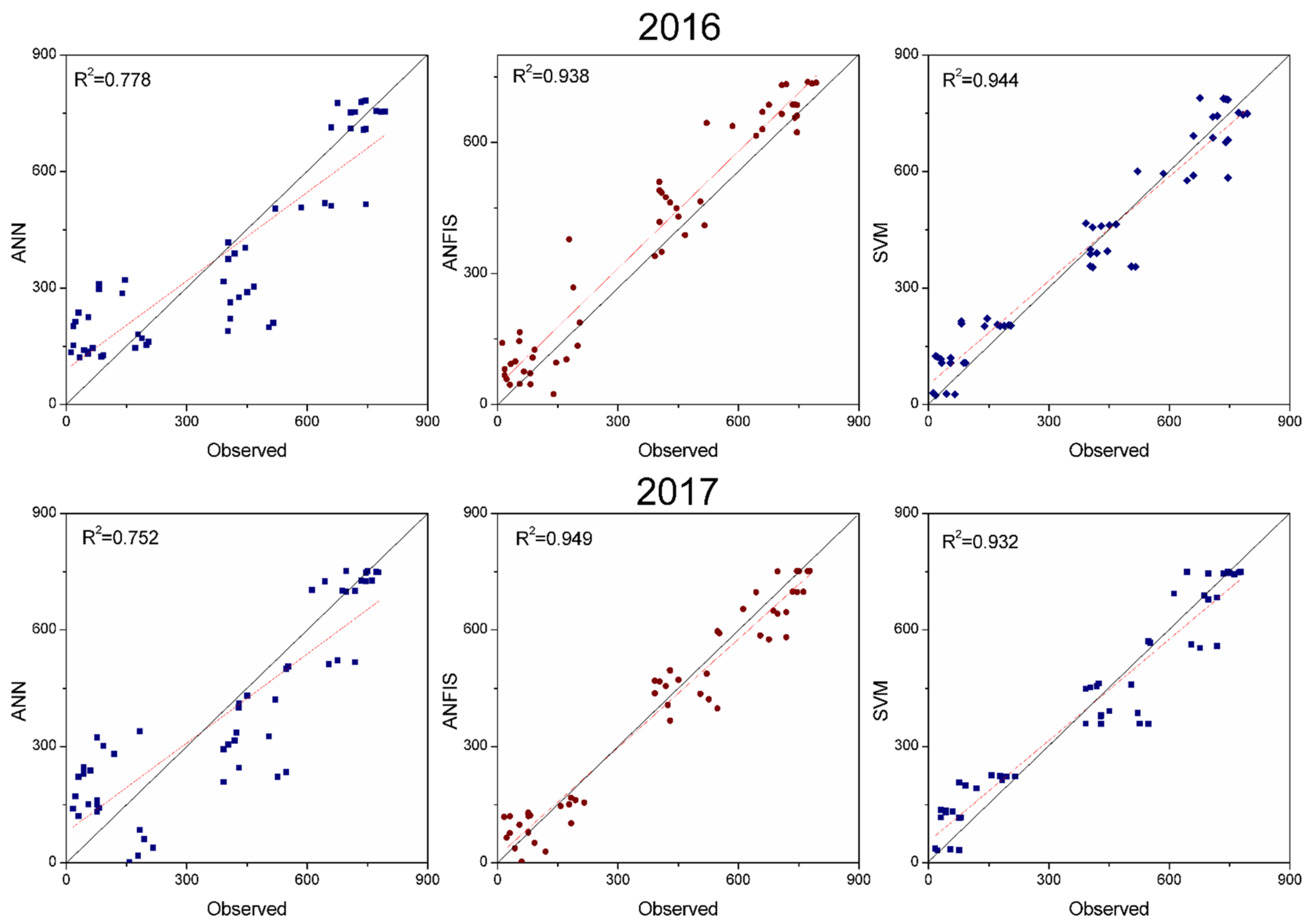

Fig. 7 Scatter plots of Strategy 1—ANN, ANFIS and SVM models during the test period

surface water seepage into aquifers needs to be studied to identify potential recharge zones along the length/stretch of the river.

Summary and conclusions

The artificial intelligence (AI) based spatial modeling schemes were tested to predict the spatial patterns of streambed hydraulic conductivity. The geographical coordinates (i.e., latitude and longitude) of the sampled locations from where the in situ hydraulic conductivity measurements were made were used as model inputs to predict streambed K_s over spatial scale using an artificial neural network (ANN), adaptive neuro-fuzzy inference system (ANFIS), and support vector machine (SVM) paradigms. The statistical measures computed by using the actual versus predicted streambed K_s values of individual models were comparatively evaluated. The spatial modeling schemes/strategies proposed were found suitable for predicting streambed K_s patterns. With such spatial modeling schemes that incorporate the neighborhood data to predict the variable of interest, one can easily predict at unknown point locations at significant confidence levels. The AI-based spatial models provided more or less satisfactory spatial K_s prediction efficiencies with respect to both the strategies/schemes considered. Although ANN and ANFIS models provided a satisfactory level of predictions, the SVM model was found to provide more accurate streambed K_s patterns due to its inherent capability to adapt to input data that are non-monotone and nonlinearly separable. The tuning of SVM parameters via 3D grid search was responsible for higher efficiencies of SVM models. The present study involved the prediction of streambed hydraulic conductivity at shorter spans or intervals. Even with limited field experimental data, the study discloses the potential of data-driven models to predict streambed K_s patterns by presenting two spatial modeling schemes. In the future, one can test the similar strategies for longer spatial scales/spans with sufficient data collected from an extensive stretch of the river.

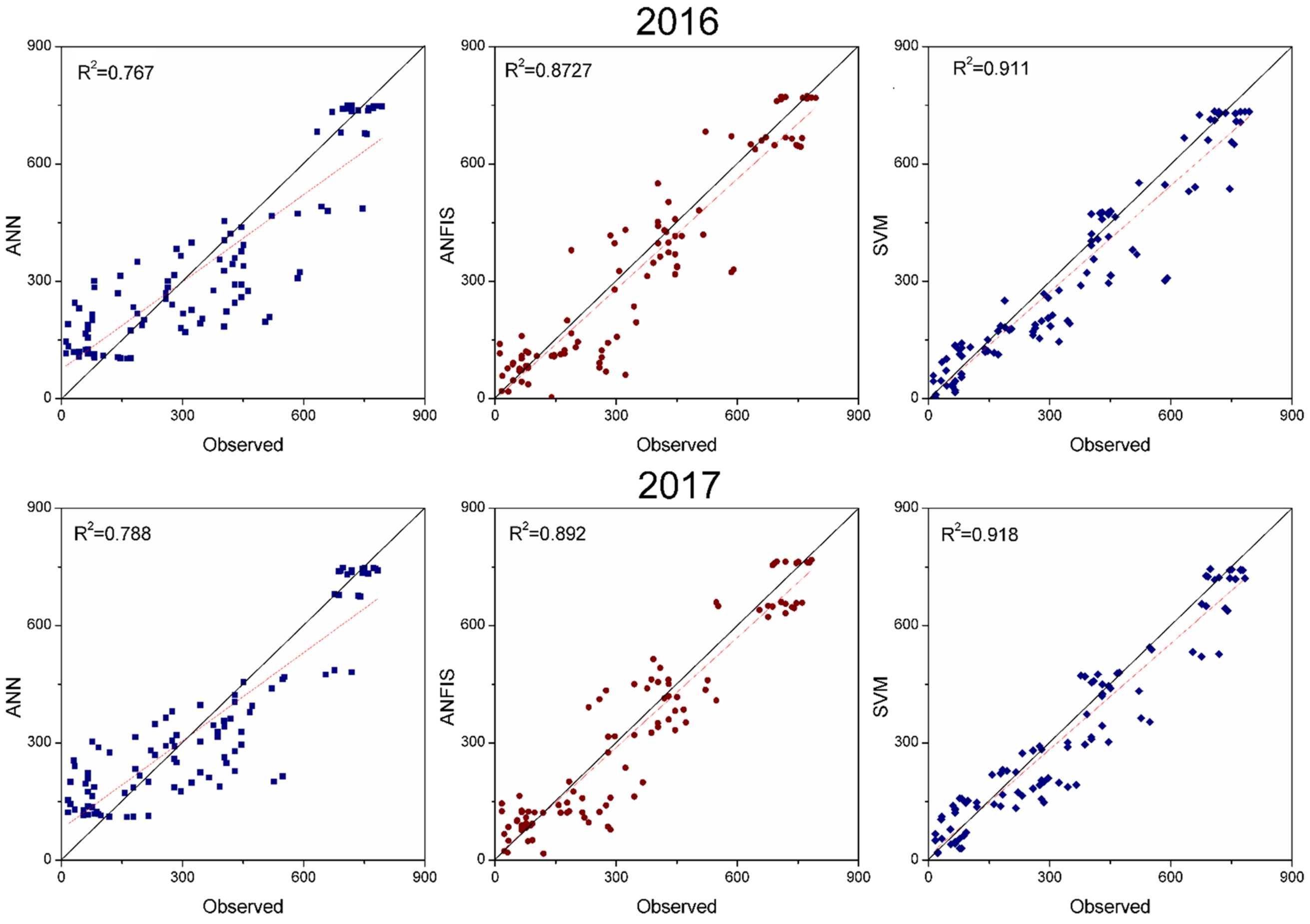

Fig. 8 Scatter plots of Strategy 2—ANN, ANFIS and SVM models during the test period

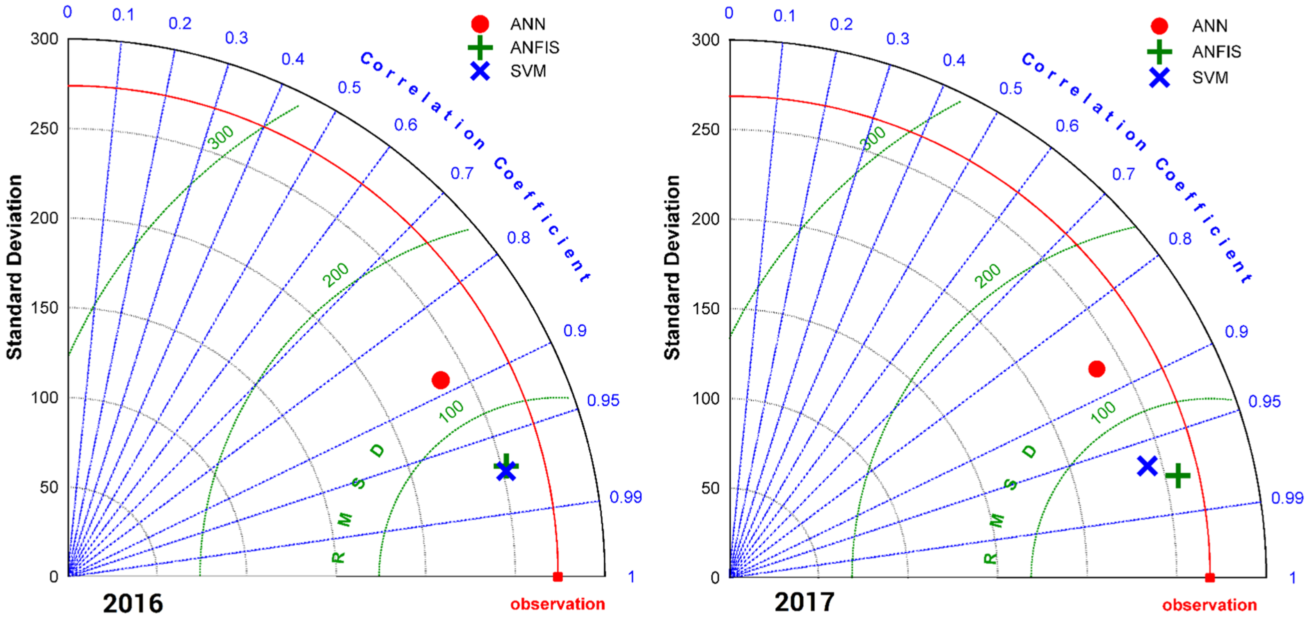

Fig. 9 Taylor diagrams plotted for comparative evaluation of Strategy 1—ANN, ANFIS and SVM models of test phase

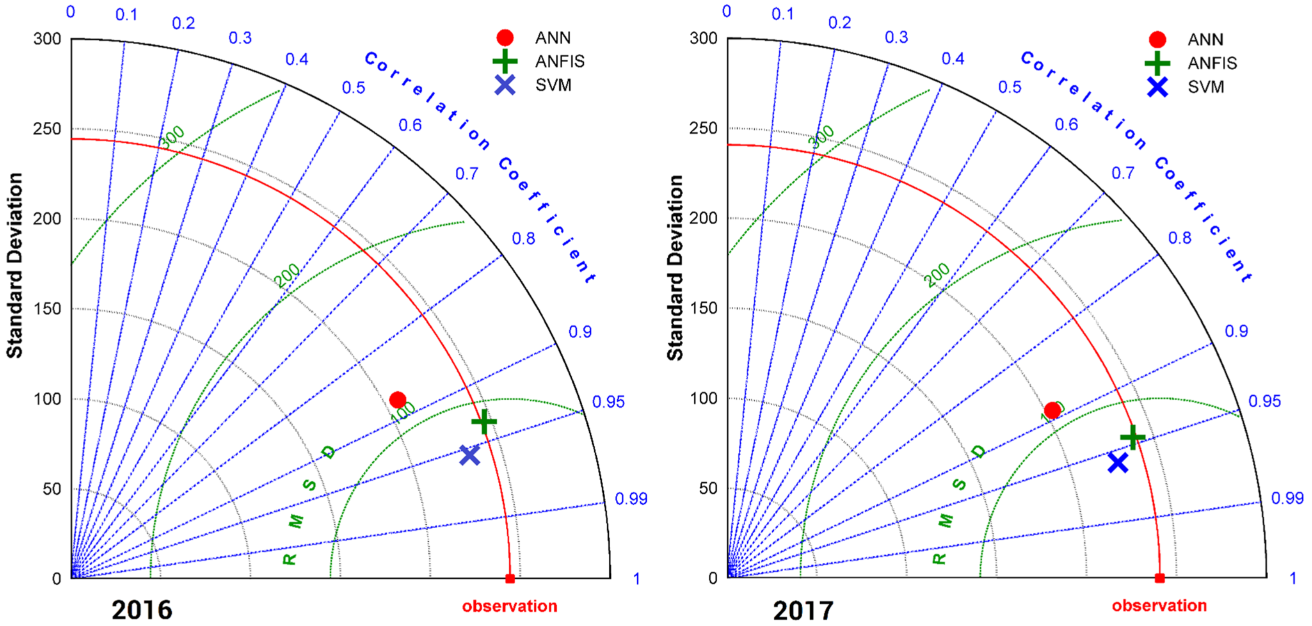

Fig. 10 Taylor diagrams plotted for comparative evaluation of Strategy 2—ANN, ANFIS and SVM models of the test phase

Fig. 11 Plot of RRMSE and NSE statistic of all the AI models

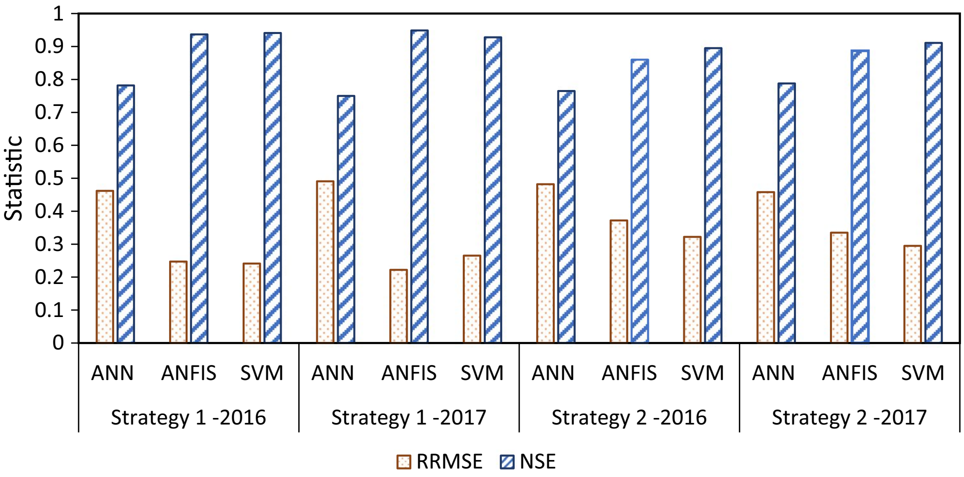

Compliance with ethical standards

Conflict of interest On behalf of all authors, the corresponding author states that there is no conflict of interest.

References

Abraham A (2005) Adaptation of fuzzy inference system using neural learning. In: Nedjah N, Macedo Mourelle L (eds) Fuzzy systems engineering. Studies in fuzziness and soft computing, vol 181. Springer, Berlin, Heidelberg. https://doi.org/10.1007/11339366_3

Cortes C, Vapnik V (1995) Support-vector networks. Mach Learn 20:273–297. https://doi.org/10.1007/BF00994018

Cristianini N, Shawe-Taylor J (2000) An introduction to support vector machines and other kernel-based learning methods. Cambridge University Press, Cambridge

Cross SS, Harrison RF, Kennedy RL (1995) Introduction to neural networks. Lancet 346:1075–1079. https://doi.org/10.1016/S0140-6736(95)91746-2

Dai F, Zhou Q, Lv Z, Wang X, Liu G (2014) Spatial prediction of soil organic matter content integrating artificial neural network and ordinary kriging in Tibetan Plateau. Ecol Indic 45:184–194. https://doi.org/10.1016/j.ecolind.2014.04.003

Forkuor G, Hounkpatin OKL, Welp G, Thiel M (2017) High resolution mapping of soil properties using remote sensing variables in south-western Burkina Faso: a comparison of machine learning and multiple linear regression models. PLoS One 12:e0170478. https://doi.org/10.1371/journal.pone.0170478

Gholami V, Booij MJ, Nikzad Tehrani E, Hadian MA (2018) Spatial soil erosion estimation using an artificial neural network (ANN) and field plot data. Catena 163:210–218. https://doi.org/10.1016/j.catena.2017.12.027

Ghorbani H, Kashi H, Hafezi Moghadas N, Emamgholizadeh S (2015) Estimation of soil cation exchange capacity using multiple regression, artificial neural networks, and adaptive neuro-fuzzy inference system models in Golestan Province. Iran. Commun Soil Sci Plant Anal 46:763–780. https://doi.org/10.1080/00103624.2015.1006367

Grekousis G, Manetos P, Photis YN (2013) Modeling urban evolution using neural networks, fuzzy logic and GIS: the case of the Athens metropolitan area. Cities 30:193–203. https://doi.org/10.1016/j.cities.2012.03.006

Jain AK, Mao Jianchang, Mohiuddin KM (1996) Artificial neural networks: a tutorial. Computer (Long Beach Calif) 29:31–44. https://doi.org/10.1109/2.485891

Jang J-SR (1992) Neuro-fuzzy modeling: architectures, analyses, and applications. University of California, Berkeley

Jang JSR (1993) ANFIS: adaptive-network-based fuzzy inference system. IEEE Trans Syst Man Cybern 23:665–685. https://doi.org/10.1109/21.256541

Jang J-SR, Sun C-T, Mizutani E (1997) Neuro-fuzzy and soft computing: a computational approach to learning and machine intelligence. Prentice Hall, New Jersey

Khosravi K, Mao L, Kisi O, Yaseen ZM, Shahid S (2018) Quantifying hourly suspended sediment load using data mining models: case study of a glacierized Andean catchment in Chile. J Hydrol 567:165–179

Kirkwood C, Cave M, Beamish D, Grebby S, Ferreira A (2016) A machine learning approach to geochemical mapping. J Geochemical Explor. https://doi.org/10.1016/j.gexplo.2016.05.003

Kisi O, Yaseen ZM (2019) The potential of hybrid evolutionary fuzzy intelligence model for suspended sediment concentration prediction. Catena 174:11–23

Kohonen T (1988) An introduction to neural computing. Neural Networks 1:3–16. https://doi.org/10.1016/0893-6080(88)90020-2

Leuenberger M, Kanevski M (2015) Extreme learning machines for spatial environmental data. Comput Geosci 85:64–73. https://doi.org/10.1016/j.cageo.2015.06.020

Merdun H, Çınar Ö, Meral R, Apan M (2006) Comparison of artificial neural network and regression pedotransfer functions for prediction of soil water retention and saturated hydraulic conductivity. Soil Tillage Res 90:108–116. https://doi.org/10.1016/j.still.2005.08.011

More SB, Deka PC (2018) Estimation of saturated hydraulic conductivity using fuzzy neural network in a semi-arid basin scale for murum soils of India. ISH J Hydraul Eng 24:140–146. https://doi.org/10.1080/09715010.2017.1400408

Motaghian HR, Mohammadi J (2011) Spatial estimation of saturated hydraulic conductivity from terrain attributes using regression, kriging, and artificial neural networks. Pedosphere 21:170–177. https://doi.org/10.1016/S1002-0160(11)60115-X

Naganna SR, Deka PC (2018) Variability of streambed hydraulic conductivity in an intermittent stream reach regulated by Vented Dams: a case study. J Hydrol 562:477–491. https://doi.org/10.1016/j.jhydrol.2018.05.006

Naganna SR, Deka PC, Ch S, Hansen WF (2017) Factors influencing streambed hydraulic conductivity and their implications on stream–aquifer interaction: a conceptual review. Environ Sci Pollut Res 24:24765–24789. https://doi.org/10.1007/s11356-017-0393-4

Raghavendra NS, Deka PC (2014) Support vector machine applications in the field of hydrology: a review. Appl Soft Comput 19:372–386. https://doi.org/10.1016/j.asoc.2014.02.002

Reid CE, Jerrett M, Petersen ML, Pfister GG, Morefield PE, Tager IB, Raffuse SM, Balmes JR (2015) Spatiotemporal prediction of fine particulate matter during the 2008 Northern California wildfires using machine learning. Environ Sci Technol 49:3887–3896. https://doi.org/10.1021/es505846r

Sanikhani H, Deo RC, Yaseen ZM, Eray O, Kisi O (2018) Non-tuned data intelligent model for soil temperature estimation: a new approach. Geoderma 330:52–64

Sivanandam S, Paulraj M (2009) Introduction to artificial neural networks. Vikas Publishing House, New Delhi

Twarakavi NKC, Šimůnek J, Schaap MG (2009) Development of pedotransfer functions for estimation of soil hydraulic parameters using support vector machines. Soil Sci Soc Am J 73:1443. https://doi.org/10.2136/sssaj2008.0021

Vapnik VN (1999) An overview of statistical learning theory. IEEE Trans Neural Netw 10:988–999. https://doi.org/10.1109/72.788640

Vapnik VN (2000) The nature of statistical learning theory. Springer, New York. https://doi.org/10.1007/978-1-4757-3264-1

Wu G, Shu L, Lu C, Chen X (2015) The heterogeneity of 3-D vertical hydraulic conductivity in a streambed. Hydrol Res 47(1):15–26. https://doi.org/10.2166/nh.2015.224

Zhao C, Shao M, Jia X, Nasir M, Zhang C (2016) Using pedotransfer functions to estimate soil hydraulic conductivity in the Loess Plateau of China. Catena 143:1–6. https://doi.org/10.1016/j.catena.2016.03.037

Acta Geophysica (2019) 67:905–920
https://doi.org/10.1007/s11600-019-00285-3

RESEARCH ARTICLE - HYDROLOGY

A multifaceted analysis of the relationship between daily temperature of river water and air

Renata Graf[1]

Received: 15 August 2018 / Accepted: 1 April 2019 / Published online: 5 April 2019

Abstract

The aim of the study was to establish the strength and direction of the relationship between daily temperature of river water and air with the use of selected estimation methods. The relationship was assessed for the River Noteć and its tributaries (Western Poland), using the cross-correlation function and Granger causality. The study established cause-and-effect relations for "water–air" and "air–water" directions of influence. It was confirmed that forecasting the pattern of flowing water temperature from changes in air temperature yields better results when done based on data from the previous day. Results of modelling the relationship between data series with the use of the linear and natural cubic splines models confirmed the presence of a nonlinear relation. It was also established that there is a statistically significant correlation of random fluctuations for both temperature series on the same days. This made it possible to confirm the occurrence of short-term connections between water and air temperature. The results can be used to determine the qualities of thermal regimes and to predict temperature of river waters in the conditions of climate change.

Keywords Cross-correlation · Granger's causality · Natural cubic splines model · Linear model · Water temperature · Air temperature

Introduction

Being prepared for climate change, the symptoms of which include an increase in air temperature and the temperature of river waters, constitutes one of the main challenges for the monitoring and assessment of the ecological state of waters and the management of water resources (Bolker et al. 2009; Arismendi et al. 2014). The thermal characteristics of waters have considerable ecological and practical significance for the economic utilisation of rivers (Allan and Castillo 2007). The temperature of river waters is a good indicator of climate change and of the degree of control of processes occurring in aquatic systems (Conlan et al. 2005; Olden and Naiman 2010; Padilla et al. 2015; Jackson et al. 2016; Letcher et al. 2016).

The temperature of river waters is subject to daily, seasonal, annual, and multi-annual change, which is the result of the impact of climatic factors, river supply conditions, thermal characteristics of tributaries, and anthropogenic factors, e.g. the inflow of wastewater, thermal pollutants, and hydromorphological changes occurring within the channel of the water course (Sinokrot et al. 1995; Caissie 2006; Webb and Nobilis 2007; Graf 2018). The specific utilisation of the catchment area and the selected method of development of the river valley may also modify the thermal characteristics of river waters (Younus et al. 2000; Wiejaczka 2007; Gallice et al. 2015; Lisi et al. 2015).

The modelling of changes in river water temperature and its relationship with air temperature is conducted on various time and space scales (Caissie 2006; Arismendi et al. 2014; Hilderbrand et al. 2014). These dependences have been confirmed at various time resolution levels, taking into consideration the nature of short-term, medium-term, and long-term fluctuations (Webb et al. 2003; Sahoo et al. 2009; Toffolon and Piccolroaz 2015). Research into the relationships between river water and air temperature is conducted using genetic and statistical models. These are developed not only in relation to air temperature, but also as a function of

---

✉ Renata Graf
rengraf@amu.edu.pl

[1] Department of Hydrology and Water Management, Institute of Physical Geography and Environmental Planning, Adam Mickiewicz University in Poznan, Bogumiła Krygowskiego 10 str, 61-680 Poznan, Poland

the transfer of heat originating from groundwaters and the exchange that takes place in the hyporheic zone. Thermal energy is exchanged primarily on the air–water level, and to a lesser extent on the river bed–water level (Sinokrot and Stefan 1994; Caissie 2006).

The statistical methods used for analysing the thermal characteristics of waters and their relationships with air temperature range from simple linear regression equations to more complex parametric and nonparametric methods (Benyahya et al. 2007; Letcher et al. 2016). A multifaceted analysis makes it possible to determine the structure of connections and interdependences existing between water and air temperature (strength, form, and direction of the relationship), and forecast the relationship between variables. For the purpose of predicting the temperature of river waters, deterministic models make use of the energy balance (Sinokrot and Stefan 1994; Benyahya et al. 2007), whereas regression and stochastic models employ air temperature data (Caissie et al. 2004; Hilderbrand et al. 2014; Li et al. 2014). Due to their good forecastability, they are used for predicting changes in water temperature in the context of climate change (Neumann et al. 2003; Webb et al. 2003; Lagergaard Pedersen and Sand-Jensen 2007). Analyses are concerned primarily with the nature and strength of the relationship between water and air temperature measurement series, and also with the synchronicity of their fluctuations. Good results are obtained, among others, through the logistic regression model, which approximates the dependence by means of an S-shaped function. This model effectively reflects the behaviour of water temperature at negative and high (in excess of 25 °C) air temperature. Its application has made it possible, among others, to confirm that the strength of logistic and linear relationships between river water and air temperature is greater for average weekly values and average maximum weekly values than for average daily values or maximum daily values (Neumann et al. 2003).

The majority of studies result in high determination coefficients ($R^2 > 0.8$), which point to the high dependence of water temperature on air temperature (Pilgrim et al. 1998; Caissie et al. 2001; Webb et al. 2003; Morrill et al. 2005). Research into the thermal regime of Polish rivers also confirms the high impact of air temperature on the course and variability of river water temperature. Goodness-of-fit values of models for the lower River Świder calculated by Łaszewski (2014) are similar to the goodness-of-fit values obtained by the aforementioned authors. When analysing the relationship between air temperature and water temperature in the River Ropa, Wiejaczka (2007) determined that this relationship is very strong, which is confirmed by the fact that the corresponding coefficient of correlation ranges from 0.90 to 0.95. The coefficient of correlation between water temperature in the River Ropa and air temperature in winter half-year periods alternated between 0.75 and 0.89, whereas in the summer half-year periods the value of this coefficient was slightly greater, fluctuating from 0.85 to 0.95. In the winter half-year periods following the commissioning of the Klimkówka reservoir on the River Ropa, there occurred a noticeable increase in the value of the coefficient of correlation (0.80–0.89), while in the summer half-year periods it was observed that its value fell to the range of 0.61–0.87. According to Wiejaczka (2011), linear regression makes it possible, among others, to estimate the value of water temperature in rivers under conditions of increased air temperature brought about by potential climate changes, and also to determine the reach of subterranean supply and its impact on the thermal characteristics of rivers. Kędra and Wiejaczka (2016) have conducted an analysis of changes in the natural relations between the water temperature of the River Dunajec and air temperature based on values of the Pearson correlation coefficient. This research has shown that the dependences between the analysed variables in the years 1978–1992, i.e. before the group of reservoirs was commissioned, were stronger during the summer period (coefficient of correlation of 0.75–0.86) and weaker in winter (coefficient of correlation of 0.54–0.73). Following the erection of the Czorsztyn–Sromowce Wyżne reservoirs, values of the coefficient of correlation fell to the range of 0.53–0.77 in the summer half-year period, while in the winter half-year period the strength of the relationship grew to 0.60–0.82. The application of a model describing the dependence between water and air temperature by means of a linear function has proved useful in the case of the River Warta (the middle section of its course) for the range of temperatures from 0.5–1.0 °C to approximately 22–23 °C (Graf 2015). The analysis confirmed that this relationship has a nonlinear form which is most significantly impacted by the behaviour of water temperature at negative air temperature values or during periods of long-term frost. When the air temperature is high, the temperature of water in rivers does not increase linearly, this because of the intense loss of thermal energy in processes of evaporation and emission of long-wave radiation (Graf 2015; Łaszewski 2014). Statistical significance was also demonstrated for the coefficient of correlation between air temperature and the water temperature of the River Warta along the section between Bobry and Skwierzyna in the years 1991–2010 (Graf et al. 2018). The coefficient assumed a high value, ranging from 0.74 to 0.83 at individual stations. The principal components analysis (PCA) of the natural variability of water temperature in surface waters of the Tatra Mountains confirmed the dependence of water temperature on weather conditions, catchment characteristics, and flow rate, explaining 88.97% of total data variability (Żelazny et al. 2018). The authors of these studies also confirmed that wavelet analysis is helpful in identifying cyclical patterns in water temperature time series. Furthermore, a number of studies were carried out of the mutual relations between water and air temperature in terms of the assessment of long-term tendencies of change therein taking into consideration climate change. As regards the Polish Lowland, a clear increase in air and inland water temperature was determined over longer periods, such as the year or half-year. In shorter periods (months), this increase is not always obvious, and sometimes even a fall in temperature was observed (Graf et al. 2018; Marszelewski and Pius 2018). The allochthonous character of rivers guarantees greater temperature stability of waters along their course, while the thermal characteristics of tributaries and spatial changes in the methods of their supply may contribute to a disruption of the thermal continuum.

Analyses of the interdependence of statistical features of water and air temperature also use multi-level regression modelling, such as—for example—the hierarchical linear model, which is known as the regression model for random effects (Hox 2002). This is elaborated on the basis of a division of measurement series into permanent and random effects, a multi-level data structure taking into consideration inter-level interaction, and a specific approach to variance components (Gelman and Hill 2006). An example is, among others, a hierarchical model of daily stream temperature using air–water temperature synchronisation, autocorrelation, and time lags, elaborated in a small stream network in western Massachusetts—USA (Letcher et al. 2016). The presented model limits analysis to days when air and water temperature is synchronised, accommodates hysteresis, incorporates time lags, can deal with missing data and autocorrelation, and can include external drivers. An interesting approach applied in research into the relationship between river water and air temperature is the hybrid model, which uses a hybrid formulation characterised by a physically based structure associated with a stochastic calibration of the parameters (Piotrowski and Napiórkowski 2018). This model has been utilised among others to predict daily averaged river water temperature as a function of air temperature and discharge in selected rivers in Switzerland (Toffolon and Piccolroaz 2015). The degree of consistency achieved for different model versions with measurements performed in the three rivers suggests that the proposed model may constitute a useful tool for synthetically describing the medium- and long-term thermal characteristics of waters, and also for capturing their changes caused by variable external conditions. Furthermore, spatial analyses of river systems make use of geostatistical models (Rushworth et al. 2015) and regional neural networks (Sahoo et al. 2009; DeWeber and Wagner 2014; Napiórkowski et al. 2014). Finally, assessments of the regularity of features of the thermal regime of rivers also utilise the equilibrium temperature concept (Caissie et al. 2005) and regional dependences connected with geographical latitude (Arscott et al. 2001; Gardner et al. 2003).

The study presents a multifaceted approach to the analysis of the relationship between daily river water and air temperature using selected estimation methods. The objective of research was to determine the character, strength, and direction of the relationship between observation series on the example of the River Noteć, which serves important economic and ecological functions (Western Poland, Polish Lowlands). For the purpose of assessing the relationship between data series, use was made of the cross-correlation function and its decay, while causality dependences were analysed in terms of Granger's causality (referred to as *G*-causality). Cause-and-effect relationships occurring on the "water–air" axes were also determined. As regards water and air temperature time series, the identification of causal patterns for the variance and the mean using Granger's causality analysis may serve to improve the quality of forecasting these values. Assuming a nonlinear relationship between water and air temperature data series, an indication was given of the usefulness and appropriateness for such research of the linear model and the natural cubic spline model.

Source material and methodology

Test area

Research into the dependences between daily river water and air temperature was conducted in the catchment area of the River Noteć that drains the western part of the Polish Lowlands (Fig. 1). The Noteć is the largest tributary of the River Warta, which itself flows into the River Oder (a drainage area of the Baltic Sea). In the division of Poland into physico-geographical regions (Kondracki 2008), the catchment area of the River Noteć is located within the reach of two macroregions: the Wielkopolskie Lake District, through which the river flows in its main bed, and the Pomeranian Lake District, which is traversed by its two right-bank tributaries—the rivers Gwda and Drawa (Fig. 1). The catchment area is located primarily within the reach of two climatic regions: that of Western Wielkopolska and that of Eastern Wielkopolska (Woś 2010), where the mean annual air temperature amounts to 8.3 °C and 8.0 °C, respectively.

There are numerous lakes along the course of the Noteć and its tributaries, and these occupy approximately 4% of the surface of the catchment area (Fig. 1). The river is regulated by means of a system of flood gates and channelled in its middle course, which impacts its hydrological features. The Noteć and its tributaries are characterised by a snow-and-rain type supply. The greatest flows usually occur in March and April, when spring run-off accounts for some 130–180% of annual run-off. Average annual specific run-off for the River Noteć in the Nowe Drezdenko profile is

Fig. 1 Location of the Noteć catchment area in Polish regions with IMGW-PIB stations measuring water and air temperature

144 mm (according to IMGW-PIB data). The lowest flow values occur from July to September. Summer–autumn low waters are predominant in the Noteć and Drawa, and their average duration is longest, totalling 75 and 97 days, respectively. The river is characterised by considerable fluctuations of water levels, and their maximum spread in its lower course amounts to 3.5 m.

Taking into consideration the abiotic type of river waters and their biotic typology (macrobenthic, phytobenthic, and macrophytobenthic), the River Noteć has been classified among the "great lowland rivers" (ETC/ICM 2015). The water course serves as a migration corridor for numerous species of fishes, while due to its excellent natural qualities the river valley has become the object of conservation measures, notably through the establishment of Natura 2000 areas (which include the "Noteć Valley" and the "Valley of the Middle Noteć and the Bydgoszcz Channel").

Database

When modelling the relationship between daily river water and air temperature, use was made of measurement data gathered by the Institute of Meteorology and Water Management—National Research Institute in Warsaw (IMGW-PIB in Warsaw) for the period 1987–2013. These data contain daily water temperature of the River Noteć registered at three points located along its course: at Pakość (upper course), Ujście (middle course), and Nowe Drezdenko (lower course), and also along its tributaries, i.e. the Gwda (Piła profile) and the Drawa (Drawiny profile)—Fig. 1. For comparative purposes, use was additionally made of daily water temperature for the River Drawa at the point in Drawsko Pomorskie, albeit for a shorter measurement period (1987–1992). Daily air temperature for the years 1987–2013 was obtained from the Piła synoptic station located in the catchment area of the Noteć. Data concerning air temperature obtained at this station are homogenous. Series uniformity was confirmed using the Alexandersson test, and therefore, these data should be considered as representative for the research area and period. The choice of research period was influenced by the ability to access a uniform observation series of water and air temperature, uninterrupted by the lack of measurement values.

Multifaceted modelling

Modelling of the relationship between time series of daily temperature values was preceded by an assessment of data series stationarity, conducted using the Augmented Dickey–Fuller (ADF) test (Dickey and Fuller 1981). As regards the analysed data series (1987–2013), it was determined that daily measurements of water and air temperature constitute stationary series (stationarity at a p value of 0.01) characterised by invariability when shifted along the time axis of the mean and the variance.

The point of departure for assessing the relationship between data series concerning daily temperature was an analysis of the cross-correlation function, which is the standard for determining the similarity of measurements. It uses value functions of the Pearson correlation coefficient for two time series shifted in relation to each other by time unit Δt either forward or backward, depending on the value of Δt. In order to provide a quantitative description of the phenomenon of decaying cross-correlations, a determination was made of the decay function of the square of cross-correlation for measurements carried out on the same day in different years. This may be interpreted as the variance percentage of one variable explained by another variable for measurements made on the same day in different years. To this end, use was made of third-degree polynomial regression for the natural logarithm of the square of correlation, where the distance between measurements—counted in years—was a dependent variable.

Further, a Granger's causality analysis (Granger 1988) was performed, and this made it possible to identify the direction of cause-and-effect relationships between water and air temperature. The Granger's causality refers to a situation where data concerning the past of one time series provide significant information that helps predict the value of a second series, which is not included in the information concerning its past values. Research utilised the Granger's causality test (Detto et al. 2012), which was conducted for stationary processes. The general test determines solely whether a linear dependence exists. Granger's causality is a statistical approach used to identify the presence of linear causal interactions between time series of data, based on prediction theory. In accordance with the assumptions of causality (Granger 1988), which makes use of only two time series and does not reference the complete information set, variable Y influences variable X if:

$$P(Xt+1 \in A|X,Y) \neq P(Xt+1 \in A|X) \text{ for a certain event } A, \tag{1}$$

X—history of time series, X, X, Y—history of time series X, and Y, $Xt+1$—value of the variable at moment $t+1$.

An analysis was also performed of the strength of the relationship between measurements of river water and air temperature on the same days, taking into consideration the possibility of occurrence of a nonlinear relationship between the two. To this end, use was made of two models—a standard linear model for predicting water temperature on the basis of air temperature and the natural cubic spline model. The degree of correlation between the random fluctuations of series, i.e. of those changes in temperature that are not the result of a long-term trend, historical values or periodicity, was also determined. It provided valuable insight into the characteristics of short-term connections between water and air temperature (Graf 2018).

$$y_t = \varphi_1 y_{t-1} + \varphi_2 y_{t-2} + \varepsilon_t \quad (2)$$

where y_t—series value at time t, y_{t-1}—series value at time $t-1$, etc., ε_t—random component, disturbance from time t, t—successive days, and φ—a parameter defining the strength of impact of the preceding value in the process (or successive ones, incrementally older) on the current value.

The above dependences were then used to determine the residues for time series of temperature, that is, that part of each measurement which may be considered as a random fluctuation. The analysis of residue series for models was augmented by means of Granger's causality. When determining the changes in coefficients of determination (R^2) for models taking into consideration the past values of the second time series, an indication was given of the strength of cause-and-effect connections existing between them.

Calculations and statistical analyses were performed in the R calculation environment, version 3.3.2 (2016 October 31). The R suite (GNU R) is a software package for analysing data, and also a programming platform (R Core Team 2015). The results of the statistical significance tests used were assessed with reference to the adopted level of $\alpha = 0.05$. Whenever a different level of significance was adopted, the relevant information was attached to the results of calculations.

Results

Cross-correlations

The analysis of cross-correlations demonstrated a very high degree of interdependence between daily data series of water temperature values for the Noteć and its tributaries, and air temperature values for the station in Piła (Fig. 2). We can clearly observe that significant positive correlations occur between daily temperature measured for the same half-year periods (cold or warm in the hydrological year), and significant negative correlations for measurements performed in different half-year periods. Equally visible is the gradual decay of process memory, i.e. measurements from successive years are less and less correlated. This means that for a zero shift we have a maximum level of interdependence between both data series. As the shift increases over time, cross-correlation adopts a minimal value.

As regards the measurement points located on the River Noteć and its tributaries, the rivers Drawa (in Drawiny) and Gwda (in Piła), a similar picture of the cross-correlation functions for daily water and air temperature was observed, and thus, Fig. 2a presents (as representative) the chart for the Noteć in Ujście (middle course). A high level of interdependence between series of daily water and air temperature, albeit lower and more rapidly decaying than that for the remaining stations, was demonstrated by an analysis of cross-correlations at the Drawsko Pomorskie point on the River Drawa. In this case, however, only a 12-year observation series of river water temperature was available (Fig. 2b).

For comparative purposes, the effect of cross-correlation was determined for monthly water temperature of the River Noteć and its tributaries, and for air temperature measured

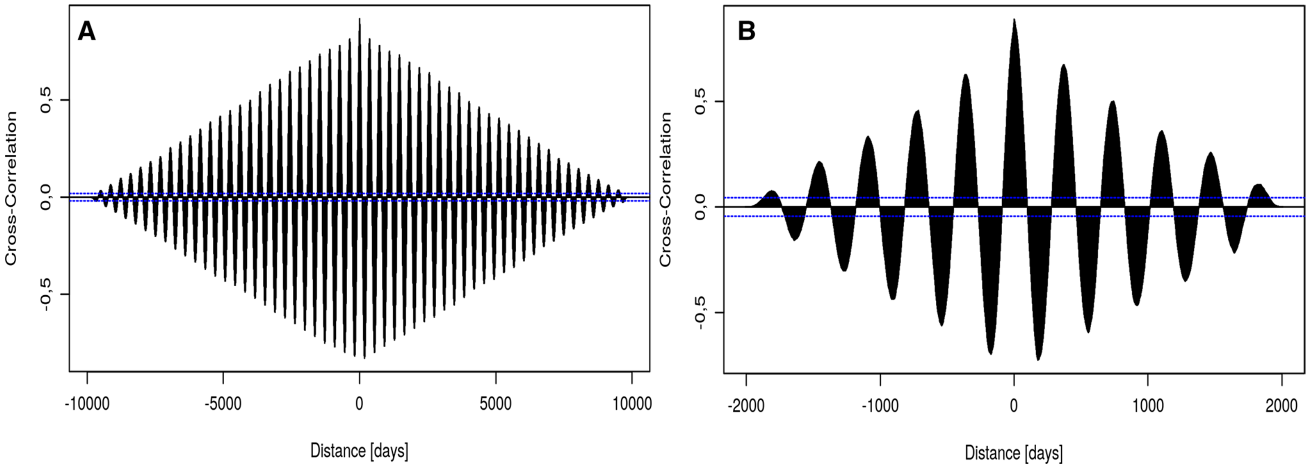

Fig. 2 Function of cross-correlations between daily water and air temperatures: **a** Noteć—Ujście (1987–2013) and **b** Drawa—Drawsko Pomorskie (1987–1991)

in Piła. In this case, too, the ADF test showed that time series are stationary, while an analysis of cross-correlations confirmed a very high level of interdependence between data series (average monthly temperature measured for the same hydrological half-year periods—cold or warm), which are additionally strictly periodic in nature (Fig. 3a, b).

In order to more precisely investigate the phenomenon of decaying cross-correlations, a determination was made of the decay function of the square of cross-correlation for measurements carried out on the same day in different years. Using third-degree polynomial regression for the natural logarithm of the square of correlation, solutions were obtained that were very well matched to the data (R^2)—Table 1. The coefficients of determination obtained were similar, falling within the range of 0.993–0.998 for the measurement series for the River Noteć, and totalling 0.997 for its tributaries. Clearly, therefore, the variance of variables registered in the water temperature measurement series is explained mainly by the variable temperature of air for measurements taken on the same day but in different years.

The decay function of the square of cross-correlation for measurements of river water and air temperature at individual measurement points located on the River Noteć and its tributaries is presented in Fig. 4. In the case of the River Gwda in Piła, due to the occurrence of problems with an unequivocal determination of the peaks of annual cross-correlations, the model was constructed taking into consideration only distances of not less than 14 years (among others, a distance of 5 years was omitted). Despite this inconvenience, we can observe that the dependence is very similar to that occurring at other measurement points (Fig. 4).

Granger's causality

When using Granger's causality to analyse dependences between daily water temperature of the River Noteć and its tributaries and air temperature (station in Piła), it was determined a cause-and-effect relationship (Table 2).

Furthermore, the test was a first-order test, which means that the cause-and-effect relationship occurs already between measurements t and $t-1$, where t stands for the distance between measurements, which is counted in years. Granger's causality was determined taking into consideration a one-day lag.

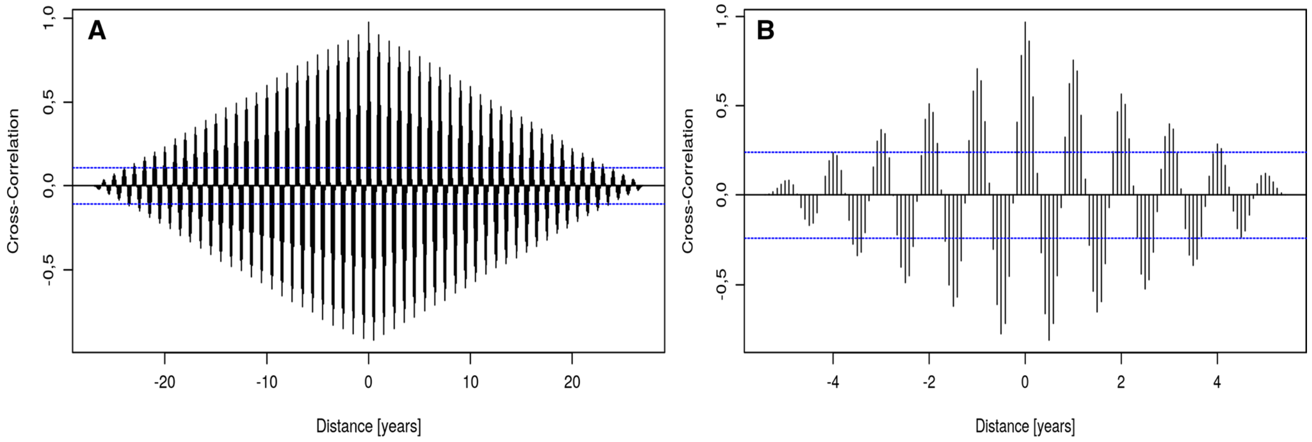

Fig. 3 Function of cross-correlations between monthly water and air temperatures **a** Noteć—Ujście (1987–2013) and **b** Drawa—Drawsko Pomorskie (1987–1991)

Table 1 Model of third-degree polynomial regression applied to the logarithm of a square of correlation between daily temperature of river water and air (Noteć River)

River—profile	Model of third-degree polynomial regression	R^2_{adj}
Noteć—Pakość	$\ln R^2 = -0.13 - 0.20t + 0.015t^2 - 0.001t^3$	0.993
Noteć—Ujście	$\ln R^2 = -0.18 - 0.16t + 0.011t^2 - 0.001t^3$	0.998
Noteć—Nowe Drezdenko	$\ln R^2 = -0.11 - 0.21t + 0.016t^2 - 0.001t^3$	0.994
Gwda—Piła	$\ln R^2 = -0.2009 - 0.1380t + 0.0082t^2 - 0.0005t^3$	0.997
Drawa—Drawiny	$\ln R^2 = -0.157 - 0.189t + 0.014t^2 - 0.001t^3$	0.997
Drawa—Drawsko Pomorskie[a]	$\ln R^2 = 0.62 - 1.90t + 0.62t^2 - 0.09t^3$	0.997

t—distance between measurements in years, R^2_{adj} adjusted parameter value

[a] Drawa—Drawsko Pomorskie: Lag order = 12 (1987–1991), for other measurement stations: Lag order = 27 (1987–2013), $\alpha = 0.01$

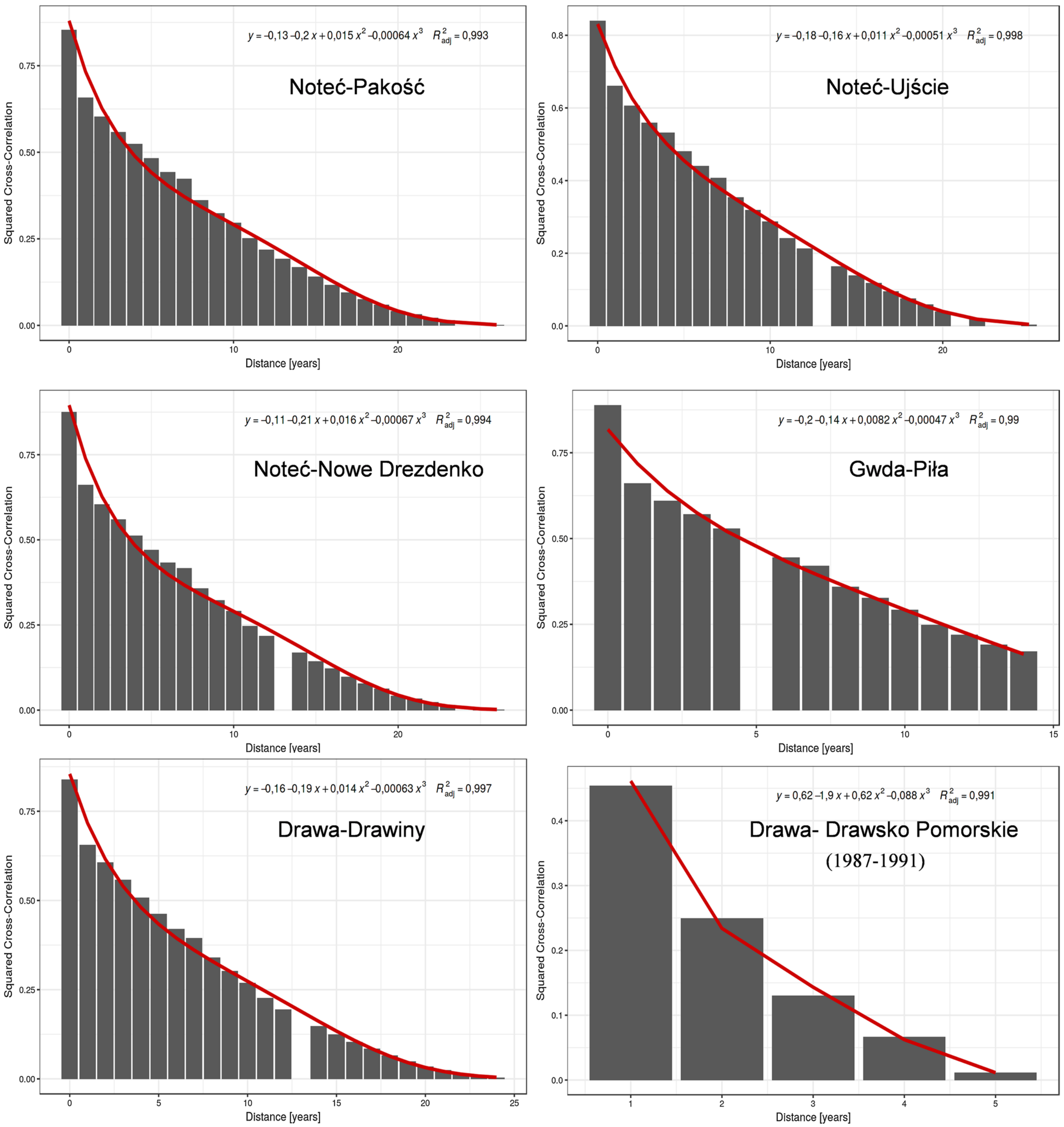

Fig. 4 Decay function of cross-correlation square for daily water temperature series (1987–2013)

Forecasting the course of water temperature fluctuations for the Noteć and its tributaries on the basis of changes in air temperature may therefore ensure better results if use is made of information from the preceding day. The hypothesis as to the dependence between water and air temperature series is confirmed by a variance analysis (test) which made use of the test statistic F. Table 2 presents the standard notation of the test result, with the numbers in parentheses representing degrees of freedom of distribution F, while the value on the right side of the "=" sign is that of the test statistic F. The results of the variance analysis indicate a considerable Granger dependence of water temperature on air temperature at $p < 0.001$. The greatest impact was determined for the River Gwda at the station in Piła, which functions as a synoptic station.

Table 2 Cause-and-effect relation between series of river water and air temperature in terms of *Granger's causality*

River—profile	Water–air
Noteć—Pakość	$F(1, 9859) = 2901$
Noteć—Ujście	$F(1, 9859) = 2476$
Noteć—Nowe Drezdenko	$F(1, 9859) = 3685$
Gwda—Piła	$F(1, 9859) = 5169$
Drawa—Drawiny	$F(1, 9859) = 1823$
Drawa—Drawsko Pomorskie[a]	$F(1, 2005) = 53.91$

t—distance between measurements in years

F—test statistic, numbers in parentheses—degrees of freedom of distribution *F*, values on the right side of the "=" sign are those of the test statistic *F*

[a] Drawa—Drawsko Pomorskie: Lag order = 12 (1987–1991), for other measurement stations: Lag order = 27 (1987–2013), $\alpha = 0.01$

Linear and natural cubic splines models

An analysis of the strength of the relationship between measurements of the water temperature of the Noteć and its tributaries and air temperature, performed on the same days, was also carried out using the linear model and the natural cubic spline model—Fig. 5.

Results confirmed the existence a nonlinear relationship between them. In all instances, the linear model recreated water temperature variance to a lesser degree (78.65–88.02%) than the natural cubic spline model (84.05–89.83%). The differences between the models ranged from 3.96 to 4.73% and were statistically significant. The greatest difference (5.67%) was determined in the models elaborated for the River Drawa in Drawsko Pomorskie, which was connected with the fact that a shorter water temperature observation series (12 years) was adopted for modelling. A high degree of conformity was obtained in the model elaborated for the Noteć water temperature series at Nowe Drezdenko (Table 3).

Prediction models

The levels of significance of standard statistical tests are a decreasing function of the number of observations, and therefore, an attempt was made at carrying out an additional assessment of the strength of the connections found. To this end, it was determined for the present instance by how much the determination coefficient (R^2) of both models increases after the past values of the second time series are taken into account. The model predicting the water temperature of the Noteć and its tributaries on the basis of water and air temperature from the preceding day (station in Piła) explains 0.01–0.27% more of the unique variance than the model which utilises solely water temperature from the preceding day (Fig. 6). In the present context, "unique variance" refers to the variance percentage that is explained by a given factor in addition to that which is explained by historical values of a given variable, i.e. in the case of water temperature—by previous temperature values. The greatest increase in the percentage of unique variance that is explained by the additional factor has been determined for the water temperature series of the River Gwda (0.27%) and the River Noteć at Nowe Drezdenko (0.19%), and the lowest for the River Noteć in Ujście (0.07%, following the exclusion of data for the River Drawa in Drawsko Pomorskie)—Fig. 6. By way of comparison, the model predicting the average monthly water temperature of the River Noteć and its tributaries on the basis of water and air temperature from the preceding month explained 0.87–2.75% more of the unique variance than the model utilising solely water temperature.

The next stage of the analysis was concerned with determining the degree of correlation of random fluctuations (chance fluctuations) for the same days of both temperature measurement series. Random fluctuations were taken to be those changes in temperature that do not result from a long-term trend, historical values, or periodicity (Table 4). This provided valuable insight into the characteristics of short-term connections between water and air temperature. The occurrence of a statistically significant correlation was determined. Random fluctuations of air temperature explain from 1.8% (River Drawa at Drawiny) to 8.0% (River Noteć at Ujście) of random water temperature fluctuation variances.

Random events and values in the measurement series that are atypical for the thermal regime of river waters appear in consequence of various disorders of its course. An analysis of the degree of correlation between random fluctuations of water temperature series for the River Noteć and its tributaries and air temperature for the same days has confirmed the short-term nature of this connection.

The strength of cause-and-effect connections was studied on the basis of an analysis of changes in the coefficients of determination (R^2) of models taking into consideration the past values of the second time series (Table 5). As regards fluctuations of water temperature, the greatest R^2 difference amounted to 9.98% (Drawa—Drawiny) in relation to R^2 equal to zero. This means that in the present instance fluctuations of air temperature have a significant and by no means small (for it explains nearly 10% of variability) impact on random fluctuations of water temperature on the next day. Furthermore, the regression coefficient—which determines the impact of air temperature fluctuations on water temperature fluctuations—indicates that this is a positive relationship: on average, positive deviations of air temperature are associated with positive deviations of water temperature on the next day, while negative deviations are associated with negative deviations on the next day. In the remaining models for predicting the water temperature of the Noteć and its tributaries, obtaining of a low R^2 value (0.56–0.94%) taking into consideration the past values of the

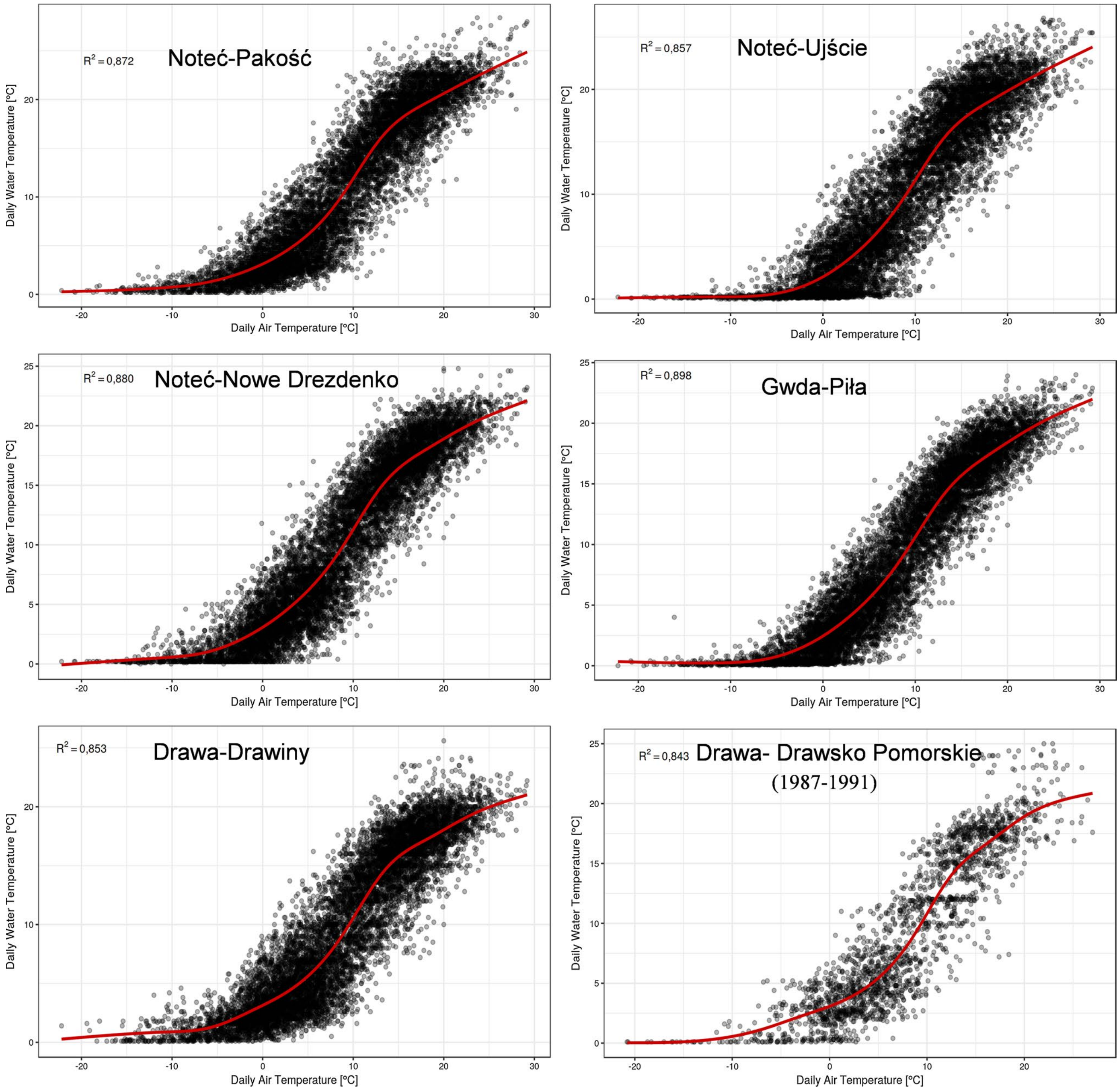

Fig. 5 Relationship between daily river water and air temperature (1987–2013) according to the natural cubic splines model

second time series, confirms that in this case water temperature fluctuations are relatively independent of each other and are not significantly impacted by air temperature fluctuations.

Discussion

Cause-and-effect relations

The existence of a relationship between fluctuations in river water temperature and air temperature has been confirmed under differing climatic and regional conditions (Bogan et al. 2003; Webb et al. 2003; Arismendi et al. 2014; DeWeber and Wagner 2014). In the case of the River Noteć and its tributaries, a high cross-correlation was established between daily water and air temperature, as well as Granger's causality. The results of analyses of cross-correlation between both variables, which are strictly periodic in nature, indicate clearly that process memory undergoes gradual decay, and this means that measurements from successive years are less and less correlated (Figs. 2, 3). This is confirmed by analyses of the decay function of the square of cross-correlation

Table 3 Degree of recreating water temperature variances for the Noteć River and its tributaries using the linear and natural cubic splines models

River—profile	Linear model (%)	Natural cubic splines model (%)	Difference in variance recreation between models (%)	Level of statistical significance $p <$ 0.001
Noteć—Pakość	82.44	87.17	4.73	$F(4, 9859) = 907.5$
Noteć—Ujście	81.06	85.65	4.60	$F(4, 9859) = 789.3$
Noteć—Nowe Drezdenko	88.02	84.05	3.96	$F(4, 9859) = 814.7$
Gwda—Piła	85.68	89.83	4.15	$F(4, 9859) = 1006$
Drawa—Drawiny	81.10	85.30	4.20	$F(4, 9859) = 686.3$
[a]Drawa—Drawsko Pomorskie	78.65	84.32	5.67	$F(4, 2005) = 181.1$

F—test statistic, numbers in parentheses—degrees of freedom of distribution *F*, value on the right side of the "=" sign are the values of test statistics *F*

[a]Drawa—Drawsko Pomorskie: Lag order = 12 (1987–1991), for other measurement stations: Lag order = 27 (1987–2013)

Fig. 6 Prediction models for the water temperature of the Noteć River and its tributaries (daily and monthly series) taking account of past values of the second time series ($tw-1$) and increase in unique variance percentage explained by an additional factor (%) ($tw-1$)—water temperature from the previous day/month (m)

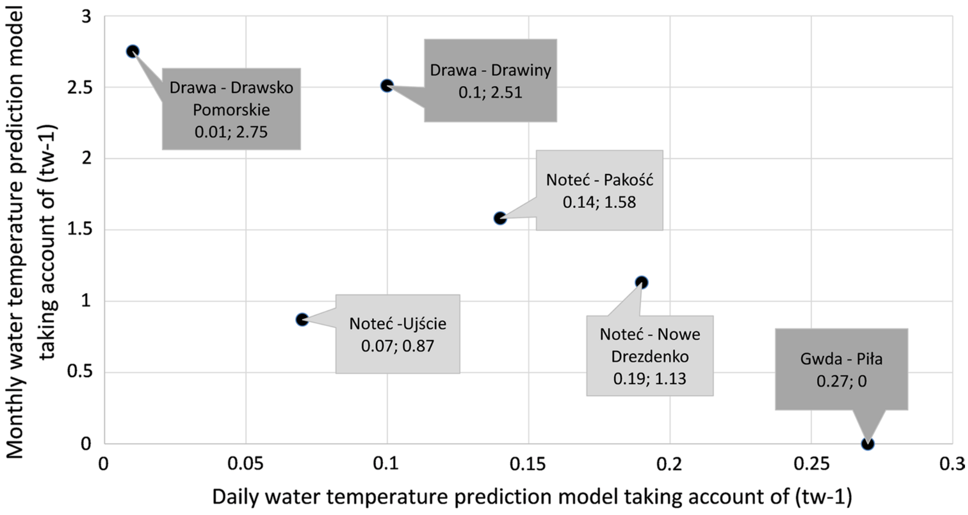

Table 4 Degree of linear correlation of fluctuations occurring in random series of river water and air temperature changes for the same days

River—profile	Linear correlation of random fluctuations for the same days (Pearson's *r*) ($p < 0.001$)	Degree of explaining random fluctuation variations (%)
Noteć—Pakość	$r = 0.24$; $t\,(9860) = 24.22$	5.61
Noteć—Ujście	$r = 0.28$; $t\,(9860) = 29.20$	8.00
Noteć—Nowe Drezdenko	$r = 0.22$; $t\,(9860) = 22.15$	4.74
Gwda—Piła	$r = 0.22$; $t\,(9860) = 22.12$	4.73
Drawa—Drawiny	$r = 0.13$, $t\,(9860) = 13.23$	1.80
Drawa—Drawsko Pomorskie[a]	$r = 0.121$; $t\,(2006) = 5.48$	1.47

t—number of days

[a]Drawa—Drawsko Pomorskie Lag order = 12 (1987–1991), other stations Lag order = 27 (1987–2013)

for measurements carried out on the same day in different years (Fig. 4). The results of cross-correlation obtained for the River Noteć and its tributaries are of significance for the short- and medium-term assessment, concordant with seasonality or cycles (Liu et al. 2005; Toffolon and Piccolroaz 2015). In the short-term perspective, however, we should turn attention to the forecast and the deviation of the actual reading from the forecast. In the present instance, the cross-correlation was examined for the entire available time series of water and air temperature and did not take into consideration the specificity of individual thermal cycles. Neither to correlation connections explain the cause-and-effect

Table 5 Increase in the coefficient of determination (R^2) in models predicting random fluctuations of water temperature taking account of past values of the second time series ($tw-1$) (%)

River—profile	Prediction model for random fluctuations of water temperature taking account of past values $tw-1$
Noteć—Pakość	0.69 (0.03)[a]
Noteć—Ujście	0.56 (0.03)
Noteć—Nowe Drezdenko	0.76 (0.03)
Gwda—Piła	0.82 (0.03)
Drawa—Drawiny	9.98 (0.00)
Drawa—Drawsko Pomorskie	0.94 (0.01)

t—number of days, ($tw-1$)—water temperature from the previous day

Drawa—Drawsko Pomorskie Lag order = 12 (1987–1991), other stations Lag order = 27 (1987–2013)

[a] The brackets contain R^2 values for the model taking account of only the random fluctuation of water temperature from the previous day

relationships between temperature, which can be achieved using the Granger's test. The determination of Granger's causality dependence (first order) between daily temperature series provides confirmation of the impact of one data series on the evolution of a second data series. In the analysed instance, data concerning the past of a time series of air temperature provide information that is of significance for predicting the values of the time series of river water temperature, which is not included in the information concerning its past values (Detto et al. 2012). In the context of Granger's causality, it is important to state that water temperature is determined causally by air temperature from the preceding day (Morrill et al. 2005; Letcher et al. 2016). These relationships occur mainly during water freezing and evaporation processes, which involve enormous quantities of energy. The latent heat of water phase transitions is collected from and given up to the environment (Hannah et al. 2004; Caissie 2006). In the local scale, these processes cause the significant heating or cooling of air above water courses and their immediate surroundings.

Local factors affecting the stream temperature

River thermal regimes are impacted first and foremost by the surface exchange of heat with the atmosphere in processes of radiation, evaporation, and convection (Caissie 2006), and also by the turbulent mixing of water of varying temperature, e.g. inflows, wastewater, thermal pollutants. It is assumed that molecular diffusion, the exchange of heat with the subsoil, and conductivity in the water mass play a less important role in shaping the thermal regime characteristics (Sinokrot and Stefan 1994). Local factors that modify the thermal characteristics of river waters usually include anthropogenic change (Olden and Naiman 2010), which may disturb the continuity of processes and the gradient nature of zones in rivers (the so-called river continuum) (Caissie et al. 2005). In the case of the catchment area of the River Noteć, local factors that impact its thermal regime include the specific morphological nature of the river valley—the flat, broad Toruń-Eberswalde Glacial Valley, springs flowing from the edges and terraces of river valleys, and the proximity of peat bogs. Vast wetlands are present in the lower and middle courses of the River Noteć (Fig. 7). These wetlands contribute to the lowering of river water temperature in the summer period due to the supply to the river of groundwater of a considerably reduced temperature.

As regards the Noteć, one of the more significant causes of undesirable changes in flowing water temperature (Poole and Berman 2001; Lisi et al. 2015) may be the degraded morphology of the channelled sections of its course. This factor usually makes it difficult to recreate the historical thermal regime of a water course.

Numerous studies concerning the dependence between times series of water and air temperature have shown that the relationship between variables is not ideally linear (Langan et al. 2001; Wiejaczka 2007; Letcher et al. 2016). This is supported among others by the results of the natural cubic spline model, which was used in research—Fig. 5. First and foremost, this is connected with the fact that water temperature, as opposed to air temperature, has a lower limit and cannot attain a value of less than 0 °C, even during periods of long-term frost. The impact of local factors modifying the thermal characteristics of river waters is also visible in the diversity of features of the winter ice regime (Graf and Tomczyk 2018; Graf et al. 2018). During the summer season, when air temperature is high, the temperature of water in the river does not increase linearly (Fig. 5), this because of the intense loss of thermal energy in processes of evaporation and emission of long-wave radiation. Changes in temperature in the aquatic environment occur at a considerably slower rate than changes in air temperature due to the lower conductivity of water in comparison with air.

Usually, a strong, nonlinear statistical dependence between the temperature of water and air is shown by the logistic (nonlinear) and linear regression models. Despite the nonlinear character of the dependence, the

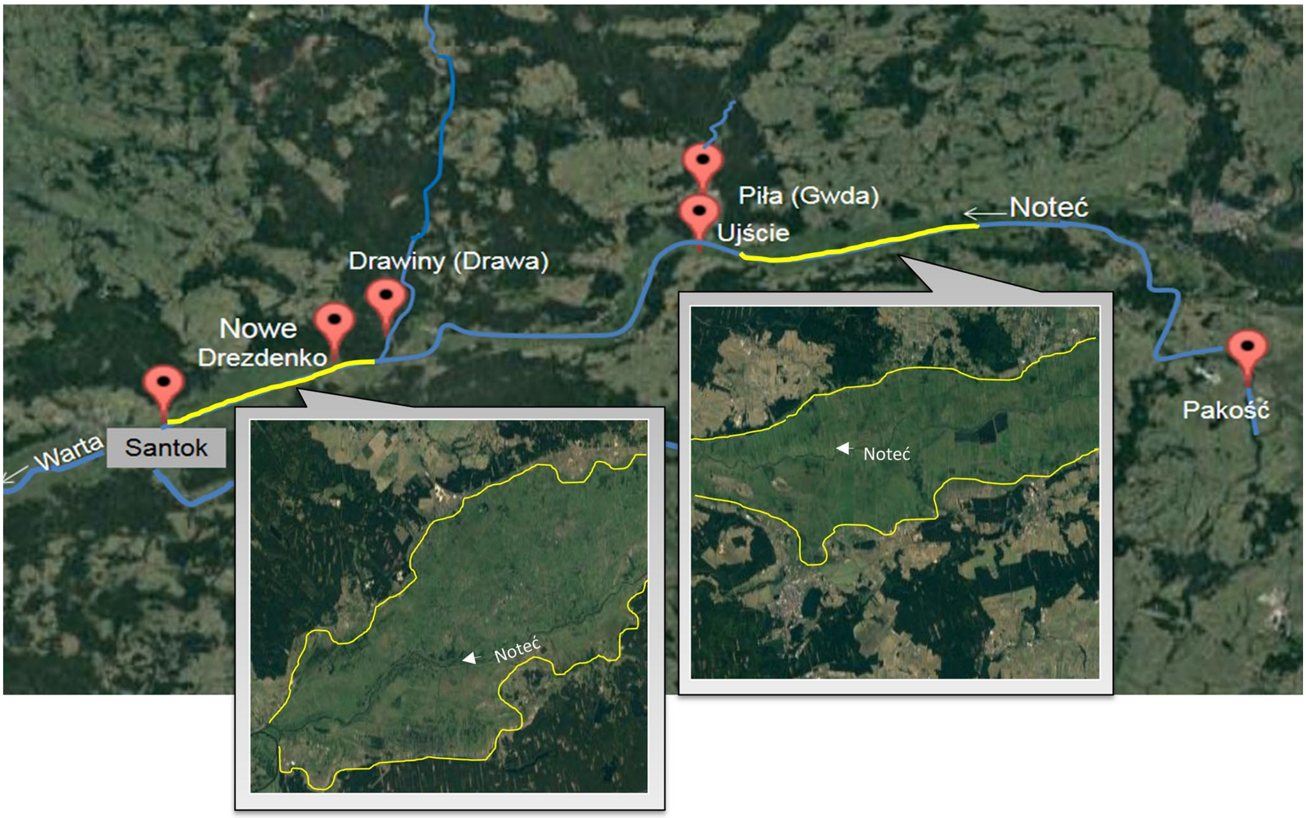

Fig. 7 Land coverage in the Noteć catchment area taking account of the extent of wetlands in the Toruń-Eberswalde Urstromtal system—orthophotomap of the Noteć catchment area [based on http://web4you.com.pl/geofinder.php]

appropriate selection of measurement data makes it possible to effectively apply the linear model (Łaszewski 2014), which accurately reflects the connection between average monthly water and air temperature. In turn, this association is weakened by the following: daily averages, weekly averages, and maximum daily or weekly values of air temperature lower than 0.0 °C (Mohseni and Stefan 1999). The nonlinear form of dependence in the logistic model is described by the *S*-shaped function (sigmoidal) with input values from the range (0,1), which properly reflects the behaviour of water temperature in the presence of negative and high (above 25 °C) air temperature (Mohseni et al. 1998; Neumann et al. 2003; Caissie et al. 2001; Łaszewski 2014), and this fact has indeed ensured the universality of application of the method. Among dependences approximated by logistic models, the strongest association was determined for the average weekly and average maximum weekly water and air temperature (Wiejaczka 2011), while the connection between the average daily and maximum daily water and air temperature (Webb et al. 2003; Morrill et al. 2005) turned out to be weakest. In turn, Zhu et al. (2018) while analysing three standard models—linear regression, nonlinear regression, and the stochastic—confirmed that the stochastic model clearly exceeds the other two. In stochastic models, water temperature is modelled as a function of time comprising two completely different components—a short-term residual component and a long-term component that is periodic in time (Caissie et al. 1998; Hadzima-Nyarko et al. 2014). Furthermore, in stochastic models water temperature is generally modelled as a function of time consisting of two entirely different components: a short-term residual component and a long-term component which is periodic in time (Zhu et al. 2018).

The natural cubic spline model used in research also confirmed the nonlinear dependence between river water and air temperature. The spline-based method resulted in an acceptable water time series temperature pattern that properly reflects its actual association with air temperature. Due to seasonal changes in water and air temperature, the model determining the dependence between them should ensure continuous seasonal patterns for each day throughout the year, and also the smooth periodicity of changes under specific boundary conditions. The spline technique additionally makes it possible to intercept the data trend irrespective of the character of the base relation, with the simultaneous reduction of the tendency to oscillate and of susceptibility to changes in data. Thus, we can use this method to, for example, supplement missing data, which frequently constitutes a significant problem in statistical research into water temperature measurement series.

Data generating process (DGP)

As regards water and air temperature time series, the identification of causal patterns for the variance and the mean using Granger's causality analysis may serve first and foremost to improve the quality of predictions of these values through the construction of models that take them into consideration. A narrowing of the interpretation concerns linear causality (for water-air temperature), whereas in the broader context we are concerned with the dependence of data generating processes (DGPs) (Cameron and Trivedi 2005). The concept of Granger's causality is not limited to the search for a variable whose presence in the model may improve the accuracy of forecasts. In line with the concept of causality, the cause in time series precedes the effect, while the causal series contains information about the variable being the effect, which was not included in other series (Granger 1988).

Conclusions

Research into the relationship between daily river water temperature registered at selected measurement profiles (the River Noteć and its tributaries) and air temperature has confirmed their considerable dependence during the analysed period. The application of multidimensional statistical modelling, taking into consideration varied methodological criteria, has made it possible to determine the nature of relationships occurring between data series. It was particularly interesting to determine cause-and-effect relationships not only along the water–air axis, but also along the air–water axis, which occur mainly during water freezing and evaporation processes. The application of Granger's causality demonstrated the existence of complex multi-level dependences that are conditioned by the number of variables used in research. When taking into consideration a one-day lag between measurements, Granger's causality was confirmed in two directions, which fact is of considerable importance for forecasting. Namely, this means that forecasting the fluctuations of the temperature of river waters on the basis of changes in air temperature may be more effective when use is made of information from the preceding day.

The results of the analysis have also confirmed the presence of a nonlinear relation between daily river water and air temperature. In all instances, the linear model recreated water temperature variance to a lesser degree than the natural cubic spline model. Differences between these models amounted to approximately 4–5% and were statistically significant. Also established was a weak, albeit statistically significant correlation of random fluctuations for the same days for both series, i.e. changes in temperature which do not follow from a long-term trend, historical values, or periodicity. This made it possible to confirm the occurrence of short-term connections between water and air temperature. The thermal regime of the researched rivers is impacted first and foremost by the surface exchange of heat with the atmosphere. Locally, the thermal characteristics of river waters may be modified by anthropogenic factors identified in the catchment area and the river valley, which may disturb the continuity of processes and the gradient nature of zones in rivers. In the case of the River Noteć, these factors include the morphological nature of the river valley and the risk of inflow of pollutants, which are the single most important factor contributing to increases in the temperature of flowing waters.

The results obtained constitute a database for reference indications of thermal parameters that are of significance for predicting climate change and for conducting research into the thermal regime of the river. On a regional scale, they may be used to assess the impact of climatic change, while on the local—to analyse anthropogenic influences on the development and nature of the relationship between river water and air temperature. Furthermore, the relations determined between thermal water and air parameters determine the degree of risk for the functioning of aquatic ecosystems represented by habitats and species susceptible to changes in river water temperature. This problem is particularly important in the case of rivers with significant ecological functions (e.g. migration corridors for various species of fishes), among which the Noteć is classified.

The results can be used to determine the qualities of thermal regimes and to predict the temperature of river waters under conditions of climate change. In light of the constant demand for information concerning the thermal regime features of waters in lowland river ecosystems (which are subjected to varying degrees of anthropogenic transformation), the results obtained constitute an important supplementation of databases used to ensure their rational management.

Acknowledgements The present paper is the result of research on thermal conditions of the river water with use of the statistical methods, carried out as part of statutory research at the Department of Hydrology and Water Management of the Institute of Physical Geography and Environmental Planning of the Adam Mickiewicz University in Poznań, Poland. The author would like to thank Szymon Talaga for his help in performing the statistical analyses.

Compliance with ethical standards

Conflict of interest The authors declare that they have no conflict of interest.

References

Allan JD, Castillo MM (2007) Stream ecology: structure and function of running waters, 2nd edn. Chapman and Hall, New York

Arismendi I, Safeeq M, Dunham JB, Johnson SL (2014) Can air temperature be used to project influences of climate change on stream temperature? Environ Res Lett 9:084015

Arscott DB, Tockner K, Ward JV (2001) Thermal heterogeneity along a braided floodplain river (Tagliamento River, northeastern Italy). Can J Fish Aquat Sci 58:2359–2373

Benyahya L, Caissie D, St-Hilaire A, Ouarda TBM, Bobée B (2007) A review of statistical water temperature models. Can Water Resources J 32:179–192

Bogan T, Mohseni O, Stefan HG (2003) Stream temperature—equilibrium temperature relationship. Water Resources Res 39:1245–1256

Bolker BM, Brooks ME, Clark CJ, Geange SW, Poulsen JR, Stevens MHH, White J-SS (2009) Generalized linear mixed models: a practical guide for ecology and evolution. Trends Ecol Evol 24:127–135

Caissie D (2006) The thermal regime of rivers: a review. Freshw Biol 51:1389–1406

Caissie D, El-Jabi N, St-Hilaire A (1998) Stochastic modeling of water temperatures in a small stream using air to water relations. Can J Civ Eng 25(2):250–260

Caissie D, El-Jabi N, Satish MG (2001) Modelling of maximum daily water temperatures in a small stream using air temperatures. J Hydrol 251:14–28

Caissie D, St-Hilaire A, El-Jabi N (2004) Prediction of water temperatures using regression and stochastic models. In: 57th Canadian water resources association annual congress, Montreal, QC, June 16–18, 2004, Ottawa, Ontario

Caissie D, Satish MG, El-Jabi N (2005) Predicting river water temperatures using the equilibrium temperature concept with application on the Miramichi River catchments (New Brunswick, Canada). Hydrol Process 19:2137–2159

Cameron AC, Trivedi PK (2005) Microeconometrics methods and applications. Cambridge University Press, Cambridge

Conlan K, Lane S, Ormerod S, Wade T (2005) Preparing for climate change impacts on freshwater ecosystems (PRINCE). Environment Agency, Science Report: SC030300/SR. http://llynbrianne-lter.org/wp-content/uploads/2013/01. Accessed 10 Feb 2018

Detto M, Molini A, Katul G, Stoy P, Palmroth S, Baldocchi D (2012) Causality and persistence in ecological systems: a nonparametric spectral Granger causality approach. Am Nat 179:524–535

DeWeber JT, Wagner TA (2014) Regional neural network ensemble for predicting mean daily river water temperature. J Hydrol 517:187–200

Dickey DA, Fuller WA (1981) Likelihood ratio statistics for autoregressive time series with a unit root. Econometrica 49:1057–1072

ETC/ICM (2015) European freshwater ecosystem assessment: crosswalk between the water framework directive and habitats directive types, status and pressures. ETC/ICM technical report 2/2015. European Topic Centre on inland, coastal and marine waters, Magdeburg. http://ecologic.eu/12451. Accessed 10 Feb 2018

Gallice A, Schaefli B, Lehning M, Parlange MP, Huwald H (2015) Stream temperature prediction in ungauged basins: review of recent approaches and description of a new physically-based analytical model. Hydrol Earth Syst Sci 19:3727–3753

Gardner B, Sullivan PJ, Lembo AJ (2003) Predicting stream temperatures: geostatistical model comparison using alternative distance metrics. Can J Fish Aquat Sci 60:344–351

Gelman A, Hill J (2006) Data analysis using regression and multilevel/hierarchical models. Cambridge University Press, Cambridge

Graf R (2015) Variations of the thermal conditions of the Warta in the profile connecting the Urstromal and gorge sections of the valley (Nowa Wieś Podgórna-Śrem–Poznań) Zmiany termiki wód Warty w profilu łączącym pradolinny i przełomowy odcinek doliny (Nowa Wieś Podgórna-Śrem-Poznań). In: Absalon D, Matysik M, Ruman M (eds) Novel methods and solutions in hydrology and water management. Hydrological Committee PTG, PTG Department, Katowice, pp 177–194

Graf R (2018) Distribution properties of a measurement series of river water temperature at different time resolution levels (based on the example of the Lowland River Noteć, Poland). Water 10:203. https://doi.org/10.3390/w10020203

Graf R, Tomczyk AM (2018) The impact of cumulative negative air temperature degree-days on the appearance of ice cover on a river in relation to atmospheric circulation. Atmosphere 9(6):204

Graf R, Łukaszewicz JT, Jawgiel K (2018) The analysis of the structure and duration of ice phenomena on the Warta river in relation to thermic conditions in the years 1991–2010 (Analiza struktury i czasu trwania zjawisk lodowych na Warcie na tle warunków termicznych w okresie 1991–2010). Woda-Środowisko Obsz Wiej 18:5–28

Granger CWJ (1988) Some recent developments in a concept of causality. J Econom 39(1–2):199–211

Hadzima-Nyarko M, Rabi A, Šperac M (2014) Implementation of artificial neural networks in modeling the water-air temperature relationship of the river Drava. Water Resources Manag 28(5):1379–1394

Hannah DM, Malcolm IA, Soulsby C, Youngson AF (2004) Heat exchanges and temperatures within a salmon spawning stream in the Cairngorms, Scotland: seasonal and sub-seasonal dynamics. River Res Appl 20:635–652

Hilderbrand RH, Kashiwagi MT, Prochaska AP (2014) Regional and local scale modeling of stream temperatures and spatio-temporal variation in thermal sensitivities. Environ Manag 54:14–22

Hox J (2002) Multilevel analysis: techniques and applications. Lawrence Erlbaum Associates, Publishers, Mahwah

Jackson MC, Loewen CJG, Vinebrooke RD, Chimimba CT (2016) Net effects of multiple stressors in freshwater ecosystems: a meta-analysis. Glob Change Biol 22:180–189

Kędra M, Wiejaczka Ł (2016) Disturbance of water-air temperature synchronisation by dam reservoirs. Water Environ J 30(1–2):31–39

Kondracki J (2008) Regional geography of Poland (Geografia regionalna Polski). Scientific Publishing House PWN, Warsaw

Lagergaard Pedersen N, Sand-Jensen K (2007) Temperature in lowland Danish streams: contemporary patterns, empirical models and future scenarios. Hydrol Process 21:348–358

Langan SJ, Johnston L, Donaghy MJ, Youngson AF, Hay DW, Soulsby C (2001) Variation in river water temperatures in an upland stream over a 30-year period. Sci Total Environ 265:195–207

Łaszewski M (2014) Methods of estimating stream water temperature and air temperature relationships—the Świder River case study (Metody określania związków temperatury wody rzecznej i temperatury powietrza na przykładzie rzeki Świder). Prace Geogr 136:45–60

Letcher BH, Hocking DJ, O'Neil K, Whiteley AR, Nislow KH, O'Donnell MJ (2016) A hierarchical model of daily stream temperature using air-water temperature synchronization, autocorrelation, and time lags. PeerJ 4:e1727

Li H, Deng X, Kim D-Y, Smith EP (2014) Modeling maximum daily temperature using a varying coefficient regression model. Water Resources Res 50:3073–3087

Lisi PJ, Schindler DE, Cline TJ, Scheuerell MD, Walsh PB (2015) Watershed geomorphology and snowmelt control stream thermal sensitivity to air temperature Geophys. Res Lett 42:3380–3388

Liu B, Yang D, Ye B, Berezovskaya S (2005) Long-term open-water season stream temperature variations and changes over Lena River Basin in Siberia. Glob Planet Change 48:96–111

Marszelewski W, Pius B (2018) Relation between air temperature and inland surface water temperature during climate change (1961–2014): case study of the Polish Lowland. In: Zelenakova M (ed) Water management and the environment: case studies. Springer, Berlin, pp 175–195

Mohseni O, Stefan HG (1999) Stream temperature/air temperature relationship: a physical interpretation. J Hydrol 218:128–141

Mohseni O, Stefan HG, Erickson TR (1998) A nonlinear regression model for weekly stream temperatures. Water Resources Res 34:2685–2692

Morrill JC, Bales RC, Conklin MH (2005) Estimating stream temperature from air temperature: implications for future water quality. J Environ Eng 131:139–146

Napiórkowski MJ, Piotrowski AP, Napiórkowski JJ (2014) Stream temperature forecasting by means of ensemble of neural networks: importance of input variables and ensemble size. In: Schleiss AJ et al (eds) River flow. Taylor & Francis Group, London

Neumann DW, Rajagopalan B, Zagona EA (2003) Regression model for daily maximum stream temperature. J Environ Eng 7:667–674

Olden JD, Naiman RJ (2010) Incorporating thermal regimes into environmental flows assessments: modifying dam operations to restore freshwater ecosystem integrity. Freshw Biol 55:86–107

Padilla A, Rasouli K, Déry SJ (2015) Impacts of variability and trends in runoff and water temperature on salmon migration in the Fraser River Basin, Canada. Hydrol Sci J. https://doi.org/10.1080/02626667.2014.892602

Pilgrim JM, Fang X, Stefan HG (1998) Stream temperature correlations with air temperature in Minnesota : implications for climate warming. J Am Water Resources Assoc 34:1109–1121

Piotrowski AP, Napiórkowski JJ (2018) Performance of the air2stream model that relates air and stream water temperatures depends on the calibration method. J Hydrol 561:395–412

Poole C, Berman CH (2001) An ecological perspective on in-stream temperature: natural heat dynamics and mechanisms of human-caused thermal degradation. Environ Manag 27(6):787–802

R Core Team (2015) R: a language and environment for statistical computing. R Foundation for Statistical Computing, Vienna, Austria. http://www.R-project.org. Accessed 10 Feb 2018

Rushworth AM, Peterson EE, Ver Hoef JM, Bowman AW (2015) Validation and comparison of geostatistical and spline models for spatial stream networks. Environmetrics 26:327–338

Sahoo GB, Schladow SG, Reuter JE (2009) Forecasting stream water temperature using regression analysis, artificial neural network, and chaotic non-linear dynamic models. J Hydrol 378:325–342

Sinokrot BA, Stefan HG (1994) Stream water temperature sensitivity to weather and bed parameters. ASCE J Hydraul Eng 120:722–736

Sinokrot BA, Stefan HG, McCormick JH, Eaton JG (1995) Modeling of climate change effects on stream temperatures and fish habitats below dams and near groundwater inputs. Clim Change 30:181–200

Toffolon M, Piccolroaz S (2015) A hybrid model for river water temperature as a function of air temperature and discharge. Environ Res Lett 10:114011. https://doi.org/10.1088/1748-9326/10/11/114011

Webb BW, Nobilis F (2007) Long-term changes in river temperature and the influence of climatic and hydrological factors. Hydrol Sci 52:74–85

Webb BW, Clack PD, Walling DE (2003) Water–air temperature relationships in a Devon river system and the role of flow. Hydrol Process 17:3069–3084. https://doi.org/10.1002/hyp.1280

Wiejaczka Ł (2007) Relationship between water temperature in the river and air temperature -on the Ropa River as an example. (Relacje pomiędzy temperaturą wody w rzece a temperaturą powietrza - na przykładzie rzeki Ropy). Folia Geogr Geograph Phys 37–38:95–105

Wiejaczka Ł (2011) Influence of storage reservoir on the relations between the temperature of water in the river and the air temperature (Wpływ zbiornika retencyjnego na relacje między temperaturą wody w rzece a temperaturą powietrza). Przegląd Naukowy Inżynieria i Kształtowanie Środowiska 53:183–195

Woś A (2010) The climate of Poland in the second half of the 20th century (Klimat Polski w drugiej połowie 20. Wieku). Scientific Publishing House UAM, Poznan

Younus M, Hondzo M, Engel BA (2000) Stream temperature dynamics in upland agricultural watersheds. J Environ Eng 126:518–526

Żelazny M, Rajwa-Kuligiewicz A, Bojarczuk A, Pęksa Ł (2018) Water temperature fluctuation patterns in surface waters of the Tatra Mts, Poland. J Hydrol 564:824–835. https://doi.org/10.1016/j.jhydrol.2018.07.051

Zhu S, Nyarko EK, Hadzima-Nyarko M (2018) Modelling daily water temperature from air temperature for the Missouri River. PeerJ 6:e4894. https://doi.org/10.7717/peerj.4894

Acta Geophysica (2019) 67:921–938
https://doi.org/10.1007/s11600-019-00288-0

RESEARCH ARTICLE - HYDROLOGY

Estimation of annual average soil loss using the Revised Universal Soil Loss Equation (RUSLE) integrated in a Geographical Information System (GIS) of the Esil River basin (ERB), Kazakhstan

Yerbolat Mukanov[1,2,3,4] · **Yaning Chen**[1] · **Saken Baisholanov**[5] · **Amobichukwu Chukwudi Amanambu**[1,2,6] · **Gulnura Issanova**[4] · **Ainura Abenova**[3] · **Gonghuan Fang**[1] · **Nurlan Abayev**[3]

Received: 21 August 2018 / Accepted: 9 April 2019 / Published online: 3 May 2019

Abstract

The Revised Universal Soil Loss Equation (RUSLE) has enormous potential for integrating remote sensing and Geographical Information System (GIS) technologies for producing accurate and inexpensive assessments of soil erosion. In this study, the RUSLE method was applied to the Esil (Ishim) River basin (ERB), which is situated in Northern and Central Kazakhstan. The northern part of the ERB extends through the Tyumen and Omsk regions of the Russian Federation to the confluence of the Irtysh River. This article may be of interest to experts and specialists in the field of agriculture, as the findings can assist agricultural producers and government entities in making decisions that prevent soil degradation and promote optimal cropping systems for land and crop cultivation. The objective of this research is to detect, estimate and map areas of land plots most vulnerable to potential soil erosion within the ERB, using the RUSLE model under Arc GIS 10.2. The results reveal that average annual soil loss during the study period ranges from 0 to 32 (t y^{-1}) and that 108,007.5 km^2 (48%) of the ERB has no erosion. The remainder of the basin is prone to soil erosion ranging from 1 to 32 t ha^{-1} y^{-1}, which comprises 117,216.9 km^2 (52%), and total soil erosion is 565,368.7 (t y^{-1}). Soil erosion in the ERB is relatively moderate due to low hill steepness and low annual precipitation (198–397 mm). Exceptions occur in plots which feature high slope length steepness, which are scattered throughout the region.

Keywords Agriculture producers · Cropping system · RUSLE · Soil erosion

Introduction

Soil degradation is a serious problem throughout the world, which ultimately affects the reduction in soil fertility—reducing productivity in the agricultural sector, creating negative impact on the environment and consequently the quality of drinking water with further effects on the quality of life (Ganasri and Ramesh 2016; Issaka and Ashraf 2017; Vaezi and Sadeghi 2011).

Topsoil is most valuable for agricultural production and most vulnerable due to natural changes in ecosystems and inappropriate land management systems (Blanco and Lal 2010).

For proper operation and use of land resources, many factors need to be taken into account, one of which is the spatial assessment of soil loss (Prasuhn et al. 2013).

To understand the degree of soil erosion over a large area, it is necessary to collect soil samples, conduct field experiments and perform required analysis for planning

---

✉ Yaning Chen
chenyn@ms.xjb.ac.cn

Yerbolat Mukanov
Yerbolat20.01.1981@gmail.com

[1] State Key Laboratory of Desert and Oasis Ecology, Xinjiang Institute of Ecology and Geography, Chinese Academy of Sciences, 818 South Beijing Road, Urumqi 830011, China

[2] University of Chinese Academy of Sciences, Beijing 100049, China

[3] Regional State Enterprise Kazhydromet, Astana 010000, Kazakhstan

[4] Faculty of Geography and Environmental Sciences, Al-Farabi Kazakh National University, Almaty 050040, Kazakhstan

[5] Institute of Geography, Astana 010000, Kazakhstan

[6] Department of Geography, University of Florida, Gainesville, USA

and decision making (Alkharabsheh et al. 2013), bearing in mind that human influences play a key role in soil degradation.

Anthropogenic factor, especially agriculture, has a strong influence on the condition of soil. Intensive development of pasture lands under the Agricultural Program of the Virgin and Fallow Lands for the period 1954–1963 in Northern Kazakhstan (including ERB) led to large-scale soil degradation (Kraemer 2015). Such a transformation of land into arable land during the first year of operation has led to a loss of 50% of organic matter in the soil. Periodic use of fallows in crop rotation also leads to the depletion of organic matter in the soil (Yanai 2005).

One of the most popular modern models for estimating soil loss is the Revised Universal Soil Loss Equation (RUSLE) (Renard 1997), which has been widely used for the past several decades. The RUSLE model is a convenient and practical approach to assessing soil loss and can be applied wherever soil erosion or the scale of erosion processes might be of concern, including in river basin watersheds or on individual properties (Chen et al. 2011; Farhan et al. 2013). This model calculates approximate annual soil losses, taking into account factors such as precipitation, soil erodibility, relief parameters (slopes), vegetation and land use schemes (Renard 1997; Wischmeier and Smith 1965, 1978). The erosion of the soil characterizes the susceptibility of the soil to biological, chemical, physical, mineralogical, hydrological and other properties (Shabani et al. 2014).

Unfortunately, however, spatial and quantitative assessment of the extent of soil loss through observation alone does not always provide objective information because of limitations in data reliability (Chen et al. 2011; Prasannakumar et al. 2011). Spatial and quantitative assessment of the extent of soil loss in sites with observations, unfortunately, does not always provide objective information, primarily because of the data limitation and cost. Despite these issues, many scientists still use the RUSLE model (Abu Hammad 2011), even though it is not capable of providing an accurate spatial representation of the scale of the erosion processes due to the lack or absence of data and the complexity of the study area (Prasannakumar et al. 2011).

Geographical Information Systems (GIS) and remote sensing technologies, by allowing for spatial analysis of soil erosion assessment over a large area (Adediji et al. 2010; Farhan et al. 2013), can be used to augment the RUSLE model. The inclusion of satellite images can provide a more comprehensive idea of the state of the vegetation cover (*C*-factor) for the area under observation (Adediji et al. 2010; Alkharabsheh et al. 2013; Chen et al. 2011). Combining DEM (Digital Elevation Model) with ArcGIS gives ample opportunities to use various methods for calculating the topographic features (LS-factor) of a specific terrain (Panagos et al. 2015).

Also, land degradation by means of vegetation removal is one of the phenomena affecting the soil the earth's surface. Soil can be detected by electromagnetic spectrum through the brightness of the soil surface, reflecting the degree of vegetation cover or the intensity of the development of vegetation. Thus, vegetation indices (e.g., NDVI, SAVI, OSAVI and MSAVI) can be useful for assessing the spatial definition of land degradation (Wu et al. 2008). Escadafal et al. (1994) and Hill et al. (1995) applied the concept of soil science and geomorphology to obtain qualitative indicators on the processes of soil degradation and erosion based on spectral vegetation indices of soil condition indicators.

Spatial and quantitative information on the extent of soil erosion in a basin, sub-basin, watershed, sub-watershed can make a significant contribution in developing measures to protect soil from erosion and manage the catchment environment (Van De et al. 2008).

The present study focuses on the following three aspects in relation to soil erosion:

(i) The application of RS and GIS technologies in combination with the RUSLE model for exploring the intensity of soil water erosion in the ERB (Esil River basin),
(ii) the delineation of the plots most vulnerable and prone to soil erosion processes, and its environmental impacts; and
(iii) recommendations and possible solutions for preventing and mitigating the effect of soil erosion.

Future researchers could use this work as an information source for similar or related research. The results of this study will be an asset to policy-makers, land use planners and nature resource managers in planning and implementing effective soil conservation strategies to prevent or reduce soil erosion.

Materials and methods

Study area

The Esil River basin (ERB) is situated in the northern and central portions of Kazakhstan between 48°39′07″ and 56°54′82″ north, and 65°45′62″ and 75°04′29″ east. The ERB covers approximately 225,224 km^2. Land use in this region is primarily agricultural (38.01%), followed by barren areas (36.26%), urban areas (17.39%), shrub (3.12%), water bodies (2.21%), wetlands (1.71%), grasslands (0.81%) and forest (0.45%). The climate conditions of the study area are generally dry (annual precipitation 198–397 mm) and windy. The climate steppe and forest steppe zones of Northern Kazakhstan, due to their remoteness from the moderating effects of seas and oceans, quickly become very hot in summer while rapidly losing heat in winter. The region's cultivated land mostly occupies low-lying plains with elevations up to 200 m as well as slightly undulating plains (250–300 m). Some agriculture also occurs in the relatively flat upland plains situated at 350–400 m above sea level. Overall, the region is characterized as steppe and forest steppe (Fig. 1).

Northern Kazakhstan, with annual precipitation of 300–400 mm, is the wettest region in the ERB. It is mostly covered by steppes. Closer to Central Kazakhstan, annual precipitation decreases to around 150 mm. The main ecosystem types, which are represented by cropland, grassland and shrubland, sequentially change from north to south (Koshim et al. 2018; Liang et al. 2017).

Data

In our study, we used the DEM 25.43 m resolution, obtained from the United States Geological Survey (USGS), to calculate the topographic parameters of the terrain slopes. To define the soil structure and physical soil properties, a digital soil map obtained from the Food Agriculture Organization Geonetwork at a scale of 1:5,000,000 was used. As well, the Normalized Difference Vegetation Index (NDVI) and satellite images from the USGS Landsat 8 (30 m resolution) for period July 2016 were used to analyze land cover. The land use/land cover map (300 m resolution) was obtained from Climate Change Initiative (CCI) on an annual basis for the period 1992–2015. Project CCI-LC provides maps of land use schemes at a resolution of 300 m (Table 1). Climate data are presented according to annual precipitation (Table 2) for a 36-year period (1981–2016) and come from Regional State

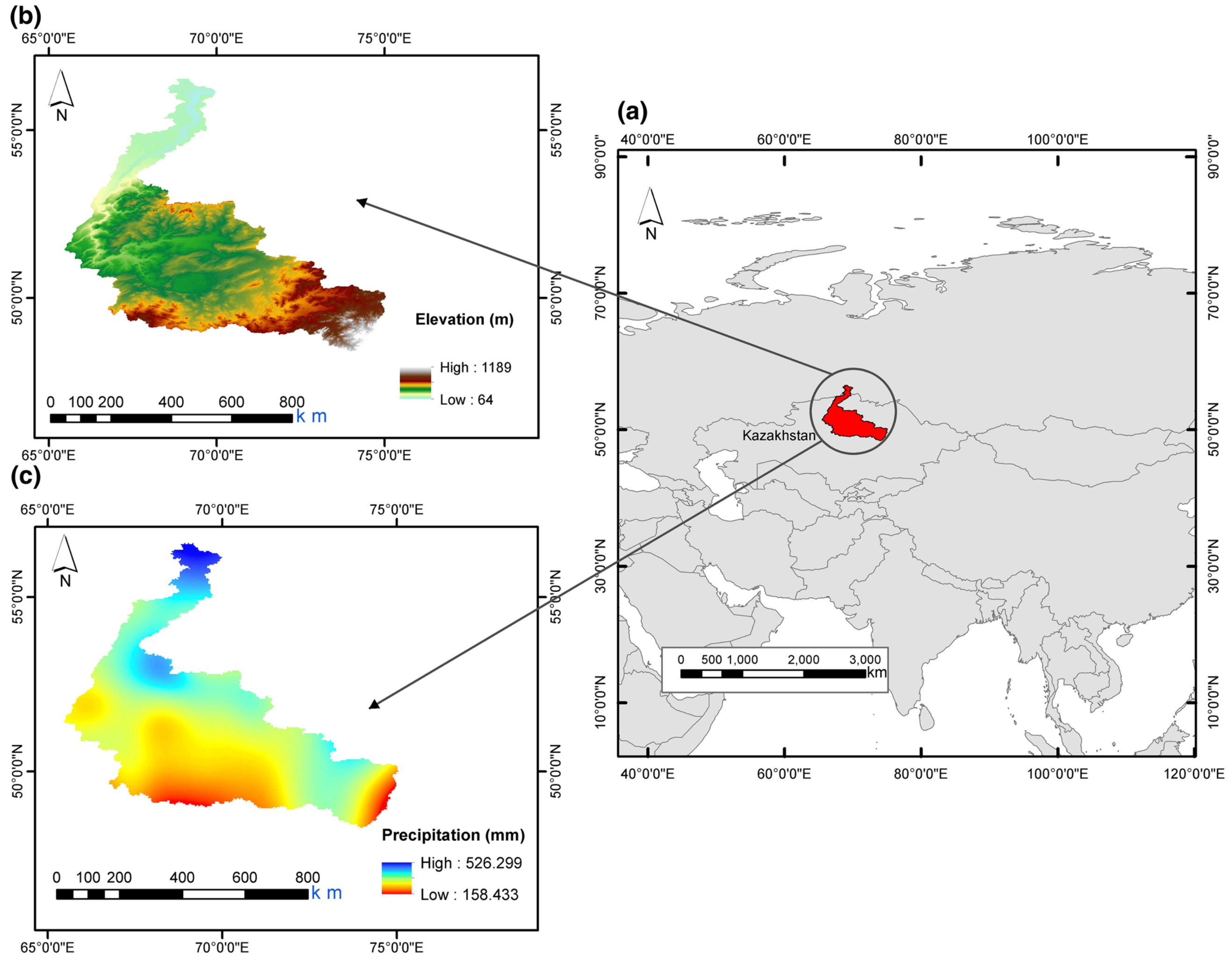

Fig. 1 Study area map of Esil River basin includes: **a** location and geographical; **b** DEM (digital elevation model); **c** spatial allocation of annual precipitation (mm)

Table 1 Datasets list used in research

Category	Source	Reference	Spatial resolution	Temporal period (years)	Variables
DEM	USGS	https://earthexplorer.usgs.gov/	25.43 m	–	Elevation
Climate	Kazhydromet	–	–	1981–2016	36 y averaged annual precipitation
Soil	FAO Geonetwork	http://www.fao.org/geonetwork/srv/en/metadata.show?id=14116	5 arcmin	2007,02,28	Sand, silt and clay fractions, organic matter (%).
Land cover	USGS Landsat 8	https://earthexplorer.usgs.gov/	30 m	July 2016	Normalized Difference Vegetation Index (NDVI)
Land use	ESACCI-LC	http://maps.elie.ucl.ac.be/CCI/viewer/	300 m	2015	Land use fraction
Vegetation indices	USGS Landsat 8	https://earthexplorer.usgs.gov/	30 m	July 2013–2018	NDVI, SAVI, OSAVI and MSAVI
Gross Regional Product	Ministry of National Economy of the Republic of Kazakhstan, Committee on Statistics	http://stat.gov.kz/beta/official/industry/11/statistic/8	–	2017	Gross Regional Product (USD) and population

Enterprise Kazhydromet, which includes observations from 39 meteorological stations (Fig. 2) covering the ERB.

Method

The Universal Soil Loss Equation (USLE) is the result of an enormous amount of labor and extensive analyses by scientists of a large amount of data published in the Agriculture Handbook 282 (Wischmeier 1976) and Agriculture Handbook 537 (Wischmeier and Smith 1978). The USLE is presented in Eq. (1) below (Fig. 3):

$$A = R * K * LS * C * P \tag{1}$$

where: the unit of average soil loss (A) is (t ha^{-1} y^{-1}); the unit of factor R is (MJ mm ha^{-1} h^{-1} y^{-1}); the unit of factor K is (t ha h ha^{-1} MJ^{-1} mm^{-1}); and the units of LS, C and P factors are dimensionless.

R-factor (rainfall erosivity factor)

To analyze the R-factor in this study, annual mean rainfall (mm) was used. The R-factor was calculated for each of the 39 meteorological stations, after which the R-factor values were interpolated by the spline interpolation method by applying Analyst Tools in ArcGIS 10.2 for the period 1981–2016. Equation (2), as proposed by Renard and Freimund (1994), was employed for calculating regressions between the R-factor and precipitation in order to calculate the effect of the kinetic energy of rain, as follows:

$$R = 0.04830 * P^{1.610} \quad (P < 850\,\text{mm}) \tag{2}$$

where R-factor is rainfall aggressiveness in (MJ mm ha^{-1} h^{-1} y^{-1}) and P is annual precipitation in mm.

K-factor (soil erodibility factor)

The equation for estimating K-factor values, as given by Williams and Singh (1995), is presented in Eq. (3):

$$K_{\text{usle}} = K_{\text{w}} = f_{\text{c/sand}} * f_{\text{cl/si}} * f_{\text{orgc}} * f_{\text{hisand}} * 0.1317 \tag{3}$$

where $f_{\text{c/sand}}$ is a factor that lowers the K indicator for soils with high or low coarse-sand content; $f_{\text{cl/si}}$ gives high soil erodibility factors for soils with low clay-to-silt ratios; f_{orgc} implies if the carbon content is high, it reduces K values in soils; and f_{hisand} increases K values for soils with extremely low sand content.

$$f_{\text{csand}} = \left(0.2 + 0.3 * \exp\left[-0.256 * m_{\text{s}} * \left(1 - \frac{m_{\text{silt}}}{100}\right)\right]\right) \tag{4}$$

$$f_{\text{cl/si}} = \left(\frac{m_{\text{silt}}}{m_{\text{c}} + m_{\text{silt}}}\right)^{0.3} \tag{5}$$

$$f_{\text{orgc}} = \left(1 - \frac{0.25 * \text{Corg}}{\text{Corg} + \exp\left[3.72 - 2.95 * \text{Corg}\right]}\right) \tag{6}$$

$$f_{\text{hisand}} = \left(1 - \frac{0.7 * \left(1 - \frac{m_{\text{s}}}{100}\right)}{\left(1 - \frac{m_{\text{s}}}{100}\right) * \exp\left[-5.51 + 22.9 * \left(1 - \frac{m_{\text{s}}}{100}\right)\right]}\right) \tag{7}$$

Table 2 The list of meteorological stations

MS	Latitude	Longitude	Elevation (m)	Years	Annual precipitation (mm)	*R*-factor	Zone
Petropavlovsk	54.82	69.12	107	36	377.0	679.0	Moderately wet
Yavlenka	54.35	68.45	111	36	376.5	677.5	Moderately wet
Sergeevka	53.88	67.40	152	36	377.9	681.6	Slightly wet
Ruzaevka	52.82	66.96	226	36	363.3	639.7	Slightly wet
Saumalkol	53.31	68.11	327	36	431.3	843.1	Moderately wet
Blagoveshenka	54.36	66.98	151	36	352.5	609.3	Slightly wet
Timiryazevo	53.76	66.49	168	36	347.0	594.1	Slightly wet
Yegindykol	51.05	69.50	338	36	299.0	467.5	Slightly arid
Esil	51.96	66.39	219	36	281.4	424.1	Slightly arid
Zhaksy	51.91	67.34	392	36	329.0	545.4	Slightly arid
Balkashino	52.53	68.74	396	36	404.8	761.2	Moderately wet
Atbasar	51.84	68.36	299	36	314.6	507.4	Slightly wet
Zhaltyr	51.63	69.82	303	36	333.0	555.9	Slightly wet
Akkol	51.99	70.94	381	36	374.5	671.7	Slightly wet
Astana	51.17	71.39	346	36	327.2	540.6	Slightly wet
Shucinsk	52.93	70.20	390	36	337.8	569.0	Moderately wet
Arshaly	50.86	72.15	426	36	318.0	516.2	Slightly wet
Derzhavinka	51.60	66.19	274	36	264.0	382.6	Slightly arid
Korgalgyn	50.59	70.00	329	36	290.0	445.0	Slightly arid
Karasu	52.65	65.48	206	36	306.4	486.1	Slightly arid
Zheleznodorozhny	52.09	65.66	246	36	285.4	433.6	Slightly arid
Amangeldy	50.20	65.21	142	36	208.0	260.6	Moderately arid
Aralkol	50.08	65.69	172	36	296.6	461.4	Moderately arid
Ekidyn	49.52	66.15	206	36	208.0	260.6	Moderately arid
Zhana-Arka	48.41	71.40	476	36	259.9	373.0	Slightly arid
Zharyk	48.51	72.50	594	36	355.0	616.4	Slightly wet
Karaganda	49.49	73.09	684	36	363.0	638.8	Slightly wet
Kertindy	49.96	71.59	421	36	292.3	450.8	Slightly arid
Korneevka	50.21	74.27	615	36	352.7	610.0	Slightly wet
Besoba	49.20	74.28	807	36	229.4	305.1	Slightly arid
Aksu-Ayuly	48.46	73.40	765	36	318.0	516.3	Slightly wet
Karkaraly	49.42	75.50	863	36	387.8	710.6	Slightly wet
Karaganda AFS	50.10	72.44	538	36	308.0	490.4	Slightly wet
Shubarkol	49.00	68.70	506	36	174.4	196.3	Slightly arid
Barshino	49.67	69.54	355	36	245.4	340.1	Slightly arid
Koskol	49.30	67.04	496	36	243.5	335.9	Slightly arid
Birlik	49.82	69.55	345	36	257.5	367.5	Slightly arid
Ishim	56.06	69.26	87	36	395	731.9	Moderately wet
Tasty-Taldy	50.44	66.37	305	32	321.2	524.6	Moderately arid

where m_s indicates the content of sand fraction (0.05–2.00 mm diameter) [%]; m_{silt} is the content of silt fraction (0.002–0.05 mm diameter) (%); m_c expresses the content of clay fraction (< 0.002 mm diameter) (%); and Corg gives the carbon content of organic matter (SOC) (%).

LS-factor (slope length and steepness factor)

The LS-factor in the RUSLE model considers the topographic features of slopes, which ultimately determines the total sediment yields from the site. Equation (8) is applied

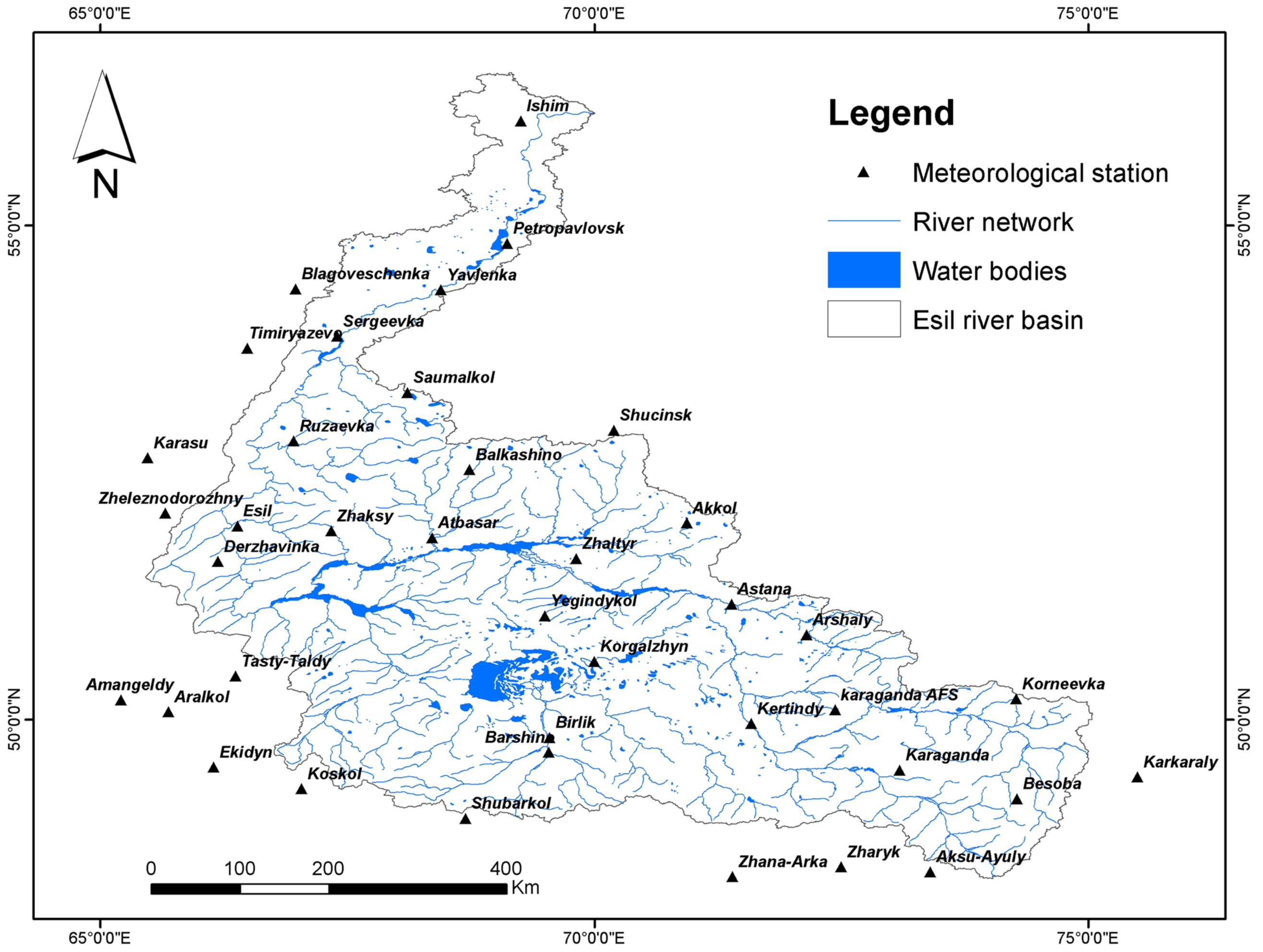

Fig. 2 Location of meteorological stations

to find the combined LS-factor by means of spatial analyst extension in ArcGIS using DEM, as proposed by Morgan (2009). Factors such as slope steepness and flow accumulation are also taken into consideration to calculate the LS-factor using the ArcGIS spatial analyst tool and the arc hydro extension using DEM:

$$LS = \sqrt{\frac{l}{22}\left(0.065 + 0.045 * S + 0.0065 * S^2\right)} \tag{8}$$

where l is slope length (m), S is slope percentage, and the size of the grid cell = cell size (in this research, 25.43 m).

C-factor (cover management factor)

The *C*-factor considers soil-disturbing activities, the sequence of crops in crop rotation, the state of the soil cover and plant biomass, and the effect of all these factors on soil erosion. Remote sensing technologies are highly informative for spatial analysis of the vegetation cover state, primarily due to the difference in land cover patterns, which is taken into account in calculating the *C*-factor (Prasannakumar et al. 2011). In addition, the Normalized Vegetation Difference Index (NDVI) is a simplistic indicator that enables potential assessment of health status, vegetation energy, and green biomass of plants (Jiang et al. 2014).

The *C*-factor value was applied in Eq. (9):

$$C = \exp\left[-\alpha\frac{\text{NDVI}}{(\beta - \text{NDVI})}\right] \tag{9}$$

where $\alpha = 2$ and $\beta = 1$ are unitless indicators which define the curve's shape to NDVI and the *C*-factor. This scaling approach was proposed by Van der Knijff et al. (2000) and gives better results versus a linear relationship.

P-factor (conservation practice factor)

The coefficient of support practice (*P*-factor) is the ratio of soil loss to the type of soil cultivation, taking into account the ratio

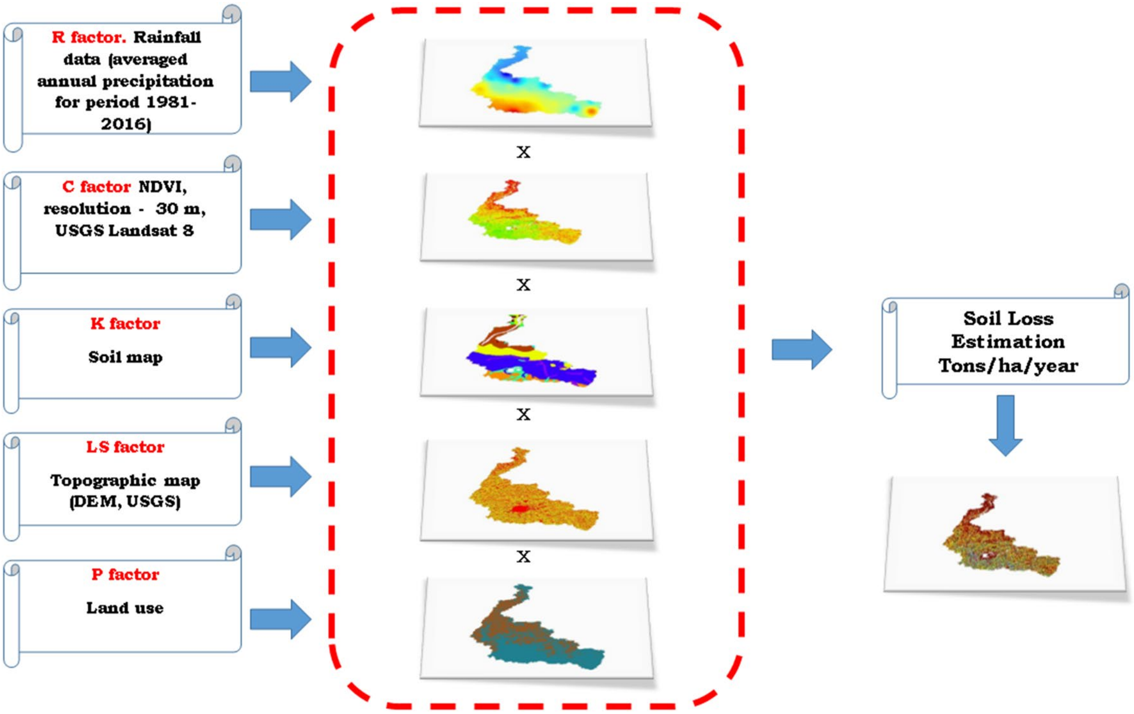

Fig. 3 Flowcharts of RUSLE methodology

of soil loss to topographic features (Renard et al. 1997). The *P*-factor shows the effects of cultivation plant technology (i.e., type of land management model, such as plowing mode and crop direction) and soil conservation practice (slope restoration), which promotes the decrease in the volume and speed of streaming water and facilitates infiltration by changing the soil structure. This helps to reduce the impact of erosion processes. In our research, the *P*-factor is defined in accordance with studies conducted by Wischmeier and Smith (1965) and Wischmeier and Smith (1981), where the values of the *P*-factor depend on the combination of slope classes and current agricultural practices. The types of agricultural practices in the ERB were identified from the land management map.

Vegetation indices

For revealing the plots of land which are prone to soil degradation, Normalized Vegetation Index (NDVI), Soil Adjusted Vegetation Index (SAVI), Optimized Soil Adjusted Vegetation Index (OSAVI) and Modified Soil Adjusted Vegetation Index (MSAVI) were used.

The calculation of NDVI (Eq. 10) look to Rouse et al. (1974) for the description of NDVI. For calculation of NDVI, we used satellite images of Landsat 8 (band 4 and 5) for period: July 2013–2018.

$$\mathrm{NDVI} = \frac{\mathrm{NIR} - R}{\mathrm{NIR} + R} \tag{10}$$

where NIR is reflectance in the near infrared and R is reflectance in the visible red band.

Huete (1988) proposed the use of soil adjustment factor L, to reduce the influence of background soil conditions, which he called Soil Adjusted Vegetation Index (SAVI) (11) and then later modified—Modified Soil Adjusted Vegetation Index by Qi et al. (1994) (MSAVI) (12) and Optimized Soil Adjusted Vegetation Index (OSAVI) proposed by Rondeaux and Baret (1996) (13).

$$\mathrm{SAVI} = \frac{\mathrm{NIR} - R}{\mathrm{NIR} + R + L}(1 + L) \tag{11}$$

$$\mathrm{MSAVI} = \frac{2\mathrm{NIR} + 1 - \sqrt{(2\mathrm{NIR} + 1)^2 - 8(\mathrm{NIR} - R)}}{2} \tag{12}$$

$$\mathrm{OSAVI} = \frac{1.5 * (\mathrm{NIR} - R)}{\mathrm{NIR} + R + 0.16}. \tag{13}$$

where $L = 0.5$

Results and discussion

Rainfall erosivity factor

The results revealed rainfall erosivity ranging from 61 to 861 (MJ mm ha^{-1} h^{-1} y^{-1}) (Table 3). Overall, annual precipitation

Table 3 The range of rainfall erosivity values

R-factor value (MJ mm ha^{-1} h^{-1} y^{-1})	Area (sq km)	Area (%)
61–200	1596.2	0.7
201–300	8685.7	3.9
301–400	29,240.0	13.0
401–500	66,669.1	29.6
501–600	48,561.2	21.6
601–700	49,414.4	21.9
701–861	21,057.8	9.3
Total	225,224.36	100

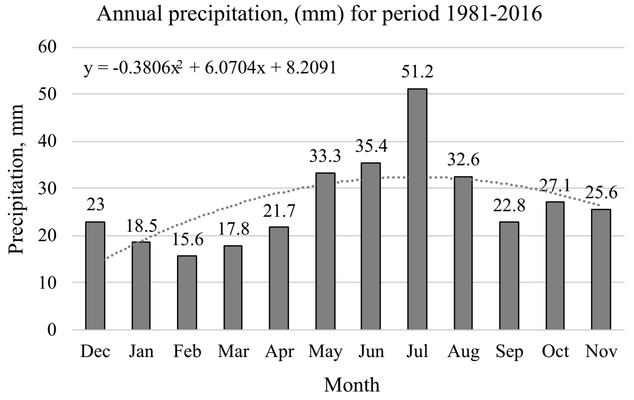

Fig. 4 Seasonal dynamic of the annual precipitation (mm)

is not very high in the ERB, giving a mid-level annual rainfall aggressiveness of 522.7 (MJ mm ha^{-1} h^{-1} y^{-1}) for our study area.

The mean annual precipitation for 1981–2016 is 324.6 mm. On average, July saw the highest amount of precipitation (up to 51.2 mm), while February saw the lowest amount (about 15.6 mm) (Fig. 4). The spatial allocation of rainfall is also uneven. The northern part of the study area, at altitudes of 64–626 m above sea level, is more humid (431.3 mm), whereas the southern part of the study area, at altitudes of 600–1189 m above sea level, is more arid (175.6 mm) (Kalb and Mavlyanova 2005; Yapiyev et al. 2017).

Soil erodibility factor

K-factor values in accordance with soil type were assigned on the soil map (Fig. 5c) toward the generation of a soil erodibility map. Inland water (WR) bodies were assigned a value of 0. In the study area, the *K*-factor ranges between 0.016264 and 0.021376 (t ha^{-1} h^{-1} ha MJ mm). A low value implies features such as low permeability, low antecedent moisture content and so on. In total, the sand content in the topsoil of our study area ranges from 26.4 to 70.8%; silt ranges from 12.8 to 46.4%; clay ranges from 14.3 to 47.7%; and OC (organic carbon) ranges from 0.39 to 41.46% (Table 4).

According to the physical properties of soils (Table 4), the values for erodibility factors range from 0.016 to 0.021 when the soil has a clay content of 14.3–47.7%. *K*-factor values less than 0.05–0.15 are considered low. Fine-textured soils with high clay content are resistant to the detachment of soil particles (Foster et al. 2003; Ganasri and Ramesh 2016). Although there are some steep slopes in the ERB, the moderate-to-low amount of precipitation (less than 250 mm y^{-1}) diminishes the influence of rain on the soil. The soil with the lowest *K*-factor value (0.0163 [t ha^{-1} h^{-1} ha MJ mm]) is located along a narrow strip stretching from the northern portion of the ERB to its middle part. Conversely, the soil plots with the highest values of *K*-factor [in the range of 0.0202–0.0214 (t ha^{-1} h^{-1} ha MJ mm)] are located in the northern part of the ERB, extending to the middle part of the basin. The soil of the remaining area has *K*-factor values ranging from 0.0171 to 0.0198 (t ha^{-1} h^{-1} ha MJ mm). High *K*-factor values indicate a higher vulnerability of the soil plot to erosion caused by rainfall and/or runoff (Ganasri and Ramesh 2016), while low *K*-factor values mean that the soil is less vulnerable to detachment by rainfall and/or runoff.

In Akmola and the North-Kazakh regions of the ERB, water erosion processes are developing intensively. The Akmola region's highly eroded soils are characterized by the absence of an arable horizon. This is because, on medium-carbon soils, 50% of the arable horizon has been washed away, while on slightly eroded soils, the humus horizon has been reduced by 30% (Mueller et al. 2013). The soil texture across the ERB region is characterized as sandy loam, sandy clay loam, clay loam, loam and clay, with local soil classification for the river basin indicating the presence of three different types of soil: Dark Chestnut, Ordinary Chernozem and Southern Chernozem (Takata et al. 2007).

Furthermore, it is estimated that in Northern Kazakhstan, the formation of 1 cm of the upper part of the soil profile occurred over a period of 100–230 years, which corresponds to an annual accumulation of soil of 0.6–1.3 t ha^{-1}. Currently, normal plowing across the slope has resulted in soil erosion of up to about 4–7 t ha^{-1} to 8–18 t ha^{-1}. This means that the fertile soil mass which took hundreds of years to form is lost in a single year (Shepelev 2014). Of the above-mentioned types of soil, the ones most stable in their physical properties in the face of erosion are the chernozems type, while the chestnuts, which are found in forest land as well as desert and semi-desert zones, are less stable. Soil erosion is affected by soil condition, season, land use type and humus content, but the largest cause of erosion currently is agricultural treatments, primarily land plowing (Zaslavsky 1983).

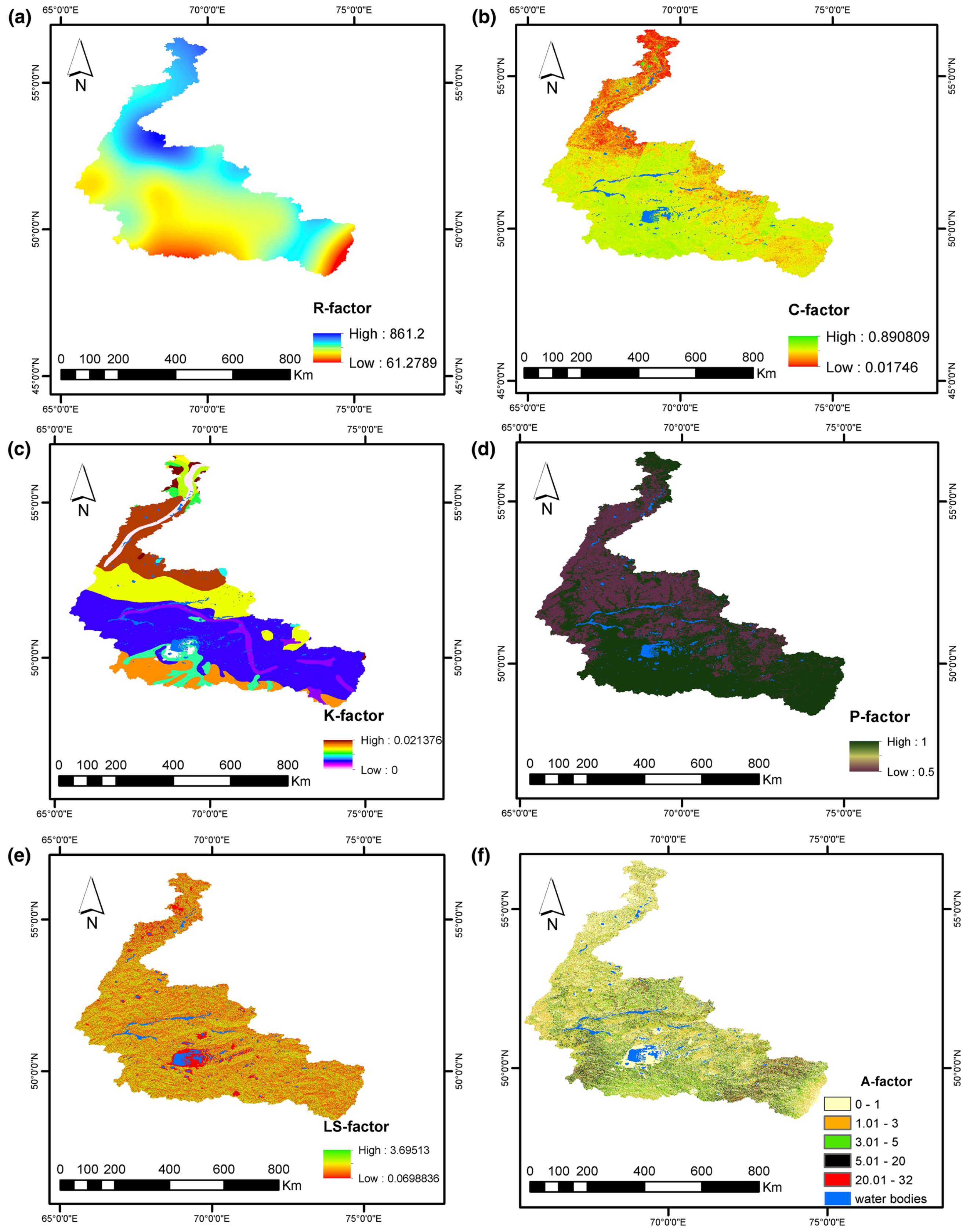

Fig. 5 Maps of the RUSLE factors included: **a** rainfall erosivity, **b** land cover management, **c** soil erodibility, **d** conservation support practice, **e** slope length and slope steepness, **f** soil erosion potential map

Table 4 The physical properties of soils for calculating *K*-factor

Soil unit symbol	*K*	Sand % topsoil	Silt % topsoil	Clay % topsoil	OC % topsoil	Fc sand	Fcl-si	Forgc	Fhisand	Kusle	*K*-factor $t\ ha^{-1}\ h^{-1}\ ha\ MJ^{-1}\ mm^{-1}$
JE	0.0163	70.8	12.8	16.5	1.15	0.2000000	2.187	0.887	0.318	0.123	0.016
MO	0.0205	33.3	46.4	20.4	3.65	0.2031096	3.208	0.750	0.319	0.156	0.021
OE	0.0194	35	40	25	41.46	0.2013879	3.060	0.750	0.319	0.147	0.019
WS	0.0193	69.1	16.7	14.3	0.72	0.2000001	2.375	0.968	0.318	0.146	0.019
CL	0.019	46.3	24.9	28.8	1.27	0.2000409	2.650	0.859	0.318	0.145	0.019
C	0.0185	42.9	27.6	29.5	1.52	0.2001057	2.733	0.809	0.318	0.141	0.019
CH	0.0202	32.2	44.1	23.7	3.04	0.2029917	3.153	0.750	0.319	0.153	0.020
SM	0.0214	51.7	31.9	16.4	1.14	0.2000365	2.876	0.889	0.317	0.162	0.021
CK	0.0192	41.6	26.6	31.8	1.32	0.2001209	2.701	0.847	0.318	0.146	0.019
I	0.0181	58.9	16.2	24.9	0.97	0.2000010	2.333	0.927	0.317	0.137	0.018
KH	0.0174	54.5	27.3	18.2	2.16	0.2000118	2.740	0.758	0.317	0.132	0.017
GM	0.0171	26.4	25.9	47.7	2.44	0.2020053	2.671	0.753	0.320	0.130	0.017
SO	0.0183	57.6	13.5	29	0.39	0.2000009	2.206	0.993	0.317	0.139	0.018
KL	0.0198	36.7	40.3	23.1	2	0.2010995	3.070	0.763	0.319	0.150	0.020

Soil Unit symbols

Je—Eutric Fluvisols, Mo—Orthic Greyzems, Oe—Eutric Histosols, Ws—Solodic Planosols, Cl—Luvic Chernozems, C—Chernozems, Ch—Haplic Chernozems, Sm—Mollic Solonetz, Ck—Calcic Chernozems, I—Lithosols, Kh—Haplic Kastanozems, Gm—Mollic Gleysols, So—Orthic Solonetz, Kl—Luvic Kastanozems

Topographic factor

Slope length and steepness are topographic factors which significantly affect the dynamics of the erosion process. Analysis shows that the values of topographic factors increase with flow accumulation as well as slope length and steepness. The values of the LS-factor in the study area range from 0.069 to 3.69513. Most parts of the ERB have an LS value of 0; this value covers 47% (106,555.52 km^2) of the total area of the ERB. Otherwise, areas with a value of 1 occupy 22.4% (50,536.19 km^2) of the study area, those with a value of 2 make up 23.99% (54,043.42 km^2), and other small plots throughout the ERB show a value of 3 (Fig. 5e). The values of the slope length are divided into seven classes ranging from 0° to 70.29° (Table 5). The slope length and steepness increase evenly from the northern portion of the region to the southeastern part. As the length and slope steepness gradient increases, so does the probability of erosion processes contributing to soil degradation. The northern part of the ERB is less vulnerable to soil erosion compared to the southern part, where slope degree in some places varies from 40° to 70.29°.

The main type of land in the Akmola region is undulating plains with isolated hills or groups of hills scattered over its surface. The altitude ranges from 300 to 400 m above sea level on the plains, with some low mountain formations rising to a height of 700–800 m. The flattest portion of the study area is the central and northern parts of the ERB (Klebanovich et al. 2016; Pashkov and Tayzhanova 2016).

According to a report from the Ministry of Agriculture of the Republic of Kazakhstan regarding the state and use of lands, the volume of eroded soil in 2017 in the Akmola, Karaganda and North-Kazakh regions of the ERB measured 818,400 ha (Karentaev et al. 2018).

Crop management factor

To assess the *C*-factor, satellite images (Landsat 8) for the vegetation period July 2016 were used. *C*-factor values ranging from 0.01746 to 0.890809 were recorded. The lowest *C*-factor values (up to 0.01746) indicate the presence of vegetation cover, which mostly covered the northern, eastern and southeastern parts of the ERB. The higher *C*-factor values on the remaining portions of the ERB reached 0.890809, which signified either sparse vegetation cover or the absence of vegetation cover. The presence of vegetation cover on the ground means that the plot is less prone to soil erosion, while its absence designates the soil as being more prone to soil degradation. The value of *C*-factor for surface water was equal to 0.0.

Bao Le et al. (2014) found that between 1980 and the mid-2000s, the conditions of the land significantly deteriorated. Soil degradation in Turkmenistan and Uzbekistan during that time frame amounted to 8%, while in Kazakhstan it reached 60% of the total area. The intensive cultivation of rain-fed wheat, combined with intensive tillage without the use of soil protection technologies, quickly led to the depletion of the fertile soil layer, especially in hilly areas. The use of fallowing during the summer period with intensive tillage to control weeds only served to exacerbate the soil erosion processes (Kienzler et al. 2012). Insufficient fertilization also led to the depletion of soil fertility.

All of the above-mentioned problems are usually the result of a lack of information on soil protection technologies and practices. However, soil erosion caused by inappropriate farming methods can also be caused by insufficient funding or lack of access to credit (Gupta et al. 2009). The degradation of pastures is aggravated by unsystematic and excessive grazing of animals, lack of conditions (infrastructure) for pasture grazing, abandoned pastures and cutting of shrubby plants (Pender et al. 2009). Tillage and plowing further decimate the SOC pool through the increase in the mineralization rate and acceleration of soil erosion.

Conservation practice factor

The *P*-factor was obtained from the land use/land cover map. The range of the *P*-factor, as indicated in Table 6, varied from 0.5 to 1, with the minimal value of 0.5 corresponding to cropland and the maximum value of 1 assigned to

Table 5 Slope steepness in the Esil River basin

Slope degree	Area (sq km)	Area (%)
0–10	82,538.06	36.65
10–20	27,421.74	12.18
20–30	27,400.82	12.17
30–40	27,096.88	12.03
40–50	30,213.25	13.41
50–60	22,545.87	10.01
60–70.3	8,007.75	3.56
Total	225,224.36	100.00

Table 6 Land use classification accordingly to the *P*-factor

No.	Class name	Area (sq km)	Area (%)	*P*-factor
1	Agriculture	85,607.79	38.01	0.5
2	Urban	39,166.52	17.39	1.0
3	Water bodies	4977.46	2.21	1.0
4	Grassland	1824.32	0.81	1.0
5	Bare area	81,666.37	36.26	1.0
6	Shrub	7027.00	3.12	1.0
7	Forest	1013.51	0.45	1.0
8	Wetland	3851.34	1.71	1.0

urban areas, water bodies, grassland, bare areas, shrub, forest and wetlands (Fig. 5d). The value of the *P*-factor depends on the cultivation method and slope length and steepness (Bouguerra et al. 2017); the averaged value of this factor is 0.75. This is relatively high for the ERB and can be explained by the lack of support practices in 62% of the total area where the *P*-factor value is 1.0. In the remaining territory, which is situated mainly in the northern and middle sections of the ERB (32%), the *P*-factor value is 0.5. This valuation covers lands that are under different cultivation cropping systems, implying that the application of a soil protection system in agriculture leads to a decrease in soil erosion processes.

The insufficient supply of organic matter, together with soil tillage practices which cause soil compaction, led to an increase in soil erosion, the breakdown of topsoil depth, and an increase in salinity, consequently inducing not only the loss of fertility but also a decrease in land value. The compaction of soil decreases the soil's capability to conduct and store water, making it less permeable to plants roots and increasing the probability of soil loss by water erosion (Jones et al. 2012). Only Kazakhstan addressed this problem, introducing Conservation Agriculture (CA) practices and supportive policies, increasing the area (including ERB) under CA-based practices from none in 2001 to 2.1 M ha in 2013 (Kienzler et al. 2012).

Assessment of potential annual soil erosion

To assess soil erosion risk, we have selected a zoning scheme used to gauge the risk of erosion soil degradation in Russia (Table 7). The potential soil loss has been categorized into five classes: not dangerous, slightly dangerous, moderately dangerous, dangerous and highly dangerous (Litvin 2002). As shown in Table 8, total soil erosion in the ERB is 565,368.7 (t y^{-1}). Since the data for recent years are unavailable, data observations of river sediment yields for 1957–1967 were used for the research results validation (Skladchikova 1977). According to the observations, the total annual river sediment yield was 570,000 (t y^{-1}) and the research result was 565,368.7 (t y^{-1}). Hence, the analysis accuracy assessment is 99.1%. The mean value of soil erosion loss throughout the ERB is 2.511 (t y^{-1}). Given the obtained results, we can conclude that 108,007.51 sq km (48%) is not prone to soil erosion processes or soil erosion intensity lower than nature soil recovery. Slightly dangerous soil erosion intensity covers 49,317.1 sq km (21.9%), moderately dangerous covers 32,686.64 sq km (14.5%), dangerous covers 35,204.43 sq km (15.6%) and highly dangerous covers 8.71 sq km (0.004%).

Results of NDVI, SAVI, OSAVI, MSAVI

The range of NDVI, SAVI, OSAVI and MSAVI results is ranging from − 1 to + 1. The positive values of vegetation indices reflect the presence of land cover, but negative values mean the reduction in biologic productivity in the ecosystem which is caused by soil and vegetation degradation (Eckert et al. 2015). The spatial allocation of soil degradation shown in Fig. 6a–d displays raster cells with values below 0 mostly in southeastern part, around water bodies throughout ERB and along the river. The

Table 7 The zoning scheme on the risk of soil erosion degradation in Russian Federation

Degree of environmental hazard	Flush intensity (t y^{-1})	Potential soil degradation, the proportion of erosive dangerous lands (%)
No dangerous	0–1.0	< 5
Slightly dangerous	1.1–3	5–20
Moderate dangerous	3.1–5	21–40
Dangerous	5.1–20	41–70
Highly dangerous	> 20	> 70

Table 8 Soil loss in Esil River basin

Intensity of soil erosion	Range of soil loss (t y^{-1})	Total soil erosion (t y^{-1})	Area (sq km)	Area (%)
No dangerous	0–1.0	33,181.1	108,007.51	48.0
Slightly dangerous	1.1–3	120,802.9	49,317.10	21.9
Moderate dangerous	3.1–5	144,119.7	32,686.64	14.5
Dangerous	5.1–20	267,065.7	35,204.43	15.6
Highly dangerous	> 20	199.3	8.71	0.004
Total		565,368.7	225,224.3965	100.000

overall square of land with negative values accounts for 1135.6 km^2, 1230.1 km^2 and 1230.1 km^2 for NDVI, SAVI, OSAVI and MSAVI, respectively, which are prone to soil gradation and soil erosion processes.

Ecological consequences

Destroying pastures and farmland

The amount of biomass carbon in the soil decreased from 0.48 PgC in 2000 to 0.47 PgC in 2010 (Zomer et al. 2016). The natural ravines observed in the valleys of the ERB usually have a length of 100–300 m, but sometimes their length can be up to 3000 m. Their width typically reaches 10–20 m and their depth 5–10 m. From 1929 to 2015, the annual increment of the ravine system at the Rabochi settlement on the outskirts of Petropavlovsk City in the northern part of the ERB was up to 132 m. Its length measured 3440 m, its width 15–20 m, and its depth 5–15 m. In the ERB valley, there are numerous river ravines at various stages of development, including gullies and beams. The gullies usually have insignificant sizes (e.g., length 10–20 m, depth 0.1–0.3 m and width 0.1–0.5 m) (Pashkov 2016). The main consequences of soil degradation are fertility depletion and soil organic matter loss of up to 40% on rain-fed cropland. The annual cost of soil degradation per capita in Kazakhstan is around 1800 USD (Nkonya et al. 2016).

Risk of flooding

At a water flow velocity of 0.4–0.9 m/s, a surface washout of the soil will take place on light loam; on denser soils (e.g., clay), surface flushing can occur at a velocity of 0.7–1.2 m/s. Even on small slopes with a decline of 1.0°–1.5°, heavy rains or spring snowmelt could cause critical speeds at the surface runoff. In cases where the soil covers a thin layer of water in the rain, soil may form 20% of the suspension, which can move even at low water velocities (0.2 m/s). The blockage of the capillary soil by dust particles disrupts filtration, promotes soil compaction, causes the formation of a soil crust, favors an increase in surface water runoff, and may later provoke other types of soil erosion (Apazhev et al. 2016). During the spring snowmelt in the ERB, the water level generally rises by 3–5 m; however, during a flood event, river levels might increase up 5–10 m or more (Plekhanov 2017). The frequency of floods exceeding the 10 m mark increased from 4 times during 1936–1965 up to 9 times during 1985–1994. In 1994, the level of the water rise exceeded 11 m, which constituted the maximum height over the entire period of observation (Lezin 1999).

GDP and poverty

The gross domestic product (GDP) per capita in Northern Kazakhstan in 2012 was 101,263 Tenge or 679 USD (Smailov 2013). Soil degradation can obstruct efforts toward poverty reduction and stable economic development, especially since the agricultural sector is a major employment provider in Northern Kazakhstan (Mirzabaev 2013; Nkonya et al. 2016). Soil erosion affects physical, chemical and biological processes in soil that later causes reductions in crop yields (FAO 2015). A recent report by the Global Assessment of Land Degradation concluded that the main reason for losses in agricultural productivity is land degradation (Mirzabaev et al. 2018). Soil degradation issues are not confined to the ERB region, however. To counteract land degradation in Africa, for instance, soil conservation measures were applied. At the initial stage, these measures led to a decrease in the farmers' profitability; however, within a decade, the farmers who used soil conservation methods saw greater income growth than farmers who used conventional land cultivation (Kruseman and Bade 1998; Pagiola 1996). About 27% losses in the agricultural sector were caused by land degradation during the 2009–2010 growing season. This had a negative impact on poverty reduction in Central Asia. In response, 25% of the poorest households applied more suitable land management than did the middle-class and wealthier households, the latter two which subsequently, due to escalating land degradation, lost profits of 30% and 34%, respectively (Mirzabaev 2018).

For a spatial assessment of incomes of the population in Agriculture sector within the ERB, the data on Gross Regional Product (GRP) for North-Kazakh, Kostanay, Akmola and Karaganda regions for 2017 were used from the Web site of the Ministry of National Economy of the Republic of Kazakhstan, Committee on Statistics. Since GDP data are available only for the republic as a whole, we used the GRP for mentioned regions to estimate the incomes of the population by region. The data about a population by regions are available from Web site of Committee on Statistics (Table 1). The total GRP for the region was divided by the population of the region in order to calculate the GRP per capita. The spatial level of GRP is reflected in Fig. 6e. According to the Statistics Committee of 2017, the GRP per capita in the North Kazakhstan region was—893.6 USD, in the Kostanay region—444.5 USD, in the Akmola region—560.8 USD and in the Karaganda region—204.1 USD (Fig. 6e).

Strategy and planning of soil conservation

Application of soil-saving technologies in Agriculture

Kazakhstan now applies a "no-till" policy in over 1.85 Mln. ha of its agricultural sector. In just five years alone,

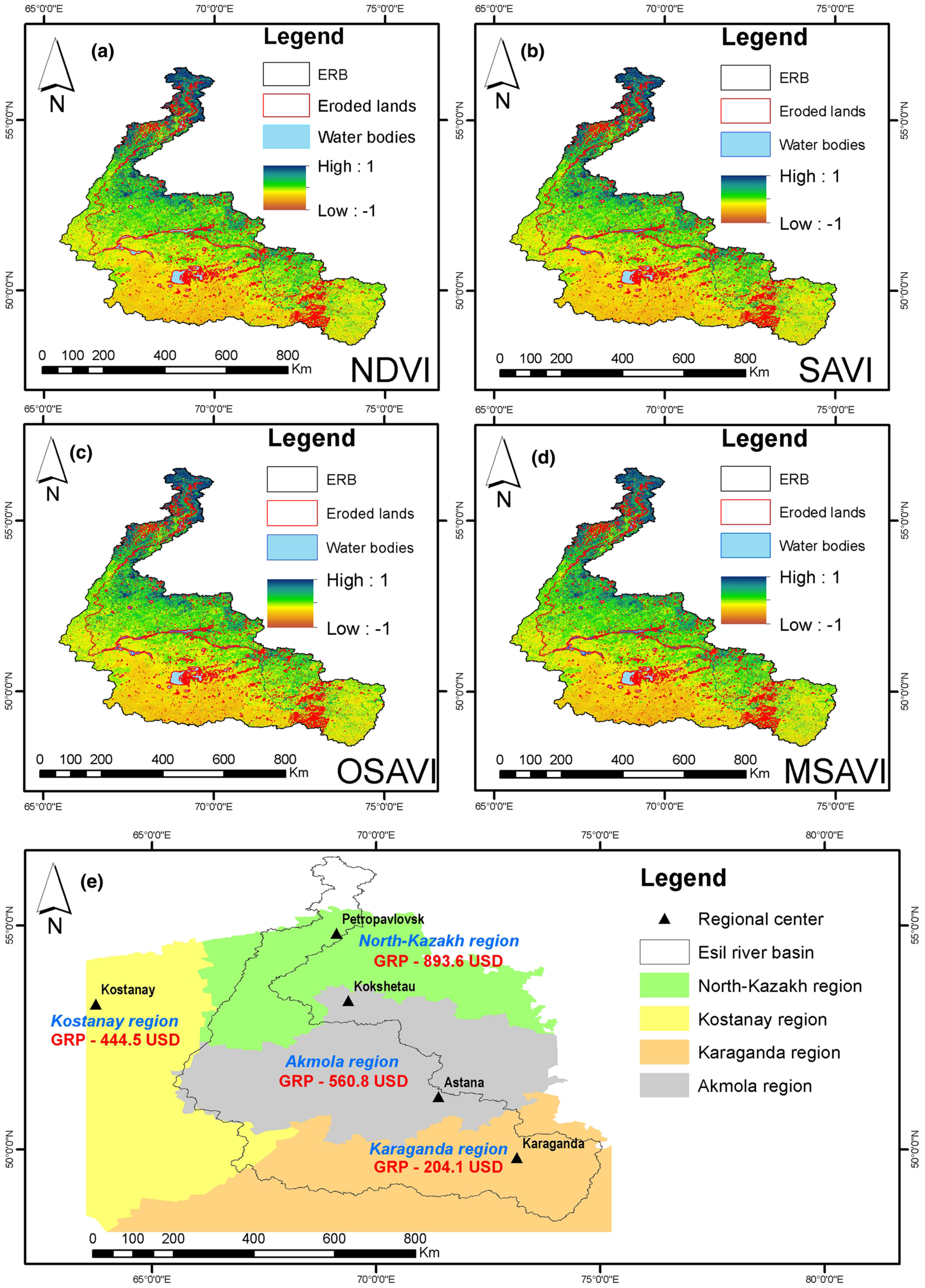
(a)
(b)
(c)
(d)
(e)
N
Legend
ERB
Eroded lands
Water bodies
High : 1
Low : -1
0 100 200 400 600 800 Km
NDVI
SAVI
OSAVI
MSAVI
65°0'0"E
70°0'0"E
75°0'0"E
80°0'0"E
55°0'0"N
50°0'0"N
Regional center
Esil river basin
North-Kazakh region
Kostanay region
Karaganda region
Akmola region
Petropavlovsk
North-Kazakh region
GRP - 893.6 USD
Kokshetau
Kostanay
Kostanay region
GRP - 444.5 USD
Akmola region
GRP - 560.8 USD
Astana
Karaganda region
GRP - 204.1 USD
Karaganda

◂**Fig. 6** Maps of the vegetation indices and RGP: **a** Normalized Difference Vegetation Index, **b** Soil Adjusted Vegetation Index, **c** Optimized Soil Adjusted Vegetation Index, **d** Modernized Soil Adjusted Vegetation Index, **e** Allocation of Regional Gross Product per capita within ERB and regions

the application of no-till cultivation grew 100%, from 600,000 ha in 2007 to 1,300,000 ha in 2012. Currently, Kazakhstan applies no-till technology to 7% of its cultivated lands, putting the country in ninth place in the world among countries applying soil-saving technologies in agriculture. This kind of cultivation technology helps to save land cover (stubble) and can decrease the dynamics of the soil erosion process (Derpsch and Friedrich 2009). Such soil-saving technologies should consider regional ecological rehabilitation as the main measurement. This usually includes conservation agriculture, raising livestock in sheep pens, forestation, establishing forbidden areas through monitored fencing, transformation of croplands to forest and pastures, and mounting of tanks or reservoirs to contribute to the self-restoration of the environment (Zhang et al. 2015). Field experiments conducted across various areas demonstrate that no-till cultivation practices can have a positive effect on the reduction in soil erosion, decreasing rill generation, soil erosion and stream sedimentation up to five-fold (Didoné et al. 2017).

Application of rotational grazing

Pastureland requires rotational grazing of animals in order to avoid excessive grazing while ensuring the restoration of degraded land to viable agricultural land (Mirzabaev et al. 2016). A field experiment was conducted at the Birlik observation site in the Zhambyl region of Almaty by the International Center for Agricultural Research which demonstrated the possibility of using farming to apply seasonal rotational grazing and the ability to restore pastureland. The pooling of small flocks into a large mobile flock allowed the animals to travel to remote unused pastures to avoid overgrazing of the rangeland around villages. Because of the concentration of livestock near populated areas, the availability of feed is 1.5 times less in those places than at a distance of 5–10 km from the villages and also 2–2.5 times more inferior than the feed on remote land (Mirzabaev et al. 2016).

Soil erosion protection measures

One of the most effective measures for the restoration of land vulnerable to soil erosion is the grass planting, in which cereal–legumes grass mixtures are usually used. The grasses help to strengthen the topsoil cover, owing to the powerful root system located close to the soil surface and prevent its washing out. Legumes are an excellent source of nitrogen. Leguminous grass mixtures are also recommended for use in soil-protective crop rotations (Paramonov and Simonenko 2007; Petelko 2016).

Green space such as shrubs and forest belts, due to their ability to withstand soil degradation, are therefore highly environmentally stable (Paramonov and Simonenko 2007). Shrubs can prevent the growth and development of ravine because they have the ability to trap sediment and organic matter and reduce the effects of precipitation on the soil (De Baets 2009). Usually, with the right farming system, there is no need for agrotechnical methods to protect against soil erosion, with local soil erosion, it is enough to use plowing across the slope or grass planting. Also, to restore and improve soil fertility, the use of fertilizers is necessary. With further aggravation of soil erosion processes, agrotechnical and forest reclamation measures are being developed (water drainage channels, loosening, contouring, shelter belts, etc.) (Klebanovich 2016). To prevent an increase and the formation of ravines, a hydraulic network of structures is used, direct water flow followed by infiltration into the soil and ensure collection of water in the catchment area. In addition, to prevent soil leaching in ravines, it is necessary to strengthen the ravine's bottom and slopes. Such activities are very expensive and usually apply if the above measures are not effective (Lareshin 2008).

Conclusion and recommendations

A qualitative study on annual soil loss in the Esil River basin (ERB) was carried out using the RUSLE model and GIS and considering the factors of rainfall, soil, land use/land cover and topographic features. The study findings indicate that different land use patterns throughout the ERB significantly affect soil loss. For instance, natural forest cover had minimal soil losses, while areas featuring intense levels of human intervention had high rates of soil erosion [>5 (t ha^{-1})]. The findings also indicate that landscape with high slope steepness and precipitation can provoke soil erosion processes that increase the soil's susceptibility to degradation. Areas with a high ratio of soil loss were the most important in terms of taking control measures to combat soil erosion. In the ERB study area, soil erosion potential ranged from 0 to 32 (t y^{-1}) and total soil erosion losses were 565,368.7 (t y^{-1}). The extent of soil erosion in the ERB as a whole is not very high due to the extreme continental climate, which is similar to other republics such as Uzbekistan and Turkmenistan (Panagos et al. 2017). This study provides a scaled vision of soil degradation in the ERB, but for future research, it would be useful to take into account prevailing climate change trends, including their effect on future precipitation and soil erosion processes in the study area.

Recommendations:

- The potential soil erosion map will help to define plots that are most vulnerable to soil erosion.
- The scaled vision of soil erosion will allow for the formation of science-based recommendations for soil conservation and will help to develop measures based on advanced international experience (multiple-cropping, strip cropping, mulching, terracing, contour plowing and other ways of soil conservation).
- Local executive bodies and authorities should implement soil conservation recommendations in situ and according to legislation.
- To prevent soil erosion processes on slopes, conservation measures such as increased forestation and shrub planting should be considered.
- The application of GIS and RS technologies allows for soil erosion assessments to be conducted. In future research, it would be helpful to focus on particular plots which are more prone to soil erosion by applying data in higher resolution.

Acknowledgements This study was financially supported by the Chinese Academy of Science (CAS) and the World Academy of Science for the Developing World (TWAS) Presidents Fellowship program for international Ph.D. students (Awardee of 2016 CAS-TWAS Presidents fellowship), together with the Strategic Priority Research Program of the Chinese Academy of Sciences, Grant No. XDA19030204.

References

Abu Hammad A (2011) Watershed erosion risk assessment and management utilizing revised universal soil loss equation-geographic information systems in the Mediterranean environments. Water Environ J 25(2):149–162. https://doi.org/10.1111/j.1747-6593.2009.00202.x

Adediji A, Tukur A, Adepoju K (2010) Assessment of revised universal soil loss equation (RUSLE) in Katsina area, Katsina state of Nigeria using remote sensing (RS) and geographic information system (GIS). Iran J Energy Environ 1(3):255–264. https://www.researchgate.net/publication/49593936_Assessment_of_Revised_Universal_Soil_Loss_Equation_RUSLE_in_Kastina_Area_Katsina_State_of_Nigeria_using_Remote_Sensing_RS_and_Geographic_Information_System_GIS

Alkharabsheh MM, Alexandridis T, Bilas G, Misopolinos N, Silleos N (2013) Impact of land cover change on soil erosion hazard in northern Jordan using remote sensing and GIS. Proc Environ Sci 19:912–921. https://doi.org/10.1016/j.proenv.2013.06.101

Apazhev AK, Shekhikhachev YuA, Fiapshev AG (2016) Analysis of factors affecting the occurrence and development of erosion processes on sloping lands. Innovative science, (3-3 (15)). (Апажев АК, Шекихачев ЮА, и Фиапшев АГ (2016) Анализ факторов, влияющих на возникновение и развитие эрозионных процессов на склоновых землях. Инновационная наука, (3-3 (15))). https://cyberleninka.ru/article/n/analiz-faktorov-vliyayuschih-na-vozniknovenie-i-razvitie-erozionnyh-protsessov-na-sklonovyh-zemlyah

Bao Le Q, Nkonya E, Mirzabaev A (2014) Biomass productivity-based mapping of global land degradation hotspots. ZEF discussion papers on development policy, 193. https://www.econstor.eu/handle/10419/106616

Blanco H, Lal R (2010) Soil and water conservation. Principles of soil conservation and management. Springer, Berlin, p 2

Bouguerra H, Bouanani A, Khanchoul K, Derdous O, Tachi SE (2017) Mapping erosion prone areas in the Bouhamdane watershed (Algeria) using the Revised Universal Soil Loss Equation through GIS. J Water Land Dev 32(1):13–23. https://doi.org/10.1515/jwld-2017-0002

Chen T, Niu RQ, Li PX, Zhang LP, Du B (2011) Regional soil erosion risk mapping using RUSLE, GIS, and remote sensing: a case study in Miyun Watershed, North China. Environ Earth Sci 63(3):533–541. https://doi.org/10.1007/s12665-010-0715-z

Derpsch R, Friedrich T (2009) Development and current status of no-till adoption in the world. In: Paper presented at the proceedings on CD, 18th triennial conference of the international soil tillage research organization (ISTRO), Izmir, Turkey, June 15–19, 2009, http://citeseerx.ist.psu.edu/viewdoc/download?doi=10.1.1.560.4625&rep=rep1&type=pdf

Didoné EJ, Minella JPG, Evrard O (2017) Measuring and modelling soil erosion and sediment yields in a large cultivated catchment under no-till of Southern Brazil. Soil Tillage Res 174:24–33. https://doi.org/10.1016/j.still.2017.05.011

Farhan Y, Zregat D, Farhan I (2013) Spatial estimation of soil erosion risk using RUSLE approach, RS, and GIS techniques: a case study of Kufranja Watershed, Northern Jordan. J Water Resour Prot 5(12):1247–1261. https://doi.org/10.4236/jwarp.2013.512134

Food and Agricultural Organization of the United Nations (FAO) (2015) Status of the world's soil resources report. FAO, Rome

Foster GR, Yoder DC, Weesies GA, McCool DK, McGregor KC, Bingner RL (2003) Revised universal soil loss equation version 2. User's reference guide, USDA-ARS, Washington, DC, USA

Ganasri BP, Ramesh H (2016) Assessment of soil erosion by RUSLE model using remote sensing and GIS—a case study of Nethrevathi Basin. Geosci Front 7(2016):953–961. https://doi.org/10.1016/j.gsf.2015.10.007

Gupta R, Kienzler K, Martius C, Mirzabaev A, Oweis T, De Pauw E, Thomas R (2009) Research prospectus: a vision for sustainable land management research in Central Asia. ICARDA Central Asia and Caucasus program. Sustainable agriculture in Central Asia and the Caucasus series, 1, 84. https://www.researchgate.net/publication/235792167/download

Issaka S, Ashraf MA (2017) Impact of soil erosion and degradation on water quality: a review. Geol Ecol Landsc 1(1):1–11. https://doi.org/10.1080/24749508.2017.1301053

Jiang B, Bamutaze Y, Pilesjö P (2014) Climate change and land degradation in Africa: a case study in the Mount Elgon region, Uganda. Geo-Spat Inf Sci 17(1):39–53. https://doi.org/10.1080/10095020.2014.889271

Jones A, Panagos P, Barcelo S, Bouraoui F, Bosco C, Dewitte O, Hiederer R (2012) The state of soil in Europe—a contribution of the JRC to the EEA Environment State and Outlook Report—SOER 2010. Publications Office of the European Union, Luxembourg, 76. https://doi.org/10.2788/77361

Kalb TJ, Mavlyanova RF (2005) Vegetable production in Central Asia: status and perspectives (vol 5, no 618). AVRDC-World Vegetable Center

Karentaev EA, Bimentin GA, Uzbaev MB, Kazhenov MA, Karzhanova JK, Bekmukashev KA, Aidarbekov TN, Seitova AS, Satybaldina LS, Zhinibekuly E, Abdili ME, Amreeva AM, Krykpaev AD (2018) Consolidated analytical report on the state and use of the lands of the Republic of Kazakhstan for

2017. Ministry of Agriculture of the Republic of Kazakhstan, Land Management Committee. Astana (Карентаев, ЕА, Бимендина МБ, Узбаев МА, Каженов ЖК, Каржанова КА, Бекмукашев ТН, Айдарбеков АС, Сеитова ГА, Сатыбалдина ЛС, Жәнібекұлы Е, Әбдіғали МЕ, Амреева АМ, Крыкпаева АД (2018) Сводный аналитический отчет о состоянии и использовании земель Республики Казахстан за 2017 год. Министерство сельского хозяйства РК, Комитет по управлению земельными ресурсами. Астана. http://mgov.kz/wp-content/uploads/2018/avgust/25.08/kuzrotchet.pdf)

Kienzler KM, Lamers J, McDonald A, Mirzabaev A, Ibragimov N, Egamberdiev O, Ruzibaev E, Akramkhanov A (2012) Conservation agriculture in Central Asia—what do we know and where do we go from here? Field Crops Res 132:95–105. https://doi.org/10.1016/j.fcr.2011.12.008

Klebanovich NV, Efimova IA, Prokopovich SN (2016) Soils and land resources of Kazakhstan: studies. materials for special students 1-56 02 02 “Geoinformation systems”, p 46 (Клебанович, Н.В, Ефимова ИА, Прокопович СН (2016) Почвы и земельные ресурсы Казахстана: учеб. материалы для студентов спец. 1-56 02 02 « Геоинформационные системы » . Стр 46)

Koshim A, Karatayev M, Clarke ML, Nock W (2018) Spatial assessment of the distribution and potential of bioenergy resources in Kazakhstan. Adv Geosci 45:217–225. https://doi.org/10.5194/adgeo-45-217-2018

Kruseman G, Bade J (1998) Agrarian policies for sustainable land use: bioeconomic modelling to assess the effectiveness of policy instruments. Agric Syst 58(3):465–481. https://doi.org/10.1016/S0308-521X(98)00041-9

Lezin VA (1999) Rivers of the Tyumen region (southern regions). Reference manual. Tyumen: Vector Book Publishing House, 196. (Лёзин ВА (1999) Реки Тюменской области (южные районы). Справочное пособие. Тюмень: Издательство Вектор Бук, стр 196)

Liang L, Wenpeng D, Huimin Y, Lin Z, Yu D (2017) Spatio-temporal Patterns of Vegetation Change in Kazakhstan from 1982 to 2015. J Resour Ecol 8(4):378–384. https://doi.org/10.5814/j.issn.1674-764x.2017.04.009

Litvin LF (2002) Geography of soil erosion on agricultural lands of Russia. IKC Akademkniga, Moscow, 255. Литвин ЛФ (2002) География эрозии почв сельскохозяйственных земель России. АкадемКнига, Москва, стр 255

Mirzabaev A (2013) Climate volatility and change in Central Asia: economic impacts and adaptation. Doctoral thesis at Agricultural Faculty, University of Bonn. urn:nbn:de:hbz:5n-3238

Mirzabaev A, Ahmed M, Werner J, Pender J, Louhaichi M (2016) Rangelands of Central Asia: challenges and opportunities. J Arid Land 8(1):93–108. https://doi.org/10.1007/s40333-015-0057-5

Mirzabaev A, Strokov A, Krasilnikov P (2018) The impact of land degradation on agricultural profits and poverty in Central Asia. In: 30th international conference of agricultural economists, Vancouver, July 28–August 2, 2018

Morgan RPC (2009) Soil erosion and conservation. Wiley, New York

Mueller L, Saparov A, Lischeid G (2013) Novel measurement and assessment tools for monitoring and management of land and water resources in agricultural landscapes of Central Asia. Springer, Berin. https://doi.org/10.1007/978-3-319-01017-5

Nkonya E, Mirzabaev A, Von Braun J (eds) (2016) Economics of land degradation and improvement: a global assessment for sustainable development. Springer, Berlin p, p 695. https://doi.org/10.1007/978-3-319-19168-3

Pagiola S (1996) Price policy and returns to soil conservation in semi-arid Kenya. Environ Resour Econ 8:255–271

Panagos P, Borrelli P, Meusburger K (2015) A new European slope length and steepness factor (LS-Factor) for modeling soil erosion by water. Geosciences 5(2):117–126. https://doi.org/10.3390/geosciences5020117

Panagos P, Borrelli P, Meusburger K, Yu B, Klik A, Lim KJ et al (2017) Global rainfall erosivity assessment based on high-temporal resolution rainfall records. Sci Rep 7(1):4175. https://doi.org/10.1038/s41598-017-04282-8

Pashkov SV, Tayzhanova MM (2016) Gully erosion determinants in northern Kazakhstan. News of Tula State University. Earth Sciences, (4), pp 50–63. Пашков СВ и Тайжанова ММ (2016) Детерминанты овражной эрозии в Северном Казахстане. Известия Тульского государственного университета. Науки о земле, (4), p 50–63

Pender J, Mirzabaev A, Kato E (2009) Economic analysis of sustainable land management options in Central Asia. Final report for the ADB. IFPRI/ICARDA, 168

Plekhanov PA (2017) Natural hydrological risks and their prevention in Kazakhstan. Cent Asian J Water Res (CAJWR) 3(1):2084

Prasannakumar V, Shiny R, Geetha N, Vijith H (2011) Spatial prediction of soil erosion risk by remote sensing, GIS and RUSLE approach: a case study of Siruvani river watershed in Attapady valley, Kerala, India. Environ Earth Sci 64(4):965–972. https://doi.org/10.1007/s12665-011-0913-3

Prasuhn V, Liniger H, Gisler S, Herweg K, Candinas A, Clément JP (2013) A high-resolution soil erosion risk map of Switzerland as strategic policy support system. Land Use Policy 32:281–291. https://doi.org/10.1016/j.landusepol.2012.11.006

Renard KG, Freimund JR (1994) Using monthly precipitation data to estimate the R-factor in the revised USLE. J Hydrol 157(1–4):287–306. https://doi.org/10.1016/0022-1694(94)90110-4

Renard KG, Foster GR, Weesies GA, McCool DK, Yoder DC (1997) Predicting soil erosion by water: a guide to conservation planning with the Revised Universal Soil Loss Equation (RUSLE) (vol 703). Washington, DC: United States Department of Agriculture. https://naldc.nal.usda.gov/download/CAT10827029/PDF

Rouse J Jr, Haas RH, Schell JA, Deering DW (1974) Monitoring vegetation systems in the Great Plains with ERTS. NASA Spec Publ 351:309

Shabani F, Kumar L, Esmaeili A (2014) Improvement to the prediction of the USLE K factor. Geomorphology 204:229–234. https://doi.org/10.1016/j.geomorph.2013.08.008

Shepelev MA (2014) Water and wind erosion and control measures. Kostanay: A. Baytursynov Kostanay State University. (Шепелев МА (2014) Водная и ветровая эрозия и меры борьбы с ними. г. Костанай: Костанайский Государственный Университет им. А. Байтурсынова). https://docs4all.com/2701659/

Skladchikova GN (1977) Resources of the surface waters of the USSR, the main hydrological characteristics (for 1963–1970. And the entire observation period). Volume 15. Altai, Western Siberia and Northern Kazakhstan. Issue 2. Upper Irtysh, Upper Ishim, Upper Tobol. Gidrometizdat, Leningrad. (Складчикова ГН (1977) Ресурсы поверхностных вод СССР, основные гидрологические характеристики (за 1963-1970 г.г. и весь период наблюдений). Том 15. Алтай, Западная Сибирь и Северный Казахстан. Выпуск 2. Верхний Иртыш, Верхний Ишим, Верхний Тобол. Гидрометиздат, Ленинград)

Smailov AA (2013) Kazakhstan in the figures. Astana: Agency of the Republic of Kazakhstan on Statistics. (Смаилов АА (2013) Казахстан в цифрах. Астана: Агентство Республики Казахстан по статистике). http://stat.ivisa.com/publishing/20131/%D0%9A%D0%B0%D0%B7.%20%D0%B2%20%D1%86%D0%B8%D1%84%D1%80%D0%B0%D1%85_%D1%80%D1%83%D1%81.pdf

Takata Y, Funakawa S, Akshalov K, Ishida N, Kosaki T (2007) Spatial prediction of soil organic matter in northern Kazakhstan based on topographic and vegetation information. Soil Sci Plant Nutr 53(3):289–299. https://doi.org/10.1111/j.1747-0765.2007.00142.x

Vaezi A, Sadeghi H (2011) Evaluating the RUSLE [Revised Universal Soil Loss Equation] model and developing an empirical equation for estimating soil erosion ability factor in a semi-arid region. Span J Agric Res 9(3):912–923

Van der Knijff J, Jones R, Montanarella L (2000) Soil erosion risk assessment in Europe. European Soil Bureau, European Commission Belgium. https://www.researchgate.net/publication/237727657/download

Williams JR, Singh V (1995) Computer models of watershed hydrology. chap. The EPIC Model, Water Resources Publications, Highlands Ranch, CO, pp 909–1000

Wischmeier WH (1976) Use and misuse of the universal soil loss equation. J Soil Water Conserv 31:5–9

Wischmeier WH, Smith DD (1965) Predicting rainfall erosion losses from cropland east of the Rocky Mountains: guide for selection of practices for soil and water conservation. U. S. Department of Agriculture. Agriculture Handbook. No. 282, p 58

Wischmeier WH, Smith DD (1978) Predicting rainfall erosion losses: A guide to conservation planning. U.S. Department of Agriculture. Agriculture Handbook No. 537

Wischmeier WH, Smith DD (1981) Predicting rainfall erosion losses: A guide to conservation planning. Supplement to Agriculture Handbook No. 537, USDA, Washington

Yapiyev V, Sagintayev Z, Verhoef A, Kassymbekova A, Baigaliyeva M, Zhumabayev D, Jumassultanova S (2017) The changing water cycle: Burabay National Nature Park, Northern Kazakhstan. Wiley Interdisciplinary Reviews: Water 4(5):e1227

Zaslavsky MN (1983) Erosiology. Moscow: High school, p 320. (Заславский МН (1983) Эрозиоведение. Москва: Высшая школа, стр 320). https://www.twirpx.com/file/1705401/

Zhang W, Zhou J, Feng G, Weindorf DC, Hu G, Sheng J (2015) Characteristics of water erosion and conservation practice in arid regions of Central Asia: Xinjiang Province, China as an example. Int Soil Water Conserv Res 3(2):97–111. https://doi.org/10.1016/j.iswcr.2015.06.002

Zomer RJ, Neufeldt H, Xu J, Ahrends A, Bossio D, Trabucco A, Wang M (2016) Global tree cover and biomass carbon on agricultural land: the contribution of agroforestry to global and national carbon budgets. Sci Rep 6:29987. https://doi.org/10.1038/srep29987

Acta Geophysica (2019) 67:939–942
https://doi.org/10.1007/s11600-019-00308-z

PREFACE - SPECIAL ISSUE

Solute transport in complex natural flows

Monika B. Kalinowska[1] · **Kaisa Västilä**[2] · **Paweł M. Rowiński**[1]

The most innovative hydraulic research flows from the needs of applications in diverse, very often complex settings. The aim of this preface is to provide a brief overview on mass transport in complex natural flows, highlighting relevant but often neglected considerations, advances presented in the articles of this Special Issue, and ways forward. Understanding and prediction of how dissolved nutrients and other solutes, suspended sediment and other particulate matter, and thermal pollution are propagated and mixed in natural channels are important for designing effective management and mitigation strategies concerning these scalars.

Complexity stressed in the title of this Special Issue is in fact a philosophical notion, typically not sufficiently well defined. *Complex* or *complexit*y is a keyword very often used in environmental hydraulics, in most cases intuitively, sometimes as synonyms of the adjective *complicated*. At the same time, *complexity* has strong scientific connotation and is treated almost as a separate research domain. In contrast to many other scientific disciplines, in environmental hydraulics, it is not well established when the subject of our investigation can be described as complex.

In principle scientists face the double, incredibly intricate problem of unraveling the cause and effect relationships between various phenomena and processes on one hand, and developing mathematical descriptions of the extraordinarily complicated reality on the other (Rowiński and Dębski 2011). Quoting (Heylighen et al. 2007), complexity science emerged in the 1980s, having the following roots:

- "nonlinear dynamics and statistical mechanics—two offshoots from Newtonian mechanics—which noted that the modeling of more complex systems required new mathematical tools that can deal with randomness and chaos;
- computer science, which allowed the simulation of systems too large or too complex to be modeled mathematically;
- biological evolution, which explains the appearances of complex forms through the intrinsically unpredictable mechanism of blind variation and natural selection;
- the application of these methods to describe social systems in the broad sense, such as stock markets, the Internet or insect societies, where there is no predefined order, although there are emergent structures."

According to Standish (2008), the term *complexity* has two distinct usages, which may be categorized as either a quality or a quantity. It is often stated that complex systems are a particular class of systems that are difficult to study using traditional analytical techniques. Standish (2008) mentions that biological organisms and ecosystems are complex, yet systems like a pendulum or a lever are simple. Complexity as a quality is therefore what makes the systems complex. Complexity maybe also treated as a quantity—with "statements like a human being being more complex than a nematode worm, for example."

Let us pay the attention of the Reader to a popular book of Johnson (2001) that explains complexity through the notion of emergence. From his fascinating story, one may read that complexity is generally used to characterize something with many parts that interact with each other in multiple ways, culminating in a higher order of emergence than the sum of its parts. In this context, emergence refers to the ability of low-level components of a system or community to self-organize into a higher-level system of sophistication. In other words, emergence occurs when an entity is observed to have properties, its parts do not have on their own. Quoting the description of the series of *Understanding Complex Systems* (Springer): "Such systems are complex in both their composition—typically many different kinds of components

---

✉ Monika B. Kalinowska
Monika.Kalinowska@igf.edu.pl

Kaisa Västilä
kaisa.vastila@aalto.fi

Paweł M. Rowiński
p.rowinski@igf.edu.pl

[1] Institute of Geophysics Polish Academy of Sciences, Warsaw, Poland

[2] Department of Built Environment, Aalto University School of Engineering, Espoo, Finland

interacting simultaneously and nonlinearly with each other and their environments on multiple levels—and in the rich diversity of behavior of which they are capable."

Whichever definition we consider, the papers presented in this Special Issue fall under the category of describing complex systems, i.e., complex open channel transport processes in the present context. The transport of constituents by advection, dispersion, and other processes in streams, rivers, and other channels is dependent on hydrological and hydrodynamic characteristics of the channel which in turn depend on the geometry and morphometry of the reach. Complexity in the physical settings may be related, e.g., to cross-sectional geometries and associated flow distributions that cannot be easily reduced into single characteristic scales, composite roughness, and multiple physical scales that interact with each other. One of the most important factors causing complexity in these categories is vegetation (e.g., Rowiński et al. 2018). The contributions in this issue address different aspects of solute transport in complex natural flows, bridging fundamental research to practical challenges in watercourses. The articles are based on selected talks presented during Special Session FM.2 entitled "Heat and mass transport under complex natural conditions" at the 5th IAHR Europe Congress that took place on 13–15 June, 2018, in Trento, Italy.

Mass transport processes of solutes can be experimentally investigated based on tests performed with soluble tracers. The most common mathematical descriptions of the processes are the one-dimensional advection–dispersion model, and the transient storage model that allows for the reconstruction of the abrupt leading edges and the long upper tails in the distributions of solute concentrations in flows including vegetation or other transient storage zones (e.g., Rowiński et al. 2008). The associated equations are typically solved using various numerical methods, which forms a distinct source of uncertainty for the parameter estimation, e.g., through numerical diffusion and dispersion (e.g., Kalinowska & Rowiński 2007). In this issue, Silavwe et al. (2019) address the reliable estimation of the parameters of the advection–dispersion model by comparing the performance of selected numerical schemes under different transport regimes. Wallis & Manson (2019) describe the sensitivity of the transient storage model parameters on the spatial and temporal resolution of the numerical solution.

In cases when tracer tests are not available, the reliable estimation of the parameters becomes extremely difficult and can be a source of large uncertainty. Dispersion coefficients are usually related to known hydraulic parameters, such as average depth, width and velocity, shear velocity, and channel sinuosity. The derived formulae are of rather limited universality, and thus, more attention should be placed on documenting their ranges of applicability and the methods used in identifying the parameters. Determining some of the basic hydraulic variables in complex natural situations constitutes a problem per se (e.g., Mrokowska and Rowiński 2017).

The complexity increases when moving from 1D to 2D or 3D approaches. For the case of depth-averaged 2D mass transport associated with incomplete lateral mixing, the dispersion tensor represents an additional significant transport mechanism, which is not a physical process, but a consequence of depth-averaging of the equation (Kalinowska & Rowiński 2012). It deserves to be stressed that the longitudinal dispersion coefficient of the 2D equation is not the same as that of the 1D equation. Despite this, 1D dispersion coefficients are often adopted to 2D models, unconsciously of the difference or since values for the 2D approach are not available. In the context of complex open channel flows, further work on parameterizing 2D transport processes is warranted.

Mass transport is particularly complicated to describe in vegetated flows since vegetation is known to control the flow and mixing at multiple scales ranging from the leaf to plant, plant stand, patch, patch mosaic, and reach scales (e.g., Marion et al. 2014). Vegetation causes strong mixing between the vegetated and non-vegetated regions, affects turbulence intensity and diffusion and often significantly alters the channel geometry (e.g., Curran & Hession 2013). Despite the fact that the rate of mass transport may notably deviate from the rate of momentum transport in vegetated settings (Ghisalberti & Nepf 2005), experiments on the influence of vegetation on dispersion coefficients and parameters of the transient storage model are limited. In this issue, Sonnenwald (2019) proposes a model to predict the longitudinal dispersion coefficient in vegetated regions based on stem spacing. Such models based on easily measurable, physically based variables are useful tools for the practitioners.

A reliable estimation of the mean and turbulent flow distribution is a prerequisite for mass transport predictions, but significant uncertainty is still present in modeling vegetation hydrodynamics. Herein, the suitable parameterization of the vegetative drag and flow resistance is a key factor (e.g., Västilä & Järvelä 2018). In their contribution, D'Ippolito et al. (2019) present an extensive dataset to investigate how the vegetative drag coefficient of rigid cylinders depends on their solid volume fraction and on flow forcing. The studies with simple plant morphology form the basis for devising investigations on flexible natural plants having multiple length scales and more complicated structures.

Because of its distinct hydrodynamic behavior, natural vegetation commonly exhibits higher complexity than simplified rigid surrogates. This is foremost associated with the strong dependency of the flow-vegetation interactions on the hydrodynamic forcing mainly through the flexibility-induced reconfiguration (e.g., Vogel 1994). Mechanisms such as bending of the stems, changes in the posture and orientation of the leaves and branches, and dynamic motions at different scales are typically observed for natural vegetation. For instance, the periodical waving of flexible plant stands significantly alters the turbulent momentum transfer between submerged aquatic vegetation and the overflow (e.g., Ghisalberti & Nepf 2006) and has been recently reported to occur at the lateral interfaces between unvegetated regions and foliated shrub-like vegetation (Caroppi et al. 2019). In this issue, Termini (2019) investigates turbulent mixing and dispersion mechanisms in flows with submerged natural herbaceous vegetation. In a highly complex setting, Przyborowski et al. (2019) explore how highly flexible plant patches of naturally occurring structure influence the turbulent flow structure in a river with movable bed. Verification of results from controlled laboratory environments in the yet more complex natural settings is required to enable up-scaling the findings for solving real-life engineering challenges.

The six papers of this issue advance our understanding, but reaching a wide-ranging impact calls for researchers to increasingly engage in science-based advising of the engineering and management of our streams and rivers. A vast challenge lies in developing robust, straightforward-to-use tools with reasonable accuracy and acceptable level of uncertainty to allow application to practical engineering. This requires new experimental data from carefully designed, executed and reported experiments, including a description of how they represent the complex physical reality. Based on the data, modeling can be further developed for different scales and purposes. Finally, coupling understanding of mass transport to the physical, chemical, and biological processes of the investigated scalar may aid in tackling water quality issues ranging from the management of riverine nutrient loads through specific nature-based channel designs (e.g., Västilä et al. 2016; Rowiński et al. 2018) to the prediction of the spreading of industrial pollutants, such as heat (e.g., Kalinowska 2019).

Acknowledgements This work has been supported within statutory activities No 3841/E-41/S/2018 of the Ministry of Science and Higher Education of Poland, the Project No 201800045 of Maj and Tor Nessling Foundation, and Project No 33271 of Maa- ja vesitekniikan tuki ry.

Compliance with ethical standards

Conflict of interest The authors declare that they have no conflict of interest.

References

Caroppi G, Västilä K, Järvelä J, Rowiński PM, Giugni M (2019) Turbulence at water-vegetation interface in open channel flow: experiments with natural-like plants. Adv Water Res 127:180–191. https://doi.org/10.1016/j.advwatres.2019.03.013

Curran JC, Hession WC (2013) Vegetative impacts on hydraulics and sediment processes across the fluvial system. J Hydrol 505:364–376. https://doi.org/10.1016/j.jhydrol.2013.10.013

D'Ippolito A, Lauria A, Alfonsi G et al (2019) Investigation of flow resistance exerted by rigid emergent vegetation in open channel. Acta Geophys. https://doi.org/10.1007/s11600-019-00280-8

Ghisalberti M, Nepf HM (2005) Mass transport in vegetated shear flows. Environ Fluid Mech 5:527–551. https://doi.org/10.1007/s10652-005-0419-1

Ghisalberti M, Nepf HM (2006) The structure of the shear layer in flows over rigid and flexible canopies. Environ Fluid Mech 6:277–301. https://doi.org/10.1007/s10652-006-0002-4

Heylighen F, Cilliers P, Gershenson C (2007) Complexity and Philosophy. In: Bogg J, Geyer R (eds) Complexity, science and society. Radcliffe Publishing, Oxford, pp 117–138

Johnson S (2001) Emergence: the connected lives of ants, brains, cities. Scribner, New York

Kalinowska MB (2019) Effect of water–air heat transfer on the spread of thermal pollution in rivers. Acta Geophys 67:597–619. https://doi.org/10.1007/s11600-019-00252-y

Kalinowska MB, Rowiński PM (2007) Truncation errors of selected finite difference methods for two-dimensional advection–diffusion equation with mixed derivatives. Acta Geophys 55:104–118. https://doi.org/10.2478/s11600-006-0046-3

Kalinowska MB, Rowiński PM (2012) Uncertainty in computations of the spread of warm water in a river—lessons from environmental impact assessment case study. Hydrol Earth Syst Sci 16:4177–4190. https://doi.org/10.5194/hess-16-4177-2012

Marion A, Nikora V, Puijalon S, Bouma T, Koll K, Ballio F, Tait S, Zaramella M, Sukhodolov A, O'Hare M, Wharton G, Aberle J, Tregnaghi M, Davies P, Nepf H, Parker G, Statzner B (2014) Aquatic interfaces: a hydrodynamic and ecological perspective. J Hydraul Res 52:744–758. https://doi.org/10.1080/00221686.2014.968887

Mrokowska MM, Rowiński PM (2017) Bed shear stresses and bed shear velocities – ubiquitous variables in river hydraulics. In: Radecki-Pawlik A, Hradecky J, Pagliara S, Hendrickson E (eds) Open channel hydraulics, river hydraulics structures and fluvial geomorphology: for engineers, geomorphologists and physical geographers, 1st edn. CRC Press, Boca Raton, pp 180–195

Przyborowski Ł, Łoboda AM, Bialik RJ (2019) Effect of two distinct patches of *Myriophyllum* species on downstream turbulence in a natural river. Acta Geophys. https://doi.org/10.1007/s11600-019-00292-4

Rowiński PM, Dębski W (2011) Mathematical modeling of inanimate natural phenomena. The living earth, ACADEMIA, The magazine of the Polish Academy of Sciences. Complexity 29(1):4–7

Rowiński PM, Guymer I, Kwiatkowski K (2008) Response to the slug injection of a tracer—large scale experiment in a natural river. Hydrol Sci J 53:1300–1309. https://doi.org/10.1623/hysj.53.6.1300

Rowiński PM, Västilä K, Aberle J, Järvelä J, Kalinowska MB (2018) How vegetation can aid in coping with river management challenges: a brief review. Ecohydrol Hydrobiol 18:345–354. https://doi.org/10.1016/j.ecohyd.2018.07.003

Silavwe DD, Brink IC, Wallis SG (2019) Assessment of some numerical methods for estimating the parameters of the one-dimensional advection–dispersion model. Acta Geophys. https://doi.org/10.1007/s11600-019-00293-3

Sonnenwald F, Stovin V, Guymer I (2018) A stem spacing-based non-dimensional model for predicting longitudinal dispersion in low-density emergent vegetation. Acta Geophys. https://doi.org/10.1007/s11600-018-0217-z

Standish R (2008) Concept and definition of complexity. In: Ang Yang A, Shan Y (eds) Intelligent complex adaptive systems. IGI Global, Hershey, pp 105–124. https://doi.org/10.4018/978-1-59904-717-1.ch004

Termini D (2019) Turbulent mixing and dispersion mechanisms over flexible and dense vegetation. Acta Geophys. https://doi.org/10.1007/s11600-019-00272-8

Västilä K, Järvelä J (2018) Characterizing natural riparian vegetation for modeling of flow and suspended sediment transport. J Soils Sediments 18:3114–3130. https://doi.org/10.1007/s11368-017-1848-4

Västilä K, Järvelä J, Koivusalo H (2016) Flow–vegetation–sediment interaction in a cohesive compound channel. J Hydraul Eng 142:04015034. https://doi.org/10.1061/(ASCE)HY.1943-7900.0001058

Vogel S (1994) Life in moving fluids—the physical biology of flow, 2nd edn. Princeton University Press, Princeton

Wallis S, Manson R (2019) Sensitivity of optimized transient storage model parameters to spatial and temporal resolution. Acta Geophys. https://doi.org/10.1007/s11600-019-00253-x

Acta Geophysica (2019) 67:943–949
https://doi.org/10.1007/s11600-018-0217-z

RESEARCH ARTICLE - SPECIAL ISSUE

A stem spacing-based non-dimensional model for predicting longitudinal dispersion in low-density emergent vegetation

F. Sonnenwald[1] · **V. Stovin**[1] · **I. Guymer**[1]

Received: 12 September 2018 / Accepted: 24 October 2018 / Published online: 1 November 2018

Abstract

Predicting how pollutants disperse in vegetation is necessary to protect natural watercourses. This can be done using the one-dimensional advection dispersion equation, which requires estimates of longitudinal dispersion coefficients in vegetation. Dye tracing was used to obtain longitudinal dispersion coefficients in emergent artificial vegetation of different densities and stem diameters. Based on these results, a simple non-dimensional model, depending on velocity and stem spacing, was developed to predict the longitudinal dispersion coefficient in uniform emergent vegetation at low densities (solid volume fractions <0.1). Predictions of the longitudinal dispersion coefficient from this simple model were compared with predictions from a more complex expression for a range of experimental data, including real vegetation. The simple model was found to predict correct order of magnitude dispersion coefficients and to perform as well as the more complex expression. The simple model requires fewer parameters and provides a robust engineering approximation.

Keywords Stem spacing · Longitudinal dispersion · Solute transport · 1D modelling · Vegetated flows · Cylinder arrays

Introduction

The fate of pollutants in stormwater is of interest to protect natural watercourses. To predict how pollutants will disperse in these systems, one-dimensional (1D) modelling based on the advection–dispersion equation (ADE) is commonly used (DHI 2009). The 1D ADE is typically given as:

$$\frac{\partial C}{\partial t} + U\frac{\partial C}{\partial x} = D_x\left(\frac{\partial^2 C}{\partial x^2}\right) \tag{1}$$

where C is cross-sectional mean concentration, t is time, U is mean longitudinal velocity, x is the longitudinal coordinate, and D_x is the longitudinal dispersion coefficient (Fischer et al. 1979). U and D_x are required to use the equation predictively.

Natural watercourses often contain vegetation (O'Hare 2015). Furthermore, prior to entering natural watercourses, stormwater is often treated within vegetated sustainable drainage systems (SuDS) to reduce the quantity of pollutants in surface runoff (Woods-Ballard et al. 2015). Applying the 1D ADE to predict pollutant transport therefore requires estimates of longitudinal dispersion coefficient (D_x) within vegetation. While velocities can be estimated from simple hydraulics or numerical models, reliable estimation of the longitudinal dispersion coefficient based on vegetation characteristics is often problematic (Sonnenwald et al. 2017). This paper investigates the prediction of the longitudinal dispersion coefficient in uniform emergent vegetation at low densities. It presents results from new laboratory measurements of longitudinal dispersion and compares new and existing predictors of longitudinal dispersion coefficient to measured values.

Predicting D_x in vegetation

Vegetation can be characterised by stem diameter d, solid volume fraction ϕ, frontal facing area a (the vegetation area perpendicular to the direction of flow per unit volume), and mean stem edge-to-edge spacing s. Assuming vegetation may be represented as an array of vertical cylinders, these parameters are related by $\phi = ad\pi 4^{-1}$. Tanino and Nepf (2008) provided:

✉ F. Sonnenwald
f.sonnenwald@sheffield.ac.uk

[1] Department of Civil and Structural Engineering, University of Sheffield, Sheffield, UK

$$s \approx d\sqrt{\frac{1+2\phi}{4\phi} - \sqrt{\pi}\sqrt{\frac{1-2\phi}{4\phi}}\frac{\left[1-\mathrm{erf}\left(\sqrt{4\phi/1-2\phi}\right)\right]}{\exp\left(-4\phi/(1-2\phi)\right)} - 1} \tag{2}$$

to estimate s based on stem diameter and solid volume fraction for a random array of cylinders. As there are multiple stem spacing values for a given vegetation configuration, stem spacing may also be characterised by s_{50}, the median stem spacing. While $s \approx s_{50}$ when vegetation stem spacing is uniformly or normally distributed, this is not the case when the distribution of stem spacing is asymmetric (e.g. many small stems but few large ones).

Tanino (2012), in a review of mixing in vegetation, suggested that there are primarily three mixing mechanisms contributing to longitudinal dispersion within emergent vegetation: turbulent diffusion; secondary wake dispersion; and vortex trapping. Turbulent diffusion within vegetation is the result of instantaneous velocity fluctuations caused by eddies generated by stems. Secondary wake dispersion is caused by velocity-field heterogeneity resulting in different travel times for particles (differential advection). Vortex trapping is caused by the temporary entrainment of particles in vortices behind stems.

Of these three processes, only secondary wake dispersion contributes significantly to longitudinal dispersion at low densities ($\phi < 0.1$). Turbulent diffusion is the primary transverse mixing mechanism at low densities (Tanino and Nepf 2008). However, as total transverse dispersion is typically an order of magnitude lower than total longitudinal dispersion (Sonnenwald et al. 2017), it does not make a significant contribution to longitudinal dispersion. Similarly, dispersion due to vortex trapping is typically much lower than secondary wake dispersion at low densities (White and Nepf 2003). Therefore, secondary wake dispersion should provide a reasonable approximation of total longitudinal dispersion within vegetation at low densities.

White and Nepf (2003) explained that secondary wake dispersion is the sum of two processes: a wake contribution and a gap contribution. The former is caused by reductions in velocity behind stems and the latter caused by increases in velocity between stems. For low densities, the gap contribution is much lower than the wake contribution, and hence, White and Nepf (2003) suggested that longitudinal dispersion in vegetation may be estimated utilising:

$$D_x = 2\sigma_u^{*2} s^* \sqrt{\frac{Sc_t}{Sc_t + 1}} Ud \tag{3}$$

where ${\sigma_u}^{*2}$ is the variance of the longitudinal velocity field normalised by mean longitudinal velocity squared, $s^* = (s + d)d^{-1}$, and Sc_t is the turbulent Schmidt number. The variance term represents the level of velocity perturbation caused by stems throughout the velocity field. These parameters can be non-trivial to estimate for a specific vegetation, and so Lightbody and Nepf (2006) combined several parameter estimates and presented:

$$D_x = \frac{1}{2} C_D^{3/2} Ud \tag{4}$$

where C_D is the drag coefficient.

Calculating C_D in vegetation depends either on having very precise measurements of the energy gradient or on having a direct force sensor (Tinoco and Cowen 2013). Both methods are difficult to apply in practice, and as such, it is often preferable to use an estimate of C_D, e.g. $C_D = 1$. C_D may also be estimated based on the Ergun (1952) expression for pressure drop in a packed column as:

$$C_D = 2\left(\frac{6475d + 32}{Re_d} + 17d + 3.2\phi + 0.5\right) \tag{5}$$

where $Re_d = Ud\nu^{-1}$ is stem Reynolds number and ν is kinematic viscosity (Sonnenwald et al. 2018b).

Comparison of Eq. (4) to experimental data suggested that it provides correct order of magnitude predictions of the longitudinal dispersion coefficient in vegetation when using values of C_D estimated with Eq. (5) (Sonnenwald et al. 2018a). However, Eq. (4) depends on several simplifying assumptions for values of ${\sigma_u}^{*2}$ and Sc_t and is insensitive to C_D. A simplified model has previously been developed by Nepf (2012) for predicting the transverse dispersion coefficient in emergent vegetation based on velocity and stem diameter. This paper aims to explore whether a similar approach could be adopted for predicting the longitudinal dispersion coefficient in emergent vegetation.

Previous studies

Several previous experimental studies have investigated the longitudinal dispersion coefficient in emergent vegetation at low density; these studies are summarised in Table 1. The majority of these studies investigated dispersion in real vegetation. As the natural variability of real vegetation does not lend itself to generalisation, additional experiments investigating longitudinal dispersion in artificial emergent vegetation have been carried out by the authors, as described below.

Methodology

A 15-m long, 300-mm-wide recirculating Armfield flume was fitted with uniform artificial emergent vegetation, and dye tracing was conducted. Uniform flow was established

Table 1 Previous studies investigating longitudinal dispersion in uniform emergent vegetation

Description	d (mm)	ϕ	s (mm)[a]	U (mm s^{-1})	References
Mixed real species	1–10	0.002–0.022	7–26	14–38	Huang et al. (2008)
Artificial random	6	0.010–0.055	8–25	29–74	Nepf et al. (1997)
Carex	10–55	0.002–0.059	70–104	99–232	Shucksmith et al. (2010)
Phragmites australis	3	0.002	28–30	171–242	Shucksmith et al. (2010)
Regular periodic	4	0.005	51.9[b]	7–50	Sonnenwald et al. (2016)
Typha latifolia	10–19	0.013–0.047	29–36	9–29	Sonnenwald et al. (2017)
Artificial random	6	0.010–0.064	7–25	12–97	White and Nepf (2003)

[a] Estimated using Eq. (2)

[b] Known, not estimated, value

at velocities of 7–122 mm s^{-1} by adjusting flume slope and tailgate, and confirmed using point gauges along the length of the flume. Flow depth was set at 150 mm. A diffuser plate was placed directly after the inlet to straighten the flow.

Three cylinder array configurations representing vegetation were examined. These were a regular periodic configuration, a pseudo-random configuration, and a random configuration. The artificial vegetation was constructed by inserting 4-mm-diameter drinking straws or 8-mm-diameter plastic dowels into plastic base plates laid into the bottom of the flume. Two types of base plates were constructed: one with a regular periodic pattern and one with a random pattern. The regular pattern base plate was drilled such that if every hole were filled with drinking straws, the solid volume fraction would be 0.02. However, stems were placed in only 1 out of every 4 holes in a regular pattern, giving $\phi = 0.005$. This allowed for the same number of stems to be repositioned on the regular plates in a new pattern with the stem positions chosen at random, giving the pseudo-random vegetation pattern. The random pattern for the second base plate was chosen so that stems would not touch, but allowed for stems to have a machined face (producing a cylinder segment) that could be placed against the flume walls. These three configurations allow the effects of stem diameter, arrangement, and density to be compared. The vegetation configurations are illustrated in Fig. 1.

The characteristics of the artificial vegetation are given in Table 2. Three different stem spacing measurements are provided: a mean value estimated using Eq. (2), the known mean value, and the median stem spacing. This illustrates how stem spacing measurements can vary depending on configuration. The regular periodic vegetation is an expanded data set from the previous Sonnenwald et al. (2016) study, and hence, comparisons are not made to that previous study.

Rhodamine WT dye tracing was carried out using four mid-channel mid-depth Turner Designs Cyclops 7 fluorometers to record temporal concentration profiles. The four fluorometers formed three 2.5-m test reaches for the 4-mm stems and three 3-m test reaches for the 8-mm stems, giving total experimental lengths of 7.5 m and 9 m, respectively. The

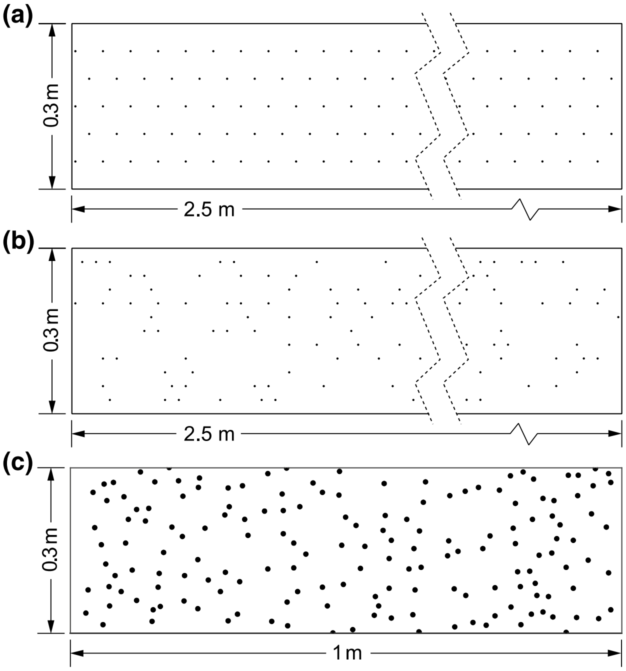

Fig. 1 Vegetation configuration illustrations **a** regular periodic vegetation reach layout with 4-mm stems, the vegetation pattern repeats every 0.05 m, **b** pseudo-random vegetation reach layout with 4-mm stems, the vegetation pattern repeats every 2.5 m, and **c** random vegetation reach layout with 8-mm stems, the vegetation pattern repeats every 1 m

Table 2 Artificial emergent vegetation characterisation

Description	d (mm)	ϕ	Estimated s (mm)[a]	s (mm)[b]	s_{50} (mm)
Regular periodic[c]	4	0.005	24.9	51.9	51.9
Pseudo-random	4	0.005	24.9	29.4	23.9
Random	8	0.027	18.0	22.7	22.3

[a] Estimated mean stem spacing using Eq. (2)

[b] Known mean stem spacing

[c] These data include additional measurements to those presented in Sonnenwald et al. (2016)

first fluorometer was located 4 m downstream of the inlet diffuser plate. The different reach lengths were to accommodate the difference in vegetation pattern repetition. The 4-mm stems covered the full length of the flume. The 8-mm stems covered between 3 m and 14 m from the inlet diffuser plate, with 1 m before and after the first and last fluorometer.

Three injections were carried out at each velocity, giving nine sets of upstream and downstream temporal concentration profiles recorded at 1 Hz. Manual pulse injections were made directly into the inlet pipe of the flume to ensure that the flow was well mixed. Regular periodic vegetation was investigated at target velocities of 7, 10, 13, 17, 20, 30, 40, and 50 mm s^{-1}, pseudo-random vegetation at 7, 10, 13, 17, 20, 30, 40, 50, 60, 90, and 110 mm s^{-1}, and random vegetation at 10, 30, 55, 80, 100, and 120 mm s^{-1}. Photographs of the experimental setup are shown in Fig. 2.

Determining D_x from experimental results

Values of D_x were found using the following routing solution to the 1D ADE,

$$C(x_2,t)=\int_{\tau=-\infty}^{\infty}\frac{C(x_1,t)U}{\sqrt{4\pi D_x\bar{t}}}\exp\left(-\frac{U^2(\bar{t}-t+\tau)^2}{4D_x\bar{t}}\right)\mathrm{d}\tau \tag{6}$$

where $C(x_1, t)$ and $C(x_2, t)$ are upstream and downstream concentration profiles, respectively, $\bar{t}$ is travel time, and τ is an integration variable (Fischer et al. 1979). The MATLAB (The MathWorks Inc. 2018) *lsqcurvefit* function was used to minimise the sum of errors squared between the measured and a predicted downstream temporal concentration profile to produce optimised values of D_x and U.

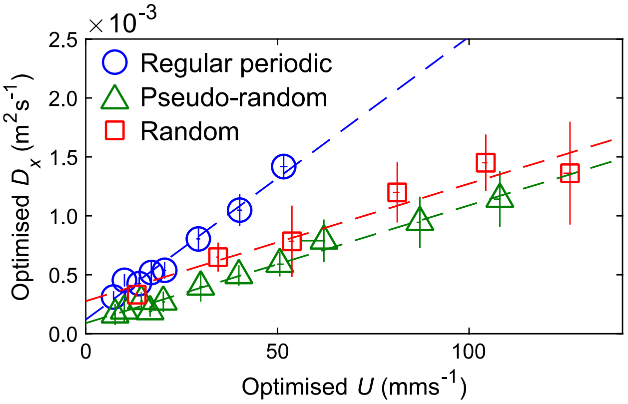

Fig. 3 Optimised longitudinal dispersion coefficient plotted against optimised velocity, dashed lines are best-fit linear trend lines with RMSE = 5.073×10^{-5}, 3.583×10^{-5}, and 1.069×10^{-4} for the regular periodic, pseudo-random, and random vegetation, respectively, vertical and horizontal error bars indicate 95% CIs

Results and discussion

Figure 3 presents mean longitudinal dispersion coefficient as a function of velocity, showing the expected linear trend of increasing D_x with U for all configurations. The near identical slope for the pseudo-random and random vegetation was not expected as the vegetation arrays are visually quite different and have different characteristics, notably different stem diameters.

Figure 4 presents non-dimensional longitudinal dispersion coefficient (with respect to stem diameter) as a function of velocity. For velocities greater than approximately 20 mm s^{-1}, the results confirm the linear dependency on U shown in Fig. 3. However, at velocities < 20 mm s^{-1}, the dependency is not linear. The lower velocities correspond roughly to $Re_d < 100$. Nepf (1999) suggested that turbulent diffusion could be significantly reduced at low velocities, which by definition corresponds with a greatly increased longitudinal dispersion, as observed here. Notably in Fig. 4,

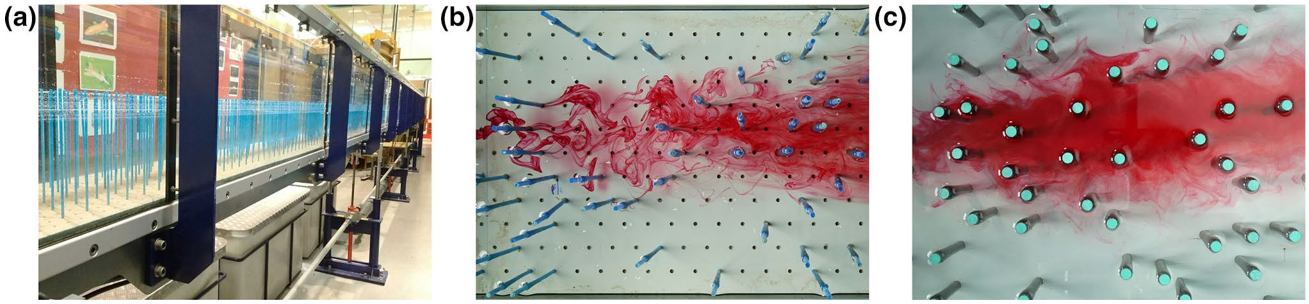

Fig. 2 Photographs of experimental setup, dye is from manual injection to water surface for illustration purpose **a** regular periodic, showing Armfield flume, **b** pseudo-random, snapshot of continuous injection at $U = 7$ mm s^{-1} and **c** random vegetation, snapshot of pulse injection at $U = 11$ mm s^{-1}

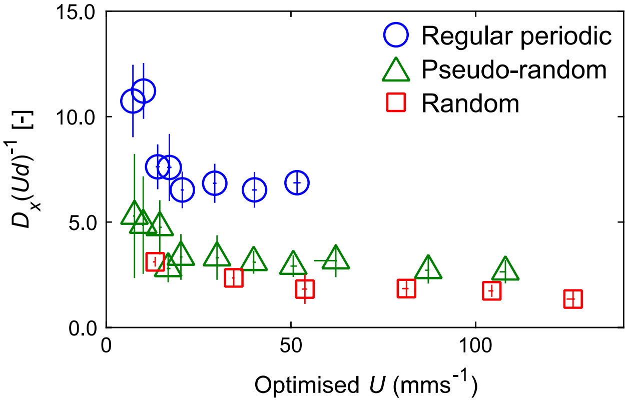

Fig. 4 Non-dimensional longitudinal dispersion coefficient with respect to stem diameter, $D_x(Ud)^{-1}$, plotted against velocity, vertical and horizontal error bars indicate 95% CIs

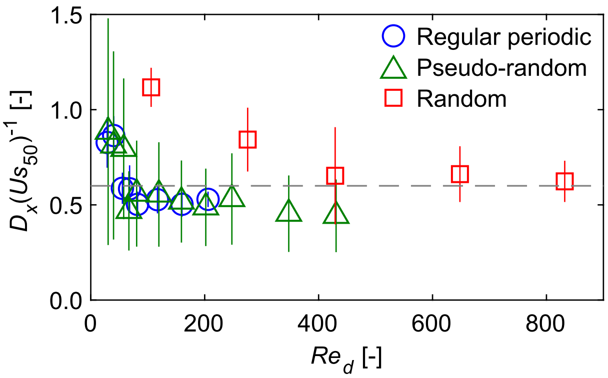

Fig. 5 Non-dimensional longitudinal dispersion coefficient with respect to stem spacing, $D_x(Us_{50})^{-1}$ plotted against stem Reynolds number, the dashed line is Eq. (7), vertical and horizontal error bars indicate 95% CIs

measurements of D_x from all three vegetation configurations do not collapse to a single line, contrary to the relationships suggested by Eqs. (3) and (4), both of which normalise by d. This suggests an alternative scale should be used for normalisation.

Figure 5 shows $D_x(Us_{50})^{-1}$, the non-dimensional longitudinal dispersion coefficient normalised by median stem spacing, plotted with respect to the stem Reynolds number. Stem spacing is used here given that it changes between the regular periodic and pseudo-random vegetation. The random vegetation has slightly higher values of $D_x(Us_{50})^{-1}$ than the regular and pseudo-random vegetation, which behave very similarly. Although there is a significant variation in $D_x(Us_{50})^{-1}$ at $Re_d < 100$, all three types of vegetation have similarly consistent values of $D_x(Us_{50})^{-1}$ at $Re_d \gtrsim 100$. This demonstrates, for the first time, the practicality of normalising longitudinal dispersion coefficient in vegetation by stem spacing. The regular and pseudo-random vegetation have similar non-dimensional dispersion coefficient values at all Re_d, including $Re_d < 100$, as would be expected for two types of vegetation with the same d and ϕ.

From the results in Fig. 5, a non-dimensional model for longitudinal dispersion based on stem spacing is proposed:

$$D_x = 0.60Us_{50} \tag{7}$$

where 0.60 is the mean value of $D_x(Us_{50})^{-1}$ at $Re_d > 100$. Equation (7) is shown as the dashed line in Fig. 5. While Eq. (7) is empirical, it is similar to Eq. (4) by analogy, containing s_{50} instead of s^*, and reflecting velocity-field heterogeneity through U and s_{50} combined.

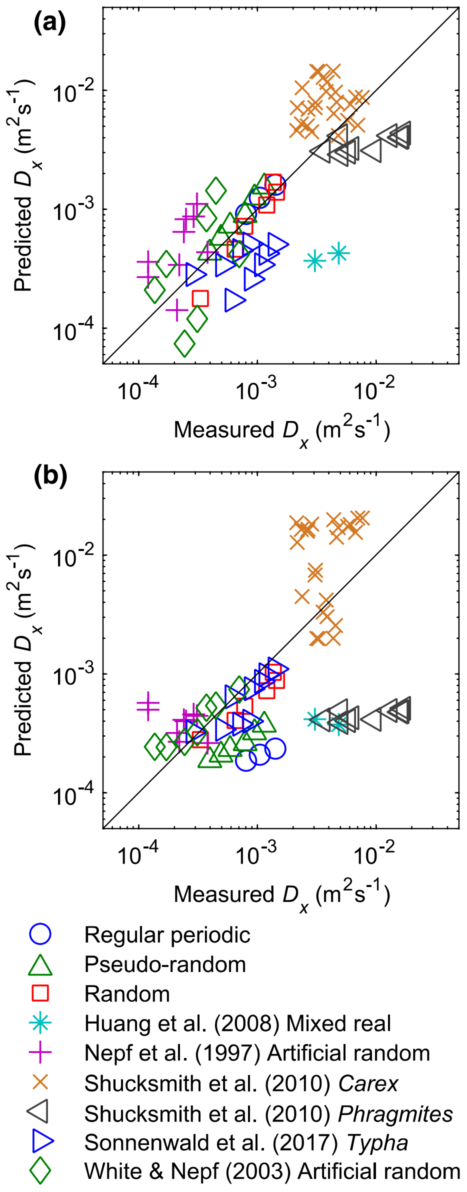

Fig. 6 Predicted D_x for $Re_d > 100$ using **a** Eq. (7) and **b** Eqs. (4) and (5) compared to measured D_x, line is line of equality

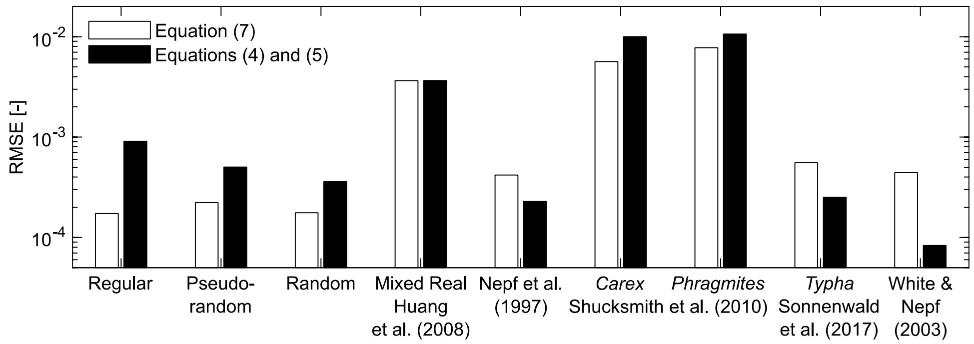

Fig. 7 Comparison of RMSE between predicted D_x and measured D_x for $Re_d > 100$ between Eq. (7) and Eqs. (4) and (5), lower values are better

Figure 6a shows predictions of D_x made using Eq. (7) compared to measured values of D_x from the present study as well as from other the experimental studies listed in Table 1. Mean s, estimated from d and ϕ, was used instead of s_{50} for the other studies as s_{50} was not available. As expected from Fig. 5, D_x is accurately predicted for the regular periodic, pseudo-random, and random vegetation configurations. The data from White and Nepf (2003) and Nepf et al. (1997), collected from cylinder arrays, are reasonably predicted. Notably, the Shucksmith et al. (2010) and Sonnenwald et al. (2017) real vegetation are also predicted well.

Figure 6b shows predictions of D_x made using Eqs. (4) and (5) compared to measured values of D_x. Equations (4) and (5) offer a better prediction of D_x for data from Nepf et al. (1997), White and Nepf (2003), and Sonnenwald et al. (2017) than Eq. (7). The vegetation from this study and the vegetation of Shucksmith et al. (2010) are less well predicted. Neither Eq. (7) nor Eqs. (4) and (5) predict the Huang et al. (2008) real vegetation well. Predictions with Eqs. (4) and (5) are biased towards underestimates of D_x. The scatter of predictions from Eq. (7) may be due to the use of an estimated value of s rather than a measured value.

Figure 7 compares RMSE goodness of fit between measured and predicted D_x made using Eq. (7) and measured and predicted D_x made using Eqs. (4) and (5). It shows the overall quality of predictions to be very similar. Equation (7) predicts the correct order of magnitude dispersion coefficient and is a suitable engineering approximation at $\phi < 0.1$. It predicts dispersion coefficient in real vegetation as well or better than Eqs. (4) and (5) in three out of four cases, despite the inherent variability of real vegetation.

Normalisation by median stem spacing, rather than stem diameter, appears to be a useful method of incorporating spatial heterogeneity into non-dimensional longitudinal dispersion coefficient, as it is successful in distinguishing between vegetation arrangements. However, it is worth noting that s_{50}, like d, is still a single length-scale characterisation. Most current theory is based on one such characterisation, while in reality multiple length scales are common, as described in Sonnenwald et al. (2017).

Future work should investigate the suitability of Eq. (7) at higher solid volume fractions and for more types of vegetation. Additional work is also needed to investigate how vegetation is described when calculating dispersion coefficient in complex vegetation arrangements, e.g. with varying stem diameter or stem spacing distributions.

Conclusions

Longitudinal dispersion coefficient (D_x) values obtained from dye tracing in artificial emergent vegetation fitted the expected trend of a linear increase with velocity, but could not be normalised using stem diameter. Stem spacing is suggested here for the first time as the appropriate length-scale normalisation for D_x in vegetation. From this, D_x in vegetation can be modelled by a new simple expression dependent on median stem edge-to-edge spacing. This new model showed reasonable performance when applied to other experimental data, including real vegetation. Although a more complex expression from the literature predicts D_x in vegetation equally well, it has multiple implicit assumptions. The new expression presented here gives robust correct order of magnitude estimates of longitudinal dispersion coefficient in vegetation suitable for engineering purposes.

Acknowledgements The authors thank Ayuk Merchant, Nathan Wilson, Alexandre Delalande, and Zoe Ball who conducted the laboratory work, and Ian Baylis for his technical support at the University of Warwick. This work was supported by the Engineering and Physical Sciences Research Council (EPSRC Grants EP/K024442/1, EP/K025589/1).

References

Danish Hydraulic Institute (2009) MIKE 11: a modelling system for rivers and channels. Reference manual. Denmark

Ergun S (1952) Fluid flow through packed columns. Chem Eng Prog 48:89–94

Fischer HB, List JE, Koh CR, Imberger J, Brooks NH (1979) Mixing in inland and coastal waters. Elsevier, Amsterdam

Huang YH, Saiers JE, Harvey JW, Noe GB, Mylon S (2008) Advection, dispersion, and filtration of fine particles within emergent vegetation of the Florida everglades. Water Resour Res 44:W04408

Lightbody AF, Nepf HM (2006) Prediction of velocity profiles and longitudinal dispersion in emergent salt marsh vegetation. Limnol Oceanogr 51(1):218–228

Nepf HM (1999) Drag, turbulence, and diffusion in flow through emergent vegetation. Water Resour Res 35(2):479–489

Nepf HM (2012) Flow and transport in regions with aquatic vegetation. Annu Rev Fluid Mech 44:123–142

Nepf HM, Mugnier C, Zavistoski R (1997) The effects of vegetation on longitudinal dispersion. Estuar Coast Shelf Sci 44(6):675–684

O'Hare MT (2015) Aquatic vegetation—a primer for hydrodynamic specialists. J Hydraul Res 53(6):687–698

Shucksmith J, Boxall J, Guymer I (2010) Effects of emergent and submerged natural vegetation on longitudinal mixing in open channel flow. Water Resour Res 46(4):W04504

Sonnenwald F, Guymer I, Marchant A, Wilson N, Golzar M, Stovin V (2016). Estimating stem-scale mixing coefficients in low velocity flows. In: sustainable hydraulics in the era of global change: proceedings of the 4th IAHR Europe congress. CRC Press

Sonnenwald F, Hart J, West P, Stovin V, Guymer I (2017) Transverse and longitudinal mixing in real emergent vegetation at low velocities. Water Resour Res 53(1):961–978

Sonnenwald F, Stovin V, Guymer I (2018a) Use of drag coefficient to predict dispersion coefficients in emergent vegetation at low velocities. Paper presented at the 12th international symposium on ecohydraulics, Tokyo, Japan

Sonnenwald F, Stovin V, Guymer I (2018b) Estimating drag coefficient for arrays of rigid cylinders representing vegetation. J Hydraul Res. https://doi.org/10.1080/00221686.2018.1494050

Tanino Y (2012) Flow and mass transport in vegetated surface waters. In: Gualtieri C, Mihailovic DT (eds) Fluid mechanics of environmental interfaces, 2nd edn. Taylor & Francis, Abingdon, pp 369–394

Tanino Y, Nepf HM (2008) Lateral dispersion in random cylinder arrays at high Reynolds number. J Fluid Mech 600:339–371

The MathWorks Inc (2018) MATLAB R2018a, Natick, MA

Tinoco RO, Cowen EA (2013) The direct and indirect measurement of boundary stress and drag on individual and complex arrays of elements. Exp Fluids 54(4):1–16

White BL, Nepf HM (2003) Scalar transport in random cylinder arrays at moderate Reynolds number. J Fluid Mech 487:43–79

Woods-Ballard B, Wilson S, Udale-Clarke H, Illman S, Scott T, Ashley R, Kellagher R (2015) The SUDS manual, report C753. CIRIA, London

Acta Geophysica (2019) 67:951–960
https://doi.org/10.1007/s11600-019-00253-x

RESEARCH ARTICLE - SPECIAL ISSUE

Sensitivity of optimized transient storage model parameters to spatial and temporal resolution

Steve Wallis[1] · **Russell Manson**[2]

Received: 28 August 2018 / Accepted: 25 January 2019 / Published online: 5 February 2019

Abstract

The transient storage model is a popular tool for modelling solute transport along rivers. Its use requires values for the velocity and shear flow dispersion coefficient in the main channel of the river together with two exchange rates between the main channel and transient storage zones, which surround the main channel. Currently, there is insufficient knowledge to enable these parameters to be predicted from the type of hydraulic variables that may typically be available. Hence, recourse is made to tracer experiments, which provide temporal solute concentration profiles that can be used to estimate the parameters by optimizing model output to observations. The paper explores the sensitivity of such parameters to the spatial and temporal resolutions used in the optimization of the model. Data from 25 tracer experiments covering a river flow rate range of 300–2250 L/s in a single reach of the river Brock in north-west England were used. The shear flow dispersion coefficient was found to be the most sensitive parameter; the velocity was found to be the least sensitive parameter. When averaged over all the experiments, mean percentage differences in parameter values between a coarse resolution case and a fine resolution case were of the order of 2% for the velocity, 70% for the shear flow dispersion coefficient and 30% and 20% for the two exchange rates. Since the shear flow dispersion coefficient was found to be small, both in numerical terms and in comparison with an estimate of the total dispersion in the reach, it is suggested that it may be viable to omit the shear flow dispersion term from the model.

Keywords Solute transport · Rivers · Transient storage model · Model resolution · Parameter optimization

Introduction

Probably the most reliable method of quantifying transport and mixing mechanisms in rivers is to undertake an in situ tracer experiment. Most often this entails the instantaneous release of a tracer followed by the measurement of temporal solute concentration profiles at one or more locations downstream of the release point. Assuming that the profiles are of good quality, i.e. the entire profile is captured at a sufficiently high temporal resolution, several methods are available for analysing the data in order to estimate parameters such as the cross-sectional average longitudinal velocity and the longitudinal dispersion coefficient. These methods range from the very simple (e.g. analysing just the evolution of the peak of the profile) to the more complex (e.g. optimizing the output of a mathematical model of the physical transport processes to all or part of the completely observed profile). Generally, there is a trade-off between a quick, easy analysis of the data and a slower, more sophisticated analysis. It is generally believed that the extra time and effort devoted to the latter is worthwhile because a more encompassing use of the data is more likely to yield reliable information than a simple one. Hence, the majority of studies undertaken since the turn of the century (e.g. Gooseff et al. 2003b; Marion et al. 2008; Briggs et al. 2009; Liao and Cirpka 2011) have focused on estimating transport and mixing parameters by optimizing one or more variants of the transient storage model (TSM). However, except for a few studies concerning parameter identifiability and uncertainty (e.g. Wagner and Harvey 1997; Wagener et al. 2002; Worman and Wachniew 2007; Kelleher et al. 2013; Zaramella et al. 2016), the

---

✉ Steve Wallis
s.g.wallis@hw.ac.uk

[1] School of Energy, Geoscience, Infrastructure and Society, Heriot-Watt University, Riccarton, Edinburgh EH14 4AS, UK

[2] School of Natural Sciences and Mathematics, Stockton University, Galloway, NJ 08205-9441, USA

reliability of the information so obtained is rarely assessed, yet alone considered.

In this paper, we consider one issue that has the potential to introduce significant errors into the results obtained when optimizing the TSM. The model consists of a pair of differential equations describing the transport of a conservative solute and contains four parameters that quantify the physical processes of: advection and shear flow dispersion in the main channel of the river; and two-way exchange of solute between the main channel and storage zones, which are located at the banks of, and in the bed of, the main channel. Application of the model entails two components: the numerical solution of the differential equations and the optimization of the model output to tracer data, thus obtaining estimates of the four parameters. This pair of operations is repeated many times until the parameter optimization converges.

There are several sources of error in this procedure among which three are particularly notable: those stemming from the numerical solution of the model equations; those stemming from convergence issues in the optimization; and those stemming from imperfections in the tracer data. This paper considers the first of these and focuses on the impact of spatial and temporal resolution issues in the numerical solution of the model equations. The paper extends some earlier work on this issue (Wallis et al. 2013; Wallis and Manson 2018). The aims of the work are to demonstrate that optimized parameter values are dependent on model resolution and to quantify the potential magnitude of resultant errors in the parameter estimates.

Methodology

Modelling

The TSM consists of the following two equations which describe the transport of a conservative solute along a river that consists of a main channel that is surrounded by storage zones:

$$\frac{\partial c(x,t)}{\partial t} + U_{\mathrm{TS}}\frac{\partial c(x,t)}{\partial x} = D_{\mathrm{TS}}\frac{\partial^2 c(x,t)}{\partial x^2} + k_1(s(x,t) - c(x,t)) \quad (1)$$

$$\frac{\partial s(x,t)}{\partial t} = -k_2(s(x,t) - c(x,t)) \quad (2)$$

Here, c is the cross-sectional average solute concentration, s is the solute concentration in the storage zones, U_{TS} is the cross-sectional average flow velocity in the main channel, D_{TS} is the shear flow dispersion coefficient in the main channel, k_1 and k_2 are exchange rates between the main channel and the storage zones ($k_2 = (A/A_s)k_1$ where A and A_s are the cross-sectional areas of the main channel and storage zones, respectively), x is the longitudinal co-ordinate direction, and t is time. Equation (1) represents solute transport in the main river channel, including advection, shear flow dispersion and the effect of transient storage, whilst Eq. (2) represents a dynamic mass balance of solute in the storage zones. In these equations, a first-order exchange mechanism is used to describe the transport of solute between the main channel and the storage zones (and back again). The origins of the model can be traced back to the 1960s (e.g. Thackston and Krenkel 1967), but the model didn't became popular until the 1980s and 1990s (e.g. Bencala and Walters 1983; Runkel and Chapra 1993; Wagner and Harvey 1997; Runkel 1998). More recently, it has become the standard approach, either in its original form or in later modified forms, for many studies of solute transport in rivers (e.g. Wagener et al. 2002; Gooseff et al. 2003a, b; Worman and Wachniew 2007; Marion et al. 2008; Briggs et al. 2009; Liao and Cirpka 2011; Kelleher et al. 2013; Zaramella et al. 2016).

When applied to a river reach, the model simulates the temporal solute concentration profile at the downstream boundary of the reach using specified values of the four (spatially and temporally constant) parameters U_{TS}, D_{TS}, k_1 and k_2 and using an upstream boundary condition provided by an observed upstream temporal solute concentration profile. A zero dispersive flux downstream boundary condition is usually used together with an initial condition of zero solute concentration throughout the reach. In this study, the numerical solution of the differential equations was achieved using a semi-Lagrangian, finite volume scheme. In Eq. 1, advection was simulated using the method of characteristics, which locates the appropriate spatial location from which information is used to calculate an unknown solute concentration, together with spatial interpolation of a cumulative solute mass function. Dispersion was computed using backward implicit finite differences in time and central differences in space, whilst transient storage was computed using a backward implicit temporal update. Equation 2 was also computed using a backward implicit temporal update. Further details are provided in Manson et al. (2001) and in earlier work cited therein.

Tracer data

The data used in this study were collected in the mid-1980s as part of a NERC-funded project undertaken by Lancaster University, UK. Data from 25 experiments undertaken in a short reach of the river Brock in north-west England were used. Each experiment consisted of the release of a known mass of Rhodamine WT followed by the measurement of temporal tracer concentration profiles at two longitudinal sites using microcomputer controlled data acquisition systems. The tracer was released using a pump-fed, laterally distributed injection system that delivered tracer evenly over the width of the river. This was located about 40 channel widths upstream of the experimental reach. Consideration of likely transverse mixing rates and the analysis in Rutherford (1994) suggests that the tracer would have been well mixed in the experimental reach for most of the river flow rates encountered. The worst cases are the low river flow rates for which an initial mixing distance of about 60 channel widths would have been required for a centre-line injection. For these experiments, this would have been reduced by the laterally distributed injection. Wallis et al. (1987) give further details of the data collection system, and Wallis and Manson (2018) give details on the recent extraction of the data from the original logged files that were archived in the 1980s.

The study reach (length 128 m; mean width 8.5 m; slope 0.006) consisted of a straight channel containing one major pool-riffle structure and with bed material of medium cobbles (Wallis et al. 1989). River flow rates, which were in the range of 300–2200 L/s, were evaluated from the tracer data using dilution gauging. They agreed closely with observations from a nearby water authority operated flow gauging weir (Wallis et al. 1987). Data were recorded at a fixed sampling interval of 15 s. Consequently, the tracer profiles were described by between 50 and 150 data points with the lowest resolution occurring at the upstream site at the highest flow rate and the highest resolution occurring at the downstream site at the lowest flow rate.

Prior to use the upstream data of each experiment was scaled (by the ratio of upstream to downstream concentration profile areas) to remove any effect from lateral inflow, non-conservative behaviour of tracer or calibration errors. Generally, this was not a major issue with the mean downstream to upstream concentration profile area ratio being 0.985 (± 0.052). This also suggests that, in general, the tracer was well mixed in all the experiments.

Optimization

For each experiment, the four model parameters (U_{TS}, D_{TS}, k_1 and k_2) were estimated by optimizing the fit of the temporal solute concentration profile simulated by the TSM to that observed at the downstream end of the reach. The observed upstream temporal solute concentration from the same experiment provided the upstream boundary condition. Optimization was achieved by minimizing the sum of squared residuals using a modified Levenberg–Marquardt algorithm (Press et al. 1992) as summarized in Manson et al. (2016). This follows common practice, but the possibility that other objective function formulations may have an impact on optimized parameter values is worthy of consideration.

The influence of model resolution was investigated by undertaking the optimization for the following cases: space steps of 0.64, 1.28, 2.56 and 5.12 m all with a time step of 15 s; time steps of 7.5, 15 and 30 s all with a space step of 1.28 m. The choice of space steps was based on an arbitrary decision to initially divide the reach into 100 space steps, followed by obvious lower and higher resolutions. As noted below, the spatial resolution of the reach is rather less important than the spatial resolution of the solute cloud being modelled. Fewer time step cases then space step cases were considered because whilst it is easy to change the space step, changes to the time step require changes to the upstream boundary condition. An increase in time step is relatively easy to accommodate because data can be omitted from the observed solute concentration profile (assuming this leaves sufficient data to adequately represent the shape of the original profile), but a reduction in time step requires data to be interpolated between observed values. This is difficult to do reliably, particularly in regions of high curvature such as around the peak and around the initial rise of the profile above the background signal. Hence, only two cases, one either side of the original time step of 15 s, were used: every other data point was removed to achieve a time step of 30 s; linear interpolation was employed to generate the data at a time step of 7.5 s.

It is important to emphasize that the magnitudes of the space and time steps control the magnitude of the numerical errors introduced into the solution of the model equations. Also, they control the resolution at which the event is modelled, but not in terms of the physical size of the river or the period of time over which solute concentrations are observed. Instead, the extent and duration of the solute cloud being modelled are the key scales against which the space and time steps need to be compared in order to quantify the spatial and temporal resolutions at which the event is modelled. Hence, as described in Wallis and Manson (2018), the spatial and temporal resolutions of a solute cloud, respectively, were evaluated by dividing its spatial extent by the space step, and by dividing its temporal duration at the upstream end of the reach by the time step. The spatial extent of a solute cloud was evaluated as the product of its temporal duration and its centroid velocity, with the former being evaluated as the time difference between the start and end of the cloud's upstream temporal concentration profile. The start and end of a profile were defined as the times at which the concentration was 10% of the peak concentration. The centroid velocity was evaluated from the first and zeroth temporal moments of the profiles.

Results and discussion

A total of 150 optimizations were undertaken of which only about 10 failed to produce physically realistic parameter values. There was no obvious cause of, or pattern to the distribution of, the failures. It is, however, possible that in these cases the initial values used in the optimization were not compatible with the search for the global minimum. They were treated as outliers and were not included in the analysis of the results. Optimized values of all four model parameters were found to be sensitive to the space step and time step used. Importantly, for each tracer experiment they converged towards what might be termed their "true" values as the spatial and temporal discretization became more refined. The convergence was smooth and showed no evidence of interaction between the parameters. The effect of increasing the spatial resolution is illustrated in Fig. 1 which shows the percentage absolute differences in U_{TS}, D_{TS}, k_1, k_2 and A_s/A between successive pairs of space steps for all experiments. A_s/A, evaluated as the ratio of k_1 to k_2, is an important

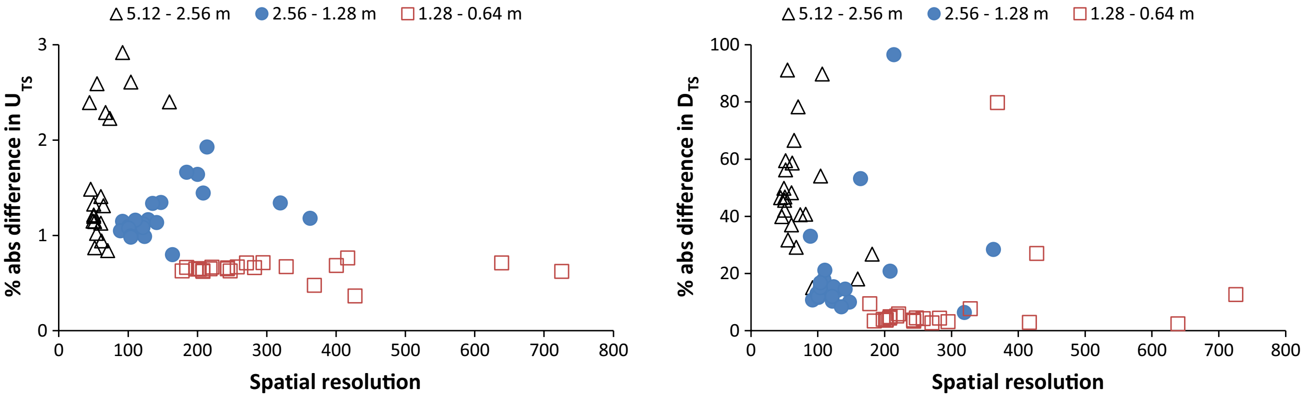

(a) Effect of space step on U_{TS} **(b)** Effect of space step on D_{TS}

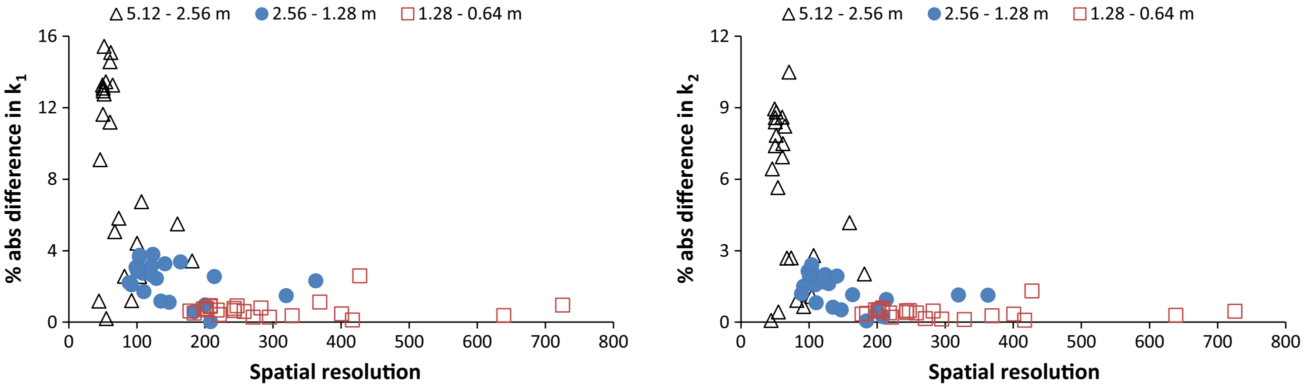

(c) Effect of space step on k_1 **(d)** Effect of space step on k_2

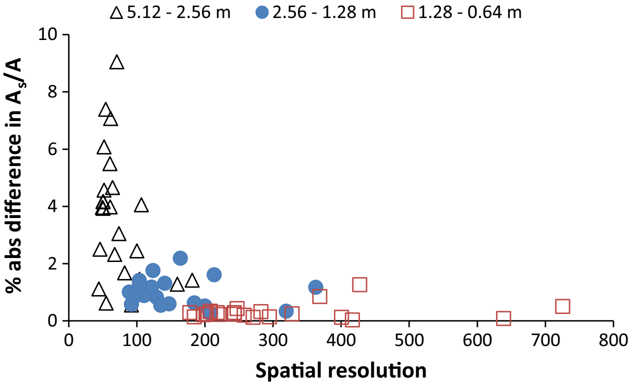

(e) Effect of space step on A_s/A

Fig. 1 Variation of change in optimized parameter values, caused by halving the space step, with spatial resolution: time step 15 s (each symbol represents one tracer experiment; spatial resolution is the ratio of tracer cloud length to space step) parameter in transient storage studies because it quantifies the physical size of the transient storage zones in relation to the physical size of the main channel.

In each panel, the triangles show the percentage absolute difference between the parameter values obtained using space steps of 5.12 and 2.56 m, and these are plotted against the spatial resolutions corresponding to the 2.56 m space step. The circles and open squares show the results presented in the same way for successive pairs of reducing space step. All these results were generated from optimizations that used a time step of 15 s.

It is evident that not only is there a reduction in the percentage difference for all the parameters with successive pairs of reducing space steps but also there is considerable variation in spatial resolution between all the experiments even when the space step is fixed. This occurs for several reasons. Most importantly, the fact that the tracer was pumped into the river over a period of about a minute meant that the tracer cloud was initially (i.e. before it reached the upstream observation location) longer in experiments undertaken at high river flow rates than in experiments undertaken at lower river flow rates. This occurred because of the higher velocity of the water in the former cases compared to the latter cases. In addition, reach travel time and overall longitudinal dispersion (main channel shear flow plus transient storage) rates varied with river flow rate, the former decreased, whilst the latter increased. In general, however, the spatial resolution increased approximately linearly with river flow rate (from about 100 to about 200 for the 1.28 m space step case), suggesting that the pumped tracer release system was the dominant issue. Results for all five parameters are summarized in Table 1 which shows percentage differences averaged over all experiments. Clearly, all five parameters converge with reducing space step. D_{TS} and U_{TS} are the most and the least sensitive parameters, respectively: k_2 is less sensitive than k_1.

The effect of increasing the temporal resolution is shown in Fig. 2, which is presented in the same way as Fig. 1. The space step was 1.28 m in all these cases. Clearly, the trends are similar to before: there is a reduction in the percentage difference in all parameter values with successive pairs of reducing time step. Table 2 shows percentage differences averaged over all experiments. Clearly, all five parameters converge with reducing time step. As was found with the space step, D_{TS} and U_{TS} are the most and the least sensitive parameters to the time step, respectively: k_2 is less sensitive than k_1. Again, as before, there were variations in temporal resolution between experiments, this time with a reduction from about 40 to about 20 for the 15 s time step case. The reduction reflects the fact that a solute cloud passes a fixed observation location more quickly at higher river flow rates than at lower river flow rates. Thus, when using a fixed sampling interval, higher river flow rate events will be observed at a poorer temporal resolution than lower river flow rate events.

It is noticeable in the figures that the temporal resolutions covered by the results are lower than the spatial resolutions covered. This is quantified in the last column of Tables 1 and 2 which show the average resolution for each case. The only approximately comparable spatial and temporal resolutions are the first row in Table 1 and the second row in Table 2.

Interestingly, the mean percentage differences in four of the parameters are also similar, but D_{TS} appears to be more sensitive to the space step than to the time step.

The optimized TSM fitted all the observed downstream concentration profiles well, with fits improving as model resolution increased. For example using a time step of 15 s, root mean square errors between observed and modelled concentrations were as follows for space steps of 5.12, 2.56, 1.28 and 0.64 m, respectively: 0.0173, 0.0129, 0.0120 and 0.0118 μg/L for an experiment with a river flow rate of 469 L/s; 0.0061, 0.0057, 0.0057 and 0.0057 μg/L for an experiment with a river flow rate of 1460 L/s. Similarly, using a space step of 1.28 m, root mean square errors between observed and modelled concentrations were as follows for time steps of 30, 15 and 7.5 s, respectively: 0.0248, 0.0120 and 0.0086 μg/L for an experiment with a river flow rate of 469 L/s; 0.0086, 0.0057 and 0.0044 μg/L for an experiment with a river flow rate of 1460 L/s.

A more meaningful assessment of model fit across all the experiments was achieved by calculating the normalized root mean square errors between observed and modelled concentrations. The normalized root mean square error for any particular case was evaluated by dividing the root mean square error between observed and modelled concentrations by the maximum observed solute concentration. Averaged over all experiments (all for a time step of 15 s, as earlier) normalized root mean square errors were 0.0113, 0.0095, 0.0092 and 0.0091 for space steps of 5.12, 2.56, 1.28 and

Table 1 Mean percentage differences in optimized parameters between pairs of space steps

Space step change (m)	U_{TS}	D_{TS}	k_1	k_2	A_s/A	Average spatial resolution
5.12–2.56	1.96	48.33	8.95	5.14	3.62	75
2.56–1.28	1.20	15.17	2.37	1.38	1.00	150
1.28–0.64	0.64	5.74	0.71	0.40	0.30	300

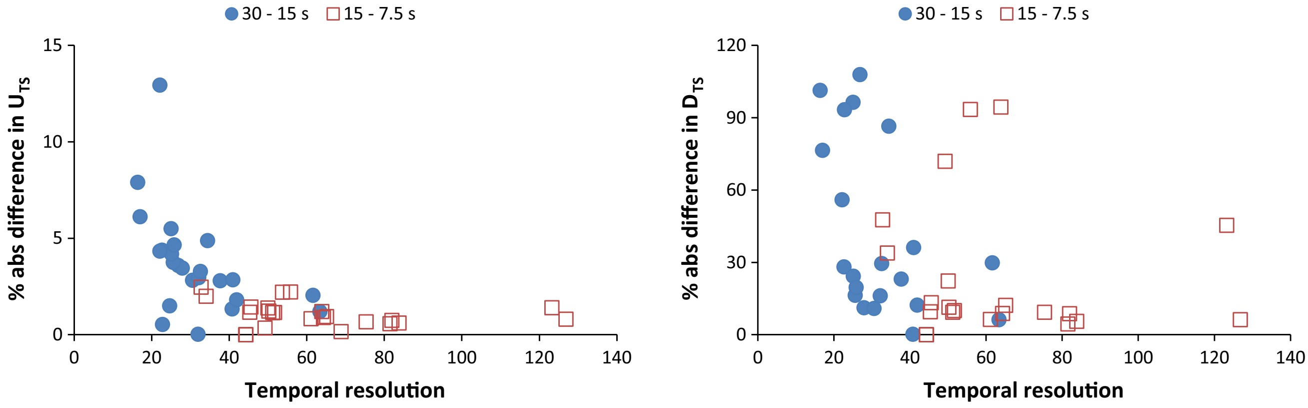

(a) Effect of time step on U_{TS} **(b)** Effect of time step on D_{TS}

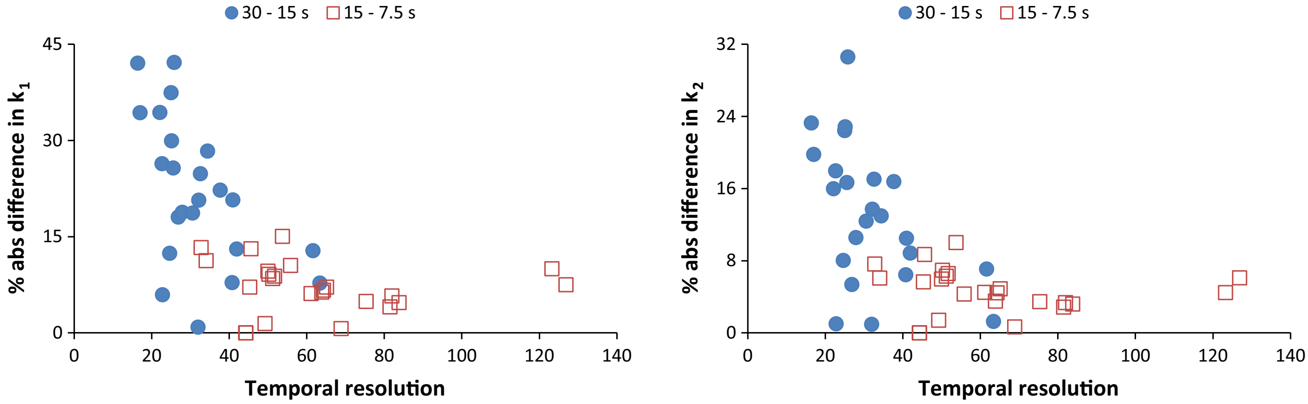

(c) Effect of time step on k_1 **(d)** Effect of time step on k_2

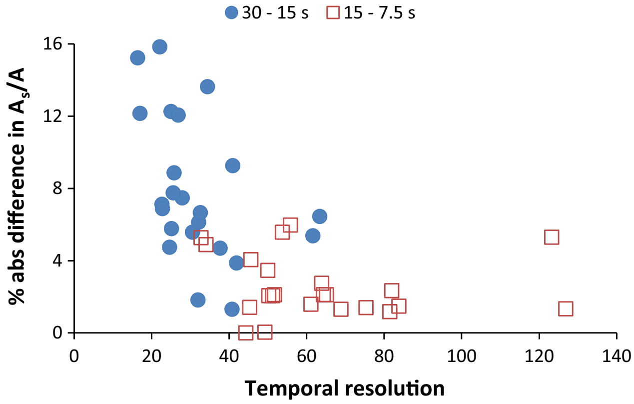

(e) Effect of time step on A_s/A

Fig. 2 Variation of change in optimized parameter values, caused by halving the time step, with temporal resolution: space step 1.28 m (each symbol represents one tracer experiment; temporal resolution is the ratio of tracer cloud length to time step)

Table 2 Mean percentage differences in optimized parameters between pairs of time steps

Time step change (s)	U_{TS}	D_{TS}	k_1	k_2	A_s/A	Average temporal resolution
30–15	3.52	27.90	23.05	14.59	7.26	31
15–7.5	1.21	20.84	8.04	5.15	2.74	62

0.64 m, respectively. Similarly, normalized root mean square errors between observed and modelled concentrations averaged over all experiments (all for a space step of 1.28 m, as earlier) were 0.0150, 0.0092 and 0.0074 for time steps of 30, 15 and 7.5 s, respectively.

An indication of the significance of the dependence of optimized parameter values on model resolution was gained by evaluating the percentage difference between results obtained using a space step of 5.12 m with a time step of 30 s (coarse resolution) and those obtained using a space step of 1.28 m with a time step of 7.5 s (fine resolution). Means and standard deviations of these differences evaluated over all experiments are shown in Table 3.

Although differences in U_{TS} are very small, differences in D_{TS}, k_1 and k_2 are substantial. Figure 3 shows how these differences vary between tracer experiments, where they are plotted against river flow rate (determined from the tracer data using dilution gauging). It appears that differences in U_{TS} increase with increasing river flow rate whilst differences in k_1 and k_2 decrease with increasing river flow rate. There is no clear pattern for D_{TS} and A_s/A.

Further detail is shown in Fig. 4 where the individual optimized parameter values from the coarse and fine optimizations are plotted together, again against river flow rate. The two sets of velocities are very close to each other and, in comparison to the fine resolution values, there are about the same number of overestimates as there are underestimates in the coarse resolution values. About 75% of the dispersion coefficients are underestimated in the coarse resolution case. In contrast about 85% of both exchange rates and the area ratio are overestimated in the coarse resolution case. Other features of the dispersion coefficient results, in particular, worth highlighting are the scatter and the very small values. These may reflect that the optimum model fit to the data is insensitive to this parameter, however, we have not investigated this.

The real significance of such potential errors lies in the use of the parameter values when formulating predictive equations for the model parameters for use in river reaches where no tracer experiments have been undertaken (e.g. Cheong et al. 2007; O'Connor et al. 2010). Clearly, parameter values obtained using numerical solutions of the TSM which employ poor spatial and temporal resolutions should not be used in such exercises. Unfortunately there is little or no evidence that such matters have been considered in previous work because the model resolutions at which parameter estimates have been obtained by optimizing the TSM to observed temporal concentration profiles are rarely, if at all, quoted alongside the published parameter values. For example, in a sample of seven published articles concerning the application of the TSM to tracer data (Hart et al. 1999; Gooseff et al. 2003a; Jin and Ward 2005; Cheong et al. 2007; Camacho and Gonzalez 2008; O'Connor et al. 2010; Kelleher et al. 2013) only one of them clearly stated what space step or time step had been used in the modelling, and there was no mention of spatial or temporal resolution in any of them. Only in 4 of them was the experimental sampling interval in the concentration profiles stated. These ranged from 10–300 s, with the majority being greater than the 15 s in the river Brock data. Hence, in view of the results presented above, it is likely that some unreliable parameter values have been reported in the literature, and therefore it is possible that some unreliable values have been used in the development of predictive equations for the TSM parameters.

Table 3 Percentage differences in optimized parameters between coarse and fine resolutions

	U_{TS}	D_{TS}	k_1	k_2	A_s/A
Mean	2.19	68.75	33.69	20.28	10.87
Standard deviation	1.50	20.06	16.88	11.06	5.24

The findings described above should provide food for thought for workers designing tracer experiments for use with parameter optimization of the TSM. In particular, we would emphasize the merits of collecting observed solute concentrations at the smallest time step possible and recognizing that high river flow rate events are particularly vulnerable to being observed too coarsely.

Finally, Fig. 4 provides evidence for how the TSM parameters vary with river flow rate, which is an issue that has not been addressed by other workers except in a very few studies (Hart et al. 1999; Gooseff et al. 2003a; Jin and Ward 2005; Camacho and Gonzalez 2008). Clearly, U_{TS} and k_1 and k_2 increase with river flow rate, as previously discussed in Wallis and Manson (2018), yet A_s/A is approximately constant at a value of about 0.3. D_{TS} shows no particular pattern although the fine resolution results are more closely grouped, and in this case, it could be argued that a constant value of about 0.25 m^2/s adequately describes the data. Similar values of D_{TS} were reported in the four studies referred to above, which were single reach studies undertaken on similar sized or smaller rivers and at similar river flow rates to the river Brock tracer experiments. Interestingly, 50 of the 51 D_{TS} values provided in those sources are < 0.6 m^2/s. Similarly, in about 60 optimizations of the TSM to mountain stream data reported in Manson et al. (2016), all the D_{TS} values were < 0.4 m^2/s. Furthermore, optimization of the advection–dispersion model (ADM) to the river Brock data yielded dispersion coefficients that increased from about 1–5 m^2/s over the river flow rate range of 300–2200 L/s. The ADM is a simplified version of the TSM in which the transient storage terms are ignored, i.e. it is simply Eq. (1) with the final

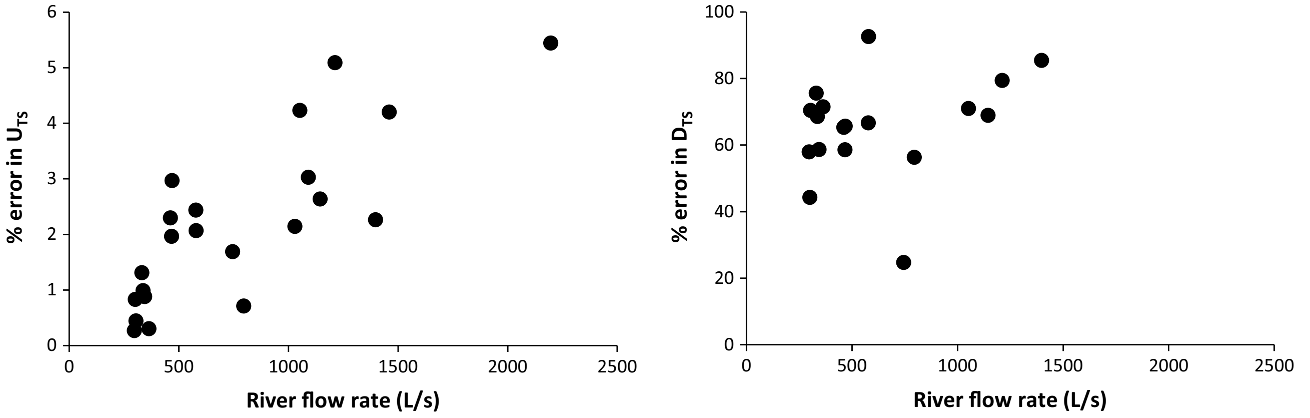

(a) % difference in U_{TS} **(b)** % difference in D_{TS}

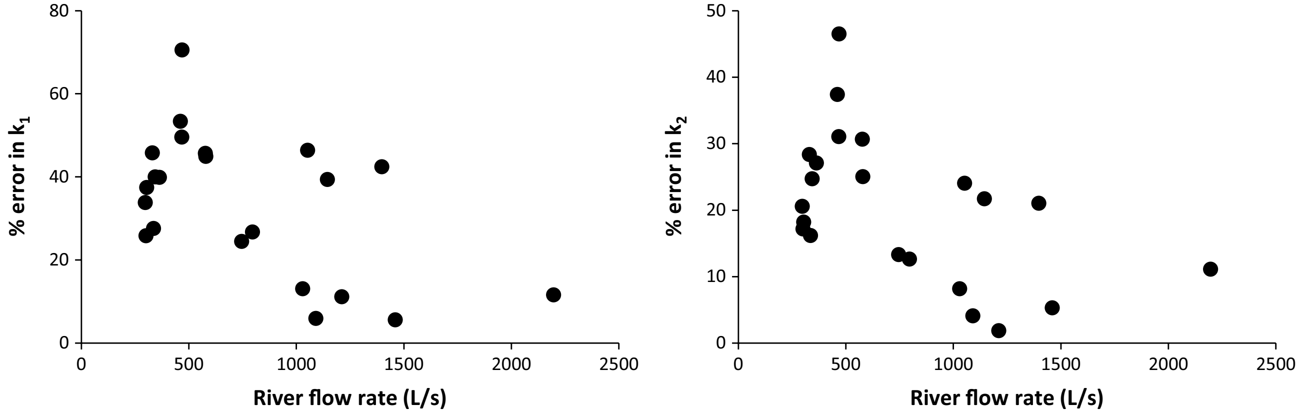

(c) % difference in k_1 **(d)** % difference in k_2

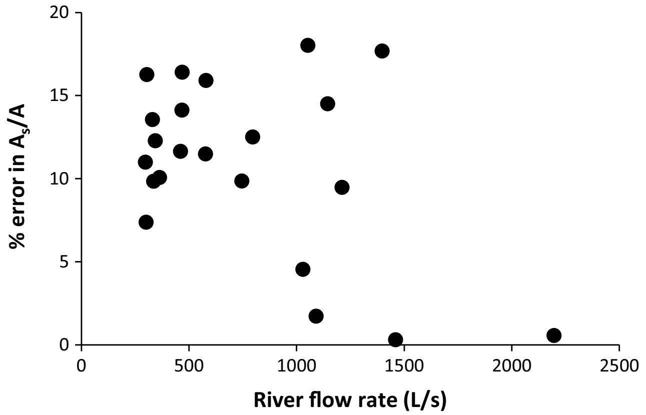

(e) % difference in A_s/A

Fig. 3 Variation of % difference in optimized parameters between coarse and fine resolutions with river flow rate

term on the right-hand side omitted. Optimizations were obtained in the same way as for the TSM model and used a space step of 1.28 m and a time step of 15 s. These dispersion coefficients are estimates of the overall longitudinal dispersion taking place in the reach, caused by shear flow in the main channel and transient storage, as measured by the increase in variance of the temporal concentration profile between upstream and downstream observation locations. Clearly, these results imply that not only are the estimates of D_{TS} in the river Brock small in numerical terms,

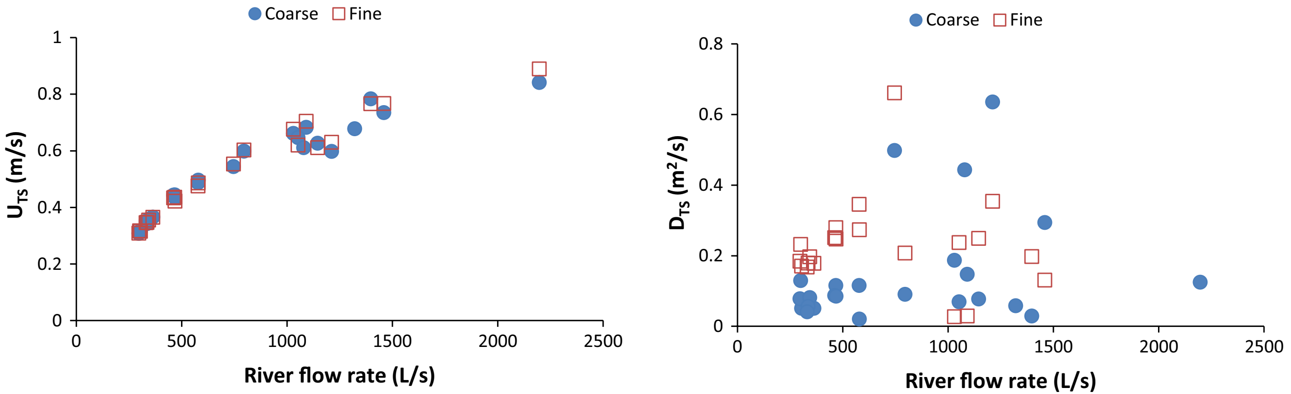

(a) Optimized U_{TS} **(b)** Optimized D_{TS}

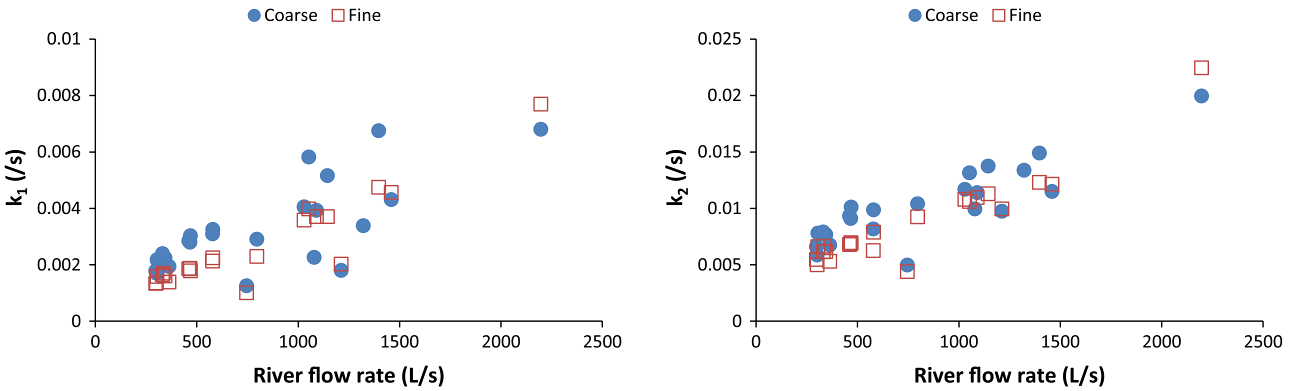

(c) Optimized k_1 **(d)** Optimized k_2

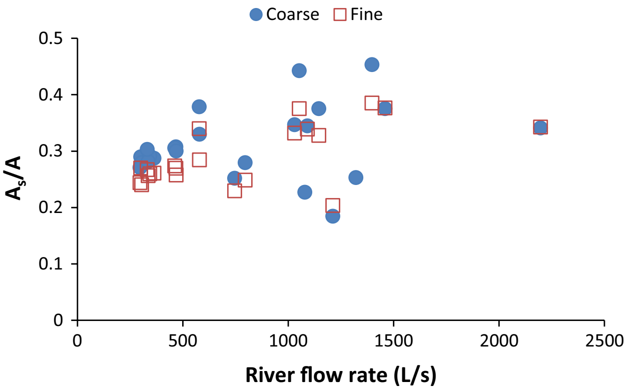

(e) Optimized A_s/A

Fig. 4 Variation of optimized parameters with river flow rate for coarse and fine resolutions

but also that transient storage is the dominant dispersive process in the reach. In view of this, and the similarly small D_{TS} values in the other sources referred to above, we postulate that omitting the dispersion term from the TSM, thus creating a three-parameter model, whose parameters might be more robustly identified than those of the four-parameter model, is worthy of examination.

Conclusions

By optimizing the TSM to observed temporal solute concentration profiles using different numerical resolutions in space and time, it has been demonstrated that the resultant estimates of the model parameters are dependent on the resolutions used. Although this will not be a surprise to numerical modellers who are well aware of the concept of grid-independent solutions, there is little evidence that the significance of numerical resolution has been recognized by workers using the TSM. In tests using 25 observed solute transport events from the river Brock in the north-west of England, mean percentage differences in parameter values between a coarse resolution model and a fine resolution model were of the order of 2% for the velocity, 70% for the shear flow dispersion coefficient and 30% and 20% for the two exchange rates. It would seem prudent that in applications of the TSM, minimum spatial and temporal resolutions of the order of 100 are used, followed by a repeat optimization at a finer resolution(s), to ensure that estimates of transport and mixing parameters are not significantly contaminated by model discretization errors. Also, we recommend that model resolutions should be published alongside the optimized parameter values. Evidence of small shear flow dispersion coefficients in the river Brock and a few other rivers of similar size suggests that a three-parameter version of the TSM is worthy of examination.

Compliance with ethical standards

Conflict of interest The authors declare that they have no conflict of interest.

References

Bencala KE, Walters RA (1983) Simulation of solute transport in a mountain pool-and-riffle stream: a transient storage model. Water Resour Res 19:718–724

Briggs MA, Gooseff MA, Arp CD, Baker MA (2009) A method for estimating surface transient storage for streams with concurrent hyporheic storage. Water Resour Res 45:W00D27

Camacho LA, Gonzalez RA (2008) Calibration and predictive ability of longitudinal solute transport models in mountain streams. Environ Fluid Mech 8:597–604

Cheong TS, Younis BA, Seo IW (2007) Estimation of key parameters in model for solute transport in rivers and streams. Water Resour Manag 21:1165–1186

Gooseff MN, McGlynn BL, McGlynn RS (2003a) Transient storage processes and stream discharge recession in a headwater stream, Maimai, New Zealand. Proc N Am Benthol Soc Annu Meet

Gooseff MN, Wondzell SM, Haggerty R, Anderson J (2003b) Comparing transient storage modeling and residence time distribution (RTD) analysis in geomorphically varied reaches in the Lookout Creek basin, Oregon, USA. Adv Water Resour 26:925–937

Hart DR, Mulholland PJ, Marzolf ER, DeAngelis DL, Hendricks SP (1999) Relationships between hydraulic parameters in a small stream under varying flow and seasonal conditions. Hydrol Process 13:1497–1510

Jin H-S, Ward GM (2005) Hydraulic characteristics of a small coastal plain stream of the southeastern United States: effects of hydrology and season. Hydrol Process 19:4147–4160

Kelleher C, Wagener T, McGlynn B, Ward AS, Gooseff MN, Payn RA (2013) Identifiability of transient storage model parameters along a mountain stream. Water Resour Res 49:5290–5306

Liao Z, Cirpka OA (2011) Shape-free inference of hyporheic traveltime distributions from synthetic conservative and “smart” tracer tests in streams. Water Resour Res 47:W07510

Manson JR, Wallis SG, Hope D (2001) A conservative semi-Lagrangian transport model for rivers with transient storage zones. Water Resour Res 37:3321–3329

Manson JR, Wallis SG, Demars BOL, Mick JD, Gislason GM, Olafsson JS, Friberg N (2016) A comparison of three solute transport models using mountain stream tracer experiments. In: Rowinski PM, Marion A (eds) Hydrodynamic and mass transport at freshwater aquatic interfaces. Springer, Switzerland, pp 77–90

Marion A, Zaramella M, Bottacin-Busolin A (2008) Solute transport in rivers with multiple storage zones: the STIR model. Water Resour Res 44:W10406

O’Connor BL, Miki H, Harvey JW (2010) Predictive modelling of transient storage and nutrient uptake: implications for stream restoration. J Hyd Eng Am Soc Civ Eng 136:1018–1032

Press WH, Teukolsky SA, Vetterling WT, Flannery BP (1992) Numerical recipes in C: the art of scientific computing, 2nd edn. Cambridge University Press, Cambridge

Runkel RL (1998) One-dimensional transport with inflow and storage (OTIS): a solute transport model for streams and rivers. Water Resour Invest Rep 98–4018 (**U S Geol Surv, Denver, Co**)

Runkel RL, Chapra SC (1993) An efficient numerical solution of the transient storage equations for solute transport in small streams. Water Resour Res 29:211–215

Rutherford JC (1994) River Mixing. Wiley, Chichester

Thackston EL, Krenkel PA (1967) Longitudinal mixing in natural streams. J Sanit Eng Div Proc Am Civ Soc Eng 93:67–90

Wagener T, Camacho LA, Wheater HS (2002) Dynamic identifiability analysis of the transient storage model for solute transport in rivers. J Hydroinformatics 94:199–211

Wagner BJ, Harvey JW (1997) Experimental design for estimating parameters of rate-limited mass transfer: analysis of stream tracer studies. Water Resour Res 33:1731–1741

Wallis SG, Manson JR (2018) Flow dependence of the parameters of the transient storage model. In: Kalinowska MB, Mrokowska MM, Rowinski PM (eds) Free surface flows and transport processes. Springer, Cham, pp 477–488

Wallis SG, Blakeley C, Young PC (1987) A microcomputer based fluorometric data logging and analysis system. J Inst Water Eng Sci 41:122–134

Wallis SG, Young PC, Beven KJ (1989) Experimental investigation of the aggregated dead zone model for longitudinal solute transport in stream channels. Proc Inst Civ Eng Part 2(87):1–22

Wallis SG, Osuch M, Manson JR, Romanowicz R, Demars BOL (2013) On the estimation of solute transport parameters for rivers. In: Rowinski P (ed) Experimental and computational solutions of hydraulic problems. Springer, Berlin, pp 415–425

Worman A, Wachniew P (2007) Reach scale and evaluation methods as limitations for transient storage properties in streams and rivers. Water Resour Res 43:W10405

Zaramella M, Marion A, Lewandowski J, Nutzman G (2016) Assessment of transient storage exchange and advection–dispersion mechanisms from concentration signatures along breakthrough curves. J Hydrol 538:795–801

Acta Geophysica (2019) 67:961–970
https://doi.org/10.1007/s11600-019-00272-8

RESEARCH ARTICLE - SPECIAL ISSUE

Turbulent mixing and dispersion mechanisms over flexible and dense vegetation

Donatella Termini[1]

Received: 9 December 2018 / Accepted: 21 February 2019 / Published online: 1 March 2019

Abstract
The present study investigates flow turbulence and dispersion processes in the presence of flexible and dense vegetation on the bed. The turbulent dispersion coefficients and the terms of the turbulent kinetic energy equation are determined by using data collected in a straight laboratory channel with living vegetation on the bed. Results show that the turbulent integral lengths assume an order of magnitude comparable to the stems' characteristic dimension independently by the direction and the turbulence assumes an isotropic behavior. The coefficients of dispersion have a trend similar to that of the turbulent lengths and assume low values in the longitudinal, transversal and vertical directions. Results also show that, in the mixing layer, the shear and wake turbulence production terms balance the dissipation; the turbulent diffusion term also assumes low values and its sign varies along the vertical indicating a transport of turbulent energy both from the vegetation to the free surface and from the free surface to vegetation.

Keywords Vegetated channels · Flexible vegetation · Turbulence · Dispersion

Introduction

Aquatic vegetation in rivers strongly affects flow structure and exchange mechanisms of substances, nutrients, dissolved oxygen and sediments. For this reason, aquatic vegetation plays a fundamental role in ecosystem services (Corenblit et al. 2007). The analysis of flow turbulence structure and exchange processes between vegetated and non-vegetated areas is important for examining river's habitat and ecological equilibrium. In the areas where submerged vegetation is present, this analysis has to be especially performed in the intermediate region (mixing layer zone) between the region inside the vegetation and that above it.

The influence of vegetation on turbulent flow structure and dispersion processes has been experimentally analyzed both in submerged and in emergent conditions (among others Nepf et al. 1997; Nepf 1999; Carollo et al. 2002; Ghisalberti and Nepf 2006; Nepf and Ghisalberti 2008; Righetti 2008; Okamoto and Nezu; 2009; Shucksmith et al. 2011; Termini 2015; Kubrak et al. 2015; Sivpure et al. 2015; Cornacchia et al. 2018). Nepf et al. (1997) verified that the presence of vegetation determines a reduced value of the longitudinal dispersion coefficient. Nepf (1999), focusing on the emergent rigid vegetation condition, developed a model to describe flow turbulence and diffusion mechanism. Ghisalberti and Nepf (2006), analyzing how the presence of submerged vegetation could affect the longitudinal dispersion coefficient, identified two zones: the zone above the vegetation, where large-scale shear dispersion occurs, and the zone within the vegetation, where stem-scale dispersion occurs. In a successive work, Nepf and Ghisalberti (2008) focused on flow transport processes in the presence of submerged vegetation providing an overview on existing models proposed to interpreter mean flow above and within the vegetated layer. Carollo et al. (2002, 2006, 2007, 2008) examined the turbulence intensity distribution and the adaptation of the mixing layer scheme to approximate the velocity profile in the case of submerged vegetation. Righetti (2008) investigated the main features of the turbulent flow field in the presence of flexible fully submerged bushes by applying the double-averaging method. Okamoto and Nezu (2009) focused their attention on the interaction processes between the flow and the waving motion of the flexible vegetation (called as "monami" by Ackerman and Okumbo 1993). Termini (2015) analyzed also the case of submerged

---

✉ Donatella Termini
donatella.termini@unipa.it

[1] Department of Engineering, Polytechnic School, University of Palermo, Palermo, Italy

vegetation condition and verified that the shape of the longitudinal velocity profile and the mixing layer thickness are mainly affected by the stems concentration and the flow submergence. Shucksmith et al. (2011), investigating the longitudinal dispersion over submerged vegetation, verified that it depends on the thickness of the mixing layer and, thus, on the difference in the flow velocity value occurring below and above it. Sivpure et al. (2015) also analyzed the flow and turbulence characteristics in the mixing layer zone over submerged and flexible vegetation but only in the case of sparse configuration. Kubrak et al. (2015), by using experimental data collected over submerged vegetation (simulated either by wooden or by plastic stems) focused on the values of the Coriolis coefficient α_c and the momentum coefficient β which have to be introduced in the energy and momentum equations to adequately simulate the velocity profile. More recently, Cornacchia et al. (2018) examined the flow effects related to the non-homogeneous vegetation distribution investigating how vegetated patches of different species could interact each other influencing flow hydrodynamics. De Serio et al. (2018) investigated the dispersion mechanisms focusing on the effect determined by different streamwise patterns of rigid vegetation and of flexible vegetation. Contributions in the knowledge of turbulent and dispersive stresses have been also obtained through numerical models and case-study simulations (Poggi et al. 2004; Defina and Bixio 2005; Coceal et al. 2007; Poggi et al. 2009; Stoesser et al. 2010).

The point is that although the studies conducted in this field have allowed to describe the characteristics of turbulent flow structure and exchange mechanisms within and away the vegetated layer (see also Schultz et al. 1995; Oldham and Sturman 2001; Nepf 2012), important aspects related to the dispersion processes and energy balance in the mixing layer zone have not systematically explored, especially in the case of flexible, submerged and dense vegetation. This is also due to the technical difficulties to collect refined experimental data. On the other side, literature (among others Ghisalberti and Nepf 2006; Termini 2015, 2016) shows that in the case of flexible and dense vegetation the flow structure in the mixing layer zone is complicated and perturbed by the stems motion. Furthermore, most of the existing experimental and numerical works consider idealized/artificial vegetation rather than living vegetation overlooking some of the key elements (such as the plant flexibility and morphology) which could affect dispersion processes (Shucksmith et al. 2011).

In such a context, the objective of the present study is to analyze the turbulent mixing and the dispersion processes restricting the attention to the case of flexible, submerged and dense vegetation. In fact, most aquatic plants in natural rivers are submerged and characterized by great flexibility (see as an example in Carpenter and Lodge 1986; Nikora et al. 2008) and the stems motion could affect the diffusion and advection mechanisms (Schnauder and Sukhodolov 2012). The paper presents estimates of the integral turbulent lengths, of the turbulent dispersion coefficients and of terms of the turbulent kinetic balance by using experimental data collected in a straight channel with living vegetation on the bed. In the next section "Methods and materials," the theoretical background and the data set used for the analysis are described; results are presented in "Results" section and are discussed in "Discussion" section; finally "Concluding remarks" section reports concluding remarks.

Methods and materials

Theoretical approach

As literature indicates (among others Nikora et al. 2001; Finnigan and Shaw 2008), because of the heterogeneity due to the presence of the vegetation, the double-averaging method should be applied to write the solving equations.

After having applied the time and space-averaging method, the transport equation of a tracer c can be written as follows (see as an example Tanino and Nepf 2008; Nepf and Ghisalberti 2008; Nepf 2012):

$$\frac{\partial\langle\bar{c}\rangle}{\partial t}+\langle\bar{v}_j\rangle\frac{\partial\langle\bar{c}\rangle}{\partial x_j}=-\frac{\partial}{\partial x_j}\left\{\underset{\text{I}}{\left\langle\overline{v'_j c'}\right\rangle}+\underset{\text{II}}{\left\langle\bar{v}''_j\bar{c}''_j\right\rangle}-\underset{\text{III}}{M\left\langle\overline{\frac{\partial c}{\partial x_j}}\right\rangle}\right\} \tag{1}$$

In Eq. (1), t indicates the time, the overbar represents the time average, the symbol $\langle\ \rangle$ represents the spatial average, the single superscript indicates the deviation from the time average and the double superscript indicates the deviation of the spatial average, x_j indicates the jth direction (with $x_1 = x$=longitudinal direction; $x_2 = y$=transversal direction; $x_3 = z$=vertical direction), M represents the molecular diffusion coefficient, v_j defines the instantaneous velocity component (with $v_1 = u(t)$ = longitudinal component, $v_2 = v(t)$ = transversal component, $v_3 = w(t)$ = vertical component).

Focusing on the right-hand side of Eq. (1), the term I defines the mass flux related to the turbulent fluctuations v'_j (with $v'_1 = u'$ = longitudinal component, $v'_2 = v'$ = transversal component, $v'_3 = w'$ = vertical component), the term II represents the dispersive flux due to the spatial heterogeneity of time-averaged velocity components, and the term III defines the flux related to the molecular diffusion. This last term (term III) is negligible compared with the turbulent diffusion (term I) and the dispersive flux (term II). By considering time-scales larger than the turbulent scales and space-scales larger than the stem's characteristic dimension or stems spacing (Rutherford

1994), the terms I and II determine Fickian transport and Eq. (1) can be rewritten as follows:

$$\frac{\partial\langle\bar{c}\rangle}{\partial t} + \langle\bar{v}_j\rangle\frac{\partial\langle\bar{c}\rangle}{\partial x_j} = K_{jj}\frac{\partial^2\langle\bar{c}\rangle}{\partial x_j^2} \tag{2}$$

In Eq. (2), K_{jj} parameterizes the turbulent diffusion and represents the dispersion coefficient along the jth direction. As the literature indicates (see as an example Tanino and Nepf 2008), K_{jj} can be determined by the product of the integral turbulent length scale, l_j, and the velocity scale, which is given by $\sqrt{k}$ (where $k = v_j v_j/2$ = the turbulent kinetic energy—see in Rutherford 1994; Pope 2000):

$$K_{jj} = \alpha\sqrt{k}l_j \tag{3}$$

α is a scale factor whose value varies in the range [0–1], as suggested by Nepf (1999).

From Eq. (3), it is clear that the evaluation of k is especially important in analyzing the dispersion processes.

After having applied the space-averaging method, the turbulent kinetic energy equation for 2-D vegetated flow can be written as (among others Brunet et al. 1994; Nezu and Sanjou 2008; Righetti 2008):

$$\frac{\partial\langle\bar{k}\rangle}{\partial t} = \underbrace{\left\langle -\overline{u'v'}\right\rangle\frac{\partial\langle\bar{u}\rangle}{\partial z}}_{P_s} + \underbrace{\left\langle -\overline{u'_i u'_j}\frac{\partial\bar{u}''_i}{\partial x_j}\right\rangle}_{P_w} + \underbrace{\frac{\partial}{\partial z}\left\langle -\overline{kw'}\right\rangle}_{T_d} + \underbrace{\frac{\partial}{\partial z}\left\langle -\overline{k''}\,\bar{v}''\right\rangle}_{T_{dis}} + \underbrace{\frac{\partial}{\partial z}\left\langle -\overline{\frac{p'}{\rho}v'}\right\rangle}_{T_p} + \underbrace{\nu\frac{\partial^2}{\partial z^2}\langle\bar{k}\rangle}_{V_d} - \langle\varepsilon\rangle \quad (4) \tag{4}$$

where ρ is the water density, ν is the kinematic viscosity, and p' represents the deviation of the pressure p. In Eq. (4), P_s and P_w are, respectively, the shear production of turbulence and the vegetation wakes production of turbulence, T_d and T_dis are, respectively, the turbulent diffusion term and the dispersive transport term, T_p represents the pressure transport term, V_d indicates the viscous term, and ε is the dissipation. According to Raupach and Shaw (1982) (see also Raupach et al. 1986 and Brunet et al. 1994), the term P_w can be estimated as:

$$P_\mathrm{w} \cong \langle u\rangle\frac{\partial\left\langle -\overline{u'v'}\right\rangle}{\partial z} \tag{5}$$

Thus, assuming steady flow and considering negligible the dispersive transport term and the viscous term, the turbulent kinetic energy equation can be written as (Nepf 1999; Nezu and Sanjou 2008):

$$\frac{\partial\langle\bar{k}\rangle}{\partial t} = 0 = P_\mathrm{s} + P_\mathrm{w} + T_\mathrm{d} + T_\mathrm{p} - \langle\varepsilon\rangle \tag{6}$$

Equation (6) indicates that the sum of shear and wakes turbulence productions, of the turbulent energy diffusion and of pressure transport balances the space-averaged turbulence dissipation.

Nepf and Vivoni (2000) examined the terms of Eq. (6) for rigid canopies and for values of the relative water depth H/kv (H = water depth, kv = vegetation height) ranging from 1 to 2.75, i.e., in the transition from emergent to submergence regimes. They verified that, for values of the stems Reynolds number $Re_\mathrm{s} > 200$, in the emergent regime P_s can be neglected and the wake production P_w balances the dissipation ε but, in the submerged regime, P_s could become significant because of the shear production at the top of vegetation.

Experimental data

Laboratory experiments were carried out in a straight rectangular laboratory channel 11.2 m long and 0.4 m wide, with transparent Plexiglass side-walls, constructed at the Department of Engineering (University of Palermo—Italy). The channel's bed, having a longitudinal slope of 0.4%, was partially covered by real flexible vegetation, as shown in Fig. 1. The first section (section *X0* of Fig. 1) of the vegetated-bed reach (1.60 m long) was 2.0 m distant from the initial section of the flume. The data used in the present work were collected during an experimental run conducted with water discharge $Q = 35$ l/s and relative water depth $H/k_\mathrm{v} = 3.6$ (with k_v = bent vegetation height). The water discharge was provided at the upstream tank of the flume through a recirculating pipe connected to the pump collocated at the downstream tank. During the experimental run, the DOP 2000 Profiler (by Signal Processing s.a.), with three probes of emitting frequency of 8 MHz, was used to measure the instantaneous velocity components in a refined measurement mesh of 9 cross sections equally spaced along the vegetated-bed reach. Because the DOP 2000 measured the velocity profile along each probe's direction, the vectorial composition of measured velocities was operated to obtain the instantaneous velocity components along *x, y, z* directions, as indicated in details in Termini (2013).

Vegetation characteristics

The vegetation used for the considered experimental runs consisted of *Festuca arundinacea* plants. The vegetated

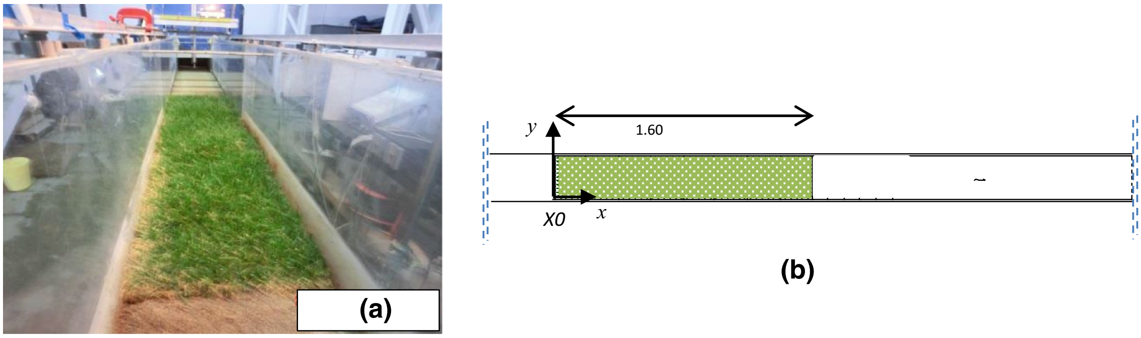

Fig. 1 **a** Frontal photograph of the channel; **b** plane view of the vegetated reach

stems were characterized by a blade geometry of width $d = 0.003$ m. In the present work, in agreement with previous works (Nepf and Koch 1999; Nepf and Ghisalberti 2008; Nezu and Sanjou 2008), such a blade width d has been assumed as the characteristic dimension of the vegetated element. The stems concentration was equal to 190 stems/dm^2 at which corresponds a value of the fractional plant area equal to $\phi = 13.5\%$ and frontal plant area per unit length $a = 57\ \mathrm{m}^{-1}$, so that this canopy can be considered dense (Nepf 2012).

The aforementioned plant species was chosen both because its straplike morphology is typical of submerged seagrasses (see as an example Chandler et al. 1996; Nepf 2012) and because it can be easily found in flooded areas (Khaleghi and Ramin 2005; Leuven et al. 2006; Ellenberg 2009) and along the Sicilian rivers. In fact, such a species presents a strong adaptability to environmental stresses and to the dry/wet changing conditions. Recently Loboda et al. (2019), by analyzing two species of a commonly growing aquatic plant (*Potamogeton*) in Poland, highlighted that the biomechanical behavior of the vegetated stems could be affected by the seasonal changes. Thus, it should be noted that, despite the great adaptability of the plant species used in the present work, according to Loboda et al. (2019) the results obtained in the present work could be restricted to the hydraulic behavior of the vegetation for the experimental conditions considered.

Results

Mean flow velocity and turbulence intensity

Figure 2 shows the vertical profiles of the mean longitudinal velocity u obtained in the vegetated-bed reach. In particular, the dots in Fig. 2 indicate the u-values at three locations (identified along the channel axis by the distance x from the section $X0$ and normalized by the stem's dimension d) and the line in Fig. 2 indicates the corresponding spatial average.

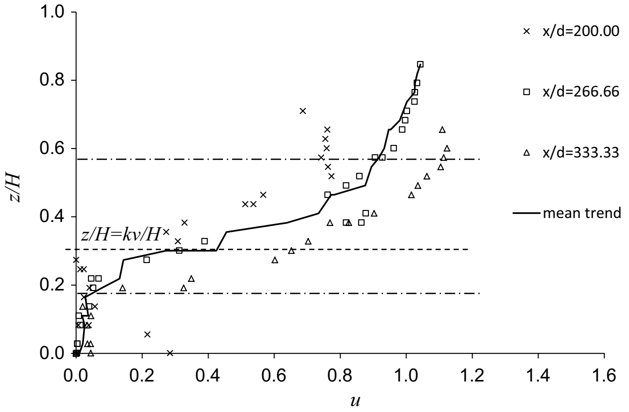

Fig. 2 Vertical profiles of the mean longitudinal velocity u (m/s) at different relative distances x/d and the corresponding spatial average

This figure shows that the velocity profile has a typical S-shape highlighting that, in agreement with other works (among others Carollo et al. 2002, 2005; Folkard 2011; Nepf 2012; Termini 2015), the presence of dense vegetation determines an evident region of shear so that an inflection point occurs close to the vegetation top. As the literature indicates (among others Ghisalberti and Nepf 2006; Carollo et al. 2006, 2007; Folkard 2011), in this case the mixing layer scheme could be applied to approximate the velocity profile. Thus, the velocity profile can be schematized as the combination of two regions (inside and outside the vegetation) characterized by a constant velocity and an intermediate region (mixing layer) which includes the inflection point. The momentum thickness and the associated transfer mechanism between the vegetation and the layer above it is related to the thickness of the mixing layer. From Fig. 2, it can be observed that in the examined case the intermediate layer (mixing layer) has an evident thickness and the flow velocity assumes very low values below the mixing layer and high values above it. This behavior could be related both to the dense vegetation and to the fact that the relative water depth ($H/k_{\mathrm{v}} = 3.6$) is > 2. In fact, following Termini's (2015) findings, for high values of stems concentration the velocity profile tends to flatten around the top of vegetation and, for relative water depths $H/k_v > 2$, the thickness of the mixing layer tends to increase as the flow submergence increases.

By using the time series of the velocity components ($u(t)$, $v(t)$, $w(t)$) and the corresponding time-averaged values (u, v, w), the longitudinal, transversal and vertical turbulent intensity components (u_{rms}, v_{rms}, w_{rms}) have been also estimated as:

$$u_{rms} = \frac{1}{N}\sum_{i=1}^{N}[u(t)-u]^2; \quad v_{rms} = \frac{1}{N}\sum_{i=1}^{N}[v(t)-v]^2 \\ w_{rms} = \frac{1}{N}\sum_{i=1}^{N}[w(t)-w]^2 \tag{7}$$

where N is the number of measured data.

Figure 3 shows the profiles of u_{rms}, v_{rms}, w_{rms}. (The dots indicate the estimates for different locations x/d, and the lines indicate the corresponding spatial average.) From Fig. 3, it appears clear that the turbulent intensity components have the peak value close to the vegetation top; inside the vegetation, the turbulent intensity components decay. Thus, the intermediate region (around the vegetation top) is that of higher turbulence intensity. In particular, the longitudinal component u_{rms} and the vertical component w_{rms} assume the peak value just below the top of the vegetated layer, while the transversal component v_{rms} has the peak just above of the vegetation top. The existence of the highest values of the turbulent intensity components close to vegetation top is related to the strong shear occurring in this zone; according to previous literature works (see as an example Ghisalberti and Nepf 2006; Carollo et al. 2008; Termini 2015), this behavior indicates the formation of vortices with the center at the top of the vegetation. The decrease in value of the turbulent intensity components inside the vegetation indicates the damping of these vortices close to the bed.

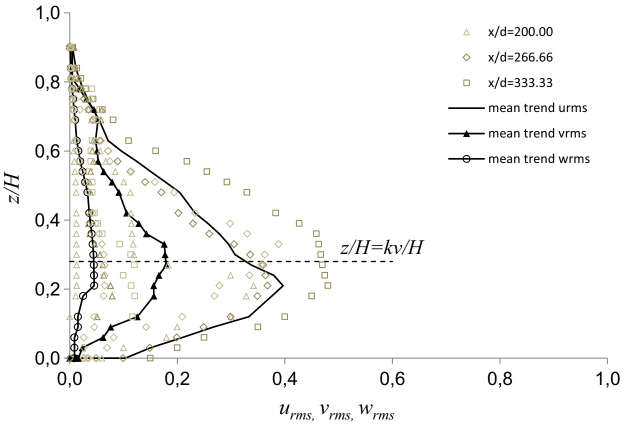

Fig. 3 Turbulent intensity components (m^2/s^2) at different relative distances x/d and the corresponding spatial average

In summary, the observed behavior suggests that the redistribution of the turbulence intensities and of the turbulent energy is affected by the presence of the vegetation.

Integral length scale and turbulent diffusion coefficients

According to Eq. (3), the knowledge of the integral length scale of turbulence is important to evaluate the turbulent dispersion and the energy transfer processes. In a cylinder array, Nepf (1999) verified that the integral length scale, l, depends on the disposition of the cylinders. In particular (see also in Tanino and Nepf 2008), l can be defined on the basis of both the cylinder's diameter, dc, and the distance between the cylinders, s. When $dc \leq s$, the turbulence is determined within stem wakes so that it can be assumed $l = dc$; when $dc > s$, the turbulence is generated in the interstices and it can be assumed $l = s$.

For the presented case, the integral length lj has been estimated by using the time series of the turbulent fluctuations and by estimating the frequency-weighted power spectral density (see also in Tanino and Nepf 2008). Figure 4 reports the integral lengths, normalized by the characteristic dimension d, estimated for individual locations x/d and the corresponding spatial average. From this figure, it can be observed that the integral scale has the order of magnitude of the stem's characteristic dimension, $O(d)$. Furthermore, we can see that such an order of magnitude remains almost constant along the directions x, y, z; this confirms that, in the case of dense vegetation, the turbulent behavior can be considered isotropic.

The vertical profiles of the dispersion coefficients K_{xx}, K_{yy} and K_{zz} are plotted in Fig. 5. From this figure, it appears clear that the dispersion coefficients assume low and almost equal values in the directions x, y, z. Thus, in the mixing layer, the longitudinal, transverse and vertical dispersion coefficients assume the same order of magnitude: $K_{xx} \cong K_{yy} \cong K_{zz} \cong O(10^{-3})$. This behavior indicates that the dense vegetation introduces turbulence at the scale of the vegetation width and limits the lateral dispersion between the vegetated elements. This result is also consistent with previous findings obtained by Termini (2016; see also in Termini and Di Leonardo 2018) in a curved vegetated-bed channel, which highlight that the presence of vegetation modifies the evolution of the turbulent structures limiting their development within and between the vegetated elements.

Terms of turbulent kinetic equation

In order to analyze the turbulence structure in the vegetated layer, the experimental data have been also used to explore the terms on right side of the turbulent kinetic energy

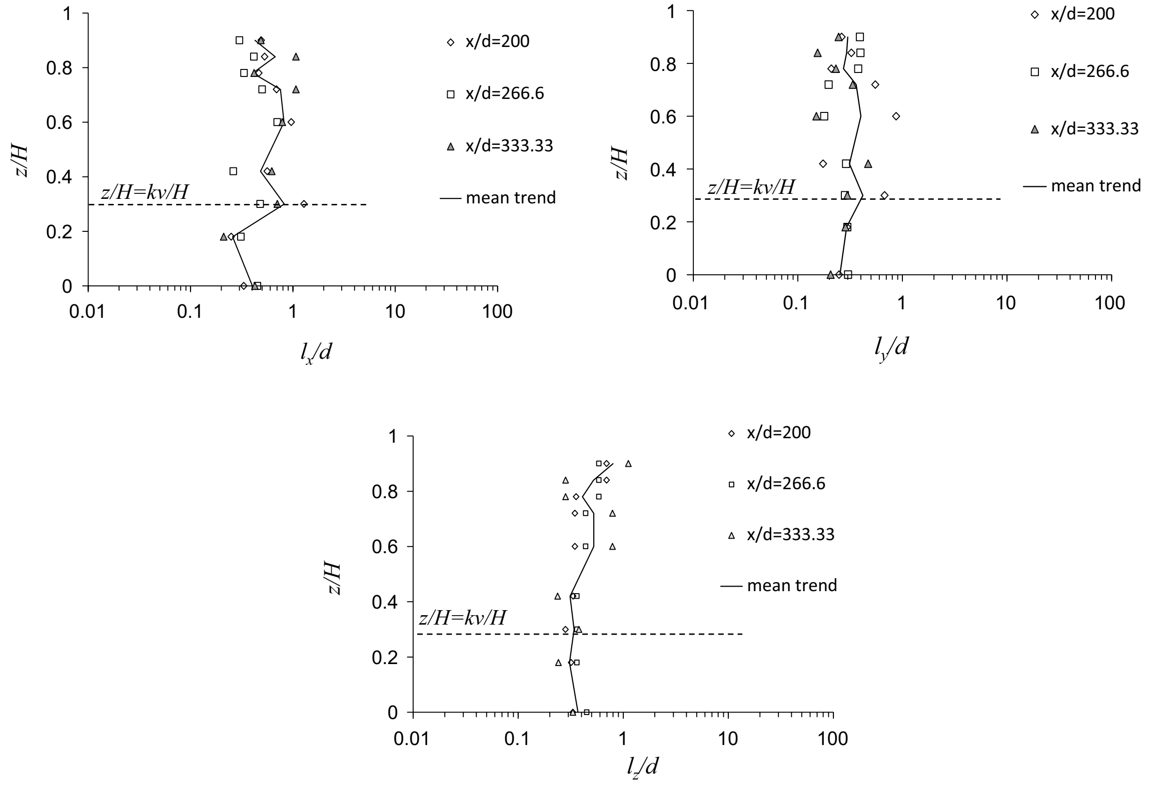

Fig. 4 Vertical profiles of the normalized integral length scales l_x, l_y and l_z

Eq. (6). In particular, the shear turbulence generation (P_s) and the turbulent transport term (T_d) have been determined according to Eq. (4) and the wakes turbulence generation (P_w) has been estimated according to Eq. (5). The pressure transport (T_p) is difficult to estimate from the measures and, according with other authors (Nepf 1999; Nezu and Sanjou 2008), it can be estimated as residual of the turbulent kinetic energy Eq. (6). The dissipation rate ε has to be estimated from theoretical considerations and different approaches have been applied in literature. Some authors (Lumley 1965; Antonia et al. 1991) evaluate the dissipation rate from the gradient of the turbulent fluctuation components; others (Lawn 1971; Nezu and Nakagawa 1993; Nezu and Sanjou 2008) consider the energy spectrum in the inertial sub-range or simplified forms of the Kolmogorov's equation (Ricardo et al. 2014).

In the present work, according to Nepf (1999), the dissipation ε has been estimated by taking into account that it scales with the ratio between the cubic of the characteristic velocity and the turbulent length scale (see in Pope 2000). Thus, on the basis of the results presented in the previous section "Integral length scale and turbulent diffusion coefficients," the turbulent length scale has been assumed equal to the stem's width, d, and, considering that the velocity scales with $\sqrt{k}$, the dissipation ε has been estimated as $\varepsilon \cong k^{3/2}d^{-1}$.

In Fig. 6, the estimated terms of the turbulent kinetic energy Eq. (6) are reported. It can be observed that, in the intermediate region, the shear production term, P_s, assumes values comparable to the wake production P_w. This is due to the fact that the shear generated in this region is a source of turbulence, in agreement to what observed by Nepf and Vivoni (2000) in the case of submerged rigid vegetation. Both the shear term and the wake production term, (P_s, P_w), assume the peak value close to the top of vegetation and then they decrease in value toward the bed; P_w assumes a second peak value slightly above the vegetation top. This could be due to the natural oscillation of the vegetation leaves. Thus, as Fig. 6 shows, in the region around the top of vegetation the sum between the terms P_w and P_s has the same order of magnitude as that of the dissipation but, inside the vegetation, and close to the bed, P_w assumes values larger than P_s. This is also in agreement with Nepf and Vivoni' (2000) findings for low submergence ratios where the wake production P_w was found larger than P_s inside vegetation so that P_w was assumed almost equal to the dissipation.

The turbulent diffusion T_d assumes positive low values near the bed and increases as one moves from the bed to the vegetation top; then it changes the sign and becomes negative. Moving toward the free surface, it changes again the sign becoming positive. This behavior demonstrates that

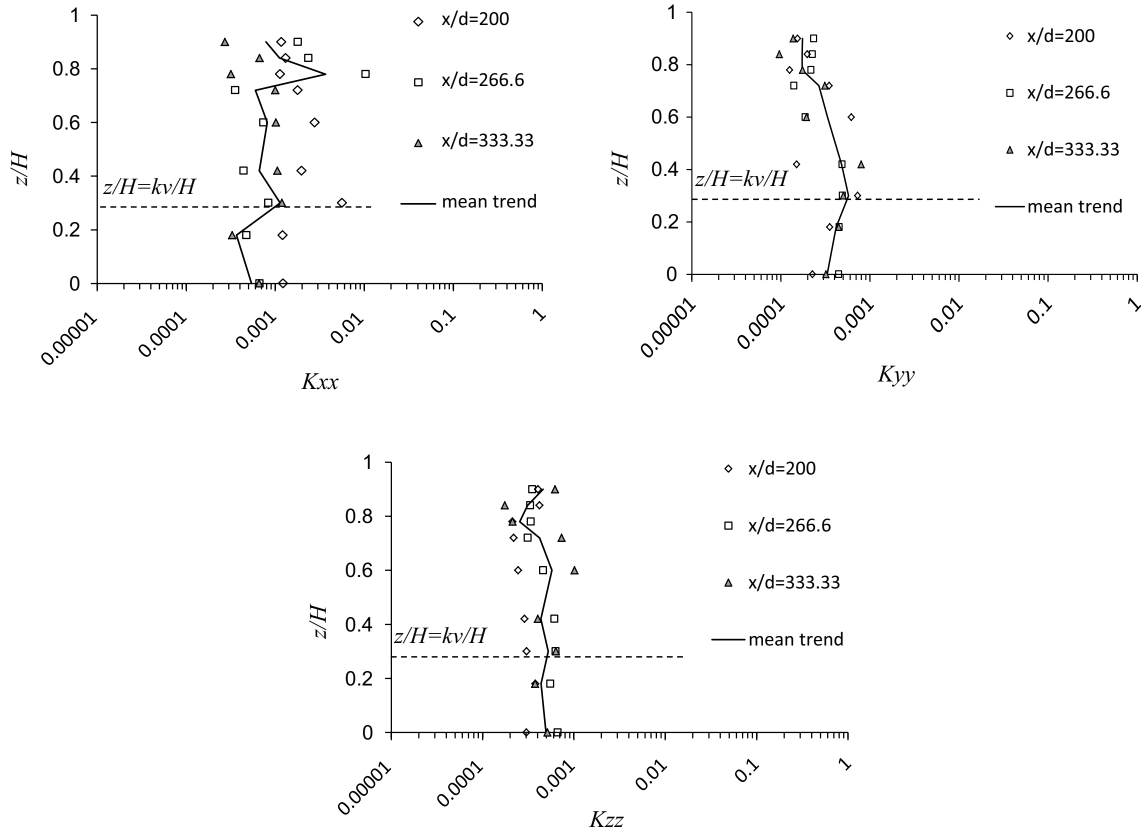

Fig. 5 Vertical profiles of the dispersion coefficients K_{xx}, K_{yy} and K_{zz} (m^2/s)

Fig. 6 Estimated terms of Eq. (6) (m^2/s^3)

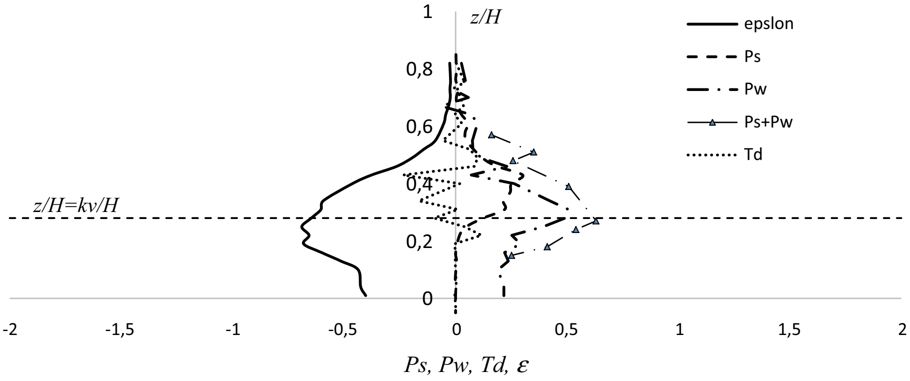

the turbulent energy is diffused both from the bed toward the free surface and from the free surface toward the bed. This could be also related to the evolution of coherent flow structures which transport turbulent energy and momentum both from the free surface toward the vegetation (sweep motion) and from the vegetation toward the free surface (ejection motion).

The contribution of the production terms can be also analyzed from Fig. 7 where the profiles of the total turbulence intensity (both for different locations *x/d* and the corresponding spatial average), given by the ratio $\sqrt{k}/u$, have been also reported. From this figure, it appears clear that $\sqrt{k}/u$ peaks slightly below the vegetation top where the sum of the production terms assumes also a peak value (see Fig. 6). This is consistent with other literature works (see among others in Nepf 1999; Poggi et al. 2004) highlighting that the turbulence produced at the vegetation top enhances the turbulence intensity affecting the turbulent diffusivity in the vegetated layer.

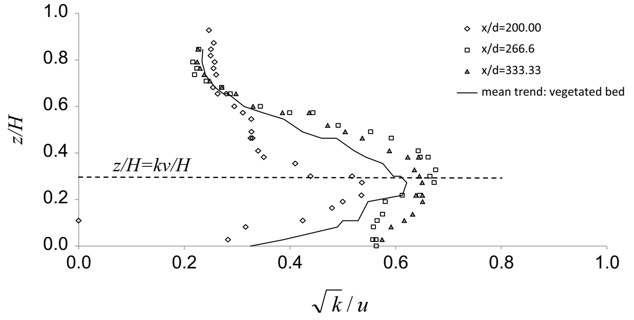

Fig. 7 Profile of the total turbulence intensity $\sqrt{k}/u$

Discussion

The knowledge of exchange processes and energy balance in the intermediate region between vegetated and non-vegetated zones is important for examining river's ecological equilibrium and dispersion of substances. But, because of the technical difficulties to collect experimental data, very few studies investigate the turbulent structure and dispersion mechanisms in the mixing layer zone in the presence of flexible submerged and dense vegetation. The presented results, based on refined velocity data collected over living flexible submerged and dense vegetation, contribute to overcome this lack.

An interesting result has been obtained for the integral turbulent length scale which is important to identify the turbulent transport processes. In particular, the analyses presented in this work have substantially shown that for submerged, flexible and dense vegetation condition the integral turbulent lengths l_x, l_y and l_z assume the order of magnitude of the vegetation width, d. This means that, in accordance with what previous researchers observed in the presence of dense rigid vegetation (Nepf 1999; Tanino and Nepf 2008; Nezu and Sanjou 2008), in the presence of dense flexible vegetation the turbulent length can be set by the stem geometry. In particular, the present research allows confirming that the integral turbulent length remains almost invariant with respect to the three directions so that the turbulence is isotropic. The fact that the turbulence is isotropic means that the turbulent eddies are intercepted and blocked by the presence of dense vegetation which limits their dimension independently by the direction. As demonstrated by De Serio et al. (2018), this behavior is different from that of flow over sparse rigid vegetation characterized by the anisotropy of the turbulence.

Furthermore, the results have shown that the dispersion coefficients assume a trend similar to that of the turbulent length scales, assuming low values along the *x, y, z* directions ($K_{xx} \cong K_{yy} \cong K_{zz} \cong O(10^{-3})$). This fatherly highlights that, the dense vegetation, introducing turbulence at the scale of the vegetation dimension, limits the lateral dispersion within the vegetated elements. This behavior is also consistent with previous findings obtained by Termini (2016—see also in Termini and Di Leonardo 2018) analyzing the turbulent flow structure in a curved channel with bed covered by flexible and dense vegetation. In particular, she verified that the vegetated elements control the size of the developing characteristic eddies which develop between them. This result suggests that, in contrast to what observed by Shucksmith et al. (2011), the trend and the value of the dispersion coefficient are not affected by the channel's plane-form.

The analysis of the terms of the turbulent kinetic energy has demonstrated that, in the intermediate region (mixing layer), the shear formed at the top of vegetation is an important source of turbulence so that the shear production term, P_s, is comparable to the wake production P_w. Inside the vegetation P_w is even larger than P_s. Both the shear and wake production terms, (P_s, P_w), assume the peak value close to the vegetation top and decrease as one moves toward the bed. In contrast to previous results obtained by Nepf and Vivoni (2000), in the presented case inside the mixing layer the dissipation balances the sum of the shear production term and the wake production term, ($P_s + P_w$). Furthermore, due to the natural oscillation of the vegetation leaves, P_w assumes a second peak value slightly above the vegetation top. This result is novel as compared to previous studies conducted in the presence either of rigid stems or of artificial cylindrical rods (Nepf and Vivoni 2000; Sivpure et al. 2015, 2016; Ricardo et al. 2014). In particular, the presented results demonstrate that the flexibility of vegetation could affect the distribution of the energy balance in the mixing layer. But, in accordance with what observed by Nepf and Vivoni (2000) for low relative water depths, the present analysis also indicates that, below the mixing layer and close to the bed, P_s assumes very small values, the dissipation decreases in value so that the dissipation balances P_w. Thus, the observed behavior indicates that, in the case of dense flexible vegetation, a wake layer characterized by low transport and low flow velocity occurs below the mixing layer and very close to the bed; inside the mixing layer, the dissipation balances the sum of the shear and wake production terms; above the mixing layer, the order of magnitude of the shear production is comparable to that of the dissipation ($P_s \cong \varepsilon$), in accordance with Nezu and Nakagawa (1993).

The term T_d, representing the turbulent diffusion, has the higher values close to the top of vegetation but it assumes peak positive values below the top of vegetation and negative peak values above it. This behavior demonstrates that the turbulent energy is diffused both from the bed toward the free surface and from the free surface toward the bed indicating the evolution of coherent flow structures which transport turbulent energy and momentum inside the vegetation (sweep motion) and toward the free surface (ejection motion). This is consistent with previous literature findings (Nezu and Sanjou 2008; Sivpure et al. 2015, 2016) indicating that ejection and sweep events govern the turbulence structure and the coherent motion between the vegetated and the non-vegetated zones. On the other hand, in agreement with others literature findings (see as an example Ghisalberti and Nepf 2006; Carollo et al. 2008; Termini 2015), the presence of the highest values of the turbulent intensity components close to vegetation top also indicates the formation of vortices with the center at the top of the vegetation.

Concluding remarks

The present study investigates the turbulent mixing and the dispersion processes in the presence of a living flexible, submerged and dense vegetation. The main results obtained in the present work can be summarized as follows:

- The turbulence intensities and energy distributions are strongly affected by the presence of the flexible vegetation;
- The integral turbulent length assumes the order of magnitude of the vegetation width, d, along the directions x, y, z so that the turbulence is isotropic. Thus, the dense vegetation introduces turbulence at the scale of the vegetation width, independently by the direction.
- The dispersion coefficients assume low and almost equal values along the directions x, y, z. Thus, the dense vegetation limits the lateral dispersion between the vegetated elements.
- The analysis of the terms of the turbulent kinetic energy has demonstrated that three layers can be distinguished along the vertical: the layer (wake layer) occurring below the mixing layer where the dissipation balances the wake production term P_w, in accordance with what observed by Nepf and Vivoni (2000) for low relative water depths; the intermediate layer (mixing layer) where the dissipation balances the sum of the shear and wake production terms ($P_s + P_w$) and the natural oscillation of the vegetation leaves could affect the energy distribution; the layer above the mixing layer where the order of magnitude of the shear production is comparable to that of the dissipation ($P_s \cong \varepsilon$), in accordance with Nezu and Nakagawa (1993);
- The vertical turbulent diffusion assumes in the mixing layer the higher values, but with variable sign, thus indicating the evolution of coherent motions between the vegetated and the non-vegetated zones.

In conclusion, the obtained results have demonstrated that in the case of dense vegetation the dispersion of the substances is strongly inhibited along all directions. In the mixing layer, the total turbulence intensity peaks where the production terms assume the higher values. In this region, the vertical turbulent diffusion assumes also the higher values with alternating positive and negative sign suggesting the generation of coherent motions which govern the turbulence structure and the transport of substances.

It should be noted that, despite the limitations related to the examined experimental conditions, the present work provides insights into complex turbulence structure and related exchange processes in the intermediate region between the region inside the vegetation and that above it.

Future research, performed by the combination of numerical and experimental simulations, will be directed toward the investigation of the evolution of turbulent coherent motions in the mixing layer and their effects on the substances transported and dissolved also varying the hydraulic and physical parameters which could influence the mixing processes.

References

Ackerman JD, Okumbo A (1993) Reduced mixing in a marine macrophyte canopy. Funct Ecol 7:305–309

Antonia RA, Kim J, Browne LWB (1991) Some characteristics of small-scale turbulence in a turbulent duct flow. J Fluid Mech 233:368–388

Brunet Y, Finnigan J, Raupach MR (1994) A wind tunnel study of air flow in waving wheat: single-point velocity statistics. Bound-Layer Meteorol 70:95–132

Carollo FG, Ferro V, Termini D (2002) Flow velocity measurement in vegetated channels. J Hydraul Eng ASCE 128(7):664–673

Carollo FG, Ferro V, Termini D (2005) Flow resistance law in channels with flexible submerged vegetation. J Hydraul Eng 131:554–564

Carollo FG, Ferro V, Termini D (2006) Experimental investigation of flow characteristics in vegetated channels. International Congress Riverflow 2006—Lisbon (Portugal) 6–8 Sept

Carollo FG, Ferro V, Termini D (2007) Analysing longitudinal turbulence intensity in vegetated channels. J Agric Eng 4:25–35

Carollo FG, Ferro V, Termini D (2008) Determinazione del profilo di velocità e di intensità della turbolenza in canali vegetati, 31° Convegno Nazionale di Idraulica e Costruzioni Idrauliche, 9–12 Sept Perugia, Italy **(in Italian)**

Carpenter SR, Lodge DM (1986) Effects of submersed macrophytes on ecosystem processes. Aquat Bot 26:341–370

Chandler M, Colarusso P, Buchsbaum R (1996) A study of eelgrass beds in Boston Harbor and Northern Massachusetts bays. Proj. Rep. Off. Res. Dev. US EPA, Narragansett, RI

Coceal O, Dobre TG, Thomas TG, Belcher SE (2007) Structure of turbulent flow over regular arrays of cubical roughness. J Fluid Mech 589:375–409

Corenblit D, Tabacchi E, Steiger J, Grunell AM (2007) Reciprocal interactions and adjustments between fluvial landforms and vegetation dynamics in river corridors: a review of complementary approaches. Earth Sci Rev 84(1–2):56–86

Cornacchia L, Licci S, Nepf H, Folkard A, van der Wal D, van de Koppel J, Puijalon S, Bouma TJ (2018) Turbulence-mediated facilitation of resource uptake in patchy stream macrophytes. Limnol Oceanog. https://doi.org/10.1002/lno.11070

De Serio F, Ben Meftah M, Mossa M, Termini D (2018) Experimental investigation on dispersion mechanisms in rigid and flexible vegetated beds". Adv Water Resour 120:98–113

Defina A, Bixio AC (2005) Mean flow and turbulence in vegetated open channel flow. Water Resour Res 41:W07006. https://doi.org/10.1029/2004WR003475

Ellenberg HH (2009) Vegetation ecology on Central Europe. Cambridge University Press, Cambridge

Finnigan JJ, Shaw RH (2008) Double-averaging methodology and its application to turbulent flow in and above vegetation canopies. Acta Geophys 56(3):534–561

Folkard AM (2011) Vegetated flows in their environmental context: a review. Eng Comput Mech ICE Proc 164(EM1):3–24

Ghisalberti M, Nepf H (2006) The structure of the shear layer in flows over rigid and flexible canopies. Environ Fluid Mech 6:277–301

Khaleghi E, Ramin AA (2005) Study of the effects of salinity on growth and development of lawns (*Lolium perenne* L., *Festuca arundinacea* and *Cynodon dactylon*). JWSS 9(3):57–68

Kubrak E, Kubrak J, Kiczko A (2015) Experimental Investigation of kinetic energy and momentum coefficients in regular channels with stiff and flexible elements simulating submerged vegetation. Acta Geophys 63(5):1405–1422

Lawn CJ (1971) The determination of the rate of dissipation in turbulent pipe flow. J Fluid Mech 48:477–505

Leuven RSEW, Ragas AMJ, Smits AJM, van der Velde G (2006) Living rivers: trends and challenges in science and management. Springer, Amsterdam

Łoboda AM, Bialik RJ, Karpiński M, Przyborowski Ł (2019) Two simultaneously occurring *Potamogeton* species: similarities and differences in seasonal changes of biomechanical properties. Pol J Environ Stud 28(1):1–16

Lumley JL (1965) Interpretation of time spectra measured in high-intensity shear flows. Phys Fluids 6:1056–1062

Nepf H (1999) Drag, turbulence and diffusivity in flow through emergent vegetation. Water Resour Res 35(2):479–489

Nepf HM (2012) Hydrodynamics of vegetated channels. J Hydraul Res 50(3):262–279

Nepf H, Ghisalberti M (2008) Flow and transport in channels with submerged vegetation. Acta Geophys 56(3):753–777

Nepf H, Vivoni E (2000) Flow structure in depth-limited, vegetated flow. J Geophys Res 105(C12):28547–28557

Nepf H, Koch EW (1999) Vertical secondary flows in submersed plant-like arrays. Limnology and Oceanography 44(4):1072–1080

Nepf H, Mugnier C, Zavistoski R (1997) The effects of vegetation on longitudinal dispersion. Estuar Coast Shelf Sci 44:675–684

Nezu I, Nakagawa H (1993) Turbulence on open channel flows. A.A. Balkema Publishers, Rotterdam

Nezu I, Sanjou M (2008) Turbulence structure and coherent motion in vegetated canopy open-channel flows. J Hydro-environ Res 2:62–90

Nikora V, Goring DG, McEwan I, Griffiths G (2001) Spatially-averaged open-channel flow over a rough bed. J Hydraul Eng ASCE 127(2):123–133

Nikora V, Lamed S, Nikora N, Debnath K, Cooper G, Reid M (2008) Hydraulic resistance due to aquatic vegetation in small streams: field study. J Hydraul Eng 134(9):1326–1332

Okamoto T, Nezu I (2009) Turbulence structure and "Monami" phenomena in flexible vegetated open-channel flows. J Hydraul Res 47:798–810

Oldham CE, Sturman JJ (2001) The effect of emergent vegetation on convective flushing in shallow wetlands: scaling and experiments. Limnol Oceanogr 46(6):1486–1493

Poggi D, Porporato A, Ridolfi L, Albertson JD, Katul GG (2004) The effect of vegetation density on canopy sub-layer turbulence. Bound-Layer Meteorol 111:565–587

Poggi D, Krug C, Katul GG (2009) Hydraulic resistance of submerged rigid vegetation derived from first-order closure models. Water Resour Res 45:W10442

Pope SB (2000) Turbulent flows. Cambridge University Press, Cambridge

Raupach M, Shaw R (1982) Averaging procedures for flow within vegetation canopies. Bound-Layer Meteorol 22:79–90

Raupach MR, Coppin PA, Legg BJ (1986) Experiments on scalar dispersion in a model plant canopy, part I: the turbulence structure. Bound-Layer Meteorol 35:21–52

Ricardo AM, Koll K, Franca MJ, Schleiss A, Ferreira RML (2014) The terms of turbulent kinetic energy budget within random arrays of emergent cylinders. Water Resour Res 50:4131–4148

Righetti M (2008) Flow analysis in a channel with flexible vegetation using double-averaging method. Acta Geophys 56:801

Rutherford JC (1994) River mixing. Cambridge University Press, Cambridge

Schnauder I, Sukhodolov AN (2012) Flow in a tightly curving meander bend: effects of seasonal changes in aquatic macrophyte cover. Earth Surf Proc Land 37(11):1142–1157

Schultz RC, Colletti JP, Isenhart TM, Simpkins WW, Mize CW, Thompson ML (1995) Design and placement of a multi-species riparian buffer system. Agrofor Syst 29:201–226

Shucksmith JD, Boxall JB, Guymer I (2011) Determining longitudinal dispersion coefficients for submerged vegetated flow. Water Resour Res 47(W10516):1–13

Sivpure V, Devi TB, Kumar B (2015) Analysing turbulent characteristics of flow over submerged flexible vegetated channel. ISH J Hydraul Eng 21(3):265–275

Sivpure V, Bebi TB, Kumar B (2016) Turbulent characteristics of densely flexible submerged vegetated channel. ISH J Hydraul Eng 22(2):220–226

Stoesser T, Kim S, Diplas P (2010) Turbulent flow through idealized emergent vegetation. J Hydraul Eng 136(12):1003–1017

Tanino Y, Nepf H (2008) Lateral dispersion in random cylinder arrays at high Reynolds number. J Fluid Mech 600:339–371

Termini D (2013) Effect of vegetation on fluvial erosion processes: experimental analysis in a laboratory flume. Procedia Environ Sci 19:904–911

Termini D (2015) Flexible vegetation behavior and effects on flow conveyance: experimental observations. Int J River Basin Manage 13(4):401–411

Termini D (2016) Experimental analysis of the effect of vegetation on flow and bed shear stress distribution in high-curvature bends. Geomorphology 274:1–10

Termini D, Di Leonardo A (2018) Turbulence structure and implications in exchange processes in high-amplitude vegetated meanders: experimental investigation. Adv Water Resour 120:114–127 **(in press)**

Acta Geophysica (2019) 67:971–986
https://doi.org/10.1007/s11600-019-00280-8

RESEARCH ARTICLE - SPECIAL ISSUE

Investigation of flow resistance exerted by rigid emergent vegetation in open channel

Antonino D'Ippolito[1] · **Agostino Lauria**[1] · **Giancarlo Alfonsi**[1] · **Francesco Calomino**[1]

Received: 13 September 2018 / Accepted: 20 March 2019 / Published online: 29 March 2019

Abstract

The issue of the resistance to flow in open channels with vegetation has been considered by several researchers mainly experimentally, but the case of rigid emergent vegetation with linear stem arrangement is scarcely investigated. In the present work, the results are presented of an experimental investigation related to the case of rigid emergent vegetation that has been modeled by placing small rods on the bottom of a laboratory flume in aligned configuration. Tests have been executed by varying the flow rate, the bottom slope and the number and the diameter of the rods, by directly measuring the drag force exerted by the flow on a given number of rods, and the water-level profiles. A new expression has been devised for the drag coefficient as a function of the vegetation density, weakly dependent on the stem Reynolds number that allows the use of the former also in large-scale cases. The experimentally measured forces exerted by the flow on the rods have been also compared with the results obtained by applying the momentum equation in integral form to given control volumes, exhibiting a general agreement, but also showing that the use of this technique for the evaluation of the drag coefficients can give rise to not negligible errors. One of the experimental tests has been numerically simulated with the RANS technique (Reynolds-Averaged Navier–Stokes equations), and it is found that the results, mainly in terms of water-level profiles, confirm the ability of such a numerical technique in investigating this complex category of flow cases.

Keywords Rigid emergent vegetation · Drag coefficient · OpenFOAM · RANS equations

Introduction

Vegetation is found in natural catchments and rivers in different forms and is of utmost importance for hydrologists and hydraulic engineers as related to flood-risk studies, sediment-transport studies and the design of river restoration schemes (among others, Bennett and Simon 2004; Aberle and Jarvela 2013; D'Ippolito et al. 2013; Vargas-Luna et al. 2016). The analysis of the interaction between fluid flow and vegetation is a fairly complex issue, due to both the different physical mechanisms that play a role in the phenomenon, and the biomechanical properties that characterize the different types of vegetation. Under a strictly hydraulic viewpoint, the vegetation basically induces an increase in the flow resistance, and this—in a constant flowrate condition—results in decreasing velocities and increasing water levels, so increasing the risk of floods. Under a general viewpoint, and in virtue of their different behavior, in the literature one usually distinguishes between flow cases with rigid and flexible vegetation in different conditions (submerged and/or emergent, with and without leaves, with or without sediment transport). A number of research works has been executed in the past on the interaction between flow and vegetation in the general case of rigid vegetation (Li and Shen 1973; Petryk and Bosmajian 1975; Pasche and Rouvé 1985; Nepf 1999; Ishikawa et al. 2000; Stone and Shen 2002; James et al. 2004; Tanino and Nepf 2008; Kothyari et al. 2009; Cheng and Nguyen 2011; Mulahasan and Stoesser 2017; D'Ippolito et. al. 2018), in the general case of flexible vegetation (Kouwen and Unny 1973; Temple 1986; Fathi-Moghadam and Kouwen 1997; Wu et al. 1999;

✉ Antonino D'Ippolito
antonino.dippolito@unical.it

Agostino Lauria
agostino.lauria@unical.it

Giancarlo Alfonsi
giancarlo.alfonsi@unical.it

Francesco Calomino
francesco.calomino@unical.it

[1] Department of Civil Engineering, University of Calabria, Via Bucci 42b, 87036 Rende, Cosenza, Italy

Kouwen and Fathi-Moghadam 2000; Jarvela 2002; Carollo et al. 2002; Jarvela 2004; Armanini et al. 2005; Carollo et al. 2005; Righetti 2008; Aberle and Jarvela 2013) and in that of both types of them (Freeman et al. 2000). Velocity distributions and turbulence properties in vegetated channels have also been observed by Liu et al. (2008), and, by means of experimental and numerical models, analyzed by Shimizu and Tsujimoto (1994), Nepf (1999), Nepf and Vivoni (2000), López and García (2001), Stephan and Gutknecht (2002), Neary (2003), Erduran and Kutija (2003), Stoesser et al. (2003), Defina and Bixio (2005), Choi and Kang (2004), Stoesser et al. (2010). It has to be noted that the majority of the aforementioned studies have been executed at low values of the Reynolds number, so that, inspite of the remarkable amount of work that has been accomplished, no expressions have been devised for the drag force as exerted by the flow when large stems or trunks are involved.

Formally, the drag force exerted by a water flow against a single vertical circular cylinder of diameter d can be expressed as $F = C_D \rho h d V^2/2$ where C_D is the drag coefficient, ρ is the water density, V is the flow mean velocity and h is the depth of the immersed portion of the body. According to Schlichthing (1979), the drag coefficient varies between 1.0 and 1.2 for the stem Reynolds numbers Re_d ranging between 10^3 and 10^5, being $Re_d = Vd/\nu$ (ν is the water kinematic viscosity, see also at the data of James et al. 2004 for a single rod of diameter 0.5 mm in Fig. 1). When a group of N cylinders is considered, the total drag force is:

$$F_D = N C_D \rho h d V^2/2 \tag{1}$$

where C_D is now an average drag coefficient and V is the mean velocity in the reach populated by the N cylinders, as given by the ratio between the discharge and the channel cross section. As can be shown by dimensional analysis, for emergent rigid vegetation the drag coefficient (1) is a function of the stem roughness, the stem shape, the stem Reynolds number, array density and pattern and flow characteristics.

With reference now to the more specific field of rigid emergent vegetation, rigid stems have been often represented by cylinders of different materials. The drag coefficient of a single cylinder is affected by the wake structure and depends on the Reynolds number at relatively low values of the latter, while in the case in which more than one cylinder is present, the phenomenon changes. For example, if two or more additional cylinders are present downstream from the first, the wake of the upstream cylinder reduces the drag on the subsequent ones, and this effect increases as the distance between the downstream cylinders decreases (Nepf 1999). Thus, the bulk drag coefficient (based on the bulk velocity) can significantly differ from that relative to an isolated emergent cylinder (Aberle and Jarvela 2013). In this context, the areal density λ, defined as:

$$\lambda = \frac{n\pi d^2}{4} \tag{2}$$

where d is the stem diameter and n the number of stems per unit area becomes a parameter of utmost importance. In the present work, we will focus on densities of the order of at most 10%, and on stem Reynolds numbers of the order of 600 and larger, because, from this value on, the C_D generally only weakly depends on Re_d.

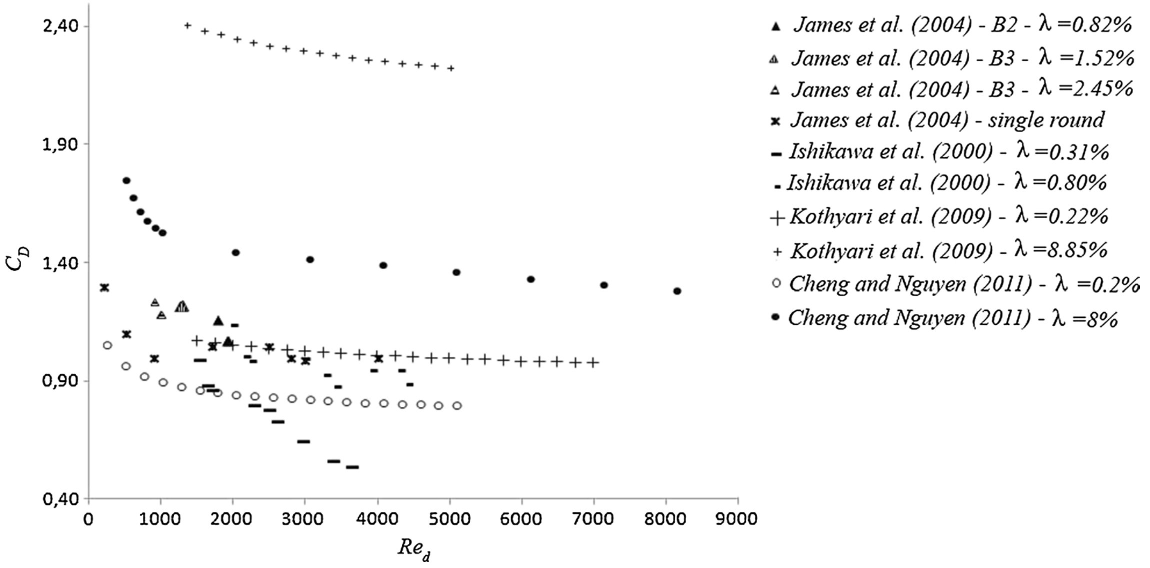

Fig. 1 Drag coefficient versus stem Reynolds number

Among the firsts, Li and Shen (1973), employing the decay and spread characteristics of wakes that form behind cylinders, studied the flow resistance of non-submerged vegetation in parallel and staggered patterns. They observed that the various patterns of tall vegetation have a rather significant effect on the retardation of flow rates, and the staggered grouping is the most effective in reducing the flowrates. The authors report the results of a series of numerical tests in which they used the drag coefficients for groups of parallel or staggered stems, considering the spread and decay rate of a wake, to obtain the water depths by a force balance equation. From their data, it is possible to calculate, for each stem configuration, an average value of the drag coefficient. Few and sparse results are obtained, and, even though one cannot observe any clear dependence on Re_{d}, one can conclude that the drag coefficients in the case of the staggered pattern are larger than those of the parallel pattern. Petryk and Bosmajian (1975) applied the momentum equation in integral form to a fluvial reach with vegetation and obtained an expression for the Manning coefficient in terms of boundary roughness, hydraulic radius and vegetation characteristics, as given by the drag coefficient times the vegetation area in the streamwise direction per unit length and unit area. According to their results, the drag coefficient is of the order of 1.0. As reported by Pasche and Rouvé (1985) and Jarvela (2004), Lindner (1982) extended the pioneering work of Li and Shen (1973) and derived an empirical relation where the drag coefficient is a function of that relative to a single cylinder in an ideal 2-D flow, and of two additional terms representing blockage and free-surface effects. Nepf (1999), in studying arrays of stems randomly arranged, noted that the C_{D} varies only weakly with the stem Reynolds number (Re_{d}), whose values ranged from 4000 to 10,000. The C_{D} was of the order of 1.0 when the areal density was of the order of a few percentages. The author considered areal densities from 3 up to 30%, and for these values the average C_{D} strongly decreased with an increasing vegetation density, due to the fact that the cylinders on the downstream portion of the channel reach are shielded by those upstream. This statement was contradicted later by Tanino and Nepf (2008), who found, for densities from 9 to 35%, C_{D} values increasing with λ. For this reason, we will not take into account the data of Nepf (1999). James et al. (2004) analyzed the variability of the drag coefficient with the stem Reynolds number in the case of single stems with and without leaves. For groups of cylinders arranged in staggered patterns, and using the momentum equation, they obtained a function that allowed the computation of the drag coefficients (one can refer to Fig. 1 in which, and among others, some of their results are reported, showing that as Re_{d} increases, C_{D} tends to remain constant). Stone and Shen (2002) developed a method for predicting the velocity in the stem layer. The values of C_{D} observed by the authors (and related to the apparent velocity = discharge/gross cross-sectional area) range between 1.10 and 1.93. Unfortunately, the authors give the C_{D} values for the experimental densities, but do not give enough information to obtain the variation of C_{D} with Re_{d}. Tanino and Nepf (2008) carried out an experimental study with randomly distributed circular cylinders with diameter of 0.64 cm, density (the cylinder area per unit bed area) varying from 0.091 to 0.35 and Reynolds stem numbers ranging from 25 to 685. They found that the drag coefficient (temporally and spatially averaged) increases with the density and, for each density, decreases as the Reynolds number increases. The range of densities considered in this research is far from the purposes of the present study, so that we will not take into account their data.

From the aforementioned literature, it emerges that C_{D} can oscillate within a wide interval of values, depending on the density, the spatial distribution of the obstacles and the flow velocity. It has also to be noted that the majority of the above results have been obtained with indirect methods. Direct measurements have been performed, among others, by Ishikawa et al. (2000) and Kothyari et al. (2009). They measured experimentally the action of the water flow onto a rigid circular cylinder located among other cylinders with the same diameter, as distributed on a grid with staggering pattern, forming an angle in the flow direction of 60° and 90°, respectively. In both cases, the force exerted by the flow in the streamwise direction on a "representative" cylinder at the center of the flume was measured by means of a load cell installed on its upper part. In Ishikawa et al. (2000), the vegetation was simulated by staggered cylindrical rods of diameter 4 mm with densities λ equal to 0.31% and 1.26%, or 6.4 mm, with densities equal to 0.8% and 3.2%. One can refer to Fig. 1 where the results of two tests presented by these authors are reported. The authors give three equations for the drag coefficient as a function of the areal density, depending on the flume slope. In the tests of Kothyari et al. (2009), the vegetation was made of staggered stainless steel rods with diameter of 1 cm and the density λ ranged between 0.22% and 8.85%. The flow velocity was estimated as the flowrate divided by the flume cross section and $(1-\lambda)$, so obtaining the so-called pore velocity V_{v}, given by:

$$V_{\mathrm{v}} = \frac{V}{(1-\lambda)} \tag{3}$$

Eight values of λ in the aforementioned interval were tested, and the authors noted how the drag coefficient remarkably increased with λ, and varied only a little with the stem Reynolds number. They proposed the equation:

$$C_{\mathrm{Dv}} = 1.53[1 + 0.45\ln(1 + 100\lambda)]Re_{\mathrm{dv}}^{-3/50} \tag{4}$$

where C_{Dv} and Re_{dv} are, respectively, the drag coefficient and the stem Reynolds number computed with V_{v}. Using Eq. (4)

of Kothyari et al. (2009), we computed the C_{Dv}, and the C_{D} values with the apparent velocity V for two densities, being:

$$C_{\mathrm{D}} = \frac{C_{\mathrm{Dv}}}{(1-\lambda)^2} \tag{5}$$

The results are shown in Fig. 1. One can observe that the drag coefficients vary a little with the stem Reynolds number, tending to become constant as the latter increases.

Cheng and Nguyen (2011) introduce the hydraulic radius r_{v} that takes the vegetation into account, being:

$$r_{\mathrm{v}} = \frac{\pi}{4}\frac{(1-\lambda)}{\lambda}d \tag{6}$$

When the wall and bottom effects are negligible, the hydraulic radius is only a function of the density and the diameter of the vegetation. This vegetation-related hydraulic radius is used together with the pore velocity to define a new Reynolds number, the vegetation Reynolds number:

$$Re_{\mathrm{v}} = \frac{V_{\mathrm{v}} r_{\mathrm{v}}}{\nu} \tag{7}$$

Using experimental data from several authors (random, staggered, only one case linear), they showed that the drag coefficient, relative to the pore velocity (C_{Dv}), decreases monotonically with the increase in the vegetation Reynolds number and propose the following equation:

$$C_{\mathrm{Dv}} = \frac{50}{Re_{\mathrm{v}}^{0.43}} + 0.7\left[1 - \exp\left(-\frac{Re_{\mathrm{v}}}{15{,}000}\right)\right] \tag{8}$$

Based on Eq. (8), in the range of Re_{v} from 1×10^2 to 6×10^5, and with λ in the range from 0.002 to 0.08, the drag coefficient varies between 8.2 and 0.87, respectively. Being:

$$Re_{\mathrm{d}} = \frac{4\lambda Re_{\mathrm{v}}}{\pi} \tag{9}$$

and based on expression (5), we computed the C_{D} values for two densities (Fig. 1). Also with expression (8) of Cheng and Nguyen (2011), the C_{D} tends to become constant with increasing Re_{d}. Wang et al. (2014) in a study of incipient bed shear-stress partition in mobile-bed channels investigate the vegetation drag coefficient. The tests were conducted in uniform flow, the diameter of one vegetation element was 6 mm and a regular vegetation parallel pattern was adopted with variable distances. By ignoring the bed surface shear stress, an empirical formula was developed by data fitting in which the drag coefficient resulted a function of the Reynolds number, as calculated with the vegetation-related hydraulic radius of Cheng and Nguyen (2011), the ratio between vegetation diameter and flow depth, and the vegetation density. This equation gives values of C_{D} decreasing with the stem density, in a difference with respect to other results presented in Fig. 1. Vargas-Luna et al. (2016) published a wide-ranging work about the effect of vegetation on river morphology. They carried out experimental tests about rigid vegetation represented by wooden rods with 2 mm diameter, finding that the flow resistance is decreasing with increasing stem Reynolds numbers. Moreover, the friction factor $C_{\mathrm{f}} = g/C^2$ (C is the Chézy coefficient resulting from both the bed and stem resistance to flow) is increasing with the vegetation density. Using a method developed by Baptist (2005) to predict the total flow resistance of a vegetated river with a C_{D} value equal to 1, and with the stem Reynolds numbers ranging from 180 to 600, they obtain valid simulations of the Chézy coefficients for the highest densities only, while, in general, these coefficients and the mean velocities were producing an underestimation of the water depths. Mulahasan and Stoesser (2017) present the results of tests concerning open-channel flow through a line of vertically oriented circular rods, representing the bank line vegetation. The tests were carried out in a uniform flow condition, and the authors compute the drag coefficient by means of the momentum equation based on the measured uniform flow depth, taking into account the bed resistance and correcting it for flow blockage. The drag coefficient exhibits a limited sensitivity to the stem Reynolds number. In this case, it is uncertain how to compute a vegetation density as defined in Eq. (2), so that, even though interesting, these results will not be considered as related to the present work.

Due to the scarcity of data in the case of parallel rod arrangement, we carried out the research mirrored in the present work. By further looking at the literature, in the numerical field, there are some studies on the resistance to flow in vegetated open channels, aiming at the understanding of the role that vegetation plays in influencing the hydrodynamic behavior of water bodies. Among others, Shimizu and Tsujimoto (1994) and López and Garcia (1997) simulated steady uniform flows through vegetation by means of the k–ε turbulence model with wall functions. They also introduced a term representing the vegetative drag in the Reynolds-averaged Navier–Stokes (RANS) equations. Neary (2003) presented a numerical solution of the RANS equations using a near-wall k–ω turbulence closure model for a one-dimensional fully developed open-channel flow with vegetative resistance, as developed and validated with the experimental measurements of Shimizu and Tsujimoto (1994). Defina and Bixio (2005) performed a number of numerical simulations using the k–ε and the two-layer model in order to test their ability to predict the flow field in the presence of rigid, complex-shaped vegetation with leaves. A good agreement was found between the results of the model and the measurements in comparing velocity and turbulent shear stress. Fischer-Antze et al. (2001) computed the velocity distributions in a channel partially covered with vegetation using the k–ε turbulence model, where the vegetation was modeled as vertical circular cylinders. All the tests showed a good agreement between computed and measured velocity profiles. Kim and Stoesser (2011) performed RANS and LES numerical simulations of flow through emergent vegetation, finding a good agreement with experimental measurements. Overall, it has to be noted again that, at least in the particular case of rigid emerging vegetation, from the results of neither the aforementioned experimental studies, nor those of the numerical, no expressions for the drag coefficient in vegetated channels have been developed that could be used in real-flow cases, i.e., characterized by high flow velocities and large rod diameters, similar to those of actual trees.

The aim of the present work is twofold: (1) presenting experimental results about the resistance to flow (in terms of drag force) due to rigid emergent vegetation in a parallel arrangements that, in a difference from the above literature, result weakly dependent on the Reynolds number at high values of the latter, so that they can be extended to cases where flow velocities and stem diameters are large, (2) investigating the accuracy and the suitability of the k–ω SST turbulence closure model in solving the RANS equations to simulate an observed water-level profile in a specific flow case (among those tested experimentally), by also monitoring the induced perturbations of the free surface.

Materials and methods

Experimental setup

The experiments have been executed in the "Laboratorio Grandi Modelli Idraulici" of the Department of Civil Engineering of the University of Calabria. A variable-slope hydraulic flume (11.13 m long) was used, with bottom made of PVC, of width $b=0.382$ m and plexiglass walls (0.21 m high). The flowrate could be regulated by means of a valve and measured with a Thomson weir downstream from the flume outlet. The vegetation has been modeled by means of two sets of small wooden circular cylindrical rods ($d=0.8$ and 1.0 cm) placed in central portions of the flume of lengths variable between 1.8 and 2.2 m (Fig. 2). The rods were vertically placed on the bottom of the flume and were secured to two wooden box-structured plates. The group of cylinders on which the drag forces were measured was maintained at a distance of about 1 mm from the bottom and was connected through another plate to a Vishay Tedea–Huntleigh load cell with sensitivity of around 0.01 N placed between the two box-structured plates mentioned above (Fig. 3), that has been calibrated against a reference laboratory load cell. In Table 1, the characteristic parameters of the 70 experimental tests are reported.

Three different bedslopes (i) have been considered, $i_1=0.48\%$, $i_2=1.35\%$, $i_3=2.02\%$, and in all tests the rods were arranged on four square meshes (D3, D4, D5, D9) at different distances, multiples of $\Delta x=\Delta y=4.24$ cm (Fig. 4).

Fig. 2 Hydraulic flume with rod-simulated vegetation

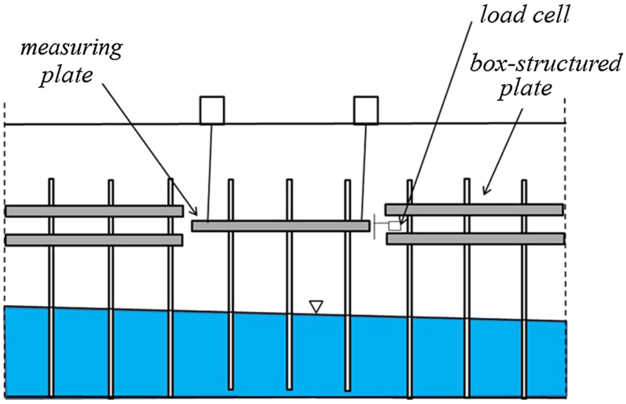

Fig. 3 Experimental setup for measurement of forces on rods

Momentum equation

In order to compare the experimental results (see "Results") with those obtained using the momentum equation in integral form (applied to given control volumes) in terms of drag forces exerted on the stems by the fluid flow, the following procedure has been followed. Consider a channel reach of width b in a steady free-surface flow (i is the slope of the bed, Q is the flowrate) and a control volume of length L containing a number N of stems (actually vertical cylinders, see also at Fig. 5). To the considered control volume, one can apply the momentum equation in integral form (bold is vector):

$$\boldsymbol{G}+\boldsymbol{T}+\boldsymbol{S}_1+\boldsymbol{S}_2+\boldsymbol{M}_1-\boldsymbol{M}_2+\boldsymbol{F}=0 \tag{10}$$

where $\boldsymbol{G}$ is the weight of the fluid in the control volume, $\boldsymbol{T}$ is the friction of the channel walls and bed, $\boldsymbol{S}$ is the hydrostatic forces, $\boldsymbol{M}$ is the momentum fluxes, $\boldsymbol{F}$ globally represents the

Table 1 Characteristic parameters of experimental tests (see at Fig. 4 for the meaning of symbols)

Test	*d* (cm)	Arrangement	*L* (cm)	λ (%)	*i* (%)
1–3	1.0	D4	25.44	0.97	2.02
4–8	1.0	D9	21.20	4.36	2.02
9–13	1.0	D3	25.44	0.48	2.02
14–16	1.0	D9	21.20	4.36	0.48
17–19	1.0	D4	25.44	0.97	0.48
20–23	1.0	D5	25.44	1.21	1.35
24–27	1.0	D4	25.44	0.97	1.35
28–31	1.0	D3	25.44	0.48	1.35
32–37	1.0	D9	21.20	4.36	1.35
38–40	1.0	D5	25.44	1.21	2.02
41–44	0.8	D3	25.44	0.31	1.35
45–48	0.8	D5	25.44	0.78	1.35
49–52	0.8	D9	21.20	2.79	1.35
53–56	0.8	D9	21.20	2.79	0.48
57–60	0.8	D9	21.20	2.79	2.02
61–64	0.8	D5	25.44	0.78	0.48
65–67	0.8	D3	25.44	0.31	0.48
68–70	0.8	D3	25.44	0.31	2.02

resistance to flow (in terms of drag force) due to the stems and subscripts 1 and 2 refer to the upstream and downstream cross sections, respectively.

By projecting expression (10) along the flow direction, one obtains:

$$F = P - T + S_1 - S_2 + M_1 - M_2 \tag{11}$$

where P is the projection of the weight term along the flow direction. The drag force F in (11) can be seen as the sum of the drag forces on the single trunks by assuming for the velocity an average value between V_1 and V_2, respectively. By knowing the values of the flowrate Q, of h_1 and h_2, and by taking into account the continuity equation in the form $Q = bV_1h_1 = bV_2h_2$, after estimating the wall and bed resistance, one ends with Eq. 11 with only F as an unknown term. The above equations are actually in some way simplified, and this gives rise to a number of uncertainties, as related to their practical application, as follows: (1) one cannot be absolutely sure that the resistance to flow of riverbed and banks can be evaluated independently from the resistance of the stems. Anyway, the resistance to flow associated to riverbed and banks is usually largely less than that of the stems, in particular when the density is high; (2) the shear stress on the wetted perimeter of a free-surface flow is not uniformly distributed; (3) the momentum coefficients in the momentum-flux terms in Eqs. (10) and (11) are taken equal to 1.

By knowing the drag force F exerted on the whole control volume, the drag force F_p exerted on the number of stems hold by the measuring plate can be expressed as:

$$F_\mathrm{s} = F\frac{N_\mathrm{p}}{N} \tag{12}$$

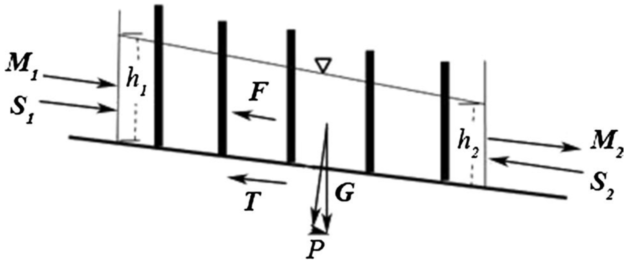

Fig. 5 Forces on control volume in free-surface flow

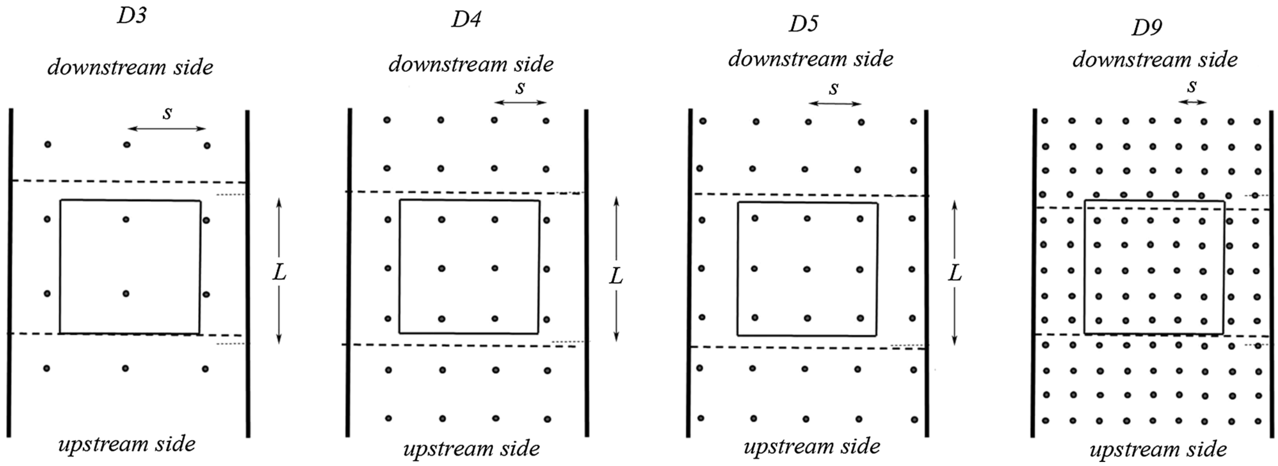

Fig. 4 Rod arrangements of types D3, D4, D5 and D9 (inner continuous lines define the measuring plate)

where N_{p} is the number of rods on the measuring plate ($N_{\mathrm{p}} = 2, 6, 9, 25$ in the D3, D4, D5 and D9 arrangements, respectively) and N is the number of rods in the whole control volume ($N = 6, 12, 15, 45$ in the D3, D4, D5 and D9 arrangements, respectively, see also at Fig. 4). It has to be also observed that, due to the relatively limited width of the flume, the force exerted by the flow on the stems along the spanwise direction may be influenced by the spanwise velocity distribution. Moreover, the mutual effect between stems depends on their distance along both the streamwise and the spanwise directions.

Numerical procedures

As mentioned before, one of the experimental tests, in particular the case in which the rod arrangement is D3, the stem diameter is 0.8 cm, the bottom slope is 0.48% and the flow rate 13.88 l/s (test 67 in Table 3) has been considered for a numerical simulation. The flow case has been simulated by solving the three-dimensional Reynolds-averaged Navier–Stokes (RANS) equations (Calomino et al. 2018, among others) in conservative form, as written here in Cartesian coordinates (the fluid is incompressible and viscous, Einstein summation convention applies to repeated indices, $i, j = 1, 2, 3$):

$$\rho \frac{\partial \bar{u}_i}{\partial t} + \rho \bar{u}_j \frac{\partial \bar{u}_i}{\partial x_j} = -\frac{\partial \bar{p}}{\partial x_i} + \frac{\partial}{\partial x_j}\left(2\mu \bar{s}_{ij} - \rho \overline{u_i' u_j'}\right) \tag{13}$$

$$\rho \frac{\partial \bar{u}_i}{\partial x_i} = 0 \tag{14}$$

where ρ is the fluid density, μ is the water dynamic viscosity, $\bar{p}$ is the mean pressure, x_i ($i = 1, 2, 3$) are the Cartesian coordinates, $\bar{u}_i$ denote the mean components of the velocity and $\bar{s}_{ij}$ is the mean strain-rate tensor:

$$\bar{s}_{ij} = \frac{1}{2}\left(\frac{\partial \bar{u}_i}{\partial x_j} + \frac{\partial \bar{u}_j}{\partial x_i}\right) \tag{15}$$

The quantity $\tau_{ij} = -\rho \overline{u_i' u_j'}$ is the Reynolds stress tensor (Wilcox 1998; Alfonsi 2009, among others). The Reynolds stresses are the components of a symmetric second-order tensor. The diagonal components are the normal stresses, while the off-diagonal elements are the shear stresses. Hence, the Reynolds averaging formulation introduces six new unknown quantities that are the six independent components of the symmetric tensor τ_{ij}, without additional equations. In order to establish a relationship between the Reynolds stresses and the mean flow field (so solving the closure problem), the k–ω SST closure model developed by Menter et al. (2003) has been used. This model has been already used in several different flow cases, always giving satisfactory results (see, among others, Calomino et al. 2018). In this model, the turbulent kinetic energy (k) and the dissipation rate (ω) are computed with the following expressions:

$$\rho \frac{\partial k}{\partial t} + \rho \bar{u}_j \frac{\partial k}{\partial x_j} = \widetilde{P_k} - \beta^* \rho k \omega + \frac{\partial}{\partial x_j}\left[\left(\mu + \sigma_{k1}\mu_t\right)\frac{\partial k}{\partial x_j}\right] \tag{16}$$

$$\begin{aligned} \rho \frac{\partial \omega}{\partial t} + \rho \bar{u}_j \frac{\partial \omega}{\partial x_j} & \\ = \alpha \rho S^2 - \beta \rho \omega^2 + \frac{\partial}{\partial x_j}\left[\left(\mu + \sigma_{\omega 1}\mu_t\right)\frac{\partial \omega}{\partial x_j}\right] & \\ + 2\left(1 - F_1\right)\rho \sigma_{\omega 2}\frac{1}{\omega}\frac{\partial k}{\partial x_j}\frac{\partial \omega}{\partial x_j} & \end{aligned} \tag{17}$$

where $\widetilde{P_k}$ represents a production limiter used in the model to prevent the buildup of turbulence in stagnation regions, and F_1 represents a blending function. The turbulent eddy viscosity is:

$$\mu_t = \frac{\rho a_1 k}{\max\left(a_1 \omega, S F_2\right)} \tag{18}$$

where $a_1 = 0.31$ (Calomino et al. 2018; Bodnár and Příhoda 2006), S is defined as the invariant measure of the strain rate and F_2 is a second blending function. All constants are predicted through a blend from the corresponding constants. For example, α is calculated as $\alpha = \alpha_1 F_1 + \alpha_2\left(1 - F_1\right)$. This model contains the following closure coefficients, $\beta^* = 9/100$, $\sigma_{k1} = 0.85$, $\sigma_{\omega 1} = 0.5, \sigma_{\omega 2} = 0.856$, $\alpha_1 = 5/9$, $\alpha_2 = 0.44$, $\beta_1 = 3/40$ (Calomino et al. 2018; Menter et al. 2003). The governing Eqs. (13) and (14), together with the equations of the turbulence model (16) and (17), have been solved numerically by means of the interFoam solver, embedded in the OpenFoam® C++ libraries (Jasak 1996). The interFoam solver has been designed for incompressible, isothermal, immiscible fluids and uses the VoF (Volume of Fluid) phase fraction-based interface capturing approach for the representation of the free-surface effects (OpenFOAM® User Guide 2012). The VoF method, as incorporated into the OpenFoam library, has been used for the analysis of several different flow cases (among others, Alfonsi et al. 2012a, b, 2013a, b, 2015, 2017) always giving satisfactory results. This method, firstly proposed by Hirt and Nichols (1981), locates and tracks the free-surface flow, in such a way as each fluid phase (air and water in the present case) occupies an individual fraction of volume. In the case in which a cell is totally empty of water but full of air, the magnitude of the volume-fraction function is 0, while, when the cell is completely full of water, the latter magnitude is equal to 1. A value between 0 and 1 is assigned when the interface intercepts the cell. The governing equations are discretized with the finite-volume method (FVM). As for the discretization of the solution domain, a structured mesh has been built, where the dependent variables are stored at the cell center of each cell space domain in a co-located arrangement. The computational domain spans 11 m in streamwise direction (x_1), 0.191 m in spanwise (x_2) direction and 0.15 m in the vertical direction (x_3). The vegetation has been represented with smooth circular cylinders. In the present study, the PISO (pressure implicit with split operator) technique suggested by Issa (1986) was employed to couple pressures and velocities in the transient computations. The stability of the solution procedure was ensured utilizing an adaptive time step with an initial value of 10^{-6} s in conjunction with a mean Courant–Friedrichs–Lewy (CFL) number limit set to 0.5. The fluid properties used in the calculations are shown in Table 2. A number of preliminary simulations have been performed before selecting the final configuration of the (multi-block) computational grid, as shown in Fig. 6. The final three-dimensional finite-volume multi-block computational domain includes about 30×10^6 grid points, with a grid spacing of approximately 1.0 mm in the blocks in the vicinity of the cylinders, and 3 mm in the blocks far from the latter. The computational domain has been rotated around the x_2 axis in order to obtain the appropriate longitudinal channel slope of the test using the rotation matrix:

$$\zeta R_{x_2}(\theta) = \begin{pmatrix} \cos\theta & 0 & \sin\theta \\ 0 & 1 & 0 \\ -\sin\theta & 0 & \cos\theta \end{pmatrix} \tag{19}$$

Table 2 Fluid properties used in the numerically simulated flow case

Air density	Water density	Air kinematic viscosity	Water kinematic viscosity
1.225 kg/m^3	1000 kg/m^3	1.48×10^{-5} m^2/s	1.0×10^{-6} m^2/s

where θ is the relevant angle of rotation. Boundary conditions of no-slip and zero wall-normal velocity at the channel and cylinders' walls have been enforced. On the two x_1–x_3 lateral boundary planes of the channel, wall boundary conditions have been set. At the x_2–x_3 inlet section, the flow depth and the discharge values have been applied, as corresponding to the companion experimental test. As for the x_2–x_3 outlet cross section, the gradient of the flow velocity was set to zero in the direction (x_1) orthogonal to the x_2–x_3 plane (outflow boundary condition), a fixed value was imposed to the pressure, while the VoF technique has been enforced for the tracking the flow free surface.

Results

Experiments

Seventy experimental tests have been executed, with different flowrates (Q), stem diameters (d) and distances along both the streamwise and the spanwise directions, in both uniform and/or steady flow conditions, the first ones obtained by operating a sluice gate on the downstream side of the flume. In a few cases, a hydraulic jump was observed in the reach populated by stems or along the flume, even though near the site were the drag force was measured, the flow was gradually varied or practically uniform. The water-level profiles (h) and the drag forces (F_p) on the rods connected to the central plate have been measured. With given stem diameters and distances, tests have been executed with flowrate values of about $Q = 3.0$, 5.0, 8.0, 11.0, 14.0 and 16.0 l/s (Table 3). The measurement relative error associated to the latter flowrates ranged from 0.007 to 0.015. The water depths were observed through the transparent flume walls and frequently checked with a point gauge. Due to the free-surface waves, the water levels varied in the portion of the flume populated by the

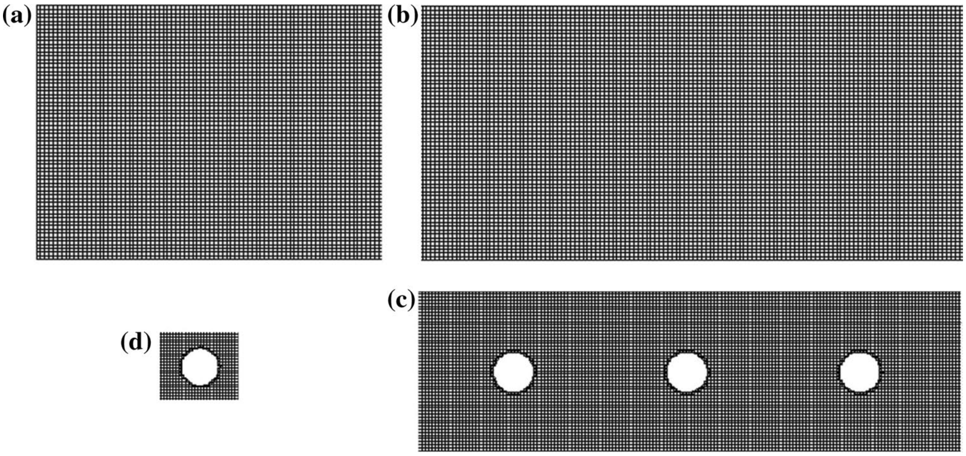

Fig. 6 Computational grid in the control volume of the simulated flow case (D3 arrangement): **a** cross-sectional view, **b** side view, **c** top view and **d** close-up around single rod

Table 3 Results of the experimental tests

Test	Q (l/s)	Flow	h_1 (cm) (upstream)	h_2 (cm) (downstream)	F_p (N)
1	5.24	GV	2.50	2.48	0.19
2	7.95	GV	3.15	3.19	0.29
3	10.83	GV	3.81	4.30	0.44
4	5.27	GV	5.39	4.96	0.55
5	7.87	GV	7.26	6.74	1.08
6	10.86	GV	9.06	8.08	1.61
7	13.55	GV	10.56	9.58	2.16
8	3.02	GV	3.50	3.50	0.29
9	5.24	GV	2.32	2.11	0.05
10	7.91	GV	2.79	2.61	0.10
11	10.92	GV	3.50	3.50	0.16
12	13.71	GV	4.02	3.91	0.20
13	16.54	GV	4.50	4.50	0.25
14	2.86	U	5.70	5.70	0.13
15	5.31	U	8.50	8.50	0.35
16	7.99	U	11.69	11.46	0.59
17	3.07	U	4.00	4.00	0.03
18	5.36	U	6.90	6.90	0.05
19	7.95	U	9.97	10.14	0.10
20	5.24	GV	3.70	3.70	0.20
21	7.99	GV	5.08	5.15	0.33
22	10.92	GV	6.50	6.50	0.50
23	13.77	GV	7.94	7.75	0.66
24	5.24	GV	3.53	3.38	0.15
25	7.96	GV	4.95	4.82	0.24
26	10.96	GV	5.94	6.29	0.33
27	13.77	GV	7.34	7.00	0.45
28	5.24	GV	2.59	2.46	0.04
29	7.91	GV	3.37	3.38	0.11
30	11.09	GV	3.93	4.15	0.16
31	13.77	GV	4.61	4.86	0.20
32	5.29	GV	5.47	5.31	0.36
33	5.29	U	7.20	7.20	0.31
34	7.90	GV	7.29	7.02	0.79
35	7.99	U	9.50	9.39	0.59
36	10.96	U	12.00	12.00	0.91
37	13.77	U	14.01	13.96	1.31
38	2.94	GV	1.94	1.58	0.10
39	5.24	GV	2.93	2.50	0.28
40	7.82	GV	3.46	4.19	0.45
41	5.73	GV	2.41	2.39	0.05
42	8.56	GV	2.89	3.14	0.10
43	11.55	GV	3.49	3.73	0.14
44	14.62	GV	4.03	4.43	0.20
45	5.18	GV	3.00	3.20	0.12
46	7.76	GV	4.33	4.56	0.26
47	11.52	GV	5.77	5.94	0.39
48	14.57	GV	7.33	7.30	0.50
49	5.83	U	6.95	7.05	0.26
50	8.58	U	8.50	8.50	0.53
51	11.65	U	11.00	11.00	0.81
52	14.53	U	13.60	13.49	1.09
53	5.77	U	7.67	7.58	0.26
54	8.55	U	9.89	9.68	0.47
55	11.61	U	11.65	11.47	0.79
56	14.62	U	13.63	13.31	1.13
57	5.77	GV	4.57	4.48	0.43
58	8.60	GV	6.34	5.95	0.78
59	11.55	GV	7.83	7.31	1.25
60	14.62	GV	9.20	8.34	1.68
61	5.77	U	6.92	7.03	0.05
62	8.60	U	9.00	9.00	0.12
63	11.65	U	11.00	11.00	0.21
64	14.62	U	12.90	12.90	0.28
65	7.99	U	8.83	8.92	0.03
66	11.01	U	10.33	10.42	0.04
67[a]	13.88	U	12.68	12.77	0.05
68	7.84	GV	2.75	2.50	0.05
69	10.83	GV	3.42	3.06	0.07
70	13.55	GV	3.87	3.51	0.11

GV gradually varied, *U* uniform

[a] The case simulated numerically

rods, and also around each single rod. As a consequence, the level measurements were not straightforward, and we associated to the latter an accuracy of about 2 mm. Thus, the drag forces measured with the load cell were fluctuating in time, so that we have considered the average values. For the highest flow velocities, on the first rows of cylinders encountered by the flow, evident run-up phenomena were observed (increasing flow levels on the upstrem portions of the cylindrical rods), that became less evident in the subsequent rows (see also "Flow visualization", Figs. 18 and 19). The flow depths in Table 3 were obtained by linearly interpolating the depths observed under the measuring plate and somewhat upstream and downstream. The mean velocity was computed on the basis of the measured discharge and the mean flow depth.

Figures 7a, b and 8a, b show, as an example, the measured water-level profiles (along the whole channel and in the zone populated by the rods) in the case of two different experimental tests (tests 3 and 19 of Table 3), respectively.

More generally, and under a qualitative viewpoint, it results that the initial flow condition is deeply altered in the zone populated by the rods, due to the process of interaction between the flow and the rods themselves. It can be noticed from Fig. 7 that the water-level profile in the zone populated

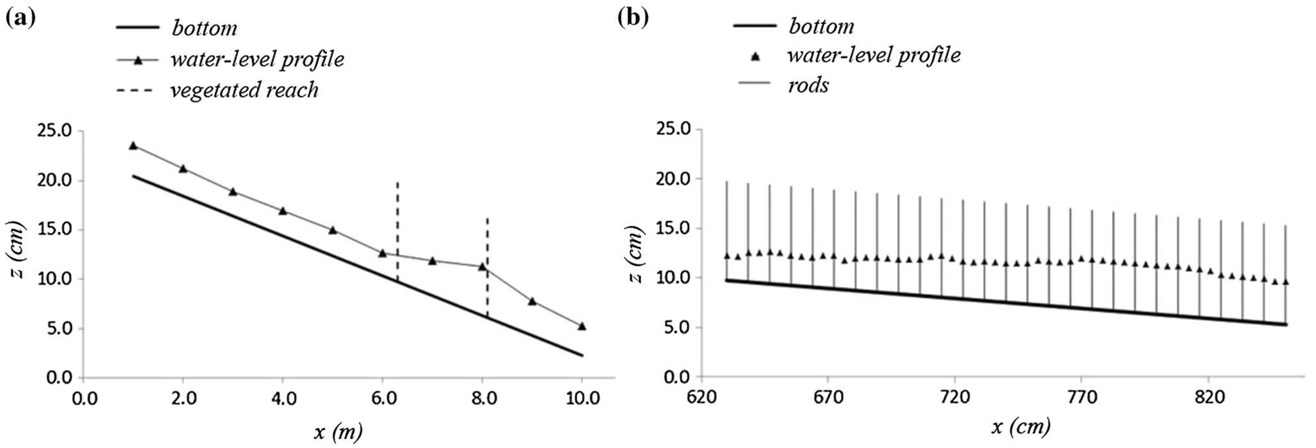

Fig. 7 Water-level profiles in the case of test 3 of Table 3 ($s = 8.48$ cm, $d = 1.0$ cm, $Q = 10.83$ l/s, $i = 2.02\%$, arrangement D4): **a** entire flume, **b** zone populated by rods

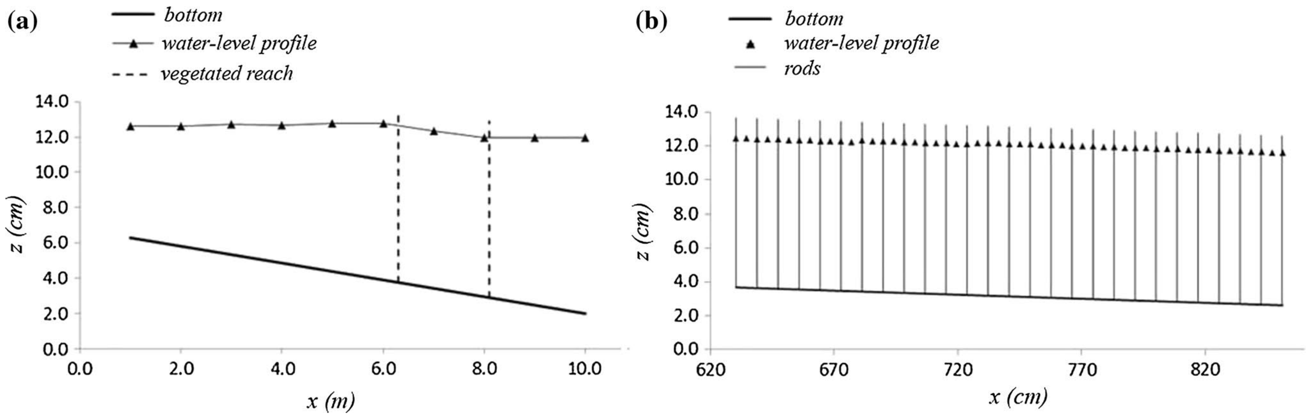

Fig. 8 Water-level profiles in the case of test 19 of Table 3 ($s = 8.48$ cm, $d = 1.0$ cm, $Q = 7.95$ l/s, $i = 0.48\%$, arrangement D4): **a** entire flume, **b** zone populated by rods

by the rods is gradually varied, while that depicted in Fig. 8 is practically uniform.

Drag coefficient

Using the values of the measured drag forces (F_p) on the group of rods connected to the measuring plate, the drag coefficient has been evaluated as (N_p is the number of stems hold by the plate):

$$C_D = \frac{2F_p}{N_p \rho h d V^2} \tag{20}$$

where h and V are the mean water depth and velocity, respectively, as computed as said above. For the evaluation of the drag coefficient, the force has been considered as equally distributed on the different rods of the group. Values of C_D in the range of about 0.3–1.4 have been obtained in executing

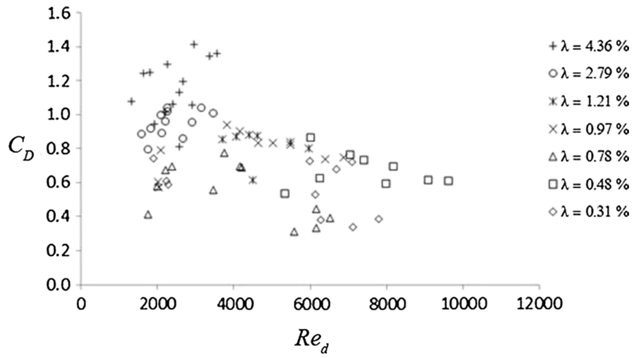

Fig. 9 Variation of C_D with Re_d at different λ

the different tests. Figure 9 reports the behavior of C_D with the Reynolds number Re_d with different values of λ (note that the values of λ are only seven, instead of eight, due to the

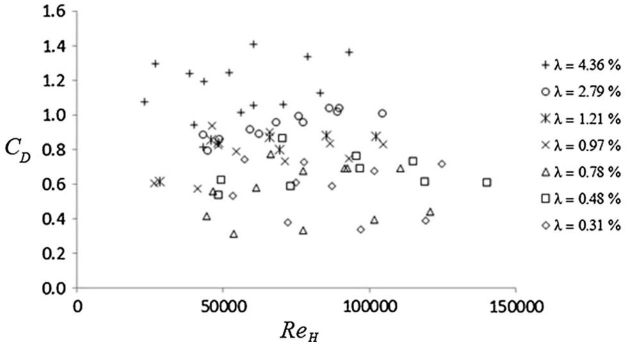

Fig. 10 Variation of C_D with Re_H at different λ

Table 4 Values of C_{Dm} and σ_{CD} at different λ

λ (%)	C_{Dm}	σ_{CD}
0.31	0.57	0.15
0.48	0.67	0.09
0.78	0.64	0.15
0.97	0.77	0.11
1.21	0.85	0.10
2.79	0.94	0.08
4.36	1.16	0.17

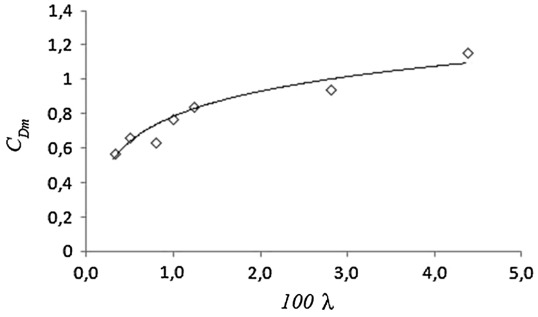

Fig. 11 Variation of C_{Dm} with λ

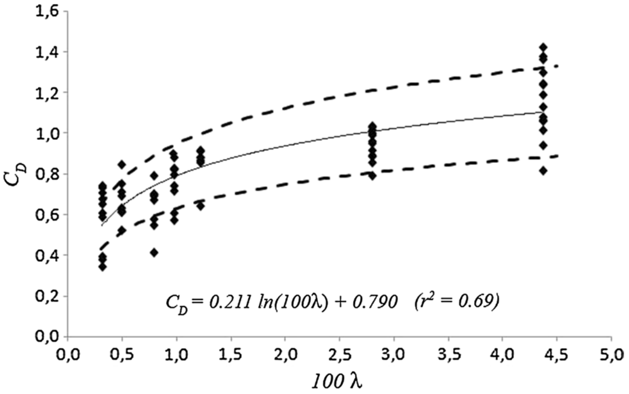

Fig. 12 Variation of C_D with λ

fact that the tests with stem diameter of 0.8 cm and arrangement D4 have not been executed).

The graph in Fig. 9 exhibits the highest values of C_D at the highest values of λ and remains more or less constant with Re_d. At increasing values of Re_d, those of C_D tend to become constant with given values of λ, and this result is similar to that of Kothyari et al. (2009). Overall, the values obtained in the present work are smaller with respect to those of Kothyari et al. (2009) with the same λ, but this has to be attributed to the different rod arrangements in the two cases (triangular mesh in the case of Kothyari et al. 2009, square mesh in the present case). Figure 10 reports the behavior of C_D with the Reynolds number $Re_H = 4VR_H/\nu$, in which $R_H = (bh)/(b+2h)$ is the hydraulic radius and V is the mean velocity with $V = Q/(bh)$. Also in this case, it can be noticed that in the graph in Fig. 10, C_D increases with λ, remaining constant with Re_H. We may note also that the Reynolds number Re_H (based on the hydraulic radius R_H) ranges between 2.3×10^4 and 1.4×10^5. However, these values correspond to the vegetation Reynolds numbers of Cheng and Nguyen (2011) of 3.0×10^4 and 1.6×10^6, being this last value remarkably larger than 6×10^5, the maximum actually considered by Cheng and Nguyen (2011). On the basis of the values given by Eq. (20), we computed the mean values of the drag coefficient (C_{Dm}) for each λ, as reported in Table 4, together with their standard deviations (σ_{CD}).

These data (also represented in Fig. 11) are satisfactorily interpolated by the following logarithmic expression ($r^2=0.92$):

$$C_{Dm} = 0.211\ln(100\lambda) + 0.784 \tag{21}$$

Equation 21 is proposed for the evaluation of the drag coefficient associated to the flow resistance due to rigid emergent vegetation as distributed on a square mesh and can be used in both gradually varied and uniform flow cases.

To assess the experimental data dispersal, we also considered all the C_D values (not only the mean for each λ), as shown in Fig. 12. The regression equation is:

$$C_D = 0.211\ln(100\lambda) + 0.790 \tag{22}$$

that is in practice the same as Eq. (21). The coefficient of determination (r^2) is 0.69, the maximum relative error is +77%, the minimum is −27% and the average of absolute values of the relative errors is 14%.

As shown in Fig. 12, most of the experimental data fall between the two lines $C_D \pm 0.2\ C_D$. To assess more completely the weak dependence of C_D on flow variables other than λ, we computed the regression equations $C_D = C_D(\lambda, Re_d)$ and $C_D = C_D(\lambda, h/d)$, seeing that neither of the two significantly improves the correlation with λ only as independent variable. As an example, in Fig. 13 we show the computed versus the experimental C_D values considering the equation $C_D = 0.341(100\lambda)^{0.293}Re_d^{0.097}$, and also in this

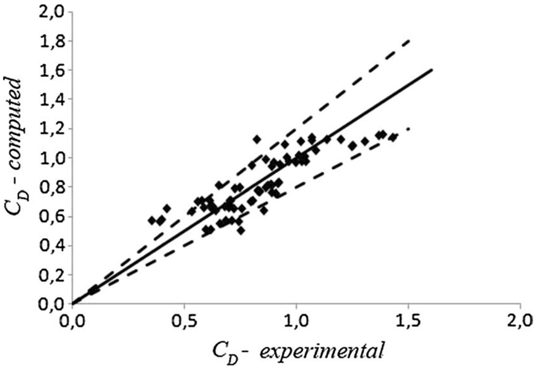

Fig. 13 Computed C_D versus experimental

case most of the experimental points are contained between the two lines $C_D \pm 0.2\ C_D$. As a conclusion, we can say that, in considering more variables than those in Eq. (22), the regression analysis does not significantly improve, and λ remains the main variable on which C_D depends. In this case, being the C_D value Reynolds number-independent, the flow structure depends only on the Froude number. Equation (4) proposed by Kothyari et al. (2009) for a staggered arrangement can be suitably used, by replacing the constant 1.53 with 0.9.

In this latter case, the maximum relative error is +74%, the minimum is −31%, the average of absolute values of relative errors is 15%. Also Eq. (8) proposed by Cheng and Nguyen (2011) can be used, by only replacing the constant 0.7 with 0.5. The max relative error is +90%, the minimum is −27%, the average of absolute values of relative errors is 16%. In Fig. 14, Eq. (21) together with experimental data obtained by other authors is shown. As for other authors, we plotted the maxima and minima drag coefficients C_D for a given density, as observed by Li and Shen (1973), James et al. (2004), Stone and Shen (2002), Ishikawa et al. (2000), Kothyari et al. (2009), and those computed by Cheng and Nguyen (2011), as they resulted from Eq. (8). One can note that (1) in any case C_D increases with λ, (2) the data related to parallel stem arrangements are limited to those gathered by Li and Shen (1973).

Momentum equation

The momentum equation applied to given control volumes has been used for the calculation of the drag force (see "Materials and methods"). Flow cases characterized by both uniform and nonuniform water-level profiles have been considered, and walls and bed were assumed as being smooth. The results have been compared with the experimental data F_p (Fig. 15a, b), as related to the laboratory tests. The comparisons shown in Fig. 15a, b exhibit mean relative errors, respectively, of 39% and 33%. In terms of drag coefficients, the agreement with the observed values is poorer, as shown in Fig. 16, where the points outside the lines $C_D \pm 0.2\ C_D$ are several. There is a reason for this fact.

If, for the sake of simplicity, in Eq. (10) one considers $S_1 = S_2 = M_1 = M_2 = 0$ (case of uniform flow), and by considering negligible the shear force T, one ends with $F = P$. It can be shown that, by considering the derivative of C_D with respect to h, the relative errors are the double with respect to those associated to the direct measurements of the force F_p. Thus, direct measurements of F_p, although in many cases not easy to perform are strongly advisable.

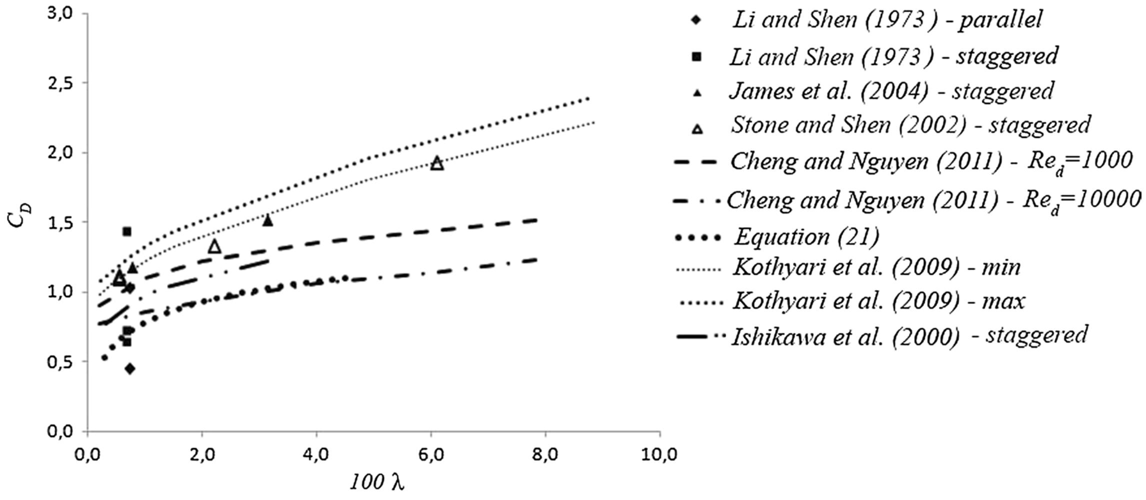

Fig. 14 Drag coefficient versus areal density

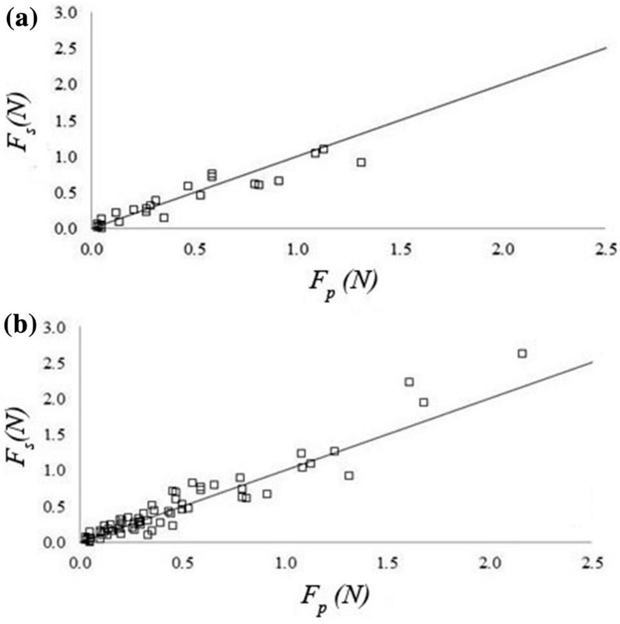

Fig. 15 Comparison between measured F_{p} and momentum equation computed values of F_{p} (F_{s}): **a** uniform flow, **b** uniform and gradually varied flow

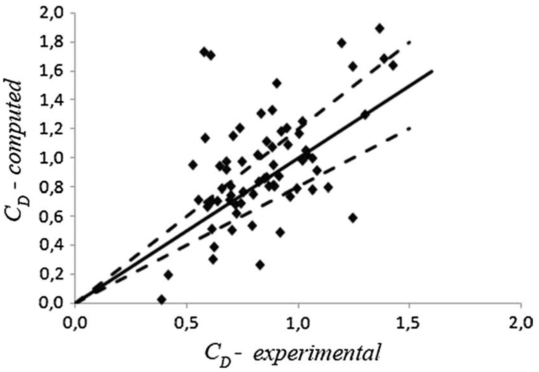

Fig. 16 Momentum equation computed drag coefficients versus experimental

Numerical results

At the beginning of the simulated test case (test 67 of Table 3, the experimentally measured flow is uniform in the reach populated by the rods), the channel was initially empty and the flow entered through the channel inlet. A CPU-based computational system has been used to execute the computations.

The simulations were carried out using 16 processors through the public domain open MPI implementation of the standard message passing interface (MPI) for parallel running. The elapsed computational time of the run was of about 144 h. The comparison between the computed and the experimental water-level profiles in the vegetated reach is shown in Fig. 17. Overall, the comparison is rather satisfactory.

Flow visualizations

The availability of numerical results (as described in "Numerical results") offers the opportunity of showing flow visualizations. In Fig. 18, a general view of the computed flow free surface is reported. It can be noticed (as mentioned before in "Experiments") how the initial free-surface condition is deeply altered in the zone populated by the rods, due to the process of interaction between the fluid flow and the set of rods. Globally, as mentioned before, and under an hydraulic viewpoint, the vegetation basically induces an increase in the resistance to flow, and this—in a constant flowrate condition—results in decreasing velocities and increasing water levels. Under a local viewpoint, in Fig. 18 the local free-surface disturbances caused by the single rods are clearly visible.

Figure 19 clearly shows the (already mentioned) run-ups, i.e., the local increases in the water levels on the upstream portions of the cylindrical rods, again due to the process of interaction between fluid flow and rods (the run-up phenomenon is a very well-known phenomenon for example in marine engineering).

Discussion and conclusions

The component of the resistance to flow due to the presence of rigid emerging vegetation has been studied experimentally, by mainly analyzing the drag forces exerted by the fluid in a laboratory flume onto a number of rigid circular cylinders. Parallel rod arrangements have been considered, with different diameters, mutual distances, flow depths and velocities. The resulting water-level profiles have been gathered, and the drag force on a given number of rods has been measured. Some factors of complexity emerged from the study, such as: (a) the measurement of the flow levels is not straightforward, due to the fact that they vary both in the portion of the flume populated by the rods, and around each single rod, (b) the drag force is fluctuating in time, so that average values have to be considered. As a main result of this work, and within the experimental range investigated, the drag coefficients were found to depend on the stem density (densities were investigated from 0.0031 to 0.04), but to be substantially independent on the Reynolds number, when the latter varies from 2.3×10^4 to 1.4×10^5. The drag forces computed by means of the momentum equation were comparable to those directly measured, even though larger

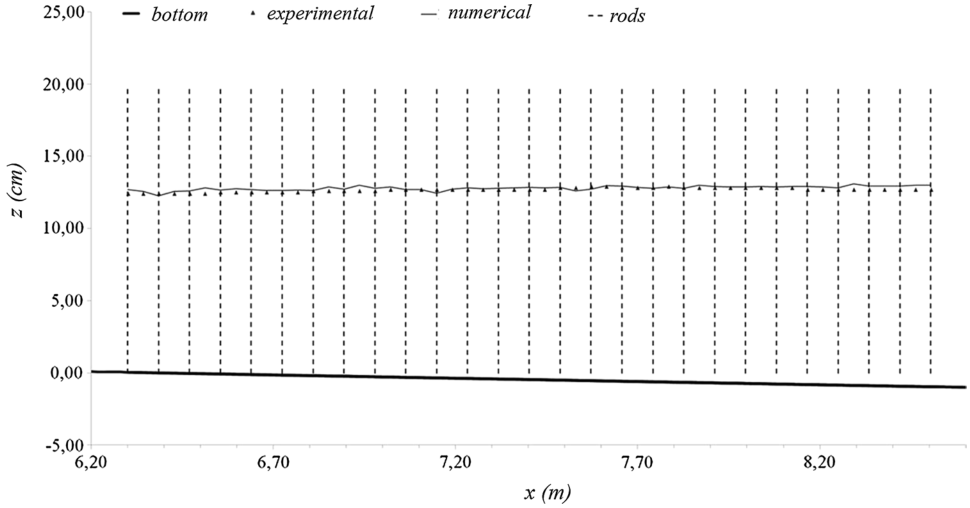

Fig. 17 Comparison between measured and numerically computed water-level profiles in the vegetated reach (test 67 of Table 3)

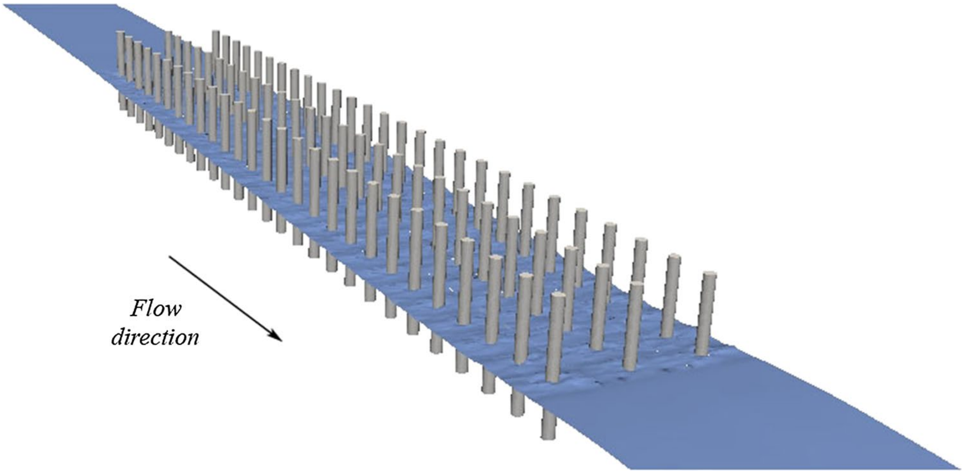

Fig. 18 Numerically simulated flow case. General view of free surface with rods

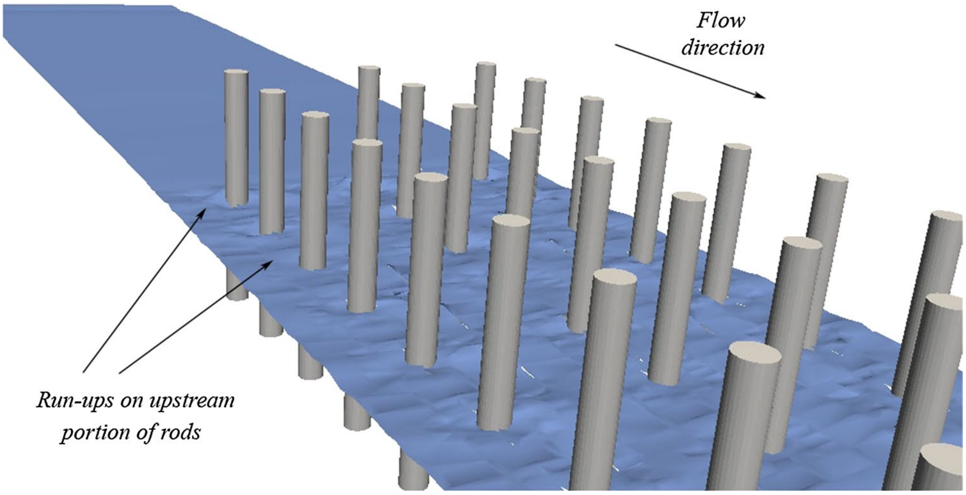

Fig. 19 Numerically simulated flow case. Close-up view of free surface with rods

errors appear in the drag coefficient values. In order to investigate the accuracy and the suitability of the k–ω SST turbulence closure model, a first numerical simulation, carried out by solving the RANS equations, has given satisfactory results. Further work is planned in this direction, toward the optimization of the numerical solution, that appears to be a favorable option in order to overcome the complexities associated to the performing of experimental measurements.

Acknowledgements The authors would like to thank the reviewers and the editor for their constructive suggestions and comments, which were very helpful in improving the quality of this work.

References

Aberle J, Jarvela J (2013) Flow resistance of emergent rigid and flexible floodplain vegetation. J Hydraul Res 51(1):33–45

Alfonsi G (2009) Reynolds averaged Navier–Stokes equations for turbulence modeling. Appl Mech Rev. https://doi.org/10.1115/1.3124648

Alfonsi G, Lauria A, Primavera L (2012a) Structures of a viscous-wave flow around a large-diameter circular cylinder. J Flow Vis Image Process 19(4):323–354

Alfonsi G, Lauria A, Primavera L (2012b) Flow structures around a large-diameter circular cylinder. J Flow Vis Image Process 9(1):15–35

Alfonsi G, Lauria A, Primavera L (2013a) Proper orthogonal flow modes in the viscous-fluid wave-diffraction case. J Flow Vis Image Process 24(4):227–241

Alfonsi G, Lauria A, Primavera L (2013b) On evaluation of wave forces and runups on cylindrical obstacles. J Flow Vis Image Process 20(4):269–291

Alfonsi G, Lauria A, Primavera L (2015) The field of flow structures generated by a wave of viscous fluid around vertical circular cylinder piercing the free surface. Procedia Eng 116:103–110

Alfonsi G, Lauria A, Primavera L (2017) Recent results from analysis of flow structures and energy modes induced by viscous wave around a surface-piercing cylinder. Math Probl Eng. https://doi.org/10.1155/2017/5875948

Armanini A, Righetti M, Grisenti P (2005) Direct measurement of vegetation resistance in prototype scale. J Hydraul Res 43(5):481–487

Baptist MJ (2005) Modelling floodplain biogeomorphology. Ph.D. thesis. Delft University of Technology, The Netherlands. ISBN 90-407-2582-9

Bennett SJ, Simon A (2004) Riparian vegetation and fluvial geomorfology. American Geophysical Union, Washington

Bodnár T, Příhoda J (2006) Numerical simulation of turbulent free-surface flow in curved channel. Flow Turbul Combust 76:429–442

Calomino F, Alfonsi G, Gaudio R, D'Ippolito A, Lauria A, Tafarojnoruz A, Artese S (2018) Experimental and numerical study of free-surface flows in a corrugated pipe. Water 10:638

Carollo FG, Ferro V, Termini D (2002) Flow velocity measurements in vegetated channels. J Hydraul Eng 128(7):664–673

Carollo FG, Ferro V, Termini D (2005) Flow resistance law in channels with flexible submerged vegetation. J Hydraul Eng 131(7):554–564

Cheng NS, Nguyen HT (2011) Hydraulic radius for evaluating resistance induced by simulated emergent vegetation in open-channel flow. J Hydraul Eng 137(9):995–1004

Choi SU, Kang H (2004) Reynolds stress modeling of vegetate open-channel flows. J Hydraul Res 42(1):3–11

Defina A, Bixio AC (2005) Mean flow and turbulence in vegetated open channel flow. Water Resour Res. https://doi.org/10.1029/2004WR003475

D'Ippolito A, Lauria A, Alfonsi G, Calomino F (2018) Flow resistance in open channel with rigid emergent vegetation. In: Armanini A, Nucci E (eds) Proceedings of the 5th IAHR Europe Congress—new challenges in hydraulic research and engineering

D'Ippolito A, Ferrari E, Iovino F, Nicolaci A, Veltri A (2013) Reforestation and land use change in a drainage basin of Southern Italy. iForest 6:175

Erduran KS, Kutija V (2003) Quasi-three-dimensional numerical model for flow through flexible, rigid, submerged and non-submerged vegetation. J Hydroinform 5(3):189–202

Fathi-Moghadam M, Kouwen N (1997) Non-rigid, non-submerged vegetative roughness on floodplains. J Hydraul Eng 123(1):51–57

Fischer-Antze T, Stoesser T, Bates P, Olsen NRB (2001) 3D numerical modelling of open-channel flow with submerged vegetation. J Hydraul Res 39(3):303–310

Freeman GE, Rahmeyer WH, Copeland RR (2000) Determination of resistance due to shrubs and woody vegetation. Technical Report-00-25. US Army Corps of Engineers. Engineer Research and Development Center

Hirt CW, Nichols BD (1981) Volume of fluid (VOF) method for the dynamics of free boundaries. J Comput Phys 39:201–225

Ishikawa Y, Mizuhara K, Ashida S (2000) Effect of density of trees on drag exerted on trees in river channels. J For Res 5:271–279

Issa RI (1986) Solution of the implicitly discretized fluid flow equations by operator-splitting. J Comput Phys 62:40–65

James CS, Birkhead AL, Jordanova AA, Sullivan JJ (2004) Flow resistance of emergent vegetation. J Hydraul Eng 42(4):390–398

Jarvela J (2002) Flow resistance of flexible and stiff vegetation: a flume study with natural plants. J Hydrol 269:44–54

Jarvela J (2004) Determination of flow resistance caused by non-submerged woody vegetation. Int J River Basin Manag 2(1):1–10

Jasak H (1996) Error analysis and estimation for the finite volume method with applications to fluid flows. Ph.D. thesis. Imperial College, London, UK

Kim D, Stoesser T (2011) Closure modeling and direct simulation of vegetation drag in flow through emergent vegetation. Water Resour Res. https://doi.org/10.1029/2011WR010561

Kothyari UC, Hayashi K, Hashimoto H (2009) Drag coefficient of unsubmerged rigid vegetation stems in open channel flows. J Hydraul Res 47(6):691–699

Kouwen N, Fathi-Moghadam M (2000) Friction factors for coniferous trees along rivers. J Hydraul Eng 126(10):732–740

Kouwen N, Unny TE (1973) Flexible roughness in open channels. J Hydraul Div 99(5):713–728

Li RM, Shen HW (1973) Effect of tall vegetations on flow and sediment. J Hydraul Div 99(5):793–814

Lindner K (1982) Der strömungswiderstand von pflanzenbeständen. Mitteilungen 75, Leichtweiss-Institut fur Wasserbau, TU Braunschweig (Doctoral thesis)

Liu D, Diplas P, Fairbanks JD, Hodges CC (2008) An experimental study of flow through rigid vegetation. J Geophys Res. https://doi.org/10.1029/2008JF001042

López F, García M (1997) Open-channel flow through simulated vegetation: Turbulence modeling and sediment transport. US Army of engineers waterway experiment station wetlands research program. Technical Report WRP-CP-10

López F, García M (2001) Mean flow and turbulence structure of open channel flow through non-emergent vegetation. J Hydraul Eng 127(5):392–402

Menter FR, Kuntz M, Langtry R (2003) Ten years of industrial experience with the SST turbulence model. In: Proceedings of the 4th international symposium on turbulence, heat and mass transfer, Antalya, Turkey, Begell House Inc., 12–17 Oct 2003, pp 625–632

Mulahasan S, Stoesser T (2017) Flow resistance for in-line vegetation in open channel flow. Int J River Basin Manag 15(3):329–334

Neary VS (2003) Numerical solution of fully developed flow with vegetative resistance. J Eng Mech 129(5):558–563

Nepf HM (1999) Drag, turbulence and diffusion in flow through emergent vegetation. Water Resour Res 35(2):479–489

Nepf HM, Vivoni ER (2000) Flow structure in depth-limited vegetated flow. J Geophys Res 105(C12):28547–28557

OpenFOAM® (2012) User guide. https://cfd.direct/openfoam/user-guide/. Accessed 3 Dec 2017

Pasche E, Rouvé G (1985) Overbank flow with vegetatively roughened flood plains. J Hydraul Eng 111(9):1262–1278

Petryk S, Bosmajian G (1975) Analysis of flow through vegetation. J Hydraul Div 101(7):871–884

Righetti M (2008) Flow analysis in a channel with flexible vegetation using double averaging method. Acta Geophys 56(3):801–823

Schlichthing H (1979) Boundary layer theory. McGraw-Hill, New York

Shimizu Y, Tsujimoto T (1994) Numerical analysis of turbulent open channel flow over a vegetation layer using a k–ε turbulence model. J Hydrosci Hydraul Eng 11(2):57–67

Stephan U, Gutknecht D (2002) Hydraulic resistance of submerged flexible vegetation. J Hydrol 269(1–2):27–43

Stoesser T, Wilson CAME, Bates PD, Dittrich A (2003) Application of a 3D numerical model to a river with vegetated floodplains. J Hydroinform 5(2):99–112

Stoesser T, Kim SJ, Diplas P (2010) Turbulent flow through idealized emergent vegetation. J Hydraul Eng 136(12):1003–1017

Stone MC, Shen HT (2002) Hydraulic resistance of flow in channel with cylindrical roughness. J Hydraul Eng 128(5):500–506

Tanino Y, Nepf HM (2008) Laboratory investigation of mean drag in random array of rigid, emergent cylinders. J Hydraul Eng 134(1):34–41

Temple DM (1986) Velocity distribution coefficients for grass-lined channels. J Hydraul Eng 112(3):193–205

Vargas-Luna A, Crosato A, Calvani G, Uijttewaal WSJ (2016) Representing plants as rigid cylinders in experiments and models. Adv Water Resour 93:205–222

Wang H, Tang HW, Yuan SY, Lv SQ, Zhao XY (2014) An experimental study of the incipient bed shear stress partition in mobile bed channels filled with emergent rigid vegetation. Sci China Technol Sci 57(6):1165–1174

Wilcox DC (1998) Turbulence modeling for CFD. DCW Industries, La Cañada

Wu F, Shen HW, Chou YJ (1999) Variation of roughness coefficients for unsubmerged and submerged vegetation. J Hydraul Eng 125:934–942

Acta Geophysica (2019) 67:987–997
https://doi.org/10.1007/s11600-019-00292-4

RESEARCH ARTICLE - SPECIAL ISSUE

Effect of two distinct patches of *Myriophyllum* species on downstream turbulence in a natural river

Łukasz Przyborowski[1] · **Anna Maria Łoboda**[1] · **Robert Józef Bialik**[2]

Received: 17 September 2018 / Accepted: 16 April 2019 / Published online: 29 April 2019

Abstract

Velocity profiles upstream and downstream of two aquatic plant species that are similar in morphology but differ in patch structures were measured in a natural river. Turbulence statistics were analyzed after thorough data filtering. In the wake of the *M. alterniflorum*, which was a slender, 0.3 m wide and 1.2 m long patch of aspect ratio 1:4, there were distinctive peaks in both, turbulence intensity and turbulent kinetic energy, which indicated increased lateral mixing. In contrast to the *M. alterniflorum*, turbulence statistics in the wake of the *M. spicatum*, which was the larger, 2 m wide and 2.4 m long patch of aspect ratio 1:1.5, indicated increased lateral shear of a greater magnitude. The turbulent kinetic energy was diminished in the closest layer to the bed downstream the both plants, although, in the case of *M. alterniflorum*, the observed values were similar to those upstream. The occurrence of the mixing layer below the height of *M. spicatum* was visible in the power spectral density plot. In both cases, ejections in the wake diminished in favor of other coherent structures. The shape and configuration of a patch are decisive factors governing the occurrence of flow instabilities downstream of the patch.

Keywords Aquatic plants · Mixing layer · Turbulence · Flow field · Flexible vegetation patches

Introduction

The role and performance of both aquatic and riparian plants in rivers have been intensively investigated in recent years by in situ measurements (e.g., Biggs et al. 2016; Cameron et al. 2013; Cassan et al. 2015; Naden et al. 2006; Sukhodolova and Sukhodolov 2012; Västilä et al. 2015) and laboratory experiments (e.g., Kubrak et al. 2015; Liu et al. 2017; Siniscalchi and Nikora 2013; Termini and Di Leonardo 2017). The growing interest in the complexity of flow–biota–sediment interactions and their impacts on flow resistance and transport processes and thus, on river management (Aberle and Järvelä 2015; Gurnell et al. 2012; Nepf 2012a; Nikora 2010) stresses the need for further studies to be conducted.

Plants in the form of individual patches that are much smaller than the river width are common in natural conditions (Siniscalchi et al. 2012). Each patch contributes to the flow blockage factor, which depends on the drag coefficient, patch density and diameter (Ortiz et al. 2013). These coefficients have a subtler influence on the detailed flow field due to the multiple scales at which a plant interacts with the flow, creating various effects in the form of boundary and mixing layers (Nikora 2010). The identification of a single phenomenon like stem induced vortices is very difficult due to the intersection of different-scale effects (Aberle and Järvelä 2013). In response to this issue, the superposition of multiple individual concepts that can describe the flow downstream of vegetation was proposed by Nikora et al. (2013).

The vortices occur at different scales; some propagate from individual stems as flows separate from their boundary, while others originate from the Kelvin–Helmholtz instability at the patch boundaries (Nikora 2010). For example, the distinct phenomena observed in the wake of a patch, which has higher drag than the bed, are patch-scale turbulences in the form of vertical and horizontal vortices, which propagate downstream (Aberle and Järvelä 2015). In the case of

---

✉ Łukasz Przyborowski
lprzyborowski@igf.edu.pl

Anna Maria Łoboda
aloboda@igf.edu.pl

Robert Józef Bialik
rbialik@ibb.waw.pl

[1] Institute of Geophysics, Polish Academy of Sciences, Warsaw, Poland

[2] Institute of Biochemistry and Biophysics, Polish Academy of Sciences, Warsaw, Poland

emergent vegetation, horizontal patch-scale vortices are prone to merge after reaching a certain distance, which depends on the patch diameter and density (Nepf 2012a). These phenomena limit the area of decreased velocity where sediment deposition is increased downstream of the plant (e.g., Liu et al. 2017).

In a vegetated channel, the energy cascade is disturbed by the occurrence of coherent structures (e.g., Nezu and Nakagawa 1993). In the flow over a sandy mobile bed without vegetation, a bursting cycle occurs, where sweeps and ejections mostly contribute to turbulence close to the boundary layer (Grass 1971). Ghisalberti and Nepf (2006) and further Chen et al. (2013) revealed that the character of secondary currents changes from ejections to sweeps within the canopy. Within a patch of flexible vegetation, sweeps bend the stems and ejections are responsible for lifting them (Sukhodolova and Sukhodolov 2012). Sweeps within the canopy are dominant over the ejections, as revealed in studies by, for example, Chen et al. (2013) and Termini and Di Leonardo (2017). In addition, within a plant patch, naturally flexible vegetation tends to undergo dynamic reconfiguration correlated with ambient flow. This behavior can suppress increased turbulence intensities, shear stresses and flow separation, which are common for rigid obstacles in water (Ghisalberti and Nepf 2006; Siniscalchi and Nikora 2013).

Theories describing flow disturbances in the presence of flexible, naturally growing aquatic vegetation are still highly limited due to the complexity of physical laws governing turbulent flow and the heterogeneity of natural conditions in each studied case. Following recent trends in vegetated flow investigations (Sukhodolov 2015), an experiment involving the deployment of an acoustic Doppler velocimeter around two common aquatic macrophytes in a natural river was conducted to measure 3D velocity field. A discussion of raw data reliability using a Vectrino Profiler was included in a previous paper by the authors (Przyborowski et al. 2018b). The two species investigated, namely, *Myriophyllum alterniflorum* L. and *Myriophyllum spicatum* L., are characterized by similar morphologies (Kłosowski and Kłosowski 2007; Wilson and Ricciardi 2009); therefore, in response to flow stresses, individual stems of comparable diameter and with the same internal structure should respond in a replicable manner. This similarity raises the question of how the dimensions and configuration of the patch alter flow properties downstream. As Nikora et al. (2008) showed, patch width (W_c) to the flow width (W) ratio is one of the meaningful plant roughness parameters. In this study, both patches had uniformly covered a small part of the bed; however, *M. spicatum* had much higher value of W_c/W, and therefore, it was expected to produce similar flow instabilities to those of submerged meadows as described by Nepf (2012a), for example. The obtained results showed differences in the velocity profiles between plant patches. This paper shows the development of these results; after thorough data filtering, the statistical analysis of turbulence was conducted to determine the flow instabilities caused by the two distinct patches.

Study site

The present experiments were conducted at two sites in the Świder River in Poland, which is a sandy bed, lowland river with a width of approximately 20 m. During the first experiment on July 16, 2016, the discharge was 2.46 $m^3 s^{-1}$. A slender, 0.3 m wide and 1.2 m long patch (aspect ratio 1:4) of *M. alterniflorum* was found approximately 2 m from the right bank in 0.35 m deep water and two pairs of velocity profiles were measured (Fig. 1a, b). During the second experiment on September 22, 2016, the discharge was lower, i.e., 1 $m^3 s^{-1}$, and the water depth was approximately 0.25 m. A patch of *M. spicatum*, which covered an approximately 2 m wide and 1.5–2.4 m long area (the aspect ratio was approximately 1:1.5 due to the irregular shape of the patch; also, the velocity profiles were placed not in the centerline of the patch but closer to its edge, as shown in Fig. 1d) was found 1 m from the left bank (Fig. 1d, e). In both experiments, the average difference in water depth between the upstream and downstream profiles was approximately 3 cm. Ripples were observed on the sandy bed. However, no bed elevation changes were observed during any 3 min long recording. In the vicinity of the experimental sites, there were no other obstacles on the riverbed; therefore, the upstream profiles represent undisturbed ambient open-channel flow.

Although the number of stems per unit bed area was not measured, the second patch was visually denser (Fig. 1b, e). Both investigated plant species belong to group of fully submerged types of vegetation. The species are characterized by similar morphologies of stems and leaves (Fig. 1c, f). The only difference was that the individual stems of *M. spicatum* were approximately 0.20 m shorter than those of *M. alterniflorum*. The diameter of the stem, which has a wheel-like internal structure (Łoboda et al. 2018b), was approximately 2 mm (Fig. 1g, h). Thin, 10–20 mm long whorled leaves grew in sets of three per node along the stem (Kłosowski and Kłosowski 2007). Differences in biomechanical properties between the two investigated species, which might influence the obtained turbulence statistics, were not evaluated due to the assumption of similar average flexural rigidities for plants with similar morphologies (Fig. 1c, f), stem diameters and cross-sections (Fig. 1g, h) (experiments were conducted after the rapid growth season of the plants; Łoboda et al. 2018a; Tymiński and Kałuża 2012).

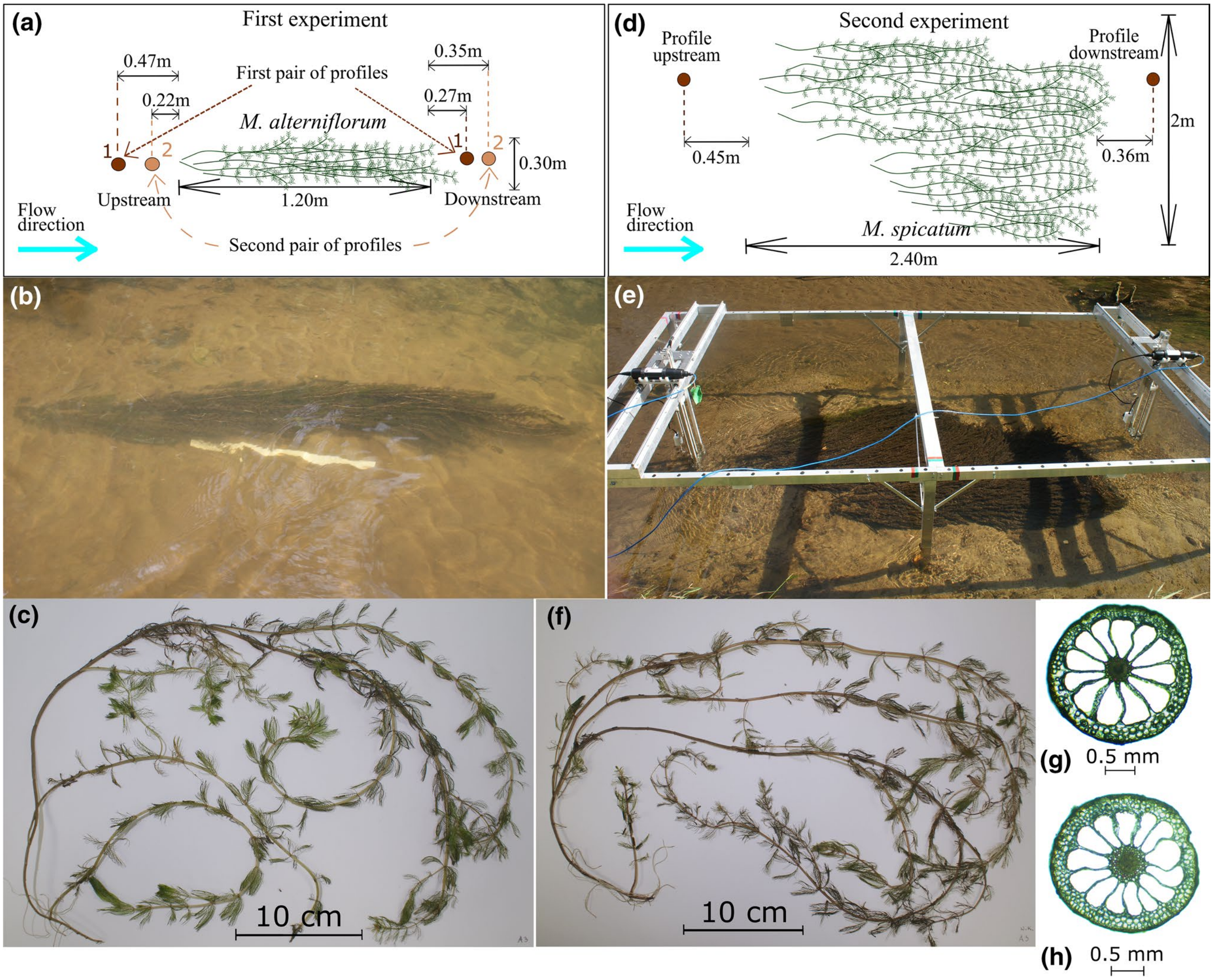

Fig. 1 Schematics of the two patches with locations of measured profiles (**a**, **d**); photographs taken at the experimental sites (**b** a patch of *M. alterniflorum*; **e** a patch of *M. spicatum* with a platform used to hold velocimeters); photographs of examples of individual stems and plant stem cross-sections (**c**, **g** *M. alterniflorum*; **f**, **h** *M. spicatum*). Please note the white strip in the photograph **b** is 0.5 m long ruler, and the photograph, **e** does not show actual placement of measurement profiles

Materials and methods

Water velocity measurements were performed using an acoustic Doppler velocimeter, the Vectrino Profiler (VP) (revision 2779/1.32, Nortek AS, Rud, Norway). During the measurements, the following VP setup was used: minimum ping algorithm; 50 Hz recording frequency; high power level; and a velocity range 0.2 m s^{-1} higher than the first recorded mean value. In the first experiment, the first pair of profiles was obtained 0.27 m downstream and 0.47 m upstream of the plant, and the second pair of profiles was obtained 0.35 m downstream and 0.22 m upstream of the plant (Fig. 1a). In the second experiment, one pair of profiles was obtained at points 0.36 m downstream and 0.45 m upstream (Fig. 1d), measured simultaneously with two VP units. It is also worth noting that the distance between upstream and downstream profiles was two times larger for the second patch than for the first patch due to the length of the patches (Fig. 1a, d). Each profile was created from a series of individual 3 min recordings taken at different water heights. Results from the velocity measurements were depicted using normalized height, i.e., a Z/H scale, where Z represents the height of the measurement point above the bed and H represents the local water depth. The average height of the main body of the plant was approximately $Z/H = 0.5$ for *M. alterniflorum* and approximately $Z/H = 0.4$ for *M. spicatum*.

Before using the recorded velocities to calculate turbulence characteristics, a filtering procedure was applied to the recorded velocities to remove low-quality or noise-related artifacts of the VP (Brand et al. 2016; Koca et al. 2017; Thomas et al. 2017). The procedure was as follows: (1) the cell with the best signal-to-noise ratio (SNR) and within a "sweet spot," i.e., the distance from the VP transducers where the signal beams were best correlated, was chosen from each data recording; (2) the record from the chosen cell was cleared of fragments with an SNR below 15 dB or correlation below 70% and replaced with interpolating neighboring values; (3) spikes were removed using a phase-space thresholding filter (Goring and Nikora 2002, with modifications by Wahl 2003 and Parsheh et al. 2010).

The signal-to-noise ratio during the velocity measurements near *M. alterniflorum* was generally above 20 dB in points in the "sweet spot," and the SNR was below this level for *M. spicatum*. To maintain the best accuracy, for a few points across profiles, bins outside the "sweet spot" had to be chosen; therefore, the results, even after filtering procedures, must be interpreted with caution. Due to the low SNR values of the points closest to the bottom, some of them were removed from results. The lowest measured point downstream of *M. alterniflorum*, showed in the results, was 7 cm above the bed in the first profile; 4 cm above the bed in the second downstream profile, whereas the lowest point downstream of *M. spicatum* was 2 cm above the bed.

Turbulence characteristics were calculated using recorded and filtered velocity fluctuations in longitudinal (u'), transverse (v') and first vertical (w') directions. The Reynolds stresses were formulated as follows:

$$\overline{u'v'},\ \overline{v'w'} \text{ and } \overline{u'w'}, \tag{1}$$

the normalized turbulence intensities are:

$$\mathrm{TI}_U = \frac{\sqrt{\overline{u'^2}}}{\bar{U}}, \quad \mathrm{TI}_V = \frac{\sqrt{\overline{v'^2}}}{\bar{U}}, \quad \text{and} \quad \mathrm{TI}_W = \frac{\sqrt{\overline{w'^2}}}{\bar{U}}, \tag{2}$$

where $\bar{U}$ denotes the time-averaged longitudinal velocity;

and the turbulent kinetic energy is:

$$\mathrm{TKE} = \frac{1}{2}\left(\overline{(u')^2} + \overline{(v')^2} + \overline{(w')^2}\right). \tag{3}$$

In addition, these characteristics were made noise-free due to the availability of redundant information for two vertical velocities recorded by the VP (Hurther and Lemmin 2001; Voulgaris and Trowbridge 1998) by subtracting the calculated noise variance in each direction from the corresponding velocity variance. To show the power spectral densities, a script implemented in MATLAB was used, i.e., the Welch (1967) method. A Hamming window function and discrete Fourier transform points equal to 512 with a 50% overlap were chosen (Koca et al. 2017).

Quadrant analysis was performed using a bursting cycle detection method (Franca et al. 2014). Shear events were detected using the following thresholds:

for outward interactions,

$$Q_{\mathrm{out}} = \left\{ u',\, w' \in R : u' > 0 \bigwedge w' > \frac{\sigma_{\mathrm{h}}}{u'} \bigwedge u' < \sigma^{+} \right\}; \tag{4}$$

for ejections,

$$Q_{\mathrm{ej}} = \left\{ u', w' \in R : u' < 0 \bigwedge \left\{ w' > \frac{\sigma_{\mathrm{h}}}{|u'|} \bigvee u' < \sigma^{-} \right\} \right\}; \tag{5}$$

for inward interactions,

$$Q_{\mathrm{inw}} = \left\{ u', w' \in R : u' < 0 \bigwedge w' < 0 \bigwedge |w'| > \frac{\sigma_{\mathrm{h}}}{|u'|} \bigwedge u' > \sigma^{-} \right\}; \tag{6}$$

and for sweeps,

$$Q_{\mathrm{sw}} = \left\{ u', w' \in R : u' > 0 \bigwedge \left\{ \left\{ w' < 0 \bigwedge |w'| > \frac{\sigma_{\mathrm{h}}}{u'} \right\} \bigvee u' > \sigma^{+} \right\} \right\}; \tag{7}$$

where the threshold σ_{h} was obtained by the following equation

$$\sigma_{\mathrm{h}} = H \times U_{\mathrm{rms}} \times W_{\mathrm{rms}}; \tag{8}$$

and the thresholds σ^{+} and σ^{-}, by:

$$\sigma^{\pm} = \pm 2.5 \times U_{\mathrm{rms}}. \tag{9}$$

H represents the hole size, which was 1.8 as this value is commonly used for open-channel flows (e.g., Liu et al. 2016), although, in order to consider weak events, this value could be lower, i.e., 1.2 as suggested by Luchik and Tiederman (1987) or even 0.2 as used by Bialik (2013). However, Poggi et al. (2004) and Chen et al. (2013) used a value of 3 in their experiments with vegetation in laboratory conditions for a classical detection method. U_{rms} and W_{rms} were equal to the root mean squares of the longitudinal and vertical velocities, respectively.

Results

The mean longitudinal velocities were decreased by 43% to 50% in each of the downstream profiles in comparison with upstream profiles (Fig. 2). The mean transverse and vertical velocities did not change significantly around *M. alterniflorum*, although in the case of *M. spicatum*, the mean transverse velocities had positive values, from 0.100 to 0.180 m s^{-1} downstream through the whole height of the plant patch, while upstream they oscillated from −0.002 to 0.009 m s^{-1} (Fig. 2).

The measured normalized turbulence intensities were, on average, 77% to 168% higher downstream of *M. alterniflorum* and 25% to 198% higher downstream of *M. spicatum*, than upstream of them (Fig. 3). Below the height of the *M. alterniflorum* patch, the highest *TI* values were detected in the downstream profile 2 which indicated that

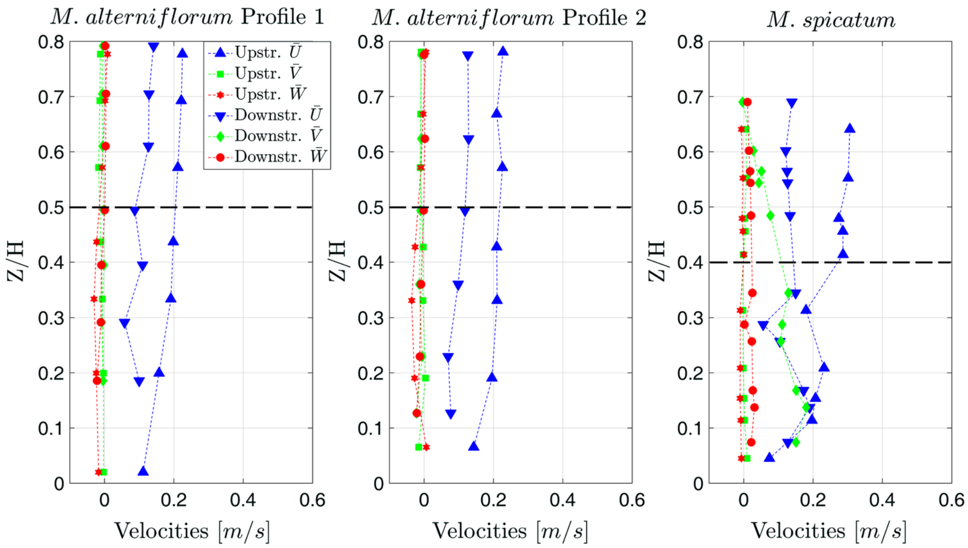

Fig. 2 Mean longitudinal $\bar{U}$, transverse $\bar{V}$ and vertical $\bar{W}$ velocities of the first and second pair of profiles downstream and upstream of *M. alterniflorum* and of one pair of profiles in the experiment with *M. spicatum*. Note that the dotted lines indicate the average height of the plant

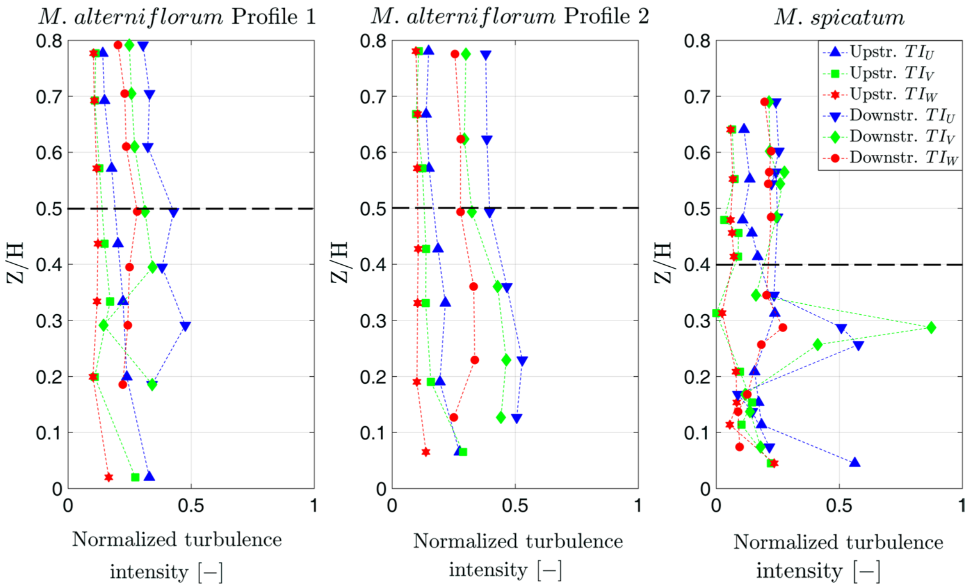

Fig. 3 Normalized turbulence intensities of the first and second pair of profiles downstream and upstream of *M. alterniflorum* and of one pair of profiles in the experiment with *M. spicatum*. Note that the dotted lines indicate the average height of the plant

mixing was developing in the farther profile. Downstream of the *M. spicatum* there was a distinctive peak in points at $Z/H = 0.29$ and $Z/H = 0.26$, where the TI_U and TI_V were four to nine times higher than closest corresponding points in height upstream, denoting increased mixing (Fig. 3), as was expected for the larger patch. However, the TI_W values in this region were noticeably low.

The turbulent kinetic energy (TKE) profiles downstream of the investigated plants showed trends opposite to those of the turbulence intensities, i.e., the TKE was higher above the main body of the plant than below that height (Fig. 4). At $Z/H = 0.5$, i.e., the height of the *M. alterniflorum* canopy, the TKE was 0.0013 $m^2\ s^{-2}$, equal in both the upstream and downstream profile 1; at $Z/H = 0.3$ the TKE was two times lower; farther in the downstream profile 2 and at $Z/H = 0.5$, the TKE value was higher than upstream (Fig. 4), while at $Z/H = 0.2$ it was similar to the upstream profile. Downstream of *M. spicatum*, the TKE profile retained a distinctive peak in the same spot as the turbulence intensities, i.e., below the maximal height of the canopy, which was 0.0029 $m^2\ s^{-2}$, and the lowest value of 0.0004 $m^2\ s^{-2}$ was registered above that height (Fig. 4).

The absolute tangential Reynolds stresses showed fewer changes between the upstream and downstream measurements than did the turbulence characteristics as described above. For *M. alterniflorum*, the $\left|\overline{u'v'}\right|$ and $\left|\overline{v'w'}\right|$ components were highest at $Z/H = 0.4$, measuring 0.35×10^{-3} $m^2\ s^{-2}$ and 0.54×10^{-3} $m^2\ s^{-2}$, respectively (Fig. 5). Farther downstream, these peaks were lower, i.e., at $Z/H = 0.2$ (Fig. 5). Profiles of $\left|\overline{u'w'}\right|$ showed elevated values of approximately 0.2×10^{-3} $m^2\ s^{-2}$ at points closest to the bed. Downstream

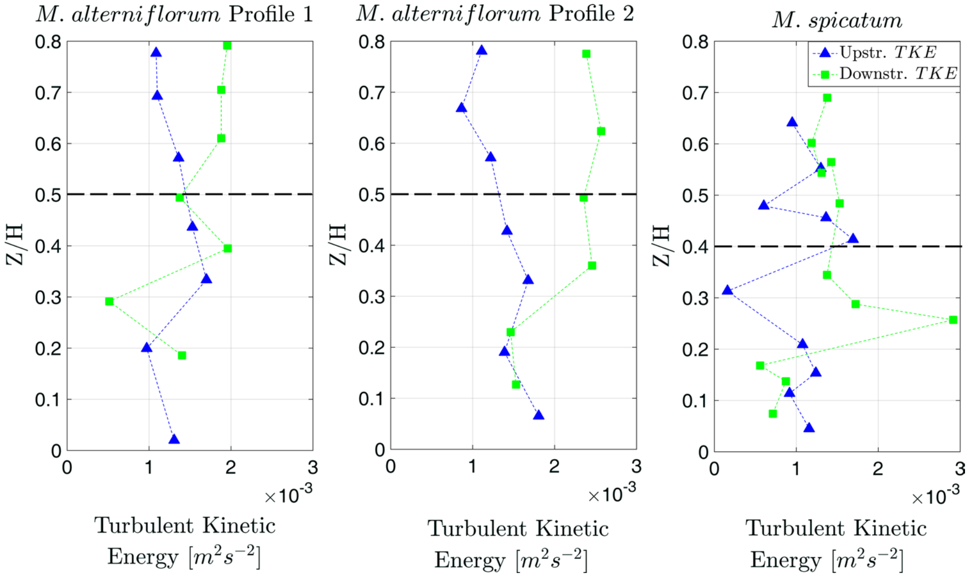

Fig. 4 Turbulent kinetic energy of the first and second pair of profiles downstream and upstream of *M. alterniflorum* and of one pair of profiles in the experiment with *M. spicatum*. Note that the dotted lines indicate the average height of the plant

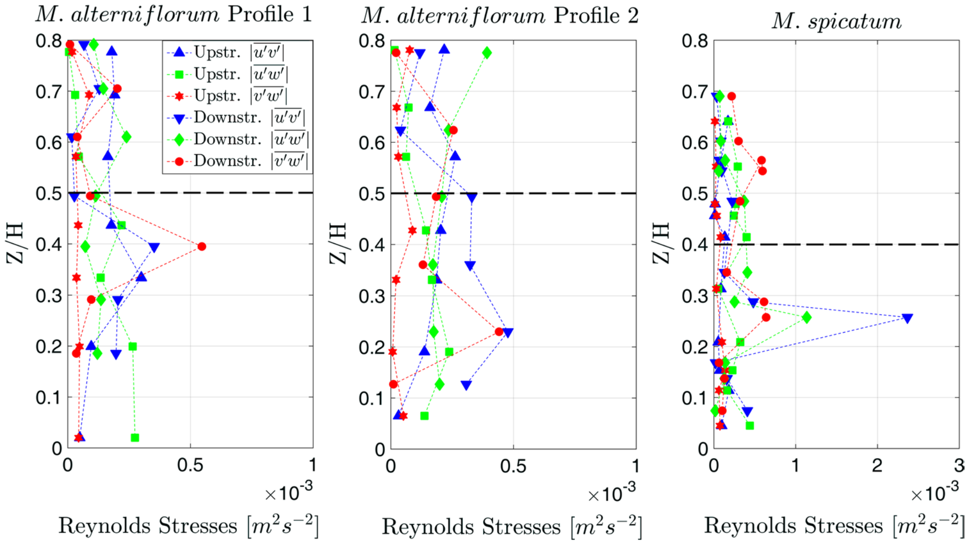

Fig. 5 Absolute tangential Reynolds stresses of the first and second pair of profiles in the experiment with *M. alterniflorum* and of one pair of profiles in the second experiment with *M. spicatum*. Note that the dotted line indicates the average height of the plant

of *M. spicatum*, the highest peaks occurred slightly below the canopy height, where the $\left|\overline{u'v'}\right|$, $\left|\overline{u'w'}\right|$ and $\left|\overline{v'w'}\right|$ components were 0.24, 0.12 and 0.06 × 10^{-3} m^2 s^{-2}, respectively, indicating a layer of increased shear (Fig. 5).

The power spectral density (PSD) plots of the longitudinal velocity fluctuations (Fig. 6) showed inconsistencies between the three measured pairs of profiles, i.e., in the first pair, the PSD was higher in the upstream profile; in the second pair, it was the same as that downstream; and, for *M. spicatum*, the downstream profile had a higher spectral density. The magnitude of downstream fluctuations throughout the whole spectrum also varied in each case, i.e., at the 2 Hz frequency in the first profile, it was below 10^{-4} (m^2 s^{-2}) Hz^{-1}; farther downstream, it increased slightly; and it was highest for the second species. Notably, the slope of the PSD in the second pair of profiles exhibited the best fit to the $-5/3$ scaling range (Kolmogorov 1991), which is common for free flow in open channels (Nezu and Nakagawa 1993).

Quadrant analysis showed frequent major events in the second and fourth quadrants in all upstream profiles (Fig. 7). At the two profiles downstream of *M. alterniflorum*, shear stress production was transferred to outward and inward interactions, but sweeps and ejections were still present. For *M. spicatum*, the quadrant plot made from a point downstream was biased because points near the bottom generally had poor quality (this was discussed more broadly in Przyborowski et al. 2018b), and 32% of the velocity values were replaced during the filtering procedure. Therefore, some information from the recording was lost, especially for inward interactions. However, sweeps tended to

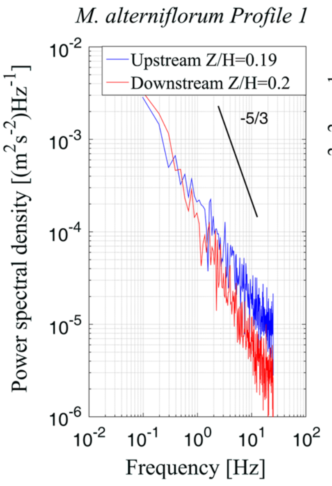

Fig. 6 Power spectrum of the longitudinal velocity fluctuations in the chosen points from the first and second pair of profiles in the experiment with *M. alterniflorum*, and of one pair of profiles in the second experiment with *M. spicatum*

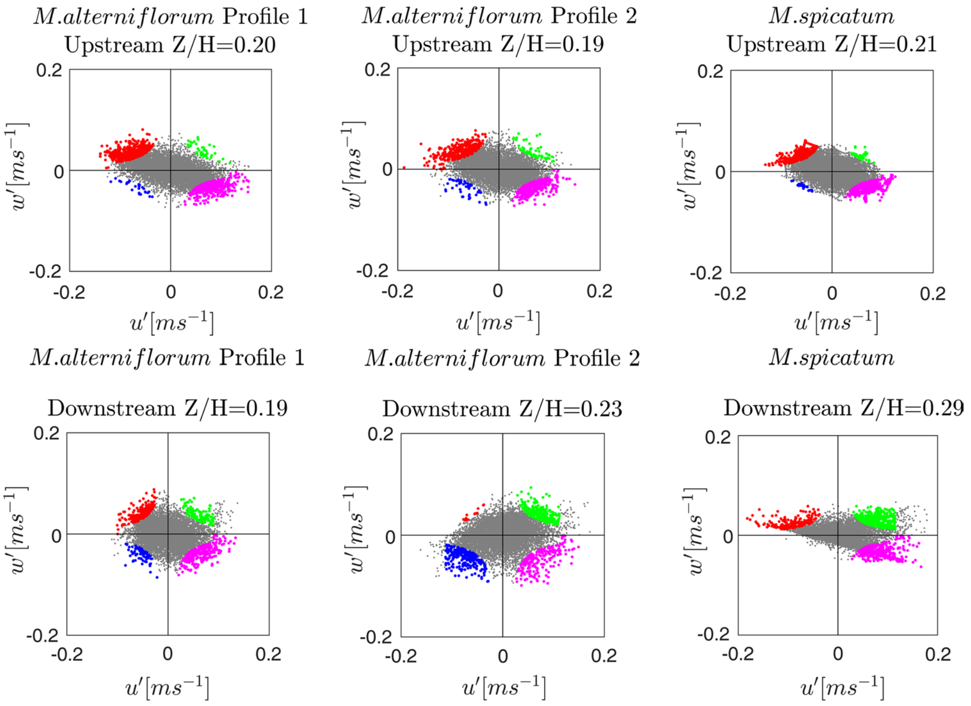

Fig. 7 Quadrant analysis using the bursting cycle detection method at points of specified height. Colors represent points that were above the threshold in each quadrant: green indicates outward interactions; red indicates ejections; blue indicates inward interactions; and purple indicates sweeps

dominate ejections, as in the two profiles downstream of *M. alterniflorum*.

Discussion

The coverage percentage of plants as well as their location in the river cross-section influence on channel blockage (Green 2005; O'Hare 2015) and sediment deposition (Västilä and Järvelä 2018). Przyborowski et al. (2018a) showed that patches of *Potamogeton pectinatus* L. varied due to bed conditions and also, that an individual plant patch had a very limited impact on the flow. The present study shows that single patches of two similar species may have varying effects on the local flow field, given the major difference in the aspect ratio between these patches, which is consistent with the Nikora et al. (2008) research about the physical vegetation parameters as roughness descriptors. The obtained results of velocities and turbulence intensities downstream of *M. alterniflorum* (Figs. 2, 3) were in line with those of Hu et al. (2018). In particular, the water velocity in the plant wake was diminished roughly by half, which showed that the patch did not completely block the flow (Fig. 2). Downstream of *M. spicatum*, of which diameter was at least three times larger and the stems visually covered the whole area densely, the results showed strongly increased, in comparison with *M. alterniflorum*, lateral shear below its maximal height. Another significant difference between the results was decreased turbulent kinetic energy observed close to the bed; at the same distance downstream, the decrease in turbulent kinetic energy was better pronounced in the case of the *M. spicatum* patch (Fig. 4). On the other hand, quadrant analysis showed the same trends in occurrence of the secondary currents downstream the both patches.

Effect of patch geometry on downstream turbulence

The turbulent kinetic energy (TKE) was elevated in majority of points downstream of *M. alterniflorum* (Fig. 4). However, in the downstream profile 1 at $Z/H = 0.3$, i.e., below the maximum height of the canopy TKE was reduced, where Hu et al. (2018) showed that TKE should be increased in this layer as a sign of elevated shear stresses. In the case of *M. spicatum*, at the maximum canopy height, TKE was similar to the profile upstream like in the case of the first patch, profile 1 (Fig. 4). For both plants, the TKE inside the wake, i.e., below $Z/H = 0.2$, was reduced, in comparison with the values above (Fig. 4), similarly to the experiments of Hu et al. (2018). The differences in the magnitude of TKE at plant height might be caused by the vertical distribution of patch density, where the majority of the stems did not reach the maximum height of the canopy (Fig. 8). Thus, these results were similar to those observed by Sukhodolov and Sukhodolova (2012), where the TKE profile bias, which indicated cumulative effect of mixing and boundary layers, grew with the density of the vegetation.

The position of the measurement profile close to the *M. spicatum* lateral edge had impact on observed turbulence intensities and tangential Reynolds stresses, as it is closer to the plant flow lateral boundary. The highest observed peak at $Z/H = 0.25$ in both, longitudinal and transverse turbulence intensities, which peak also appeared in $\left|\overline{u'v'}\right|$ stress, indicated the presence of a lateral shear layer (Rominger and Nepf 2011). In comparison with *M spicatum*, downstream of *M. alterniflorum* patch, $\left|\overline{u'v'}\right|$ and $\left|\overline{v'w'}\right|$ stresses showed about five times smaller lateral transport of momentum at $Z/H = 0.4$ in the first downstream profile, which corresponded to the upper part of the plant and in a lower point, i.e., $Z/H = 0.25$, in the second profile (Fig. 5). That difference between produced shear was the direct result of the distinct spatial dimensions of the patches (Ortiz et al. 2013).

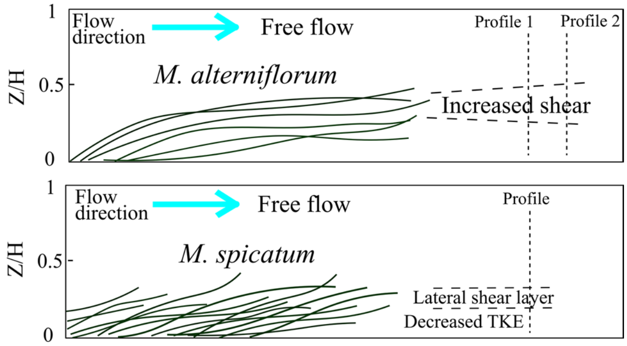

Fig. 8 Schematics of observed flow layers: downstream of the *M. alterniflorum* patch, where a slightly increased turbulent kinetic energy indicated elevated mixing; downstream of the *M. spicatum* patch, where increased turbulence in transverse direction was observed below the height of the canopy, and decreased TKE were observed closer to the bottom

Similar results as those presented in the paper, showing increased Reynolds stresses, were obtained by Biggs et al. (2016) in an experiment with a *Ranunculus penicillatus* patch; however, the $\left|\overline{u'w'}\right|$ shear stress was also elevated, in contrast to the present study, which may be due to differences in bed structure, i.e., sand versus gravel/cobbles. The comparison of the observed $\left|\overline{u'w'}\right|$ stress and corresponding to it turbulence intensities do not support the presence of vertical Kelvin–Helmholtz vortices in either of patches, phenomenon which was described, e.g., by Nepf (2012b). The cause of such result may be wavy motions of plant stems, which is in line with results obtained by Ghisalberti and Nepf (2006), who observed that an increase in the variability of vegetation height resulted in decreased shear stress.

The PSDs of both the longitudinal and vertical velocities in a wake should have distinct peaks at lower frequencies, marking the passage of vortices. In the case of the occurrence of a mixing layer, the spectral density should be higher than that in the free flow (Ghisalberti and Nepf 2006; Sukhodolov and Sukhodolova 2012). Such phenomenon occurred in the case of the *M. spicatum* patch, where a distinctive peak in the turbulence intensity (Fig. 3) translated into the higher energy visible in the PSD from that point. In this experiment, the PSD showed peaks similar in magnitude at lower frequencies; however, at higher frequencies, energy dissipated faster in the downstream profile closer to *M. alterniflorum*, than in the profile farther away (Fig. 6), where the turbulence intensity was elevated (Fig. 3). This indicated that the energy transport in profile 2 downstream was the same as in the free flow, but with increased mixing.

The main differences between complex natural vegetation and simplified rigid laboratory studies

The present study showed that differences in turbulent statistics describing phenomena such as a mixing layer were not as clearly distinguishable as in flumes with rigid rods (Chen et al. 2013). However, such a comparison of artificial rigid patches to real flexible vegetation has limitations. Ortiz et al. (2013) showed that flexible patches have much lower impact on the flow than its rigid counterpart. What is more, there are major differences in biomechanical properties between rigid and flexible materials, which influence plant responses to flow and thus, flow resistance (Łoboda et al. 2018a). For instance, lower flexural rigidity indicates that the plant bends and moves with the flow and thus, decreases its frontal area (Nikora 2010). Additionally, for real patches of vegetation, the majority of species such as *Myriophyllum* have stems reaching far beyond the area of the roots, floating above the bed, as was depicted in Siniscalchi and Nikora (2013). Therefore, it is difficult to compare the number of stems per unit bed area. Moreover, the ratio of water depth (H) to patch height (h) was considered shallow in the present case ($H/h \sim 2$), although there was no solid upper boundary of the patches, as observed in laboratory studies (e.g., Chen et al. 2013), thus expected velocity gradient downstream the patch was not pronounced.

In the present study, quadrant analysis at points in the wake of *M. alterniflorum* revealed that ejections were diminished in favor of inward and outward interactions. This behavior implies that the energy of ejections was allocated to the force needed to lift the patch canopy or that the flow in the wake was returning to its ambient state by inflow from the high-speed free flow layer above.

Limitations of the present study and future directions

One possible reason for the substantial difference in the power spectral density results for *M. spicatum* (Fig. 6) may be the noise contamination of the signal. Brand et al. (2016) depicted how PSD values differ when using certain bins, due to different noise contributions connected to the SNR level. Although bins were chosen using the best mean SNR in the present study, the noise contribution was found to affect higher frequencies. An effect of noise was also visible in the increased contribution of longitudinal velocity fluctuations in the quadrant analysis of point downstream of *M. spicatum* (Fig. 7). On the other hand, the used SNR and correlation thresholds were the same as in field experiments conducted by Cassan et al. (2015) or Afzalimehr et al. (2017), and with the used filtering procedure, the obtained results were not below accepted requirements. Though, a caution in generalization of the presented interpretation is advised due to a scarcity of similar experiments.

Nikora et al. (2008) and Cornacchia et al. (2018) showed how dimensions of aquatic plants and their positions in the river channel determine their impact on the flow. The presented outcomes of two distinct patches showed how big influence on water mixing may have patch dimensions. However, without further downstream profiles and accurate plant density values it is impossible to determine, whether the *M. spicatum* canopy resembles one of the patches used in laboratory studies such as in Zong and Nepf (2012), where vortex street was generated. What is more, patches with enhanced horizontal flow deflection, i.e., which are denser and with lower submergence ratio, should produce greater velocity gradient at patch edge and therefore changing the sedimentation process, while wide patches, i.e., patch width/$h > 4$ produce vertical deflection (Ortiz et al. 2013). However, the results of the present study, were not sufficient enough to prove this relationship, but we do believe that additional field measurement of velocity profiles at the edges of the patches of different dimensions will provide valuable information about this interaction, which finally should help in building advanced hydrodynamics flow-biota models.

In the perspective of river ecology, the existence of a large patch promotes increased sedimentation in its wake (e.g., Cotton et al. 2006; Ortiz et al. 2013) and stimulates further growth downstream (Cornacchia et al. 2018). The question arises of whether impact on the flow and the sediment of wide patches is equal to the impact of more slender ones, assuming that the covered area of the patches is the same. Further case studies including plant growing in different configurations with a denser grid of velocity profiles, sediment traps and biomechanical tests of aquatic plants should provide relevant data to unify vegetated flow models and the impact of patch characteristics on river morphology.

Summary

Turbulent statistical analysis of the 3D velocity recorded with Vectrino Profilers in two distinct aquatic plant patches provided the following insights:

- Distinctive peaks in both, the turbulence intensity and turbulent kinetic energy downstream of *M. spicatum*, indicated the increased lateral mixing, which was also present downstream *M. spicatum*, but of a smaller magnitude.
- Comparing the TKE values in the downstream points closest to the bed, i.e., below $Z/H = 0.2$, as in case of the second patch, a layer of the decreased TKE was observed, while at the same distance downstream of *M. alterniflorum*, i.e., at the profile 2, the TKE was similar to the profile upstream.
- The power spectral density of the velocity fluctuation below the plant height showed the occurrence of a mixing layer downstream of *M. spicatum* and the energy downstream of *M. alterniflorum* dissipated faster in the closer profile.
- The bursting cycle downstream of both plants was disturbed, i.e., the ejections diminished and the number of sweeps, as well as inward and outward interactions increased.

These results are generally in line with the findings of similar investigations of flow around natural aquatic plants, especially in the case of *M. spicatum*. The smaller and slenderer patch of *M. alterniflorum* influenced the flow field less than did the second plant patch. The presented analysis showed that after thorough evaluation, filtering and despiking procedures, velocity recordings of a lower quality than those acquired in laboratory conditions can lead to meaningful results.

Acknowledgements This work was supported by the National Science Centre, Poland, Grant No. UMO-2014/13/D/ST10/01123 "Field experimental investigation of hydrodynamics of water flow–vegetation–sediment interactions at the scale of individual aquatic plants." The publication has been partially financed from the funds of the Leading National Research Centre (KNOW) received by the Centre for Polar Studies for the period 2014–2018.

Compliance with ethical standards

Conflict of interest On behalf of all authors, the corresponding author states that there is no conflict of interest.

References

Aberle J, Järvelä J (2013) Flow resistance of emergent rigid and flexible floodplain vegetation. J Hydraul Res 51(1):33–45. https://doi.org/10.1080/00221686.2012.754795

Aberle J, Järvelä J (2015) Hydrodynamics of vegetated channels. In: Rowiński P, Radecki-Pawlik A (eds) Rivers: physical, fluvial and environmental processes. GeoPlanet: earth and planetary sciences. Springer, Cham, pp 519–541. https://doi.org/10.1007/978-3-319-17719-9_21

Afzalimehr H, Barahimi M, Sui J (2017) Non-uniform flow over cobble bed with submerged vegetation strip. In Proceedings of the institution of civil engineers-water management. Thomas Telford Ltd, London, pp 1–16

Bialik RJ (2013) Numerical study of near-bed turbulence structures influence on the initiation of saltating grains movement. J Hydrol Hydromech 61(3):202–207. https://doi.org/10.2478/johh-2013-0026

Biggs H, Nikora VN, Papadopoulos K, Vettori D, Gibbins C, Kucher M (2016) Flow-vegetation interactions: a field study of ranunculus penicillatus at the large patch scale. In: Webb JA, Costelloe JF, Casas-Mulet R, Lyon JP, Stewardson MJ (eds.) Proceedings of the 11th international symposium on ecohydraulics, Melbourne, Australia, 7–12 Feb 2016 Paper number 26153

Brand A, Noss C, Dinkiel C, Holzner M (2016) High-resolution measurements of turbulent flow close to the sediment-water interface using bistatic acoustic profiler. J Atmos Ocean Technol 33(4):769–788. https://doi.org/10.1175/JTECH-D-15-0152.1

Cameron SM, Nikora VI, Albayrak I, Miler O, Stewart M, Siniscalchi F (2013) Interactions between aquatic plants and turbulent flow: a field study using stereoscopic PIV. J Fluid Mech 732:345–372. https://doi.org/10.1017/jfm.2013.406

Cassan L, Belaud G, Baume JP, Dejean C, Moulin F (2015) Velocity profiles in a real vegetated channel. Environ Fluid Mech 15(6):1263–1279. https://doi.org/10.1007/s10652-015-9417-0

Chen Z, Jiang C, Nepf H (2013) Flow adjustment at the leading edge of a submerged aquatic canopy. Water Resour Res 49(9):5537–5551. https://doi.org/10.1002/wrcr.20403

Cornacchia L, Folkard A, Davies G, Grabowski RC, van de Koppel J, van der Wal D, Wharton G, Puijalon S, Bouma TJ (2018) Plants face the flow in V formation: a study of plant patch alignment in streams. Limnol Oceanogr. https://doi.org/10.1002/lno.11099

Cotton JA, Wharton G, Bass JAB, Heppell CM, Wotton RS (2006) The effects of seasonal changes to in-stream vegetation cover on patterns of flow and accumulation of sediment. Geomorphology 77(3–4):320–334. https://doi.org/10.1016/j.geomorph.2006.01.010

Franca MJ, Santos BO, Antico F, Ferreira RML (2014) Quadrant analysis of coherent structures in open channel flows over mobile and immobile hydraulically rough beds. ERCOFTAC Bull 100:29–36

Ghisalberti M, Nepf H (2006) The structure of the shear layer in flows over rigid and flexible canopies. Environ Fluid Mech 6(3):277–301. https://doi.org/10.1007/s10652-006-0002-4

Goring DG, Nikora VI (2002) Despiking acoustic Doppler velocimeter data. J Hydraul Eng 128(1):117–126. https://doi.org/10.1061/(ASCE)0733-9429(2002)128:1(117)

Grass AJ (1971) Structural features of turbulent flow over smooth and rough boundaries. J Fluid Mech 50(2):233–255. https://doi.org/10.1017/S0022112071002556

Green JC (2005) Modelling flow resistance in vegetated streams: review and development of new theory. Hydrol Process 19(6):1245–1259. https://doi.org/10.1002/hyp.5564

Gurnell AM, Bertoldi W, Corenblit D (2012) Changing river channels: the roles of hydrological processes, plants and pioneer fluvial landforms in humid temperate, mixed load, gravel bed rivers. Earth Sci Rev 111(1–2):129–141. https://doi.org/10.1016/j.earscirev.2011.11.005

Hu Z, Lei J, Liu C, Nepf H (2018) Wake structure and sediment deposition behind models of submerged vegetation with and without flexible leaves. Adv Water Resour 118:28–38. https://doi.org/10.1016/j.advwatres.2018.06.001

Hurther D, Lemmin UA (2001) Correction method for turbulence measurements with a 3D acoustic Doppler velocity profiler. J Atmos Ocean Technol 18(3):446–458. https://doi.org/10.1175/1520-0426(2001)018%3c0446:ACMFTM%3e2.0.CO;2

Kłosowski S, Kłosowski G (2007) Aquatic and marsh plants. MULTICO, Warsaw **(in Polish)**

Koca K, Noss C, Anlanger C, Brand A, Lorke A (2017) Performance of the Vectrino Profiler at the sediment-water interface. J Hydraul Res 55(4):573–581. https://doi.org/10.1080/00221686.2016.1275049

Kolmogorov AN (1991) Dissipation of energy in the locally isotropic turbulence. Proc R Soc Lond A 434(1890):15–17. https://doi.org/10.1098/rspa.1991.0076

Kubrak E, Kubrak J, Kiczko A (2015) Experimental investigation of kinetic energy and momentum coefficients in regular channels with stiff and flexible elements simulating submerged vegetation. Acta Geophys 63:1405–1422. https://doi.org/10.1515/acgeo-2015-0053

Liu D, Liu X, Fu X, Wang G (2016) Quantification of the bed load effects on turbulent open-channel flows. J Geophys Res Earth 121(4):767–789. https://doi.org/10.1002/2015JF003723

Liu C, Hu Z, Lei J, Nepf H (2017) Vortex structure and sediment deposition in the wake behind a finite patch of model submerged vegetation. J Hydraul Eng 144(2):04017065. https://doi.org/10.1061/(ASCE)HY.1943-7900.0001408

Łoboda AM, Karpiński M, Bialik RJ (2018a) On the relationship between aquatic plant stem characteristics and drag force: is modeling application possible? Water 10(5):540. https://doi.org/10.3390/w10050540

Łoboda AM, Przyborowski Ł, Karpiński M, Bialik RJ, Nikora VI (2018b) Biomechanical properties of aquatic plants: the effect of test conditions. Limnol Oceanogr Methods 16(4):222–236. https://doi.org/10.1002/lom3.10239

Luchik TS, Tiederman WG (1987) Timescale and structure of ejections and bursts in turbulent channel flows. J Fluid Mech 174:529–552

Naden P, Rameshwaran P, Mountford O, Robertson C (2006) The influence of macrophyte growth, typical of eutrophic conditions, on river flow velocities and turbulence production. Hydrol Process 20(18):3915–3938. https://doi.org/10.1002/hyp.6165

Nepf HM (2012a) Hydrodynamics of vegetated channels. J Hydraul Res 50(3):262–279. https://doi.org/10.1080/0221686.2012.6965599

Nepf HM (2012b) Flow and transport in regions with aquatic vegetation. Annu Rev Fluid Mech 44:123–142. https://doi.org/10.1146/annurev-fluid-120710-101048

Nezu I, Nakagawa H (1993) Turbulence in open-channel flows. IAHR-Monograph, Balkema

Nikora V (2010) Hydrodynamics of aquatic ecosystems: an interface between ecology, biomechanics and environmental fluid mechanics. River Res Appl 26(4):367–384. https://doi.org/10.1002/rra.1291

Nikora V, Larned S, Nikora N, Debnath K, Cooper G, Reid M (2008) Hydraulic resistance due to aquatic vegetation in small streams: field study. J Hydraul Eng 134(9):1326–1332. https://doi.org/10.1061/(ASCE)0733-9429(2008)134:9(1326)

Nikora N, Nikora V, O'Donoghue T (2013) Velocity profiles in vegetated open-channel flows: combined effects of multiple mechanisms. J Hydraul Eng 139(10):1021–1032. https://doi.org/10.1061/(ASCE)HY.1943-7900.0000948

O'Hare MT (2015) Aquatic vegetation: a primer for hydrodynamic specialists. J Hydraul Res 53(6):687–698. https://doi.org/10.1080/00221686.2015.1090493

Ortiz AC, Ashton A, Nepf H (2013) Mean and turbulent velocity fields near rigid and flexible plants and the implications for deposition. J Geoph Res Earth 118(4):2585–2599. https://doi.org/10.1002/2013JF002858

Parsheh M, Sotiropoulos F, Porte-Agel F (2010) Estimation of power spectra of acoustic-Doppler velocimetry data contaminated with intermittent spikes. J Hydraul Eng ASCE 136(6):368–378. https://doi.org/10.1061/(ASCE)HY.1943-7900.0000202

Poggi D, Porporato A, Ridolfi L, Albertson JD, Katul GG (2004) The effect of vegetation density on canopy sub-layer turbulence. Bound Layer Meteorol 111(3):565–587. https://doi.org/10.1023/B:BOUN.0000016576.05621.73

Przyborowski Ł, Łoboda AM, Bialik RJ (2018a) Experimental investigations of interactions between sand wave movements, flow structure, and individual aquatic plants in natural rivers: a case study of *Potamogeton Pectinatus* L. Water 10(9):1166. https://doi.org/10.3390/w10091166

Przyborowski Ł, Łoboda AM, Karpiński M, Bialik RJ (2018b) Characteristics of flow around aquatic plants in natural conditions: experimental setup, challenges and difficulties. In: Kalinowska MB, Mrokowska MM, Rowiński PM (eds) Free surface flows and transport processes. GeoPlanet: earth and planetary sciences. Springer, Cham, pp 347–361. https://doi.org/10.1007/978-3-319-70914-7_23

Rominger J, Nepf H (2011) Flow adjustment and interior flow associated with a rectangular porous obstruction. J Fluid Mech 680:636–659. https://doi.org/10.1017/jfm.2011.199

Siniscalchi F, Nikora V (2013) Dynamic reconfiguration of aquatic plants and its interrelations with upstream turbulence and drag forces. J Hydraul Res 51(1):46–55. https://doi.org/10.1080/00221686.2012.743486

Siniscalchi F, Nikora VI, Aberle J (2012) Plant patch hydrodynamics in streams: mean flow, turbulence, and drag forces. Water Resour Res. https://doi.org/10.1029/2011WR011050

Sukhodolov AN (2015) Field-based research in fluvial hydraulics: potential, paradigms and challenges. J Hydraul Res 53(1):1–19. https://doi.org/10.1080/00221686.2015.1012126

Sukhodolov AN, Sukhodolova TA (2012) Vegetated mixing layer around a finite-size patch of submerged plants: Part 2. Turbulence statistics and structures. Water Resour Res. https://doi.org/10.1029/2011WR011805

Sukhodolova TA, Sukhodolov AN (2012) Vegetated mixing layer around a finite-size patch of submerged plants: 1. Theory and field experiments. Water Resour Res. https://doi.org/10.1029/2011WR011804

Termini D, Di Leonardo A (2017) Turbulence structure and implications in exchange processes in high-amplitude vegetated meanders: experimental investigation. Adv Water Resour. https://doi.org/10.1016/j.advwatres.2017.11.020

Thomas RE, Schindfessel L, McLelland SJ, Creëlle S, De Mulder T (2017) Bias in mean velocities and noise in variances and covariances measured using a multistatic acoustic profiler: the Nortek Vectrino Profiler. Meas Sci Technol. https://doi.org/10.1088/1361-6501/aa7273

Tymiński T, Kałuża T (2012) Investigation of Mechanical Properties and Flow Resistance of Flexible Riverbank Vegetation. Pol J Environ Stud 21(1):201–207

Västilä K, Järvelä J (2018) Characterizing natural riparian vegetation for modeling of flow and suspended sediment transport. J Soils Sediments 18(10):3114–3130. https://doi.org/10.1007/s11368-017-1776-3

Västilä K, Järvelä J, Koivusalo H (2015) Flow–vegetation–sediment interaction in a cohesive compound channel. J Hydraul Eng 142(1):04015034. https://doi.org/10.1061/(ASCE)HY.1943-7900.0001058

Voulgaris G, Trowbridge JH (1998) Evaluation of the acoustic Doppler velocimeter (ADV) for turbulence measurements. J Atmos Ocean Technol 15(1):272–289. https://doi.org/10.1175/1520-0426(1998)015%3c0272:EOTADV%3e2.0.CO;2

Wahl TL (2003) Discussion of 'Despiking acoustic Doppler velocimeter data' by Derek G. Goring and Vladimir I. Nikora. J Hydraul Eng 129(6):484–487. https://doi.org/10.1061/(ASCE)0733-9429(2003)129:6(484)

Welch PD (1967) The use of fast Fourier transform for the estimation of power spectra: a method based on time averaging over short, modified periodograms. IEEE T Acoust Electr 15(2):70–73. https://doi.org/10.1109/TAU.1967.1161901

Wilson SJ, Ricciardi A (2009) Epiphytic macroinvertebrate communities on Eurasian watermilfoil (*Myriophyllum spicatum*) and native milfoils *Myriophyllum sibericum* and *Myriophyllum alterniflorum* in eastern North America. Can J Fish Aquat Sci 66(1):18–30. https://doi.org/10.1139/F08-187

Zong L, Nepf H (2012) Vortex development behind a finite porous obstruction in a channel. J Fluid Mech 691:368–391. https://doi.org/10.1017/jfm.2011.479

Acta Geophysica (2019) 67:999–1016
https://doi.org/10.1007/s11600-019-00293-3

RESEARCH ARTICLE - SPECIAL ISSUE

Assessment of some numerical methods for estimating the parameters of the one-dimensional advection–dispersion model

Davy D. Silavwe[1] · **Isobel C. Brink**[1] · **Steve G. Wallis**[2]

Received: 18 September 2018 / Accepted: 16 April 2019 / Published online: 30 April 2019

Abstract

This study appraised optimisations of numerical solutions of the one-dimensional advection–dispersion model (AD-Model) to synthetic data generated using an analytical solution. The motivation for the work was to identify reliable methods for estimating stream solute transport parameters from observed events in small rivers. Numerical solutions of the AD-Model must contend with several effects that might disturb the solution, with the introduction of numerical diffusion and numerical dispersion being particularly important issues. This poses a problem if physical dispersion is being identified by optimising model coefficients using observations of solute transport from field experiments. The discretisation schemes used were the Backward-Time/Centred-Space, Crank–Nicolson, Implicit QUICK, MacCormack and QUICKEST methods. Optimisations were obtained for several grid resolutions by keeping the time step constant whilst varying the space step: the range of Peclet number, P_e, was 1.5–12.0. Generally, increasing the space step led to poorer estimated coefficients and poorer fits to the synthetic concentration profiles. For $P_e < 5$ only Crank–Nicolson, MacCormack and QUICKEST gave reliable optimised dispersion coefficients: those from Backward-Time/Centred-Space and Implicit QUICK being significantly underestimated. For $P_e > 5$ Crank–Nicolson and MacCormack gave slightly overestimated dispersion coefficients whilst the other methods gave significantly underestimated dispersion coefficients. These findings were generally consistent with the known presence of numerical diffusion and numerical dispersion in the methods.

Keywords Advection–dispersion model · Numerical methods · Solute transport parameters · Numerical properties · Optimisation

Introduction

Worldwide, there is a constant threat of high-level contamination of freshwater resources such as streams through, inter alia, discharge of effluents from treatment plants, accidental industrial spillage or intentional disposal of pollutants. In many cases, unintentional spills are the most significant economic danger to fresh water resources (USEPA 2009). Prediction of the subsequent movement and longitudinal spreading of contaminants in streams is necessary for a timely response by water authorities in respect of downstream consumers and purposes of alleviation. Alleviation can only be possible if the characteristics of pollutant migration in such streams are reliably known. There are numerous processes that transport matter within streams. In the present context these processes can be categorised as either advection or mixing, and they exist in three spatial dimensions. However, we will assume they do not vary in time.

Attempting to include the processes in a 2- or 3-dimensional spatial framework would result in a complex model with difficulties associated with the availability of data for development of the model. A 1-dimensional model, conversely, has the advantages of improved ease of application as well as more easily obtainable data. However, all the mixing processes become combined in a single term, creating some separation between the model and the real world. Furthermore, the use of the 1-dimensional model is only suitable beyond an initial mixing zone, in which a pollutant becomes sufficiently well distributed within the cross section of the flow. Once achieved, the 1-dimensional mixing

---

✉ Steve G. Wallis
s.g.wallis@hw.ac.uk

[1] Department of Civil Engineering, Stellenbosch University, Stellenbosch, Cape Town, South Africa

[2] School of Energy, Geoscience, Infrastructure and Society, Heriot-Watt University, Riccarton, Edinburgh EH14 4AS, UK

is usually termed longitudinal dispersion, represented by a dispersion coefficient (Fischer et al. 1979; Rutherford 1994; Martin and McCutcheon 1999; Ani et al. 2009), and the corresponding 1-dimensional advection is quantified by the cross-sectional average longitudinal velocity. Both of these vary with the flow rate and the size of the stream channel. Although stream geometry is usually variable along the stream, introducing significant complexities into the dispersive aspects (Ani et al. 2009), lack of data often prevents the inclusion of such detail and, therefore, streams are often modelled as uniform 1-dimensional systems. Consequently, application of the models produces reach-averaged solute transport parameter values (Wallis et al. 2013; Wallis and Manson 2004).

Most of the mass transport modelling in streams has been undertaken using the 1-dimensional governing transport equation known as the advection–dispersion model (AD-Model) (Fischer et al. 1979; Rutherford 1994). It has been observed that best practices for estimating solute transport parameters combine tracer experiments with the AD-Model (Rutherford 1994). In this, workers combine solutions of the model equation with some form of parameter estimation. Experimental data is in the form of solute concentration–time profiles (or breakthrough curves), obtained by conducting slug-release tracer experiments. Several types of solution of the governing equation are available which include analytical solutions (Ogata and Banks 1961; Kumar et al. 2009) and numerical solutions (Abbott and Basco 1989; Versteeg and Malalasekera 2007).

In most practical situations the solution to governing equations is through numerical approaches because the initial and/or boundary conditions of analytical solutions are rarely satisfied in the field. There is evidence to suggest that, depending on the numerical method used, different solute transport parameter values can be estimated with the same observed data, such that prediction and interpretation of mass transport in streams may depend on the numerical approach used (Wallis and Manson 2004; Wallis et al. 2013). Numerical solution methods of the AD-Model must deal with several effects that disturb a solution. Primarily, these effects are a result of numerical approximation of the advective term (Sobey 1984; Abbott and Basco 1989), which may introduce artificial mixing (see later) into the solution. In the computed solution it may not be possible to differentiate between the artificial mixing introduced by a numerical scheme and the physical process of longitudinal dispersion (Sobey 1984). Therefore, it would be prudent to compare solutions given by various numerical methods. This is the theme of the current paper. The aim of the work was to investigate the reliability of several numerical methods for estimating stream solute transport parameters in a small stream using the AD-Model. The primary objective of the study was to estimate solute transport parameters using synthetic data generated with an analytical solution over a range of numerical grid resolutions. Since the parameter values used to generate the data were known, the accuracy of the estimated parameters could easily be assessed.

Background

The spreading of solutes in a fluid is termed as mixing (Chin 2013). Mixing occurs because of molecular diffusion, turbulent diffusion and shear dispersion. Longitudinal mixing in streams is primarily caused by shear dispersion which results from the stretching effect of cross-sectional velocity gradients combined with cross-sectional turbulent diffusion. The longitudinal dispersion coefficient is used to measure the longitudinal mixing of a solute which is well mixed across a channel (Chin 2013). Taylor (1954) argued that when a solute is well mixed in turbulent pipe flow longitudinal dispersion can be described by Fick’s law. Based on this, Fischer argued that in open channels, sufficiently downstream of an initial mixing zone, concentration distributions can be modelled using an analogy of Fick’s law (Fischer et al. 1979). In this zone there is an equilibrium between longitudinal velocity shear and transverse mixing. Depending on the release conditions of the solute, the zone may extend by up to 100 stream widths: Rutherford (1994) provides more detail on this issue. The general 1-dimensional equation describing longitudinal transport is expressed as (Rutherford 1994):

$$\frac{\partial(A\varphi)}{\partial t}+\frac{\partial(A\upsilon\varphi)}{\partial x}=\frac{\partial}{\partial x}\left[DA\frac{\partial\varphi}{\partial x}\right] \tag{1}$$

where A is the cross-sectional area of the channel, D is the longitudinal dispersion coefficient, υ, is the cross-sectional average longitudinal velocity, φ, is the cross-sectional average solute concentration, x is the longitudinal coordinate and t is the time. The above equation is Taylor’s (1954) and Fischer et al.’s (1979) 1-dimensional advection–dispersion model (AD-Model). Commonly, constant mixing rates and cross-sectional average velocities are assumed (Chanson 2004). Therefore, for constant dispersion coefficient and velocity, the 1-dimensional advection–dispersion model is:

$$\frac{\partial(\varphi)}{\partial t}+\upsilon\frac{\partial(\varphi)}{\partial x}=D\frac{\partial^2\varphi}{\partial x^2} \tag{2}$$

In this equation, the longitudinal dispersion coefficient quantifies the rate of longitudinal stretching of a solute cloud, and the cross-sectional average velocity quantifies the rate of downstream movement of the whole cloud (Chanson 2004; Wallis 2007). Application to a particular advection–dispersion problem requires a complete mathematical statement consisting of the AD-Model and specific boundary and initial conditions. The AD-Model is implemented through calibration, i.e. selection of values for coefficients υ and D for use in solutions of Eq. (2), and several types of solution exist. The available solutions include analytical solutions (Ogata and Banks 1961; Kumar et al. 2009), numerical solutions (Wallis et al. 1998; Hoffman 2001; Manson et al. 2001; Chapra 2008) and routing procedures (Rutherford 1994; Singh and Beck 2003). There are very many solutions to the AD-Model depending on which boundary and initial conditions are specified (Fischer et al. 1979; Barnett 1983; Graf and Altinakar 1998; Chanson 2004; Chin 2013). Analytical approaches are derived to obtain solutions that are precise and continuous in time and space whereas numerical and routing approaches are inherently approximate and discrete.

There are essential analytical solutions of the AD-Model that are considered as the bases from which other solutions can be developed. These essential solutions mostly correspond to instantaneous slug releases of a solute in a stream in which the velocity and mixing fields are longitudinally uniform. One such solution is Taylor's solution of the AD-Model with constant coefficients, written as (Rutherford 1994):

$$\varphi(x,t) = \frac{M}{A\sqrt{4\pi Dt}} \exp\left[-\frac{(x-\upsilon t)^2}{4Dt}\right] \tag{3}$$

where M = mass of the solute released, and the other variables are as previously defined. The solution is based on the situation where concentration is known as a spatial distribution at an initial time, and it satisfies the following initial and boundary conditions (Rutherford 1994; Graf and Altinakar 1998):

$$\varphi(x,0) = M_1\delta(x) \tag{4}$$

$$\varphi(+\infty,t) = 0 \tag{5}$$

$$\varphi(-\infty,t) = 0 \tag{6}$$

where M_1 is the mass of solute released per unit cross-sectional surface area and δ is the Dirac delta function. The Taylor solution is reliable in the equilibrium zone, i.e. at some distance downstream from the point where the slug is released (Rutherford 1994).

Equation (3) predicts Gaussian spatial concentration profiles and slightly skewed temporal concentration profiles. Observations of solute transport in streams are usually undertaken in the time domain and they too are not Gaussian, but they do not necessarily obey Taylor's solution (Chapra 2008). There are several reasons for this, e.g. the conditions in the field may not be consistent with the initial and boundary conditions of the solution, the stream may not be longitudinally uniform and the assumption of uniform concentration across the stream section may not hold. In addition, dead zones in the stream often create long tails in concentration profiles resulting in further deviations of temporal profiles from Gaussianity (Singh and Beck 2003).

Most practical situations require the use of a numerical solution because ultimately the models are required for more complex problems than those that allow the use of analytical solutions (Martin and McCutcheon 1999; Wallis 2007). Unfortunately, numerical solutions are neither exact nor continuous in both time and space, producing discrete solutions. Numerical solution techniques involve converting the governing differential equation into algebraic difference equations that can be solved for values at incremental points, or nodes, in space and time (Abbott and Basco 1989; Wallis 2007; Szymkiewicz 2010; Chapra and Canale 2015). In applying numerical methods, accurate results may be obtained when the number of nodes is infinitely large regardless of the method used. However, practical calculations can only use a limited number of nodes. In that case, results can only be physically realistic when the discretisation scheme has important properties, namely that they be stable, conservative, bounded and transportive (Ferziger and Peric 2002; Versteeg and Malalasekera 2007).

A solution method is said to stable if the errors that appear during the numerical solution process do not magnify; a conservative method is one that maintains the original mass of solute throughout the calculations. A bounded method entails that solutions remain within appropriate physical limits. Therefore, in the absence of sources, the concentration values at internal nodes should be bounded by boundary values, which in the context of solute transport in rivers implies that internal concentrations should be less than the concentrations propagated into the solution domain from the upstream boundary (because the physical system is advection dominated). A transportive method is one that recognises the directionality of influence in the flow. For solute transport in rivers conditions at a downstream location are heavily influenced by conditions further upstream with there being little or no influence from locations further downstream (because the physical system is advection dominated). In the numerical solution, the Peclet number (see below) plays an important role because it is a measure of the relative strength of advection and dispersion.

There are various discretisation schemes with varying properties (Leonard 1979; Abbott and Basco 1989; Hoffman 2001; Versteeg and Malalasekera 2007). Numerical solutions are discretised using one of the three basic approaches, namely: finite differences, finite volumes and finite elements (Abbott and Basco 1989; Ferziger and Peric 2002; Versteeg and Malalasekera 2007; Szymkiewicz 2010). However, the two most common discretisation approaches used in modelling solute transport in streams are the finite difference and finite volume methods. The finite volume approach has an advantage in that mass conservation is guaranteed (Versteeg and Malalasekera 2007) whereas finite difference schemes

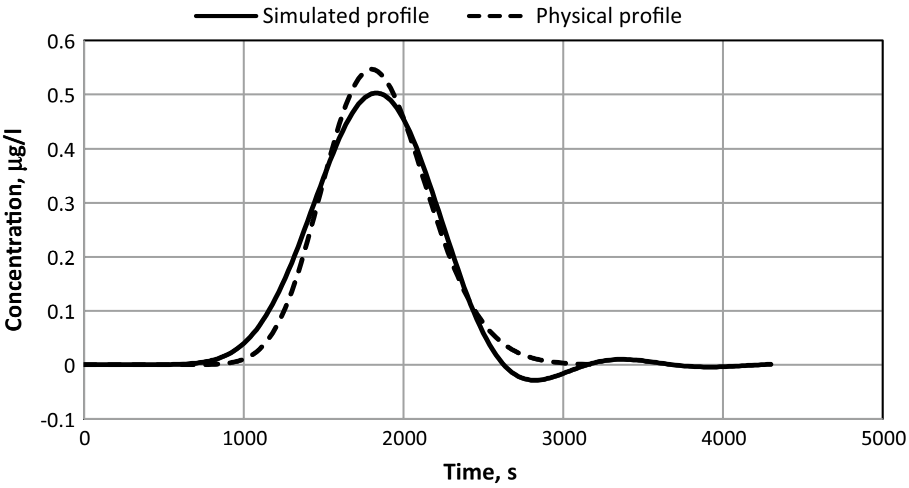

Fig. 1 Comparison of a simulated concentration profile using the Crank–Nicolson scheme with the corresponding physical concentration profile

may require that special care is taken (Ferziger and Peric 2002). A solution method for a time-variable problem can be advanced in time in two ways, namely: explicitly and implicitly (see next section).

The main issue in the application of numerical methods to Eq. (2) is the formulation of an appropriate scheme for the values of the transported property when accounting for the advective contribution to the solution (Abbott and Basco 1989; Wallis and Manson 1997; Versteeg and Malalasekera 2007; Wallis 2007).

It is now necessary to define and explain some terminology in order to help mitigate some unavoidable confusion. Mathematically, Eq. (2) is of the form of an advection–diffusion equation. When the truncation errors of numerical solutions to it are examined, it is possible that they include the second, third and higher spatial derivatives of concentration. Mathematically, such terms introduce unwanted errors known as numerical diffusion (from the second spatial derivative) and numerical dispersion (from third spatial derivative). Similar errors are introduced by the higher spatial derivatives, but the second and third ones are the dominant terms. In the context of the application of Eq. (2) to longitudinal mixing in rivers the numerical diffusion enhances the physical dispersion causing greater longitudinal spreading and amplitude attenuation to occur in solutions than would be expected based on the value of the dispersion coefficient specified by the modeller (Chapra 2008; Szymkiewicz 2010). In contrast, numerical dispersion encourages the appearance of oscillations (or wiggles) in the numerical solutions (Leonard 1979; Manson and Wallis 1995; Chapra 2008) caused by the various components of the solution being propagated at different wave celerities (Szymkiewicz 2010). Usually the presence of these oscillations is most noticeable on the leading or trailing edge of a concentration profile and as a consequence the non-zero part of the profile extends further than it would if numerical dispersion were not present. In order to conserve the mass of the solute, some amplitude reduction and phase shift of the profile is often observed also. This is illustrated in Fig. 1 using a simulation with the Crank–Nicolson scheme (one of the schemes described later in the paper). Although it appears that the simulated concentration profile has spread further than the corresponding physical profile, the cause is not numerical diffusion, but is numerical dispersion. Since, physically, diffusion and dispersion are different processes, and dispersion has two quite different meanings to mathematicians and river modellers, in this paper we use the term artificial mixing when discussing the modified longitudinal spreading caused by any truncation error terms. Usually, the majority of this is due to numerical diffusion from the second spatial derivative in the truncation error.

The typical ways of judging the suitability of a numerical solution of the AD-Model, i.e. stability, boundedness, mass conservation etc., reveal little about the accuracy of a numerical solution (Sobey 1984). The fact that a scheme is numerically bounded or stable does not guarantee its accuracy. The grid resolution (i.e. the magnitude of the time and space steps in comparison with the duration and length, respectively, of the solute cloud being modelled) also has a considerable influence on the accuracy of a numerical scheme though it is often given little attention (Sobey 1984). Overall, the suitability of a numerical solution depends on the relative strength of the transport processes of advection and dispersion, the characteristics of the numerical method and the grid resolution used (Wallis and Manson 1997; Versteeg and Malalasekera 2007; Wallis 2007). Although these issues are inter-related the performance of a numerical method is heavily influenced by two non-dimensional properties known as the advection (or Courant) and dispersion (or diffusion) numbers. The ratio of the advection number to the dispersion number is known as the Peclet number (Ferziger and Peric 2002; Versteeg and Malalasekera 2007), which indicates whether the solution is dominated by advection or by dispersion (Chapra 2008; Chin 2013). An important application of the Peclet number is that it can be used to predict the appearance of oscillations (Abbott and Basco 1989; Versteeg and Malalasekera 2007; Szymkiewicz 2010).

In contrast to simulating a solute transport event, estimating solute transport parameters using observed concentration data requires an inverse modelling method. In this, values of model parameters are determined which give the best fit between the simulated and the observed data (Semuwemba 2011; Chin 2013). The level of agreement between the model output and the observations is used to assess the capability of the model (Runkel and Broshears 1991; Wallis et al. 2013), which can be assessed using one or more performance measures (Bennett et al. 2013).

Applied numerical methods

Several numerical methods were applied in this investigation. The choice of various discretisation schemes was based on discretisation type, solution method and scheme order. Hence, finite difference (FD) and finite volume (FV) discretisation approaches, explicit and implicit solution methods and first, second and third-order accurate discretisation schemes were chosen. The FD schemes were the Backward-Time/Centred-Space method, the Crank–Nicolson method and the MacCormack method (Ferziger and Peric 2002; Chapra 2008). The FV schemes were the Implicit QUICK (quadratic upstream interpolation for convective kinetics) method (Leonard 1979; Versteeg and Malalasekera 2007) and the QUICKEST (quadratic upstream interpolation for convective kinetics with estimated streaming terms) method (Leonard 1979).

The FD approach subdivides the solution domain into a mesh, in which grid lines serve as local coordinates. The derivatives in the AD-Model are expressed in terms of nodal quantities of both dependent and independent variables at the intersection of the grid lines. The discretisation results in algebraic equation(s) with all unknowns prescribed at discrete mesh points of the solution domain. The FV approach subdivides the solution domain into several control volumes (CVs) each of which is centred at a node of the mesh. The derivatives in the AD-Model equation are integrated over the CV allowing the net solute mass entering the CV to be expressed in terms of the differences in advective and dispersive solute fluxes passing through the faces of the CV. The nodal values are then used in an interpolation formula to approximate the solute fluxes at the CV faces. Consequently, one obtains an algebraic equation for each CV, in which several neighbouring nodal values appear (Ferziger and Peric 2002; Versteeg and Malalasekera 2007). "Appendix 1" provides explanatory figures for the two approaches.

A general approach for advancing a FD solution over time employs a temporal weighting, θ, and is expressed as (Abbott and Basco 1989):

$$\frac{\varphi^{n+1}-\varphi^{n}}{\Delta t}+(1-\theta)\frac{\upsilon\partial\varphi}{\partial x}\bigg|^{n}+\theta\frac{\upsilon\partial\varphi}{\partial x}\bigg|^{n+1} = (1-\theta)\frac{D\partial^2\varphi}{\partial x^2}\bigg|^{n}+\theta\frac{D\partial^2\varphi}{\partial x^2}\bigg|^{n+1} \tag{7}$$

where Δt is the time step and the superscripts n and $n+1$ refer to the times at the start and end of the time step, respectively. Once the spatial gradients have been replaced by finite difference approximations, Eq. (7) is used to evaluate the solute concentration at time $n+1$ for all the nodes, assuming all nodal solute concentrations at time n and all boundary conditions at the edges of the computational domain are known. When applying Eq. (7), if $\theta=0$ only transported variable values at the old time are used to evaluate one unknown concentration, resulting in an explicit calculation; if $\theta=1$, transported variable values at the new time level are used; and if $\theta=0.5$ transported variable values at both time levels are used. The latter two cases give a set of simultaneous equations containing all the unknown concentrations, resulting in an implicit calculation. In principle, the $\theta=0.5$ case is superior to the other cases because it is second-order accurate in time whilst the other cases are only first-order accurate in time. FV schemes can be expressed in a similar temporal weighting framework.

The non-dimensional numerical properties introduced earlier, which have an important bearing on the behaviour of the numerical schemes (advection number, dispersion number and Peclet number) are expressed as follows (Abbott and Basco 1989; Versteeg and Malalasekera 2007), where Δx is the space step:

$$\text{Advection number: } c=\frac{\upsilon\Delta t}{\Delta x} \tag{8}$$

$$\text{Dispersion number: } d=\frac{D\Delta t}{(\Delta x)^2} \tag{9}$$

$$\text{Peclet number: } P_e=\frac{\upsilon\Delta x}{D} \tag{10}$$

Each of the numerical methods used is described in the following sub-sections. Information on the expected behaviour of the methods is considered later.

The Backward-Time/Centred-Space method

Using Eq. (7) with $\theta=1$, the method approximates the spatial derivatives at time level $n+1$ by the centred difference approach. Thus, the method is a Backward-Time/

Centred-Space Implicit scheme (Chapra 2008). The method is a FD scheme and is expressed as:

$$\varphi_j^{n+1} = \varphi_j^n + \left[-\upsilon\frac{\varphi_{j+1}^{n+1} - \varphi_{j-1}^{n+1}}{2\Delta x} + D\frac{\varphi_{j+1}^{n+1} - 2\varphi_j^{n+1} + \varphi_{j-1}^{n+1}}{(\Delta x)^2}\right]\Delta t \tag{11}$$

For computational purposes, the above equation can be expressed in terms of the non-dimensional numerical properties introduced above as:

$$-\left(d + \frac{c}{2}\right)\varphi_{j-1}^{n+1} + (1 + 2d)\varphi_j^{n+1} - \left(d - \frac{c}{2}\right)\varphi_{j+1}^{n+1} = \varphi_j^n \tag{12}$$

In this method values of the transported variable at the new time level are evaluated in terms of other unknown variable values at the new time level, requiring the solution of a set of simultaneous equations. This method is first-order accurate in time and second-order accurate in space and is unconditionally stable, allowing arbitrarily large time steps to be taken (Chapra 2008). In advection dominated flows Wallis (2007) warns that the promise of stability is outweighed by increasing inaccuracy as c increases above unity because the implicit nature of the method compromises the upstream-biased transportive nature of the physical system.

The Crank–Nicolson method

Using Eq. (7) with $\theta = 0.5$ the method employs a centred-time/centred-space approach in which estimates of the spatial derivatives are expressed using values of the transported property at time levels n and $n + 1$. This is an implicit FD scheme and is expressed as:

$$\begin{aligned}\varphi_j^{n+1} = \varphi_j^n &+ \frac{\Delta t}{2}\left[-\upsilon\frac{\varphi_{j+1}^{n+1} - \varphi_{j-1}^{n+1}}{2\Delta x} + D\frac{\varphi_{j+1}^{n+1} + \varphi_{j-1}^{n+1} - 2\varphi_j^{n+1}}{\Delta x^2}\right]\\ &+ \frac{\Delta t}{2}\left[-\upsilon\frac{\varphi_{j+1}^{n} - \varphi_{j-1}^{n}}{2\Delta x} + D\frac{\varphi_{j+1}^{n} + \varphi_{j-1}^{n} - 2\varphi_j^{n}}{\Delta x^2}\right]\end{aligned} \tag{13}$$

For computational purposes the above equation can be written as:

$$\begin{aligned}&-\left(\frac{d}{2} + \frac{c}{4}\right)\varphi_{j-1}^{n+1} + (d + 1)\varphi_j^{n+1} - \left(\frac{d}{2} - \frac{c}{4}\right)\varphi_{j+1}^{n+1}\\ &\quad= \left(\frac{d}{2} + \frac{c}{4}\right)\varphi_{j-1}^{n} + (1 - d)\varphi_j^n + \left(\frac{d}{2} - \frac{c}{4}\right)\varphi_{j+1}^{n}\end{aligned} \tag{14}$$

In this method, values of the transported variable at the new time level are evaluated in terms of variable values from both the old and the new time levels, requiring the solution of a set of simultaneous equations. The scheme is based on centred differencing in time and space and is thus second-order accurate in time and space. The scheme is unconditionally stable, but it has been observed to be inaccurate at high values of P_e (Chapra 2008) and its implicit nature implies that the warnings of Wallis (2007) apply to it.

The Implicit QUICK method

This is a FV approach with CV face values of the transported variable expressed in terms of an upstream weighted parabolic interpolation and spatial gradients of the transported variable expressed using linear interpolation (Leonard 1979). Using $\theta = 1$ in the FV equivalent version of Eq. (7) gives:

$$\begin{aligned}\varphi_j^{n+1} - \varphi_j^n = &-\frac{\Delta t\upsilon}{\Delta x}\left(\varphi_{j+1/2}^{n+1} - \varphi_{j-1/2}^{n+1}\right)\\ &+ \frac{\Delta tD}{\Delta x}\left[\left(\frac{\partial\varphi}{\partial x}\right)_{j+1/2}^{n+1} - \left(\frac{\partial\varphi}{\partial x}\right)_{j-1/2}^{n+1}\right]\end{aligned} \tag{15}$$

Using Hayase et al.'s formulation (Hayase et al. 1992; Versteeg and Malalasekera 2007) to express variable values at the CV surfaces gives:

$$\varphi_{j+1/2}^{n+1} = \varphi_j^{n+1} + \frac{1}{8}\left(3\varphi_{j+1}^{n+1} - 2\varphi_j^{n+1} - \varphi_{j-1}^{n+1}\right) \tag{16}$$

$$\varphi_{j-1/2}^{n+1} = \varphi_{j-1}^{n+1} + \frac{1}{8}\left(3\varphi_{j}^{n+1} - 2\varphi_{j-1}^{n+1} - \varphi_{j-2}^{n+1}\right) \tag{17}$$

The discretised equation for a general FV centred at node, j, is expressed as:

$$\begin{aligned}&\frac{c}{8}\varphi_{j-2}^{n+1} - \left(d + \frac{7}{8}c\right)\varphi_{j-1}^{n+1} + \left(1 + 2d + \frac{3}{8}c\right)\varphi_j^{n+1}\\ &\quad- \left(d - \frac{3}{8}c\right)\varphi_{j+1}^{n+1} = \varphi_j^n\end{aligned} \tag{18}$$

The scheme is first-order accurate in time and third-order accurate in space. Its implicit nature offers unconditional stability, but the warnings of Wallis (2007) apply to it.

The MacCormack method

The MacCormack (or Predictor–Corrector) method is a two-step FD method, unlike the above-discussed techniques which are one-step methods. There are various formulations of the approach (e.g. MacCormack 1982; Fürst and Furmánek 2011). Here we follow the semi-implicit formulation described in (Chapra 2008). The first step (predictor) uses the following explicit estimator, which uses forward spatial differencing for the advective term and centred spatial differencing for the dispersion term:

$$\varphi^* = \left(\frac{\varphi_j^{n+1} - \varphi_j^n}{\Delta t} \right) = -\upsilon \frac{\varphi_{j+1}^n - \varphi_j^n}{\Delta x} + D \frac{\varphi_{j+1}^n - 2\varphi_j^n + \varphi_{j-1}^n}{\Delta x^2} \tag{19}$$

The second step (corrector) uses the following implicit estimator, which uses backward spatial differencing for the advective term and centred spatial differencing for the dispersion term:

$$\varphi^{**} = \left(\frac{\varphi_j^{n+1} - \varphi_j^n}{\Delta t} \right) = -\upsilon \frac{\varphi_j^{n+1} - \varphi_{i-1}^{n+1}}{\Delta x} + D \frac{\varphi_{j+1}^{n+1} - 2\varphi_j^{n+1} + \varphi_{j-1}^{n+1}}{\Delta x^2} \tag{20}$$

Finally, an average of the two estimators is used to obtain the result expressed as:

$$\varphi_j^{n+1} = \varphi_j^n + \left(\frac{\varphi^* + \varphi^{**}}{2} \right) \Delta t \tag{21}$$

This method, in a similar way to the Crank–Nicolson method, uses an average of an explicit scheme and an implicit scheme. For computational purposes, Eq. (21) can be expressed as:

$$\begin{aligned} &-\left(\frac{d}{2} + \frac{c}{2}\right)\varphi_{j-1}^{n+1} + \left(1 + d + \frac{c}{2}\right)\varphi_j^{n+1} - \frac{d}{2}\varphi_{j+1}^{n+1} \\ &= \frac{d}{2}\varphi_{j-1}^n + \left(1 + \frac{c}{2} - d\right)\varphi_j^n + \left(\frac{d}{2} - \frac{c}{2}\right)\varphi_{j+1}^n \end{aligned} \tag{22}$$

This has the same form as other implicit methods described above and is similar to that presented by Fürst and Furmánek (2011). The scheme is second-order accurate in time and space. Chapra (2008) claims that the scheme is conditionally stable, but Fürst and Furmánek (2011) claim it is unconditionally stable.

The QUICKEST method

The QUICKEST method (Leonard 1979) is a FV approach similar to, but superior to, the QUICK method. As well as using the upstream weighted parabolic interpolation of the QUICK method (Abbott and Basco 1989; Versteeg and Malalasekera 2007) it is an explicit formulation, using the $\theta = 0$ version of the FV equivalent of Eq. (7). In addition, it includes 'estimated streaming terms' (EST) to account for advection and dispersion occurring during the time step (Leonard 1979). Variable values at CV faces are given by the following expressions (Leonard 1979; Abbott and Basco 1989):

$$\varphi_{j+1/2}^n = \frac{1}{2}\left(\varphi_j^n + \varphi_{j+1}^n\right) - \frac{1}{6}\left(\varphi_{j-1}^n - 2\varphi_j^n + \varphi_{j+1}^n\right) \tag{23}$$

$$\varphi_{j-1/2}^n = \frac{1}{2}\left(\varphi_{j-1}^n - \varphi_j^n\right) - \frac{1}{6}\left(\varphi_{j-2}^n - 2\varphi_{j-1}^n + \varphi_j^n\right) \tag{24}$$

For computational purposes the method may be expressed as (Leonard 1979; Abbott and Basco 1989):

$$\begin{aligned} \varphi_j^{n+1} = &\left[d(c) + \frac{c}{6}\left(c^2 - 1\right)\right]\varphi_{j-2}^n \\ &+ \left[d(1 - 3c) - \frac{c}{2}\left(c^2 - c - 2\right)\right]\varphi_{j-1}^n \\ &- \left[d(2 - 3c) - \frac{c}{2}\left(c^2 - 2c - 1\right) - 1\right]\varphi_j^n \\ &+ \left[d(1 - c) - \frac{c}{6}\left(c^2 - 3c + 2\right)\right]\varphi_{j+1}^n \end{aligned} \tag{25}$$

This shows that unknown variable values at the new time level can be computed one at a time (an explicit calculation). In principle, the scheme is third-order accurate, but its explicit nature leads to conditionally stability. Thus, it can be unstable at modest values of P_e: Leonard (1979) provides some detail on this issue.

Expected behaviour of applied numerical methods

Although the order of accuracy, given above, of the numerical methods gives an insight into how their performances might compare, a deeper study of the truncation error is much more revealing. This is achieved by substituting Taylor series expansions into the algorithms and identifying any temporal and spatial derivatives that might be a source of poor performance. As introduced earlier, the second and third spatial derivatives are particularly problematic so that methods which minimise the magnitude of such terms, or better still eliminate them, are likely to be among the better performing methods. Since the lowest spatial derivative emanating from the physical dispersion term is the 4th one it is only necessary to examine the truncation terms from the temporal and advective terms in order to quantify the numerical diffusion and numerical dispersion (from the dominant terms) of a numerical method. It is also necessary to replace any second or third temporal derivative with a corresponding spatial derivative, considering advection only. The procedure is often referred to as the modified equation approach (Szymkiewicz 2010) but appears elsewhere without being named (Abbott and Basco 1989).

Table 1 shows the results of this analysis for the five methods considered in the paper. "Appendix 2" summarises the method, provides intermediate expressions for all five methods and shows completed analyses for two of the schemes, namely Implicit QUICK (IQ) and MacCormack (M). Completed analyses for Crank–Nicolson (CN) and Backward-Time/Centred-Space (BTCS) are readily available elsewhere (Szymkiewicz 2010). The reader is left to confirm the result for QUICKEST (Q) for themselves. In

Table 1 Coefficients of numerical diffusion and numerical dispersion derived from the modified equation approach: c is the advection number, as defined in Eq. (8)

Scheme	Coefficient of numerical diffusion	Coefficient of numerical dispersion
BTCS	$\Delta t \upsilon^2/2$	$-\Delta x^2 \upsilon(-c^2+1)/6$
CN	0	$-\Delta x^2 \upsilon(c^2+2)/12$
IQ	$\Delta t \upsilon^2/2$	$-\Delta x^2 \upsilon(-c^2+1/4)/6$
M	0	$-\Delta x^2 \upsilon(c^2+3c+2)/12$
Q	0	0

the remainder of the paper we use the abbreviations introduced above to refer to the five numerical methods.

These results suggest that CN, M and Q are free from numerical diffusion, but that BTCS and IQ contain the same amount of numerical diffusion, which depends only on the time step and the velocity. All the methods except Q contain numerical dispersion, but to differing degrees which are dependent on the space step, velocity and advection number. These results are consistent with those given elsewhere, e.g. Leonard (1979), Chapra (2008) and Szymkiewicz (2010).

Computational procedure

This study used Microsoft Excel spreadsheets to apply the numerical methods and followed the design described by Karahan (2006, 2007, 2008). Excel spreadsheets have the advantages of computational speed and visual feedback through cell values and graphical displays (Billo 2007; Karahan 2006). Also, they can be configured to solve implicit numerical methods without the need for matrix algebra by writing algorithms in a direct form and using an iterative technique (Karahan 2006).

A separate workbook was created for each numerical method (Eqs. 12, 14, 18, 22 and 25). The general structure of the calculations for each implicit method is shown in Fig. 2. The input values were Δx, Δt, υ and D, and these were written to cells B1, B2, B3 and B4, respectively. The three numerical properties (Eqs. 8–10) were evaluated in cells B5, B6 and B7 and were derived from the input values. In the main calculation area columns represent different spatial locations or grid points (defined in row 8) and rows represent different times (defined in column C). The time step was fixed, but the spatial resolution of the computational domain was varied so that model parameters could be estimated over a range of numerical properties. Each space step case had its own worksheet tab in each of the workbooks. Initial conditions were provided in row 10 (zero concentration at all locations), and the upstream boundary condition was provided in column E.

In each worksheet the direct form (see below) of the numerical method being tested was written to the cells in the main calculation area. Having entered the equation in cell F10, it was then copied along the row as far as a location well beyond the downstream end of the reach being modelled where a zero concentration downstream boundary condition was supplied. Provided that Excel's iterative

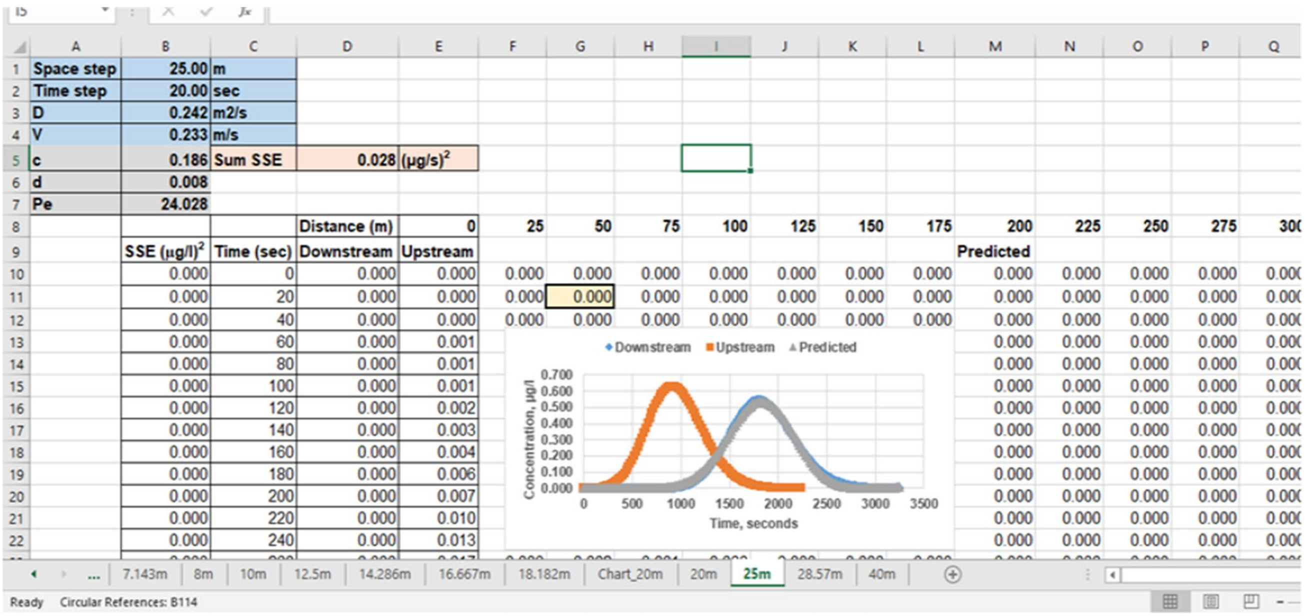

	A	B	C	D	E	F	G	H	I	J	K	L	M	N	O	P	Q
1	Space step	25.00	m														
2	Time step	20.00	sec														
3	D	0.242	m2/s														
4	V	0.233	m/s														
5	c	0.186	Sum SSE	0.028	(μg/s)^2												
6	d	0.008															
7	Pe	24.028															
8				Distance (m)	0	25	50	75	100	125	150	175	200	225	250	275	30
9		SSE (μg/l)^2	Time (sec)	Downstream	Upstream								Predicted				
10		0.000	0	0.000	0.000	0.000	0.000	0.000	0.000	0.000	0.000	0.000	0.000	0.000	0.000	0.000	0.00
11		0.000	20	0.000	0.000	0.000	0.000	0.000	0.000	0.000	0.000	0.000	0.000	0.000	0.000	0.000	0.00
12		0.000	40	0.000	0.000	0.000	0.000	0.000	0.000	0.000	0.000	0.000	0.000	0.000	0.000	0.000	0.00
13		0.000	60	0.000	0.001								0.000	0.000	0.000	0.000	0.00
14		0.000	80	0.000	0.001								0.000	0.000	0.000	0.000	0.00
15		0.000	100	0.000	0.001								0.000	0.000	0.000	0.000	0.00
16		0.000	120	0.000	0.002								0.000	0.000	0.000	0.000	0.00
17		0.000	140	0.000	0.003								0.000	0.000	0.000	0.000	0.00
18		0.000	160	0.000	0.004								0.000	0.000	0.000	0.000	0.00
19		0.000	180	0.000	0.006								0.000	0.000	0.000	0.000	0.00
20		0.000	200	0.000	0.007								0.000	0.000	0.000	0.000	0.00
21		0.000	220	0.000	0.010								0.000	0.000	0.000	0.000	0.00
22		0.000	240	0.000	0.013								0.000	0.000	0.000	0.000	0.00

Fig. 2 Example spreadsheet showing the structure of the solution method (Backward-Time/Space-Centred method) for one space step case

Fig. 3 Flow chart of the optimisation process

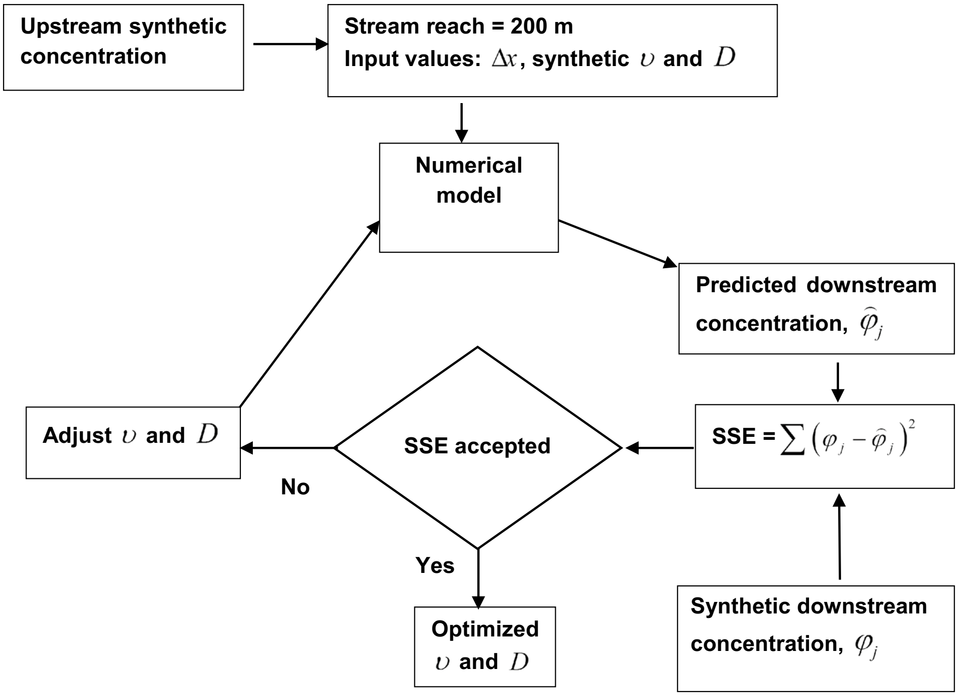

calculation mode was enabled, a solution to the set of simultaneous equations thus entered was automatically achieved. The complete row of calculations was then copied to all subsequent rows thus obtaining a solution at every time denoted in column C.

The direct forms of the implicit methods were simple rearrangements of the algorithms such that the concentration in the target cell was expressed as a function of unknown concentrations in neighbouring cells. For the case shown in Fig. 2, the direct form of the BTCS method is a re-arrangement of Eq. (12) to give:

$$\varphi_j^{n+1} = \left[\varphi_j^n + (d - c/2)\varphi_{j+1}^{n+1} + (c/2 + d)\varphi_{j-1}^{n+1}\right] \Big/ (1 + 2d) \tag{26}$$

for which the calculation in the worksheet for cell G11, for example, is:

$$\begin{aligned}\text{G11} = \big(&\text{G10} + (\$\text{B}\$6 - \$\text{B}\$5/2) * \text{H11} \\ &+ (\$\text{B}\$6 + \$\text{B}\$5/2) * \text{F11}\big)/(2 * \$\text{B}\$6 + 1)\end{aligned} \tag{27}$$

where cell G11 contains the concentration at time $n + 1$.

Optimisation of the model parameters (υ and D contained in cells B3 and C4, respectively) was achieved by minimising the sum of squared errors (SSE) between calculated concentrations at the downstream end of the reach being modelled (column M) and the synthetic data for that location (column D). The SSE was minimised using Excel's solver function which uses a steepest descent optimisation code (Lasdon et al. 1978; van den Bos 2007; Fylstra et al. 1998). Figure 3 summarises the procedure.

Implementation of the Q method followed the same spreadsheet design as used for the implicit methods except that an iterative solution of the direct form of the algorithm wasn't required (it being an explicit method an unknown concentration is only dependent on other concentration values in the previous row). In addition, however, a special treatment of the upstream boundary was needed because when applied to the cells in column F (see Fig. 2) a concentration value further upstream than the boundary is required. To overcome this, the CN scheme was applied to the cells in column F. Solving this simultaneously with the Q algorithm in column G yielded an explicit solution for column F. A similar CN implementation in column F was also used for the IQ method, but within the direct form of solution.

Some of the direct form implementations of the implicit methods did not always yield robust solutions (particularly higher Peclet number cases for BTCS). To remedy this, such cases were solved (also using Excel) using a double-sweep elimination method, which is described briefly in "Appendix 3". The opportunity was also taken to confirm a sample of the results from the other three implicit methods because the double-sweep elimination method could be applied to them with only a little extra work.

Application of the numerical methods

To assess the reliability of the numerical methods for identifying the velocity and the dispersion coefficient from temporal concentration profiles, synthetic data was

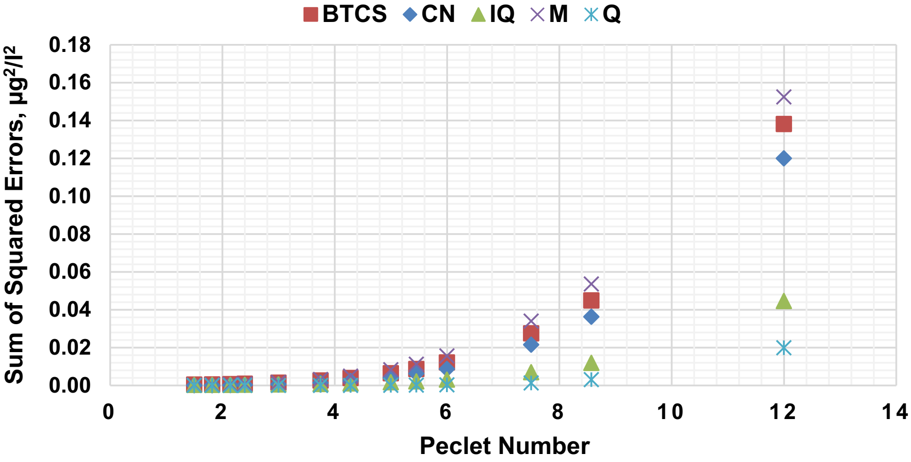

Fig. 4 Variation of sum of squared errors (between simulations with optimised velocity and dispersion coefficient and synthetic downstream data) with Peclet number for the first data set

generated using Eq. (3). The use of synthetic data derived from analytical solutions has become common (Semuwemba 2011; Vaghela and Vaghela 2014) and has several advantages over using observed data. For example: conditions can be tailored for a particular situation, the values of solute transport parameters are known precisely and analytical solutions can provide results for a broad range of conditions that would not be practically possible with observed data (Semuwemba 2011). As well as attempting to estimate the parameter values used with the analytical solution, the numerical methods were also required to simulate the temporal concentration profiles given by the analytical solution at the downstream end of the reach.

Application of the numerical methods was made to synthetic data generated using two different sets of parameter values and time steps. The first set was generated using $\upsilon=0.225$ m/s and $D=0.750$ m^2/s with a time step of 20 s and the second set was generated using $\upsilon=0.150$ m/s and $D=0.500$ m^2/s with a time step of 30 s. The parameter values were selected based on previous studies of the stream where the AD-Model was going to be applied in later research by the authors, namely the Murray Burn in Edinburgh, UK. A hypothetical stream reach of length 200 m was used, which was similar to the Murray Burn study reach length. Hence, for each synthetic data set an upstream and a downstream temporal concentration profile were generated at 600 m and 800 m, respectively, from the solute source. The mass of solute was 1 kg and the cross-sectional area of the channel was 1 m^2. The numerical methods were applied to the synthetic data over a range of space steps (5–40 m), such that optimisation of the model parameters was observed under different values of the non-dimensional numerical properties (e.g. P_e being 1.5–12). The parameter values of the second set were deliberately chosen to yield the same values of the non-dimensional numerical properties as those for the first set.

Results and discussion

Results from the two sets of synthetic data were very similar in nature such that only one set of results is considered in detail here, namely that from the first set ($\upsilon=0.225$ m/s, $D=0.750$ m^2/s, time step = 20 s). In all cases the numerical schemes behaved conservatively and simulations were stable. In several of the figures referred to below various aspects of the results are plotted against Peclet number, P_e. As shown previously, numerical discretisation can be expressed in terms of velocity, dispersion coefficient, space step and time step or in terms of advection number, dispersion number and Peclet number. The results were plotted against P_e because it combines the effects of the other two non-dimensional properties and the plots are an effective way of showing the behaviour of the numerical methods when the space step is varied.

Figure 4 shows plots of the sum of squared errors between simulated and synthetic concentration profiles at the downstream end of the reach plotted against P_e for the first data set. In every case the simulated profile was generated using the optimised velocity and dispersion coefficient. In general, simulation errors increased with increasing P_e for all the numerical methods. Simulation errors obtained for $P_e < 5$ were very small (<0.01 µg^2/l^2) for all the methods, whilst for $P_e > 5$ simulation errors increased significantly with increasing P_e for all the methods. Generally, the finite difference methods gave higher simulation errors than the finite volume methods. The methods could be ranked in the following order of decreasing accuracy: Q, IQ, CN, BTCS, M. To a great extent this reflects the spatial orders of accuracy of the methods noted earlier. However, this is a rather superficial analysis to which some refinements are required, as described below.

Tables 2 and 3 show optimised values of velocity and dispersion coefficient. It should be noted that the values of the non-dimensional numerical properties, i.e. advection

Table 2 Non-dimensional numerical properties and optimised velocities for first data set (synthetic velocity of 0.225 m/s)

Δx (m)	Advection number	Dispersion number	Peclet number	BTCS	CN	IQ	M	Q
5.00	0.900	0.600	1.500	0.226	0.225	0.226	0.226	0.225
6.06	0.743	0.408	1.818	0.226	0.225	0.226	0.226	0.225
7.14	0.630	0.294	2.143	0.226	0.226	0.226	0.226	0.225
8.00	0.563	0.234	2.400	0.226	0.226	0.226	0.226	0.225
10.00	0.450	0.150	3.000	0.227	0.226	0.226	0.227	0.225
12.50	0.360	0.096	3.750	0.227	0.227	0.226	0.228	0.225
14.29	0.315	0.073	4.286	0.228	0.227	0.227	0.228	0.225
16.67	0.270	0.054	5.000	0.229	0.228	0.227	0.229	0.225
18.18	0.248	0.045	5.454	0.229	0.229	0.227	0.230	0.225
20.00	0.225	0.038	6.000	0.230	0.229	0.228	0.231	0.226
25.00	0.180	0.024	7.500	0.233	0.232	0.229	0.234	0.226
28.57	0.158	0.018	8.571	0.235	0.234	0.230	0.236	0.227
40.00	0.113	0.009	12.000	0.243	0.242	0.235	0.244	0.231

Table 3 Non-dimensional numerical properties and optimised dispersion coefficients for first data set (synthetic dispersion coefficient of 0.750 m^2/s)

Δx (m)	Advection number	Dispersion number	Peclet number	BTCS	CN	IQ	M	Q
5.00	0.900	0.600	1.500	0.235	0.749	0.255	0.749	0.746
6.06	0.743	0.408	1.818	0.235	0.749	0.260	0.748	0.749
7.14	0.630	0.294	2.143	0.234	0.748	0.264	0.747	0.750
8.00	0.563	0.234	2.400	0.233	0.747	0.267	0.746	0.750
10.00	0.450	0.150	3.000	0.231	0.746	0.273	0.745	0.749
12.50	0.360	0.096	3.750	0.228	0.743	0.278	0.744	0.744
14.29	0.315	0.073	4.286	0.226	0.742	0.279	0.744	0.739
16.67	0.270	0.054	5.000	0.225	0.741	0.278	0.745	0.728
18.18	0.248	0.045	5.454	0.225	0.750	0.275	0.747	0.718
20.00	0.225	0.038	6.000	0.226	0.739	0.269	0.751	0.704
25.00	0.180	0.024	7.500	0.238	0.752	0.240	0.770	0.649
28.57	0.158	0.018	8.571	0.255	0.766	0.207	0.790	0.594
40.00	0.113	0.009	12.000	0.316	0.827	0.032	0.854	0.332

number, dispersion number and Peclet number, shown in the tables were calculated using the parameter values used for generating the synthetic data so that the results of all methods could be easily compared. It can be observed that there is variation of optimised velocity and dispersion coefficient both with the numerical method used and with the numerical properties. In all cases the optimised velocity is greater than the synthetic value. For $P_e < 5$ the percentage errors in the velocities are typically less than 2%. They increase to about 8% when $P_e = 12$. Generally, Q has the smallest velocity errors and M has the largest.

Turning attention to the optimised dispersion coefficients, which generally show greater errors than the optimised velocities, Fig. 5 shows results for all the numerical methods for the first data set (i.e. the data in Table 3). It can be observed that for $P_e < 5$, the results fall into two distinct groups. Here, CN, M and Q yield optimised dispersion coefficients that agree closely with the synthetic value; BTCS and IQ yield values that are similar to each other, but which are considerably too small. This is consistent with the analysis of the numerical diffusion in the methods shown in Table 1. Furthermore, the error in the optimised dispersion coefficients (i.e. the difference between the optimised value and that used to generate the synthetic data) for BTCS and IQ is very close to the value given by the numerical diffusion coefficient in the table (~0.5 m^2/s, using the synthetic value of velocity). In other words, the presence of numerical diffusion means that a smaller physical dispersion coefficient than the synthetic value is required to fit the model to the data.

For $P_e > 5$, optimised dispersion coefficients for all the methods diverge from the synthetic value. Those from CN, M and BTCS show a small increase from the value in the lower P_e range whilst those from IQ and Q show a

Fig. 5 Variation of optimised dispersion coefficient with Peclet number for first data set (synthetic dispersion coefficient of 0.750 m^2/s—indicated by dashed line)

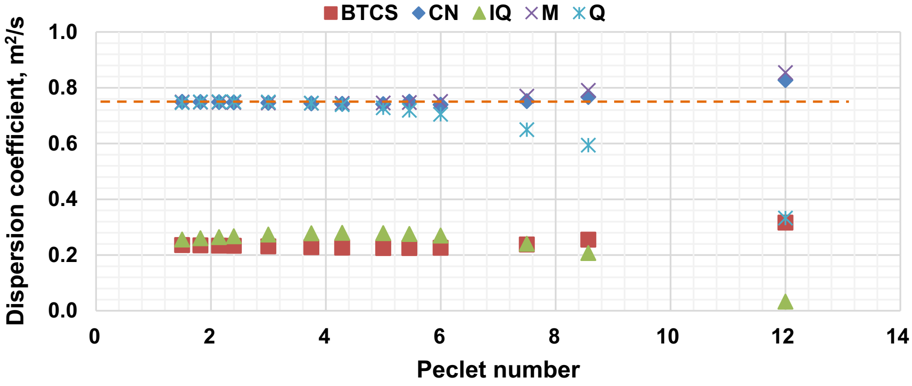

Fig. 6 Simulation results for five numerical methods using a space step of 20 m and a time step of 20 s for first data set (synthetic dispersion coefficient of 0.750 m^2/s, synthetic velocity of 0.225 m/s, Peclet number = 6.0)

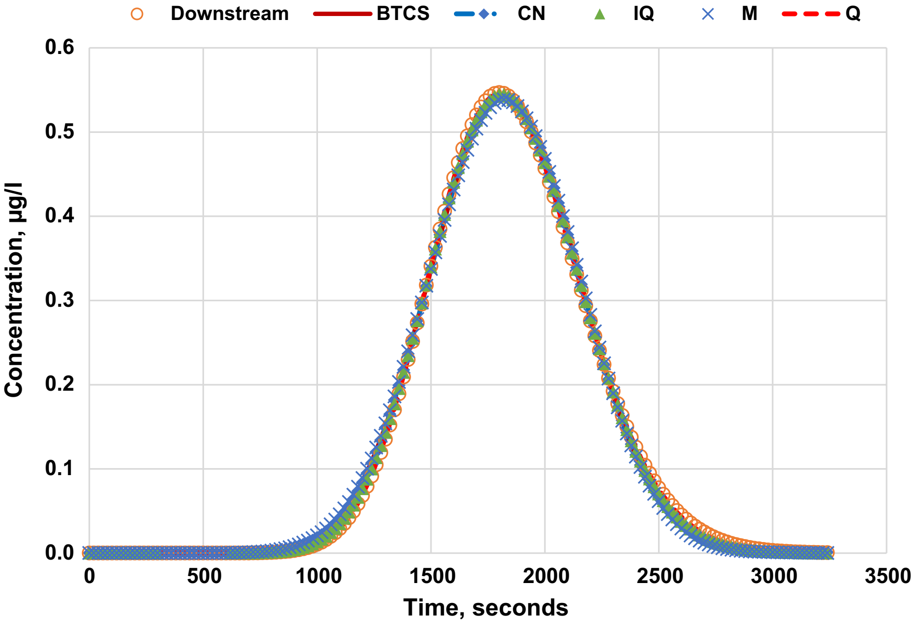

substantial decrease from the value in the lower P_e range. In both cases, the divergence increases with increasing P_e.

In order to aid the interpretation of these results, Figs. 6 and 7 show composite plots (i.e. results from all 5 methods) of the simulated concentration profiles for two values of P_e, namely, 6 and 12, respectively. The downstream synthetic concentration profile is also shown. For the lower P_e case, there is little difference between the simulated profiles and they all match the synthetic profile well. This reflects the relatively low modelling errors shown in Fig. 4 (described earlier). In contrast, Fig. 7 shows that, to a greater or lesser extent, all 5 simulated profiles are distorted, being characterised by a reduced amplitude (compared to the synthetic profile), a little more spreading (particularly on the rising limb) and an oscillation on the trailing edge. Such behaviour is caused by numerical dispersion, as described earlier (see Fig. 1).

Table 4 shows the coefficients of numerical dispersion, obtained using the formulae in Table 1, for four values of P_e from the range covered in the optimisations. Clearly, these coefficients increase with increasing P_e for all schemes, and they are significantly larger for $P_e = 12$ than for $P_e = 6$. Furthermore, the degree of distortion of the simulated profiles in Fig. 7 (for the higher P_e case) mirrors the magnitude of the numerical dispersion coefficients. Thus, the ranking order of the degree of distortion is similar to the ranking order of the coefficients of numerical dispersion. For example, the errors in the peak concentrations are −8.6%, −9.2%, −12.0%, −12.4%, −13.5% for Q, IQ, CN, BTCS and M, respectively.

For CN and M in the higher P_e range the generally larger dispersion coefficient than the synthetic value (see Fig. 5 and Table 3) helps to damp out the oscillation, but sacrifices the fit around the peak of the profile. Of course, the optimisation finds the combination of velocity and dispersion coefficient

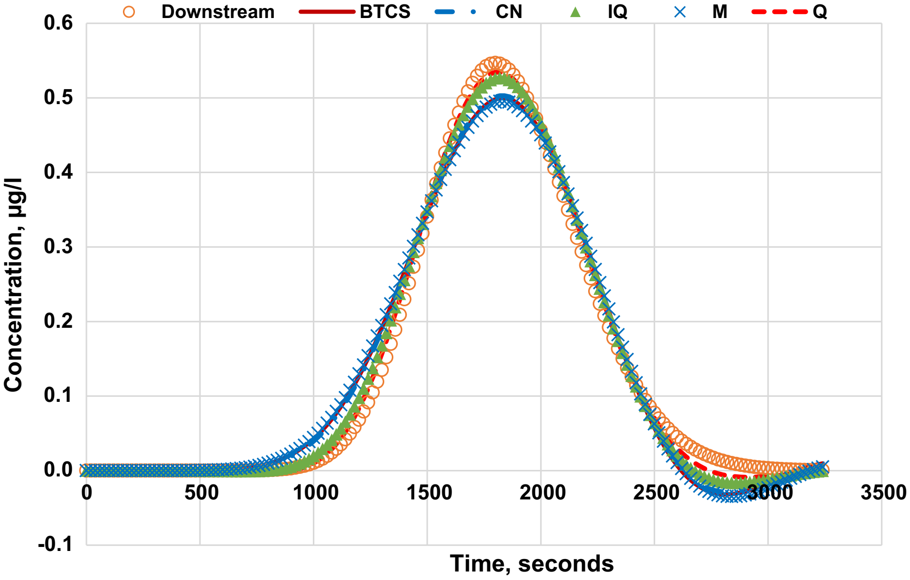

Fig. 7 Simulation results for five numerical methods using a space step of 40 m and a time step of 20 s for first data set (synthetic dispersion coefficient of 0.750 m^2/s, synthetic velocity of 0.225 m/s, Peclet number = 12.0)

Table 4 Coefficients of numerical dispersion evaluated using the formulae in Table 1

Δx (m)	Advection number	Dispersion number	Peclet number	BTCS	CN	IQ	M	Q
5.00	0.900	0.600	1.500	− 0.2	− 1.3	0.5	− 2.6	0
10.00	0.450	0.150	3.000	− 3.0	− 4.2	− 0.27	− 6.8	0
20.00	0.225	0.038	6.000	− 14.5	− 15.7	− 3.0	− 21.1	0
40.00	0.113	0.009	12.000	− 63.8	− 65.0	− 14.8	− 77.6	0

that gives the best fit considering the whole profile. In these cases where the optimised dispersion coefficient is larger than the synthetic value, artificial mixing arises from the fitting of the model to the distorted profile and so is related to the presence of numerical dispersion rather than numerical diffusion. Similarly for BTCS, and allowing for the numerical diffusion it contains, some additional physical dispersion (compared to the lower P_e range) is helpful in damping out the oscillations in the higher P_e range leading to a better fit to the whole concentration profile. Although the presence of numerical dispersion influences the optimised dispersion coefficient via model fitting to the distorted profile (similarly to CN and M), in these BTCS cases artificial mixing is dominated by the presence of numerical diffusion.

The results from IQ and Q in the higher P_e range display smaller oscillations than the other three methods which enables the optimisation to find better fits to the synthetic profile (see Fig. 4), but the dispersion coefficients are too small suggesting that additional numerical errors become significant in the higher P_e range. Regarding Q, it is interesting that the profile in Fig. 7 shows a distortion, yet according to Table 1 the method contains no numerical dispersion. Similarly, the optimised dispersion coefficients are very small (implying that numerical diffusion is present), in contrast to the result in Table 1. It seems very likely, therefore, that higher-order truncation error terms than the second and third spatial derivatives are playing a significant role. Such higher-order terms were not included in the modified equation analysis because usually the second and third spatial derivatives are the dominant terms for numerical diffusion and numerical dispersion, respectively. Since even truncation error terms are associated with numerical diffusion (Szymkiewicz 2010), the source of this numerical diffusion in Q is likely to be the 4th spatial gradient term. The trend of the IQ results in Fig. 5 in the higher P_e range is similar to that of Q, reflecting their common basis (quadratic upstream interpolation of control volume face concentrations). So it seems that higher-order truncation error terms affect the IQ results also, but of course in this case numerical errors from the second and third spatial derivatives are also present (see Tables 1 and 4). However, the latter is much smaller than for the other implicit methods (see Table 4), as reflected in the modelling errors shown in Fig. 4.

IQ and Q may also be affected by the CN treatment of the first computational cell next to the upstream boundary. This will introduce a little numerical dispersion, and the effect will be greater for the higher P_e case than for the lower P_e case because (a) the CN method contains more numerical dispersion in the former than in the latter (see Table 4) and (b) there is a greater ratio of affected computational cells

Table 5 Non-dimensional numerical properties and ratio of optimised dispersion coefficients to synthetic dispersion coefficient for the first data set

Δx (m)	Advection number	Dispersion number	Peclet number	BTCS	CN	IQ	M	Q
5.00	0.900	0.600	1.500	0.314	0.999	0.340	0.998	0.995
10.00	0.450	0.150	3.000	0.308	0.994	0.364	0.993	0.998
20.00	0.225	0.038	6.000	0.301	0.985	0.359	1.001	0.939
40.00	0.113	0.009	12.000	0.421	1.103	0.043	1.139	0.443

Table 6 Non-dimensional numerical properties and ratio of optimised dispersion coefficients to synthetic dispersion coefficient for the second data set

Δx (m)	Advection number	Dispersion number	Peclet number	BTCS	CN	IQ	M	Q
5.00	0.900	0.600	1.500	0.314	0.999	0.340	0.998	0.995
10.00	0.450	0.150	3.000	0.308	0.994	0.364	0.993	0.998
20.00	0.225	0.038	6.000	0.301	0.985	0.359	1.001	0.939
40.00	0.113	0.009	12.000	0.421	1.103	0.043	1.139	0.443

to unaffected computational cells in the former than in the latter (1 to 5 compared to 1 to 11). However, simulations of an initial value problem (for which the upstream boundary concentration was zero for all time) using Q under similar numerical conditions also showed some oscillatory behaviour. So the source of the numerical dispersion appears to be a truncation error term (probably the 5th spatial gradient).

We have not investigated the cause of the underestimation of the dispersion coefficient for Q and IQ in the higher a P_e range any further because in practice there is little point in using these (or any) methods under conditions when oscillations affect simulations. Better to decrease P_e so that artificial mixing, stemming from the second, third or higher spatial derivatives in the truncation errors is reduced to acceptable limits.

Optimised dispersion coefficient and velocity results from the second set of synthetic data showed very similar patterns of results to those from the first data set. The degree of similarity was investigated by computing the ratio of the estimated parameters to the corresponding values used to generate the synthetic data. Example results (for 4 P_e values) for the dispersion coefficients are shown in Tables 5 and 6 for the first and second data sets, respectively.

As well as highlighting differences between optimised values from the 5 numerical methods, the identical results in the two tables highlights the way in which the non-dimensional numerical properties, rather than the individual parameter values, control the behaviour of the numerical solutions. As might be expected from the velocity results shown earlier, the ratios of optimised to synthetic velocity values were much closer to unity than for the dispersion coefficients for all the methods over the range of P_e used (for both synthetic data sets).

Overall, the dispersion coefficient results cast doubt on the reliability of obtaining them by optimising numerical models of the AD-Model unless due attention is paid to the characteristics of the numerical method and the numerical properties under which the models are applied. In particular, the presence of artificial mixing needs to be taken into account. Optimised dispersion coefficients will be underestimated in the presence of numerical diffusion (very significantly in some cases) and will be overestimated (but not significantly) in the presence of numerical dispersion, assuming numerical diffusion is absent.

Conclusions

Five different numerical methods were applied to synthetic solute concentration data under the same grid resolutions and non-dimensional numerical conditions, and optimised dispersion coefficients and velocities were obtained. The ranges of advection number, dispersion number and Peclet number covered were 0.900–0.113, 0.600–0.009 and 1.5–12.0, respectively. For $P_e < 5$, using the optimised dispersion coefficients and velocities, all the numerical methods were able to simulate the synthetic data well (sum of squared errors being < 0.01 μg^2/l^2 and with little visual difference between synthetic and simulated concentration profiles), but simulations were increasingly inaccurate as P_e increased beyond 5. However, optimum model fits to the synthetic data were only achieved by adjusting, to greater or lesser extents, the velocity and dispersion coefficient to accommodate the presence of numerical errors. Differences between the optimised and synthetic velocity values were typically less than 2% for $P_e < 5$, but increased to about 8% for $P_e = 12$. The methods yielded a range of optimal values of the dispersion coefficient some of which were significantly different to the value used to generate the synthetic data. The behaviour of the methods was generally consistent with the known presence of artificial mixing, caused by numerical diffusion and/or numerical dispersion, in them. In this regard, numerical diffusion in Backward-Time/Centred-Space and Implicit QUICK reduced the optimised dispersion coefficient from 0.75 m^2/s to about 0.25 m^2/s for $P_e < 5$, whilst optimisations with Crank–Nicolson, MacCormack and QUICKEST, which contain no numerical diffusion, produced reliable optimised dispersion coefficients in this P_e range. For $P_e > 5$ the simulations from all five methods were affected by an oscillatory distortion which became more prominent with increasing P_e, this being generally consistent with the known presence of numerical dispersion in the methods. In this higher P_e range optimised dispersion coefficients for Crank–Nicolson, MacCormack and Backward-Time/Centred-Space increased a little from the values in the lower P_e range due to the fitting of the distorted simulated concentration profile to the whole synthetic one, whilst those from Implicit QUICK and QUICKEST showed a substantial decrease from the value in the lower P_e range due to numerical diffusion. It was suggested that results for these two methods were affected by numerical errors from higher-order truncation error terms than the second and third spatial derivatives.

Acknowledgements The authors would like to thank an anonymous reviewer for suggesting that an improved interpretation of the results could be achieved by using the modified equation approach to highlight the nature of the numerical errors in the five methods used in the work.

Compliance with ethical standards

Conflict of interest The authors declare that they have no conflict of interest.

Appendix 1

See Figs. 8 and 9.

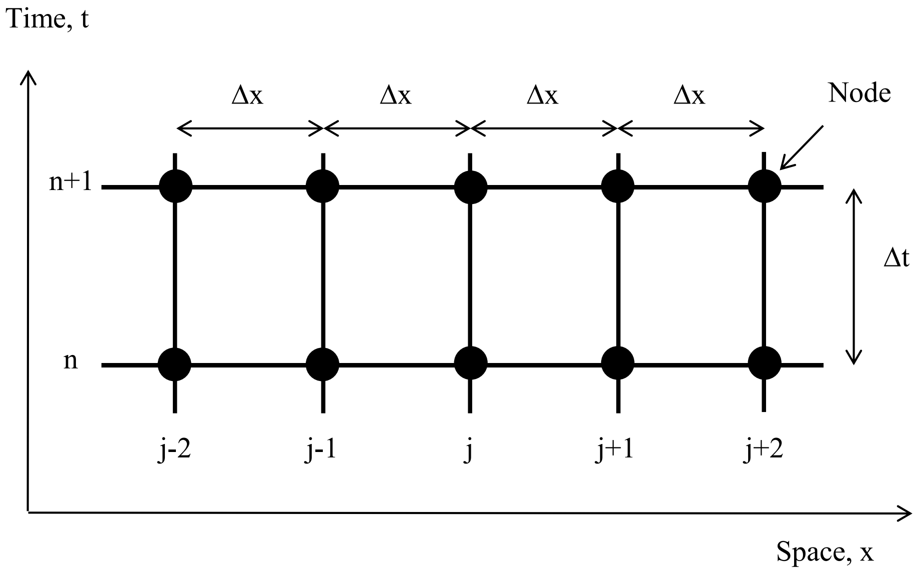

Fig. 8 Computational grid for a finite difference method: information at the nodes is used directly to express solute concentration derivatives

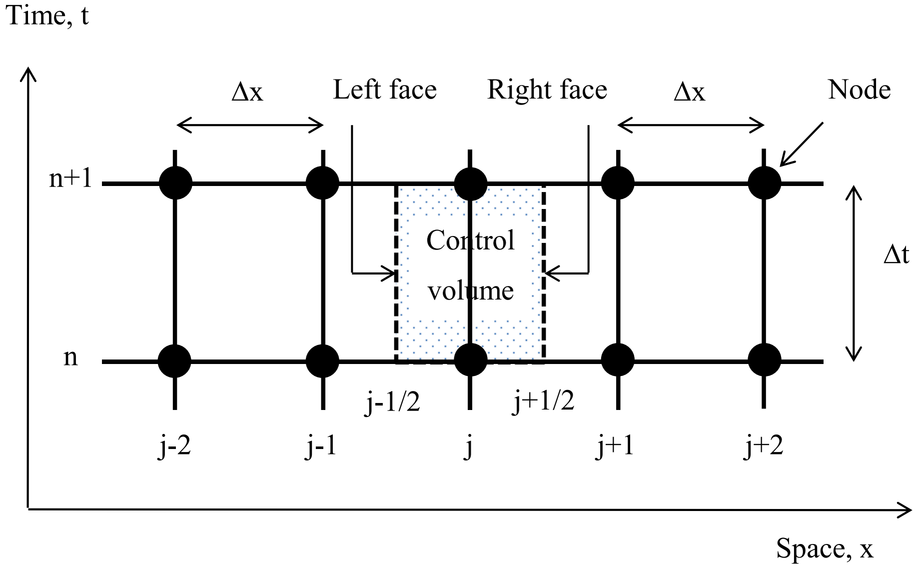

Fig. 9 Computational grid for a finite volume method: advective and dispersive solute fluxes passing through the control volume faces are interpolated from information at the nodes

Appendix 2

Following Szymkiewicz (2010), the modified equation approach aims to write a numerical method in the following form:

$$\varphi_t + \upsilon\varphi_x = D_n\varphi_{xx} + E_n\varphi_{xxx} + \cdots \tag{28}$$

where φ_t, represents the first temporal concentration derivative and φ_x, φ_{xx} and φ_{xxx} represent the first, second and third spatial concentration derivatives. D_n and E_n are termed the coefficients of numerical diffusion and numerical dispersion, respectively. Only advection is considered because it is only truncation errors emanating from the first temporal and first spatial derivatives that contribute to the second and third spatial derivative terms in Eq. (28). By using Taylor series expansions to express a nodal concentration in terms of a neighbouring nodal concentration that is typically separated from it by one space step (Δx) or one time step (Δt), the following expressions can be obtained for the five numerical methods used in the paper.

Backward-Time/Centred-Space

$$\varphi_t - \frac{\Delta t}{2}\varphi_{tt} + \frac{\Delta t^2}{6}\varphi_{ttt} + \upsilon\left(\varphi_x + \frac{\Delta x^2}{6}\varphi_{xxx}\right) + \cdots = 0 \tag{29}$$

Crank–Nicolson

$$\begin{aligned}&\varphi_t + \frac{\Delta t}{2}\varphi_{tt} + \frac{\Delta t^2}{6}\varphi_{ttt}\\ &\quad + \upsilon\left(\varphi_x + \frac{\Delta x^2}{6}\varphi_{xxx} + \Delta t\varphi_{tx} + \frac{\Delta t^2}{2}\varphi_{ttx}\right) + \cdots = 0\end{aligned} \tag{30}$$

Implicit QUICK

$$\varphi_t - \frac{\Delta t}{2}\varphi_{tt} + \frac{\Delta t^2}{6}\varphi_{ttt} + \upsilon\left(\varphi_x + \frac{\Delta x^2}{24}\varphi_{xxx}\right) + \cdots = 0 \tag{31}$$

MacCormack

$$\begin{aligned}&\varphi_t + \frac{\Delta t}{2}\varphi_{tt} + \frac{\Delta t^2}{6}\varphi_{ttt} + \upsilon\left(\varphi_x + \frac{\Delta x^2}{6}\varphi_{xxx}\right)\\ &\quad + \frac{c}{2}\left(\Delta x\varphi_{xt} - \frac{\Delta x^2}{2}\varphi_{xxt} + \frac{\Delta t\Delta x}{2}\varphi_{xtt}\right) + \cdots = 0\end{aligned} \tag{32}$$

QUICKEST

$$\varphi_t + \frac{\Delta t}{2}\varphi_{tt} + \frac{\Delta t^2}{6}\varphi_{ttt} + \upsilon\left(\varphi_x - \frac{\Delta xc}{2}\varphi_{xx} + \frac{\Delta x^2}{6}c^2\varphi_{xxx}\right) + \cdots = 0 \tag{33}$$

where c is the advection number, as previously defined (Eq. 8). Note that the time-centred methods contain cross-derivatives (φ_{xt}, φ_{ttx}, φ_{xxt}) as a result of the need to express everything in terms of a concentration and its derivatives at the same node. This involves using Taylor series expansions of concentration derivatives in exactly the same way as Taylor series expansions are used to express concentrations. Finally use is made of the following relationships, obtained by differentiating the advection equation (Szymkiewicz 2010), to replace all temporal derivatives and cross-derivatives:

$$\varphi_{tt} = \upsilon^2\varphi_{xx} \tag{34}$$

$$\varphi_{ttt} = -\upsilon^3\varphi_{xxx} \tag{35}$$

$$\varphi_{tx} = \varphi_{xt} = -\upsilon\varphi_{xx} \tag{36}$$

$$\varphi_{xxt} = -\upsilon\varphi_{xxx} \tag{37}$$

$$\varphi_{ttx} = \varphi_{xtt} = \upsilon^2\varphi_{xxx} \tag{38}$$

The analysis is completed below for two of the methods.

Implicit QUICK

Equation (31) becomes:

$$\varphi_t - \frac{\Delta t v^2}{2}\varphi_{xx} - \frac{\Delta t^2 v^3}{6}\varphi_{xxx} + v\left(\varphi_x + \frac{\Delta x^2}{24}\varphi_{xxx}\right) + \cdots = 0$$

Thus:

$$\varphi_t + v\varphi_x = \frac{\Delta t v^2}{2}\varphi_{xx} - \frac{\Delta x^2 v}{6}\left(-c^2 + \frac{1}{4}\right)\varphi_{xxx} + \cdots$$

MacCormack

Equation (32) becomes:

$$\varphi_t + \frac{\Delta t v^2}{2}\varphi_{xx} - \frac{\Delta t^2 v^3}{6}\varphi_{xxx} + v\left(\varphi_x + \frac{\Delta x^2}{6}\varphi_{xxx}\right)$$
$$+ \frac{c}{2}\left(-\Delta x v\varphi_{xx} + \frac{\Delta x^2 v}{2}\varphi_{xxx} + \frac{\Delta t \Delta x v^2}{2}\varphi_{xxx}\right) + \cdots = 0$$

Thus:

$$\begin{aligned}\varphi_t + v\varphi_x = {} & -\frac{\Delta t v^2}{2}\varphi_{xx} + \frac{\Delta t^2 v^3}{6}\varphi_{xxx} - \frac{\Delta x^2 v}{6}\varphi_{xxx} \\ & + \frac{c}{2}\Delta x v\varphi_{xx} - \frac{\Delta x^2 vc}{4}\varphi_{xxx} - \frac{\Delta t \Delta x v^2 c}{4}\varphi_{xxx} + \cdots\end{aligned}$$

$$\begin{aligned}\varphi_t + v\varphi_x = {} & -\frac{\Delta t v^2}{2}\varphi_{xx} + \frac{\Delta t^2 v^3}{6}\varphi_{xxx} - \frac{\Delta x^2 v}{6}\varphi_{xxx} \\ & + \frac{\Delta t v^2}{2}\varphi_{xx} - \frac{\Delta t \Delta x v^2}{4}\varphi_{xxx} - \frac{\Delta t^2 v^3}{4}\varphi_{xxx} + \cdots\end{aligned}$$

$$\varphi_t + v\varphi_x = -\frac{\Delta x^2 v}{12}\left(c^2 + 3c + 2\right)\varphi_{xxx}$$

Appendix 3

The algorithm for any implicit method involving three unknown nodal concentrations surrounding the jth node can be written in the following form:

$$\alpha\varphi_{j-1} + \beta\varphi_j + \gamma\varphi_{j+1} = \delta_j \tag{39}$$

where α, β and γ are constant functions of time step, space step, velocity and dispersion coefficient, δ_j is a spatially varying function of time step, space step, velocity, dispersion coefficient and known concentration values (at time level, n) and φ_{j-1}, φ_j and φ_{j+1} are unknown concentrations (at time level $n+1$). Letting $j=2$ represent the first internal node and recognising that φ_1 is known from the upstream boundary condition, Eq. (39) can be written as:

$$p_2\varphi_2 + q_3\varphi_3 = r_2 \tag{40}$$

where p_2, q_3 and r_2 are functions of α, β, γ, δ_2 and φ_1. For $j=3$, Eq. (39) can be written as:

$$p_3\varphi_3 + q_4\varphi_4 = r_3 \tag{41}$$

where φ_2 has been eliminated using Eq. (40). Repeating this process for successively increasing j, we eventually obtain:

$$p_{m-1}\varphi_{m-1} + q_m\varphi_m = r_{m-1} \tag{42}$$

where φ_m is the known concentration at the downstream boundary (at time level $n+1$) and p_{m-1}, q_m and r_{m-1} are given by:

$$p_{m-1} = \frac{-\alpha q_{m-1}}{p_{m-2}} + \beta \tag{43}$$

$$q_m = \gamma \tag{44}$$

$$r_{m-1} = \delta_{m-1} - \frac{\alpha r_{m-2}}{p_{m-2}} \tag{45}$$

The solution is summarised by the following three steps, which are repeated for every time step:

Calculate α, β, γ and, for $j=2$ to $m-1$, δ_j: then calculate p_2 $(=\beta)$, q_3 $(=\gamma)$ and r_2 $(=\delta_2-\alpha\varphi_1)$.
Undertake a forward sweep: for $j=4$ to $m-1$ calculate p_{j-1}, q_j and r_{j-1} [using Eqs. (43)–(45)].
Undertake a backward sweep: for $j=m-1$ to 2 calculate φ_j [using Eq. (42)].

It is straightforward to derive a similar solution for an implicit method containing a fourth unknown nodal concentration (e.g. φ_{j-2} needs to be included in Eq. (39) for Implicit QUICK) assuming that both the boundary value and the value at the first interior node are known. In this, Eqs. (42) and (44) remain the same, but Eqs. (43) and (45) are modified.

References

Abbott MB, Basco DR (1989) Computational fluid dynamics: an introduction for engineers. Longman Scientific & Technical, Harlow

Ani E-C, Wallis S, Kraslawski A, Agachi S (2009) Development, calibration and evaluation of two mathematical models for pollutant transport in a small river. Environ Model Softw 24:1139–1152. https://doi.org/10.1016/j.envsoft.2009.03.008

Barnett AG (1983) Exact and approximate solutions of the advection-dispersion equation. In: Proceedings of the 20th IAHR Congress, Moscow, vol 3, pp 180–190

Bennett ND et al (2013) Characterising performance of environmental models. Environ Model Softw 40:1–20. https://doi.org/10.1016/j.envsoft.2012.09.011

Billo EJ (2007) Excel for scientists and engineers: numerical methods. Wiley, Hoboken

Chanson H (2004) Enviromental hydraulics for open channel flows. Elsevier, Oxford

Chapra SC (2008) Surface water-quality modeling. Waveland Press, Long Grove

Chapra SC, Canale RP (2015) Numerical methods for engineers. McGraw-Hill Education, New York

Chin DA (2013) Water-quality engineering in natural systems: fate and transport processes in the water environment. Wiley, Hoboken

Ferziger JH, Peric M (2002) Computational methods for fluid dynamics. Springer, Berlin

Fischer HB, List EJ, Koh RCY, Imberger J, Brooks NH (1979) Mixing in inland and coastal waters. Academic Press, San Diego

Fürst J, Furmánek P (2011) An implicit MacCormack scheme for unsteady flow calculations. Comput Fluids 46:231–236. https://doi.org/10.1016/j.compfluid.2010.09.036

Fylstra D, Lasdon L, Watson J, Allan W (1998) Design and use of the Microsoft Excel solver. Interfaces 28:9–55

Graf WH, Altinakar MS (1998) Fluvial hydraulics: flow and transport processes in channels of simple geometry. Wiley, Chichester

Hayase T, Humphrey JAC, Greif R (1992) A consistently formulated QUICK scheme for fast and stable convergence using finite-volume iterative calculation procedures. J Comput Phys 98:108–118

Hoffman JD (2001) Numerical methods for engineers and scientists. Marcel Dekker, New York

Karahan H (2006) Implicit finite difference techniques for the advection–diffusion equation using spreadsheets. Adv Eng Softw 37:601–608

Karahan H (2007) Unconditional stable explicit finite difference technique for the advection–diffusion equation using spreadsheets. Adv Eng Softw 38:80–86. https://doi.org/10.1016/j.advengsoft.2006.08.001

Karahan H (2008) Solution of weighted finite difference techniques with the advection–diffusion equation using spreadsheets. Comput Appl Eng Educ 16:147–156. https://doi.org/10.1002/cae.20140

Kumar A, Jaiswal DK, Kumar N (2009) Analytical solutions of one-dimensional advection–diffusion equation with variable coefficients in a finite domain. J Earth Syst Sci 118:539–549

Lasdon LS, Waren AD, Jain A, Ratner N (1978) Design and testing of a generalized reduced gradient code for nonlinear programming. ACM Trans Math Softw 4:34–50

Leonard BP (1979) A stable and accurate convective modelling procedure based on quadratic upstream interpolation. Comput Methods Appl Mech Eng 19:59–98. https://doi.org/10.1016/0045-7825(79)90034-3

MacCormack RW (1982) A numerical method for solving the equations of compressible viscous flow. AIAA J 20:1275–1281

Manson JR, Wallis SG (1995) An accurate numerical algorithm for advective transport. Commun Numer Methods Eng 11:1039–1045

Manson JR, Wallis SG, Hope D (2001) A conservative semi-Lagrangian transport model for rivers with transient storage zones. Water Resour Res 37:3321–3329. https://doi.org/10.1029/2001WR000230

Martin JL, McCutcheon SC (1999) Hydrodynamics and transport for water quality modeling. CRC Press, Boca Rotan

Ogata A, Banks RB (1961) A solution of the differential equation of longitudinal dispersion in porous media. Geological Survey Professional Paper 411-A, US Department of Interior, Washington, USA

Runkel RL, Broshears RE (1991) One-dimensional transport with inflow and storage (OTIS): a solute transport model for small streams. CADSWES, Department of Civil, Environmental and Architectural Engineering, University of Colorado, Boulder

Rutherford JC (1994) River mixing. Wiley, Chichester

Semuwemba J (2011) Modelling tracer breakthrough curves to determine stream reaeration and hydrodynamic properties. Ph.D. thesis, Queens University Belfast, UK

Singh SK, Beck MB (2003) Dispersion coefficient of streams from tracer experiment data. J Environ Eng ASCE 129:539–546. https://doi.org/10.1061/(ASCE)0733-9372(2003)129:6(539)

Sobey RJ (1984) Numerical alternatives in transient stream response. J Hydraul Eng ASCE 110:749–772

Szymkiewicz R (2010) Numerical modelling in open channel hydraulics. Water science and technology library, vol 83. Springer, Berlin

Taylor GI (1954) The dispersion of matter in turbulent flow through a pipe. Proc R Soc Lond A223:446–468

USEPA (2009) Guidance on the development, evaluation and application of environmental models. NSCEP, Cincinnati

Vaghela CR, Vaghela AR (2014) Synthetic flow generation. Int J Eng Res Appl 4:66–71

van den Bos A (2007) Parameter estimation for scientists and engineers. Wiley, Hoboken. https://doi.org/10.1002/9780470173862

Versteeg HK, Malalasekera W (2007) An introduction to computational fluid dynamics: the finite volume method. Pearson Education Ltd, Harlow

Wallis SG (2007) The numerical solution of the advection–dispersion equation: a review of some basic principles. Acta Geophys 55:85–94. https://doi.org/10.2478/s11600-006-0044-5

Wallis SG, Manson JR (1997) Accurate numerical simulation of advection using large time steps. Int J Numer Methods Fluids 24:127–139

Wallis SG, Manson JR (2004) Methods for predicting dispersion coefficients in rivers. Water Manag ICE 157:131–141. https://doi.org/10.1680/wama.2004.157.3.131

Wallis SG, Manson JR, Filippi L (1998) A conservative semi-Lagrangian algorithm for one-dimensional advection–diffusion. Commun Numer Methods Eng 14:671–679

Wallis SG, Osuch M, Manson JR, Romanowicz R, Demars BOL (2013) On the estimation of solute transport parameters for rivers. In: Rowiński P (ed) Experimental and computational solutions of hydraulic problems. Springer, Berlin, pp 415–425. https://doi.org/10.1007/978-3-642-30209-1_30